THE RELATIONSHIP BETWEEN FLUIDS AND STRUCTURE AT THE PATCHWAY GOLD MINE, ZIMBABWE

by

Richard Jeremy Herrington BSc. ARSM

A thesis submitted for the degree of Doctor of Philosophy
of the University of London

Department of Geology
Royal School of Mines
Imperial College of Science,
Technology and Medicine
London SW7 2BP

September 1991

Errata

p17 para 3 line 2 for "Foster 1986" insert "Foster 1985"

p22 line 16 for "examination" insert "examination of"

p25 2nd para. for "youngest" insert "oldest"

p31 3rd para. for "remarkeably" insert "remarkably"

p36 line 1 delete first "lead"

p36 line 15 delete "in"

p36 at the end of line 17 insert of

p37 last line for "Ba" insert "Ga"

p47 2nd para. final line for "link" insert "links"

p49 line 3 for "is" insert "are"

p56 after "data from other geothermal fields" insert (Henley 1984)

p66 Figure caption 3.14c ends "the vein", insert "the vein results in faulting of the dyke and rotation of faulted segments"

p76 Figure caption last line for "measures" insert "measured"

p83 3rd para last line should read "nature of the veining with introduction of SiO_2"

p85 Figure 3.24 upper figure is 3.24b and lower figure is 3.24a

p86 line 6 omit "with the"

p86 2nd para line 3 replace "to" with "of"

p87 3rd para last line replace "may" with "is"

p89 4th para line 5 "dominantly"

p89 4th para line 3 replace "are" with "is"

p121 2nd para first line add "to" at the end

p125 2nd para line 6 "Pitfield & Campbell 1990"

p125 2nd para line 7 "complement"

p143 Figure caption 5.15 line 5 "vein"

p147 4th para line 6 "extensional"

p173 3rd para "NE-SW directed compression" should read "NNE-SSW directed compression"

p173 3rd para line 6 delete "is"

p174 Figure caption 5.44 no.1 "roughly N-S compression" should read "NNE-SSW compression"

p176 Figure caption 5.45 no.1 "roughly N-S compression" should read "NNE-SSW compression"

p178 3rd para. "ENE to WSW direction" should read "NE to SW direction"

p186 line 4 for "are" insert "is"

p186 2nd para line 1 for "there" insert "the"

p187 Table 6.4 (upper) n.b. grains from 20-14 are free grains and those from 18-1 and 10-29 are associated with pyrite and pyrrhotite (see p391). Only grains from 18-1 and 10-29 are suitable for use in geobarometry projection, although a further caveat is that the presence of hexagonal pyrrhotite was not proven. It is therefore suggested that any conclusions are tentative. Pressure estimates from these analyses suggest pressures much lower than 2.5 kbars (not as suggested on p199).

p199 3rd para. line 3 for "are" insert "is"

p202 3rd para "remobilisation"

p210 2nd para line 10 delete "is"

p212 4th para. use of the term "pseudo-secondary" is misleading here and all inclusions are considered "primary" consistent with Figure 7.1 (p214)

p220 2nd para line 9 delete "was"

p239 the final sentence "The plot of ..... homogenisation temperatures" should be omitted.

p241 the first sentence "The T_{mCO2} ..... inclusion population" should be omitted.

p252 note that the bulk volatile analyses involve thermally decrepitating the sample at 600°C and it was pointed out that any calcite present as solid inclusions in the quartz may lead to enhanced CO_2 levels

p252 para 4 line 3 delete "To date"

p254 note that the volatile analyses are in fact expressed as mole%

p256 para 2 line 3 "reproducibility"

p256 para 4 line 7 "Comparative"

p266 para 2 line 13 "Fouillac & Michard (1981)"

p270 Table 7.16 caption for "see Table 7.16" insert "see Table 7.15"

p272 line 2 "assemblage"

p274 Figure caption 7.29 line 2 for "B:Na" insert "Na:B"

p276 line 1 delete "an"

p276 3rd para last line after "error" insert "can"

p281 line 7 after "invoked" insert "to"

p296 3rd para line 4 "comparative"

p300 last para line 4 "equilibrate"

p300 last para lines 6 and 8 "8-10" should read "8-9"

p307 line 7 delete one "the"

p319 para 3 line 3 for "heavier" insert "heavy"

p321 para 4 lasr line "Reproducibility"

p324 line 4 at end of line insert "be"

p326 line 2 for "2 to 3%" insert "2 to 3‰"

p326 para 4 line 4 "reproducibility"

p330 para 5 line 1 for "helps" insert "help"

p333 2nd para line 13 for "proposes" insert "propose"

p333 3rd para. line 3 for "volumatic" insert "volumetric"

p343 3rd para line 4 for "HS°" insert "AuHS°"

ABSTRACT

Patchway mine is a lode gold deposit hosted in sheared ca.2700 Ma, Fe-rich, tholeiitic lavas in the Midlands greenstone belt of Zimbabwe. Gold veins occurs as a complex array linked to the regional Lily Fault zone, initiated under NW-SE directed transpression, in response to shortening in the ca. 2700 Ma Limpopo Mobile Belt in southern Zimbabwe. Early regional folding gave way to deformation and mineralisation focussed along narrow shear-zones which, in the Patchway region, are dominated by 020/30W and 070/60NW trending structures. The former structures host the most productive quartz veins in the Patchway region and show classic ribbon texture. Mineralogy is dominated by quartz with minor sulphides and gold. Towards the culmination of this transpression, large diapiric tonalite bodies (ca. 2690 Ma) were intruded, post dating mineralisation on the main shear structures. Later deformation is related to E-W extension, expressed as normal faulting and intrusion of mafic dykes.

Early, locally derived aqueous (4.5 wt% NaCl) metamorphic fluids ($\delta^{18}O = +6$) were mobilised during folding and regional metamorphism. During focussed shearing, an exotic carbonic fluid (3.5 wt% NaCl) containing around 15 mole% CO_2-CH_4 ($\delta^{18}O = +4$), formed the gold-bearing ribbon quartz veins. This fluid was buffered by the vein-margin wallrock assemblage of largely chlorite, K-rich white mica and carbonate, and had a pH of 5.5 and a calculated log fO_2 of -30. The ribbon veins formed in response to cyclic stick-slip failure, where catastrophic pressure drop caused fluid unmixing and precipitation of the main mineral phases. Gold, probably carried as the $AuHS^o$ complex, destabilised during unmixing and resultant partial oxidation. Silica may have initially precipitated in an amorphous form. Later deformation and waning mineralisation culminated in intrusion of the large tonalite diapirs, formed through granulitisation of the lower crust which also produced the gold-bearing fluid. Late quartz-tourmaline veining formed from a moderate salinity (14 wt% NaCl) fluid ($\delta^{18}O \approx +2$) and existing mineralisation was locally remobilised.

Acknowledgements

Many people have contributed to the success of the research project but I must firstly thank my two "official" supervisors, Prof. Dennis Buchanan and Prof. Andy Rankin. I particularly thank Andy for kindling my spark of research interest whilst I was still in the world of industry. To Dennis I owe thanks for the chance to see one of Africa's most impressive countries, both through the eyes of a geologist and those, albeit too briefly, of a tourist.

Very big thanks must go to the many persons in Zimbabwe who helped the project; Prof. Keith Viewing and the staff of the Institute of Mining Research in Harare who helped with permits, advice, sample preparation and the loan of a precious vehicle! I thank all the staff at Patchway Mine who made my stay so highly productive and enjoyable. Particular thanks go to Trevor and Leigh who were so hospitable to their foreign houseguest(s) and to the late Bart Kuipers who was so indulgent towards a research geologist at the mine. Thanks Isaac for not getting me lost underground and introducing me to some of the more interesting parts of the mine. A special thanks to the many members of the Patchway Club (Daffy, John, Mike, Harold to name but a few) who were such good company. I am greatly endebted to Rob Teesdale of Golden Valley Mine who permitted me free access underground there and likewise to the operators of Hamburg Mine for similar access. Many thanks to the management of Rio Tinto Zimbabwe (particularly Ant Marsh) for logistical help and shipping of my samples.

I must thank Prof. Stan White for his brief field visit and longer periods of discussion of structural geology. I must also thank the technical staff at Imperial for their help, particularly Liz and Gill for the exotic fluid inclusion wafer demands. Thanks to Peter Watkins (whole-rock ICP), Rich Giddens for his help on the SEM and to Alan Jones for showing me how to prepare thin sections by hand (a dubious pleasure) and encouraging my golf! (a veritable pleasure). Thanks to Barry and Mike for the ICP analyses of inclusion fluids, wish you could have helped with the grain picking! "Tracer Tone" gets a special mention for his indulgent permission to use Adobe Illustrator and his untiring effort as Geology cricket captain.

At the old London BGS-NIGL lab I must thank Peter Greenwood, Baruch Spiro and Tom Shepherd for the stable isotope and bulk volatile analyses and help with their interpretation. I specially thank "Gentleman" Jim Coppard for his help with the gas analyses and XRF data.

I owe much to my comrades in arms, my fellow post-grads, particularly Chris, Frazer, Mike A., Mike J., Mick and Claudio for the intense discussion over various types of beverage (with and without "bubbles"). Latterly many thanks must go to Jamie who has foolishly kept the flame of research burning in me and given me much food for thought.

Financial support during the project was provided through an RTZ bursary and the work would not have been possible without this. Generous financial help to travel to the 8th IAGOD conference in Ottawa was provded by the Robinson-Oldfield travel fund and I thank the trustees for their support.

Finally and fundamentally my special thanks go to you Den for your unfailing support. Without you this would never have happened, or indeed been possible. I dedicate the thesis to you and our wonderful new son, Tom.

TABLE OF CONTENTS

Page

CHAPTER ONE - INTRODUCTION

1.1 Background 17

1.2 Location 20

1.3 Mine History 20

1.4 Project Objectives 21

1.5 Layout of Thesis 23

CHAPTER TWO - REGIONAL STRATIGRAPHY AND METALLOGENESIS OF THE ZIMBABWEAN CRATON

2.1 Greenstone Terrains of the Zimbabwean Craton 25

2.2 Granitic Terrains of the Zimbabwean Craton 28

2.3 Archaean Gold Mineralisation 29

2.3.1 Introduction 29

2.3.2 Gold Mineralisation in the Zimbabwean Craton 31

2.4 Structural Framework of the Zimbabwean Craton 32

2.5 Geology of the Kadoma Region 37

2.6 Description of the Gold-Bearing Structures in the Kadoma Region 40

2.7 Summary 46

CHAPTER THREE - PETROLOGY AND MINERAL CHEMISTRY

3.1 Introduction 47

3.2 Methodology 47

3.3 Mine Host Rock Petrography 49

3.3.1 Mafic Flow Rocks 48

3.3.2 Intrusive "Felsites" 60

3.3.3 Regional Tonalite Intrusives 64

3.3.4 Mafic Dykes 64

3.4 Whole Rock Geochemistry 67

3.4.1 Introduction 67

3.4.2 Previous Work 67

3.4.3 Mafic Lavas 68

3.4.4 Mine Felsite and Regional Tonalite Intrusives 75

3.4.5 Mafic Dykes 77

3.5 Chemistry of Deformed Vein Host Rocks 77

3.5.1 Mass Balance Calculations 77

3.6 Conclusions 89

Page

CHAPTER FOUR - DEFORMATION FLUIDS AND MESOTHERMAL QUARTZ VEINS

4.1 Introduction 91
4.2 Fluids and Deformation 91
4.3 Deformation Models 93
4.4 Fault Rocks 98
4.5 Crustal Scale Fault Structures 101
4.6 Fluids in Crustal Scale Shear Zones 103
4.7 Shear Zone Hosted Ribbon Quartz-Gold Veins 105
4.8 Type Examples of Shear Vein Systems 111
4.9 Detailed Study of Patchway Ribbon Veins 114
4.10 Behaviour of Transported Fluid Soluble Species in Shear Vein Systems 119

CHAPTER FIVE - STRUCTURAL EVOLUTION OF THE PATCHWAY REGION

5.1 Introduction 125
5.2 Structural Framework of the Kadoma Region 126
5.2.1 Aeromagnetic Data 126
5.2.2 Air Photographs 126
5.2.3 Gravity Profile 129
5.2.4 Integration with Geology 129
5.3 Synthesis of Observed Key Regional Structural Elements 133
5.4 Analysis of Deposit Scale Structure 134
5.4.1 Deposit Structural Evolution 134
5.5 Deformation Model for the Kadoma Region with Reference to Regional Events 173

CHAPTER SIX - MINERALISATION

6.1 Introduction 180
6.2 Mineralisation Predating Gold-Bearing Veins 180
6.3 Gold-Bearing (D2) Mineralisation 180
6.3.1 Gangue Mineralogy 180
6.3.2 Gold and Sulphide Mineralogy 181
6.3.3 Detailed Electron Microprobe Study of Sulphides 190
6.3.4 Discussion 193
6.4 Later Mineralisation 202
6.5 Summary 206

Page

CHAPTER SEVEN - FLUID INCLUSION STUDIES

7.1 Introduction 208
7.2 Previous Work 208
7.3 Methodology 210
7.4 Optical Characterisation of Inclusion Types 212
7.5 Microthermometric Study 229
7.5.1 Microthermometry Results 235
7.5.2 Discussion of Microthermometry Results 244
7.6 Bulk Volatile Analysis of Fluid Inclusions 252
7.6.1 Bulk Volatile Analysis Results 252
7.6.2 Discussion of Bulk Volatile Analysis Results 253
7.7 Fluid Inclusion Bulk Analysis by ICP-AES 255
7.7.1 Comparison of ICP Techniques 256
7.7.2 D-ICP Fluid Chemistry Results 263
7.7.3 Discussion of D-ICP Results 269
7.8 Calculated Trapping Temperatures and Pressures 275
7.8.1 Fluid Inclusions as P-T Indicators 275
7.8.2 Calculated Conditions of Trapping 276
7.9 Detailed Study of D2 Ribbon Quartz Veins 288
7.9.1 Microthermometry and Volatile Analysis Results 288
7.9.2 Discussion 292
7.10 Summary of Fluid Characteristics of the Evolving Mineralised System 294

CHAPTER EIGHT - HYDROTHERMAL FLUID MODELLING

8.1 Introduction 296
8.2 (D2) Gold-Bearing Fluid Cation Activities and pH 296
8.3 (D2) Fluid C-O-H-S Species Activities 298
8.3.1 Oxygen Fugacity 300
8.3.2 Sulphur Species Fugacities 305
8.4 Stable Isotope Study 310
8.4.1 Introduction 310
8.4.2 Experimental Methods 310
8.4.3 Oxygen Isotope Study 311
8.4.4 Carbon Isotope Study 319
8.4.5 Sulphur Isotope Study 324
8.5 Discussion 329

Page

CHAPTER NINE - DEPOSIT MODEL

9.1 Introduction 332
9.2 Timing of Gold Mineralisation 332
9.3 Detailed Mechanical Controls to Mineralisation 333
9.4 Nature of the Gold-Bearing Hydrothermal Fluid 336
9.5 Fluid Source 336
9.6 Gold Transport and Deposition 341
9.7 Fluid Evolution During Regional Deformation 349
9.8 Exploration Significance 351
9.9 Suggestions for Future Research 353

REFERENCES 355

APPENDIX I - Sample Locations 379

APPENDIX II - Electron Microscopy and Microprobe Analysis 384

APPENDIX III - Whole Rock Analyses 392

APPENDIX IV - Fluid Inclusion Microthermometry 400

APPENDIX V - ICP Analyses of Inclusion Fluids 412

APPENDIX VI - Stable Isotope Analysis 424

INSERT POCKET - Sample Location Plans 426

LIST OF FIGURES AND TABLES

FIGURES		Page
1.1	Location map of Zimbabwe	18
1.2	Locality map Patchway - Golden Valley	19
2.1	Summary geological map of the Zimbabwe Craton	26
2.2	Principal features of the Archaean craton areas of Southern Africa indicating principal gold mines and major structures	30
2.3	Summary of structural elements in the greenstone belts of Zimbabwe	34
2.4	Provisional timetable of deformation events in the Kadoma region with respect to craton scale deformation events in Zimbabwe	35
2.5	Simplified geology of the Patchway - Golden Valley area	39
2.6	Mineralised structures in the Patchway region	41
2.7	Patchway - Golden Valley mining plan	42
2.8	Cross section drawn along 10 level to 9 level raise	43
2.9	Typical ribboned quartz veining on 10 level south, Patchway mine	44
3.1	Diagram showing links between deformation, alteration and possible driving processes	48
3.2	Pillow lavas on 10 level south	50
3.3	Pyrite cubes developed in deformed mafic lava marginal to gold-quartz vein on 10 level north	51
3.4	Highly pyritic wallrock mined adjacent to the gold-quartz mineralisation studied in detail on 6 level north	51
3.5	High constrast backscattered SEM image of iron bearing phases in sulphidised wallrock (Sample 30-2)	52
3.6	Well deformed mafic lava into the hanging wall of the gold quartz vein on 22 level	54
3.7	Deformed lava on 22 level	54
3.8	Highly deformed wallrock hosting thin quartz sulphide segregations	55
3.9	Carbonate rich unmineralised shear zone 15 level north	55
3.10	Plot of Fe^{2+}/total $^{2+}$ ions versus Al (IV) ions for chlorite probe analyses	58
3.11	Photographs showing variable age relationships of felsite intrusive bodies underground at Patchway	63
3.12	Hand specimen of Whitewaters tonalite body (sample LH7)	65
3.13	Photomicrograph of thin section cut from LH7	65
3.14	Photographs of field relationships of mafic dykes underground at Patchway	66
3.15	AFM diagram plotted for Patchway mafic lavas	71

FIGURES (cont.) Page

3.16 SiO_2 versus Zr/TiO_2 discrimination plot for mafic volcanic rocks at Patchway 72

3.17 Alkali plot for determination of Na-K metasomatism of mafic volcanic rocks at Patchway 73

3.18 Geochemical sample traverses on 5 and 15 level Patchway mine 74

3.19 Lithogeochemical profiles for Na_2O/Al_2O_3 and K_2O/Al_2O_3 for sample traverses on 5 and 15 level Patchway mine 76

3.20 Nb, Y, Rb and SiO_2 discriminant diagrams for granitic rocks plotted for Patchway felsic intrusive rocks 78

3.21 Ti-Zr discriminant diagram plotted for Patchway mafic lavas and mafic dykes 79

3.22 "Isocon" plots for deformed mafic lavas at Patchway 81

3.23 *Plot of Ba versus K_2O for deformed mafic lavas at Patchway* 84

3.24 "Isocon" plots for deformed veined mafic lavas at Patchway 85

3.25 "Isocon" plots for deformed felsite intrusives at Patchway 88

4.1 Diagram indicating the effect of fluid pressure on the Mohr stress circle 92

4.2 Diagram showing relationship between hydrostatic and lithostatic pressure in the crust 94

4.3 Model for fluid ascent in the crust proposed by Gold & Soter (1985) 95

4.4 Schematic diagram indicating deformation regimes likely as a function of depth 97

4.5 Mohr's construction for failure of intact rock on a failure surface 99

4.6 Diagrams to show three modes of brittle failure for intact rock 100

4.7 Model fault plane with resolved forces defined 102

4.8 Diagram of Riedel geometry developed around dextral sense central failure plane 102

4.9 Close up photograph of ribbon gold-quartz vein at Patchway 106

4.10 Stylolitic texture in ribbon quartz veins 107

4.11 Common shear zone vein geometries 106

4.12 Mechanically induced dilatancy in shear veins 110

4.13 Mesothermal gold veins of Grass Valley, California 112

4.14 Mesothermal gold veins of Sigma Mine, Quebec 113

4.15 Typical ribbon vein textures at Patchway and Golden Valley mines 115

4.16 Ribbon vein profiles studied in detail at Patchway mine 116

4.17 Visible gold in ribbon quartz veins 117

4.18 Proposed cyclic model of failure for the formation of ribbon quartz veins 118

4.19 Effect of temperature and pressure on silica species solubility 120

FIGURES (cont.)		Page
4.20	Effect of dissolved NaCl and pH on quartz solubility	122
4.21	Temperature composition diagrams in the systems H_2O-CO_2-NaCl, H_2O-CO_2 and H_20-CH_4 at variable temperature and pressure	124
5.1	Interpreted 1:500,000 aeromagnetic map of Zimbabwe	127
5.2	Air photograph interpretation of the Patchway - Golden Valley region	128
5.3	Gravity profile across Lion Hill	130
5.4	Possible interpretation of gravity profile, Lion Hill	131
5.5	Structural compilation of elements in the Kadoma to Kwekwe region	132
5.6	Schematic diagram of a typical brittle-ductile shear zone summarising features and kinematic indicators present in the shear zones examined in the Patchway region	135
5.7	Photograph of Basil vein	137
5.8	Stereonet plot of poles to D2 ribbon quartz veins from Patchway, Golden Valley, Basil and Hamburg mines	138
5.9	Stereonet plot of poles to S2 shear fabric from Patchway and Golden Valley	139
5.10	Minor structure in main vein hanging wall 10 level indicating reverse shear sense	140
5.11	Domino veining in hanging wall 10 level of main vein structure	140
5.12	Extension veining and shear folding related to D2 deformation	141
5.13	Stereonet plot of intercepts of D2 ribbon vein and D2 extension veining	142
5.14	Thin section photomicrographs of deformed wallrocks	143
5.15	Thin section photomicrograph of recrystallising vein quartz	145
5.16	Thin section photomicrograph of quartz-veined deformed felsite	145
5.17	Thin section photomicrograph of deformed felsite	145
5.18	Location plan of the Patchway mine showing location of detailed maps	146
5.19	Stereonet plot of S3 shear fabric from Patchway and Erin mines	148
5.20	Structural detail of mineralisation on 10 level north	149
5.21	Stereonet plot of vein boudinage and minor fold axes plunges related to D3 deformation	150
5.22	Structural detail of mineralisation on 10 level north	151
5.23	Structural detail of mineralisation on 28 level north	152
5.24	Structural detail of mineralisation on 4 level north	153
5.25	Structural detail of mineralisation on 9 level north	154
5.26	Extension veining and boudinage related to D3 deformation	156
5.27	Deformed rocks in the Erin mine shear zone on 90 fathom level	157
5.28	Folded foliation (intrafolial fold) in the Erin shear zone, 90 fathom level	157

FIGURES (cont.) Page

5.29 Structural detail of mineralisation on 90 fathom level at Erin mine 158
5.30 Minor folding in the Erin shear zone 159
5.31 Stereonet plot of D3 gold-sulphide veins and S3 shear fabric 160
5.32 Distinctive alteration marginal to Kabanga mineralisation seen on 4 level north 161
5.33 Kabanga vein exposed on 4 level north 161
5.34 Cross-veining exposed on 4 level north 161
5.35 Stereonet plot of D2, S2 and S3 fabric 163
5.36 Diagram showing the possible linked initiation of D2 and D3 structures 164
5.37 Summary plan showing key mineralised structures related to A: D2 and B: D3 structures at Patchway 165
5.38 Section drawn through the level 18 to 15 raise on the south orebody 167
5.39 Ribbon vein exposed in the 18 to 15 level raise looking south 168
5.40 Late normal faulting of mineralisation 169
5.41 Stereonet plot of D4 features at Patchway 170
5.42 Late deformation to mineralisation on 5 level north 171
5.43 Stereonet plot of tonalite hosted quartz scheelite veins at Lion Hill 172
5.44 Summary of deformation events at Patchway with respect to mineralisation events 174
5.45 Provisional timetable of deformation events in the Kadoma region with respect to deposit scale deformation events 176
5.46 Block diagram showing initiation of the Patchway and associated mineralised structures under transpression 177

6.1 Scheelite rich (D2) ribbon quartz vein at Golden Valley mine 182
6.2 Photomicrograph of scheelite and pyrite in (D2) ribbon quartz veining 182
6.3 Backscattered SEM photomicrograph of sulphides, quartz and phyllosilicates 184
6.4 Photomicrographs indicating the association of gold in the (D2) ribbon quartz veins at Patchway mine 185
6.5 Backscattered SEM photomicrograph of pyrite, sphene and rutile in sulphidised wallrock, Patchway mine 187
6.6 Photomicrograph of pyrite grain enclosing ilmenite 188
6.7 Photomicrograph of pyrite grain enclosing pyrrhotite 188
6.8 Photomicrograph of pyrite grain, showing evidence of complex internal growth banding 188
6.9 Backscattered SEM image of pyrite grain enclosing other sulphide grains 188
6.10 High contrast backscattered SEM image of pyrite grain (Sample 18-1) 191
6.11 High contrast backscattered SEM image of pyrite grain (Sample 18-1) 192

FIGURES (cont.) Page

6.12 As-Ni WD map of pyrite grain (Sample 6006b) 194
6.13 As-Ni WD map of pyrite grain (Sample 6006b) 195
6.14 As-Ni-Au WD map of pyrite grain (Sample 6006b) 196
6.15 As-Au WD map of pyrite grain (Sample 6008a) 197
6.16 As-A and Ni WD maps of pyrite veins in "barren" portions of vein (6007b) 198
6.17 S_2 activity-temperature projection of the stability field of arsenopyrite 200
6.18 *T-X* projection of the sphalerite, pyrite and hexagonal pyrrhotite solvus isobars 201
6.19 Composition of pyrrhotite in atomic % Fe as a function of aS_2 and temperature 203
6.20 Photograph of late D4 quartz tourmaline vein 204
6.21 Photomicrograph of coarse chalcopyrite segregation in D4 veining 204

7.1 Photomicrographs of quartz stage 1 fluid inclusions 214
7.2 Histograms showing degrees of fill for all fluid inclusion types 215
7.3a Photomicrographs of quartz stage 2 fluid inclusions 217
7.3b Photomicrographs of quartz stage 2 fluid inclusions 218
7.4 SEM cathodoluminescence images of quartz stage 2 219
7.5 Fluid inclusion bearing quartz grains associated with gold and sulphides 221
7.6 Scheelite associated with quartz stage 2 containing primary inclusions 222
7.7 Fluid inclusion detail from gold bearing quartz grain in quartz stage 2 223
7.8 Solid phases present in fluid inclusions in quartz stage 2 224
7.9 Photomicrographs of quartz stage 3 fluid inclusions 226
7.10 Photomicrographs of quartz stage 4 fluid inclusions 227
7.11 Photomicrographs of quartz stage 5 fluid inclusions 228
7.12 Photomicrographs of quartz stage 6 fluid inclusions 230
7.13 Synoptic sketches of all fluid inclusion types 231
7.14 Histograms for microthermometric data from Type 1 inclusions 236
7.15 Histograms for microthermometric data from Type 2B inclusions 236
7.16 Histograms for microthermometric data from Type 2A inclusions 238
7.17 Plots of T_{hCO2} versus T_{mCO2} and T_{mClath} versus T_{mCO2} for Type 2A inclusions 240
7.18 Histograms for microthermometric data from Type 2C and Type 3B inclusions 242
7.19 Histograms for microthermometric data from Type 3a inclusions 243
7.20 Histograms for microthermometric data from Type 4 inclusions 245
7.21 Histograms for microthermometric data from Type 5 inclusions 246

FIGURES (cont.) Page

7.22 Histograms for microthermometric data from Type 6 inclusions 247
7.23 Graph showing temperature of depression of ice melt caused by various alkali salts 247
7.24 Histograms for combined microthermometric data from Type 2C and Type 4 inclusions 249
7.25 Comparison of Na:Ca:K ratios for Q2 and Q4 quartz inclusion fluids determined by different ICP methods 258
7.26 Comparison of Na:K and Na:Li ratios for Q2 quartz inclusion fluids 261
7.27 Comparison of Na:K and Na:Li ratios for Q4 quartz inclusion fluids determined by D-ICP and CL-ICP methods 262
7.28 Graph showing derived temperatures for different empirical Na:K fluid geothermometers 268
7.29 Graphs showing derived Na:B, Na:Cu, Na:Fe, Na:Ba and Na:Zn ratios for inclusion fluids determined by D-ICP 274
7.30 Fluid isochore constructed for conditions during Q1 quartz formation 278
7.31 Average fluid isochore constructed for conditions during Q2 quartz formation 280
7.32 T-X diagram constructed for solvi of H_2O-CO_2-3wt% NaCl fluid at 350°C and 2000 bars pressure 282
7.33 Fluid isochore constructed for conditions during Q3 quartz formation 283
7.34 Fluid isochore constructed for conditions during Q4 quartz (and Type 2C inclusion) formation 285
7.35 Fluid isochore constructed for conditions during Q5 quartz formation 286
7.36 Fluid isochore constructed for conditions during Q6 quartz formation 287
7.37 Sketch showing location of detailed fluid inclusion samples from gold quartz veins on 6 and 10 level 289
7.38 Plot of T_{mClath} versus T_{mCO2} of inclusions measured from 6 level pillar 290
7.39 Plot of depression of T_{mCO2} measured in inclusions, versus molar ratio CH_4:CO_2 measured by bulk volatile gas analysis 291
7.40 Plot of T_{mClath} versus T_{mCO2} of inclusions measured from 10 level pillar 293

8.1 Expanded Debye-Hückel equation for simple ionic solutions 297
8.2 Stability diagram for Na-K-silicate minerals as a function of Na and K ionic activity at 350° C and 2.5 Kbars 299
8.3 Graphic representation of fO_2 values calculated from inclusion volatile analyses 306
8.4 Log aS_2 temperature plot for major species in the Cu-Fe-S system 309

FIGURES (cont.) Page

8.5 Plot of $\delta^{18}O$ quartz versus Na:K alkali geothermometer for fluid inclusion fluids calculated from D-ICP analysis 314

8.6 Replot of $\delta^{18}O$ versus calculated Na:K alkali geothermometer for Q2 samples only 316

8.7 Graphic representation of $\delta^{18}O$ quartz values for Q2 ribbon vein quartz from the Patchway mine 317

8.8 Graph showing calcite-dolomite-magnetite-CO_2 fractionation factors versus temperature 322

8.9 Plot of $\delta^{13}C$ calcite versus distance from the Q2 ribbon quartz vein on 15 level 323

8.10 Graph showing positions of $\delta^{13}C$ contours fluid versus calcite as a function of fO_2 and pH 325

8.11 Graph showing positions of $\delta^{34}S$ contours H_2S versus fluid as a function of fO_2 and pH 327

9.1 Summary sketch of effects of D3 and D4 deformation on the D2 ribbon quartz vein at Patchway 335

9.2 Fugacity buffers plotted at 2.5 Kbars from 300° to 800° C 337

9.3 Graph showing relative gold solubility with respect to pH at various temperatures for gold-sulphur complexes commonly present in hydrothermal systems 344

9.4 Figure showing the variation in gas:liquid partition coefficients in water for major miscible gas species present in hydrothermal systems 346

9.5 Synoptic model for vein formation and gold-sulphide precipitation at Patchway during D2 deformation 348

9.6 Summary of the key regional structural elements in the northwest Kadoma region 352

TABLES		Page
2.1	Upper Bulawayan stratigraphy	38
3.1	EPMA analyses of chlorite	57
3.2	Calculated mineral geothermometry from chlorite	57
3.3	EPMA analyses of sericite	59
3.4	EPMA analyses of pyrophyllite	61
3.5	EPMA analyses of carbonate	61
3.6	EPMA analyses of epidote	62
3.7	EPMA analyses of sphene	62
3.8	EPMA analyses of albite	62
3.9	Whole rock geochemical analyses of mafic lavas	70
3.10	Whole rock chemical analyses of deformed mafic lavas	82
5.1	Summary table of proposed deformation events in the Patchway region	175
6.1	EPMA analyses of scheelite	183
6.2	EPMA analyses of ribbon vein sericite	183
6.3	EPMA analyses of gold grains	187
6.4	EPMA analyses of sphalerite	187
6.5	EPMA analyses of tourmaline	205
7.1	Published fluid inclusion studies for selected Archaean gold deposits	209
7.2	Published fluid inclusion fluid cation determinations for selected Archaean gold deposits	211
7.3	Published volatile analyses for selected Archaean gold deposits	211
7.4	Summary of fluid inclusion types identified in the different vein assemblages	213
7.5	Summary statistics of fluid inclusion types 1, 2B, 3B	232
7.6	Summary microthermometry statistics for inclusion types 2A, 3A, 5	233
7.7	Summary microthermometry statistics for inclusion types 2C, 4, 6	234
7.8	Physical properties of one component fluids likely to be present in hydrothermal systems	249
7.9	Volatile analyses for picked quartz samples	254
7.10	Comparison of cation ratios with respect to Na for comparative ICP analysis techniques	257
7.11	Charge balanced ICP analyses	260
7.12	D-ICP data table	264
7.13	Fluid compositions calculated for fluids from various quartz stages	265
7.14	Fluid geothermometers	267

TABLES (cont.) Page

7.15 Calculated alkali fluid geothermometers for Q1 quartz sample 270
7.16 Calculated alkali fluid geothermometers for Q2 quartz sample 270
7.17 Calculated alkali fluid geothermometers for Q3 quartz sample 271
7.18 Calculated alkali fluid geothermometers for Q4 quartz sample 271
7.19 Calculated alkali fluid geothermometers for Q5 quartz sample 272
7.20 Calculated alkali fluid geothermometers for Q6 quartz sample 272
7.21 Summary of fluid parameters used in isochore construction 277

8.1 Calculated fluid characteristics of aqueous part of the D2 gold bearing hydrothermal fluid 297
8.2 Tabulated thermodynamic constants used in fugacity calculations 303
8.3 Calculated oxygen fugacities generated from the volatile analysis data 304
8.4 Compilation of $\delta^{18}O$ hydrothermal quartz values in Archaean gold deposits 312
8.5 Tabulated $\delta^{18}O$ quartz values for Patchway samples analysed 313
8.6 Compiliation of $\delta^{13}C$ hydrothermal carbonate values in Archaean gold deposits 320
8.7 Carbon isotope determinations from calcite in samples peripheral to (D2) ribbon quartz veins 323
8.8 Sulphur isotope determinations from pyrite for Patchway samples 328

9.1 Summary table of D2, gold bearing hydrothermal fluid characteristics 338
9.2 Equilibrium constants for the formation of aqueous Au(I) complexes at 25° C 342
9.3 Summary of characteristics of the hydrothermal fluid during the deformation 350

CHAPTER ONE - INTRODUCTION

1.1 Background

To date studies of the geological controls of gold mineralisation hosted within shear-zones of the Archaean are largely confined to the major greenstone belts of the Canadian Shield and the Australian Yilgarn Block (e.g. Colvine *et al.* 1984, 1988, Groves *et al.* 1987). Relatively few studies of Zimbabwean Archaean gold deposits have been carried out, despite the Zimbabwean greenstones representing the most gold productive belts, with gold production at over 42kg of gold per km^2 of greenstone stratigraphy (Foster 1985). In addition, few studies anywhere have examined the role and detailed behaviour of the evolving hydrothermal fluids active during deformation and mineralisation. The excellent exposure afforded by the many developed mines, together with the good standard of basic geological mapping performed by the government geological survey, makes Zimbabwe an ideal field area for a detailed study of Archaean greenstone gold mineralisation.

Brief visits by Mike Jones of the Mining Geology Research Group of Imperial College to the Dalny and Midwinter deposits in central Zimbabwe, indicated that many of the deposits in the Midlands greenstone belt of Zimbabwe could well be shear-zone hosted with some key kinematic indicator elements present (Jones 1986). The collaborative work of Fraser Tabeart (Tabeart 1988) at Rio Tinto Zimbabwe's Renco deposit indicates the usefulness of detailed structural study in unravelling the mode of formation of gold deposits in structurally complex areas.

The Kadoma region of the Midlands greenstone belt of Zimbabwe (Figure 1.1) has a number of producing gold mines, many of which show classic features of a shear-zone host (Foster 1986, 1989). The good working relationship developed between Imperial College and Rio Tinto Zimbabwe lead to the choice of this region for a collaborative project to study the relationship between structure and the mineralising fluids in the system centred on the Patchway gold deposit.

Patchway Mine is a small, but extensively developed lode gold deposit in the Midlands greenstone belt operated by Rio Tinto Zimbabwe, part of an area of highly mineralised greenstone stratigraphy near Kadoma. Several deposits close to Patchway are also accessible including the major Golden Valley deposit operated by John Mack Ltd. and the small Hamburg deposit, mined by a private small-worker (Figure 1.2). This offered the opportunity to study a classic vein system on a semi-regional scale. Most of the 30 levels, each separated by 100 vertical feet, are still accessible at the Patchway Mine. Furthermore, the mining method of room and pillar extraction has left complete sections of the mineralised structure throughout the deposit.

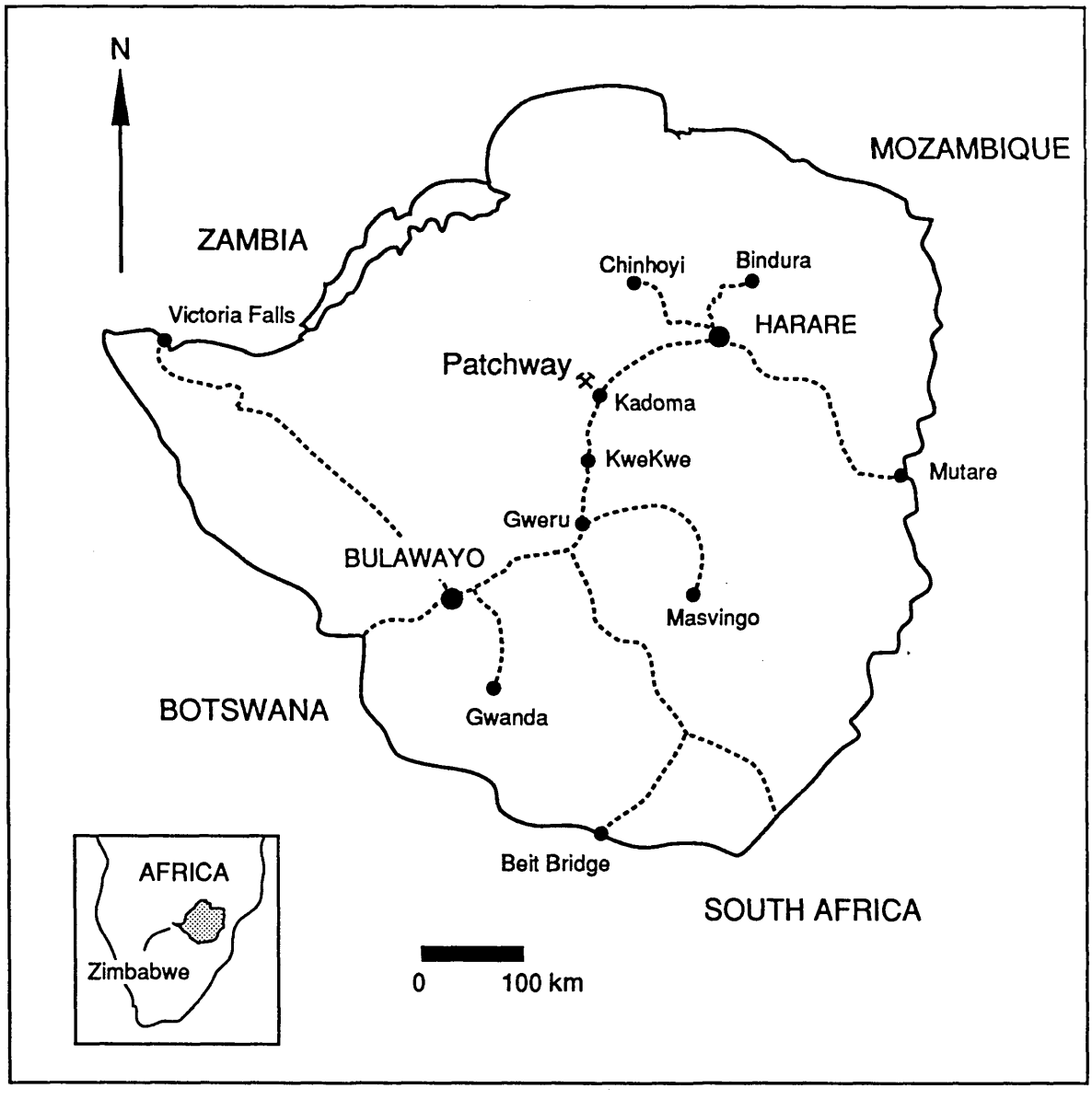


Figure 1.1 - Location map of Zimbabwe indicating major settlements, railways and position of Patchway gold mine.

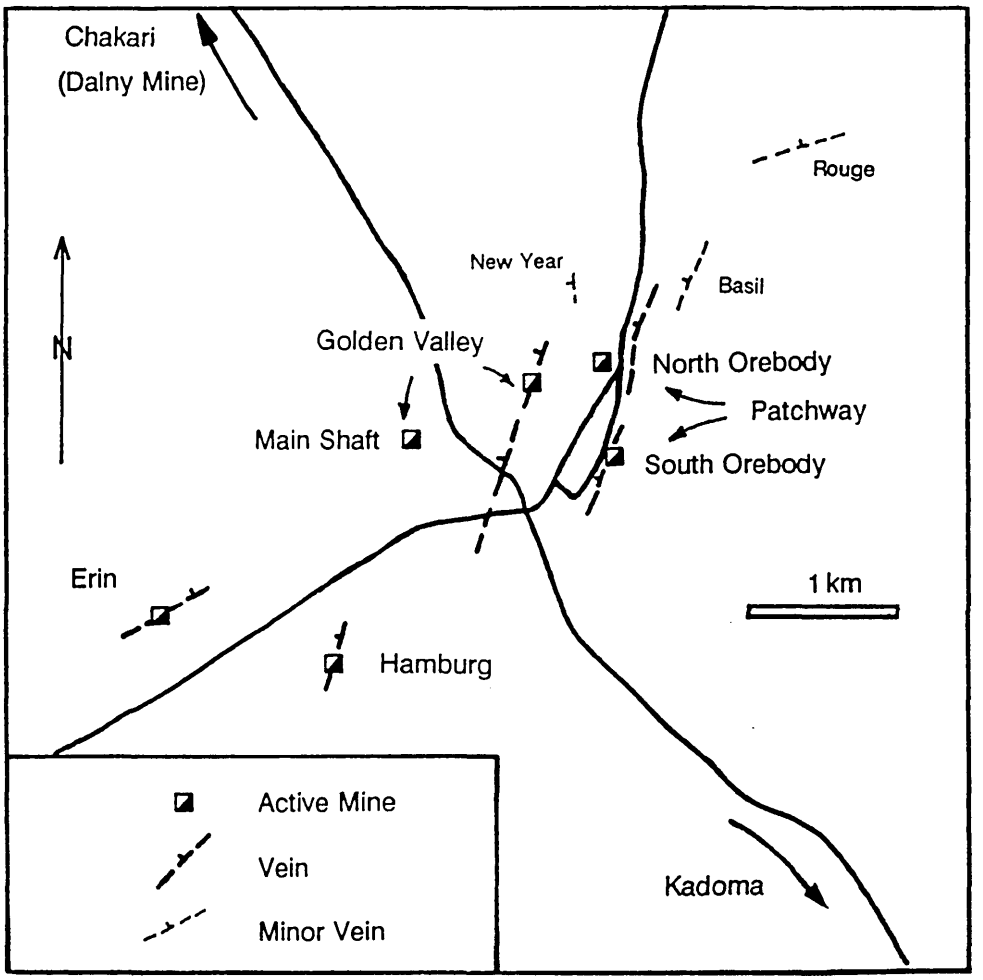


Figure 1.2 - Locality map of the Patchway - Golden Valley region showing the main gold deposits

1.2 Location

Patchway Mine lies some 20km northwest of Kadoma, some 150km southwest of Harare (Figure 1.1). The mine lies close to the settlement of Golden Valley, which forms the centre to the local mining community. Immediately adjacent to Patchway is the larger Golden Valley deposit, and both the Erin and Hamburg deposits lie within a few kilometres to the southwest (Figure 1.2).

The Midlands of Zimbabwe is characterised by flat plains with relatively few topographic features with a mean altitude of 1000 metres above sea level. The climate is Steppe type, with 50 to 80 centimetres of rain annually. Natural vegetation is dominated by scrubby thornbush, gorse and small trees, similar to the high veldt of South Africa, although in the region the land is currently extensively farmed for maize and cotton. Surface exposure is poor, particularly in the greenstone areas, where a distinctive, red, deeply-weathered soil is developed.

1.3 Mine History

The southern part of Patchway Mine (Figure 1.2), known as the south orebody (SOB) was first pegged in 1906. It was worked by a series of small syndicates and companies until 1959 when it was aquired by Rio Tinto Rhodesia (Bliss 1970), later to become Rio Tinto Zimbabwe Ltd. During 1960 exploratory drilling located the zone now known as the north orebody (NOB). The surface expression of the NOB was obscured by a large dolerite dyke, since located by underground development. In 1967 mining was partly suspended underground as a heavily faulted section between 1500 and 1800 feet below surface (15 to 18 levels) was encountered. The small New Year deposit helped supplement ore production during this period. Since then the NOB has been developed extensively down to a current 3000 foot depth (30 level - as at end of February 1990). Mining is largely from a single ribbon quartz vein, which splits in places leading to apparent duplication. The adjacent Golden Valley mine was discovered around the same time as Patchway. Mineralisation is parallel to the main Patchway vein, and mining has similarly focussed on a single, large ribbon quartz vein.

The Erin deposit lies some 2.5km southwest of Patchway. It was discovered in 1960 by Rio Tinto and the zone was investigated in the following years via a small shaft. In 1964 the shaft was deepened to 30 metres and trial mining took place. In 1981 renewed interest resulted in trial open pit mining. The oxidised ore proved difficult to treat in the Patchway mill so the shaft was deepened to 60 metres and then 90 metres with further trial mining and milling of sulphide ore. The Hamburg deposit is currently being mined by as a "smallworker" operation, leased from Rio Tinto Zimbabwe. Production amounts to only a few tonnes per day.

Cumulative production of gold metal from Patchway is estimated at around 20 tonnes gold metal to date from ore with a historical estimated average grade of 10 grammes per tonne (g/t). Annual production is now in the order of 300 kg gold per year from Patchway, although the mill also processes ore from the nearby Erin and Brompton mines. The cumulative production of gold from Golden Valley is estimated at 30 to 35 tonnes gold metal at an average estimated historical grade of 20 g/t Au (after Foster 1986).

1.4 Project Objectives

Classification of Archaean gold deposits from a genetic point of view suffers from a lack of consistency in approach to detailed deposit descriptions. Phaup (1964) crudely divided deposits into veins and replacements, which implied an epigenetic origin for all deposits. Boyle (1979) subdivided deposits on lithological association and hence developed a very complex classification. More recent studies such as Hodgson & MacGeehan (1982) propose subdivisions based on intrusive-extrusive igneous and sedimentological characteristics. These classifications are very often based on geological data collected with preconceived genetic models and thus become either over-simplistic or conversely over complicated. The argument between syngenesis and epigenesis has embraced Phaup's (1964) broadly epigenetic model at one extreme, to proposals by Fripp (1976) and Hutchinson (1986) who invoke models of early syngenetic gold deposition remobilised to form ore bodies. Colvine *et al.* (1984), Groves *et al.* (1984) and Groves & Foster (1990) have further developed the original idea of epigenetic formation suggested by Phaup (1964), basing their conclusions on more detailed study of a selection of Archaean deposits.

Fluids are ubiquitous features of all geological processes in the magmatic, metamorphic or meteoric domains. Since fluids form important natural solvents to metal ions in the presence of suitable anion complexes, they have the potential of transporting dissolved species and to later precipitate them in selected areas in high concentration. This concept is fundamental to understanding how epigenetic ore deposits form. Fluids are also shown to have a key dynamic role in some deformation processes (Fyfe *et al.* 1978) and thus the link between fluid dynamic and chemical behaviour is crucial in structurally controlled mineral deposits.

Intense hydrothermal wallrock alteration is a feature of most Archaean gold deposits. A clear understanding of the induced chemical changes in the wallrock peripheral to the gold-bearing zone or structure is a critical part of any quantitative study of the hydrothermal fluid responsible for such alteration and presumably the associated gold mineralisation. The chemical change observed in the wallrock coupled with the study of the fluids themselves (from fluid inclusions), can be used to determine characteristics of the hydrothermal fluid likely to be responsible for the deformation-mineralisation event.

Host rocks for epigenetic gold deposits in the Archaean of Zimbabwe show a broad range of compositional types and metamorphic grade (Foster 1989). This indicates that other key parameters in the mineralised system may hold the key to the location of gold deposits other than simple geological setting. Studies in Archaean deposits worldwide are confirming the unifying crucial role of deformation in the development of a suitable structural environment for a) the collection, b) the transportation and c) the subsequent precipitation of gold in a suitable hydrothermal fluid (Colvine *et al.* 1984). There is a need to understand the detailed structural controls to the gold mineralisation and, as a complimentary study, the nature and composition of the mineralising fluids. Structures are the essential channelways for mineralising fluids and the nature of the fluid determines its ability to transport and precipitate gold.

The Patchway and its associated gold deposits appeared from the literature (Ward 1968, Bliss 1970 and Foster *et al.* 1979) to be classic examples of structurally controlled epigenetic deposits. Since access to a number of deposits was possible, the region offered the opportunity to undertake an integrated study, in order to constrain the mineralisation within a structural framework. Recent study of crustal-scale, seismogenic structures (Sibson 1984) point to their ability to support widespread fluid flux during slip. Such models of linked deformation and fluid flux have been used in general terms to explain some of the features of Archaean gold-vein systems (Sibson *et al.* 1988). Examination of structurally constrained mineralised assemblages, by mineralogical and fluid inclusion study, could allow definition of the P-T conditions required for a favourable environment for the formation of gold mineralisation. The detailed study of fluid inclusions in the vein assemblage might link fluid evolution to the dynamic structural model for vein formation. It was hoped to examine inclusion-bearing vein phases (particularly quartz) which may have been precipitating at the same time as gold, permitting the precise definition of fluid parameters during gold precipitation.

The main aims of the project were therefore:

i) Develop a deposit-scale deformation model of the Patchway host structural system.

ii) Constrain mineral paragenesis within the evolving structural framework of the deposit.

iii) Determine fluid compositional and PT parameters of the fluids responsible for the various mineralisation stages, relating these stages with possible fluid sources.

iv) Determine fluid evolution the actual precipitation of the gold mineralisation, through examination of mineral phases contemporaneous with gold precipitation.

v) Develop a regional dynamic structural-fluid model for evolution of the mineralised shear system which hosts the Patchway and associated gold deposits.

Detailed mapping of the Patchway vein system allowed a suite of well controlled samples of both host rocks and mineralisation to be collected. These samples formed the basis of the petrological and mineral chemical study and more importantly the suite of mainly quartz samples used for the detailed fluid inclusion and stable isotope study. The fluid inclusion study of phases formed at different stages

of the deformation-mineralisation event was crucial to the development of a detailed fluid evolution model.

1.5 Layout of the Thesis

Chapter 2 reviews the published regional geology and evolution models for the Zimbabwe craton, focussing on the geology of the Patchway-Kadoma region. The chapter incorporates the established models for Archaean gold deposits and relates these models to the gold deposits discussed in this study.

Chapter 3 presents the petrology and geochemistry of the Patchway mine host stratigraphy, with the emphasis on defining any chemical change in the deformed rocks marginal to the gold-bearing veins. The study assesses the effect of any fluid metasomatism during deformation.

Chapter 4 discusses the physical parameters controlling the development of large, complex mesothermal gold-quartz veins, comparing similar deposits described in the literature with the Patchway vein system. The broad nature of the hydrothermal fluids active in the shear-systems hosting such deposits is discussed and the physical and chemical behaviour of such fluids during deformation is addressed.

Chapter 5 is a key chapter, presenting a detailed structural study of the gold deposits at Patchway together with complimentary studies at the Golden Valley, Erin and Hamburg deposits. The structural history outlined is integrated into the regional deformation model previously presented in Chapter 2. From the structural mapping, multiple deformation and vein mineralisation events can be discriminated, providing an excellent relative age constraint on different assemblages in the paragenetic sequence.

Chapter 6 describes these assemblages in the paragenetic sequence and clearly defines the gold-bearing stage of mineralisation, identifying contemporaneous sulphide and gangue mineral phases which could be used to provide constraint on PT conditions during gold precipitation.

Chapter 7 presents a detailed fluid inclusion study of the quartz from the various vein assemblages, with limited data from scheelite, collected from various stages of the paragenetic sequence characterised in Chapter 5. The fluids are characterised by fluid inclusion study, utilising classic microthermometry and chemical analysis of inclusion fluids. Detailed study of quartz directly hosting gold grains allows excellent study of the evolution of the gold-bearing hydrothermal fluid during the actual process of gold precipitation. Estimates of ambient formation temperatures and pressures are defined from the fluid inclusion study in conjunction with other mineral geothermometry and geobarometry.

The implications of the proposed model of fluid evolution during the mineralisation event is quantified in Chapter 8, by thermodynamic calculations made for the fluid during vein formation. The effects of

the chemical changes in the gold-bearing hydrothermal fluid during gold precipitation on speciation in the C-O-H-S fluid system are considered. A stable isotope study of mineral phases from the various stages of the mineralisation is presented, discussed within the constraints of the fluid system imposed by the results of the fluid inclusion study and the thermodynamic modelling.

Chapter 9 incorporates the conclusions, and links the model of fluid evolution during mineralisation stages to the deformation model proposed. Discussion of gold transport and precipitation models allows conclusions, precisely linking gold transport and precipitation with the observed deformation and mineralisation style, to be made. Incorporation of these conclusions into the regional geological evolution leads to a model for regional metallogenesis. Finally suggestions are made as to suitable areas for future research.

CHAPTER TWO - REGIONAL STRATIGRAPHY AND METALLOGENESIS OF THE ZIMBABWEAN CRATON

2.1 Greenstone Terrains of the Zimbabwe Craton

Exposed rocks of Archaean age which form part of the Zimbabwe craton make up the dominant succession in central and eastern Zimbabwe. The rocks of the craton can be usefully divided into the complex greenstone belt regions and the more abundant areas of granitic rocks.

The Zimbabwean Craton is recognised to have three major greenstone sequences which listed from youngest first are 1) Sebakwian 2) Bulawayan and 3) Shamvaian. (Anhaeusser 1976, Wilson *et al.* 1978, Wilson 1979). Figure 2.1 shows the regional distribution of the various sequences within the Zimbabwe craton.

Sebakwian

The Sebakwian is developed in the central part of the craton forming a sequence of ultramafics, komatiites, minor mafic volcanic, iron formations and clastic meta-sediments. Closely associated intrusive granites are dated at 3500 Ma (Foster & Wilson 1984), and thus this represents the earliest of the greenstone sequences. Recent dating of sediments in the Shurugwi and Mweza greenstone belts yields detrital zircon ages of 3800 Ma (Dodson *et al.* 1988).

The volcanic part of the sequence is dominantly Mg-rich and has been interpreted as being emplaced in a proto-rift (Foster 1985), partly based on the lack of associated sediments other than chemically precipitated cherts and ironstones. The uppermost part of the Sebakwian is marked by the Wanderer formation where a transition to sediments more indicative of active syn-sedimentary tectonism, such as conglomerates and greywackes, are present. In the Shurugwi belt, deeper basinal conditions are likely at this time as the sequence is marked by 600 metres of banded-iron formation (BIF) and shale, succeeded by the Tibilikwe formation. This formation comprises around 1km of tholeiitic basalt. The Sebakwian is succeeded by a second major phase of greenstone belt development resulting in the Bulawayan and Shamvaian Groups.

Bulawayan

The Bulawayan Group forms the most extensive of the later sequences, with the group in the central portion of the craton conveniently subdivided into the Lower and Upper Greenstones (Martin 1978). A distinct sulphide facies iron formation forms the boundary between these two units.

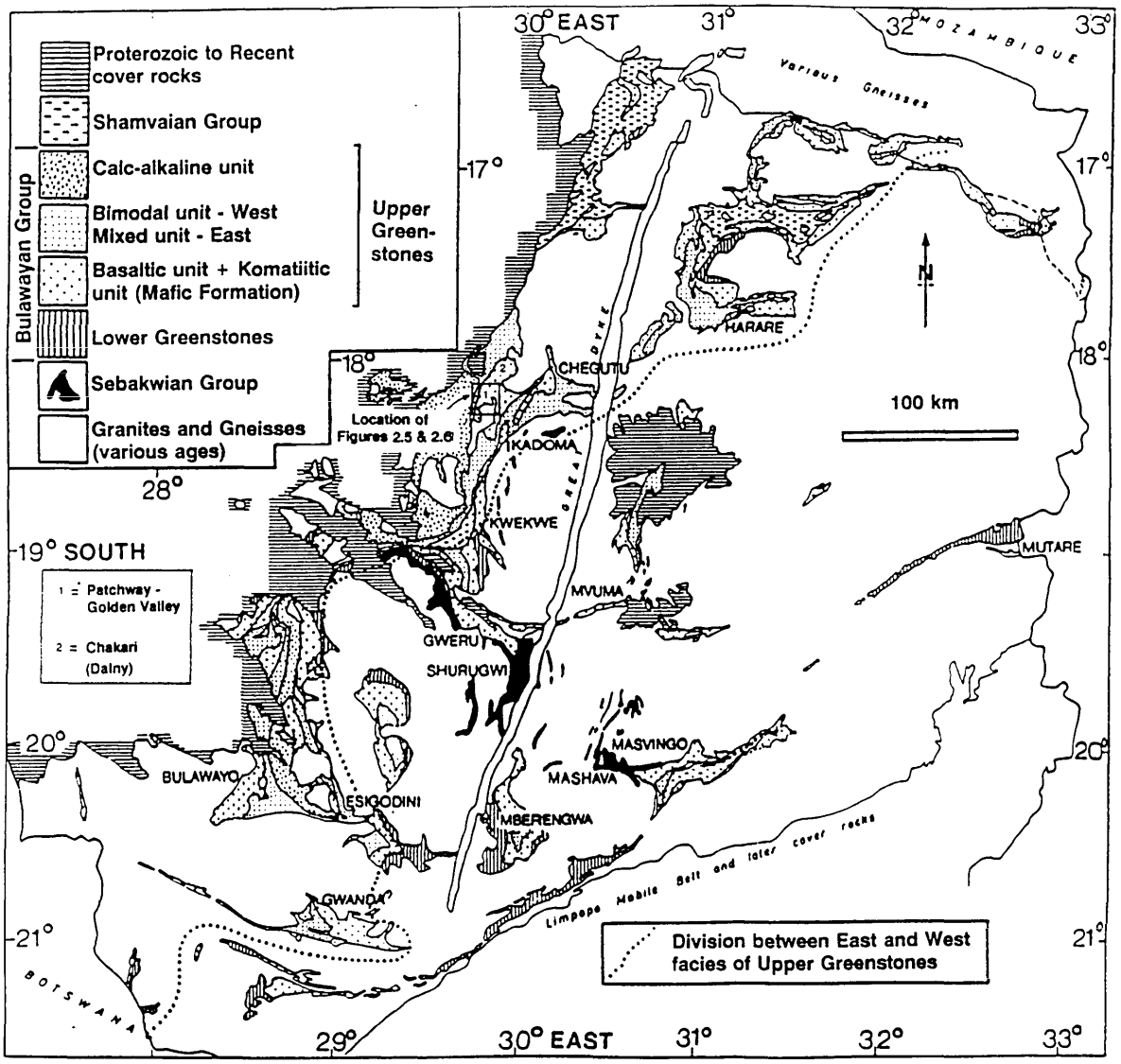


Figure 2.1 - Summary geological map of the Zimbabwe craton (after Foster *et al.* 1986)

The Lower Greenstones are best developed in the Mberengwa belt and comprise felsic meta-volcanic, volcanoclastics and komatiites together with komatiitic basalts, iron formations and polymictic conglomerates (Wilson 1981). Dating of these rocks suggests an age of 2900 Ma (Wilson 1979).

The variously dated 2800 to 2700 Ma (Hawkesworth *et al.* 1975, Moorbath *et al.* 1987) Upper Greenstone sequence can be subdivided stratigraphically, but also shows marked facies contrast between western and eastern portions of the craton. The initial basal sedimentary unit is succeeded by a sequence of between 1 and 2 km of komatiites and tholeiitic basalts which are often pillowed. Mafic sills are common in this unit, referred to as the Reliance Formation in the Mberengwa belt, or more recently as the 'Komatiitic Unit' by Foster *et al.* (1986). Sediments are poorly developed or absent, comprising mainly minor inter-flow sediments or iron formation. Following the Reliance Formation is a sequence of up to 6 km of extrusive tholeiitic basalts with minor komatiitic basalts. This is well developed throughout all the greenstone belts, being termed the Zeederbergs Formation in the Mberengwa belt which Foster (1985) has termed the 'Basaltic Unit' for this equivalent unit elsewhere in the craton. It is apparent although Foster (1985) proposes a "rift" setting for the unit, the lateral persistence of thick sequences of mafic and ultramafic flows is indicative of fairly subdued relief, and a stable tectonic setting. The lack of thick sediment sequences in this unit is notable (with no high energy sediments), particularly in the Midlands greenstone belt. The Patchway, Golden Valley, Erin and Hamburg deposits are all hosted within rocks of the Zeederbergs equivalent Basaltic unit. Collectively the Reliance and Zeederbergs Formations form the Mafic Formation and have been described by Wilson (1981).

Above the Mafic Formation lies the Bimodal Unit (Foster 1985). The Bimodal Unit shows a very distinct east-west facies divide. The sequence in the west comprises an alternating mafic-felsic sequence, consisting of felsic, andesitic and basaltic lavas with minor pyroclastics, reworked volcano-sediments and abundant iron formations. Succeeding the Mafic Formation in the eastern part of the craton is the much thinner Mixed unit which contains far more sediments in the sequence. A sequence dominated by phyllites with minor conglomerates, grits and limestones is overlain by a 1 to 2 km thick sequence of tholeiitic basalts with minor komatiites.

The Bimodal Unit is overlain in the western part of the craton by a calc-alkaline succession (Munyati Formation) which comprises a thick sequence of dacitic to andesitic lavas and pyroclastic flows. The calc-alkaline sequence can be interpreted as early rift volcanism followed by development of a volcanic arc (Nisbet *et al.* 1981, Wilson 1981, Foster 1985). The eastern part of the craton has no equivalent sequence.

Shamvaian

The Shamvaian Group is mainly restricted to the central and northern parts of the craton and is largely formed of poorly sorted arkosic and wacke grits together with minor felsic lavas and volcanoclastics.

An unconformity separates the Shamvaian from the Bulawayan (Wilson 1979). No dating is available from this Group but dating of later cross-cutting granites puts the minimum age at 2700 Ma (Hawkesworth *et al.* 1975).

The Upper Greenstones of the Bulawayan Group together with the Shamvaian forms the greater part of the exposed greenstone terrain.

2.2 Granitic Terrains of the Zimbabwe Craton

Granitic intrusives and subordinate mafic and ultramafic intrusive suites occupy some 85% of the exposed craton (Anhaeusser 1976). Granite suites are intimately associated with each of the three greenstone successions based on age dating and spatial association. The oldest 3580 Ma (Hawksworth *et al.* 1975) tonalite gneisses of the Mashava, Shurugwe and Masvingo areas are closely followed by the Mushadike granite (Wilson 1973) and Mont d'Or granite of 3420 Ma (Moorbath *et al.* 1976). The early Mashaba ultramafic suite and Mashaba-Chibi dykes are restricted to rocks older than the Bulawayan Upper Greenstones and may also be of similar age. These may have formed feeders for the Upper Greenstone sequences.

All the early granite suites, except the Mont d'Or granite (which Moorbath *et al.* (1976) suggest may be a partial melt of early sialic crust), have $^{87}Sr/^{86}Sr$ ratios suggestive of upper mantle or base of lithosphere origin (Wilson *et al.* 1978). Two important younger granite or tonalite suites can be defined (Wilson *et al.* 1978) and are collectively known as "Younger granites" (Stagman 1978). The Sesombi and Chilimanzi tonalite suites are both dated at 2700 Ma by the Rb-Sr method (Wilson 1979) but less reliable K-Ar dates indicate a 2900 Ma age for the Sesombi suite and a 2600 Ma age for the Chilimanzi bodies (Hickman 1974 and Hawkesworth *et al.* 1975). The Sesombi suite is suggested as the plutonic equivalent of the Bulawayan age calc-alkaline Munyati (Umniati) Formation (Hawkesworth & Bickle 1977) based on geochemical evidence. The Sesombi suite is certainly seen to cut rocks of the Mafic Formation of the Bulawayan age Upper Greenstones in the Kadoma region (Bliss 1970). The Chilimanzi suite is suggested as representing a later phase formed from the remelting of earlier sialic crust (Hickman 1978) and is rarely seen to cut the greenstone belt rocks.

Possibly even later than the "Late granites" are the Zimbabwe and Chibi potassic granites developed close to the Limpopo Marginal Zone (2700 Ma after Robertson 1973). If these are the latest granites, this indicates a marked age related trend of increasing K versus Na contents of the felsic intrusives with time, similar to a trend in data from the Kaapvaal Craton intrusives (Tankard *et al.* 1982) and from published data on the Norseman-Wiluna belt of West Australia (Hallberg 1985, Perring *et al.* 1988). This may well represent the product of repeated anatexis.

2.3 Archaean Gold Mineralisation

2.3.1 Introduction

Gold deposits in Archaean terrains are almost always restricted to the greenschist to lower amphibolite metamorphic grade portions of granite-greenstone areas as noted in Canada by Goodwin & Ridler (1970), in Western Australia by Groves *et al.* (1988) and in southern Africa by Anhaeusser (1976). This P/T environment conveniently falls in the region of brittle to ductile deformation processes in normal sialic crust (Sibson 1983). The higher grade terrains and "mobile belts" are traditionally less productive with notable exceptions of Big Bell, Western Australia (Phillips 1985), Hemlo, Ontario, Canada (Valliant *et al.* 1986) and Renco, Zimbabwe (Tabeart 1988). In almost all cases Archaean deposits occupy specific structural positions such as fold hinges, shear-zones or fracture networks. Many of these important features are recurrent on a regional scale, leading to distinct concentrations of deposits in any particular "camp".

Typical granite-greenstone terrains show broadly similar morphological features. Negative cuspate and elongate "greenstone belts" form enclaves within batholithic granite gneiss areas and comprise a distinctive stratigraphy dominated by mafic volcanic rocks. The greenstone belts show large areas of low penetrative strain with preservation, very often, of delicate primary textural features (e.g. pillow lavas). There is a broad synclinal aspect to most belts which often show strongly differing sequences in the opposing limbs. These limbs are often separated by major stuctures or deformation zones ("breaks" in Canadian literature). The "breaks" roughly parallel the main strucural axes of the belts and are a strong aspect to the tectonic evolution of the granite-greenstone terrains.

The importance of these tectonic discontinuities for mineralisation in the Canadian Shield was recognised early on (Gunning & Ambrose 1937). Workers such as Jensen & Landford (1983) suggested that these structures are fundamental, long lived and may even have played a role during sedimentation, volcanism and/or intrusive events. In the Norseman-Wiluna belt of Western Australia such structures were related to gold deposits by Gee (1979) and even the distribution of original volcano-stratigraphy (Groves & Batt 1984). Nutt *et al.* (1988) discuss this further and indicate similar relationships in the Archaean of southern Africa. These structures often take the form of large brittle-ductile shear zones and these are outlined on Figure 2.2.

Other regionally defined structural sites related to mineralisation are high-strain zones marginal to diapiric granitoids. Anhaeusser (1976) demonstrated this spatial relationship in Zimbabwe, and productive parts of the Pilbara block in Western Australia would appear to relate to similar features (Vearncombe 1988).

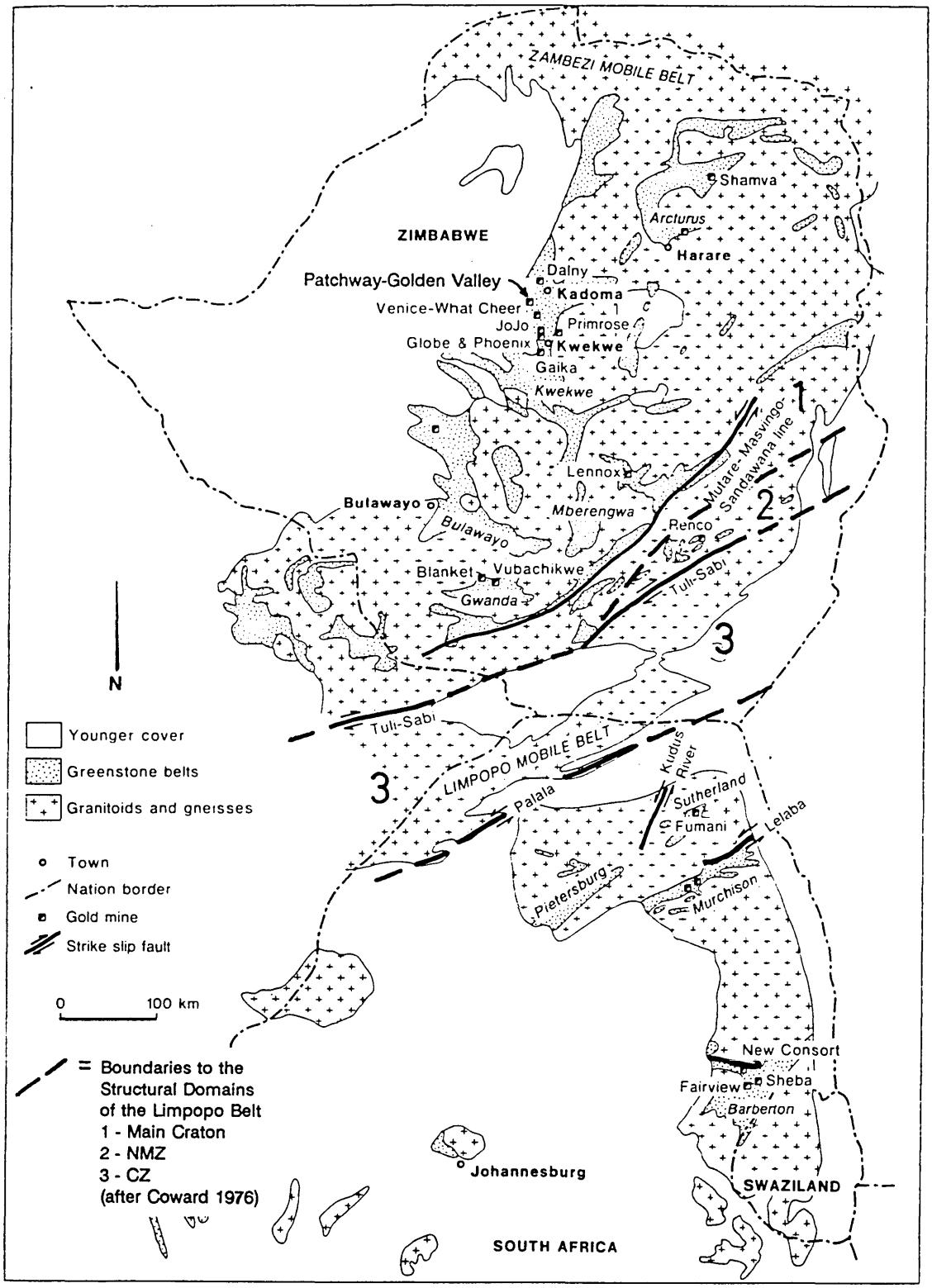


Figure 2.2 - Principal features of the Archaean cratons of southern Africa indicating principal gold mines and major structures (modified from Vearncombe *et al.* 1989). Also shown are the key structural domains of the Limpopo Mobile Belt 1 = Craton, 2 = Northern Marginal Zone, 3 = Central Zone (after Coward 1976)

The presence of ubiquitous felsic intrusive bodies is also an important feature of the Archaean gold deposits. Ferguson *et al.* (1968) suggested this association for some Canadian deposits, and many workers (e.g. Burrows & Spooner 1986, Smith *et al.* 1984) invoke a strong genetic relationship between intrusions and mineralisation. Felsic intrusives are common in the Norseman-Wiluna belt of West Australia, where there is an undoubted spatial relationship between internal granitoids, shear zones and mineralisation (Golding *et al.* 1987, Swarnecki 1988). Cameron & Hattori (1987) are even more specific, noting a favourable association of sodic, magnetic (hence oxidised) felsic intrusions with gold deposits. This magmatic association is still subject to much debate, but it is clear that very few of currently known ore-bodies occur deep within batholith complexes (Saager & Meyer 1984), and most seem restricted to the high strain marginal areas where genetic associations are equivocal.

Distinctive alteration mineral assemblages are noted for most Archaean deposits. Individual descriptions show variable elemental behaviour but most studies (e.g. reviews by Colvine *et al.* 1984, Vearncome *et al.* 1989, Kerrich 1989a) concur on common enrichments or depletions in Si, CO_2, K, Rb, Ba, Cs and B together with Au, Ag and W. These changes are consistent with massive fluid flux during formation of many of these deposits, indicative of epigenetic, focussed fluid processes. This alteration seems largely confined to the greenstone portions of the terrains, best developed in mafic to ultramafic lithologies (Fyon & Crockett 1981). There is a strong relationship between distribution of these alteration patterns and the major regional structures. This alteration can often be related chronologically to deformation events, peak metamorphism and mineralisation.

2.3.2 Gold Mineralisation in the Zimbabwe Craton

Colvine *et al.* (1984) points out an empirical relationship between greenstone belt age and gold production. Pre 3000 Ma parts of greenstone belts such as in the Kaapvaal Craton southern Africa, Slave province Canada and Pilbara block Western Australia are remarkably less productive than post 3000 Ma stratigraphy. Groves & Batt (1984) link tectono-stratigraphy and age with observed metallogenesis. The subdivision of "Rift" greenstones covers the most productive regions of the Yilgarn block, whilst the poorly mineralised older Pilbara is what he calls a "Platform" greenstone area based largely on the lack of komatiites and felsic volcanics. The Mafic Formation of the Bulawayan Group in the Zimbabwean Archaean, however, appears to more closely resemble a "Platform" sequence, yet is demonstrably a highly productive terrain for gold mineralisation (Foster *et al.* 1986).

The Zimbabwean Archaean Craton has itself produced some 1500 tonnes of gold (extrapolated from data in Foster & Wilson 1984) with historical production starting at least as far back as 600 AD (Summers 1969). Production levels are currently at 15 tonnes per annum which places Zimbabwe in 12th place in world production rankings.

The geological setting of gold deposits in Zimbabwe has been discussed in several treatises including Phaup (1964), Fripp (1976), Anhaeusser (1976), Foster *et al.* (1986b) and most recently by Foster (1989). Classifications have been attempted by Lightfoot (1934) and genetic models proposed in discussions by Fripp (1976) and Anhaeusser (1976). The most recent review, Foster (1989), subdivides deposits into Lode deposits, BIF deposits and Volcanoclastic hosted deposits. Of these, the Lode deposits have accounted for over 80% of the gold produced in Zimbabwe between 1892 and 1977 (Foster *et al.* 1986). Adding the, probably structurally controlled, replacement iron formations gold deposits (13%) (Fuchter & Hodgson 1986, Foster *et al.* 1986b, Gilligan & Foster 1987), and even the, possibly epigenetic, Shamva-type volcanic-hosted deposits (S. Mundondo *pers. comm.*, Foster 1989), then probably over 95% of the gold is produced from structurally controlled deposits. In the terminology adopted in Foster (1989), Patchway and Golden Valley should be included in the Lode deposit category.

A study of the lithological distribution of deposits in Zimbabwe by Foster *et al.* (1986), indicates a strong association between structurally controlled gold mineralisation, and the basaltic Upper Greenstones of the western portion of the Bulawayan Group (38% of production). These rocks are dominantly Fe-rich tholeiites and together with the iron formations host over 50% of Zimbabwe's gold. This relationship between highly competent, Fe-rich rocks, and gold is clear in other Archaean terrains such as Western Australia (Phillips & Groves 1983). Patchway, Golden Valley, Erin and Hamburg are all hosted in iron-rich volcanic rocks of the Upper Greenstones of the Bulawayan.

2.4 Structural Framework of the Zimbabwe Craton

Early discussions of the regional structures of Zimbabwe, centre on the review by Macgregor (1951) who introduced the concept of "gregarious batholiths", expanding upon earlier ideas of broadly synclinal aspects to Archaean greenstone belts. Stowe (1971, 1974, 1980) describes multiple deformation phases with widespread deformation features characterised by cross folding, together with vertical structures marginal to the various granitic bodies.

It is clear that structural evolution of the Zimbabwe Craton was inexorably linked to that of the Limpopo belt and Kaapvaal Craton (Coward 1976). Events affecting the Limpopo belt are probably the most significant from a deformation point of view, and the broad relationships and fabrics developed in the Zimbabwean cratonic block owe their origin to such events (Coward *et al.* 1976).

Several models for the formation of the Limpopo belt have been proposed (Intracratonic rifting - Barton & Key 1981, Back arc - Fripp 1982, Inter plate collision - Light 1982 and more recently Continental collision - Van Reenan *et al.* 1987). The continental collision model appears to be the best explanation, accommodating most of the observed features, as well as the lack of generated intrusive suites (this lack tends to negate the rifting and subduction related models). What is certain, however, is that strong

compressional tectonics were active across the Limpopo belt and structures well into the Zimbabwe Craton were influenced by this. Studies such as Coward *et al.* (1976) and Key *et al.* (1976) recognised the regional aspect to deformation patterns and the influence of the craton-bounding mobile belts. This work compiled and expanded by Coward (1980), outlined three broad structural domains in Zimbabwe : 1) The Craton, 2) Northern Marginal Zone (of the Limpopo belt) and 3) Central Zone (of The Limpopo belt) which are also outlined on Figure 2.2.

Domain 1, the main craton, forms a domain dominated by strongly arcuate foliation, often focussed into restricted structural zones. In the southwest portion of the area, which covers the Bulawayo, Gwanda, Shangani and Mberengwa greenstone belts, NW to SE trending upright to inclined tectonic fabric is developed in granitic gneisses and greenstones. Further east this fabric is deflected to form steep NE to SW shear zones. Some of these shears show evidence of extensive strike slip motion (Stowe 1974). In the KweKwe area of the Midlands greenstone belt the fabric is mainly steep and arcuate around the older gneiss complex at its eastern margin. The northern greenstone belts of Mount Darwin, and Harare are again dominated by NE to SW structures.

The main fabrics developed in the greenstone belt areas of the main cratonic areas (Coward's domain 1) are summarised on Figure 2.3. The eastern part of the craton is dominated by structures developed in response to some form of NNW to SSE imposed shortening across the craton, whilst structure in the more western part indicates some lateral shortening in a WSW to ENE direction to the west of the main Rhodesdale Gneiss block.

Domain 2, the Northern Margin of the Limpopo belt, is dominated by a series of NE-SW thrust faults (James 1975, Coward & Fairhead 1980). Major shortening and thickening of the crust in a NW to SE direction is apparent from gravity surveys. Much of this deformation would appear later than that in the south of the cratonic area.

Domain 3, the Central Zone of the Limpopo belt is dominated by intense ENE to WSW trending shears where strong lateral movement is recorded (Coward *et al.* 1976). The Central Zone comprises high grade granites folded with a strongly developed N-S grain. Much of this deformation is probably early Proterozoic (Wilson & Prendegast 1989), and similar ENE to WSW structures (e.g. Gurungwe fault) are seen to cut the Great Dyke in the cratonic area (Wilson & Prendegast *et al.* 1989). Relative timing of the events resulting in this framework is not rigidly defined but a broad two-phase chronology can be established. The proposed sequence of regional events is summarised graphically in Figure 2.4 :

1 - Early Deformation

Early deformation in the Shurugwi greenstone belt in the south of the cratonic area probably predates the bulk of the deformation elsewhere (Stowe 1974). After this event NNW to SSE directed shortening

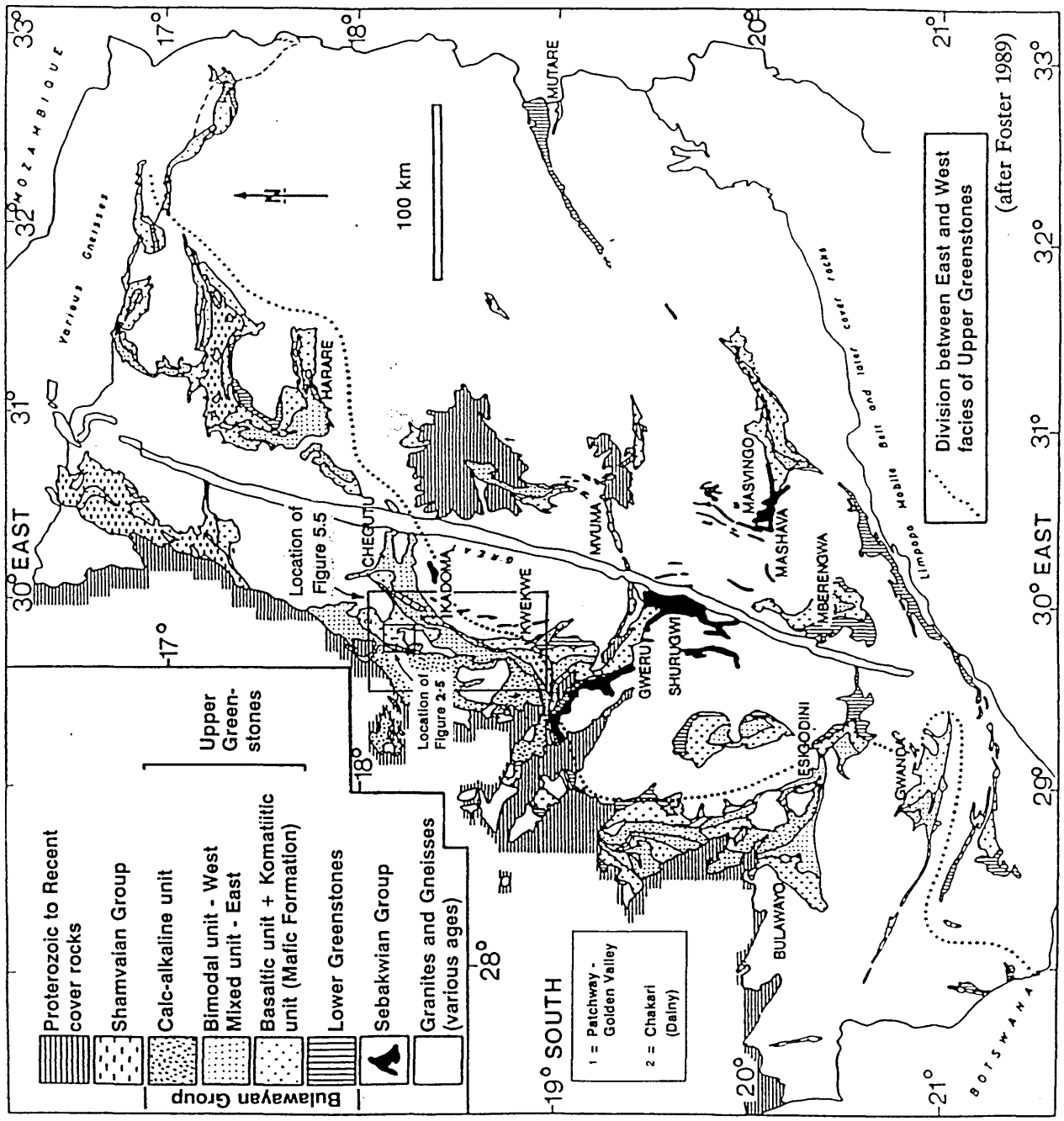


Figure 2.3 - Summary of key structural elements of the Zimbabwe craton (shown on overlay). (Compiled from Bliss 1970, Harrison 1970, Coward 1976, Coward *et al.* 1976, Stowe 1971, 1974, 1980, Nutt *et al.* 1988, Pitfield & Campbell 1989, Wright 1975).

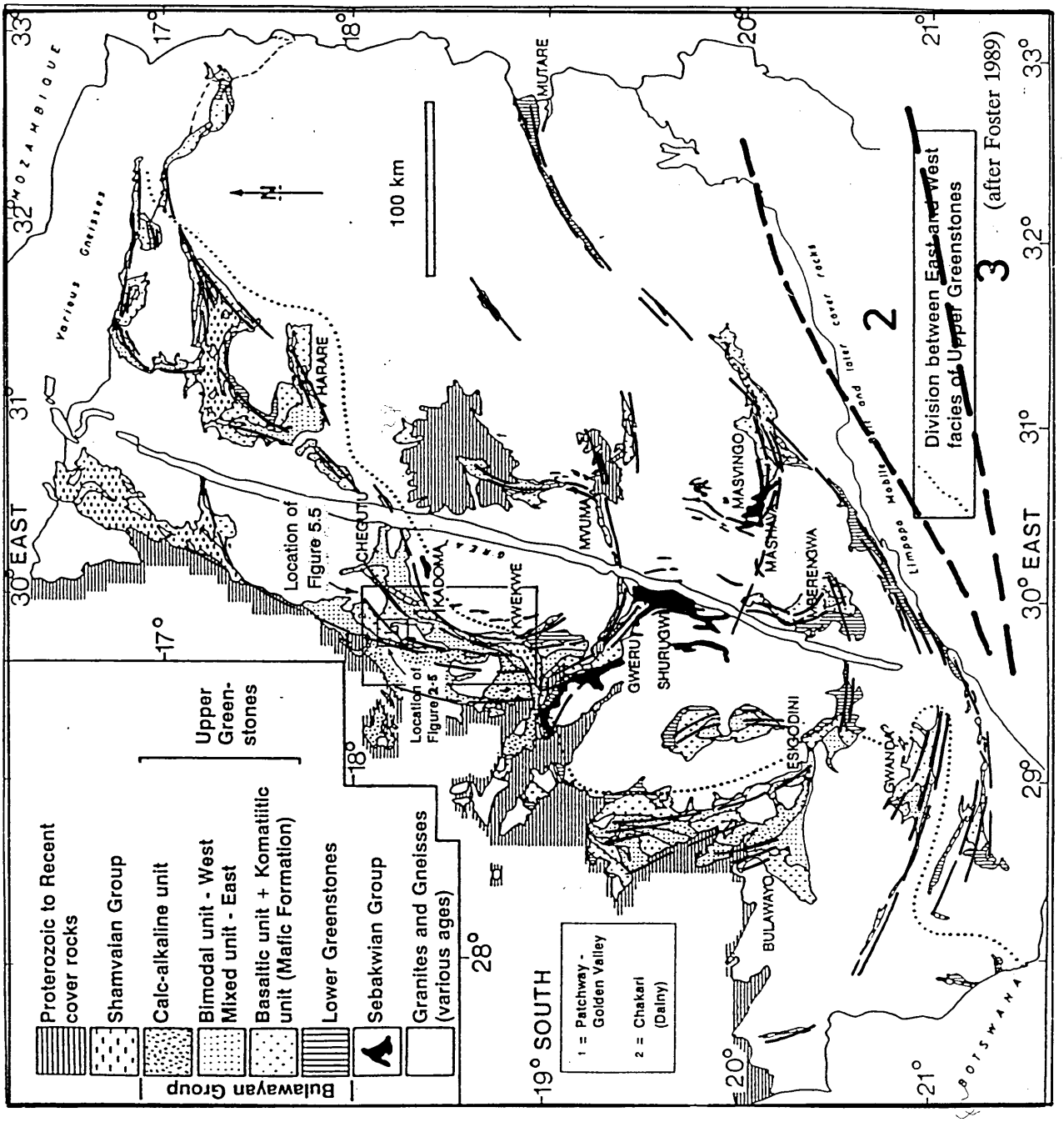


Figure 2.3 - Summary of key structural elements of the Zimbabwe craton (shown on overlay). (Compiled from Bliss 1970, Harrison 1970, Coward 1976, Coward *et al.* 1976, Stowe 1971, 1974, 1980, Nutt *et al.* 1988, Pitfield & Campbell 1989, Wright 1975).

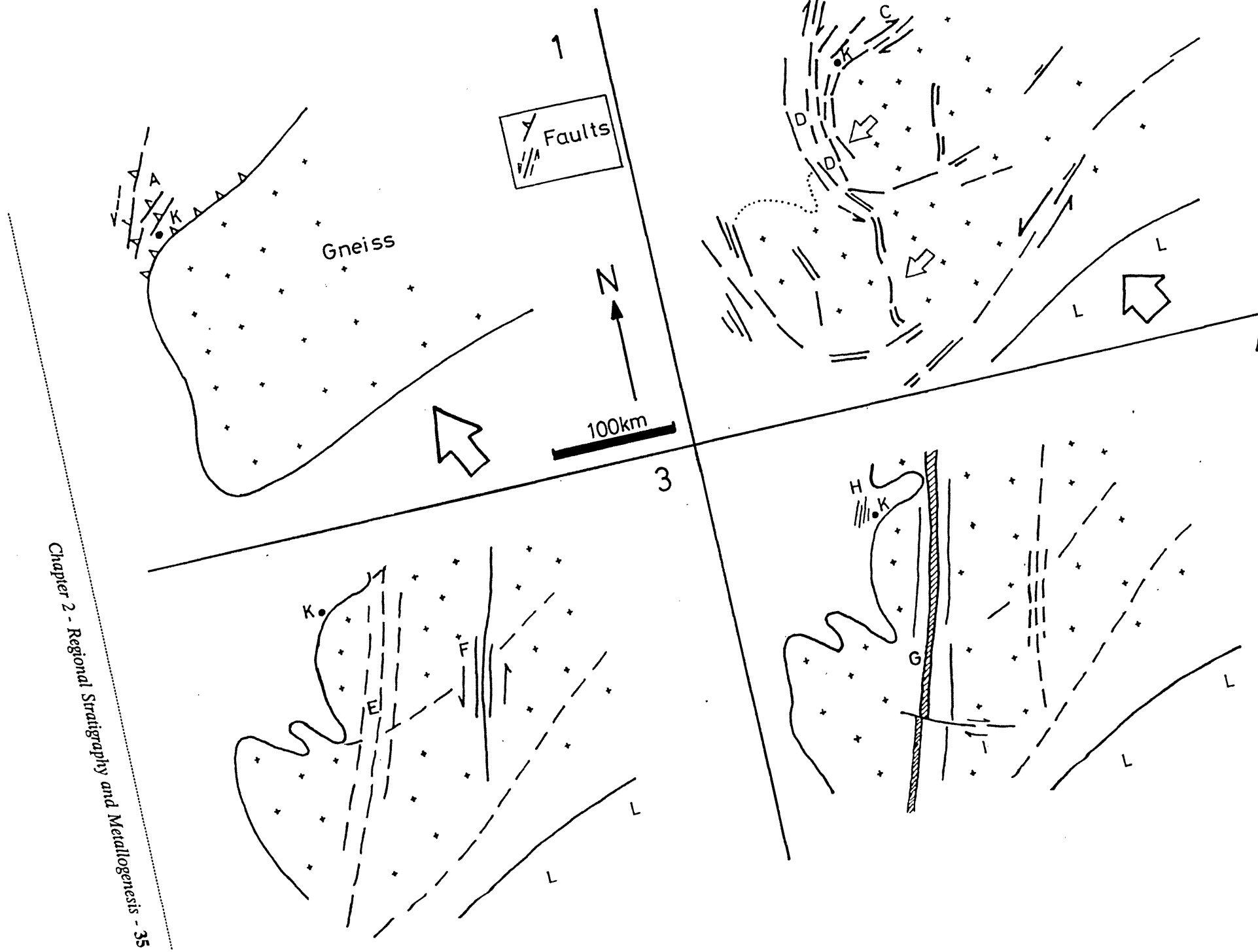
1 - Initiation of major structures (A) in the Kadoma region (K = Kadoma) after early folding following N-S compression. Beginning of Limpopo deformation due to movement of Kaapvaal craton northwards.

2 - Evolution of deformation to compression from Limpopo region (L = Limpopo Belt), combined with lateral expulsion of gneiss block westwards (small arrows). Lily Fault (B) and Rhodesdale boundary shear (C) suffer strike-slip displacement. Shears in southern part of Midlands region (D) suffer mainly high-angle reverse motion.

3 - Late Archaean "lock-up" of greenstone-belt structures. Brittle deformation on Popoteke fault set (F). Development of parallel fracture set (E) prior to Great Dyke intrusion.

4 - Intrusion of Great Dyke (G) and associated dykes into fractures sub-parallel to Popoteke faults. Similar stress field persists for intrusion of late (Proterozoic ?) dykes in Kadoma region (H). Great Dyke cut by reactivated Jenya-Mushandike shear (I).

Figure 2.4 - Provisional timetable of deformation events in the Kadoma region with respect to craton scale deformation events in Zimbabwe.


1
Faults
A
K
Gneiss
N
100km
3
4
B
C
K
D
D
L
L
L
H
K
G
K
E
F
L
L

across the belt lead probably lead to the regional folding events in the 2700 Ma greenstone belts, which largely predated intrusion of the Sesombi suite of granitoids (Coward 1976, Coward *et al.* 1976). Intrusion of these granitoids followed with the contemporaneous development of migmatites and granite sheets in the Limpopo belt itself.

The arcuate forms of the regional fabric around these granitoids have been alternatively explained in part by cross-folding (Snowden & Bickle 1976, Snowden 1984) or forceful emplacement and "billiard ball" deformation (Coward *et al.* 1976).

2 - Later deformation

The development of the WSW-ENE shortening in the Midlands and Bulawayo greenstone belts cannot be explained by a simple compression event. McCourt & Vearncome (1987) propose a component of an E-W collision event lying to the east to account for the westerly directed thrusting of the Limpopo Central Zone. This could result in the observed westerly movement of the Rhodesdale Gneiss complex. It is clear that the cratonic area 1) moved some 200 km west with respect to the Limpopo belt (Coward 1976). This led to major shortening in the south-west greenstone belts (Coward 1980). It now seems clear that the whole of the cratonic area was not displaced however, as dextral strike-slip movement is recorded on some of the NE - SW trending shears in on the northern margin of the Rhodesdale Gneiss block (Pitfield & Campbell 1989). It seems the Rhodesdale Gneiss block alone may have moved westwards withbounding shears both north and south. This type of event could lead to a complex series major strike-slip movement on the previously developed NE-SW thrust faults. Recent models for emplacement of the Great Dyke point to crustal extension during a period of pure shear (Wilson & Prendegast 1989) with development of the Popoteke Fault set. Light (1982) relates this to collision of the Zimbabwe and Kaapvaal cratons, which infers a continued period of NNW to SSE oriented compression right up to the end of the Archaean. In this case the only way for the Rhodesdale Gneiss block to have moved westwards, is in some kind of lateral secretion model, where the central portions of the largely undeformed Rhodesdale Gneiss are squeezed westwards (Coward *pers. comm.*). Support for the lateral movement of the block comes from the observation of dominantly reverse thrust movement on N-S trending mineralised structures in the KweKwe area (Nutt *et al.* 1988).

This model could lead to the observed NNW-SSE fabric in the south-west coupled with the strike slip movement on the NE-SW shears. Locking up of the latter structures could lead to development of the brittle Popoteke fracture set which are the parallel precursors to the Great Dyke fracturing (Wilson & Prendegast 1989).

2.5 Geology of the Kadoma Region

The Patchway mine is hosted within the Upper Bulawayan sequence of rocks of the Midlands greenstone belt. These rocks can be compared to similar rocks in the Mberengwa area where a reasonable stratigraphic succession has been established (Wilson 1979). Age dating in the Mberengwa area suggests greenstone dates of 2760 ± 80 Ma (Jahn & Condie 1976) and from comparable rocks at KweKwe at 2700 Ma (Hawkesworth & Bickle 1976). Based on Wilson's work (Wilson 1979) and the sub-divisions outlined by Foster *et al.* (1986) the Upper Bulawayan of the Kadoma region can be subdivided as shown in Table 2.1. All the deposits studied are hosted in the Basaltic Unit of the Upper Bulawayan which is the most important stratigraphic unit for gold production in the region (Foster & Wilson 1984). The Basaltic Unit forms the core of the major Kadoma anticline and extends from Chegutu in the north to an area to the southwest of Kadoma in the south. The unit is dominated by flow rocks, mainly of basaltic and andesitic composition and often pillowed (Bliss 1970; Foster *et al.* 1979). Subordinate inter-flow sediments and volcano-sediments are also recorded. This package of flow rocks is accompanied by numerous thin quartz porphyry intrusives (termed "felsites" locally), probably high-level dykes or sills, which show variable age relationships but the majority apparently intruded later than the original mafic flow rocks. These intrusives are recorded at a number of mines within the region as Bliss (1970) notes, particularly in the Golden Valley region. The intrusive "felsites" were seen underground at Patchway, Golden Valley and Erin during the course of this study. Bliss relates these intrusives to the small stocks of Marizani, Chadshunt and Polperro (west of Golden Valley and north near Chakari respectively).

The nearby Lion Hill intrusive stock is part of the much larger Whitewaters tonalite (Figure 2.5) and together they form part of the series of sodic intrusives which form the 2700 Ma Sesombi tonalite suite. (Bliss 1970, Hawkesworth & Bickle, 1976). The suite of intrusives probably forms the plutonic expression of the magmatic episode responsible for the andesites and dacites of the overlying Calc-alkaline Unit (Hawkesworth & Bickle, 1977). Work by Bellamy (1975) suggests that the Whitewaters complex intruded in two stages as an early sodic phase which was deformed before a later more potassic facies. Bliss (1970) suggests that the Grandeur potassic granite (located at the southern tip of the Whitewaters body) is a late expression of this major granitic intrusive event.

Clearly post-dating all these rocks are a series of generally NE trending dolerite dykes. Recorded extensively in the belt (Bliss 1970) these are seen to cut the Lion Hill stock and Whitewaters tonalite bodies. Macgregor (1930) proposes an age of Upper Karoo for these dykes, although the undoubted tectonism of some of the intrusives seen at Patchway would appear to indicate that at least some of the intrusives are much earlier, possibly part of the Plumtree swarm of 2.15 Ga (Wilson *et al.* 1987).

Unit Name (after Foster *et al.* 1986)	Thickness	Description
CALC-ALKALINE	± 4000m	Calc-alkaline volcanic suite of basalt, andesite and rhyolite; flows and pyroclastics, some mafic sills
BIMODAL	± 4000m	Bimodal volcanic succession. Tholeiitic and Mg-rich basalts, peridotites alternating with dacites; tuffs and agglomerates. Grits and conglomerates locally derived from pyroclastics; mafic sills, phyllites, BIF and limestone
BASALTIC	4000 - 6000m	Pillowed and massive basalts, mainly tholeiitic, some komatiitic and sills. Minor pyroclastics
KOMATIITIC	< 2000m	Komatiites, pillowed and massive. Some tholeiitic basalts and associated sills. Minor pyroclastics
BASAL SEDIMENTARY	< 250m	BIF, local conglomerates, grits and some limestones

Table 2.1 - Western succession of the Upper Greenstones of the Bulawayan Group, central Zimbabwe. The Patchway mine host rocks (Basaltic Unit) are highlighted (modified from Foster 1985, Foster *et al.* 1986).

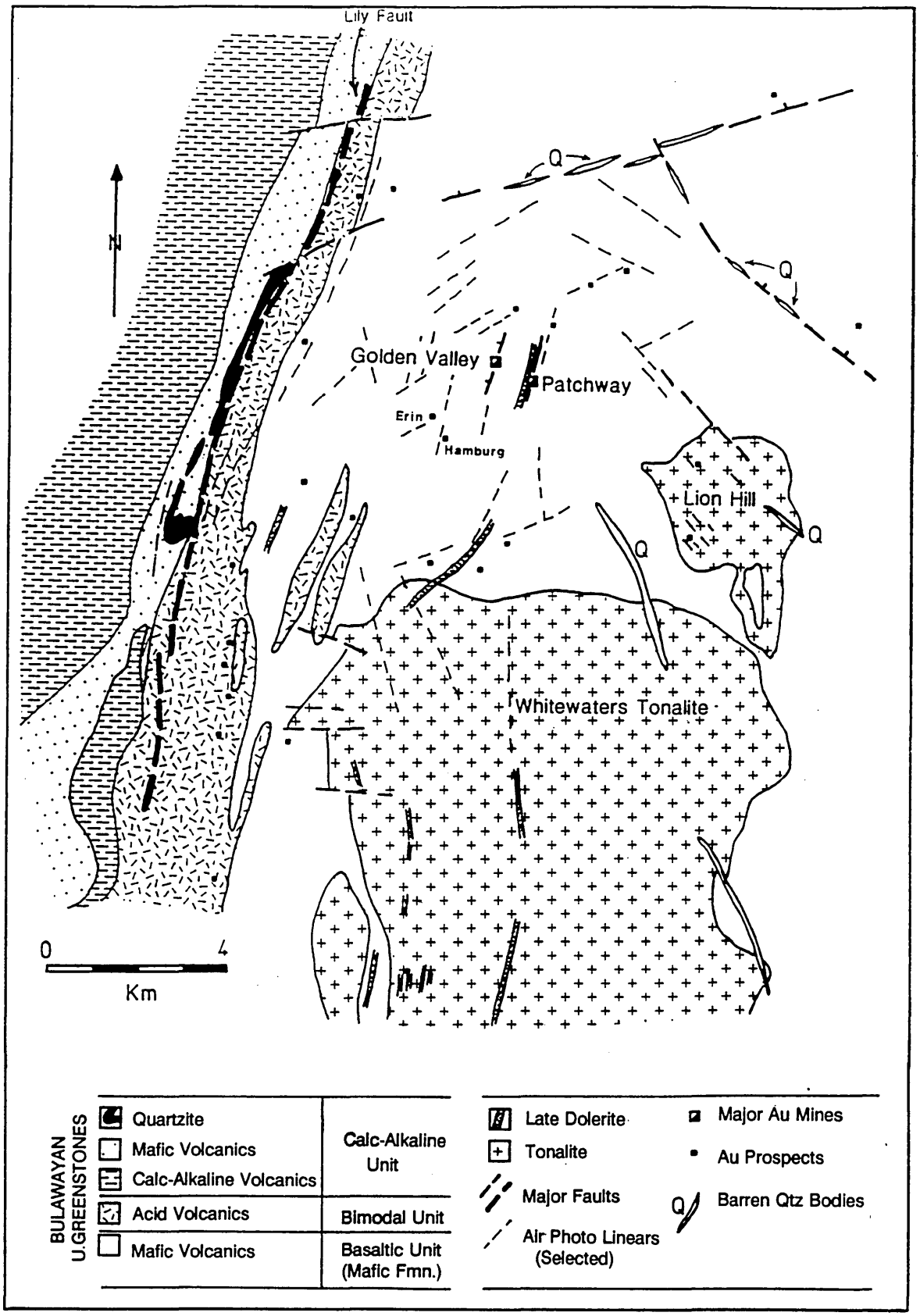


Figure 2.5 - Simplified geology of the Patchway - Golden Valley region (modified with additions from Bliss 1970)

2.6 Description of Gold-Bearing Structures in the Kadoma Region

The gold deposits in the region northwest of Kadoma are almost entirely hosted within vein structures of clearly defined orientations. Figure 2.6 is a sketch map of the area based on the work of Bliss (1970), who compiled data on vein orientations at the various deposits. The mines of Patchway, Golden Valley, Hamburg and Erin are also indicated on Figure 2.6 and the underground development of Patchway and Golden Valley, are detailed on the plan, Figure 2.7. The minor deposits of Basil (3), Hal (4), Rouge (5), New Year (6) and Simba (7) are also indicated. Of these, significant production is recorded only from the Rouge (5) and New Year (6) deposits.

Mineralisation at Patchway is confined to a single complex vein within an envelope of sheared mafic volcanics. Bifurcations and duplications are not uncommon, particularly where the vein hosting shear is also intruded by acid intrusive bodies, locally known as "felsites" (Bliss 1970) (Figure 2.8). The strike of the vein varies from 005° in the south to 025° in the northern part and dip is within the range 25° to 30° westwards. Golden Valley shows a very similar style of mineralisation. Mineralisation at Patchway, Golden Valley and Basil is very similar texturally (Figure 2.9), all forming classic veins of ribboned appearance. At Patchway vein widths rarely exceed 2.5 metres, whilst at Golden Valley 5 metre widths are recorded. The mineralisation at Basil rarely exceeds 1.5 metres in thickness. Where the mineralisation duplicates at Patchway, particularly when acid intrusive dykes are present in the hosting shear zone, an aggregate vein thickness of over 5 metres is known. At Golden Valley, vein duplications are almost unknown with mineralisation restricted to a single, albeit somewhat wider (up to 5 metre width), complex vein. Almost without exception at Golden Valley a felsite intrusive forms the immediate hanging wall to the vein.

The Patchway workings are subdivided into two distinct orebodies, South Orebody (SOB) and North Orebody (NOB). The most extensive, accessible level at Patchway, 10 level, is shown, as a surface projection, on Figure 2.7. Since the bulk of this level is developed within the vein host structure, the workings indicate the strike of the main gold-bearing vein. The Basil mineralisation, can be considered as a parallel structure in the footwall of the NOB. Separating the two, North and South, Patchway orebodies, is a well defined barren zone termed the "Central Shear Zone". The trace of the intercept of this zone with the orebodies are shown clearly as parallel, east-west trending lines on Figure 2.7, forming a loss of mineralisation, some 200 metres wide on all mine levels. An east-west trend alignment of individual mining blocks is a strong feature of other areas of the mine and constitutes one of the two major "payshoot" directions at the Patchway mine. This trend parallels the "Central Shear Zone" and suggests that structure may play a key role in the distribution of economic mineralisation.

In addition to the east-west trend, the NOB shows clearly a break between mineralisation on the upper and lower mine levels. A 100 metre wide "barren" section trending approximately 030° is present and

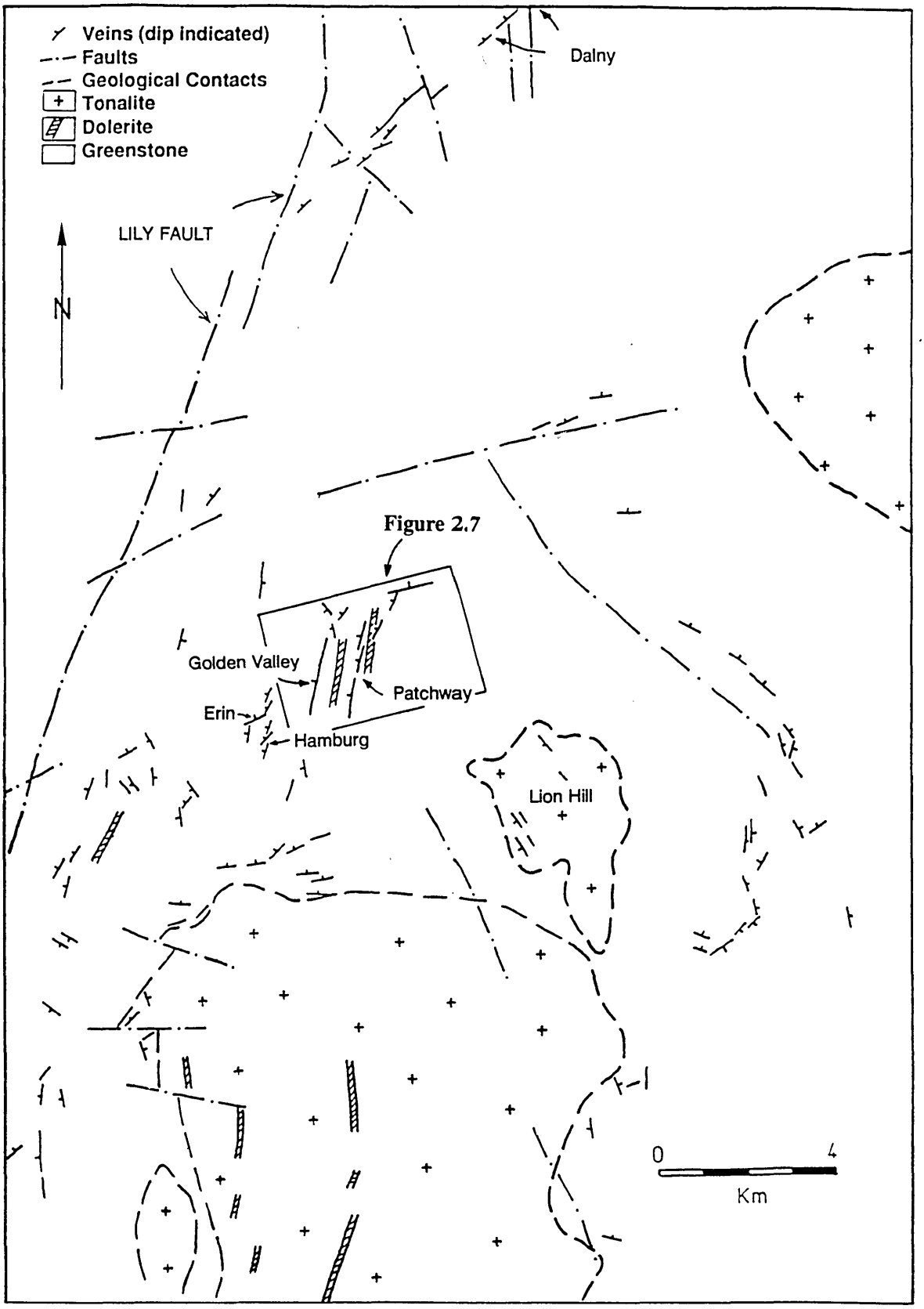


Figure 2.6 - Mineralised structures in the Patchway - Golden Valley region (compiled from Bliss 1970)

FIGURE CAPTION FOR FIGURE 2.7

Patchway mine

1 - South Orebody
2 - North Orebody
3 - Basil Reef

4 - Hal Reef

5 - Rouge Reef

6 - New Year Reef

7 - Simba

Golden Valley mine

8 - Maida Vale
9 - Southern Orebody
10 - Northern Orebody
11 - North Prospect Orebody

N.B. Extra-lateral mineral rights legislation in Zimbabwe permits the mining of a structure outcropping on a mining lease, down dip to any depth, even if the surface projection of the vein is outside the mineral lease. In the case of the Patchway mine, both the North and South Orebodies are currently being mined below the surface projection of the Golden Valley mine workings and mining lease.

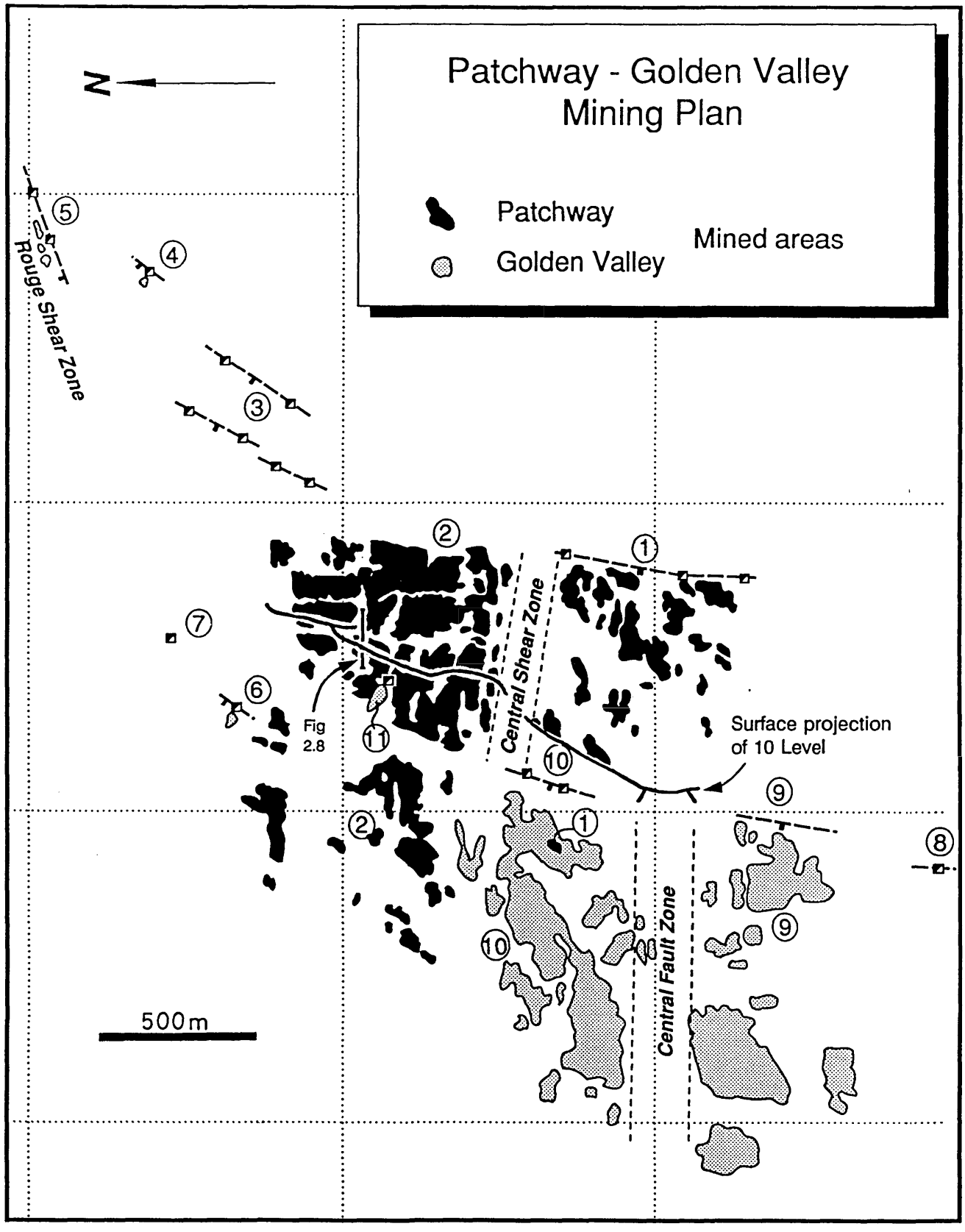


Figure 2.7 - Plan of the Patchway and Golden Valley mineworkings projected to surface. See caption left for explanation
(compiled by the author from mine plans)

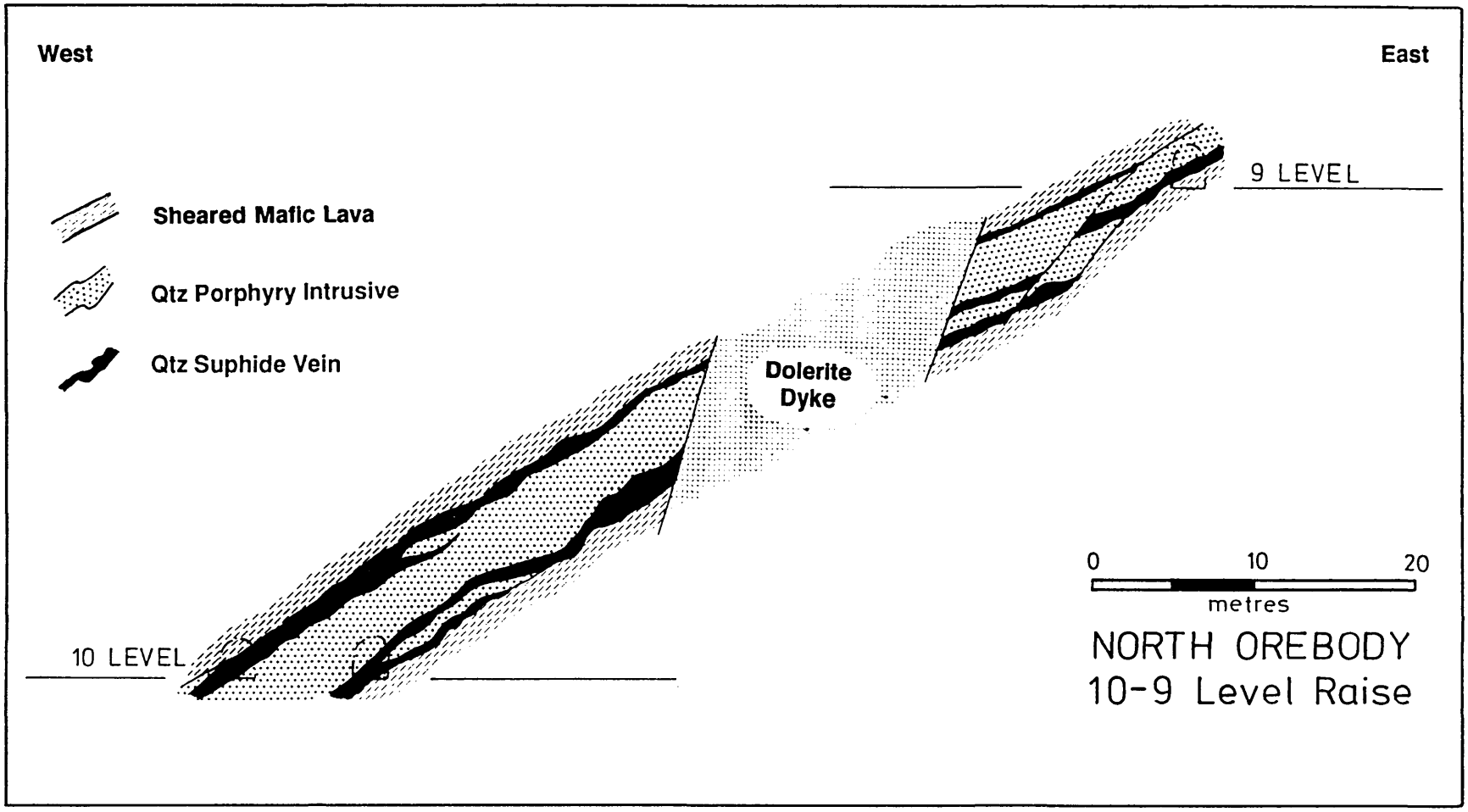


Figure 2.8 - Cross section drawn along Level 10 to 9 raise (Line of section on Figure 2.7). Section clearly shows vein duplication around felsite intrusive body. Also shown is one of the larger dykes intruded into a late fault (showing normal displacement). Vein shows asymmetric boudinage with its axis parallel to this faulting and dyke intrusion.



Figure 2.9 - Typical ribboned quartz veining on 10 Level south, Patchway mine.

this break in mineralisation in the NOB, resulted in production loss at the mine whilst the deeper extensions were developed. In other areas of the mine, minor sub-parallel faults cause disruption to mineralisation and the intercept of these faults and the orebody, constitutes the second "payshoot" trend. Also apparent from the plan, particularly on the upper parts of the NOB, there are a series of roughly north-south trending zones where mineralisation is missing across normal faults, which simply displace the mineralisation. Many of these normal faults are intruded by dolerite dykes (see Figure 2.7).

The Golden Valley orebodies show a very similar spatial pattern to those at Patchway. Most of the production at Golden Valley is from the two orebodies (9) and (10). In a similar pattern to the Patchway "Central Shear Zone", there is a clear, 200 metre wide break between two separate bodies. This ground loss at Golden Valley is the on-strike extrapolation of the Patchway "Central Shear Zone". Again, one of the payshoot trends at Golden Valley is parallel to the almost due east-west intercept of this zone on the dipping orebodies. The Golden Valley mineralisation has further extensions both to the north, and south, of the two main orebodies. North Prospect (11) and Maida Vale (8) are two such extension zones, where limited mining has been carried out. North Prospect appears to be similar mineralisation to the main bodies but is apparently more tectonised (R. Teesdale pers. comm.). There is also some suggestion of the second trend of payshoot being present at Golden Valley, but the lower mine cut-off grade at Golden Valley means that direct comparison is difficult. The deeper levels of the Golden Valley mine have similar fault disruptions to mineralisation to that seen at Patchway, which are associated with late dolerite dykes. The Golden Valley workings have reached one such structure named the "Terminal Fault" at the level of deepest workings. Beneath this fault, no mineralisation has yet been developed despite cross-cutting and drilling.

At the Rouge mine workings (5), the trend of the mineralisation is approximately 070°, dipping some 55° to 60° northwest. Mineralisation style is clearly different to that of the Patchway and Golden Valley veins, being described by Bliss (1970) as:

"schist impregnated with pyrite, pyrrhotite and minor amounts of quartz in lenses and stringers. The zone is normally wide, varying from 44 inches to over 100 inches but the distribution of ore was irregular".

This observation is confirmed by the author's examination of drill logs from diamond drill holes intersecting this structure. The description of mineralisation is somewhat similar to the style and trend of mineralisation displayed at the Erin mine. At Erin, a broad zone of deformation containing strong carbonate alteration, disseminated pyrite and erratic pods of quartz-sulphide veining is developed. This mineralisation style is quite different from the discrete, classic ribbon-veins seen at Patchway, Basil and Golden Valley (Figure 2.9).

Of the other minor deposits, New Year appears from description to resemble the Patchway mineralisation, the vein having a typical ribboned appearance, and has a similar strike (Bliss 1970). The

small orebody was worked in the early 1960s as part of the Patchway operations. Since the workings are now inaccessible, this deposit was not examined.

2.7 Summary

The gold deposits of the Patchway region are all hosted in mafic lavas of the ca.2700Ma (Moorbath *et al.* 1987) Upper Greenstone sequence of the Bulawayan Group. The environment of deposition is interpreted as a "rift" setting (Foster 1985), although little tectonic disturbance is indicated during formation. The Upper Greenstones are flanked by the overlying Bimodal, mixed volcanic sequence, together with much younger Calc-alkaline volcanics to the west and older, 3580 Ma (Hawksworth *et al.* 1975) tonalitic gneisses in the east.

Later tonalitic granites, dated at 2700 Ma (Wilson 1979), intrude the greenstone sequence, and thin, possibly associated, felsite intrusives are common at all the mines.

The location of major Archaean, greenstone gold deposits in distinctive structural settings is ubiquitous (Gee 1979, Colvine *et al.* 1984, Vearncombe *et al.* 1988), and Zimbabwe is no different with over 80% of gold production from structurally contolled veins, or lode deposits (Foster 1989). The gold deposits of the Patchway region fall into the lode category of deposit. The further relationship of the gold deposits of the region with the Upper Greenstone Unit of the Bulawayan is notable. Gold deposits hosted in this unit, dominated by Fe-rich lavas, accounting for 38% of Zimbabwe's gold production (Foster *et al.* 1986).

The structural framework of the Zimbabwe Craton is dominated by the evolution of the ca.2700 Ma Limpopo Belt (Coward 1976). Strongly developed, major shear-zones initiated at this time (Stowe 1974, Coward *et al.* 1976, Pitfield & Campbell 1989). These major shear-zones focussed strain, which evolved from pure N-S compression, to lateral secretion of the main Rhodesdale gneiss block westwards. Late locking-up of the structures resulted in the Popoteke fault set, precursors to the fracturing hosting the Great Dyke (Wilson & Prendegast 1989).

Mineralisation in the Patchway region is entirely hosted in discrete veins within shear-zones which show two clear 020/30W and 070/60N trends. These structures show clear evidence for a complex structural history, which undoubtedly relates to the structural evolution of the craton.

CHAPTER THREE - PETROLOGY AND MINERAL CHEMISTRY

3.1 Introduction

This chapter addresses the petrology and chemistry of the host rocks to the mineralisation. The main aim is to characterise the original mafic-volcanic host-rock lithotypes, together with the various acid and basic intrusives. A suite of samples was taken from rocks believed to represent least altered examples of the original lithofacies. However, it is clear that the whole sequence has undergone sea-water reaction, regional deformation, metamorphism to lower greenschist facies and some degree of alteration is ubiquitous.

Archaean supracrustal sequences all appear to have fairly complex patterns of hydrothermal history (Barley & Groves 1987). Barley & Groves (1987) suggest, a three part division of alteration types in such sequences: i) synvolcanic and diagenetic hydrothermal alteration (together with burial metamorphism), ii) regional metamorphism during deformation and granitoid emplacement and iii) hydrothermal alteration around large scale faults. Such effects are the result of processes summarised in Figure 3.1, where the link between processes and alteration are summarised.

Intensive hydrothermal alteration (metasomatism) is a characteristic of many Archaean gold deposits (Ludden *et al.* 1984, Roberts 1987, Colvine *et al.* 1988, Groves & Foster 1990). Such metasomatism leads to dramatic chemical and mineralogical change marginal to mineralisation, overprinting the original chemical and mineralogical composition. Samples were taken from the highly deformed zone marginal to the mineralisation at Patchway, in order to assess any metasomatism during the deformation and mineralisation event.

3.2 Methodology

Representative samples for characterisation of the least altered lithotypes were chosen for study. For the mafic lavas, the samples were restricted to underground cross-cuts developed away from mineralisation into "barren", undeformed rocks. Two traverses across the main mineralised structure, into undeformed lava, were also made in order to define any alteration effects around the vein-hosting shear-zone. Sample locations and descriptions for all the samples discussed are in Appendix I.

Representative samples were also examined in polished thin section, by both transmitted light microscopy and scanning electron-microscope (SEM). Use of the SEM also allowed electron microprobe analyses (EMPA) of mineral phases in the polished thin sections. Equipment used and operating conditions are detailed in Appendix II. Stoichiometric calculations of mineral chemistry were performed using the MINFILE MS-DOS software package (Affifi & Essene 1988).

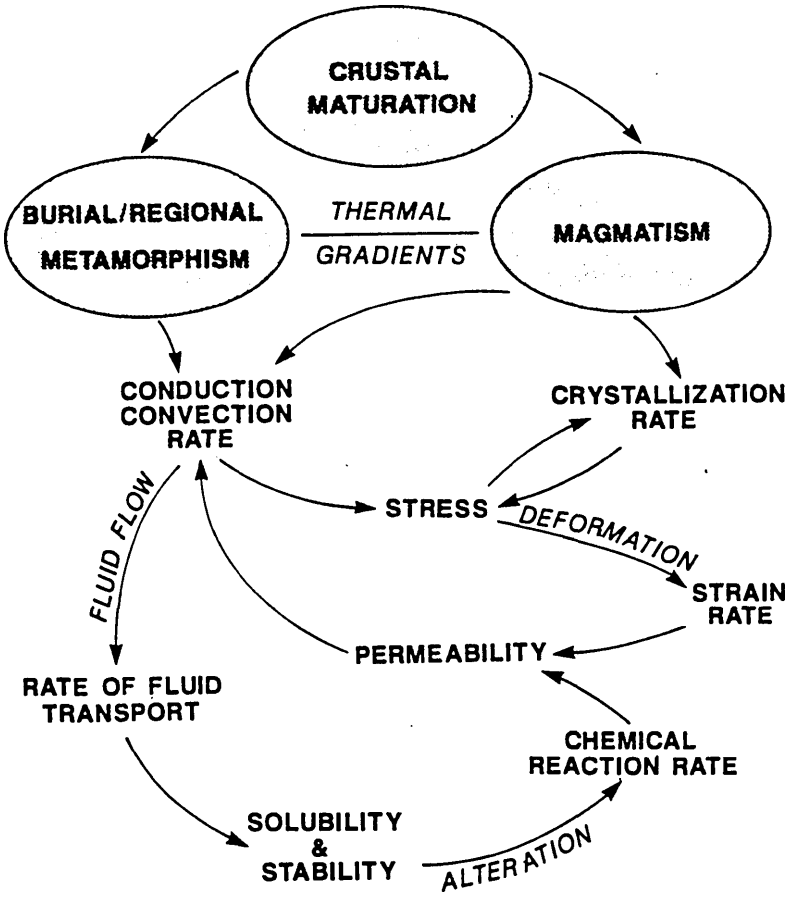


Figure 3.1 - Diagram showing links between deformation, alteration and possible driving processes (after Norton 1984)

Analysis of whole rocks were also performed by inductively-coupled-plasma atomic-emission-spectroscopy (ICP-AES) and X-Ray fluorescence spectroscopy (XRF) at the British Geological Survey facility in London. The methods for both these analytical procedures is outlined in Appendix III.

3.3 Mine Host Rock Petrography

3.3.1 Mafic Flow Rocks

The rocks of the Basaltic Unit at Patchway are almost entirely flow rocks. Pillow lavas are common with pillows of generally 30 to 50 cms. in diameter. Pillow margins are often clearly defined by a thin, light yellow-green, carbonated zone. Tri-cuspate carbonate-chlorite-epidote segregations are frequently seen at the pillow junctions. Flow-top breccia textures are well preserved in less deformed areas. In addition to the pillow lavas, massive lavas form the bulk of the remaining host rocks.

The rocks are aphanitic, fine grained microcrystalline and are generally light to olive green in colour. The rocks show some alteration at pillow margins where they develop an apple green hue due to the presence of epidote. Well developed pillow margins, flow-top breccias and tri-cuspate infillings of quartz, carbonate and epidote are preserved in many places (Figure 3.2). In thin section it is evident that the rocks have been metamorphosed to lower greenschist facies. Metamorphism has resulted in replacement of plagioclase, pyroxene and olivine by actinolite, epidote, chlorite, albite, sericite and carbonate.

Deformed Lava

Marginal to mineralisation, the mafic lavas are strongly deformed with a clearly defined penetrative fabric. Thin section study of samples taken marginal to mineralisation demonstrates a crudely defined zonation of rock mineralogy from the vein margin to undeformed mafic lava. This can be broken down into two subdivisions based on hand specimen and complimentary thin section study.

a) Pyritic Zone

Mafic rocks in the zone up to 0.5m immediately adjacent to the vein form the most highly deformed facies of the mafic lavas. Pyrite is strongly developed as generally cubic grains, up to 3mm in size, with pressure shadow fibre trails evident in thin section (Figure 3.3). Pyrite can comprise up to 25% of the rock by volume (Figure 3.4). Thin sections indicate the complex relationships of the Fe-bearing phases (Figure 3.5).

The pyrite zone also commonly contains veinlets of quartz-carbonate-sulphide, mostly developed sub-parallel to the main vein fracture. The included wallrock slivers are mineralogically identical to the



Figure 3.2a - Well formed pillow lavas on 10 Level South (south-western limit of workings). Pillow rims show evidence of epidotisation, pillow cores show ovoid quartz infillings. Pillows here are clearly the right way-up.



Figure 3.2b - Close up of Fig 3.2a showing pillow margin infilling and flow-top breccia. White area is coarse quartz-carbonate infilling (quartz stage Q1 - Chapter 7) with yellow-green epidote clots.

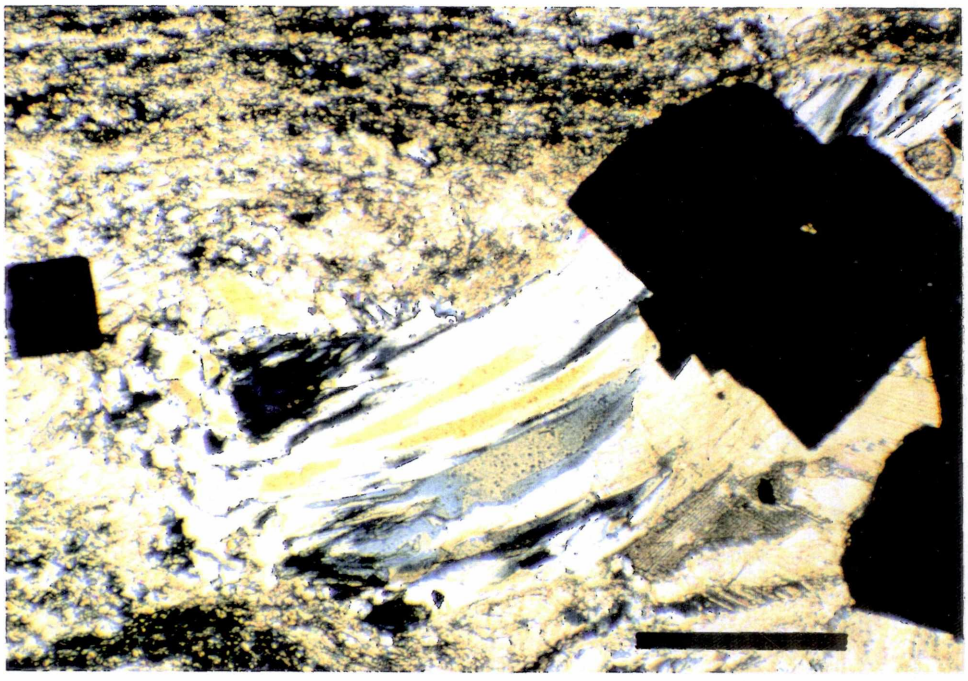


Figure 3.3 - Pyrite cubes developed in deformed mafic lava marginal to the gold quartz vein on 10 Level North (Sample 10-29). Arcuate pressure shadows comprising quartz fibres are apparent. Late buff carbonate infills close to the pyrite grain bottom right. Scale bar = 0.5mm.



Figure 3.4 - Highly pyritic wallrock, immediately adjacent to the gold-quartz vein studied in detail on 6 Level North (see Fig. 4.16). Wallrock here is also highly silicified with abundant quartz segregations (upper left). Section of tape = 10cm.

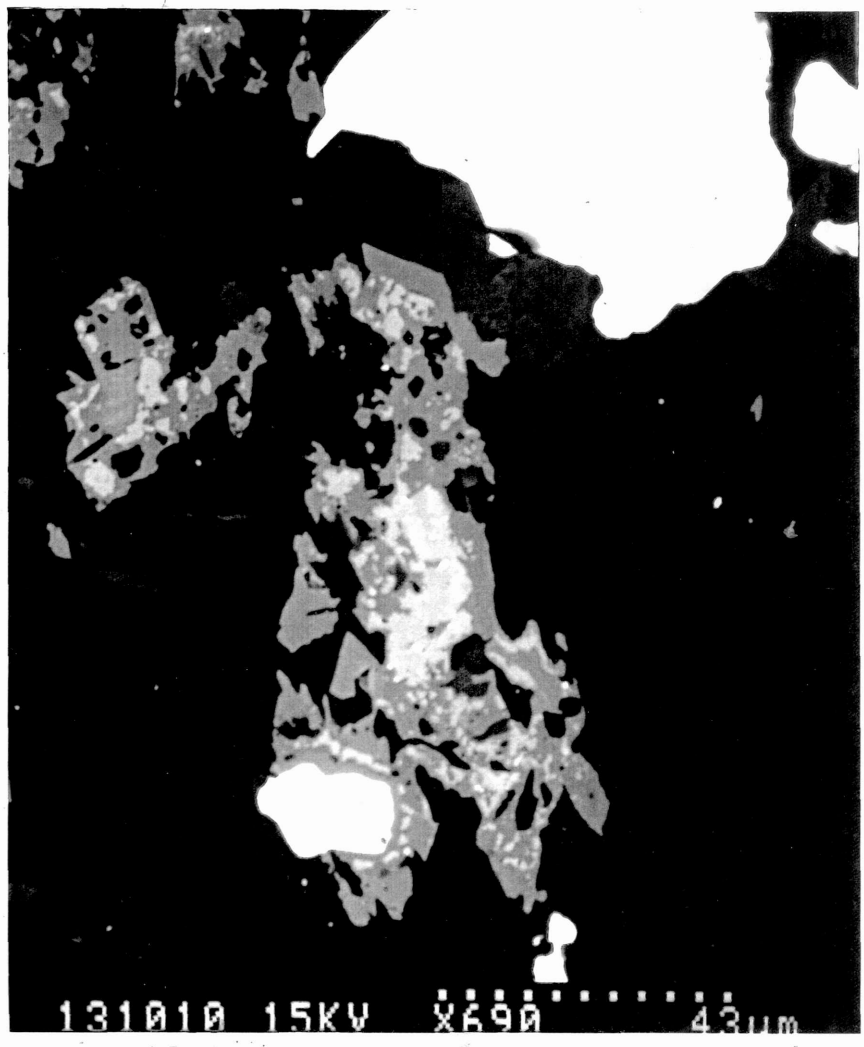


Figure 3.5 - High-contrast backscattered SEM image from sulphide rich wallrock marginal to gold-quartz ribbon vein (Sample 30-1). Image shows complex relationships of Fe-bearing phases. Phases identified are, from brightest to darkest: Pyrite, forms large white grains; Rutile, forms light grey, fairly amorphous areas; Sphene, comprises grey areas enclosing rutile, often euhedral grain-boundaries seen; chlorite, darker grey area between largest pyrite grain and mass of sphene; Sericite, darkest grey area , forms >50% of field; Quartz, black areas. Scale: as shown on scale bar (43 μm)

deformed mafic rocks in the pyritic zone around the vein, and thus can be considered to belong to the pyritic zone.

b) White Mica (Muscovite)-Chlorite-Carbonate Zone

This zone includes the pyritic zone which differs only by its increased sulphide content and the often dominant silica-carbonate laminae and veinlets. Zone b) is characterised by well aligned phyllosilicate grains which form the strong continuous foliation, which is clearly seen in hand specimen (Figure 3.6). Original textures such as pillow margins are often preserved, although heavily deformed (Figure 3.7), even close to the vein fracture. Although less frequent than in zone a), quartz-carbonate-sulphide stringers are still present, usually as thin, often highly deformed, laminae parallel to the foliation. In thin section, fine grained sericite, chlorite, carbonate and quartz are the dominant phases. The minerals frequently segregate into distinct domains, with phyllosilicate rich cleavage bands dividing quartz-carbonate micro-lithons (Figure 3.8). Later coarse carbonate is common. Pyrite commonly occurs as up to 2mm idioblastic grains and as laminate clusters of smaller grains. Rutile and sphene are common, the former as small grains frequently associated with irregular aggregates of the latter.

Lastly, the mafic lava sequence also contains numerous, minor, unmineralised shears. These shears can be seen underground (Figure 3.9). Such shears are not related to gold bearing veins and show some mineralogical differences to the deformed rocks marginal to the gold veins. In thin section these foliated rocks comprises albite, epidote, white mica, chlorite and carbonate. Although some white mica (muscovite) is developed, some tremolite-actinolite is still preserved. Ilmenite is still present together with minor sphene. No original pyroxene is preserved.

Electron Microprobe Data

Microprobe analysis was carried out on minerals in the mafic lavas, in order to establish mineral chemistry. Attention was focussed on chlorite, since this mineral is abundant in all lithotypes examined. Chlorite is a potential mineral geothermometer (Cathelineau 1988) and this might help establish ambient temperature of formation. The other minerals investigated were white mica (muscovite), carbonate, epidote and sphene. The feldspar phenocrysts in the less deformed mafic lava were also analysed.

a) Chlorite

Chlorite normally conforms to the formula $A_6B_4O_{10}(OH)_8$ (Deer *et al.* 1966), where A refers to the "O" (octohedral) site which may be filled by Al(VI), Ti, Fe^{3+}, Fe^{2+}, Mn^{2+}, Mg, Ca, Na or K. B refers to the "T" (tetrahedral) site which is filled by Al(IV) or Si(IV).

Recent studies of active geothermal areas has indicated the use of relative contents of Al(IV) in the T site as an empirical geothermometer (Cathelineau 1988). His work in the range 130 to 310° C indicates a strong linear relationship between temperature and Al(IV) and data from other geothermal field

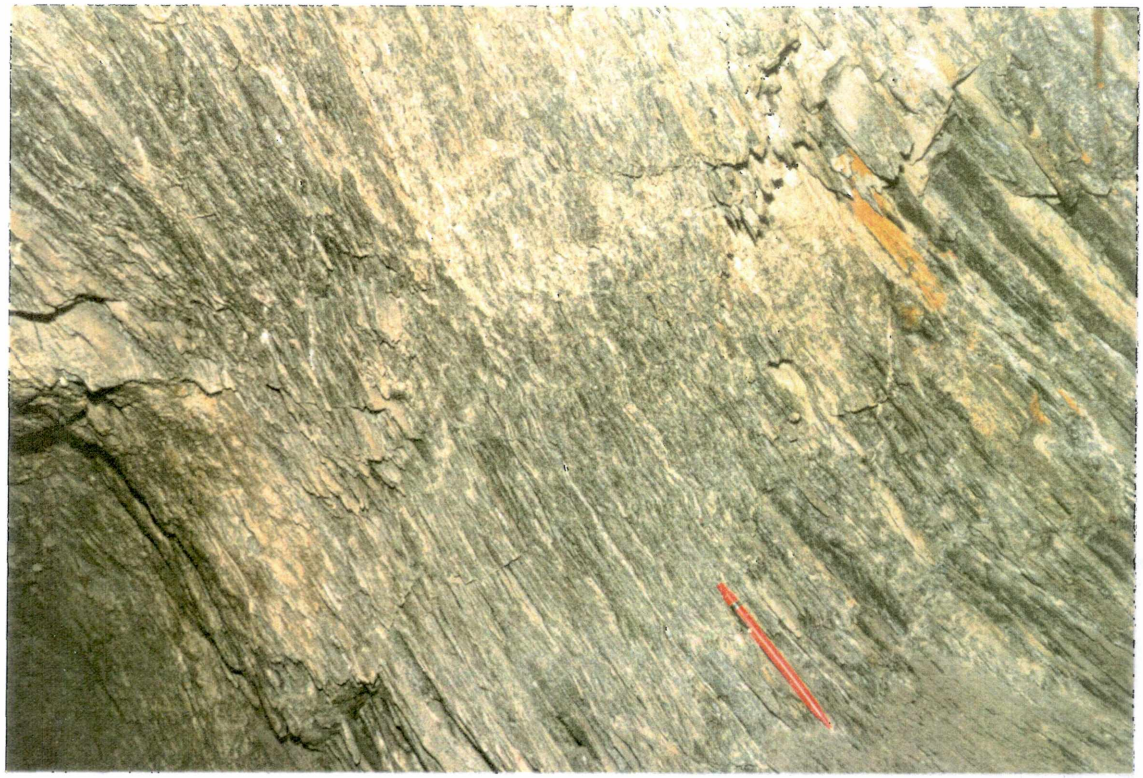


Figure 3.6 - Well deformed mafic lava, 1.5m (true thickness) into the hanging wall of the gold-quartz vein on 22 Level North. Photograph shows the typical, well foliated nature of the lava close to the vein (pen 12cm long).



Figure 3.7 - Deformed lava on 22 Level, 4m (true thickness) into the hanging wall of the gold-quartz vein. Relict pillow texture is still visible (acute V-shaped grey banding, traversed by pen), despite moderate deformation. Pen 12cm long.



Figure 3.8 - Photomicrograph of strongly deformed wallrock marginal to gold-quartz mineralisation on 10 Level North (Sample 10-22). Sample shows thin, deformed quartz veinlet (centre), surrounded by phyllosilicate rich domains with a strong planar fabric. Scale disk = 5mm diameter



Figure 3.9 - Carbonate rich unmineralised shear zone on 15 Level South. Shear contains no sulphides and only minor quartz although developed sub-parallel to the main mineralised vein.

suggests that extrapolation to temperatures above 350°C is valid. Substitution into the O site is largely dependent upon chemistry, although Bryndzia & Scott (1987) have shown that fS_2 and fO_2 may play a role in the Mg^{2+} : Fe^{2+} ratio, largely due to the incorporation of Fe^{2+} into pyrite under high fS_2 conditions, and a similar incorporation of Fe into magnetite under high fO_2 conditions.

Chlorite was examined from undeformed lava, highly deformed lavas close to the mineralised vein and chlorite actually from the the vein itself where gold intimacy was demonstrated. These data are summarised in Table 3.1, with all normalisation calculations (including stochiometric substitutions) performed using MINFILE.

From the work of Cathelineau (1988), the empirically derived formula of :

$$T(°C) = -61.92 + 321.98 \times [Al\ (IV)]$$

permits calculation of formation temperature. The generated results are tabulated in Table 3.2 for the various chlorite types. The range of data for the chlorite from undeformed lavas is from 350° to 360°C and is consistent with formation under greenschist facies metamorphic conditions. The results from the chlorites probed in deformed lavas collected marginal to mineralisation show a higher temperature range between 380° and 400°C. Lastly, the data for the chlorite intimate with gold grains in samples show a narrow Al (IV) range from 1.30 to 1.37, indicative of temperatures in the range 357° to 379°C.

All Fe analyses for chlorite are reported as Fe^{2+}, as discrimination between oxidation state is not possible by EMPA techniques. Iron, quoted as Fe^{2+} here, shows some distinct variation. The chlorite directly co-existing with gold grains is clearly different to both the other chlorite types, the vein chlorite being more Fe^{2+} rich (Figure 3.10). For the other two associations, the chlorite from the deformed lavas appears to have a higher Fe^{2+} content than the chlorite from the undeformed lava.

b) Sericite

The analyses of sericite are from samples believed to be representative of deformed lavas. These data are summarised in Table 3.3, and from this an approximate average formula can be determined:

$$Na_{0.1}K_{1.9}(Al_{3.3}Fe_{0.3}Mg_{0.4})(Si_{6.2}Al_{1.8})O_{20}(OH)_4$$

This clearly indicates the dominance of potassium over sodium in the mica, and thus it is clearly of muscovite composition.

c) Pyrophyllite

The analysis of some of the fine grained white phyllosilicate in the groundmass of the same highly deformed samples indicated the presence of pyrophyllite. EMPA data is shown in Table 3.4, indicating a fairly ideal composition, with only minor substitution of alkalis.

Sample	10-25 (n=10) (A)	20-14 (n=8) (B)	10-29 (n=16) (C)	18-26 (n=12) (D)	10-2 (n=14) (E)
wt% oxide					
SiO_2	24.49	24.21	24.72	26.38	26.83
TiO_2	0.01	0.01	0.05	0.08	0.05
Al_2O_3	21.26	23.53	21.77	21.81	20.55
Fe_2O_3	0.00	0.00	0.00	0.00	0.00
FeO	35.81	25.79	27.95	25.28	22.31
MnO	0.31	0.27	0.18	0.26	0.34
MgO	7.57	13.87	13.50	16.35	18.41
CaO	0.08	0.00	0.04	0.05	0.21
Na_2O	0.21	0.17	0.47	0.39	0.57
K_2O	1.48	0.04	1.14	0.71	2.17
H_2O	10.83	12.04	11.25	11.47	11.50
Total	102.04	99.90	101.06	102.79	102.94
no. of atoms					
Si(IV)	2.65	2.55	2.60	2.68	2.71
Al(IV)	1.35	1.48	1.31	1.28	1.16
Al(VI)	1.36	1.48	1.31	1.28	1.16
Ti	0.00	0.00	0.00	0.01	0.00
Fe^{3+}	0.00	0.00	0.00	0.00	0.00
Fe^{2+}	3.25	2.27	2.46	2.14	1.88
Mn^{2+}	0.03	0.02	0.02	0.02	0.03
Mg	1.21	2.18	2.12	2.47	2.77
Ca	0.00	0.01	0.00	0.01	0.02
Na	0.04	0.03	0.10	0.08	0.11
K	0.20	0.00	0.15	0.09	0.28
O	10.00	10.00	10.00	10.00	10.00
OH	8.00	8.00	8.00	8.00	8.00

Table 3.1 - Chlorite EPMA analyses for different associations. A and B types are from ribbon quartz veins. A = chlorite intimate with Au, B = chlorite intimate with scheelite. C and D are chlorites from deformed vein margin lavas. E is chlorite from undeformed lava.

Sample	Chlorite type	$\bar{x}$ Al(IV) [range]	$\bar{x}$ Temperature (°C) [range]
10-25	Vein - Au adjacent	1.35 [1.30 - 1.42]	372.8 [356.7 - 395.3]
20-14	Vein - scheelite adjacent	1.45 [1.39 - 1.49]	405.0 [385.6 - 417.8]
20-12	Vein - stylolite sulphides	1.34 [1.32 - 1.35]	369.5 [363.1 - 372.8]
10-29	Vein margin wallrock	1.40 [1.20 - 1.47]	388.9 [324.5 - 411.4]
18-26	Vein margin wallrock	1.32 [1.28 - 1.38]	363.1 [350.2 - 382.4]
10-2	Undeformed lava	1.29 [1.18 - 1.40]	353.4 [318.0 - 388.9]

Table 3.2 - Calculated geothermometry from chlorite analyses in Table 3.1.

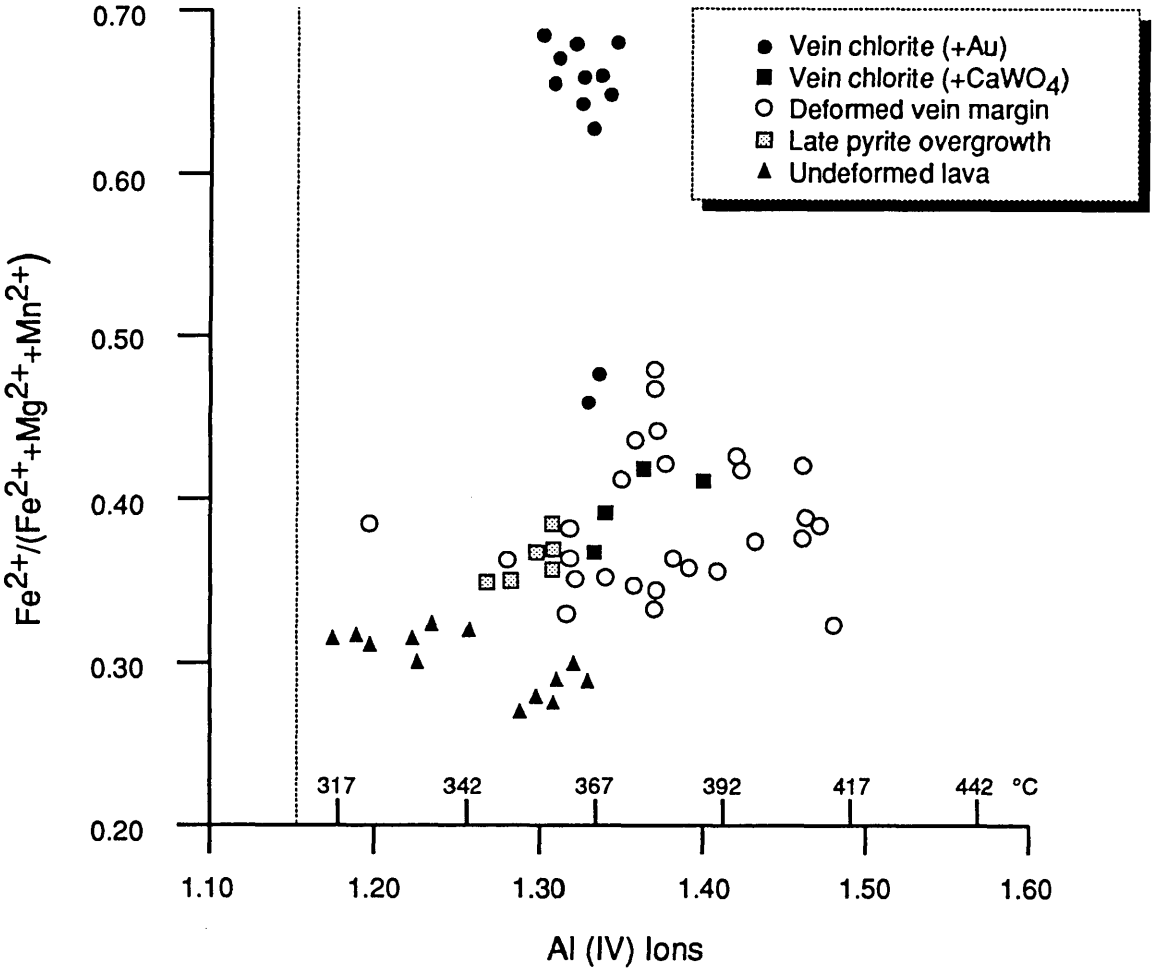


Figure 3.10 - Graphic presentation of Fe^{2+}/total $^{2+}$ ions versus Al (IV) ions, both calculated from stoichiometry using MINFILE (Affifi & Essene 1988). Also shown on the X-axis is the geothermometer calculated on the basis of Al (IV) atoms (Cathelineau 1988). Dotted verical line represents upper limit of precise calibration of thermometer (310° C), although extrapolation above 350° C seems valid (Cathelineau 1988).

Sample	10-25 (n=5) (A)	20-12 (n=5) (B)	18-26 (n=4) (C)
wt% oxide			
SiO_2	46.26	47.61	48.28
TiO_2	0.39	0.37	0.39
Al_2O_3	32.33	33.90	33.42
Fe_2O_3	0.00	0.00	0.00
FeO	2.51	1.81	2.00
MnO	0.00	0.00	0.00
MgO	0.89	1.19	1.46
CaO	1.52	0.18	0.22
Na_2O	0.31	0.34	0.44
K_2O	10.56	11.14	11.46
H_2O	4.48	4.49	4.49
Total	98.51	101.03	102.16
no. of atoms			
Si(IV)	6.31	6.29	6.37
Al(IV)	1.69	1.72	1.62
Al(VI)	3.51	3.57	3.48
Ti	0.04	0.03	0.03
Fe^{3+}	0.00	0.00	0.00
Fe^{2+}	0.29	0.20	0.22
Mg	0.18	0.24	0.28
Ca	0.08	0.02	0.03
Na	0.08	0.09	0.11
K	1.84	1.89	1.92
O	20.00	20.00	20.00
OH	4.00	4.00	4.00

Table 3.3 - EPMA analyses of sericite grains. Type A sericite is intimate with Au grains, type B associated with ribbon vein sulphides and type C from deformed lava at the vein-wallrock margin.

d) Carbonate

Data from the limited analyses of carbonate in both deformed and undeformed lavas is summarised in Table 3.5. The carbonate is shown to be calcite with only minor substitution of iron, magnesium and manganese.

e) Epidote

Analyses of epidote in the deformed lavas are summarised in Table 3.6. From this an average composition can be calculated :

$$Ca_2(Al_{2.5}Fe_{0.5})Si_3O_{12}(OH)$$

This lies well within the field for typical epidote in the clinozoisite-epidote series.

f) Sphene

Sphene is very common in the deformed lavas, particularly notable in samples adjacent to the main vein. In most cases sphene is probably the product of the breakdown of original ilmenite to rutile, the sphene accommodating calcium released during breakdown of epidote. This is supported by the common intimacy of rutile and sphene (Figure 3.5). Microprobe analyses are summarised in Table 3.7, where the mean is seen to define a mineral formula close to a low-iron sphene, with minor substitution of Fe and Al for Ti.

g) Albite

Feldspar suspected to be albite has only been seen in undeformed lava samples, and probe analysis of selected grains in the undeformed mafic lava was carried out to confirm chemistry. Table 3.8 confirms that it is close to being an end member albite, with minor Fe substitution for Al.

3.3.2 Intrusive "Felsites"

Within the mafic lithologies of the mine sequence are a series of more felsic units. These units by their distribution and morphology are most probably sills or dykes, but vary in their texture and fabric. The widely accepted mining term for these units is "Felsite" but they vary from quartz porphyry units to aphanitic massive units to quartz sericite schists. Colour is quite variable from grey quartz porphyry to buff-grey massive units to buff, waxy looking, well foliated schists. These intrusives are laterally relatively continuous, intercepting the main mineralised shear zone trend at a low angle, almost sub-parallel to the trend of the main mineralisation. Some of the bodies have undergone the same deformation features as the mafic lava wallrock within the mineralised shear zone, although some clearly post date these events. The intrusives may be linked to the more extensive diapiric intrusive suite seen regionally. Age relationships with regard to the mineralisation indicates intrusion both prior to and post-dating mineralisation. Figure 3.11 shows these relationships which might point to a close temporal association with the intrusives and gold mineralisation.

wt% oxide	10-25 (n=8)
SiO_2	60.60
TiO_2	0.25
Al_2O_3	32.01
FeO	0.20
MnO	-
MgO	0.30
CaO	0.10
Na_2O	0.35
K_2O	0.00
Total	93.81
H_2O	5 - 7

Vein pyrophyllite (associated with Au)

Table 3.4 - EPMA analyses of pyrophyllite grains in gold-bearing vein sample (10-25). H_2O content shows general range for published analyses (Deer *et al.* 1966).

wt% oxide	10-29 (n=4)	10-25 (n=10)
FeO	0.62	0.43
MnO		-
MgO	0.24	0.38
CaO	55.85	57.83
Total	56.71	58.64
CO_2 (est.)	44	42

Carbonate analyses
10-29: deformed wallrock groundmass
10-25: vein (associated with Au grain)

Table 3.5 - EPMA analyses for carbonate from gold-bearing vein and deformed wallrock. CO_2 values are purely estimates.

Sample	10-18 (n=10) wt%	18-10 (n=7) wt%
SiO_2	38.56	39.84
TiO_2	0.07	0.16
Al_2O_3	25.80	28.44
Fe_2O_3	10.06	6.89
Mn_2O_3	0	0
FeO	0.01	0
MnO	0.12	0.06
CaO	23.43	24.20
Na_2O	0.04	0.01
H_2O	1.91	1.96
Total	100.00	101.57

Table 3.6 - Analyses of epidote from deformed vein margin lavas.

Sample	18-10 (n=8) wt%	18-26 (n=5) wt%
SiO_2	32.48	30.23
TiO_2	33.53	38.70
Al_2O_3	5.12	1.42
CaO	27.52	28.65
FeO	0.70	0.61
MgO	0.52	0.18
Cr_2O_3	0.26	0
Total	100.13	99.79

Table 3.7 - Analyses of sphene from deformed vein margin lavas.

Sample	10-2 (n=5) wt%	13-1 (n=4) wt%
Na_2O	10.97	10.41
SiO_2	68.20	67.70
Al_2O_3	19.74	18.76
FeO	1.01	1.76
CaO	0.53	0.64
Total	100.45	99.27

Table 3.8 - Analyses of albite in undeformed lavas.

Figure 3.11A - Felsite in footwall to gold-quartz vein on 28 Level North. Highly sheared footwall felsite has suffered the same degree of deformation as the sheared hanging wall mafic unit. Both units contain disseminated sulphides developed during mineralisation and so the felsite is interpreted as pre-dating much of the deformation and mineralisation. Late extension veining cuts both the brittle ribbon vein and felsite footwall but does not extend into the more ductile mafic hangingwall.

Figure 3.11B - Felsite exposed on 4 Level North cross-cut. The highly deformed felsite unit occurs within a narrow shear-zone in deformed mafic lavas. Both host lavas and felsite are highly sheared, but no gold-bearing mineralisation is developed.

Figure 3.11D - Thin felsite intrusion on Main Haulage Drive, Golden Valley. Here the thin buff felsite (20cm wide) is clearly seen to cut both deformed mafic lavas and ribbon vein mineralisation. The felsite here is interpreted as post-dating the bulk of deformation and gold-bearing mineralisation.

Figure 3.11C - Thin felsite intrusion on 15 Level North, hand specimen (black bars are 1 cm long). In this sample the thin felsite dykes are intruded syn-tectonically into deformed mafic lava. The felsite clearly fills two distinctly different planes at this scale, which are interpreted as conjugate planes or Riedel fractures developed during strike-slip shearing which closely accompanied mineralisation (sample viewed looking east, up-dip, perpendicular to the strike of the host shear-zone).







C



In thin section the undeformed dykes are finely crystalline aphanitic rocks, with ubiquitous quartz phenocrysts up to 0.5mm in diameter. The dykes also contain K-feldspar phenocrysts which are often saussëritised. White mica is a common alteration product together with minor carbonate. Chlorite forms clusters, apparently after primary hornblende which was detected in one sample. Fine plagioclase is common in the matrix.

The "felsite" intrusive bodies close to mineralisation are deformed in similar fashion to the mafic lavas. These rocks are also quite distinctly foliated, with a continuous cleavage developed. In hand specimen the rocks develop a buff waxy colouration, largely due to the abundant phyllosilicates developed on cleavage surfaces. Pyrite is common, forming up to 5% of the rock by volume in intensely altered zones. The ubiquitous quartz phenocrysts seen in the undeformed intrusives elsewhere are preserved even in quite deformed and altered rocks, and these behave as porhyroclasts in places, defining a poorly developed stretching lineation (see Chapter 5).

3.3.3 Regional Tonalite Intrusives

Samples from the Whitewaters tonalite body exposed southeast of Patchway in a roadstone quarry were examined. The rock is a medium grained, leucocratic, grey unit with a granitic texture (Figure 3.12). Feldspar is visible in hand specimen, up to several millimetres in length. Plagioclase, microcline, quartz and brown biotite are readily visible in thin section (Figure 3.13), together with more minor hornblende, epidote and iron-oxides. Deformation and alteration in this rock type was only noted around minor quartz-scheelite veins developed in the Lion Hill satellite body of the Whitewaters tonalite body (Figure 3.1). Here abundant white mica in rocks marginal to the veins is testament to some limited retrograde alteration but this was not examined in detail.

3.3.4 Mafic Dykes

The mine is characterised by a series of mafic intrusive bodies, which by their morphology, and field relationships, indicate that they are dykes. In general they are much younger than the other mine lithologies and are seen to cut all the mafic and felsic units as well as the mineralisation. Ward (1968) noted the presence of mafic dykes, pre-dating mineralisation, in the upper levels of the south orebody at Patchway. There was no access to this area, and so the relationship could not be examined.

A number of these dykes were examined underground and appeared quite similar in composition, with minor differences in texture. All the dykes examined in this study show cross-cutting relationships with the mineralisation, although some post-dyke deformation of both vein and dyke can be seen in places. Contacts with wallrocks are sharp with thin chill-margins (Figure 3.14).

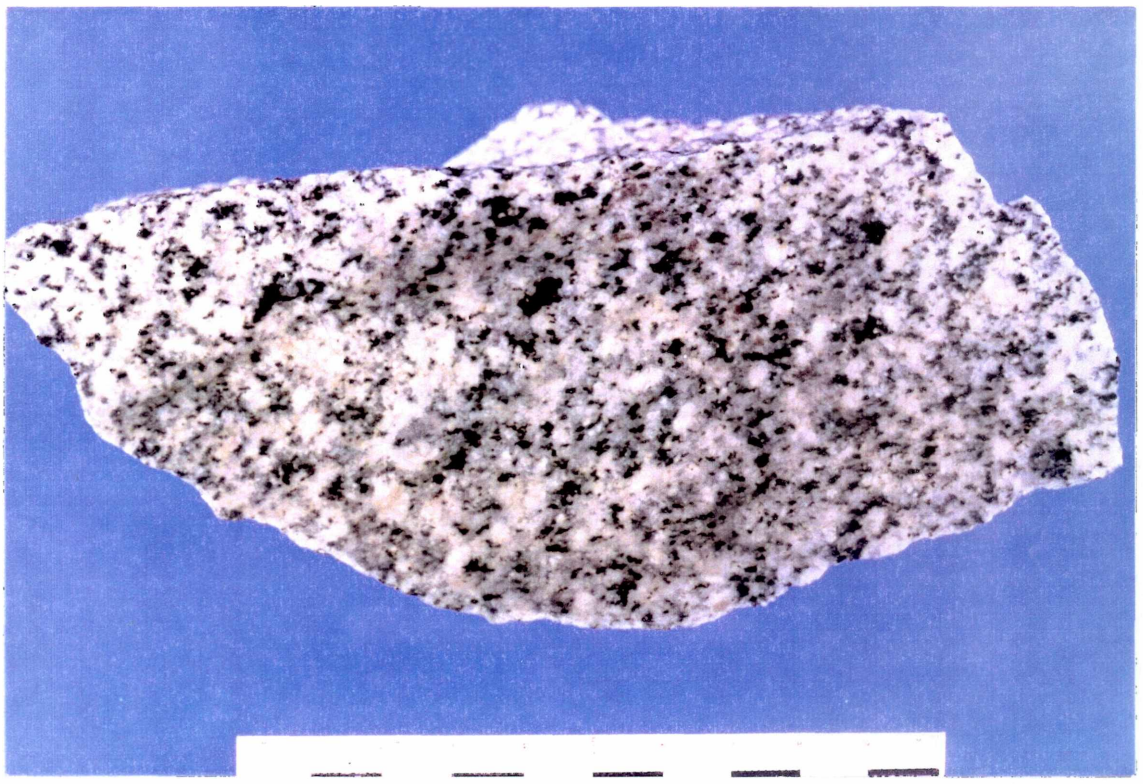


Figure 3.12 - Photograph of hand specimen of the Whitewaters tonalite body (see Figure 2.5). Coarse white feldspar laths are visible together with coarse brown-black biotite aggregates (Black scale bars are 1 cm long).

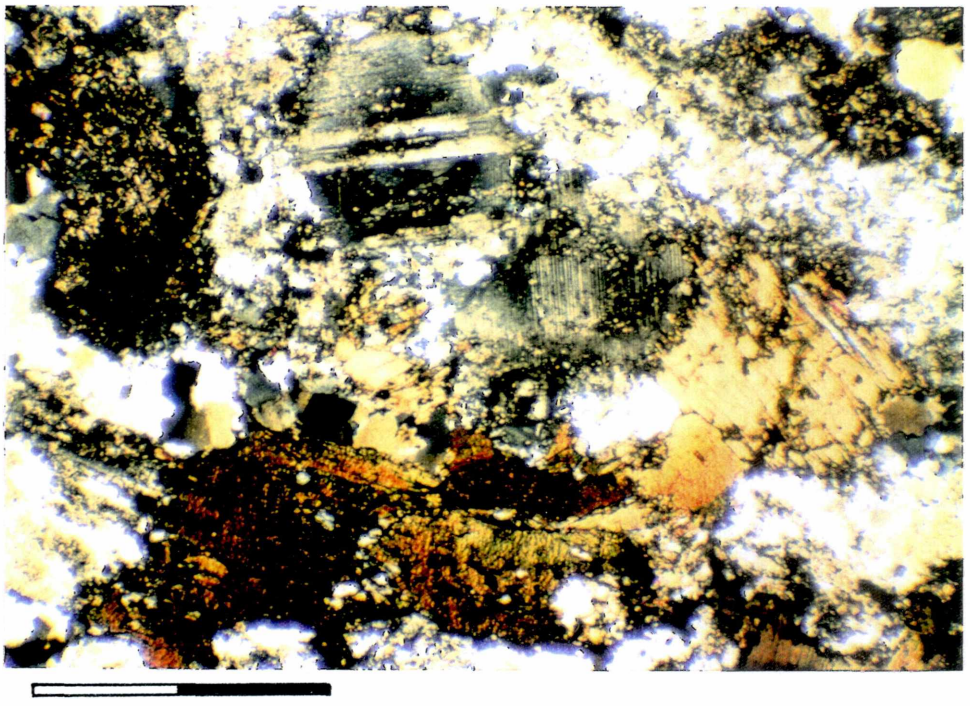


Figure 3.13 - Photomicrograph of sample LH6 (above). Microcline is common, together with plagioclase and quartz, together with coarse brown biotite laths. This sample shows little evidence of major hydrothermal alteration (Scale bar = 2 mm).



Figure 3.14a - Dolerite dyke contact 4 Level North cross-cut. Sharp contact between paler dyke and mafic lava shows evidence of a thin chilled margin.



Figure 3.14b - Thin dolerite dyke on 18 Level North. The undeformed dyke clearly cuts the foliated mafic lava.



Figure 3.14c - Thin dolerite dyke in 7 Level North 8 Stope. Thin dyke clearly cuts gold-bearing quartz-vein but is itself deformed. Late movement along the margin of the vein

The dykes are generally aphanitic, fine grained ranging in colour from pale grey to dark green. Porphyritic examples were only seen when the dyke thickness exceeded a few metres.

Phenocrysts of plagioclase are mostly altered to fine sericite and carbonate. Actinolite is very common, possibly replacing pyroxene. Some brown hornblende is preserved although mainly altered to chlorite and Fe-oxides. The matrix appears to be fine chlorite, sericite, epidote and some fibrous serpentine minerals.

3.4 Whole Rock Geochemistry

3.4.1 Introduction

The samples analysed together with sample locations are shown in Appendix I. Sample descriptions are based on examination of hand specimens. "Undeformed" refers to the lack of a developed penetrative fabric and these samples were all collected well away from mineralised structures in an attempt to sample the least altered material possible. The interpretation of pillow lavas is based on the interpretation of pillow margin textures and/or flow-top breccia and tri-cuspate infill textures, which can still be observed in even highly deformed samples. A number of the samples were deliberately taken with regard to spatial distribution around the mineralised structure, with the aim of assessing any possible wallrock alteration accompanying mineralisation in both the mafic lavas and the "felsites".

3.4.2 Previous Work

The most comprehensive study to date on the Bulawayan Group volcanics of the Basaltic Unit in the region is confined to the KweKwe area (Condie & Harrison 1976). Some additional data are given by Bliss (1970), Robertson (1976) and Foster *et al.* (1979). Foster *et al.* (1979) report on lavas analysed from the adjacent Golden Valley deposit as well as samples collected from the Dalny gold deposit which lies some 15km north of Patchway. These studies all suggest the lavas are of tholeiitic affinity, similar in composition to mid-oceanic ridge tholeiites. The REE and Ti-Zr values suggest that the tholeiites are ridge or volcanic arc basalts, whilst mid-ocean ridge affinity is favoured by Condie & Harrison (1976). Evidence cited for this conclusion is the lack of clearly demonstrated andesites and particularly the low strontium, rubidium and potassium levels. Direct comparison of the chemistry of Archaean rocks with more recent types must be speculative (Pearce *et al.* 1977). However, basic sub-divisions can be made based on standard criteria.

Numerous thin felsic intrusive bodies are seen underground at Patchway, Erin and Golden Valley. These intrusives are often closely associated with the mineralised shear-zones (Ward 1968, Bliss 1970). Previous chemical analyses of these are limited (Bliss 1970, Robertson 1976), but show them to be

granodiorite to tonalite in composition. The ages of the intrusives are poorly constrained, but they are most likely to be associated with the major Sesombi intrusive suite, dated at 2.69 Ga. They show a geochemical affinity with the volcanics of the Calc-alkaline Unit of the Bulawayan (Hawkesworth & Bickle 1977), which overlie the Basaltic Unit rocks. At least part of the Whitewaters is deformed close to the main Lily Fault (Bliss 1970), supportive of intrusion before the end of major regional deformation and compatible with the association of the main tonalite and the variably deformed thin felsic intrusives seen at the mines.

Previous studies of Archaean greenstone-hosted gold deposits highlight the ubiquitous presence of high-level intrusive suites in the mineralised sequence (Colvine *et al.* 1988). These intrusives also commonly show a degree of concordance with the mineralised structural features. The intrusions are often of two magma types i) felsic (TTG or Tonalite-Trodhjemite-Granodiorite) and ii) shoshonitic (lamprophyres). The alternative roles of these two magma types has been variously discussed (Burrows & Spooner 1986, Rock *et al.* 1987) but no unequivocal connection has yet been established.

Studies in Australia of the TTG bodies (Perring *et al.* 1988), indicate that these so called "internal granitoids" can be variable in composition but are quite distinct geochemically from the older granite terrains bounding the greenstone belts. Perring *et al.* (1988) note the relationship of the location of larger stocks and favourable structural sites, and the clearly associated thin TTG intrusive bodies spatially associated with mineralisation. Barley *et al.* (1989) link this type of internal granitoid with possible convergent margin tectonics at this time in the Archaean, based on the LILE (large-ion lithophile elements) enriched and Nb depleted nature of the magmas. These studies suggest that comparison of these Archaean granites with more modern tectonically constrained analogues may in fact be valid.

Recent reviews on granite classification (Lameyre & Bowden 1982, Hussein *et al.* 1982, Pearce *et al.* 1984) expand on the earlier work of Streckeisen (1976) which Lameyre & Bowden (1982) adapted to discriminate tectonic setting. Hussein *et al.* (1982) proposed a new classification scheme and Pearce *et al.* (1984) clearly relate tectonic settings of granites with incompatible trace element content.

3.4.3 Mafic Lavas

The analyses of the mafic lavas are shown in Appendix III. The description "deformed" is applied to samples where a continuous cleavage is developed. "Undeformed" is used to describe samples where the original primary fabric of the rock is preserved. The data can be compared to the published analyses of Condie & Harrison (1976). One immediate feature is the loss on ignition (LOI) value for the samples. Even the "undeformed" samples show LOIs between 3 and 11%, indicative of carbonatisation in the form of calcite (confirmed by a positive reaction with HCl to liberate CO_2 by all samples) and hydration, confirmed by the presence of abundant chlorite seen in thin section. The highly deformed

samples show much higher LOIs, and in hand specimen appear to contain more abundant phyllosilicate, and probably carbonate, than the undeformed samples.

The AFM plot (Jensen 1976) provides a useful discrimination diagram for mafic lavas. This type of plot has been used to classify rocks both in the Canadian Abitibi belt (Jensen & Pyke 1981) and in Zimbabwe in the Mberengwa belt (Nisbet *et al.* 1977). The AFM plot for rocks of the Patchway deposit (Figure 3.15) puts all the "undeformed" samples in a tight cluster clearly in the high Fe-tholeiite field. Samples from the "deformed" sample set plot quite similarly but indicate a wider spread with some falling into the andesite field. An alternative method of classification scheme proposed by Winchester & Floyd (1977) confirms the samples fall within the sub-alkalic basalt field except for four of the deformed samples (Figure 3.16).

Since pillow texture is common in the mafic lavas at Patchway, some degree of sea-water metasomatism is expected, and this may have given rise to the epidote-rich pillow infillings and altered rinds to undeformed pillows which are occasionally seen underground. Hughes (1973) suggests that alkali ratios can be used as a test of significant metasomatism. This type of data must be interpreted with caution however, as alkali exchange between major silicate phases and fluid is likely to be a function of temperature of the fluid (Truesdell 1984). However, the diagram is useful to assess changes in alkali ratios due to diagenesis or alteration. The Patchway data plotted (Figure 3.17) shows that strong changes in the alkali contents of the lavas may indeed be the case in at least some of the samples. Interestingly, the undeformed samples show indications of Na metasomatism whilst most of the deformed samples show values indicative of K metasomatism. However, Winchester & Max (1984) demonstrate that many of the elements of intermediate ionic potential (e.g. Ti, Zr, Cr as well as Y, Hf, Nb, Ta and most of the REE) remain immobile during most sub-greenschist facies processes. These less mobile elements are utilised as useful geochemical discriminants.

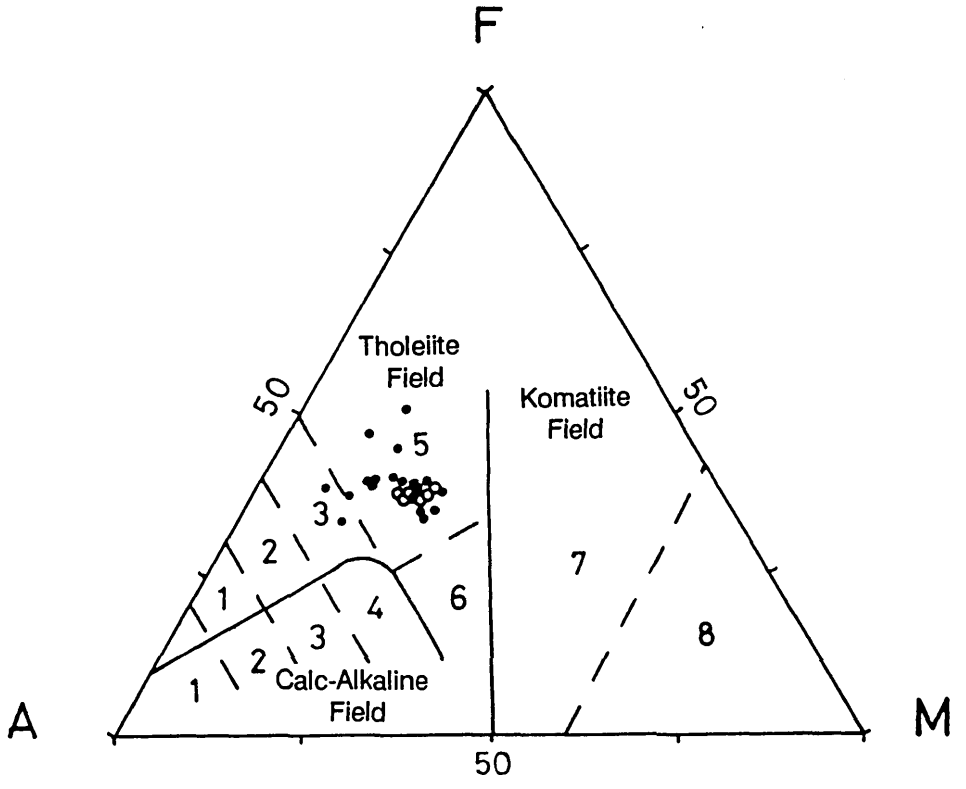
The Patchway samples show results generally comparable to the analyses of Condie & Harrison (1976) (Table 3.9). Silica levels are slightly lower at Patchway, but most major elements can be seen to be quite similar.

Deformed versus Undeformed Samples

Both the major and trace element contents of the deformed samples show major variations both from the undeformed samples, and amongst themselves (Appendix III). In assessing the deformed samples analysed, it becomes clear from the alkali ratios, Na : K particularly, that there are major changes in these elements during deformation, which appear related to formation of the gold mineralised veins.

		Patchway Lava Samples					
	Ave. Mafic Formation[1]	15-1	15-2	10-18	10-6	18-8	10-2
%							
SiO_2	50.50	47.23	43.20	49.53	48.77	42.26	48.02
Al_2O_3	14.00	14.70	13.53	14.47	13.78	13.01	13.49
Fe_2O_3	11.50	14.24	11.29	12.03	11.79	11.47	11.09
MgO	7.34	9.42	7.59	7.73	7.81	7.75	6.71
CaO	11.60	7.94	9.29	9.01	10.33	11.00	13.98
Na_2O	2.05	1.82	1.54	2.54	2.69	2.01	0.79
K_2O	0.06	0.06	0.04	0.05	0.08	0.02	0.04
P_2O_5		0.09	0.06	0.07	0.07	0.07	0.07
TiO_2	0.65	0.73	0.66	0.71	0.67	0.63	0.64
MnO		0.20	0.17	0.18	0.18	0.18	0.17
LOI	2.15	4.35	8.89	3.60	3.06	11.73	4.62
Total	99.80	100.78	101.24	99.93	99.22	100.12	99.61
ppm							
Ba	110	11	10	13	23	19	12
Cr	338	405	366	391	379	359	365
Co	50	62	53	60	48	52	46
La	4	14	13	3	0	8	3
Ni	122	190	200	173	181	169	171
Sr	82	83	67	179	115	65	200
Zr	100	54	51	37	35	34	37

Table 3.9 - Wholerock analyses of mafic lava samples from Patchway mine. For comparison, 1 is the published average analysis of the Mafic Formation of the Upper Bulawayan (from Condie & Harrison 1976).



NUMBERED FIELDS

1 - Rhyolite
2 - Dacite
3 - Andesite
4 - Basalt
5 - High Fe tholeiitic basalt
6 - High Mg tholeiitic basalt
7 - Basaltic komatiite
8 - Ultramafic komatiite

Figure 3.15 - AFM (Al_2O_3 - [Total Iron + TiO_2] - MgO) Plot for Patchway mafic lavas. Open circles are undeformed samples, solid circles deformed samples (after Jensen & Pyke 1981).

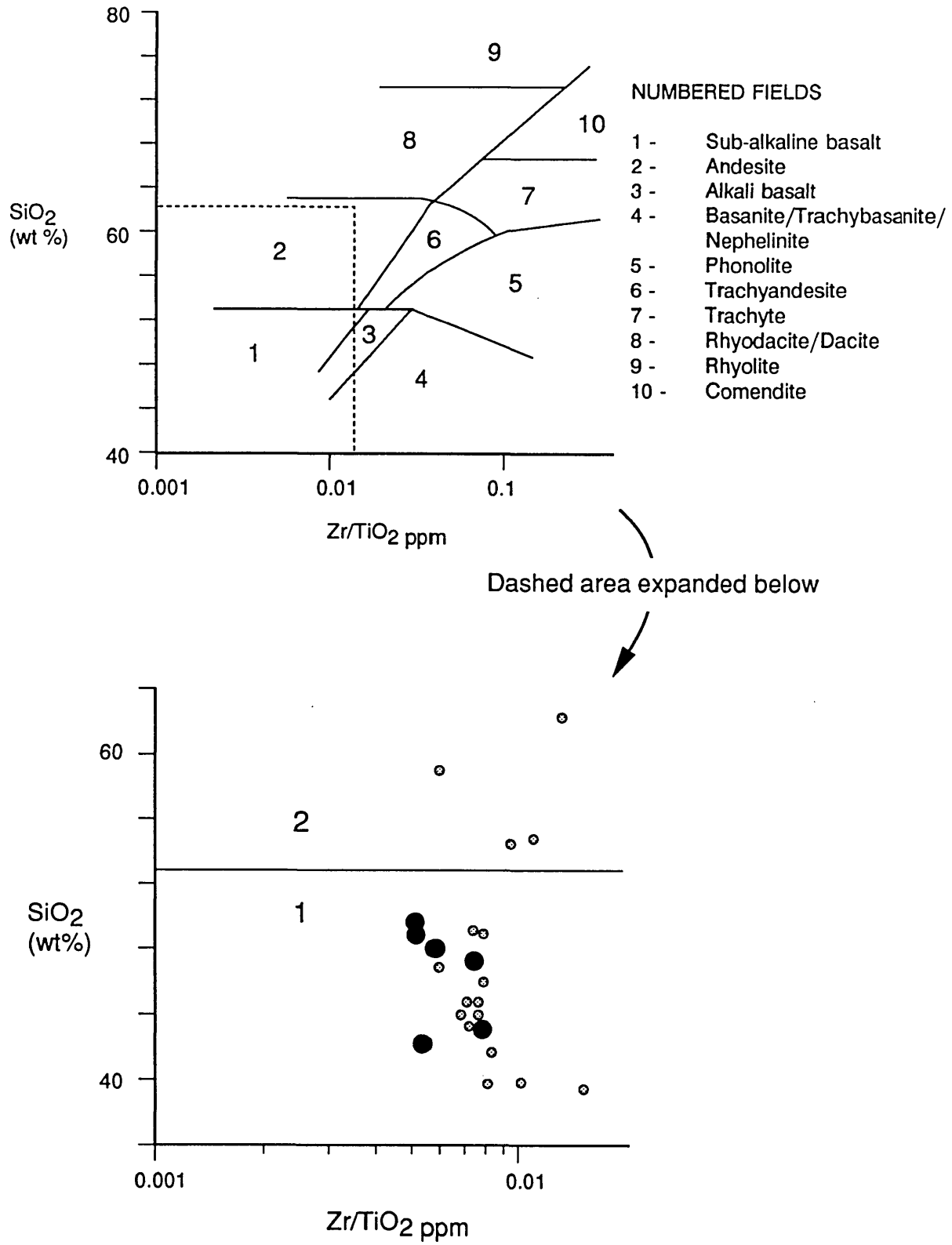
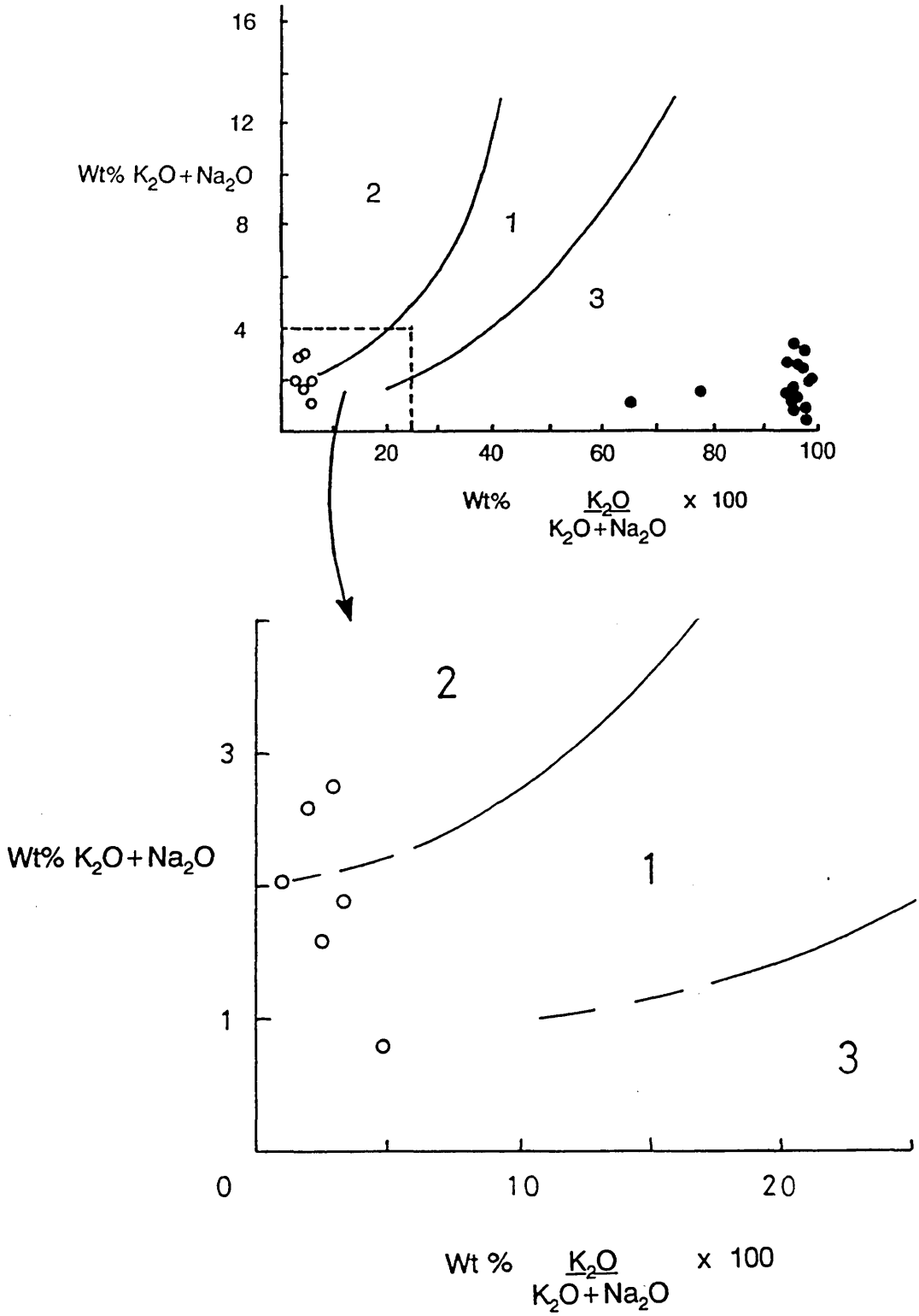


Figure 3.16 - SiO_2 - Zr/TiO_2 discrimination plot for mafic volcanic rocks at Patchway (after Winchester & Floyd 1977). Mafic samples from Patchway plotted in lower diagram which is expanded from the upper diagram. Large dark circles are undeformed samples, smaller circles are deformed samples.



Numbered Fields : 1 - Normal igneous rocks
2 - Na-metasomatised rocks
3 - K-metasomatised rocks

Figure 3.17 - Alkali plot for determination of Na-K metasomatism (after Hughes 1973). Open circles represent undeformed samples, deformed samples plotted as filled circles. Expanded field shown in lower graph.

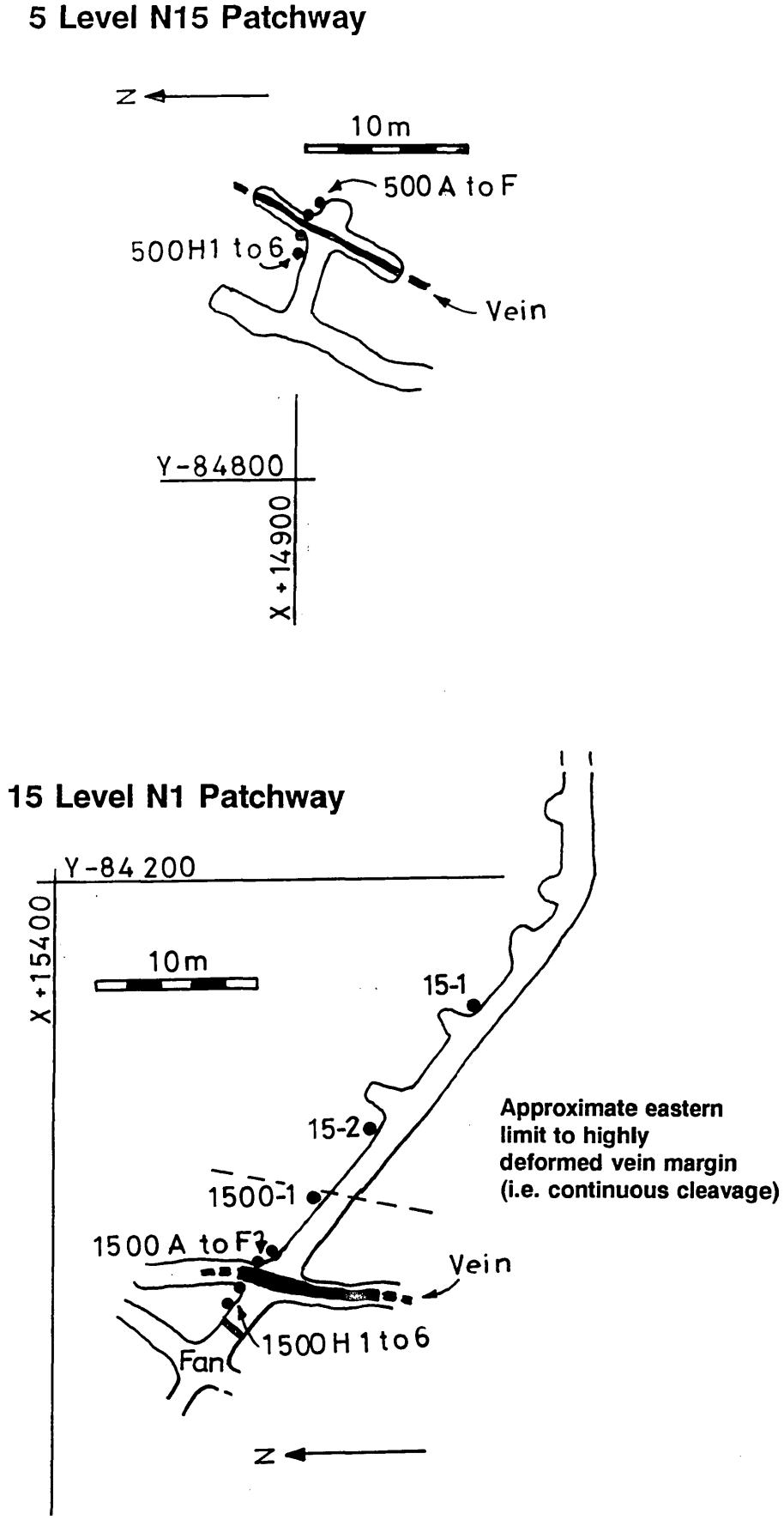


Figure 3.18 - Detailed location of geochemical sample profiles on 5 and 15 Levels, Patchway. For location of small plans with respect to mine plan, see Figure I.1 (insert pocket)

To assess this observation, two areas were sampled on 5 and 15 level (Figure 3.18), from the mineralised gold-bearing structure, away into the undeformed wallrock. The simple geochemical profiles of total Na_2O and K_2O are shown on Figure 3.19, where striking variation is shown marginal to the mineralisation. Simply based on these elements, there is a clear antithetic change in Na and K in the deformation zone close to mineralisation. Because of this geochemical variability, it was decided to exclude all the deformed lava samples, where a penetrative cleavage is present, from any subsequent discussion of magma type and provenance for the mafic rocks.

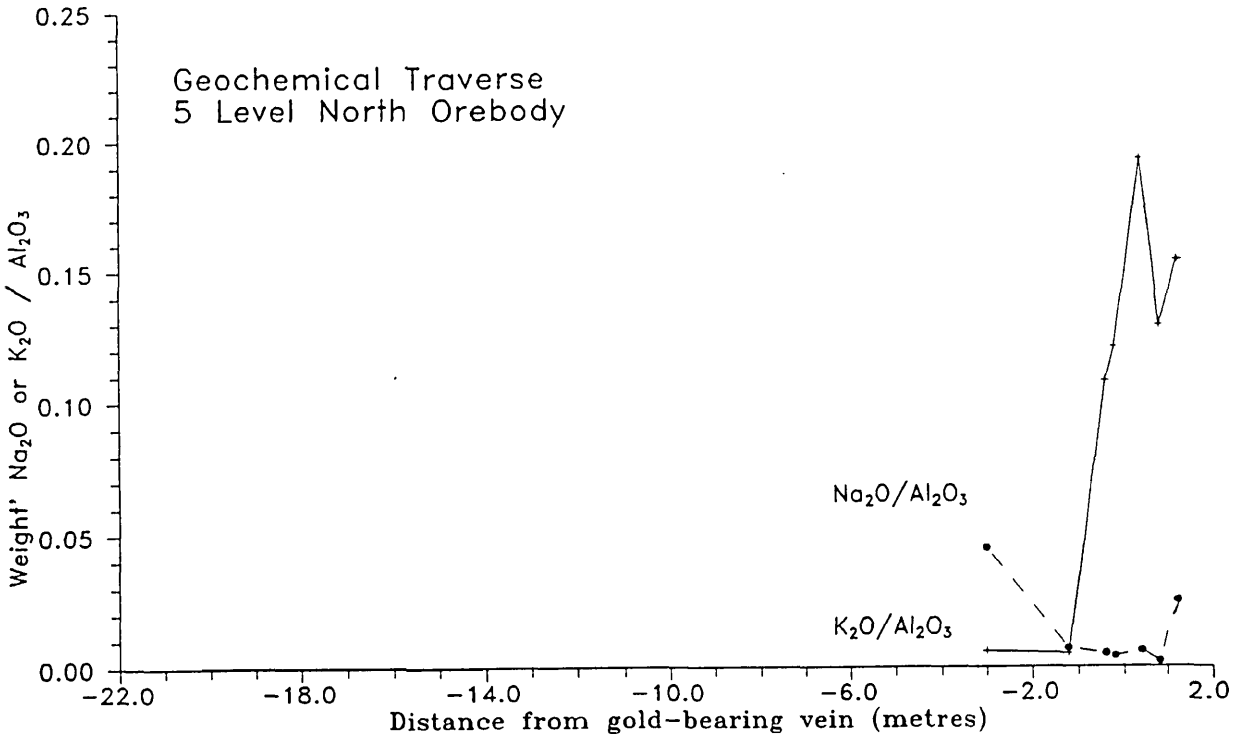
Discussion on Environment of Formation of Mafic Lavas

Major element values for both undeformed mine samples, and the published data in Table 3.9. show values very similar to the published data of modern arc and mid-ocean ridge tholeiites, as pointed out by Condie & Harrison (1976). Trace element contents of the undeformed lavas are also comparable except for higher Ni and Sr values from the Patchway analyses. Sr behaves in a very similar fashion to Ca which also show highly variable values, probably due to alteration described earlier. Zr levels are close to averages of modern tholeiites, somewhat lower than the published analyses. Importantly, Cr values are consistent in the undeformed rocks, similar to the published analyses for the more recent tholeiites. Both Cr and Zr can be considered generally incompatible with the major phases, and largely immobile during alteration events. The chemistry of the lavas is thus broadly comparable to modern ridge or arc tholeiites, although any conclusions as to geological setting is fairly speculative due to the problems of interpreting Archaean tectonics.

3.4.4 Mine Felsites and Regional Tonalite Intrusives

Deformed and undeformed rocks are again discriminated in the mine intrusive samples. This deformation is manifest in hand specimen by a variable development of foliation. In all cases these deformed samples are taken from intrusive bodies immediately adjacent to gold-bearing quartz mineralisation. Again, only undeformed lithotypes are considered for classification, and the intrusives analysed all fall into the broad classification of granite (>65 % SiO_2). They are all tonalitic to granodioritic in composition (see Appendix III for analyses) and published analyses from Bliss (1970) are included for comparison. It is immediately apparent that the deformed samples show distinctly higher LOI values, indicative of the presence of significant carbonate and/or hydrated phyllosilicates which is in agreement with the petrographic observations.

In view of the problems of including deformed samples into the geochemical discussion relating to environment of formation for the mafic lavas, deformed samples of the felsites are excluded from the discussion on original rock chemistry, since these samples also occur proximal to mineralisation and major changes in alkali contents are indicated.



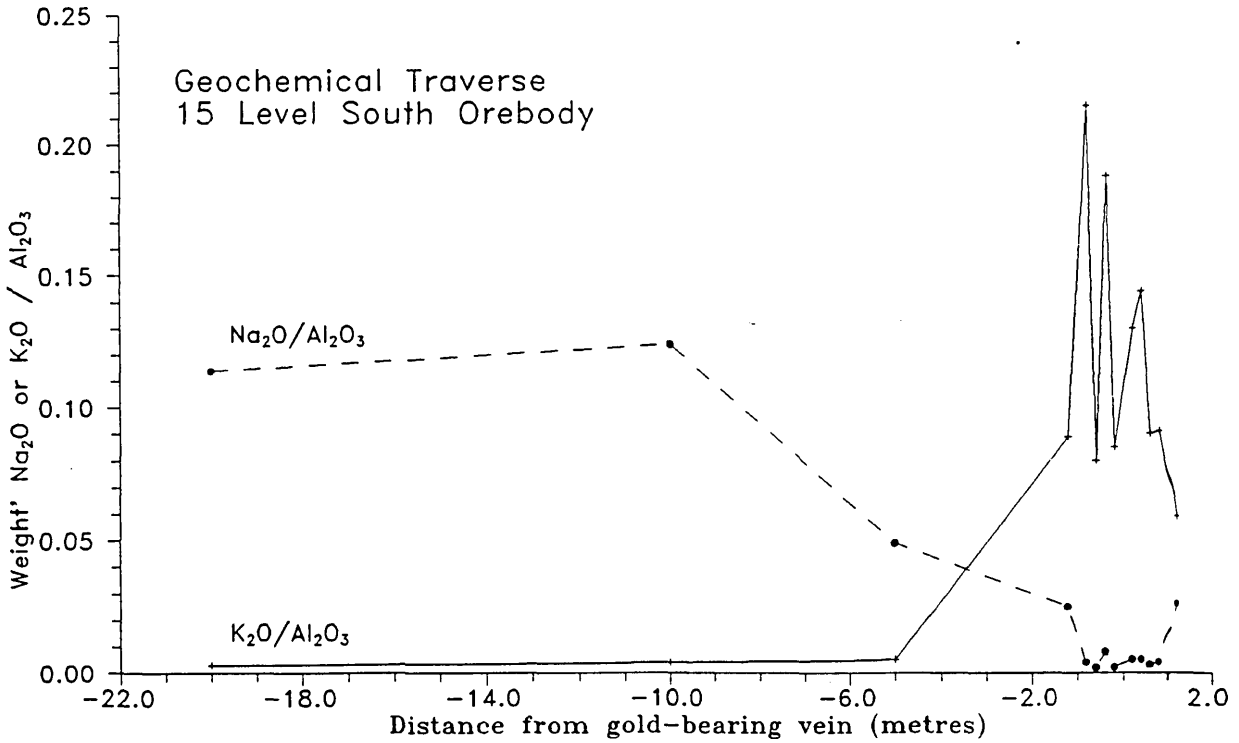


Figure 3.19 - Lithogeochemical profiles on 5 and 15 Level, Patchway mine. Point 0 represents the quartz vein margin with samples shown at negative metres into the footwall, positive metres into the hangingwall, distances measures horizontally.

Environment of Formation

Some caution is necessary when making comparisons between Archaean rocks and more modern analogues, since conclusions from this are tentative at best. Sub-division of granites into two broad catagories, I and S - types (Chappell & White 1974) is broadly co-incident with proposed distinctly different magma origins. This difference in origin was related to different tectonic settings (Pitcher 1983), the appreciation of which lead to expansion of the "types" to include granites of A and M - type (Collins *et al.* 1982, White 1979). Pearce *et al.* (1984) reviewed classification and demonstrated that incompatible trace elements Rb, Y, Nb, Ta, and Yb are probably a better way to discriminate granites.

The samples analysed by XRF provided Rb, Nb and Y data which are used on the discriminant plots of Pearce *et al.* (1984) in Figure 3.20. On these plots, the intrusives show a clear affinity with the more modern volcanic arc or syn-collision granites and fit into the broad category of I - type granites (Chappell & White 1974).

3.4.5 Mafic Dykes

These dykes are common underground and are seen to cut all the other lithologies at the mine. Generally in hand specimen they appear fresh with little visible alteration except where isolated deformation has resulted in minor asbestos veining. Representative analyses (Appendix III), show the dykes to be quite different in chemistry to the mafic lavas. A plot of Zr/Ti (Figure 3.21) puts the dykes distinctly in the "within plate" field, quite different to the mafic lavas.

The dykes would appear to be similar to the sub-parallel Plumtree dyke swarm (Wilson *et al.* 1987). The age of this event, 2150 Ma, is consistent with observed field relationships.

3.5 Chemistry of Deformed Vein Host Rocks

3.5.1 Mass Balance Calculations

In order to calculate the net chemical gains and losses during any hydrothermal alteration, it is implicit that some assumptions of either single or multiple element immobility or of well constrained volumetric change during alteration must be made. Gresens (1967) developed a method which utilised specific gravity data into two-way, mass-balance calculations, by fixing a value for volumetric change or the behaviour of one component during the alteration. This involves the calculation of volumetric factors for each of the isochemical species, and the plotting of composition-volume diagrams for the various species. Common intercepts of lines constructed for elements near to the isochemical axis infers immobility for those elements. From this, volumetric change for the whole rock together with the relative increase and decrease of the various other species can be inferred. This rather involved

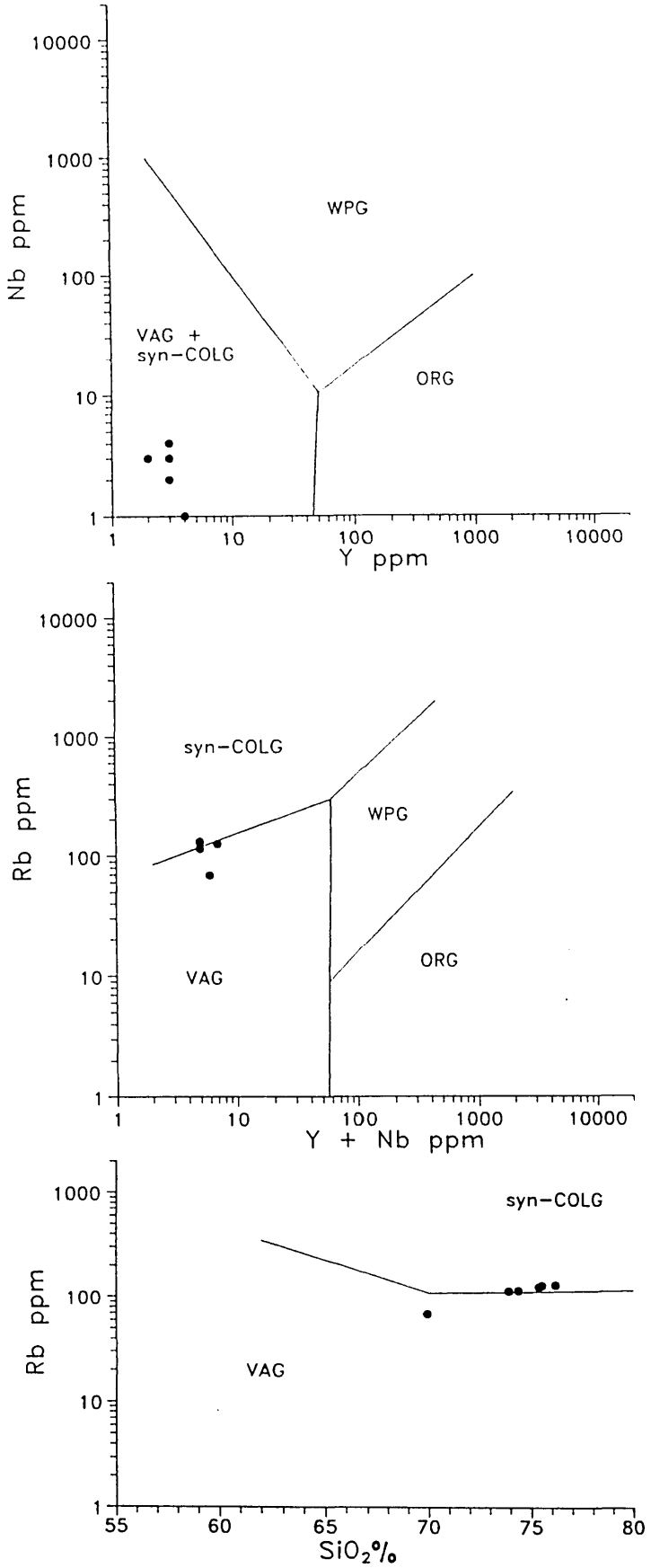


Figure 3.20 - Nb, Y, Rb and SiO_2 discriminant diagrams for granitic rocks plotted for Patchway felsic intrusive rocks (after Pearce *et al.* 1984). Samples shown are unaltered felsic intrusives. Key to diagrams : VAG - volcanic arc granites, WPG - within plate granites, ORG - ocean ridge granite, syn COLG - syn-collision granite.

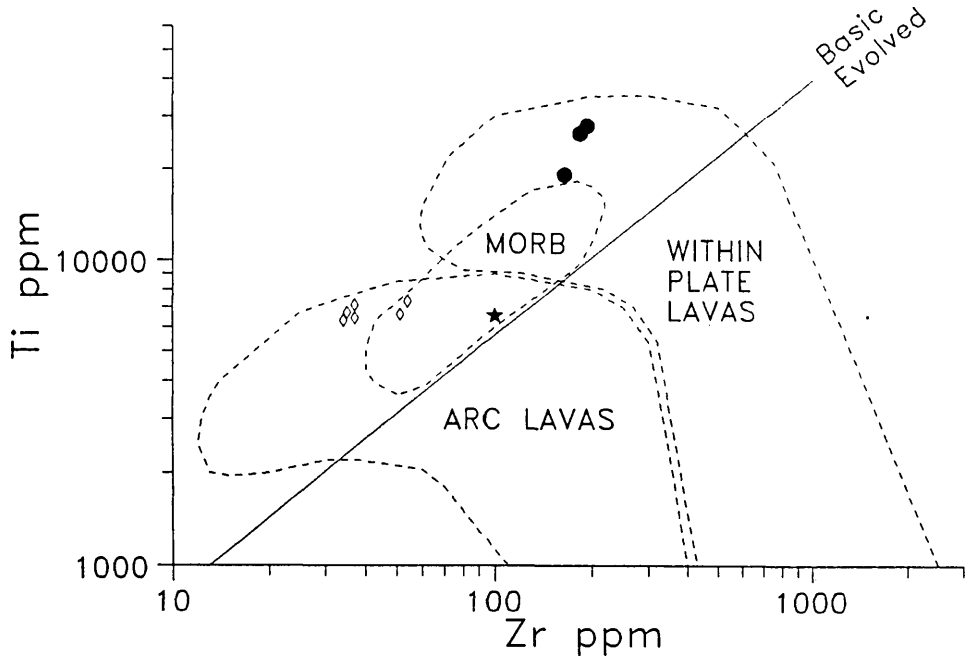


Figure 3.21 - Ti-Zr discrimination plot for Patchway mafic rocks. Diagram discriminates basic and evolved lavas (after Winchester & Floyd 1977). Diamond symbols show undeformed mafic lava samples and the solid circles show the mafic dykes which clearly plot in a different field. The star shows the plot for the average Mafic Formation analysis of Condie & Harrison (1976).

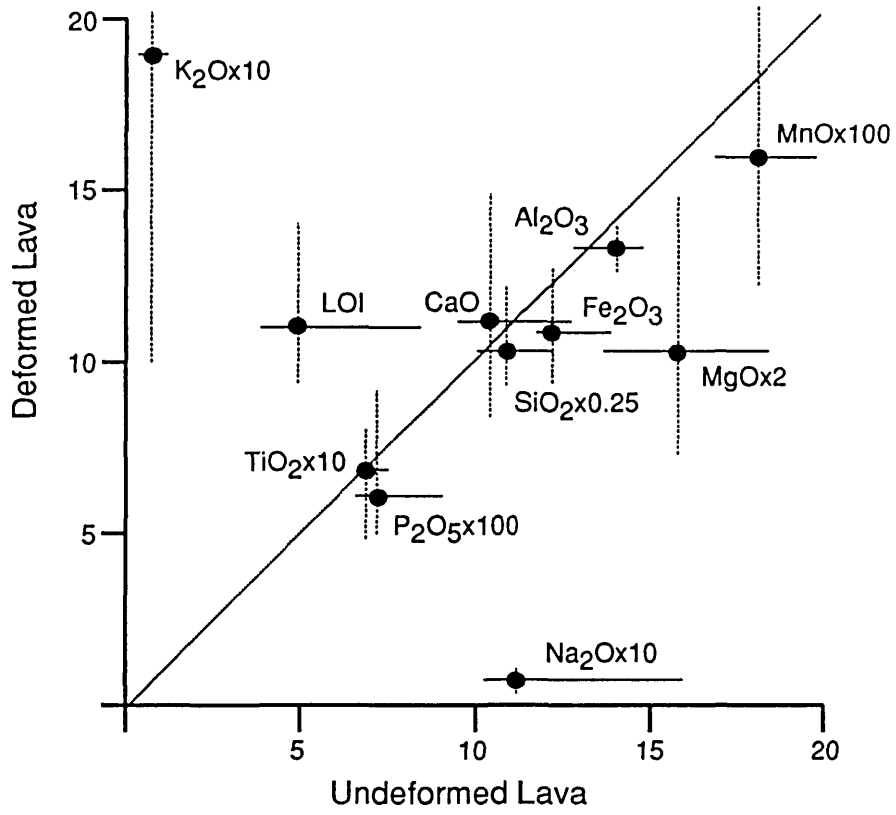
technique is contingent on accurate specific gravity measurements. The presence of quartz and carbonate veinlets, which are the result of mechanical volumetric inflation, play no part in the mass balance calculations of the main rock mass. The inclusion of such introduced phases in any specific gravity measurements would cause error to mass balance estimates by this method.

To avoid the problems with precisely measuring specific gravity, Grant (1986) proposed a simple graphical method of plotting values from isochemical species for the most altered samples versus the least altered samples. This simple plot permits direct observation of the divergence of elements from the "isocon" or line of no relative change (which has a slope of 1 on an X-Y plot of any element "A" in the most altered sample versus element "A" in the least altered sample). The isocon plot can thus have simple axes with no need to define units as long as consistent units are used for both axes (e.g. both in ppm or wt%). Definition of a best fit line through several "immobile" elements in the same fashion as Gresen's intercept on the "volume factor" axis, can be used to indicate relative volume change. The magnitude of any change is proportional to the slope of such a defined best-fit line, where a slope is greater than 1, a volume decrease is implied, and conversely a slope less than 1 implies volumetric increase.

Results of Deformed Mafic Lavas

The ICP-AES analyses of the mafic lavas comprised two traverses (total 16 samples plus duplicates) on two levels at the mine (Figure 3.18 and Table 3.10). Four of the analyses from the traverses which show abnormally high silica contents are seen to have abundant quartz-carbonate veinlets and are not considered truly representative of the mafic rock, due to an undoubted degree of volumetric inflation and carbonate-silica addition. Samples with high sulphide contents were avoided due to problems during the fusion of the samples prior to preparation of the ICP solution.

Average values of results of the deformed samples from the traverses are plotted on "isocon" plots in Figure 3.22. Results for particular elements have been multiplied by a suitable factor to keep the values for major elements in the range 0 to 20 and minor elements in the range 0 to 200. On the plot for major elements (Figure 3.22a) there is very clear enrichment of K_2O above the normal isocon (+3800%), with LOI (loss on ignition or $\Sigma H_2O+CO_2+SO_2$) enriched to a smaller degree (+250%). Significant losses are primarily recorded by Na_2O (-96%) and MgO (-35%). There is, however, very strong correlation between Al_2O_3 and TiO_2 for all the samples and the average values of these together with other elements lie very close to the ideal isocon (Figure 3.22b). The elements, Cr and V, which are usually considered "immobile", plot very close to the ideal isocon. This observation leads to the suggestion that the geochemical changes are approximately isovolumetric. This observation is particularly significant given the major mineralogical changes observed between deformed and undeformed lava samples.



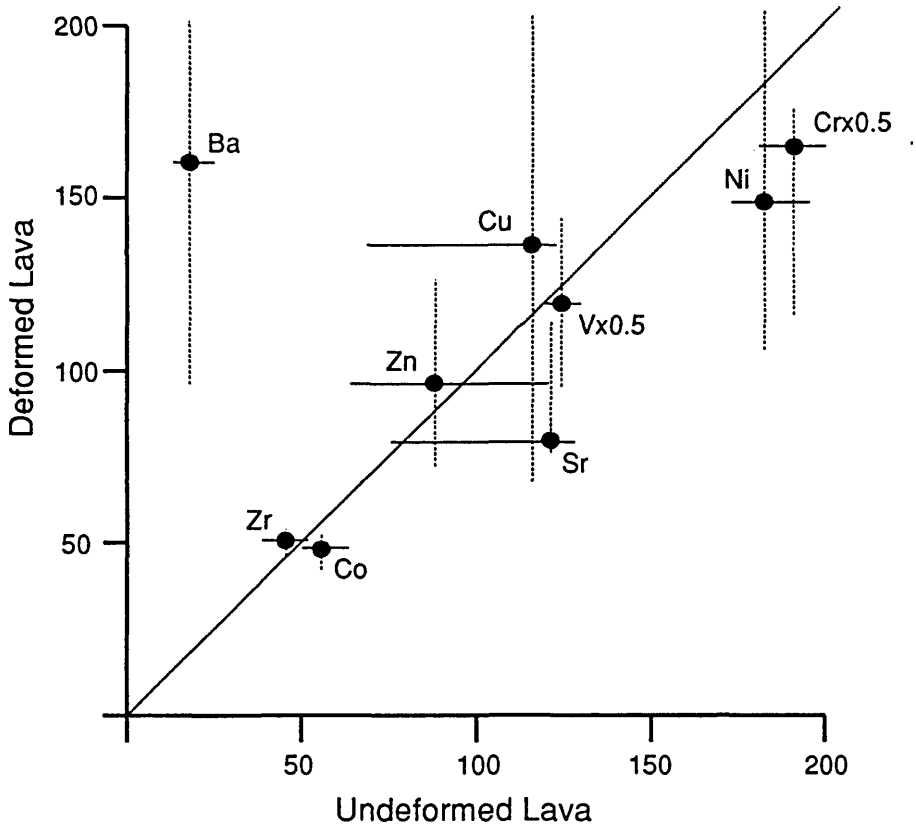


Figure 3.22 - "Isocon" plots for deformed versus undeformed mafic lava samples from Patchway mine (after Grant 1986). Upper plot 3.22a is for major oxides, axes are relative with wt% oxide plotted except when the wt% oxide is multiplied by a factor for both deformed and undeformed value so the point lies within the range of the diagram (e.g. K_2O wt% x 10 is plotted). Lower plot 3.22b is for traces and a similar method of plotting the ppm values is used.

Sample	SiO_2	Al_2O_3	Fe_2O_3	MgO	CaO	Na_2O	K_2O	P_2O_5	TiO_2	MnO	LOI	Total
15/1	47.23	14.70	14.24	9.42	7.94	1.82	0.06	0.09	0.73	0.20	4.35	100.78
15/2	43.20	13.53	11.29	7.59	9.29	1.54	0.04	0.06	0.66	0.17	8.89	101.24
1500/1	49.11	13.93	11.53	6.98	13.04	0.98	0.07	0.07	0.67	0.18	3.21	99.77
1500/H/1	39.90	11.71	8.98	7.08	14.55	0.02	1.00	0.08	0.53	0.12	14.39	98.81
1500/H/2	49.03	12.73	9.83	4.18	9.48	0.10	2.39	0.06	0.61	0.13	9.95	98.49
1500/H/3	61.99	8.33	11.04	3.45	6.91	0.02	0.67	0.06	0.40	0.12	7.39	100.40
1500/H/4	58.67	16.23	10.60	2.96	1.72	0.07	3.49	0.05	0.82	0.06	4.77	99.43
1500/H/6	45.97	13.07	10.94	6.80	9.85	0.33	1.16	0.06	0.63	0.14	8.89	101.24
1500/A	54.42	9.18	11.44	3.49	8.89	0.05	1.19	0.05	0.46	0.13	8.68	97.99
1500/B	44.28	14.01	11.11	4.82	10.81	0.07	2.02	0.05	0.68	0.20	11.76	99.82
1500/C	39.77	12.72	10.35	6.26	13.99	0.04	1.41	0.06	0.61	0.14	3.21	99.82
1500/D	43.51	13.64	10.55	7.99	10.34	0.05	1.24	0.05	0.64	0.14	12.21	100.36
1500/F	44.06	13.29	10.76	8.89	9.61	0.35	0.73	0.05	0.64	0.15	11.96	100.50
500/2	39.47	13.61	13.85	3.58	12.07	0.06	2.62	0.05	0.67	0.14	12.78	98.90
500/4	41.87	13.17	11.22	5.71	12.74	0.02	1.70	0.07	0.64	0.15	13.36	100.67
500/6	44.85	12.57	10.07	4.61	12.44	0.04	1.93	0.04	0.62	0.13	12.43	99.73
500/A	54.69	7.42	8.92	3.77	11.72	0.03	0.90	0.02	0.46	0.13	10.89	99.04
500/B	44.90	13.54	13.91	5.56	8.42	0.07	1.46	0.06	0.83	0.16	10.25	99.19
500/F	46.90	16.77	10.01	4.70	7.05	0.12	3.18	0.09	1.04	0.16	9.30	99.32

Sample	Ba	Cr	Sr	V	Zr	Distance from vein margin (in metres)
15/1	11	405	83	266	54	-20
15/2	10	366	67	242	51	-10
1500/1	9	372	173	242	53	-5
1500/H/1	67	296	124	196	55	0.2
1500/H/2	158	340	75	228	47	0.4
1500/H/3	63	236	53	183	50	0.6
1500/H/4	225	445	30	286	48	0.8
1500/H/6	129	361	73	235	51	1.2
1500/A	93	261	71	182	44	-0.2
1500/B	136	374	80	245	47	-0.4
1500/C	134	343	96	224	50	-0.6
1500/D	112	360	76	243	47	-0.8
1500/F	135	384	75	227	50	-1.2
500/2	170	351	82	243	54	0.4
500/4	120	344	80	228	54	0.8
500/6	190	322	70	218	48	1.2
500/A	60	135	75	143	51	-0.2
500/B	105	265	56	264	60	-0.4
500/F	296	308	58	331	60	-1.2

Table 3.10 - Whole-rock analyses of sampling traverses on 5 and 15 Level, Patchway. Full trace element analyses are presented in Appendix III. Samples highlighted were used for constructing the isocon diagram Fig 3.22. Samples 1500/H/3, 1500/H/4, 1500/A and 500/A had visible quartz veining; these samples were selected to construct the isocon diagram Fig. 3.24. In both Fig. 3.22 and 3.24, the range of data is expressed as error bars shown on the diagram.

The presence of pyrite disseminations in some of the deformed samples gives the impression of iron enrichment but total analysed iron (here quoted as Fe_2O_3) shows no change from the undeformed lavas. Ba is highly enriched in the deformed assemblage (+1100%), whilst Sr shows strong depletion (-35%). Comparing these traces with the major changes, strong correlation is indicated between Ba and K_2O enrichments (Figure 3.23). Sr, which might be expected to relate to either the Na_2O or MgO depletion shows no clear correlation. Other elements showing partial mobility are Zr and perhaps Cu, Zn, Cr and Ni. Zr is enriched (+24%) while Cr and Ni are depleted (-13% and -17% respectively). The base metals Cu and Zn are enriched (+22% and +14% respectively).

The samples where visible quartz veining is present are shown on Figure 3.24. The apparent shift of Al_2O_3, TiO_2 and V, which plot on, or close to, the ideal isocon in Figure 3.22, implies that volumetric increase is indicated if similar immobility is implied, which fits with the demonstrated volumetric inflation due to SiO_2 influx in dilatant veining. If the isocon for the samples is redrawn through Al_2O_3, TiO_2 and V, then a very similar pattern to that for Figure 3.24 is shown.

In conclusion, strong chemical changes appear to have accompanied the deformation around the mineralised structure, together with mineralogical change to a more hydrated, carbonatised assemblage. The changes can be demonstrated to be largely isovolumetric, except in the case where macroscopic quartz veining occurs. In this case a volume increase is clearly demonstrated confirming the dilatant nature of the veining introduction of SiO_2.

During deformation K_2O shows massive increase, coupled with concomitant Ba increase. Na_2O shows strong depletion, as do MgO and Sr. Most other elements indicate approximation to immobility with perhaps the exception of Zr, Cu, Zn and perhaps Ni and Cr. The geochemical traverses shown on Figure 3.19 indicate that major chemical change is confined to the strong deformation envelope, which in the broadest example is limited to two metres either side of the vein. The changes in the mafic lavas during deformation around the mineralisation can be considered, for all intents and purposes, to be isovolumetric. Major increases in both K and Ba can be linked to decrease in Na, Mg and Sr. LOI increases indicative of major influx of volatile components, probably S and CO_2, from the hydrothermal fluid.

Strong carbonatisation in the deformation is apparent from the increase in LOI and the presence of large amounts of carbonate in the deformed wallrock. This carbonate is largely calcite, with subordinate dolomite. The deformed zone is phyllosilicate rich which undoubtedly adds to the LOI figure with increase in bonded OH groups.

Mineralogically, the increase in K is reflected in the major presence of muscovite, confirmed in thin section. Albite, which is present in the undeformed lava, is destroyed in the deformed zone which

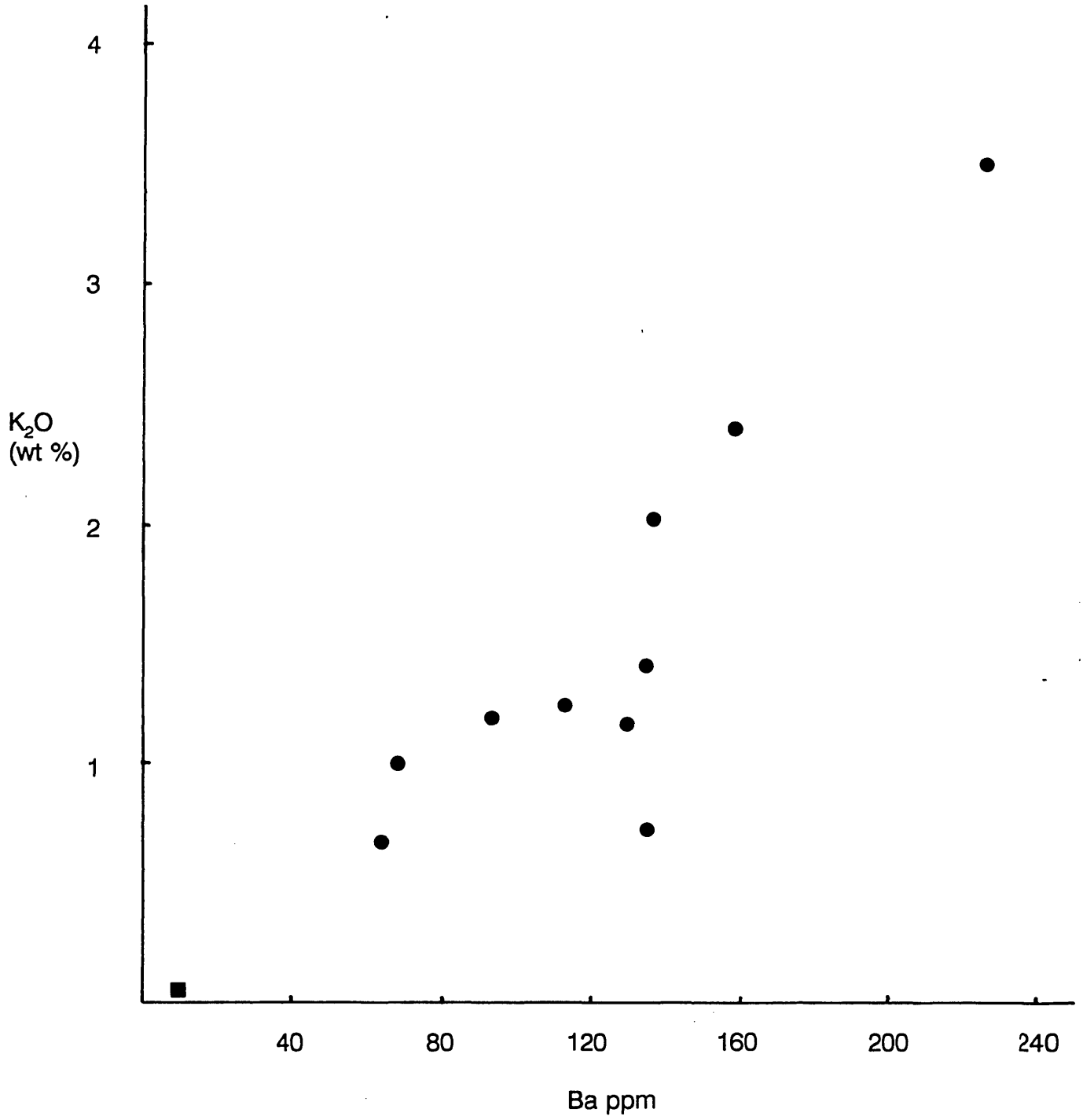


Figure 3.23 - Plot of K_2O wt% versus Ba ppm for deformed mafic lavas at Patchway.
Circles represent individual analysis points, square shows average value for undeformed lava.

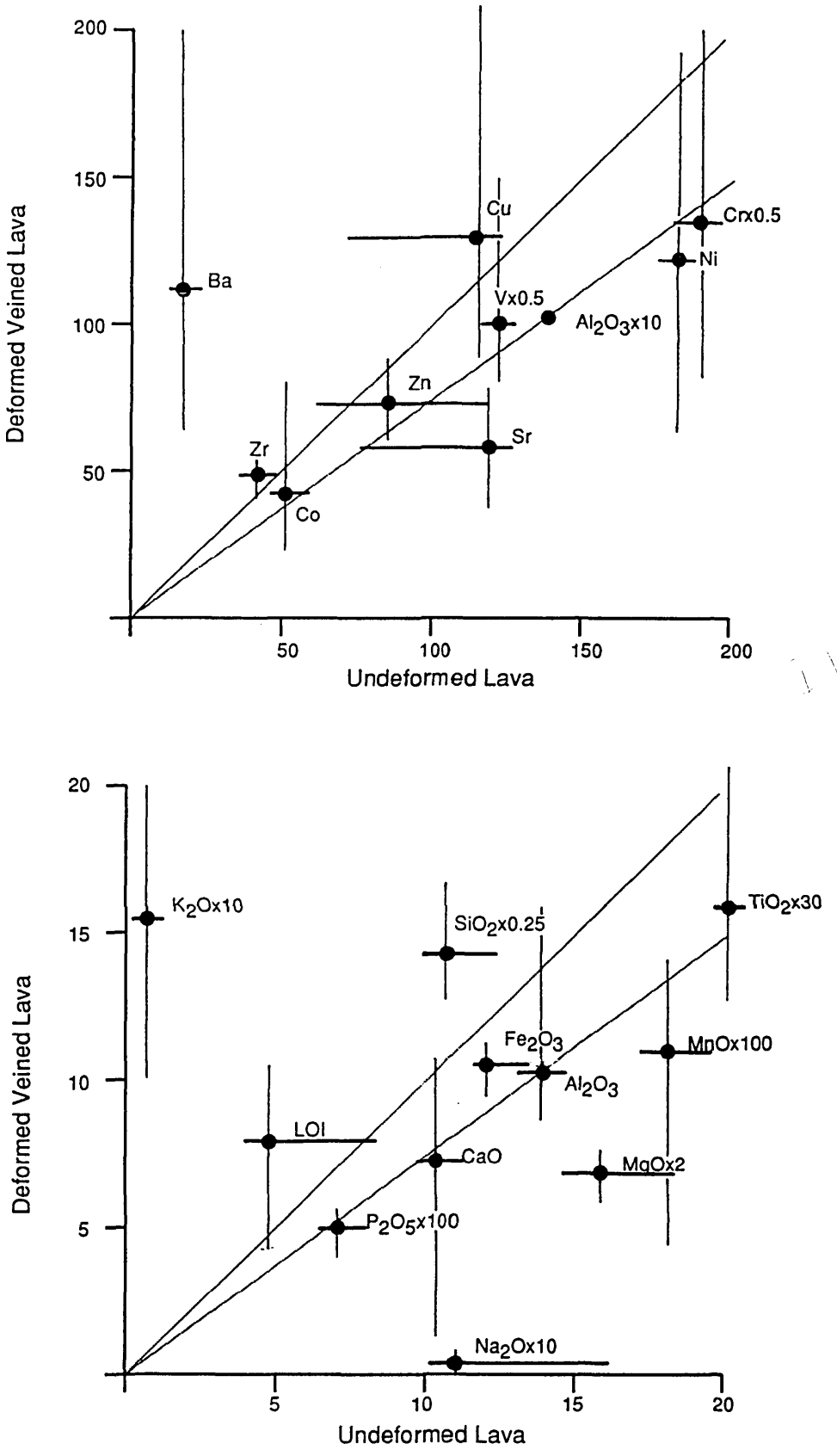


Figure 3.24 - "Isocon" plots for deformed mafic lava with quartz veins versus undeformed lava samples from Patchway mine (after Grant 1986). Upper plot 3.24a is for major oxides, axes are relative with wt% oxide plotted except when the wt% oxide is multiplied by a factor for both deformed and undeformed value so the point lies within the range of the diagram (e.g. K_2O wt% x 10 is plotted). Lower plot 3.24b is for traces and a similar method of plotting the ppm values is used.

accounts for the loss of Na. Sympathetic to K increase is the enrichment of Ba which is compatible in the muscovite lattice. Sr is known to be compatible in the albite lattice, but no clear correlation is seen between Na and Sr levels. However, Sr can substitute into the calcite lattice to some degree and this may fix Sr released by albite breakdown. Loss of Mg can perhaps be explained by the evident destruction of chlorite during sulphidation of the wallrocks to form pyrite. The Fe from the chlorite is fixed as pyrite whereas the Mg is incompatible. Although with the abundant carbonate formed as a result of massive CO_2 flux, dolomite is less common than calcite in the deformation zone and perhaps calcite is the more stable carbonate. This can occur at high Ca^{2+}/H^+ activity conditions (Bowers *et al.* 1984), perhaps indicating the high Ca levels in the hydrothermal fluid.

In terms of mineralogy, the initial mafic lava is seen to be dominated by albite, tremolite-actinolte, chlorite, epidote, together with some muscovite (sericite), carbonate, quartz and iron oxides, generally ilmenite. This is the result of greenschist metamorphism to the original tholeiitic basalt.
Thin section examination suggests that in the undeformed material lavas, relict orthopyroxene may be present in some of the tremolite masses.

Deformation around the mineralised structure accompanied by the chemical change documented earlier results in a fairly simple mineralogy of muscovite, chlorite, calcite and quartz with minor sphene and rutile. This mineralogical change can perhaps be outlined in the charge-balanced reactions outlined below:

$$\underset{\text{Tremolite-Actinolite}}{Ca_2(Mg,Fe)_5SiO_8(OH)_2} + \underset{\text{Albite}}{2NaAlSi_3O_8} + \underset{\text{Epidote}}{2Ca_2Al_3Si_3O_{12}(OH)}$$

$$+ \underset{\text{Ilmenite}}{FeTiO_3} + 5CO_2 + 4\,H_2O + 2K^+$$

gives:

$$\underset{\text{Muscovite}}{2KAl_3Si_3O_{10}(OH)_2} + \underset{\text{Chlorite}}{(Mg,Fe)_5Al_2SiO_{10}(OH)_8} + \underset{\text{Sphene}}{CaTiSiO_5}$$

$$+ \underset{\text{Calcite}}{5CaCO_3} + \underset{\text{Quartz}}{10SiO_2} + 2Na^+ + Mg^{2+}\ (\text{or } Fe^{2+})$$

The reactions outlined require an addition of K^+ to the system whilst Na^+ and Mg^{2+} or Fe^{2+} are released. The geochemistry supports the addition of K^+ coupled with Na^+ loss. The breakdown of ilmenite would be expected to release Fe but the geochemistry suggests that Fe is not lost. Fe might be expected to enter chlorite preferentially under certain fO_2 conditions (Bryndzia & Scott 1987). If Fe did enter chlorite, excess Mg^{2+} might be expected which could be lost in solution, partly explaining variations in the MgO values in the whole-rock geochemical study. Alternatively, the Fe could form pyrite reacting with sulphur from the fluid responsible for the hydrothermal alteration during deformation. Other possible reactions involve the partial breakdown of chlorite by sulphidation to form muscovite and pyrite liberating more Mg.

The behaviour of sulphur probably influences the behaviour of Mg, thus:

$$3(Mg,Fe)_5Al_2Si_3O_{10}(OH)_8 + 18H_2S + 2K^+ + 7O_2 + 10H^+$$
Chlorite

gives:

$$2KAl_3Si_3O_{10}(OH)_2 + 9FeS_2 + 3SiO_2 + 33H_2O + Mg^{2+}$$
Muscovite

Pyrophyllite is also seen in some of the rocks marginal to the mineralisation. The presence of this mineral can perhaps be explained by the following reaction:

$$4(NaAlSi_3O_8) + 4H+$$
Albite

gives:

$$Al_4Si_8O_{20}(OH)_4 + 4SiO_2 + 4Na+$$
Pyrophyllite Quartz

Both these reactions above consume H^+ ions and are thus more likely in increasingly acidic solutions.

The felsite intrusive bodies also show changes in the alkali contents during deformation which again points to the dominant reaction of breakdown of Na bearing feldspar to form muscovite. A slight increase in LOI points to an enrichment in both carbonate in the form of calcite, and hydrous phyllosilicates. Ba and Rb are enriched as a result of their introduction into the muscovite lattice and Sr is depleted, again not correlated with Na, consistent with its loss from feldspar and partial incorporation into calcite.

Ti, Cr and V are likely to be accommodated in the minor oxide phases present in the undeformed intrusives. Sphene is however present in some of the thin sections studied which may be host to Ti.

Results of Felsic Intrusives

No geochemical sampling traverses across the intrusive bodies were attempted as they are generally thin (<5m thick), and the bodies appear either entirely deformed, or else relatively massive. Isocon diagrams for deformed versus undeformed samples are shown on Figure 3.25.

What is immediately apparent on the plot for major elements is the fact that Al_2O_3 and TiO_2 plot close to the ideal isocon. Such a result is likely to indicate that very little volume change has occurred, a similar observation to the deformed mafic lavas. The plot for minor elements shows that Co, Cr, V and Zr show some depletion, indicating a loss of these elements. Most of the major elements plot close to the ideal isocon with the exception of K_2O, Na_2O, MgO and $P2O_5$. K_2O shows a gain with respect to this isocon, whilst Na_2O, is very greatly, and P_2O_5 and MgO, less substantially, depleted. For the other trace elements, Ba, Rb and Cu show gains, whilst Sr, and Ni show losses.

Compared to the effects on the mafic rocks, chemical change in the felsites is quite similar. The key similarities are the intense K_2O and Ba enrichment coupled with Na_2O and Sr depletion. MgO is

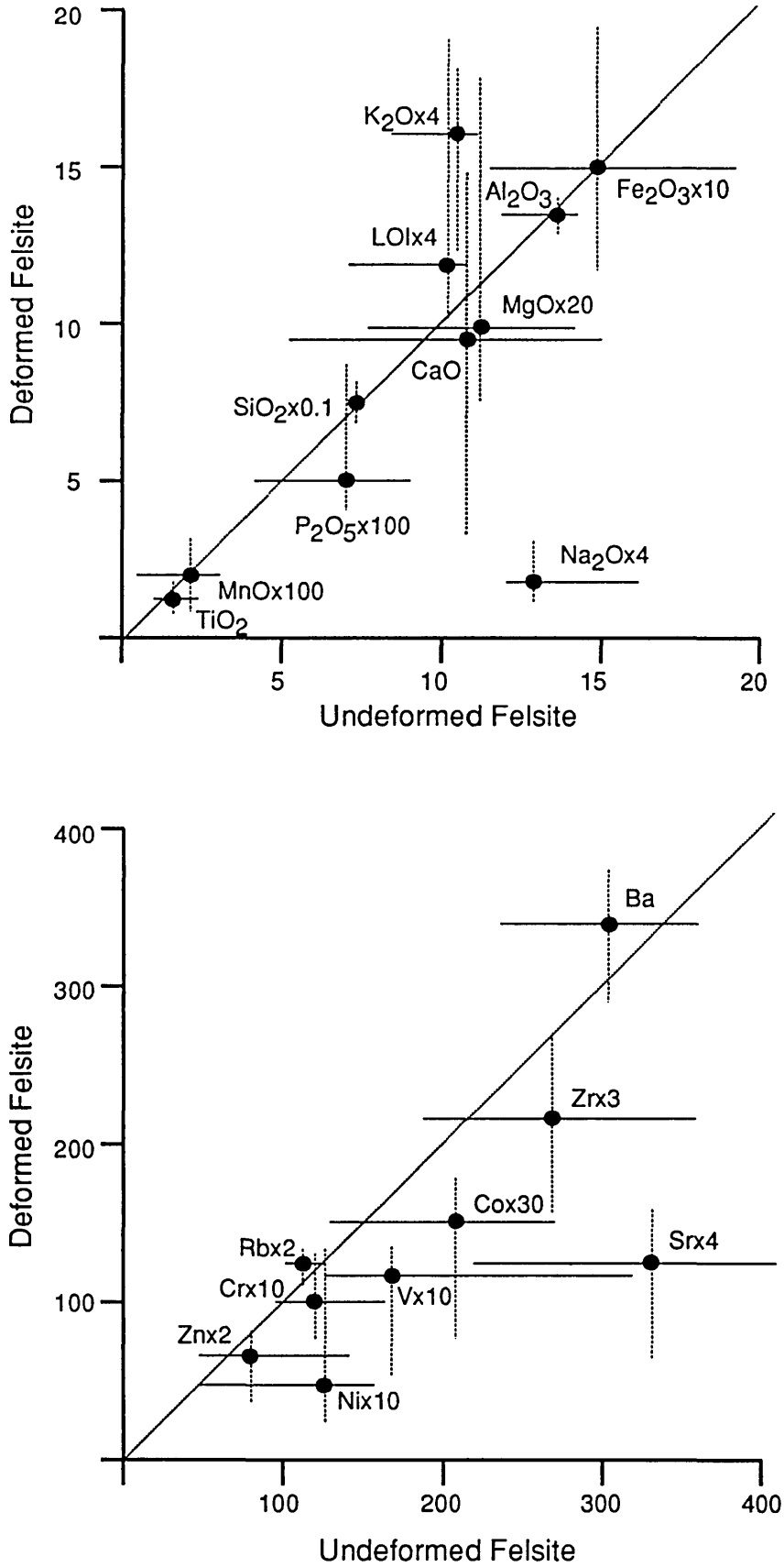


Figure 3.25 - "Isocon" plots for deformed felsic intrusive versus undeformed felsic intrusive samples from Patchway mine (after Grant 1986). Upper plot 3.25a is for major oxides, axes are relative with wt% oxide plotted except when the wt% oxide is multiplied by a factor for both deformed and undeformed value so the point lies within the range of the diagram (e.g. K_2O wt% x 10 is plotted). Lower plot 3.25b is for traces and a similar method of plotting the ppm values is used.

depleted in the same fashion as the mafic rocks. The behaviour of base metals is somewhat different. Cu is added whereas Zn is removed during deformation. Both appear to be added to the mafic rocks during the deformation and hydrothermal alteration process.

The chemical changes suffered by both the mafic lavas and felsic intrusives are very similar.

3.6 Conclusions

In establishing a tentative model for the petrogenesis of the Bulawayan greenstones and later intrusive suites seen in the Patchway region, some regard must be paid to recent suggestions of Archaean plate tectonic processes (Barley *et al.* 1989, Hodgson & Hamilton 1989). Indeed, for at least parts of the upper parts of the greenstone belt development, such a model has been explored by Nisbet *et al.* (1981).

The current geochemical study of the Patchway mafic lavas, when considered together with the published data of Condie & Harrison (1976) shows the lavas to be iron-rich tholeiites. They were most likely erupted in a sub-aqueous environment where they suffered later diagenesis and Na-metasomatism. The rocks have then suffered greenschist facies metamorphism. Indications are that the rocks show an affinity to more recent arc-lavas, although the sequence is dominantly basaltic with seemingly no evolved component.

On a regional scale the sequence of mafic flow rocks is extensive (Bliss 1970), with few interbedded sediments apart from some minor BIFs and shales. This shows a strong similarity with a similar sequence in the Pilbara of Western Australia (Groves & Batt 1984), which are interpreted as a "platform" sequence, extruded into an environment of low topographic relief.

Cutting the mafic volcanics is the 2700 Ma Sesombi intrusive suite (Hawkesworth & Bickle 1977), together with the related suite of thin TTG ("felsite") intrusives seen underground at the Patchway and Golden Valley mines.

Geochemically these intrusives are consistent with either arc-granites or alternatively could be the result of partial melting of earlier mafic crust. Support for the arc model comes from the proposed association with the Calc-alkaline unit which overlies the mafic lavas (Hawkesworth & Bickle 1977). The Calc-alkaline unit is only developed west of the major facies divide (see Figure 2.1), which could be due to a plate tectonic boundary.

This type of model is proposed as a possible scenario by Nisbet *et al.* (1981), although any plate tectonic model might be expected to be quite different in Archaean times compared to more recent events. However, some continental crust undoubtedly existed to the southeast during Bulawayan times and the

movement of this crustal block during Limpopo deformation may be linked to deformation in the Kadoma region. A model of some type of underplating/subduction in the Kadoma region which generated the magma resulting in the Sesombi and related intrusives, together with eruption of late Bulawayan calc-alkaline volcanics might be speculated. It is probable that this major tectonic and magmatic event was responsible for the regional greenschist metamorphism event coupled, perhaps, with the initiation of the regionally gold-bearing structures.

The zone of deformed rocks seen marginal to the gold-bearing mineralisation shows accompanying alteration which is testament to large scale fluid flux of an H_2O-CO_2-K^+-Ba^{2+} bearing fluid which largely resulted in breakdown of feldspar, amphibole and epidote to hydrous phyllosilicates, carbonate and quartz. Sodium, and perhaps magnesium, are lost from the wallrock and are released to the fluid. This fluid flux clearly post-dates the mafic lavas and at least some of the "felsite" intrusions.

Cross-cutting all these features are the mafic dyke phases. Geochemical studies indicate that they are dolerites, of possible within-plate tectonic setting. From the work of Wilson *et al.* (1987), it is probable that these dykes are part of the 2150 Ma Plumtree swarm, which are feeders to Proterozoic lavas. These dykes are approximately sub-parallel to the Great Dyke structure and may have been intruded in a similar stress field (see Chapter 2).

CHAPTER FOUR - DEFORMATION, FLUIDS AND MESOTHERMAL QUARTZ VEINS

4.1 Introduction

The association of Archaean gold deposits with regional fault systems was recognised by early workers (Hurst 1935, Gunning & Ambrose 1937). It is now clear that these structures form shear systems within which smaller scale structures localise gold orebodies. These same shear systems also played the part of conduits, either from deep fluid sources or a focus for locally derived fluids. These same fluids were largely responsible for the transport and deposition of the ore and gangue mineralogy.

This chapter aims to examine the dynamic relationship between faulting, fluid flow and mineral deposition in large, shear-hosted quartz vein systems. Although the literature contains many reviews of fluid-structural behaviour associated with shearing, this chapter aims to focus on the possible mode of formation of quartz veins which show characteristic ribbon-banding. The laminated texture of these veins is indicative of transient, episodic mineralisation processes which can be directly related to a structural and fluid evolution model.

Firstly the physico-chemical role of fluids in deformation is examined and the effect of fluids on deformation style is outlined. The types of fault rocks developed record the deformation style and are a key to fluid P-T conditions. Relating this role of fluids in deformation to the large, crustal-scale structures which often control the distribution of mesothermal gold deposits, leads to a conceptual model of fluid-fault behaviour under fluctuating high fluid pressure and stick-slip fault movement, responsible for ribboned quartz veins. The behaviour of a hydrothermal fluid during such cyclic events is addressed in terms of chemical effects to dissolved, transported species.

4.2 Fluids and Deformation

"...when water is collected into one place it softens the rock by its liquid nature, and by its weight and pressure, breaks and divides it." (Agricola 1546)

The connection between deformation and fluid behaviour is extensively described in the literature (Fyfe *et al.* 1978, Sibson 1981a, 1981b, 1986, Sibson *et al.* 1975, Fyfe & Kerrich 1984, 1985, Etheridge *et al.* 1984, Kerrich 1986). High fluid pressures have important rheological and geochemical consequences as indicated by Etheridge *et al.* (1984). Rutter (1986) has already demonstrated that brittle processes can occur at temperatures and pressures where plastic deformation processes normally dominate, simply as a result of high fluid pressures. The effect of fluid pressure (P_f) can be demonstrated graphically on the Mohr stress circle (Figure 4.1). Increasing fluid pressure serves to shift the stress circle to the left, in other words toward the failure envelope.

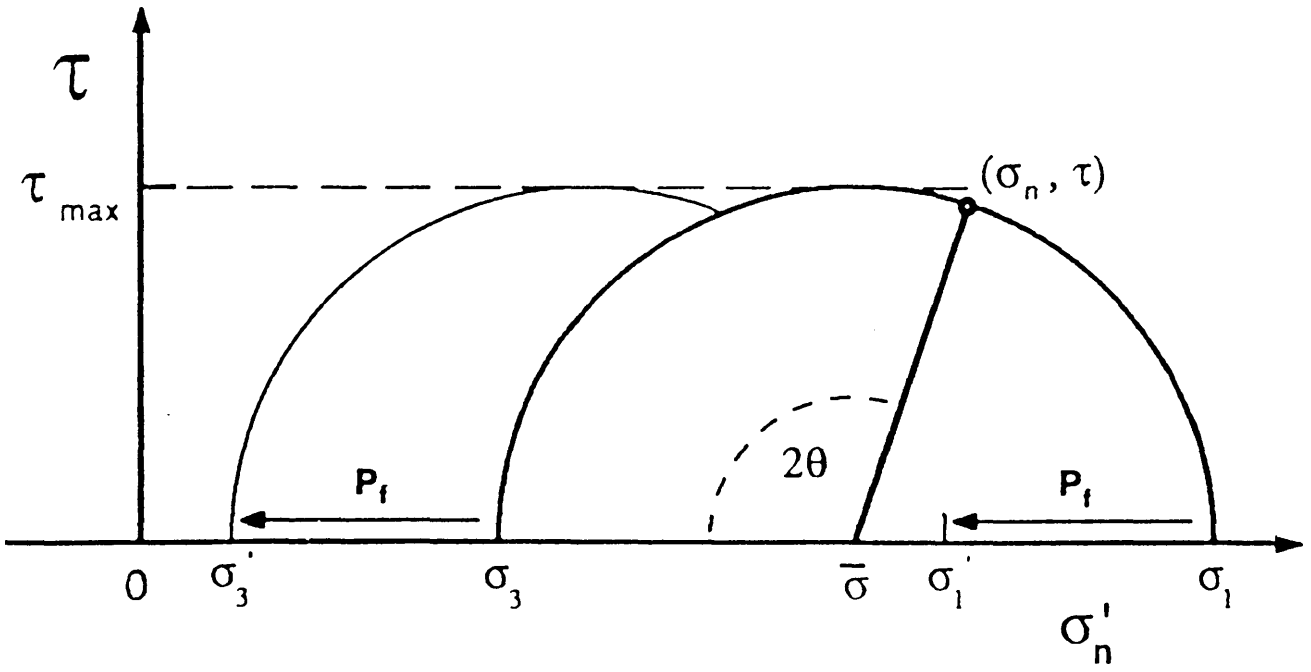


Figure 4.1 - Diagram indicating the effect of fluid pressure (P_f) on the Mohr stress circle. (σ_1 and σ_3 are maximium and minimum principal stresses respectively, σ_n is the normal stress and τ the shear stress)

In normal circumstances, fluid pressure should relate to hydrostatic pressure. Theoretically, the ratio of fluid (P_f) to lithostatic pressures (P_{lith}) should be approximately 0.4. Since both fluid pressure under true hydrostatic conditions relates to fluid density (ρ_f) and gravitational constant (g) and depth (z) by $P_f = \rho_f.g.z$ and hence $P_{lith} = \rho_{lith}.g.z$. The relationship can be seen graphically in Figure 4.2 together with some real examples where values for $P_f : P_{lith}$ of up to 0.8 are not exceptional in stable crust (Fyfe *et al.* 1978). In this case the state of fluid overpressure exists where fluid is not continuously interconnected throughout the crust to surface. The classic study of Hubbert & Rubey (1959) demonstrated that during thrusting, to cause failure, fluid pressure must exceed lithostatic pressure ($P_f : P_{lith} > 1$). It thus follows that fluid pressure in this case becomes the key control to fault movement. In strike slip systems in the seismic portion of the crust (< 15 km depth) Sibson *et al.* (1975) modelled a passive role for fluids which were essentially sucked into a displacement dilatancy ("seismic pumping") but it became clear that perhaps the fluid could play an active role in faulting and that a "seismic valve" model was perhaps more appropriate in many fault systems (Sibson 1981). This type of synthesised fluid-deformational model for major structures was expanded by Gold & Soter (1985) into their model of "compartmentalised" crustal fluid domains (Figure 4.3).

It is clear then that structure and fluid are likely to be fundamentally linked during the formation of epigenetic mineral deposits, both as mineral solvents and through its hydraulic effect. The relationship seems particularly strong for mesothermal veins hosted in shear zones like Patchway, where recent work demonstrates that such deposits may have formed in seismogenic ("stick-slip" deformation) portions of the crust (Sibson *et al.* 1989).

4.3 Deformation Models

Three fundamental deformation mechanisms for rock deformation are defined in the literature (Rutter 1986), and deformation in the crust is a product of any one or combination of cataclasis, diffusive mass transfer or crystal plasticity. The behaviour of rocks and hence the preferred mechanism or mechanisms is determined by several variables of which the most important are: applied external stress, temperature, pressure, fluid pressure, stress and strain rate. Rock type should also be considered a variable (Obee 1985) since this has bearing on the manner stress is accommodated within the rock, and also the rocks inherent porosity and permeability.

The crust shows strong evidence for transition in rheological behaviour at depth. Although transition from brittle to ductile processes in the crust is dependent on several variables including the rheological properties of the rock as well as external physical parameters (Fyfe *et al.* 1978), broad generalisations are possible. Under crustal conditions with a "normal" temperature gradient of 25° C per kilometre, the transition between brittle and ductile processes occurs at lithostatic pressures of some 2 to 3 KBars at a temperature of 240 to 360° C (Sibson 1983, 1984). Seismic studies (Meissner 1986) show that

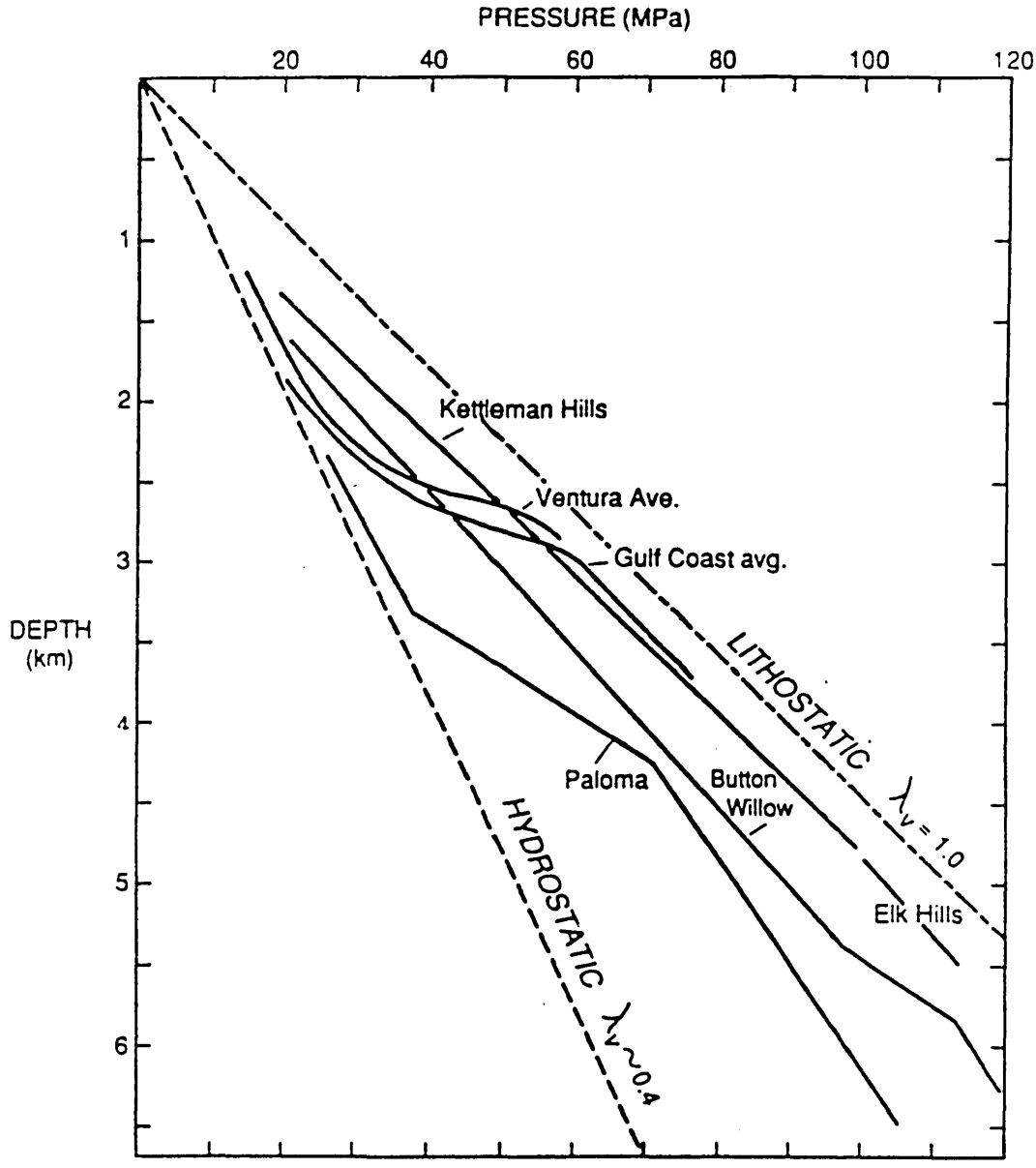


Figure 4.2 - Diagram showing relationship between Hydrostatic and Lithostatic Pressure. Also shown are examples of fluid pressures for reservoirs in tectonically active zones of the western USA (after Yerkes *et al.* 1985).

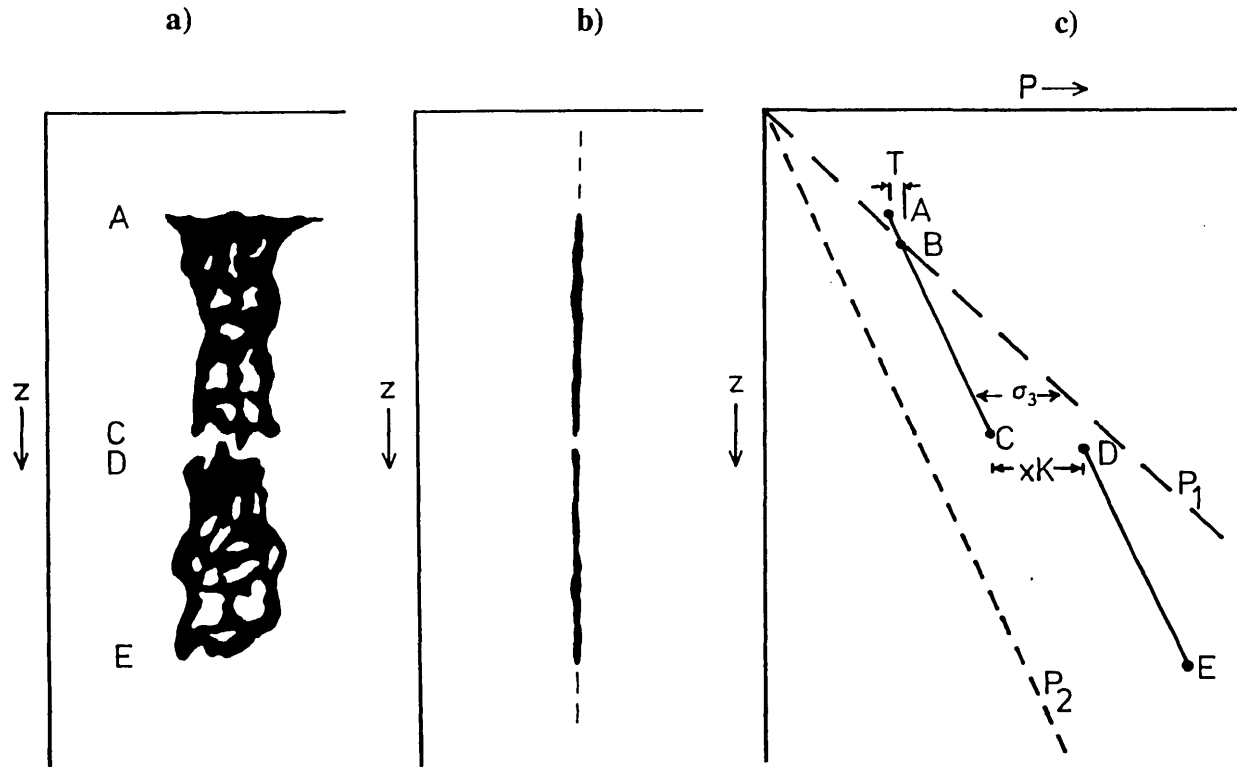


Figure 4.3 - Model for fluid ascent in the crust proposed by Gold & Soter (1985). Two vertically adjacent fluid domains following the same fracture are shown in a) longitudinal section b) cross-section and c) as depth-pressure profiles. In all cases z = depth, A-C and D-E the two discrete fluid domains, each domain fully interconnected and supported by 'bridges'across the structure [white areas in a)]. P_1 represents the least principal external stress, from which the least principal effective stress, σ_3, is derived from P_1 - P_{fluid}. P_2 represents the simple hydrostatic head (ρ.g.z). T represents the maximum tensile strength of the rock, which permits the overpressured fluid reservoir at point A. xK is a fraction of K, the compressive strength of the rock, where x → 1, sufficient to seal the lower from the upper domain. It can be seen from the diagram that in this case of a simple vertical fracture, an increase in the fluid pressure in the lower domain [which serves to force point D to the right on c)], will cause failure of the seal betweeen C and D. This allows fluid to "valve" from the lower to the upper domain.

seismic events peak at a depth of 10 to 15 km, rapidly dropping off below 16 km allowing the crust to be divided into seismic and aseismic portions.

In studies of seismogenic (elastico-frictional) portions of the crust and palaeocrust, cataclasis is the dominant deformation mechanism (Sibson 1986). Cataclasis is accompanied by dilatancy and hence is highly pressure sensitive. The creation of dilatancy obviously has strong implications for behaviour of any fluid accompanying cataclastic deformation. As Maddock (1986) demonstrates an important feature of cataclasis is distributed fracturing including shear and extension fractures.

In aseismic portions of the crust, deformation is by dominantly plastic processes which by definition, cause the process of softening. Softening can take the form of either mechanical or chemical softening by the processes outlined below. The onset of this process can be considered as the product of localised stress concentration caused by three likely methods: material inhomogeneity, localised high fluid pressure and non-uniform temperature field.

Crystal plasticity is sensitive to temperature, stress and strain rate and probably forms the dominant deformation mechanism in the deeper quasi-plastic regions of the crust (Sibson 1986). Deformation is through reorganisation of crystal lattice defects, which after initial strain hardening evolves to dislocation creep and thus strain softening (Obee 1985). Dynamic recrystallisation results in grain growth and polygonal subgrain textures which, in fault rocks, generally means reduction in grain size (Bell & Etheridge 1973). Although normally not dependent on fluids, there is some evidence for crystal plastic behaviour in quartz to be enhanced by the presence of water (Griggs 1967).

The mechanism of diffusive mass transfer occurs by two mechanisms i) intracrystalline diffusion or Nabarro-Herring creep and ii) grain boundary diffusion or Coble creep. Difficult to distinguish in nature, Coble creep is more favourable at lower temperatures due to its lower activation energy. Coble creep is particularly important in the presence of an intergranular fluid when it is termed pressure solution (McClay 1977). Rutter (1983) describes pressure solution processes where pressure enhanced dissolution and transfer of material through the intergranular fluid leads to precipitation at less stressed sites. White & White (1981) suggest that interconnective grain boundary bubbles and tubes in tectonites would enhance strain rates during deformation by this process.

Dislocation or diffusion creep (DAGBS) in certain conditions can lead to adjacent grains in deforming rocks sliding along their boundaries. This creep process involves neighbour grains switching bonds (White & White 1981). DAGBS is likely to be an important mechanism of deformation in rocks (Rutter & Brodie 1987) particularly in rocks of fine grain size or containing well oriented phyllosilicate bands (White *et al.* 1986).

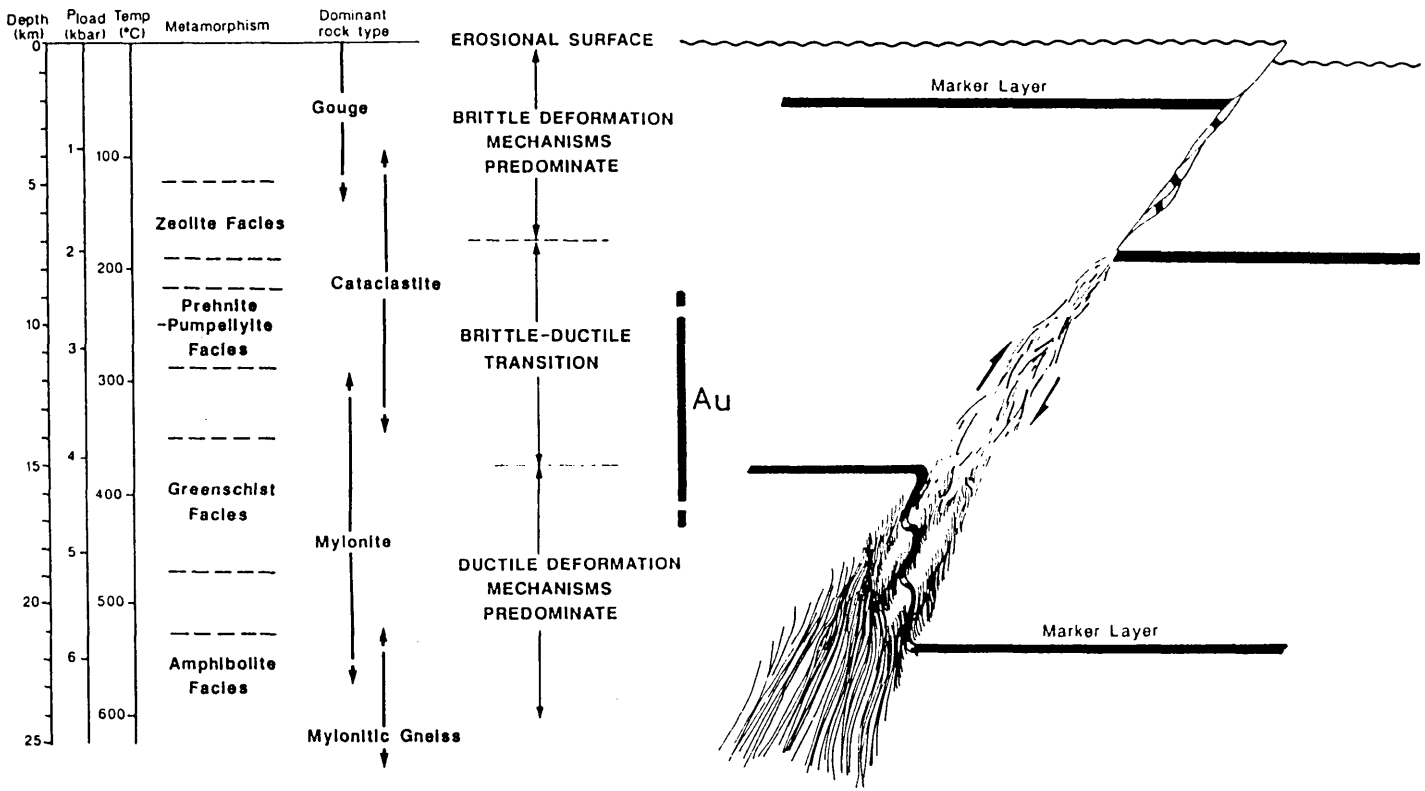


Figure 4.4 - Schematic diagram indicating deformation regimes likely as a function of depth. (Diagram modified from Colvine *et al.* 1988 after Sibson 1977, 1981) The black bar labelled "Au" shows the approximate range of conditions during formation of most mesothermal gold deposits.

4.4 Fault Rocks

Two major fault rock types can be identified (based on Sibsons 1977 classification): 1) Cataclasites and 2) Mylonites. The classification can be clarified with reference to the three major deformation mechanisms already discussed : i) cataclasis ii) intra-crystalline plasticity and iii) diffusive mass transfer or flow. The last two processes are, by definition, plastic and as such give rise to mylonites and obviously cataclasis leads to cataclasites. Terms such as brittle and ductile are somewhat entrenched in the literature as descriptions of respectively cataclastic and plastic processes, but since it can be argued that cataclastic flow is in fact a "ductile" process (Rutter 1986) confusion can occur. The terms brittle and ductile are retained here as their use is widespread as useful textural descriptive terms for the two main fault rock groupings.

Since the mechanisms for deformation are to a large part dependent upon temperature and confining pressure, generalisations based on Sibson's (1977) and Wise *et al.* (1984) classification show a generally depth related transition between major process domains of brittle and plastic (ductile). Further generalisation shows that the transition from cataclastic to plastic mylonitic processes occurs at the approximate boundary between greenschist and amphibolite metamorphic grades. This division of crust into broad zones defined by deformation style and mechanism can be summarised diagrammatically (Figure 4.4). Although these models have been developed for quartzo-feldspathic rock types, modification based on lithotype is likely to be fairly minor on a crustal scale (Tabeart 1989). This boundary is also shown to be the approximate boundary between seismic and aseismic slip on major structures (Sibson 1983), above which, faults show frictional stick-slip motion whilst at deeper levels quasi-plastic flow is recorded. The greenschist-amphibolite facies boundary then becomes extremely pertinent when it is linked to the observation that the majority of structurally controlled Archaean gold gold deposits occur at the greenschist-amphibolite facies boundary (Colvine *et al.* 1984). As a general rule, when mean stress and temperature are low, or if pore fluid pressure or strain rate is high, rocks are likely to fail by brittle, extensional failure. Fractures are likely to develop parallel to $\sigma 1$ (maximum principle stress). An increase in one or more of the variables; mean stress, fluid pressure or temperature means that tensile failure gives way to shear failure. If the pore fluid pressure and/or strain rate are decreased the same is true. Perfectly homogeneous, isotropic media will suffer brittle failure under stress subject to predictions according to Coulomb-Griffith criteria (Figure 4.5). However rocks are not homogeneous (Ramsay 1980), and indeed suffer from mechanical inhomogeneities from an individual grain to regional formational scale. Furthermore deformation induced inhomogeneity such as reaction softening further complicate analysis of systems.

The formation of mineral veins implies discrete brittle failure. Three broad types of brittle failure from homogeneous isotropic intact rock can be modelled based on the Mohr circle (Etheridge 1983). The conditions for failure are summarised by Sibson (1990) and his diagrams are shown on Figure 4.6 with

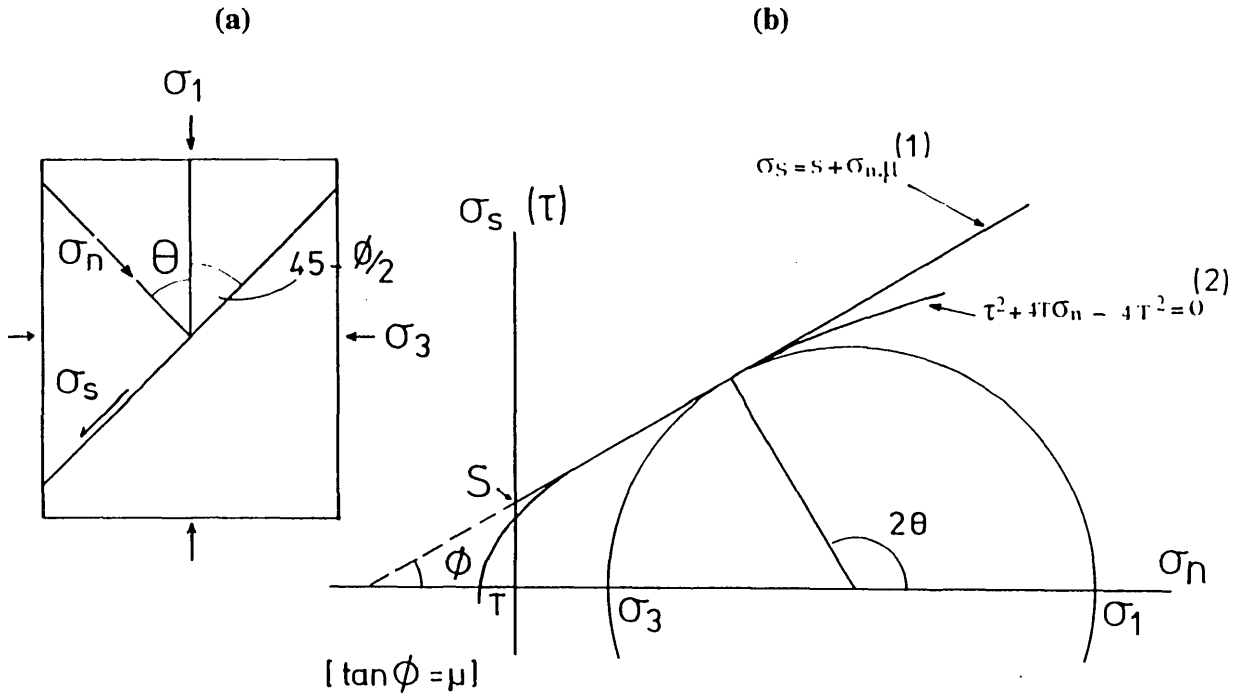


Figure 4.5 - Mohr's construction (b) for failure of intact rock around failure surface defined by (a). Shown on the diagram are (1) Coulomb's costruction for shear failure and (2) the parabolic failure envelope embracing Griffith crack theory. Symbols on the figure are as follows : σ_1 and σ_3 are maximum and minimum principal stresses respectively; σ_n is normal stress; $\sigma_S = \tau$ = shear stress; μ is the coefficient of internal friction of the rock; T and S are the uniaxial tensile and shear strengths of the rock respectively. As stated above (1) is the construction for shear failure $\sigma_S = S + \sigma_n.\mu$ and (2) is the parabolic construction where $\tau^2 + 4T\sigma_n - 4T^2 = 0$.

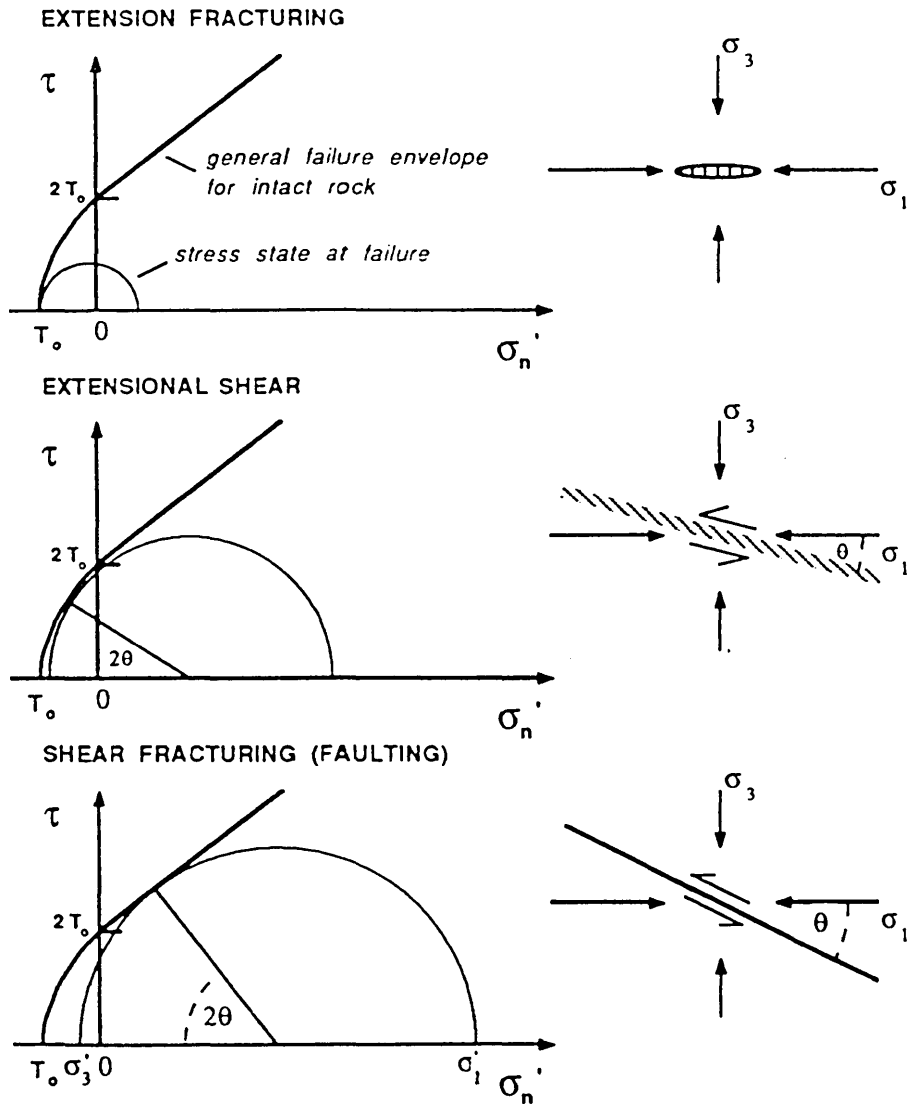


Figure 4.6 - Diagrams to show three modes of brittle failure for intact rock (from Sibson 1990, after Etheridge 1983). The most common situation for discrete faulting is shown at the bottom.

reference to the Mohr stress circle. The differing failure is due to differences in differential stress states ($\sigma 1$ - $\sigma 3$) in relation to tensile strength of the rock (T_o).

To study the conditions for failure, a hypothetical fault surface is modelled as in Figure 4.7. For compressional shear failure, as shown in the adjoining Mohr circle, movement on the fault is normally governed by the Coulomb Criteria:

$$\tau = C_o + \mu_i \sigma_n'$$

where:

$$\sigma_n' = \sigma_n - P_f$$

In this case C_o, the cohesive strength which in intact homogeneous rock approximates $2T_o$ (twice the tensile strength of the rock) and $0.5 < \mu_i < 1.0$ (Jaeger & Cook 1979). However, for re-shear of an existing fault, C_o is effectively zero and the equation reduces to a function of the frictional strength of the plane. In this case the equation becomes:

$$\tau = \mu_s(\sigma_n - P_f)$$

Byerlee (1978) showed that in this case, for most rocks $0.6 < \mu_s < 0.85$ which Sibson (1983) further simplifies to a useful average of 0.75. Sibson further notes that for the Byerlee friction model, structures tend to "lock-up" when dip values approach 35° unless $P_f > \sigma_3$. This has major implications for reverse faults as motion on, even a well established, fault surface with a dip greater than 30° implies high fluid pressures. Because in most of such cases σ_3 equals lithostatic pressure, fluid pressure to lithostatic pressure ratios close to or exceeding unity are necessary.

4.5 Crustal Scale Fault Structures

Faults, and particularly faults which form part of more complex shear zones, have long been recognised as loci for gold mineralisation (e.g. Gunning & Ambrose 1937, Boyle 1979, Colvine *et al.* 1984, White & Baxter 1987). It is further widely recognised that deep seated crustal fractures, commonly referred to as lineaments or "breaks" in the literature, exert a major influence on the localisation of Archaean gold deposits. These structures are long-lived strike-slip or dip-slip, ductile to brittle, shear zones which are associated with secondary and tertiary structures and show that they must have formed focused channelways for episodic hydrothermal fluid flow during deformation. Such structures often form, or are closely related to, major features which separate contrasting geological terrains.

In Canada the regionally important Campbell Shear is host to the major Yellowknife gold deposits (Boyle 1961). The Destor-Porcupine and Kirkland Lake-Larder Lake faults in Ontario and the Cadillac-Bouzon fault in Quebec have been recognised as major foci for gold mineralisation in the Superior province of Canada (Gunning & Ambrose 1937, Colvine *et al.* 1988). Similarly the Boulder-LeFroy fault as it transects the Norseman-Wiluna belt of the Yilgarn Block, Australia is a clear focus for the many structurally controlled gold deposits (Groves *et al.* 1987).

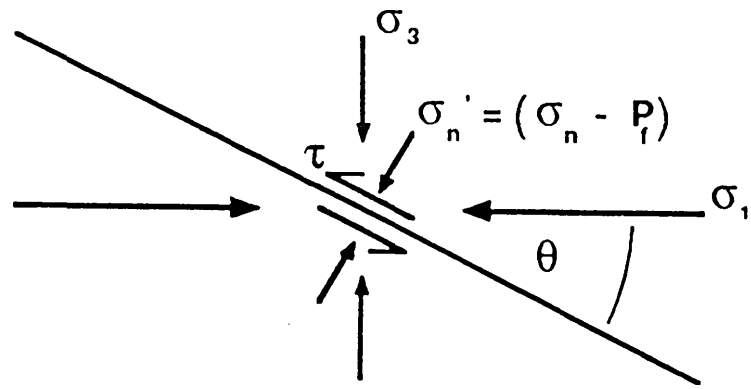


Figure 4.7 - Model fault plane with resolved forces defined.(for definition of terms see Figure 4.5)

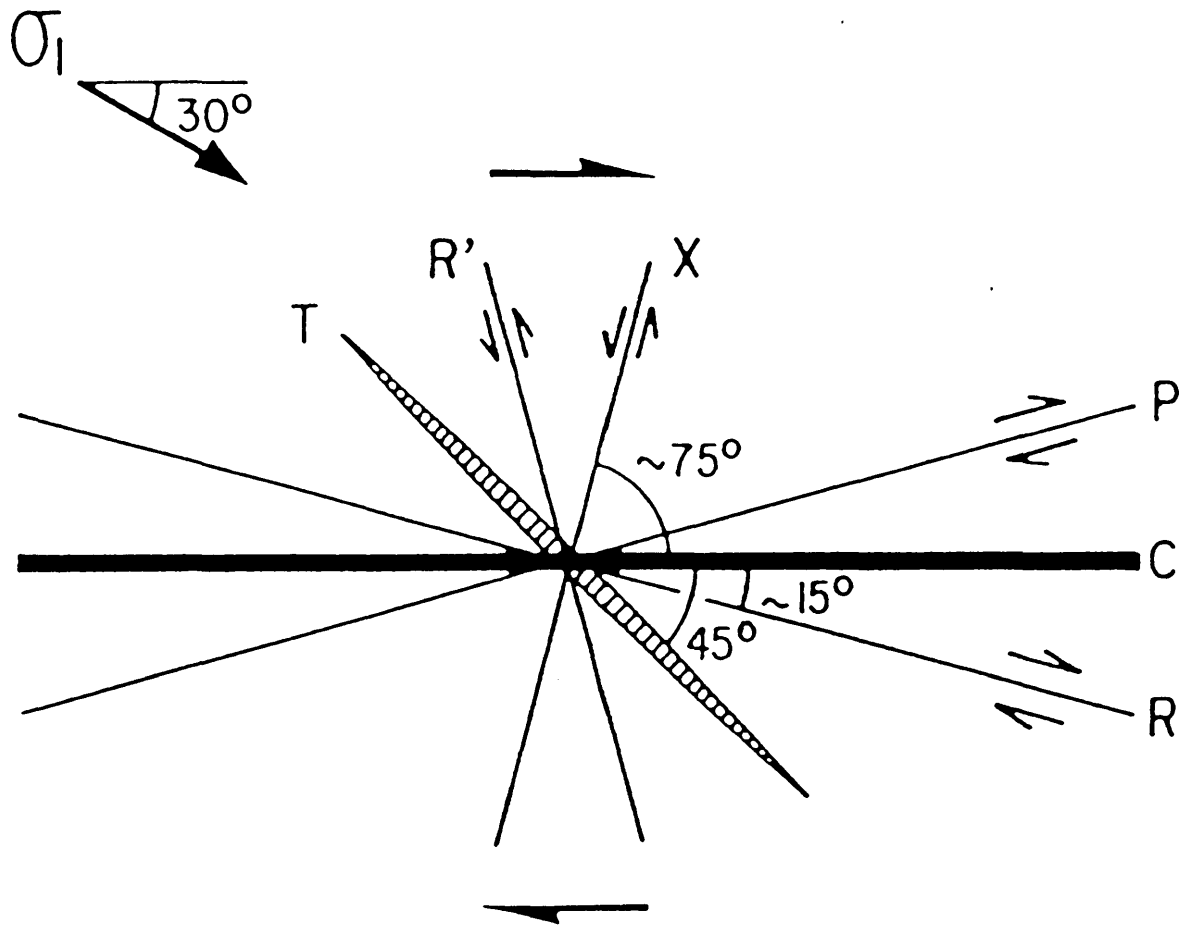


Figure 4.8 - Diagram of Riedel geometry developed around dextral sense central failure ("C" plane). Geometric array described in the text.

Shear zones are complex fault zones where deformation is accommodated by a series of related structures, and nucleate when the hardening capacity of the host is exceeded, thus indicating the rock has initiated some degree of softening (White *et al.* 1980). This softening can take the form of either mechanical or chemical softening and was discussed earlier.

Sibson (1986) noted that as faults form through such concentration of deformation, shear resistance is either maintained or decreases. Thus, once a fault has been initiated, further deformation is likely to be focussed in the same structure unless major changes in the stress regime of a particular field can be envisaged. In addition to this deformation focus, the later reactivation of an existing structure seems highly likely (White *et al.* 1980). In real terms undeformed sialic crust can support differential stresses of some 1.5 Kbars (Jefferys 1952). This figure compares with a strength of a few hundred bars in fault rocks in seismogenic structures (Ambraseys 1969), so it is easy to see how once faults are initiated, strain readily partitions into existing structures, increasingly isolating undeformed host lithologies, leading to *strain partitioning*, or focus of deformation into discrete interconnected zones.

Simple strike-slip fault arrays have been modelled in the now classic Riedel experiments (Riedel 1929, Tchalenko 1968, Wilcox *et al.* 1973). Discussion of the geometrical relationships within such systems have been covered by various authors (Casey 1980, White & Baxter 1987 and Hodgson 1989) and the patterns of Riedel geometries to fault systems have been applied to the analysis of complex shear zones (Figure 4.8). Several authors including Harris (1987) and White (1990) have applied the Reidel geometry model on a regional scale within long-lived shear systems. While in detail it is true that array relationships are modified in any dynamic system, broad generalities of preferred fracture arrays can be defined. From this geometric array, prediction of sites more favourable for extension, and hence dilation, can be made. In such sites the precipitation of dissolved species from the hydrothermal fluid is likely to be more focussed.

4.6 Fluids in Crustal Scale Shear Zones

The source of crustal hydrothermal fluids responsible for the transport and deposition of minerals within crustal scale structures has received a great deal of attention in the literature (e.g. Fyfe & Kerrich 1985, Kerrich 1986, Groves & Phillips 1987, Cameron & Hattori 1987, Cameron 1988, Colvine *et al.* 1988, Nesbitt *et al.* 1989). From the literature it is clear that the nature of the fluids responsible for the major vein systems in terrain boundary fault systems developed in generally compressive strike-slip (transpressive) regimes, such as the Destor-Porcupine, Kirkland Lake-Cadillac "Breaks" in the Archaean Abitibi of Canada, the Boulder-LeFroy fault in the Archaean Norseman-Wiluna belt of Western Australia together with possible modern analogues such as the Jurassic Melones fault system of California (Mother Lode) and the Cretaceous-Tertiary Coast Range Megalineament of Juneau Alaska is fairly similar. Epigenetic vein deposit types in all these previously mentioned environments are similar

with quartz-carbonate-sulphide-gold bearing veins commonly developed in structural favourable environments within the fault arrays. As well as common structural features, the deposits developed share a number of common features pertinent to discussion of possible fluid source for the mineralisation.

In the study of fluids active in structural systems, like the Boulder-LeFroy and Cadillac-Larder Lake structures, which are responsible for these gold deposits, certain common key features emerge. These common features are indicative of perhaps common source, common protracted evolution within the structures or a combination of both. Fluid inclusion studies of mesothermal gold deposits show that the deposits probably formed from very similar fluids. The fluids are generally of low salinity (generally less than 5 wt% NaCl equivalent), and contain significant CO_2 (5-30 mol%). The gangue mineralogies are often similar, and the restricted stable isotope signature support regionally common hydrothermal fluid reservoirs (Kyser & Kerrich 1990). Furthermore, the largely, mineralogically unzoned nature of most of the large deposits, the late kinematic timing for much of the mineralisation, and restriction of deposits to constrained P-T conditions, leads to the suggestion of common fluid behaviour during mineralisation.

Numerous hypotheses for fluid source have been proposed for the "family" of mesothermal gold deposits, and these were recently reviewed by Kyser & Kerrich (1990). Of these models, the four most likely possibilities appear to be: i) fluid released during granulitisation, i) orthomagmatic fluid, iii) cycled meteoric fluid and iv) metamorphically-derived fluid. These conflicting models will not be discussed here but are reviewed together with the results of the current study in Chapter 9.

Fluid flow is undoubtedly focussed dramatically through shear-zones which form major fluid conduits. Disagreement on the mode of formation of the epigenetic deposits centres mainly on the way the fluid becomes focussed and behaves within the shear zone. The literature contains several models of fluid behaviour within such a zone, which are outlined below:

i) Grain boundary diffusion, where the lateral diffusion of CO_2 and H_2O from host rocks into the major structure is proposed (Boyle 1979).

ii) Fluid convection under hydrostatic conditions within the structure (Kerrich & Allison 1978, Allison & Kerrich 1980, Nesbitt *et al.* 1986).

iii) Fluid circulation in convective cells constrained by impermeability barrier such that $P_f : P_{lith}$ approaches 1.0 (Etheridge *et al.* 1983).

iv) Fault valve model of suprahydrostatic fluids in single or multiple crustal cells - "Seismic Valving" (Sibson 1981, Gold & Soter 1985, Sibson *et al.* 1988).

v) Fluid pressure gradient from contractional sites in the wallrock to dilational zones in the structure - "Seismic Pumping" (Sibson *et al.* 1975, Guha *et al.* 1983, Ledru & Autron 1987).

There is strong support for models iv) and v) for the formation of complex veins and this is discussed below in the light of published studies.

4.7 Shear Zone Hosted Ribbon Quartz-Gold Veins

Fracture-hosted, mesothermal gold-quartz veins form the most common type of structurally-controlled gold deposit type throughout the geological record. The deposit type is similarly common in the Archaean. Similar morphological features are recorded in deposits with ages as diverse as the Yellowknife deposits in the Canadian Archaean (Boyle 1979), to Tertiary age Monta Rosa deposits in the Alps of northern Italy (Curti 1987). The common features recurrent despite the broad ranges in age for the deposits is likely to be due to development from common geodynamic processes (Kyser & Kerrich 1990).

"Ribbon" or "book" quartz veins are a typical sub-type of mesothermal vein, described again in deposit types as diverse as Archaean to Mesozoic. The literature demonstrates the similarity of textures from the Canadian Archaean, the Palaeozoic of eastern Australia and the Mesozoic of south-west USA (Hurst 1935, McKinstry & Ohle 1949, Chace 1949, Farmin 1941). The ribbon-veins seen at Patchway are clearly shown in Figure 2.9. As well as the broad morphological analogies, mineralogically the veins are all very similar and comprise >95% quartz in the white "ribbon" areas together with subordinate carbonate and phyllosilicates. Darker bands are of two distinct types. They can comprise slivers of wallrock, often altered and/or mineralised or else thin phyllosilicate laminations, often containing sulphide and gold bearing mineralisation (Figure 4.9). Historical descriptions of such deposit types (e.g. Hulin 1929, Ferguson & Gannett 1932, Hurst 1935, Farmin 1941, Chace 1949 and McKinstry & Ohle 1949) lead to the conclusion that most of such veins owed their origin to episodic, discontinuous processes. Veins with a dominance of quartz ribbons separated by wallrock slivers are often termed "book" texture, whilst the veins dominated by thin phyllosilicate septa are termed "ribbon" veins. These contrasting textures may give important clues to the mode of formation.

An important observation in the study of this ribboned quartz vein type is the nature of the inclusion band types (dark bands) within the complex quartz veins. The presence of stylolitic septa is very common in such veins (Figure 4.10). The other major textural type of inclusion band is where subparallel wallrock slivers are incorporated in complex veins, and yet they do not show this stylolitisation. This texture, where vein inclusions are parallel sided slivers of wallrock, often likened to the leaves of a book ("book texture"), may be the result of faulting under quite different fluid pressure conditions.

In their analysis of vein systems, Hodgson (1989) and Poulsen & Robert (1989) classify continuous ribbon-vein types as "shear veins", developed along the main failure of the shear zone (Figure 4.11).

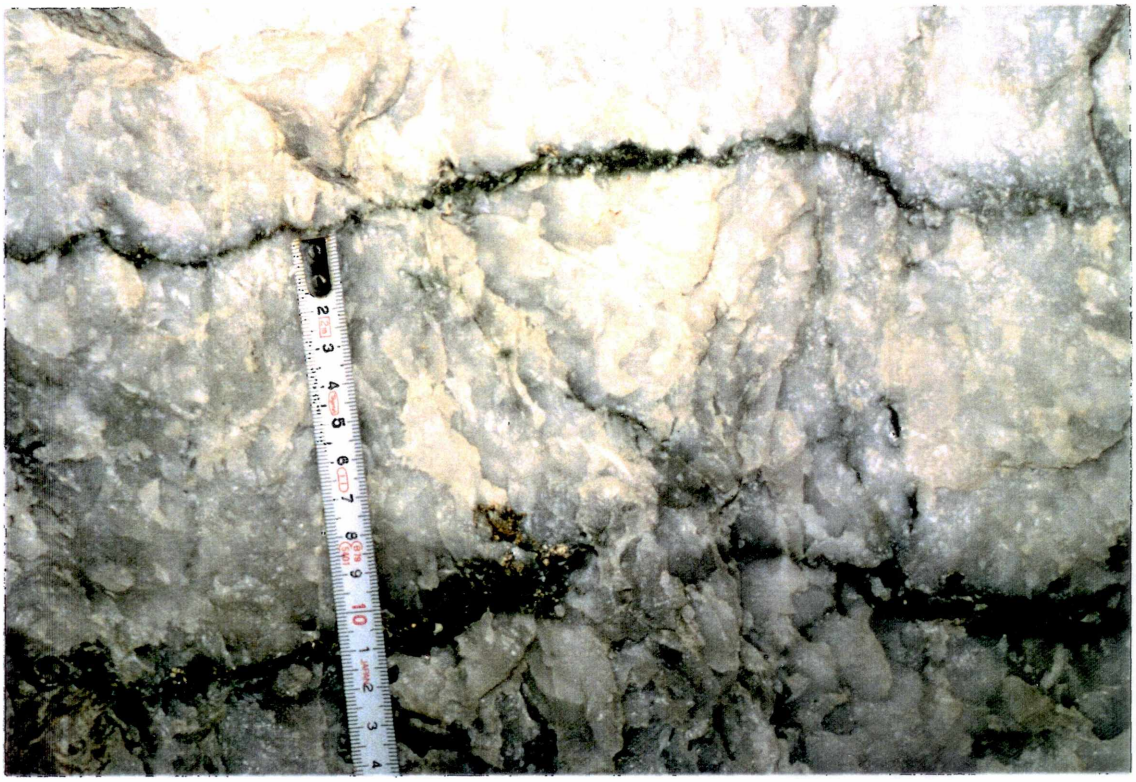


Figure 4.9 - Close-up photograph of ribbon vein texture on 6 Level North showing thin phyllosilicate septa clearly associated with sulphides (and gold). White quartz areas are generally devoid of other mineral phases. Tape shows centimetre divisions.

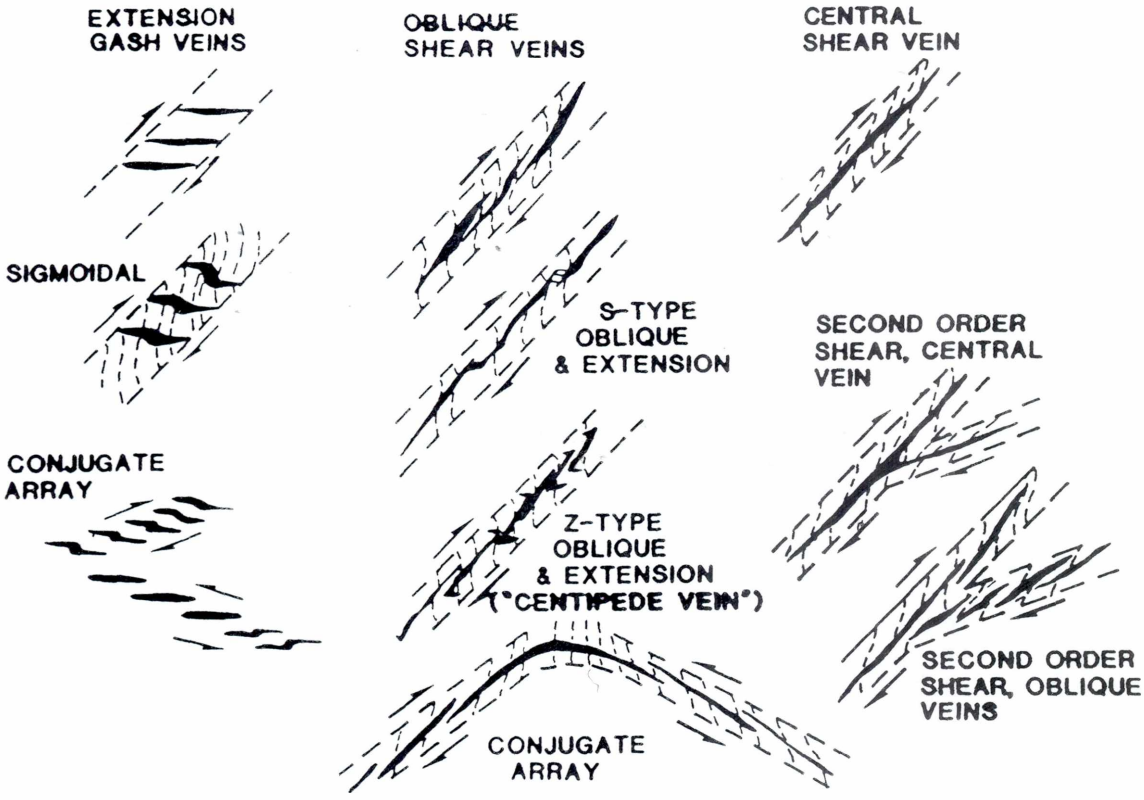


Figure 4.11 - Diagram showing common shear-zone vein geometries (from Hodgson 1989).

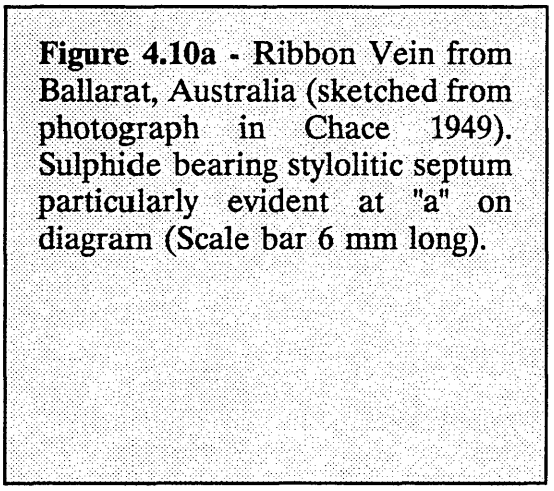


Figure 4.10a - Ribbon Vein from Ballarat, Australia (sketched from photograph in Chace 1949). Sulphide bearing stylolitic septum particularly evident at "a" on diagram (Scale bar 6 mm long).

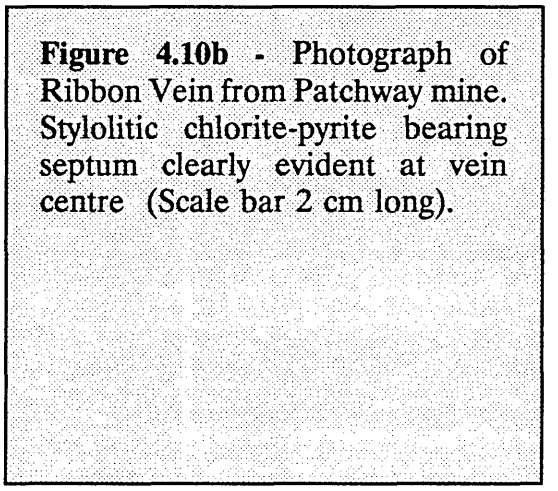


Figure 4.10b - Photograph of Ribbon Vein from Patchway mine. Stylolitic chlorite-pyrite bearing septum clearly evident at vein centre (Scale bar 2 cm long).

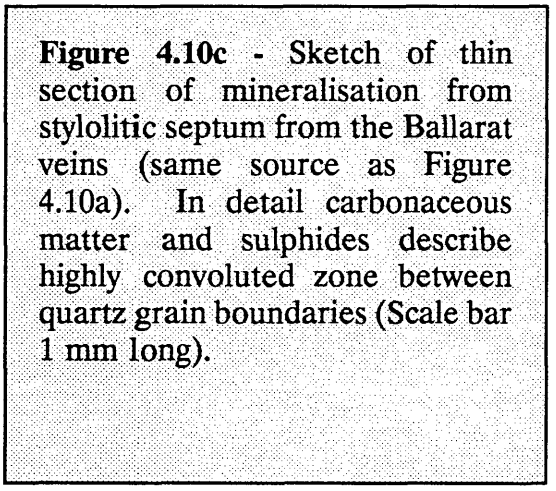


Figure 4.10c - Sketch of thin section of mineralisation from stylolitic septum from the Ballarat veins (same source as Figure 4.10a). In detail carbonaceous matter and sulphides describe highly convoluted zone between quartz grain boundaries (Scale bar 1 mm long).

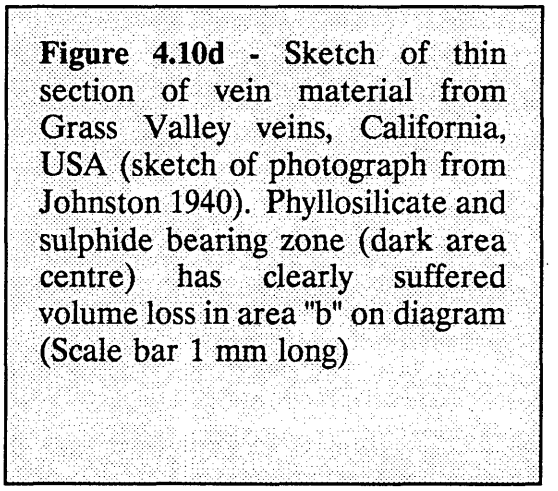
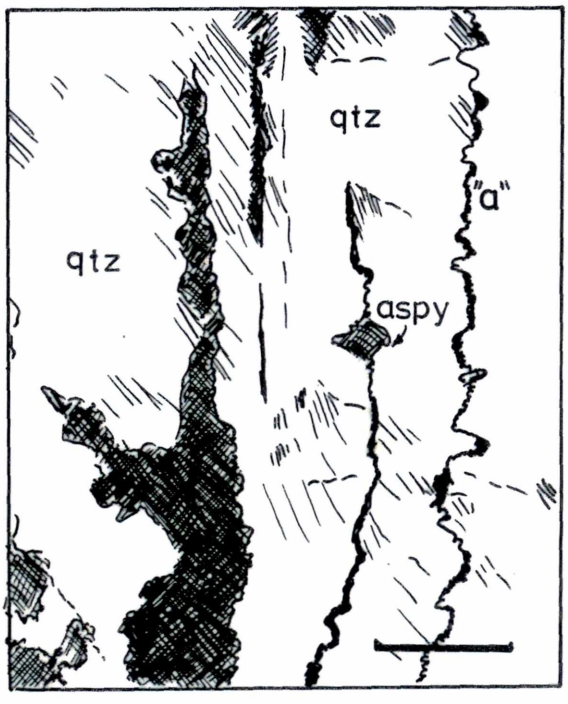
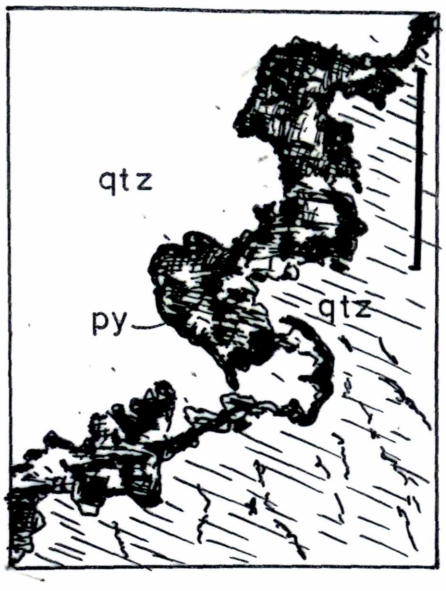
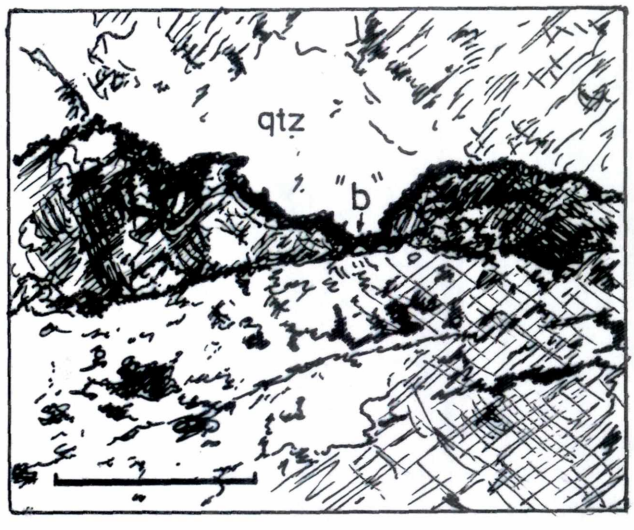


Figure 4.10d - Sketch of thin section of vein material from Grass Valley veins, California, USA (sketch of photograph from Johnston 1940). Phyllosilicate and sulphide bearing zone (dark area centre) has clearly suffered volume loss in area "b" on diagram (Scale bar 1 mm long)


qtz
"a"
qtz
aspy




qtz
py
qtz


qtz
"b"

Hodgson notes a strong dominance of Riedel geometries to developed veining and concludes that shear veins follow the central or "C" fracture. Such veins often demonstrate a common association with "R" and "P" oriented veins as well as purely extensional "T" veins (see Figure 4.8). The earlier observations of McKinstry & Ohle 1949, that the contact surface between included wallrock septa and quartz ribbon often show slickensides, supports this idea of the complex vein following the main shear fracture plane "C". Such central shear veins are typically laterally extensive from tens of metres to, in the case of the Patchway deposit, thousands of metres of strike. Although within the central shear fracture, the individual ribbons cannot be traced over this distance, unequivocal lateral persistence of ribbons over many tens of metres has been seen observed. Such veins clearly follow a single regionally persistent fault zone which has been subject to reactivation.

The fact that these veins might be the result of successive vein wall focussed brittle failure - dilation - infilling events was noted early on in the literature (Hulin 1929). Cox (1987) has shown that what he terms antitaxial "crack-seal" vein processes can lead to a diversity of vein microstructures which include irregular grain fabrics typical of rapid quartz growth occlusion as well as fibrous and laminated microstructures. "Crack-seal" as described by Ramsay (1980) is a term commonly used in the literature to describe episodic failure and infilling in veins, but in fact Ramsay describes fracture and infill in fairly static conditions, where infilling of the fracture by delicate mineral overgrowth occurs. It is therefore a misleading term in the case of fractures formed under conditions of high shear stress where deformation may be controlled by an exotic, probably overpressured, hydrothermal fluid.

Ramsay's "crack-seal" model describes the case where a simple opening extensional fracture generates a moderate fluid pressure gradient from the surrounding rock to the fracture, and silica transported in solution from the wallrock is precipitated in fairly static condition as quartz in optical continuity with previously precipitated crystals. This situation is somewhat similar to the model of shear zone fluid flow proposed by Guha *et al.* (1983) (see model v) in section 4.6), whereby the mechanical creation of a physically bridged dilatancy effectively causes a fluid pressure gradient from wallrock to fracture. Locally derived dissolved species precipitate from this fluid drawn into the fracture to fill the dilatancy.

However, the model proposed by Sibson *et al.* (1989) (see model iv in section 4.6), suggests that in unfavourably oriented fault-vein systems, fluid pressure must approach lithostatic pressure in order for failure, and thus P_f becomes the failure controlling parameter. In such a dynamic system, the term "crack-seal" is a misleading description of the failure mechanism and, in this case, perhaps "jack-seal", implying a hydraulic component to the stress field, is a better description. In the case of the ribbon-type shear veins generally, perhaps "dilatant shear veining" is a better general descriptive term for these texturally similar veins, avoiding any assumptions of the actual mode of formation.

The vein texture offers clues to the likely stress regime during vein formation. In the case of the stylolitic bands, such features are undoubtedly the result of pressure solution (diffusive mass transfer). The presence of these features developed with variable intensity across the whole vein is good evidence that such the veins were formed under generally compressive conditions, causing pressure solution between successive vein openings. Indeed, degree of stylolitisation may be an indicator of relative chronology of a given ribbon, since the last formed ribbons are likely to be the least stylolitised. As these features are evidence for the generally compressive nature of the applied stress fields. Under such conditions, transient high fluid pressures would be likely, in order to reactivate the failure and lead to multiple veining events.

By contrast, "book texture" shows no such stylolitisation and may be the result of faulting under quite different fluid pressure conditions. In certain circumstances, mechanical dilatancy, possibly due to fracture margin asperities or favourable Riedel arrays (Figure 4.12) could occur. In this situation, fluid pressure in the dilatancy may be lower than that of the surrounding wallrock (Etheridge *et al.* 1983, Guha *et al.* 1983). The dilatancy is effectively maintained by a mechanical "bridge", which stops the fracture collapsing. In this situation the pore fluid gradient would allow fluid to pass from the wallrock into the dilatancy, obviously transporting any dissolved species. "Seismic pumping" (Sibson *et al.* 1975) can be considered to be a particular manifestation of such a process and more closely resembles Ramsay's (1980) "crack-seal" mechanism. This mechanism might furthermore be expected to occur catastrophically if the fluid pressure difference between wallrock and dilatancy were greater than the tensile strength of the wallrock. In such a case, sub-parallel slivers of wallrock or brecciated wallrock fragments might suffer hydraulic ejection into the dilatancy (Allman-Ward *et al.* 1982, Halls 1987). This effect could also occur in a cyclic fashion and would result in "book textured" veins.

Another interesting feature of the ribbon-veins at Patchway, which is a common feature of textures described elsewhere in mesothermal gold-quartz veins, is the generally equant, anhedral nature of the quartz grains. In true "crack-seal" veins, syntaxial or epitaxial quartz textures (Ramsay 1980), indicative of consistent overgrowth of crystalline quartz on to an existing crystal, are noted. Interestingly, work in epithermal vein systems (Fournier 1985), suggests that milky, inclusion rich equant grains may indicate quartz formed initially as an amorphous gel, later fully crystallising to quartz. Furthermore, Fournier suggests such textures are typical of high-temperature (> 300°C) epithermal systems, where rapid fluid pressure drop would induce amorphous quartz precipitation in a super-saturated solution. Such a dynamic system of rapid change of fluid pressure is predicted for a ribbon-vein system like Patchway and similar chemical behaviour might be expected. It is suggested that the quartz in the Patchway veins may therefore have initially precipitated as amorphous, partially structured silica, quickly annealing to crystalline quartz. Careful study of vein texture may, therefore, give vital clues to fluid chemical behaviour.

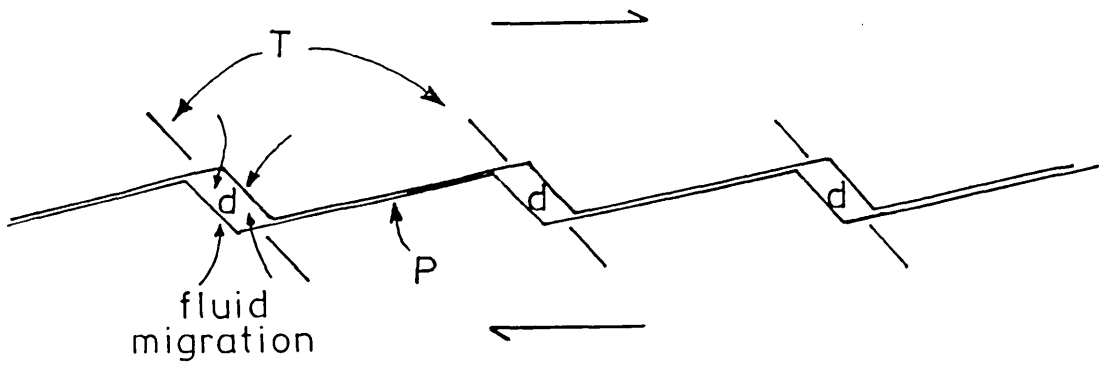


Figure 4.12a - Mechanically induced dilatancy caused by failure on preferential planes. In this case, shear focussed on the P plane of the Riedel array coupled with extension fracturing parallel to the T plane (see Fig. 4.8) causes the dilatancy "d". Since "d" is under extension, a fluid pressure gradient from wallrock to dilatancy is created, resulting in fluid migration shown by the arrows.

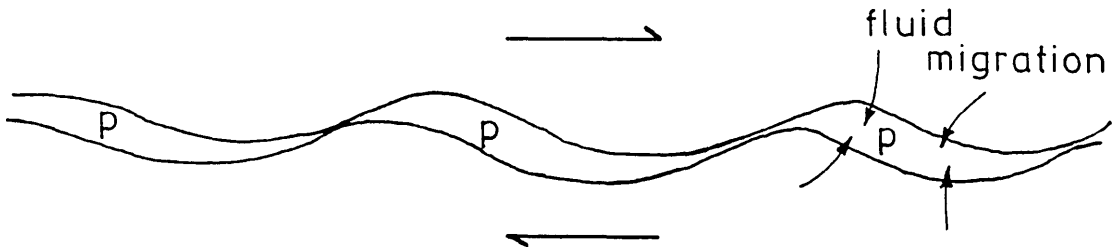


Figure 4.12b - Mechanical dilatancy caused by failure on an irregular fault surface. Here dilatancy is caused by the irregularites of the fault surface causing creation of space "d" under simple shear. Again, the effect is to create a fluid pressure gradient from the wallrock to the fracture (model after Johnston 1940, Guha *et al.* 1983).

Mawer (1987) reviewed the processes of fracture opening and subsequent quartz infilling and demonstrates that feasible rates of opening and subsequent quartz precipitation are possible in natural systems.

4.8 Type Examples of Shear Vein Systems

The geological literature contains numerous studies of mesothermal quartz-gold veins which can help establish the likely dynamic parameters necessary for their formation (Hulin 1929, Hurst 1935, Farmin 1941, Chace 1949, McKinstry & Ohle 1949). From the previously established fault theory, movement on reverse faults systems is highly dependent on fluid pressure if the fault has anything more than a shallow dip. Most mesothermal gold deposits are formed in transpressive terrains (Colvine *et al.* 1988), and although perhaps initially activated as strike-slip or normal faults, some mineralised structures with much higher dips clearly evolved under reverse (thrust) conditions.

Two examples of mesothermal deposits are outlined here, which are both reverse fault systems. The examples serve to illustrate the two extremes of shallow and steeply dipping fault systems. Evidence from these two systems can then be compared with the studied Patchway shear-system.

The first example is a mesothermal gold deposit from the Mesozoic of western USA. Figure 4.13 details the Grass Valley deposit which has shallow dipping (30°) ribbon veins, very similar in texture to Patchway. At Grass Valley a true conjugate set of veins is developed, although as can be seen at the southern margin of the system, one of the conjugate system dominates. This domination of one of the conjugate fault set is quite typical for most stress systems (Hodgson 1989). The key textural features of the deposit are almost identical to those seen in the Patchway veins. The Grass Valley veins would appear to follow classic Andersonian orientation for initiation and reactivation as thrust faults. Continued multiple reactivation of these structures seems clear, resulting in the development of the ribbon quartz-gold veins described by Farmin (1941).

It is clear, that once these compressional shears initiated in classic Andersonian orientation, reactivation under even a waning stress regime is possible. This reactivation is is particularly true if high fluid pressures continue during the deformation. Interestingly Farmin (1941) made the following observation at Grass Valley:

"*.... vein deposition through inflation of partings in the country rock by an injected quasi-magmatic fluid is the mechanism which best explains the occurrence.*"

The development of quartz veins, several metres thick, in the Grass Valley shear fractures is a testament to the passage of large volumes of hydrothermal fluid through the structures. It is believed that the high fluid pressure would aid the formation of such a vein system in a dynamic sense.

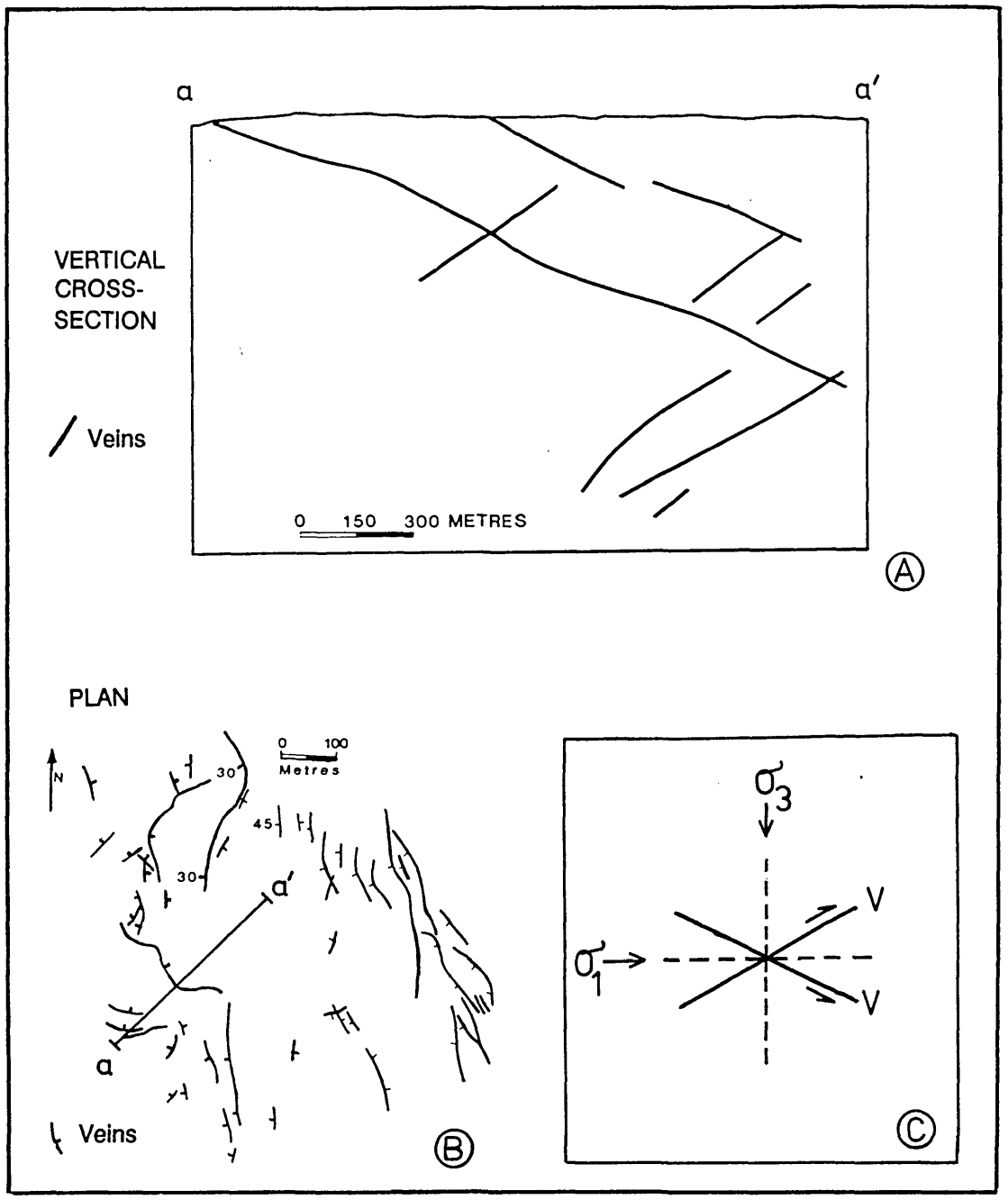


Figure 4.13 - Diagram showing A, vertical cross-section (no vertical exaggeration) and B, plan of the mesothermal gold veins of Grass Valley, California (after Farmin 1941). Diagram C shows the interpreted horizontal compressive stress regime during formation and subsequent reactivation of the veins. Two conjugate vein sets "V" are clearly developed in classic "Andersonian" orientation ("C" fracture and central shear veins on Fig 4.8 and 4.11 respectively).

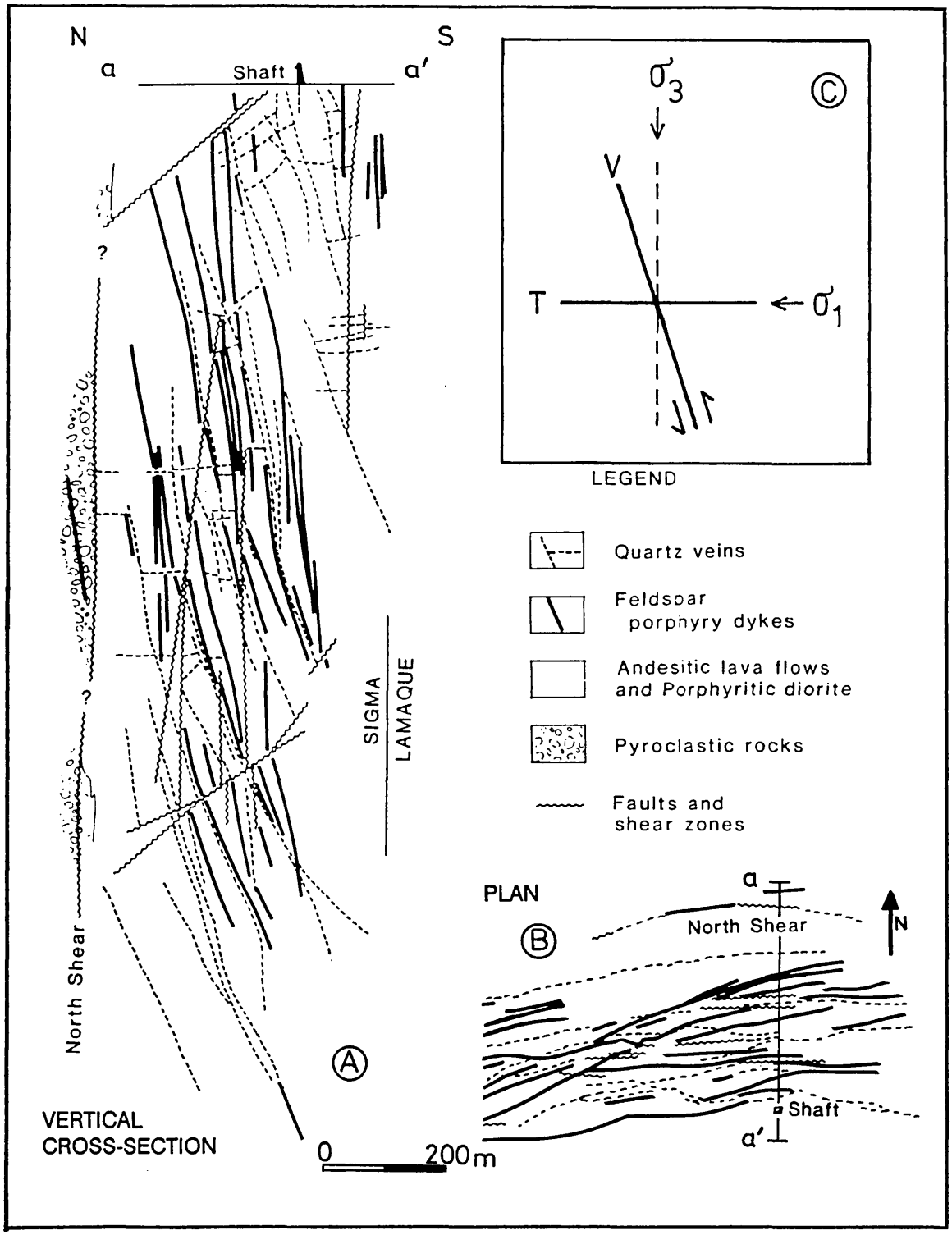


Figure 4.14 - Diagram showing A, vertical cross-section (no vertical exaggeration) and B, plan of the mesothermal gold veins of Sigma Mine, Canada (after Sibson *et al.* 1989). Diagram C shows the interpreted horizontal compressive stress regime during formation of the veins. Two vein sets "V" and "T" are developed in mechanically unfavourable orientation. The "T" vein follows the "T" plane of the Riedel diagram (Fig. 4.8) while "V" is the main shear zone, originally formed under much different stress conditions. Both "T" and "V" veins evolve as the result of cyclic, high ($P_f = P_{lith}$) fluid pressures.

The role of high fluid pressure can be even more profoundly demonstrated in the second example of the Archaean ribbon quartz-gold vein deposit at Sigma Mine, Canada (Sibson *et al.* 1989), where the fault orientation is far less favourable. Figure 4.14 shows the development of both steep ladder veins and vein flats by essentially horizontal compressive stress linked to high fluid pressure.

4.9 Detailed Study of Patchway Ribbon Veins

The Patchway mineralisation is largely confined to a single or duplicate complex ribbon vein (Figure 4.15a). The Golden Valley mineralisation is very similar (Figure 4.15b), although almost exclusively forms a single vein, albeit generally wider than Patchway. The veins are interpreted as shear veins following the "C" failure plane of the Riedel geometry (Figures 4.8 and 4.11).

The ribbon veins were studied in detail in two locations at Patchway, on 6 and 10 levels, and these profiles and location are shown in Appendix II. The same vein pillars were selected for detailed fluid inclusion study which is described in Chapter 7. The profiles in Figure 4.16 clearly define three distinct regions within the vein system which are :

A - *Quartz dominated areas ("barren" white quartz ribbons)*

B - *Phyllosilicate and sulphide septa (thin dark ribbons)*

C - *Silicified wallrock inclusion bands (thick dark ribbons)*

These three regions can be discriminated visually on the parameters above, and it is clear that gold is particularly concentrated in the regions B and C. This gold association can be clearly demonstrated by high grade mineralisation from Patchway (Figure 4.17a). Significantly high grade samples seen at other similar deposits indicate that this is a common feature (Figure 4.17b).

From the previous discussion of fluid behaviour and deformation models, high fluid pressures, close to lithostatic, are likely during the formation of ribboned quartz veins, particularly those showing stylolitic textures. From this assumption, a model of cyclic shear failure and fluid "valving" (Sibson 1981) is proposed for the formation of such vein systems. The likely events accompanying this cyclic event, leading to the textures shown in Figure 4.16 are summarised diagramatically in Figure 4.18. The vein-hosting shear failure would occur parallel to the vein margin (Riedel "C" plane) and the most likely point for the failure to occur would be the rheological boundary between previously precipitated quartz and wallrock. This initial fracturing event might be expected to pluck fragments of wallrock from the wallrock face of the opening fracture which would form a thin screen on the previously precipitated quartz vein (region B). The mineralising fluid would then be expected to flood the opening dilatancy with a possible concomitant drop in fluid pressure if any mechanical "bridging" of the formed dilatancy occurred. Quartz is seen to infill the dilatancy forming the quartz bands (A). It also appears that the bulk of sulphide minerals and gold precipitation occurs mainly at the fracture margins (region B),

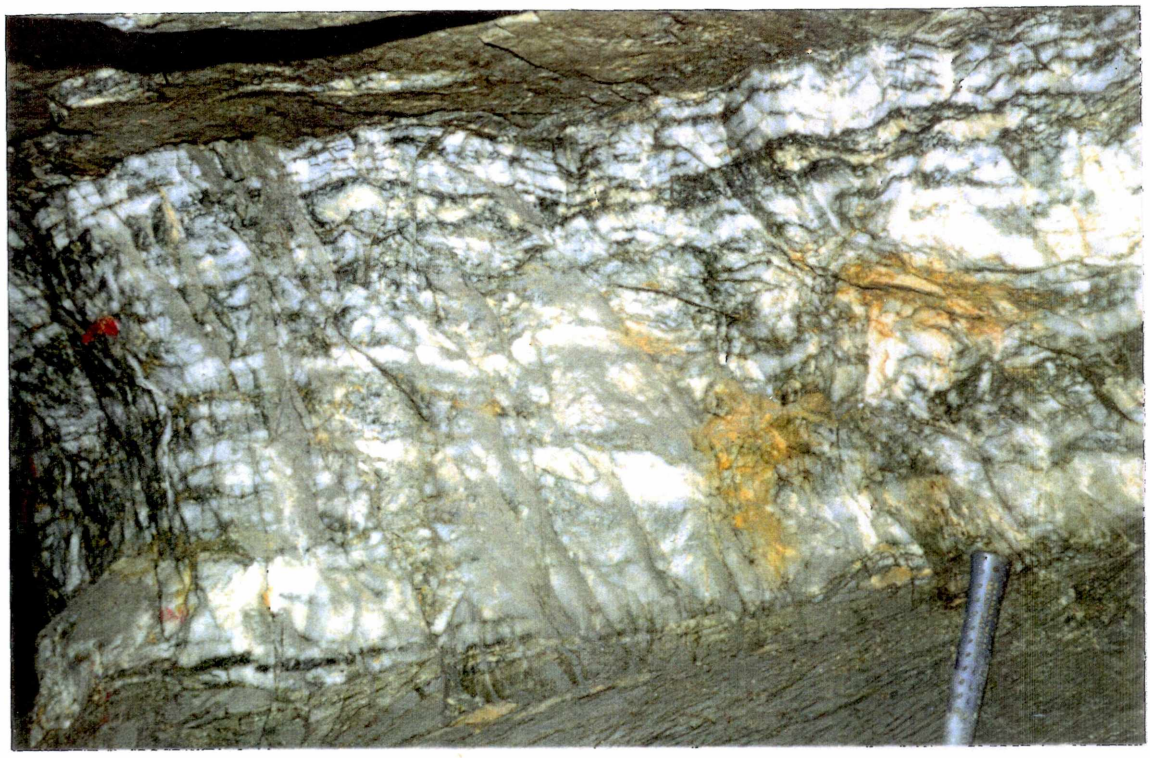


Figure 4.15a - Typical ribboned vein on 6 Level North, Patchway mine.



Figure 4.15b - Typical ribboned vein on 32 Level, Golden Valley mine.



Figure 4.16a - Vein pillar on 6 Level N18 stope.



Figure 4.16b - Vein pillar on 10 Level S9 stope.



Figure 4.17a - High-grade visible gold sample from Patchway (from 19 Level North Orebody). Coarse gold clearly closely follows phyllosilicate septum at the margin of the white quartz ribbon.

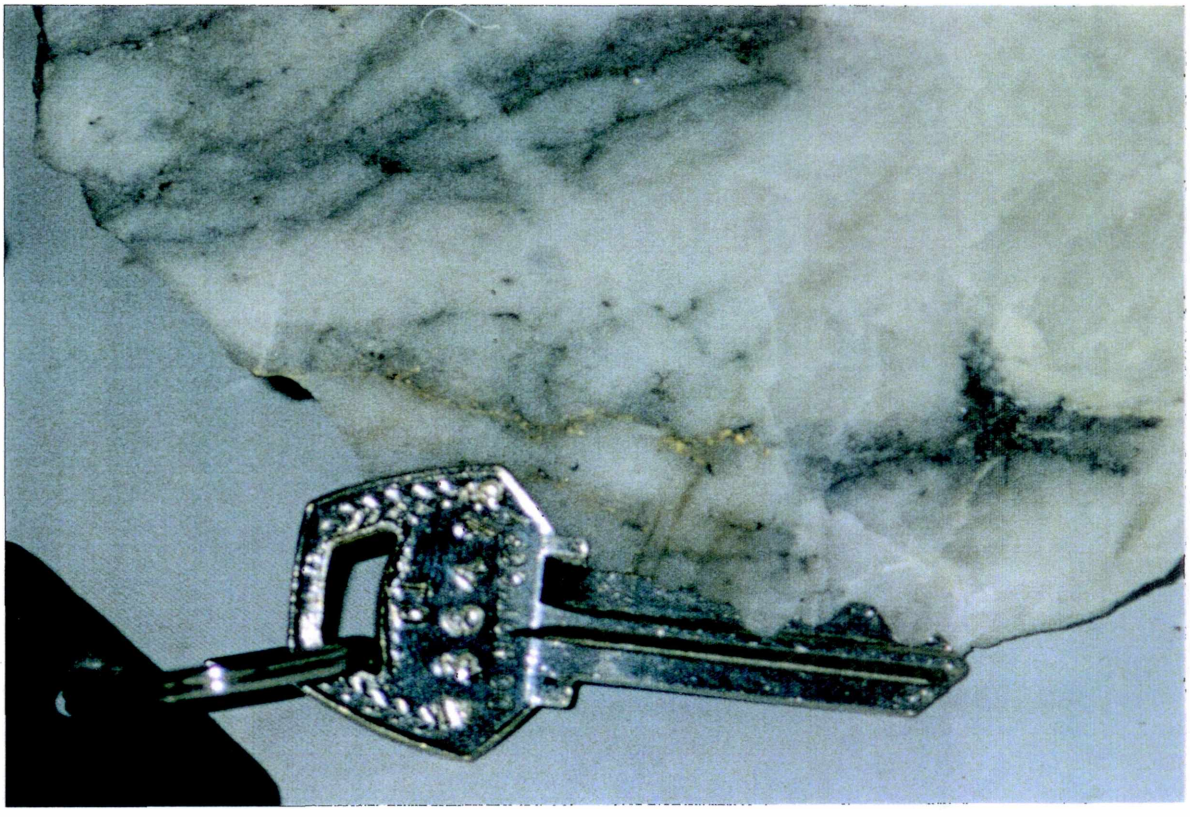


Figure 4.17b - High-grade gold sample from Owl Creek gold deposit, near Timmins, Ontario Canada. Thin septum above key is defined by bright native gold. Sulphides can be seen in other septa.

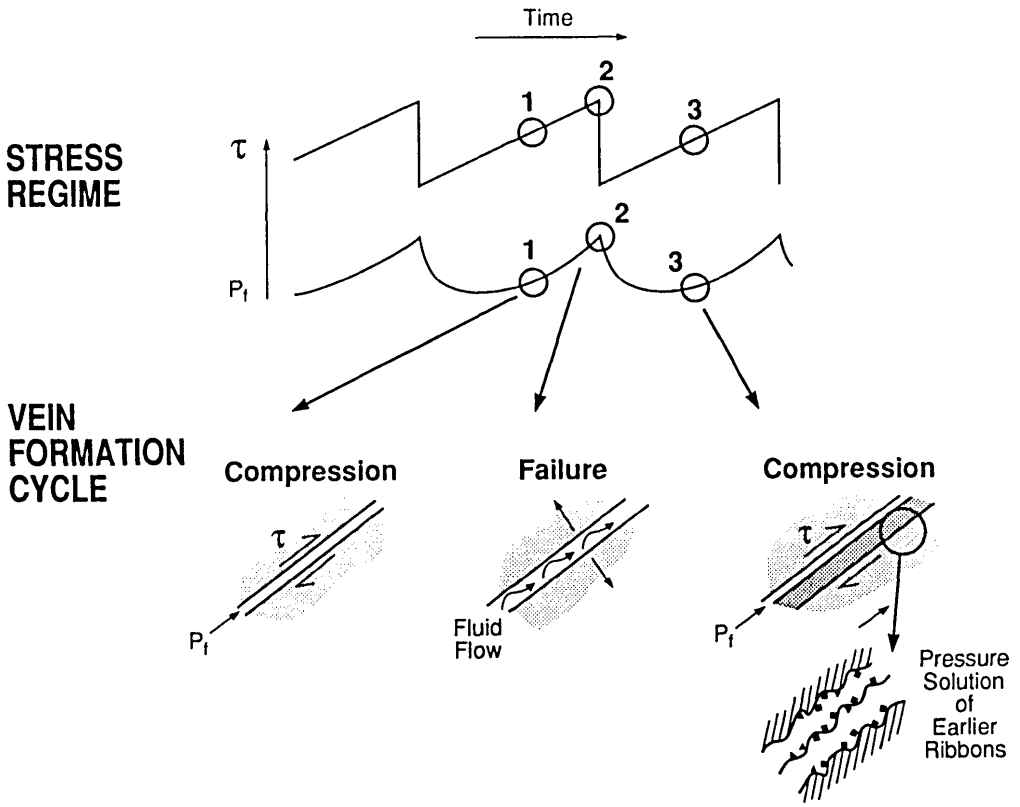


Figure 4.18 - Proposed cyclic model for failure and mineralisation of mesothermal ribbon quartz veins (modified from Sibson 1981). Upper part of diagram shows Sibson's proposal for cyclic stress during stick-slip on seismogenic structures. From his cycle, 2 points of the cycle are important, compression and failure. The diagram below details the events during the cycle. At point 1, fluid pressure and shear stress are increasing until failure at 2. At point 2, hydrothermal fluid flows into the open fault, precipitating dissolved species in a distinct zoned ribbon (margins of altered, mineralised wallrock and cores of mostly quartz). The massive fluid pressure drop causes the structure to lock-up and generally compressive conditions continue (3). Evidence for this compressive regime is provided by the stylolitic texture of previously formed "ribbons".

perhaps due to fluid interaction with the included fragments. The central portion of the fracture (A) appears to contain mainly barren quartz, sometimes scheelite and some carbonate.

This dynamic model is quite different to that proposed for crustiform and drusy veins, where a symmetrical mineralogical zonation developed about a central fracture is evident. In the model for ribbon veins, the fracture repeatedly opens at one of the margins of the vein material, not at the centre of the vein.

Explanation for incorporation of the large wallrock slivers (B) can perhaps be explained by some degree of fault generated dilation resulting in pressure gradient from the wallrock to fracture (the model of Guha *et al.* 1983, Halls 1987). This situation would be caused by wide fluctuation in hydrothermal fluid pressures from overpressured ($P_f \approx P_{lith}$) to underpressured ($P_f < P_{lith}$) conditions particularly if the dilation becomes mechanically bridged by asperity on the fault surface. Rapidly fluctuating levels of fluid pressure would influence chemical equilibration of dissolved species within the hydrothermal fluid.

4.10 Behaviour of Transported, Fluid Soluble Species in Shear Vein Systems

The fluids active during formation of mesothermal gold deposits must have been capable of transporting and precipitating the phases seen in the veins. Such fluids show clear similarities between different deposits, regardless of age or association (Kerrich 1989), and hence generalisations about dominant fluid species can be made. The most important species is silica which forms the dominant vein phase (quartz). Carbon dioxide ($CO_{2(aq)}$) and soluble chlorides form the bulk of the other dissolved species. The behaviour of these species as a function of the two fundamental physical parameters of pressure and temperature will be considered.

The solubility of silica in essentially water dominated fluids, has been studied extensively over a range of conditions (see review by Fournier & Potter 1982). Walther & Helgeson (1977) formulated a theoretical back-up to the experimental data of Kennedy (1950) which Fournier & Potter (1982) extrapolated to cover low to high temperatures and pressures. In general, the solubility of all the silica species in water is highly sensitive to temperature (Figure 4.19a). Quartz is clearly less soluble than the less structured chalcedony, opal or amorphous silica. The effect of temperature on the solubility of all the silica types is seen to constant over the complete temperature range up to 300°C. Below 300°C, temperature is the most important parameter controlling silica solubility.

Above 300°C, pressure has a very important effect on silica solubility. The work of Walther & Helgeson (1977) gave good indication of the effect of both the ambient pressure and temperatures. A distinct zone of retrograde solubility is experienced at pressures below 1 Kbar between temperatures of 450 and 350° C (Figure 4.19b). Above 300° C, pressure change causes major change in quartz solubility.

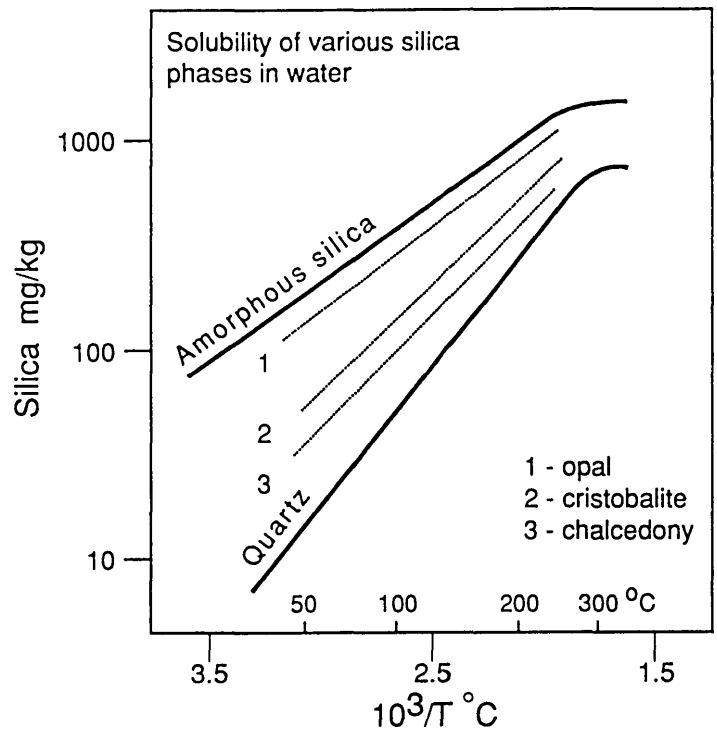


Figure 4.19a - Solubility of silica species in pure water at 1 bar pressure as a function of temperature (after Fournier & Potter 1982).

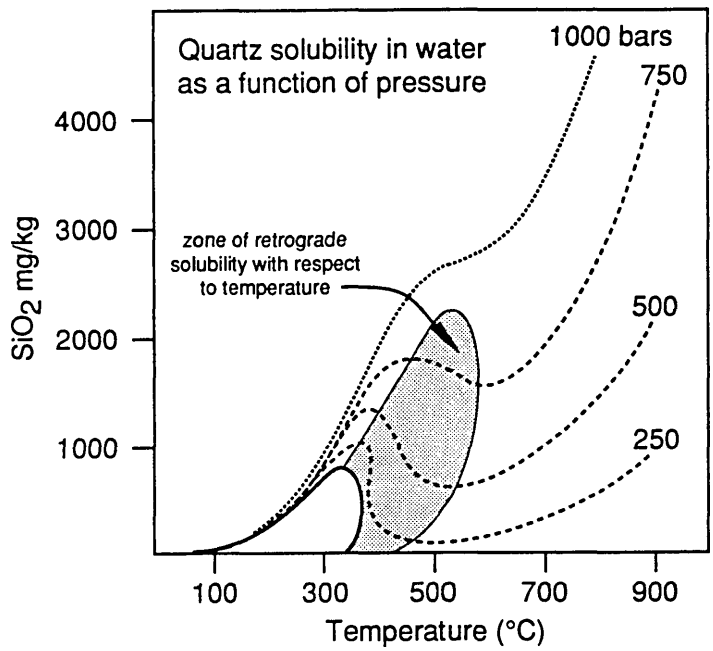


Figure 4.19b - Solubility of quartz in pure water as a function of temperature and pressure (after Walther & Helgeson 1977).

Walther & Helgeson (1977) calculate that a switch from lithostatic to hydrostatic pressures at a depth of 12km would precipitate 2300 ppm quartz from a pure water solution, indicating the magnitude of the effect of a major fluid pressure change.

Fournier (1985) suggested that the equant quartz grain textures of some quartz veins might be due to precipitation of quartz initially as amorphous silica (see earlier discussion). This could occur in a silica-saturated fluid, under pressure, above 300°C, which has suffered dramatic fluid pressure drop, pushing the fluid well above even the amorphous silica saturation curve (Figure 4.19a). Since the temperature at which this might occur is critical, it is tentatively suggested that syntaxial quartz textures in veins may only occur through "crack-seal" or "jack-seal" processes below the temperature of around 300°C, with quartz forming directly from solution. Below this temperature, quartz solubility is no longer pressure sensitive and simple pressure decrease would not significantly over-saturate the fluid with respect to silica, and since quartz is the least soluble silica species, this would precipitate. Conversely, above 300°C, fluctuation of fluid pressure during "crack-seal" or "jack-seal" events is likely to result in the initial precipitation of amorphous silica, subsequently recrystallising to quartz.

This modelling of quartz behaviour is based on pure water. In reality, geological fluids contain other solutes, particularly dissolved ionic salts. Fournier (1985) shows that the addition of NaCl to water has an effect on the solubility of quartz in the retrograde solubilty zone shown on Figure 4.19b. The addition of NaCl to the system is shown on Figure 4.20a, where an increased solubility of quartz is demonstrated. Quartz solubility is little changed by pH in the range pH 0 to 7 up to temperatures of 300°C (Iler 1955, Okamoto *et al.* 1956), but solubilty increases at very high pH values, due to the increased dissociation of silicic acid Figure 4.20b (Fournier & Potter 1982). However, buffering by wallrock silicate assemblages usually limits hydrothermal fluid pH to below 7, except when extreme boiling may raise pH by loss of the gas phase in the sub-surface environment (Fournier 1985).

CO_2 rich fluid inclusions and strong wallrock carbonatisation are testament to the presence of carbon dioxide as a major component in the fluid of most mesothermal gold-quartz veins. The chemical role of this dissolved gas in the transportation of gold or metals generally has not been addressed in this environment. Dissolved CO_2 lowers the activity of water (Shettel 1974) and hence has the effect of decreasing quartz solubility. However, both the carbonate and bicarbonate ions are shown to enhance quartz solubility (Lovering 1922, Carr & Fyfe 1958). Since dissolved CO_2 is likely to hydrate to form carbonic acid, which in turn dissociates to bicarbonate, some increased quartz solubility is likely to counteract the decrease in H_2O activity due to the dissolved gas. In addition, since CO_2 is a polar molecule, its addition to water is likely to cause a decrease in the static dielectric constant of water (Dubessy *et al.* 1989). Decreasing this constant has the effect of raising the stability of metal chloride complexes. Furthermore, Walther & Schott (1988) have shown that the solubility of quartz increases in a fluid, directly proportional to the decrease of the dielectric constant, due to addition of CO_2. This

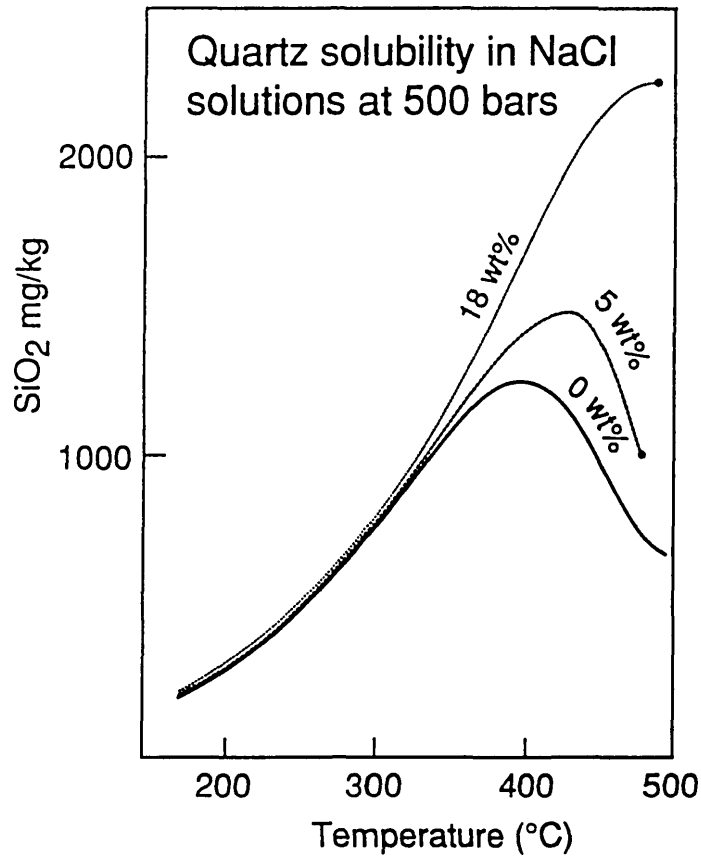


Figure 4.20a - Solubility of quartz in NaCl solutions at 500 bars pressure as a function of temperature (after Fournier 1985).

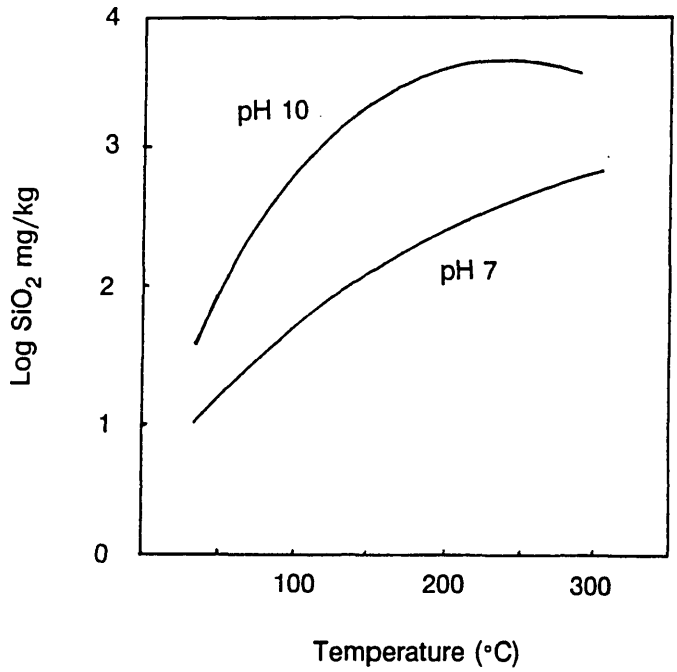


Figure 4.20b - Solubility of quartz in pure water at 1 bar pressure as a function of pH (after Okamoto *et al.* 1956).

effect of CO_2 on the static dielectric constant is an important feature. However, very little experimental data is available for major species in natural fluids.

The physical behaviour of water-carbon dioxide mixed fluids, as observed in fluid inclusions, can help define ambient conditions during the formation of the host phase. Experimental studies of fluids in the system H_2O-CO_2-NaCl and H_2O-CH_4-NaCl (Takenouchi & Kennedy 1964, Bowers & Helgeson 1983a and 1983b, Gehrig *et al.* 1986, Krader & Frank 1986 and Haas 1978) allow for modelling of the fluid miscibilities in carbonic and methanoic ore-fluid systems. The behaviour of other, potentially important, miscible gases such as H_2S has also been investigated (Huang *et al.* 1985) which is relevant to the behaviour of any sulphur-species complexed ions.

Figure 4.21 shows solvus curves constructed for a range of conditions to illustrate the key points of fluid behaviour in the H_2O-CO_2-CH_4-NaCl system. Figure 4.21a shows the position of the solvus for a CO_2-H_2O-NaCl fluid at a fixed pressure (here 2 Kbars) for various weight % dissolved NaCl, showing that the solvus curve is clearly raised by increasing salinity. A similar plot in Figure 4.21b shows the same system for a fixed salinity (6 wt% NaCl) at various confining pressures showing a very similar effect of decrease in confining pressure on the solvus curve. Figure 4.21c shows the effect of methane on the fluid system where in this case the solvus curve for pure CO_2-H_2O and pure CH_4-H_2O is plotted as an illustration of the general effect of methane on the system. For any given fluid in the system CO_2-H_2O-NaCl, the addition of dissolved CH_4 serves to raise the solvus line for a particular set of physical parameters.

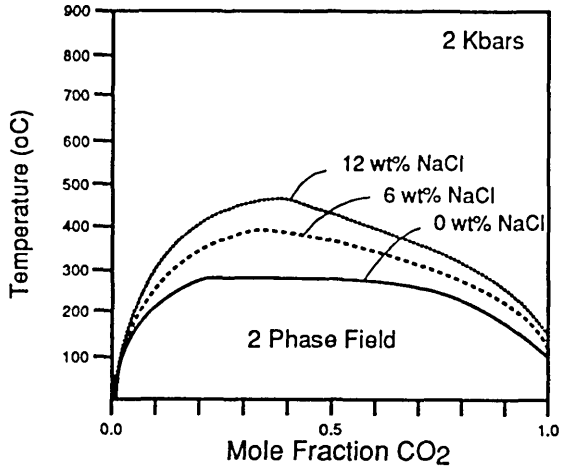
In summary then, the hydrothermal fluid dynamically active in the host structure during deformation was also responsible for the transport of the introduced silica, carbonates, sulphides and gold. The continued stability of this carbonic, saline fluid as a homogeneous, one phase fluid is dependent upon maintaining physical conditions at a point above the particular solvus curve defined for that fluid. Changes in any of i) pressure, ii) temperature, iii) salinity and iv) miscible gas levels can significantly change the position of the solvus line even maintaining all other parameters fixed. If unmixing is a crucial factor in mineral precipitation then change in one or more of these parameters could provide the necessary trigger. Silica solubility is also seen to be closely linked to pressure and temperature and changes in these two parameters offers a potential mechanism for triggering both fluid unmixing *and* silica/quartz precipitation.

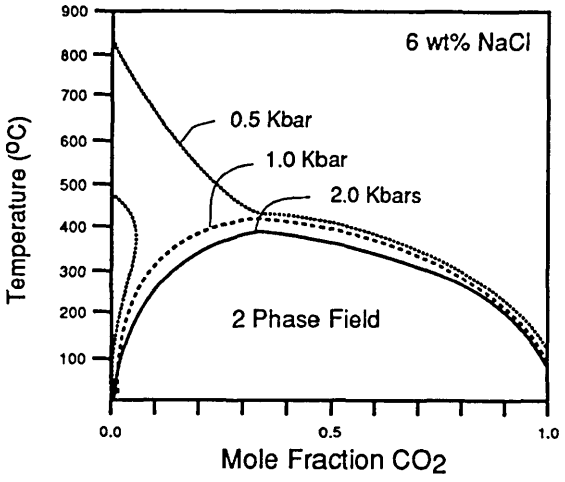
It was demonstrated in 4.7 that a rapid fluid pressure changes may be expected to occur during cyclic vein formation. There is, therefore, a possible link between the dynamic evolution of host structure, mineralising fluid introduction possible and fluid unmixing and silica/quartz precipitation triggered by fluid pressure drop. Other physical and chemical change may cause precipitation of other phases.

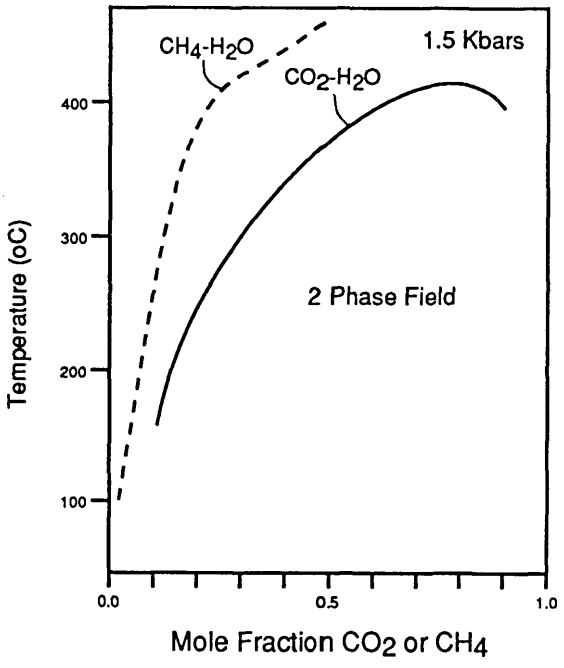
Figure 4.21a - Temperature-composition diagram for fluids in the H_2O-CO_2-NaCl system at fixed 2 Kbars pressure (data from Bowers & Helgeson 1983). Curves shown are for 1) 0 wt% NaCl, 2) 6 wt% NaCl and 3) 12 wt% NaCl. Two-phase region is constrained below the curves, single phase above.

Figure 4.21b - Temperature-composition diagram for fluids in the H_2O-CO_2-NaCl system at fixed 6 wt% dissolved NaCl (data from Bowers & Helgeson 1983). Curves shown are at 1) 2 Kbars, 2) 1 Kbar and 3) 500 bars pressure. Two-phase region is constrained below the curves, single phase above except in the case of 3) where the two-phase region is constrained by the two curves marked 3).

Figure 4.21c - Temperature-composition diagram for part of the system for fluids in the H_2O-CO_2 and H_2O-CH_4 systems at fixed 1.5 Kbars pressure (diagram from Naden & Shepherd 1990). Curves shown are 1) CH_4-H_2O and 2) CO_2-H_2O (0 wt% NaCl). Two-phase region is constrained below the curves, single phase above. X-axis shows mol% dissolved gas (either CO_2 or CH_4).


2 Kbars
12 wt% NaCl
6 wt% NaCl
0 wt% NaCl
2 Phase Field
Temperature (oC)
900
800
700
600
500
400
300
200
100
0.0
0.5
1.0
Mole Fraction CO2


6 wt% NaCl
0.5 Kbar
1.0 Kbar
2.0 Kbars
2 Phase Field
Temperature (oC)
900
800
700
600
500
400
300
200
100
0.0
0.5
1.0
Mole Fraction CO2


CH4-H2O
CO2-H2O
1.5 Kbars
2 Phase Field
Temperature (oC)
400
300
200
100
0.0
0.5
1.0
Mole Fraction CO2 or CH4

CHAPTER FIVE - STRUCTURAL EVOLUTION OF THE PATCHWAY REGION

5.1 Introduction

Very little work has been published regarding the major structural framework of the the Zimbabwe Midlands greenstone belt. On a local scale at Patchway, Ward (1968) recognised the development of strong shear fabrics developed marginal to the Patchway mineralisation. He further suggested that the fabrics are consistent with a Riedel geometric array to the main mineralised vein structure and cross-cutting barren shear zones. The recognition of regional deformation confined to narrow zones of high strain shear-zones in the Archaean of Zimbabwe has been more recently emphasised, largely as a result of regional studies such as Coward *et al.* (1976) and Stowe (1980). Recently studies have been initiated in the Midlands greenstone belt (Pitfield & Campbell 1989) focusing on the structural aspects to mineralisation in the KweKwe to Kadoma region. This work highlights the structural inhomogeneity of the belt with large areas of low strain, low to very low metamorphic grade bordered by high strain zones. Deformation in these latter zones is largely ductile to brittle-ductile in the first order structures, whilst related second order structures show brittle to brittle-ductile behaviour. Stowe (1980) was the first to systematically describe the evidence of strike-slip movement on structures in the Midlands region. Nutt *et al.* (1988) propose largely reverse dip-slip movement on the mineralised structures they examined in the KweKwe region and conclude that this is the major style of movement throughout the belt. Clearly a great deal of the deformation in the region has been focussed within major regional scale structures.

The main aim of this chapter is to incorporate the craton scale structural evolution model summarised in Chapter 2 into the analysis of the structural elements of the Patchway-Golden Valley region. In this regard, a review of regional and detailed aeromagnetic data together with air-photographs has been made. This review is integrated into published studies of the geology of the region, to help outline a structural framework of the belt. In addition, data from the preliminary results of the joint UK Overseas Development Administration and Government of Zimbabwe study (Pitfield & Campbell 1989) has also been used, which includes some TM image processing to compliment their more traditional structural analysis of the southern portion of the belt.

The synthesis of all this data forms the framework for interpreting the deposit scale structural mapping. At Patchway mine mapping was carried out on a number of levels, but focussing on 10 Level (see Figure 2.7) where access was possible to at least 1.5 km of development in the mineralised structures. The detailed mapping, which forms the basis of the interpretation, is available with the sample collection and only key sections of this work are presented in the main text. As well as mapping the main gold-bearing structure at Patchway, access to the Basil and other associated mineralised structures was possible from the underground workings at Patchway. Some limited mapping was carried out at the neighbouring Golden Valley deposit for comparative purposes. The Hamburg mine (Figure 2.5) was also briefly

examined, as it was known to lie on a structure with a similar trend to the Patchway and Golden Valley main structures.

As well as mapping of macrostructural elements, oriented samples provided oriented thin sections for a complimentary microscopic study of the host rocks. The use of kinematic indicators is a key part of the geometrical analysis of shear zones and a number of studies have summarised these (Simpson & Schmid 1983, White *et al.* 1986, Bjornerud 1989).

5.2 Structural Framework of the Kadoma Region

5.2.1 Aeromagnetic Data

An interpretation of the published regional aeromagnetic data produced at 1:500,000 scale for the Zimbabwe government helps very clearly in defining major structures. A summary of interpreted features is shown on Figure 5.1 where a number of linears and regions have been defined and shown on the overlay. Additional detailed aeromagnetic data at 1:50,000 scale was examined around the deposits, which although not very detailed and pre-dating the regional survey, confirms the large-scale features.

If the Great Dyke features are ignored, since they post date mineralisation, a broad three domain division of the major fabric of the Midlands belt is suggested by the aeromagnetic data:

1) The area between KweKwe northwards to just south of Kadoma is dominated by a major N to NE trending, clearly defined, linear "D" running from KweKwe to Battlefields.

2) The area north of 1), from Kadoma towards Chegutu, is dominated by NE trending linears, "F". These linears show evidence of branching ("splaying") from where they meet the domain 1) linear. In area 2) the main part of the Bulawayan age greenstones are bounded by the major "a" and "b" structures in the east and west respectively.

3) Although data in the south is sparse (no data around the industrial town of KweKwe), there is evidence for a switch to NW trending linears towards the area of Gweru, "G".

5.2.2 Air Photographs

Stereo air photographs of the Patchway region were studied and interpreted. The air-photo study was felt to be an effective geological tool since a) outcrops are notoriously poor in the Patchway region b) air-photographic study is particularly suitable in this type of flat grass/farmland terrain, especially with

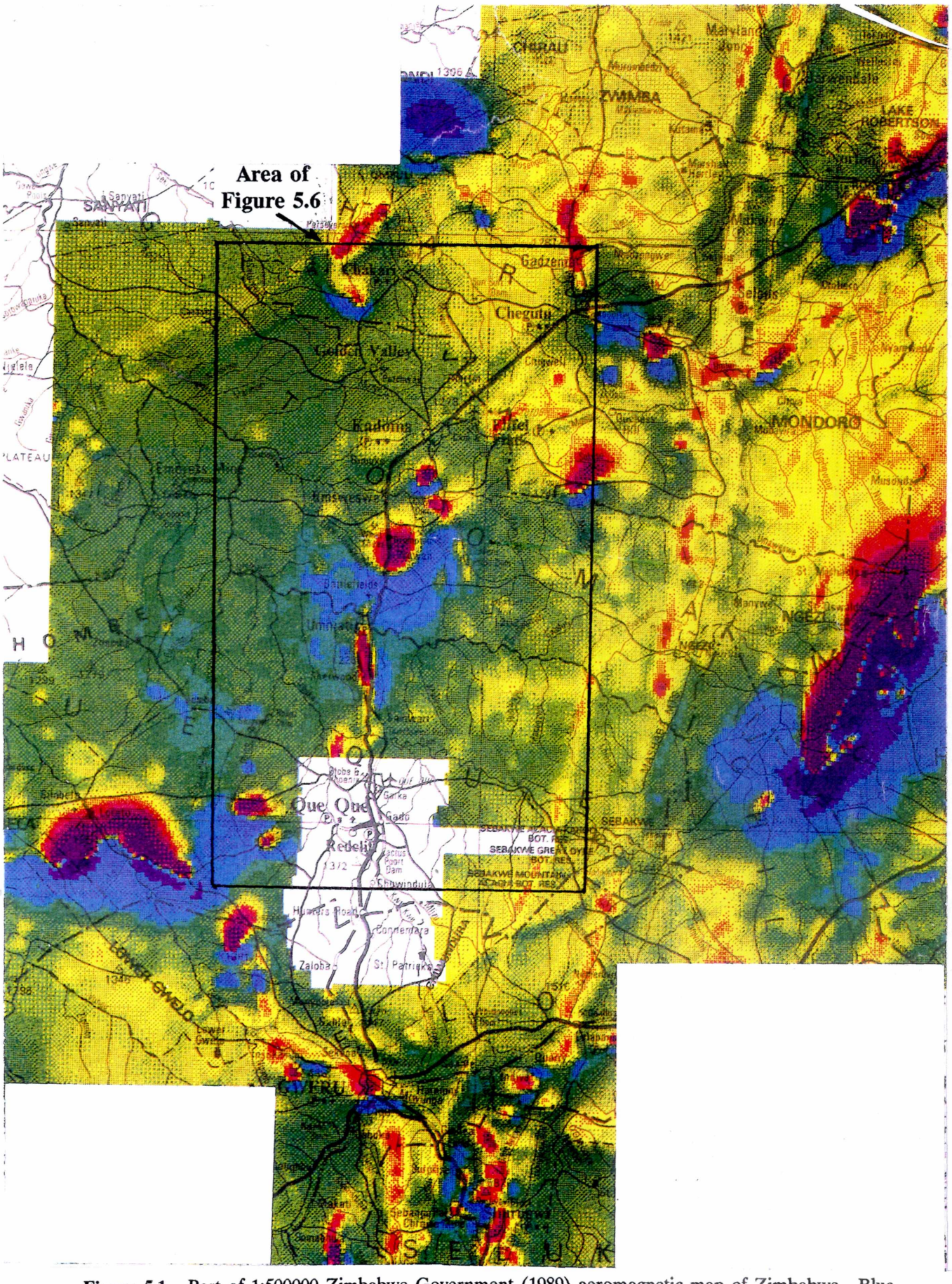


Figure 5.1 - Part of 1:500000 Zimbabwe Government (1989) aeromagnetic map of Zimbabwe. Blue areas represent areas of low response, through green and yellow moderate, to red high response. Of interest here are the boundaries between high and low areas, indicating deep structural features.

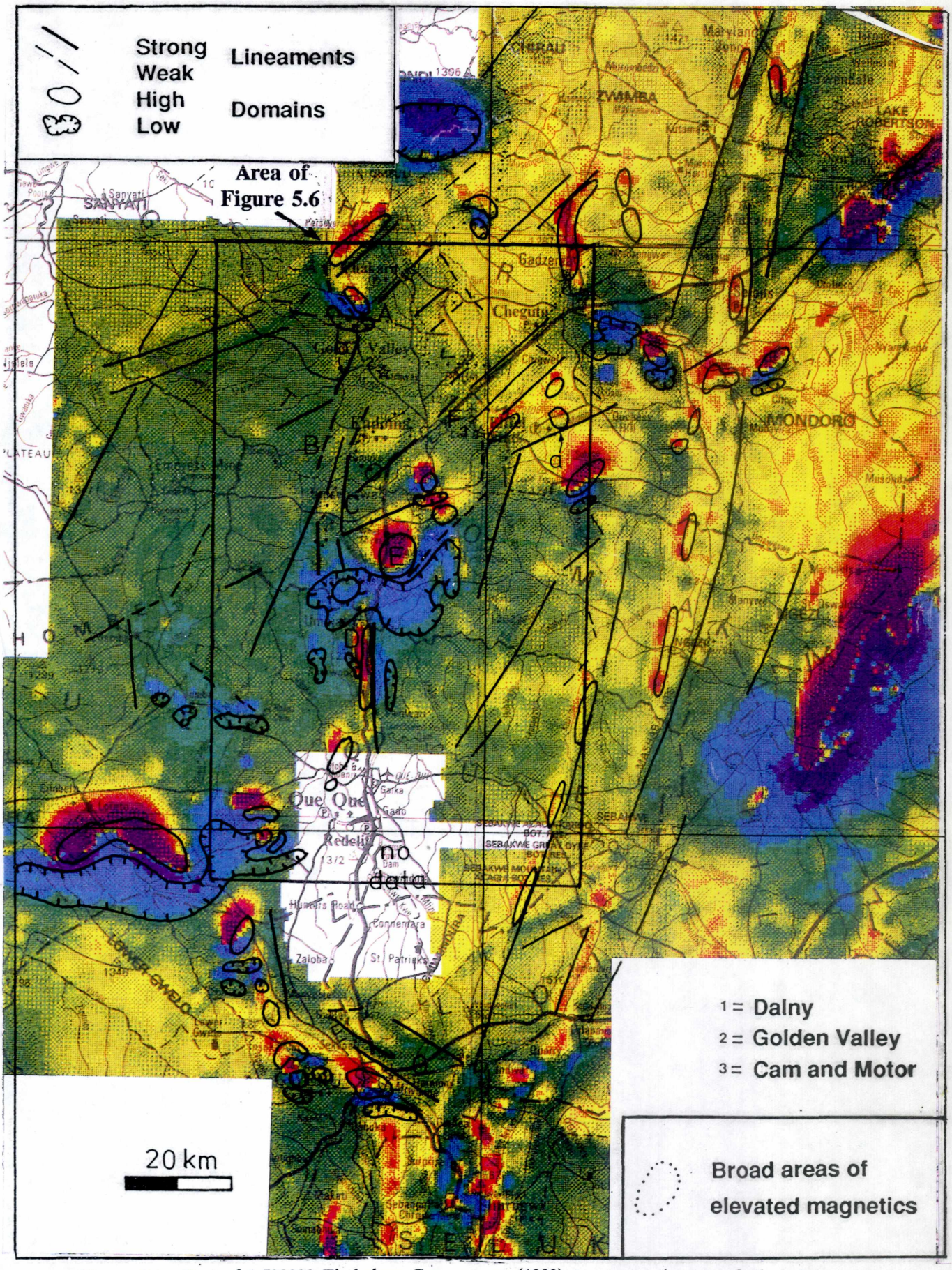
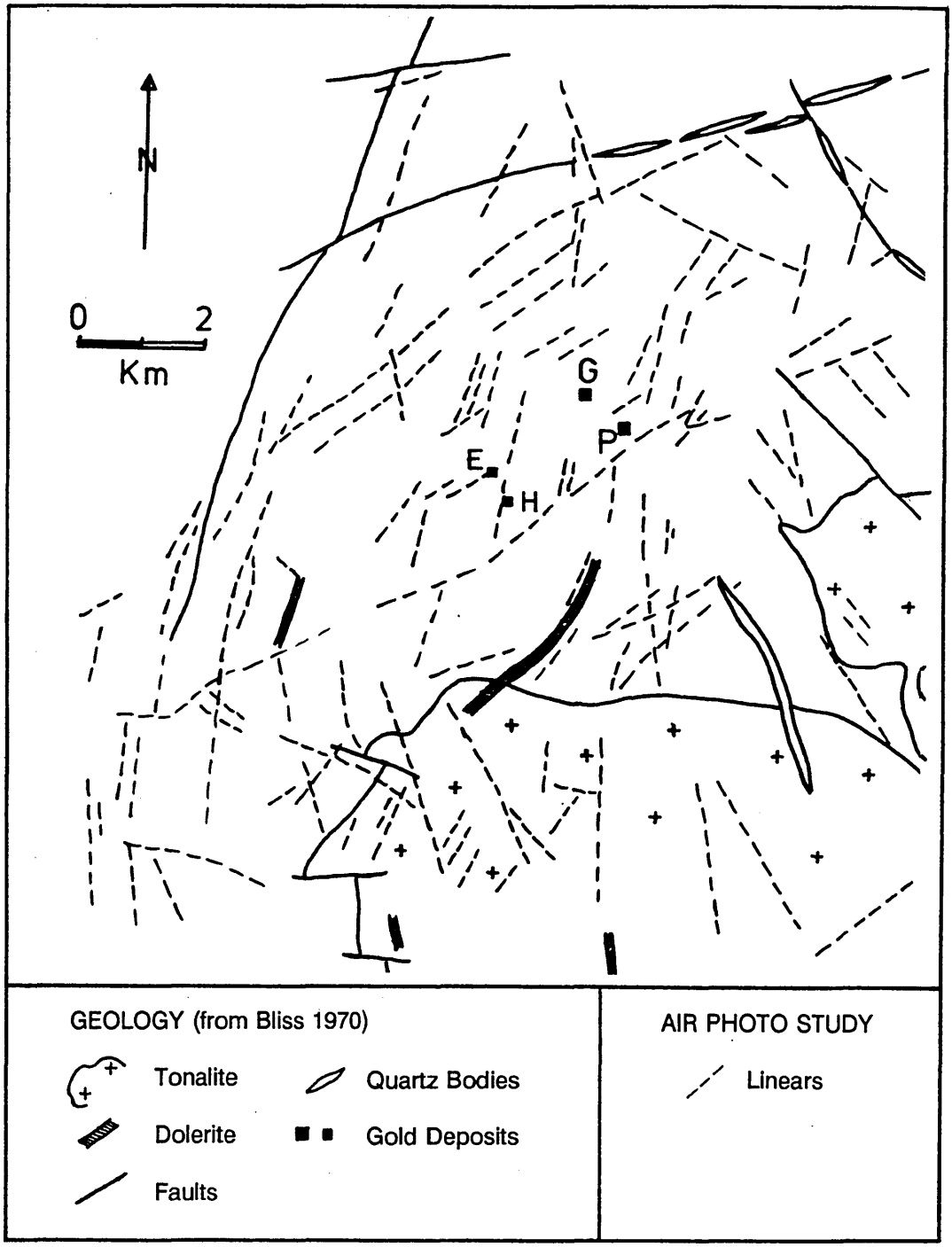


Figure 5.1 - Part of 1:500000 Zimbabwe Government (1989) aeromagnetic map of Zimbabwe. Blue areas represent areas of low response, through green and yellow moderate, to red high response. Of interest here are the boundaries between high and low areas, indicating deep structural features.



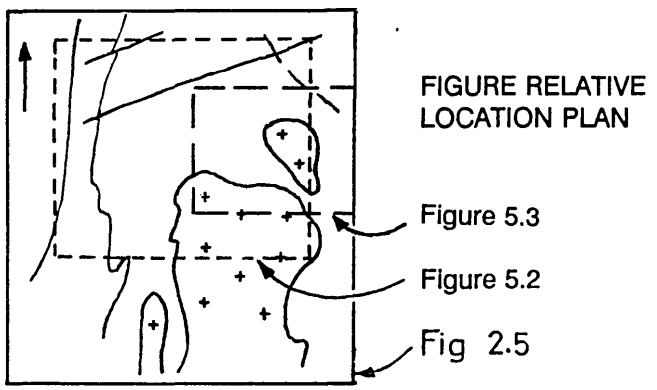


Figure 5.2 - Air-photograph interpretation of the Patchway - Golden Valley region. Simplified geology from Bliss (1970). P = Patchway, G = Golden Valley, E = Erin and H = Hamburg.

regard to interpreting structure. The results of this study (Figure 5.2) highlight a number of features. Several sub-parallel 020° trending lineaments are indicated paralleling the Patchway and Golden Valley orebodies, which are themselves not seen on the air-photos due to cultural cover (mine-buildings). Another trend of 070° structures is also prominently highlighted, with one of these coincident with the Erin orebody. These 070° structures are seen to truncate the 020° structures, particularly immediately north and south of Patchway - Golden Valley. Lineament patterns in the main tonalite bodies are clearly different to those in surrounding greenstones, suggesting contrasting tectonic histories. Several major structures are indicated coincident with, and probably contolling the distribution of, the major drainages.

5.2.3 Gravity Profile

In 1981 the Department of Physics at the University of Zimbabwe carried out a gravity profile across the northern margin of the Whitewaters tonalite body from Golden Valley mine in the west to Guelph mine in the east. Modelling of the subsurface geology (Foster 1982) indicates that the western margin of the tonalite dips at some 50 to 60° at outcrop, but that the contact rapidly flattens to some 10 to 20° beneath Golden Valley and Patchway. The consequence of this is that based on the reasonable estimate of greenstone to tonalite density contrast of 0.25 gcm^{-3}, the tonalite-greenstone contact only lies some 1.3 km below Golden Valley's current workings. The same thing happens in reverse on the eastern side of the tonalite body with the contact only some 1.6 km below Guelph workings based on the same density contrast (Figure 5.3). This feature has interesting implications for structure of the area, and permits speculation that the greenstones in the central portion of the Kadoma anticline may show a relatively shallow dipping discontinuity overlying granitic rocks. In this case it could be evidence for either an allocthonous package of greenstone stratigraphy thrust over old granitic basement or alternatively evidence of a much larger extent to the Whitewaters batholith beneath the Upper Greenstone package which has major significance for the heat flow regime during deformation and mineralisation. The former idea permits the suggestion that the Golden Valley and Patchway structures are in fact linked structures which merge with a flat lying basal fault over granitic basement (see Figure 5.4). Alternatively, the latter idea might, as Foster (1982) suggested, indicate that complex heat flow patterns could have existed around the Whitewaters pluton. Obviously, if there were a relationship between the intrusive and mineralisation the latter would have implications for mineralisation zonation in a vertical sense down the Patchway and Golden Valley structures.

5.2.4 Integration with Geology

The framework of structures indicated by the aeromagnetic interpretation can now be integrated with the regional geological maps of Bliss (1970) and Robertson (1976) together with the more recent interpretation of Pitfield & Campbell (1989). It becomes clear that several of the major magnetic linear features are regional scale structures. The compiled summary is shown on Figure 5.5.

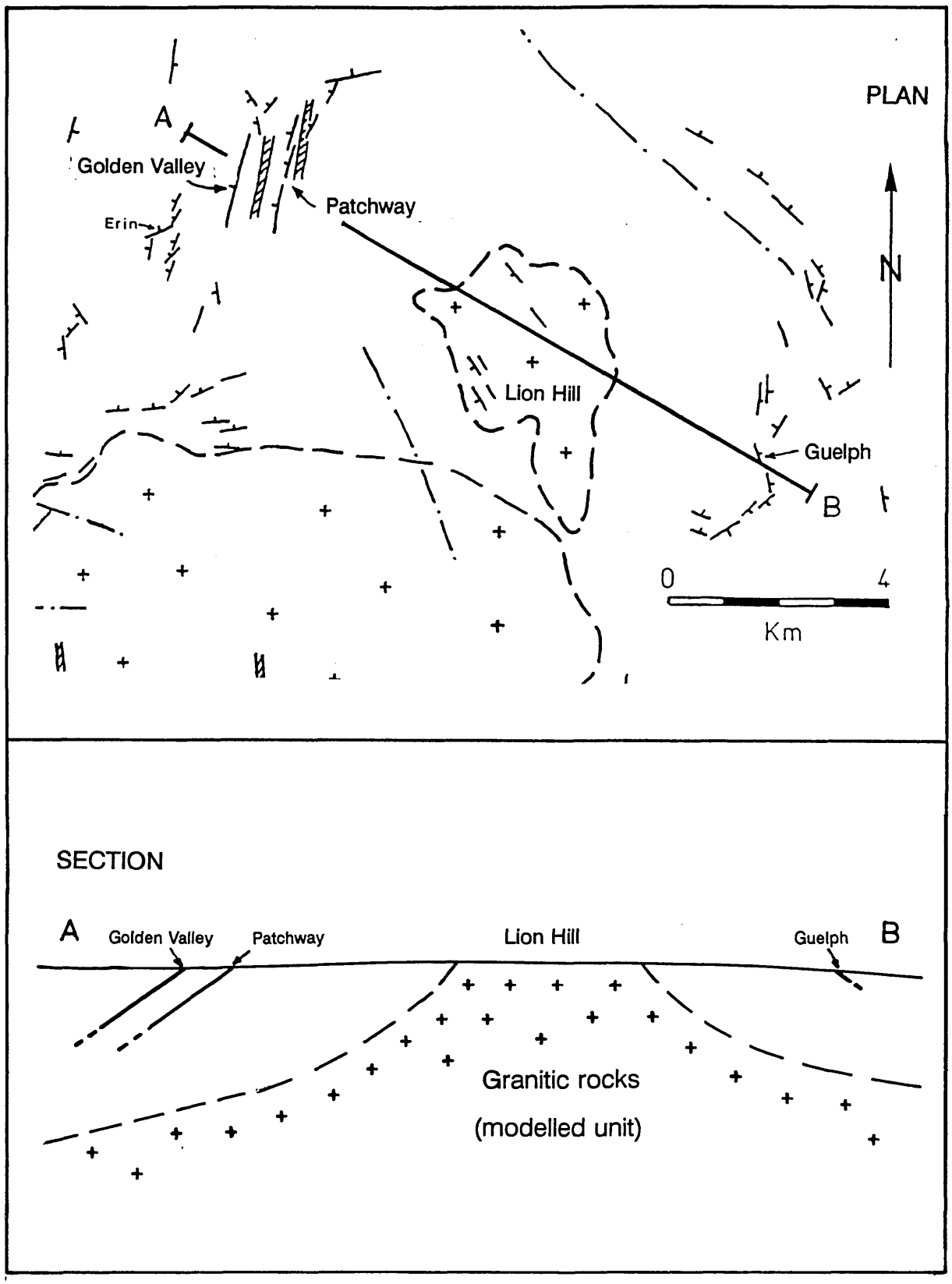


Figure 5.3 - Gravity profile across Lion Hill. Profile performed by the University of Zimbabwe Physics Department 1981, reported and modelled by Foster (1982). Section scale as for Plan, no vertical exaggeration.

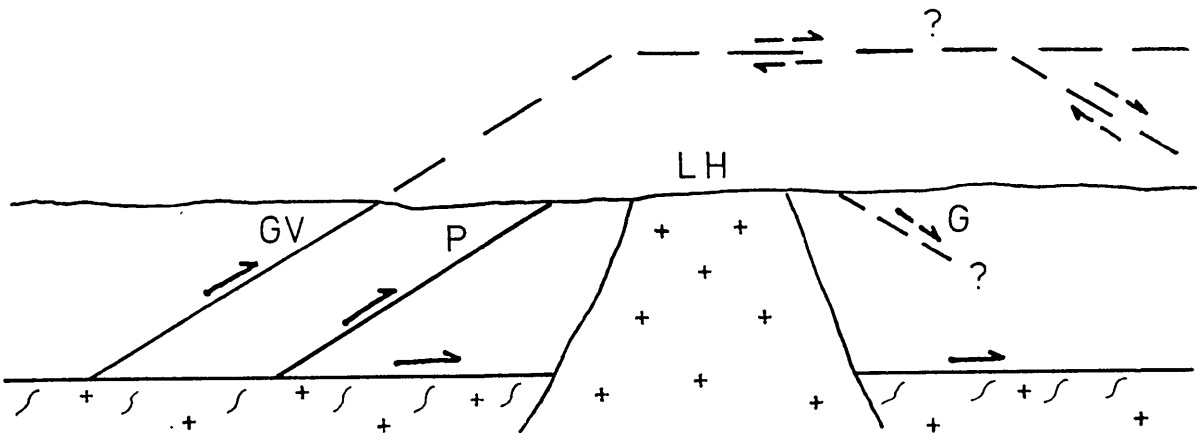


Figure 5.4 - Possible interpretation of gravity profile, Lion Hill. The diagram shows how the Golden Valley and Patchway structures may in fact be linked duplex thrust structures. Boyer & Elliot (1982) indicate that this type of structure may initiate over an early, major thrust sheet. At Lion Hill, the granitic rocks at depth below Patchway and Golden Valley may in fact be the much earlier tonalite gneiss (seen in the east as the ca. 3.5 Ba Rhodesdale complex). This would have the same density characteristics as the younger (2.69 Ba) Lion Hill stock.

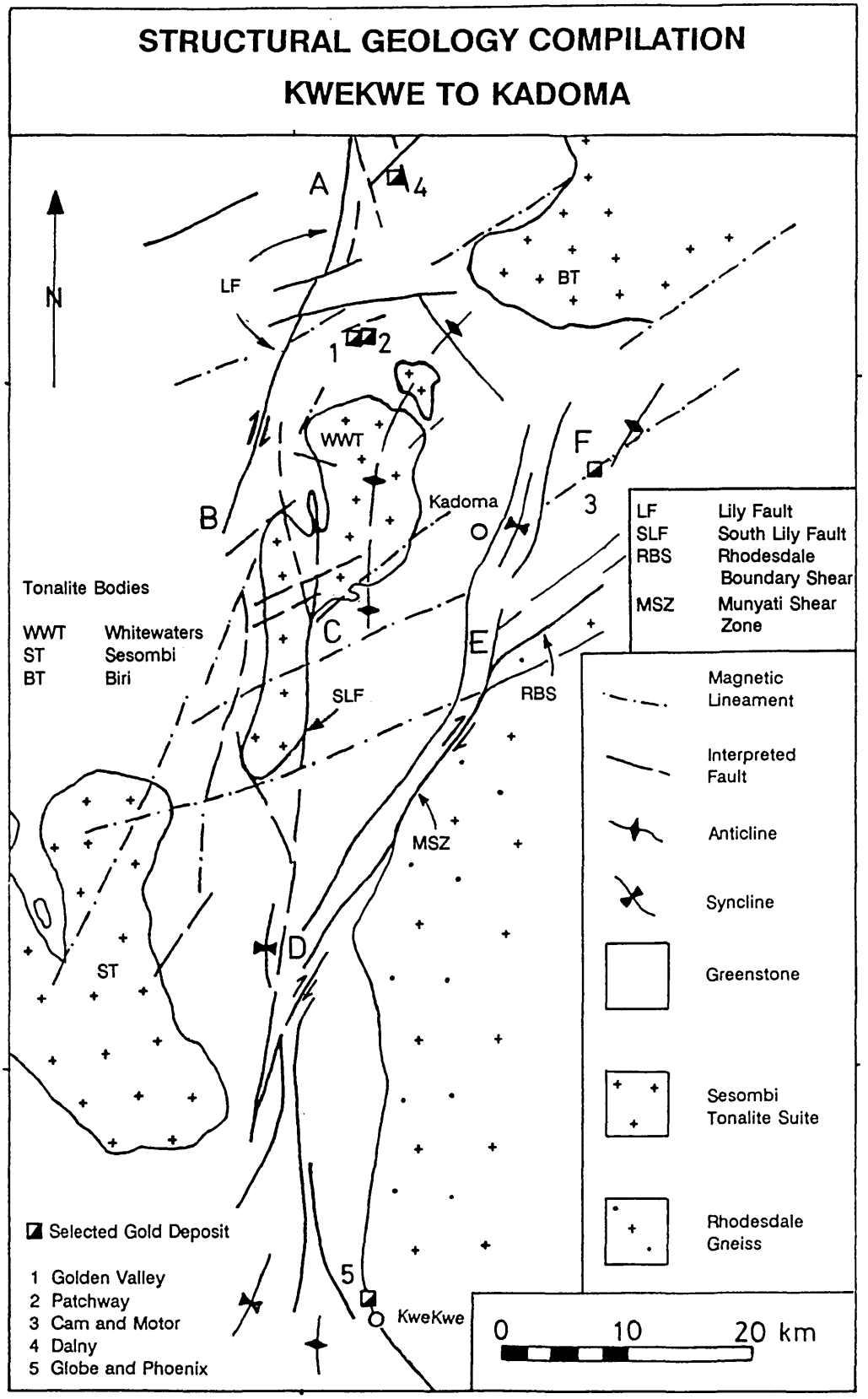


Figure 5.5 - Structural compilation of elements in the Kadoma to KweKwe region (compiled from Bliss 1970, Harrison 1970, Pitfield & Campbell 1989 and the authors own aeromag and air-photo interpretation).

The strongest feature in the Patchway - Golden Valley area is the Lily Fault, described by Bliss (1970) as a major strike-slip structure. On Figure 5.5 this is shown as feature "A" to "B". In the south at "B" the Lily Fault is strong feature parallel to the western margin of the Whitewaters tonalite body. At its southern limit, the structure steps across the tonalite to join with structure "C", whilst at "A" the structure forms a major splay towards Dalny (Chakari). "C" continues south to "D" where it joins with the major Munyati Shear system (Pitfield & Campbell 1989), a complex shear zone previously mapped by Robertson (1976). Mapping together with magnetic data suggests that north of Battlefields the Munyati shear intercepts the Rhodesdale Boundary Shear complex at "E", close to Kadoma. Stowe (1980) had previously identified both of these structures as major strike-slip shears. North of Kadoma town the structures then swings to follow a northeast orientation. At this point a number of sub-parallel features running northeast are indicated including a strong feature which runs through the Eiffel Flats area "F", coincident in part with the Cam and Motor gold deposit.The zone between the major Lily and Munyati-Rhodesdale structures in the Kadoma region shows a fairly subdued magnetic response but some linears are suggested, largely sub-parallel to or splays off the major first order structures. Interestingly a broad area of elevated magnetic response is indicated over the Whitewaters and Biri tonalite bodies. The relevance of this is not clearly understood, but this may be due to the presence of magnetite in these intrusives.

These observations show a zone of very intense deformation in the KweKwe to Battlefields ("D") area which to the north opens into more complex splay structures branching northwards to Dalny ("A") and northeastwards to Kadoma ("E") and Cam and Motor ("F"). This structural pattern is compatible with some degree of "lateral secretion" of the eastern Rhodesdale Gneiss block during deformation with the regional structural pattern being modified around the laterally squeezed block (Chapter 2).

5.3 Synthesis of Observed Key Regional Structural Elements

In review, three major lineaments, or "breaks" can be now defined which have a major role in the location of gold-bearing structures. These most likely represent first order shear zones where strain has been most focussed during craton-scale deformation. Using terminology chosen by Pitfield & Campbell (1989) these are: 1) The Rhodesdale Boundary Shear Zone, 2) The Munyati Shear Zone and 3) The Lily Fault.

1) The Rhodesdale Boundary Shear Zone

The shear-zone runs along the eastern margin of the greenstone belt, running roughly north-south in the KweKwe area, curving around to run northeast-southwest toward Chegutu. It is marked by a zone of distinctly foliated granitic gneiss in the Rhodesdale Gneiss unit and contains zones of locally silicified and carbonatised rocks.

2) The Munyati Shear Zone

In the southern part of the Midlands belt this forms the boundary between the Shamvaian and the Upper Greenstones of the Bulawayan Group. In the north it merges with the Rhodesdale Shear in the Battlefields area and south of the Munyati river it swings west around the Sesombi tonalite.

3) The Lily Fault

The fault is well defined in the northern part of the belt, specifically to the west of the Patchway-Golden Valley region where it forms the boundary between the Calc-alkaline and Bimodal units of the Upper Greenstones. Towards the north, a northeast trending splay runs through the Chakari region with development of parallel north-south structures accommodating movement around a large infold of Proterozoic rocks. In the south the Lily fault appears to cross the Umsweswe river in a series of steps, merging to the south with the Munyati shear.

5.4 Analysis of Deposit Scale Structure

Kinematic indicators are a key guide to the dynamics of any shear system, Figure 5.6 highlights the indicators identified and utilised in the following section. The figure is for an idealised shear-zone developed during a single deformation regime.

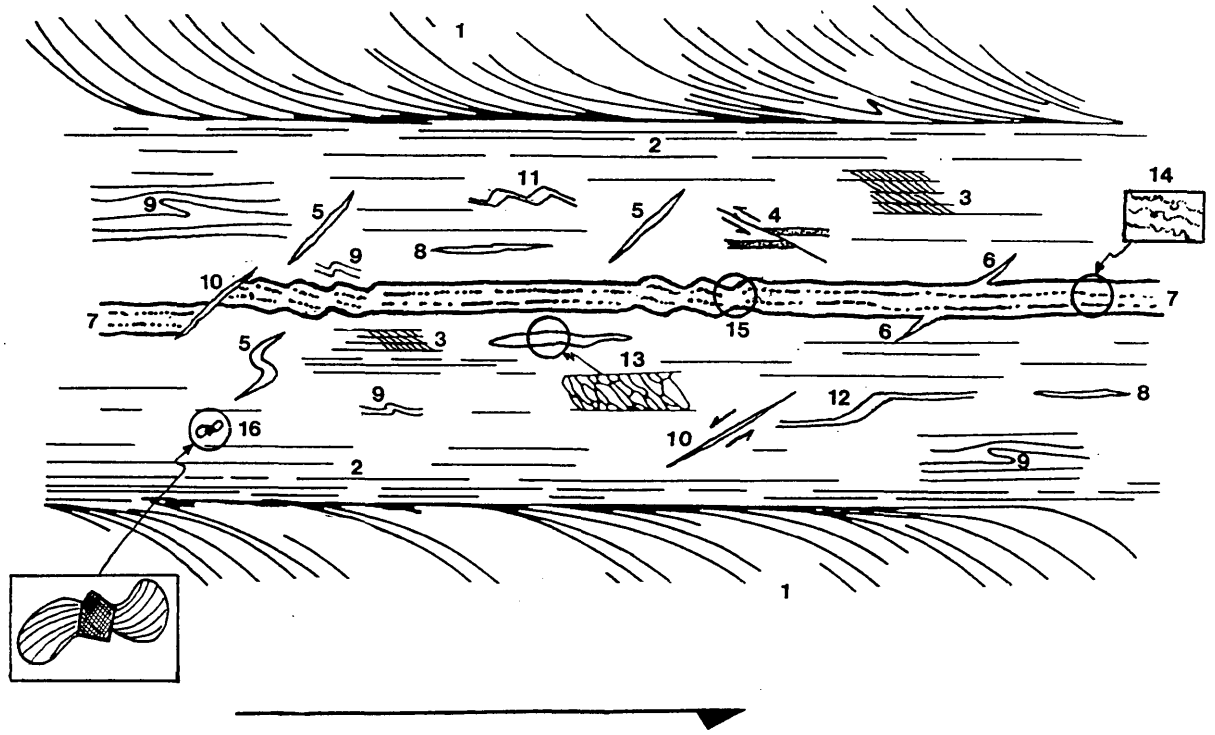
5.4.1 Deposit Structural Evolution

Early Folding

The earliest recorded deformation event in the greenstone belt as described earlier is the development of large scale regional folding (Bliss 1970). The folding has lead to formation of the so called Kadoma anticline and the Patchway area would lie on the northwest limb of this feature. At Patchway primary bedding features are rare, but there is indication of a generally shallow northwest dip to the package of flow rocks, with units being the right way up in agreement with other authors.

D2 Deformation

The next feature observed at both Patchway and Golden Valley is the development of the structures which host the main gold-quartz mineralisation, the event which here is termed D2. The structures themselves are represented by ductile to brittle-ductile zones which can be traced for over 1.5km of strike. They have, within this extent, contiguous zones of deformed mafic host rocks over uninterrupted strike lengths of up to 600 metres. Down-dip the structures are known to a depth of 1km which at 30° dip means a true extent of at least 2km. Unfaulted sections of the host shear zone have individual dip extents of up to 500m. Within these contiguous sections ribboned quartz-gold veins (Figure 4.15) themselves form the most continuous elements of the structures, which at Patchway have continuous vein



NUMBERED ELEMENTS

1 - Shear fabric (Ramsay 1980) rotated into plane of shear (White *et al.* 1986)
2 - Fabric sub-parallel to main failure in shear-zone core
3 - S-C fabric (Berthé *et al.* 1979, Lister & Snoke 1984)
4 - Sympathetic compressional "P" shears (Tchalenko 1968)
5 - Extensional "T" veining, sygmoidal in places due to rotation (Hodgson 1989)
6 - "Caterpillar" extension veining (Hodgson 1989)
7 - Main "C" failure shear veining (Tchalenko 1968, Hodgson 1989)
8 - Minor shear veins
9 - Intrafolial folds (White *et al.* 1986)
10 - Dilational "R" shears (Tchalenko 1968)
11 - "Domino" veins (Gamond 1983)
12 - Dilational "R-C" jogs (White & Baxter 1987)
13 - Asymmetric recrystallisation to quartz grains (Simpson & Schmid 1983)
14 - Stylolitic grain boundaries in compressional sites (McClay 1976)
15 - Asymmetric boudinage with dilational neck infilling (Hanmer 1986)
16 - Asymmetric pressure shadows (Durney & Ramsay 1973)

Figure 5.6 - Schematic diagram of a typical brittle-ductile shear zone summarising features and kinematic indicators present in the shear zones examined in the Patchway region. The presence of all indicators at any one stage of the deformation history is not implied. Indicators are all drawn for sinistral shear-sense.

sections of up to 300 metres in strike extent with a down dip extent of up to 250 metres. At Golden Valley the continuous sections of vein may be over 300 metres in strike length with dip extents of up to 500 metres. The Basil vein ("3" on Figure 2.7) is a similar sub-parallel structure partially tested by underground workings at Patchway which shows identical textures (Figure 5.7), although gold grades do not currently support mining. In addition, the Hamburg structure which lies south of Patchway (Figure 5.2) follows a similar structure, and is considered to have formed contemporaneously. From the broad relationships the veins would all appear to represent a shear vein parallel to the main failure plane of the zone (the main "C" plane of Figure 4.8). Figure 5.8 shows a composite plot for poles to gold bearing vein for Patchway, Basil, Golden Valley and Hamburg deposits. The great circle plotted is drawn about the central point of the >30% contour plot of all the poles to vein. The data shows a relatively small spread, consistent with all the deposits being developed on parallel, regionally significant, structures. In all cases there is strong development of a shear fabric marginal to the quartz veins (Figure 3.6). The shear fabric has a generally consistent relationship with the main vein. The angular relationship of this S-fabric versus the main failure plane, C (Berthé 1979), together with the limited stretching lineation data, is supportive of a reverse plus sinistral strike-slip movement on the C failure plane (Figure 5.9). Other macroscopic kinematic indicators are rare, but there is a suggestion of minor reverse thrusting in flow tops on 10 level (Figure 5.10), which would equate to failure on the "P" shear planes on Figure 4.8. Figure 5.11 shows "domino" veins formed by the mechanism described in Figure 4.12 supporting this sense of shear. In places a poorly developed stretching lineation is developed in sheared felsite bodies, where the quartz phenocrysts form hard grains. These few data are plotted on Figure 5.9, compatible with the shear sense derived from the S-C fabric and domino veins. Reverse plus strike-slip movement accompanied the periodic hydrothermal fluid flow through the main failure surface ("C" or the shear vein) which lead to formation of the ribbon quartz veins. Evidence for the broadly compressive nature of the stress field on the main mineralised structure is seen in the intense flattening of pillows seen in the shear zone (Figure 3.7) and within the quartz vein itself where a variable development of stylolitisation of the veins and wallrock septa is seen across the vein. However it is clear that for the main failure plane, the quartz veining is evidence for volume inflation across the structure.

The (D2) deformation along the 020° failure then later evolved into periods of more brittle strike-slip motion. Evidence is provided by extension veining and shear folding in the foot and hanging walls of the veins (Figure 5.12). The extension veins follow the classic simple extension ("T") site and the "R" extensional Riedel (Figure 4.8) orientation and thus can be used to accurately confine the shear sense. In most cases these veins are clearly indicative of dextral strike slip movement and a stereonet plot of all the measured intercepts corroborates this (Figure 5.13).

Microstructure

The laminated marginal phyllonite around the vein is shown in thin section to comprise fine-grained phyllosilicate, quartz and carbonate immediately adjacent to the main vein (Figure 5.14). There is a



Figure 5.7 - Photograph of Basil vein on 4 Level. Vein is clearly ribboned, developed between a sheared mafic lava footwall and a similarly sheared "felsite" intrusive hanging-wall. The intrusive has the characteristic buff colouration and waxy appearance, common for felsite marginal to mineralisation.

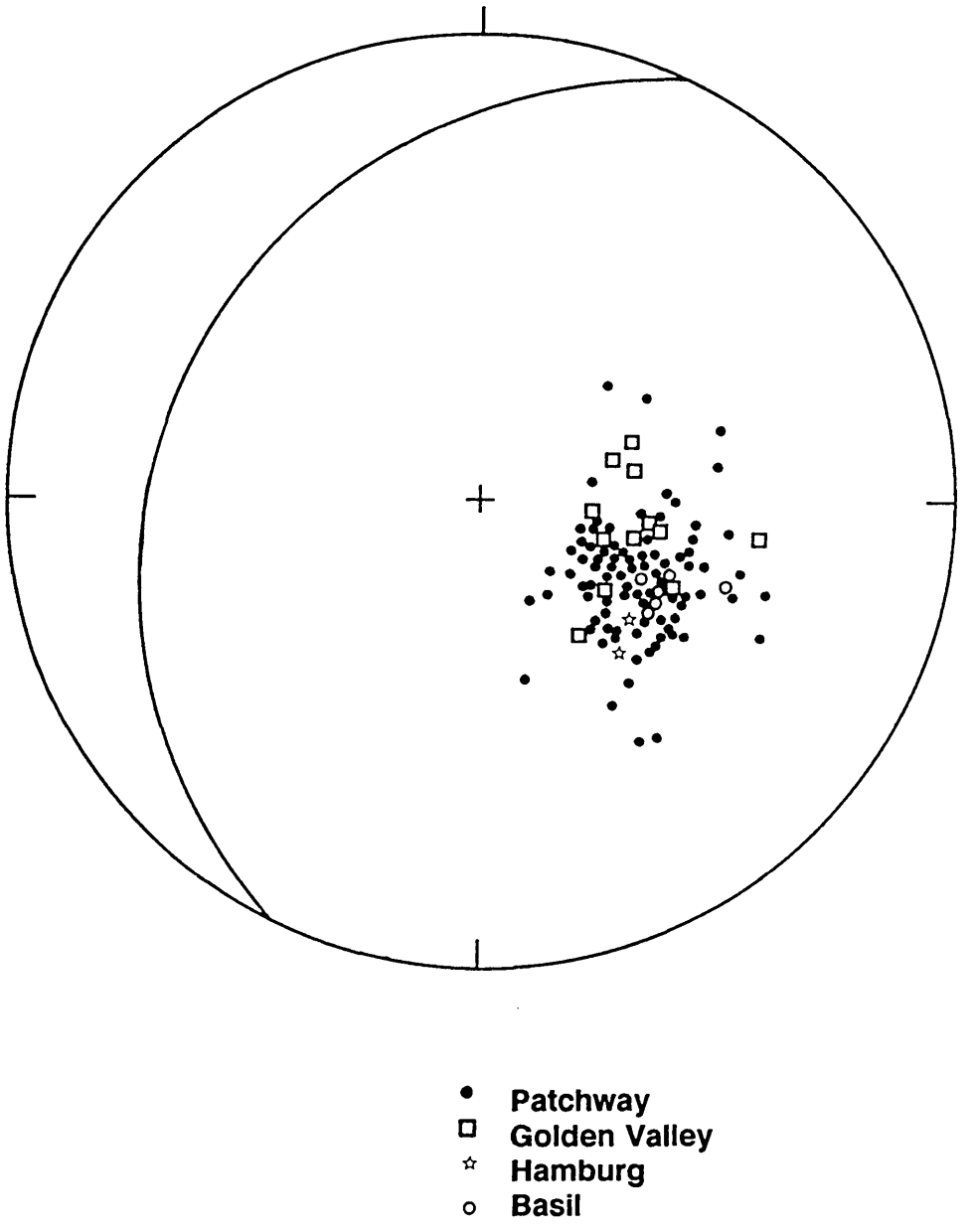


Figure 5.8 - Stereonet plot of poles to main gold-bearing ribbon quartz veins (D2). Average great circle for all data also plotted (020/30W). Sources of data from the mines indicated.

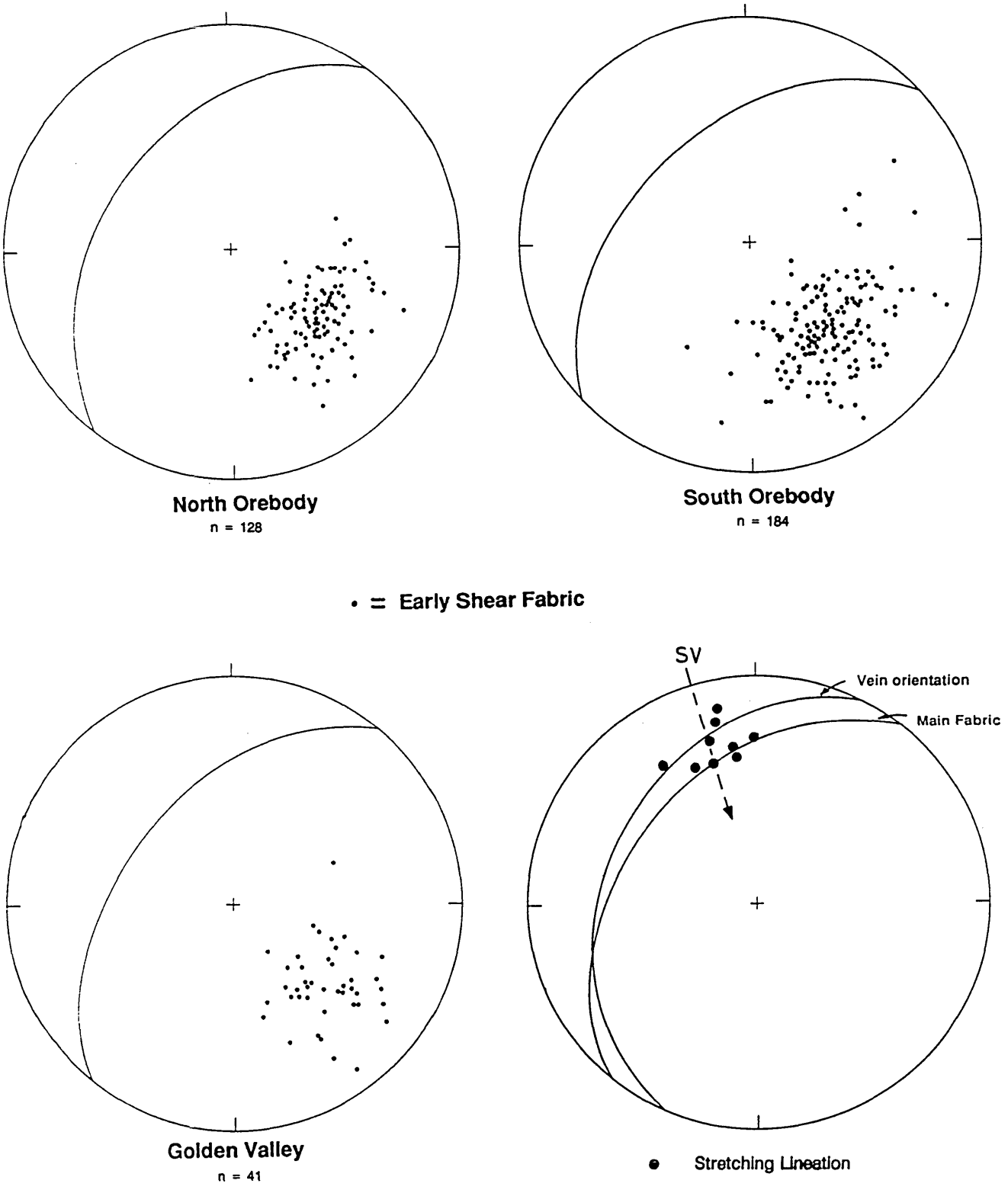


Figure 5.9 - Stereonet plot of poles to main shear fabric marginal to the D2 veins. Average great circles for each data set are also plotted. Sources of data from the areas indicated. Stereonet bottom right summarises all the data as a single great circle and the great circle from Fig 5.8 is also plotted to show angular relationship. Limited stretching lineation data collected is shown on this stereonet, with the estimate of the slip vector during D2 plotted as "SV" (Reverse + component of sinistral slip).

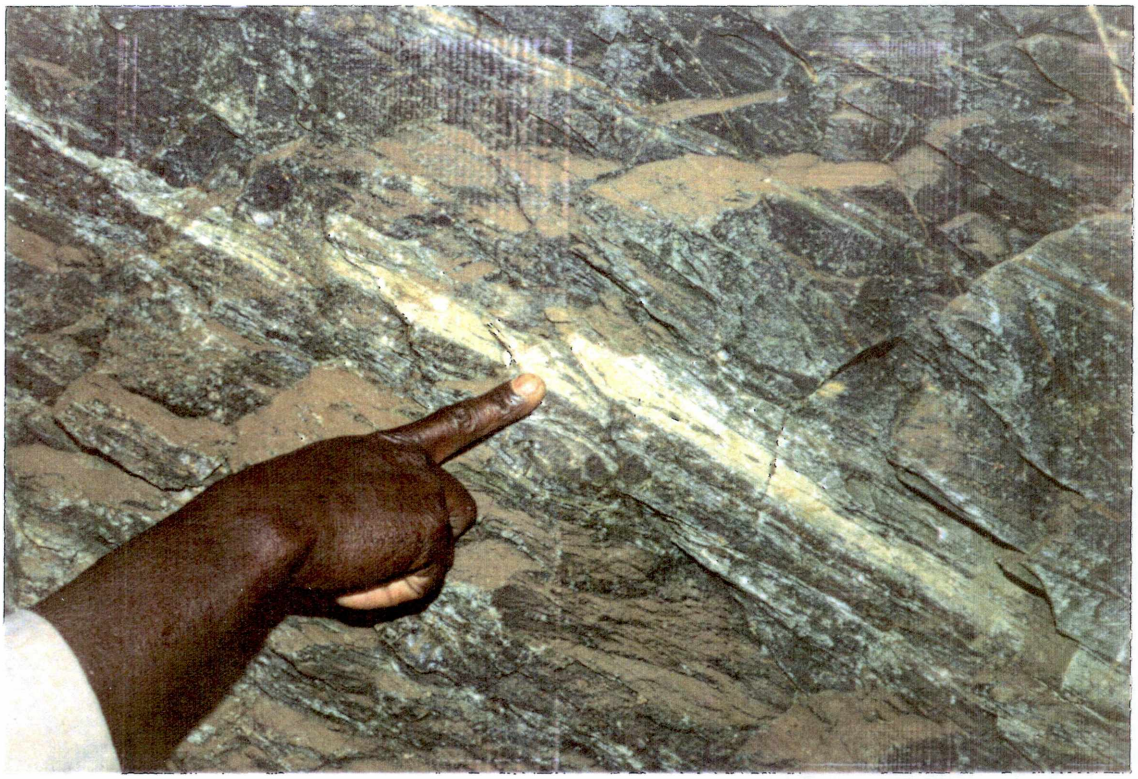


Figure 5.10 - Minor structure in main vein hanging wall, indicating reverse shear sense (10 Level South main drive looking south). Small reverse shears developed, probably in "P" orientation to main vein, disrupting sheared flow top unit.

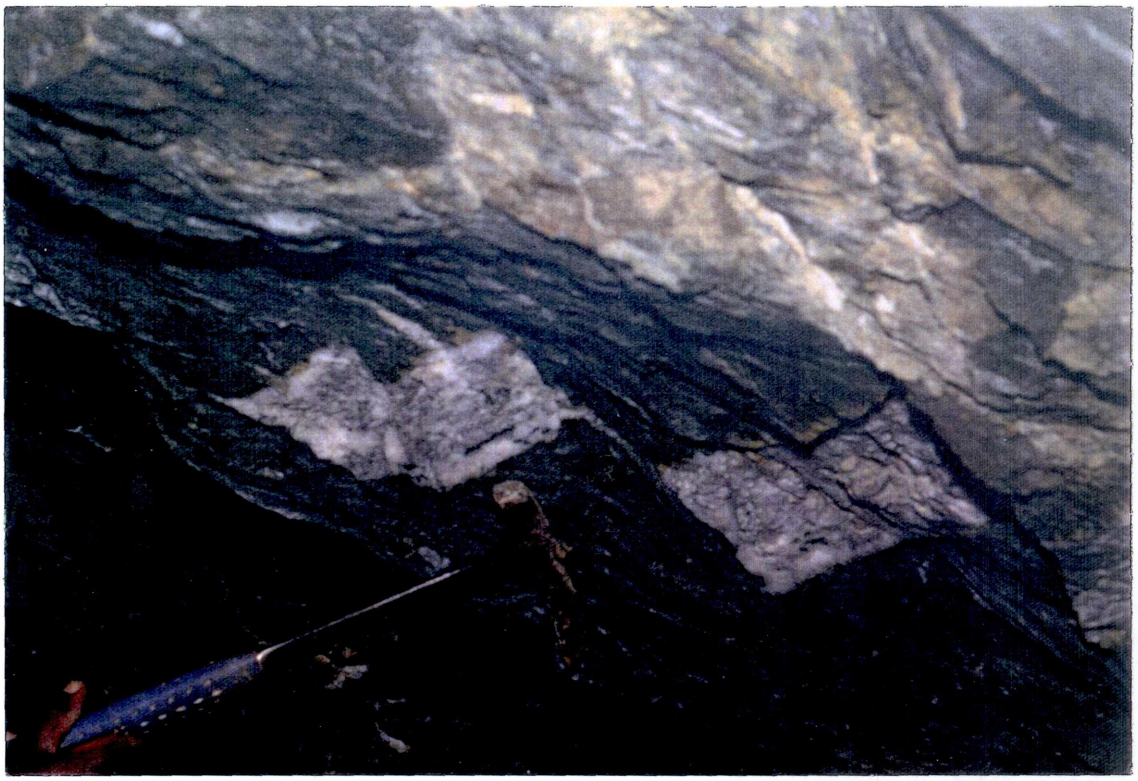


Figure 5.11 - Minor structure indicating reverse shear sense on main vein structure (10 Level South main drive looking south). "Domino" veining developed due to shearing on "P" shear combined with extension perpendicular to the "T" direction (see Figure 4.14 for mechanism).

Figure 5.12a - Ribbon Vein 8 Level N16 stope. Later strike slip shear (looking down-dip, dextral sense) causing narrow veining both parallel to the main ribbon vein and in "T" extension site (pencil 12cm long)

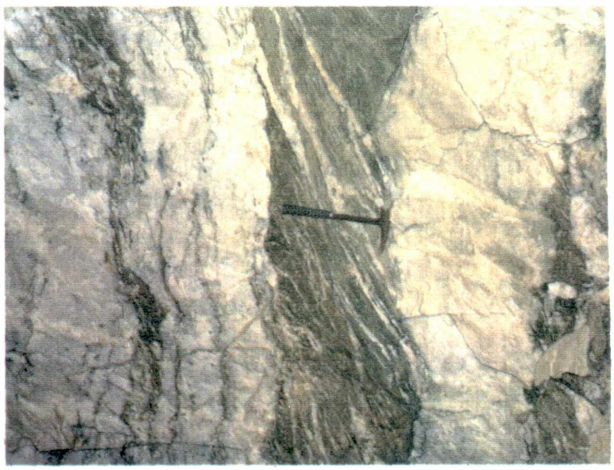
Figure 5.12b - Ribbon Vein 8 Level N16 stope. Later strike slip shear (looking down-dip, dextral sense) causing en-echelon quartz veining in the "T" extension site. Note sygmoidal aspect to some of the veining, supportive of the shear sense (pencil 12cm long)

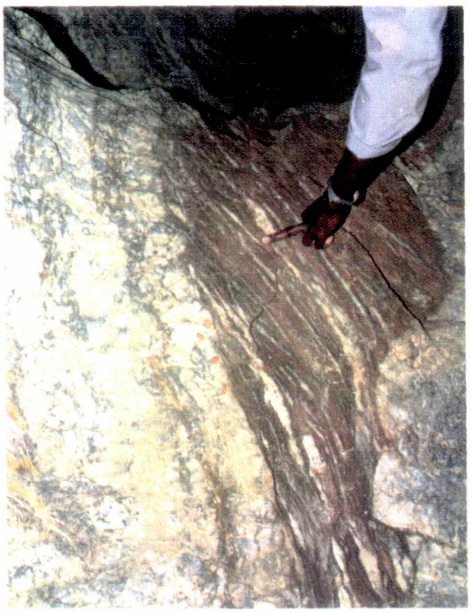
Figure 5.12c - Ribbon vein on 7 Level South main drive (looking up-dip, hence view shows reversed sinistral shear-sense). Narrow veining may fill "R" Riedel site. Veinlet "a" is seen to join main ribbon vein with no interruption, indicative of synchronous, related development of thin footwall veining and at least some of the ribbon vein.

Figure 5.12e - Intrafolial folding of individual quartz ribbon, 9 Level N2 stope. Looking up-dip, small drag fold indicates sinistral shear-sense as viewed (hence looking down-dip dextral). Undisturbed nature of complex ribbon vein indicates either later shearing responsible for folding was focussed into discrete zones or that shear-folding occurred during ribbon vein development.

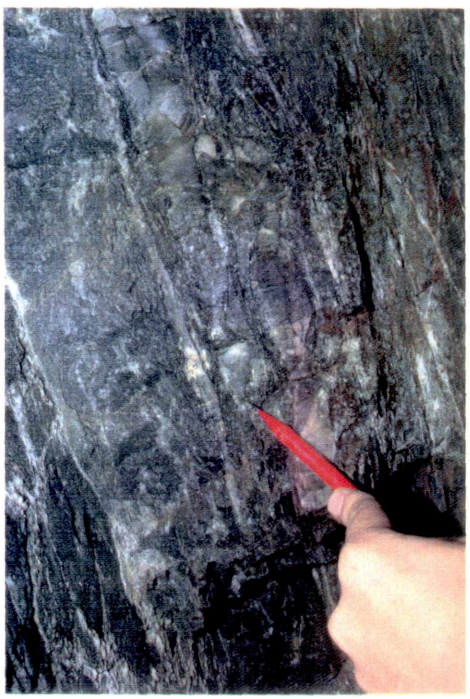
Figure 5.12

Figure 5.12d - Ribbon vein on 10 Level South main drive (looking up-dip, hence view shows reversed sinistral shear-sense). Narrow veining may again fill "R" Riedel site (see Figure 4.8).






B




A

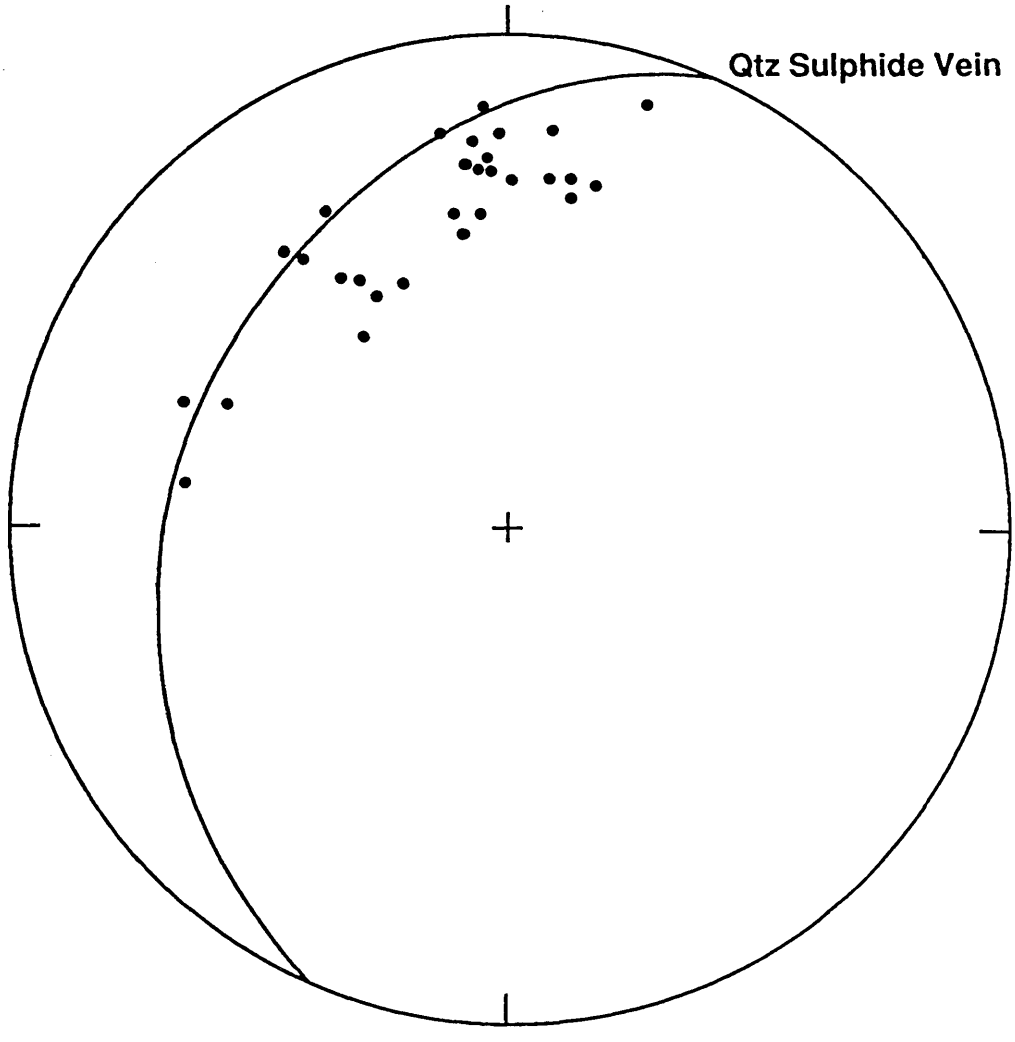


Figure 5.13 - Stereonet plot of plunges of intercepts between late D2 extension veinlets and D2 ribbon veins. Average great circle for D2 ribbon vein also plotted. Plot of data suggests dextral strike-slip shearing occurred during late D2 (n = 29).



Figure 5.14 - Photomicrograph of highly deformed sheared mafic lava comprising dominantly phyllosilicate and carbonate with deformed quartz veining (Sample 10-29, immediately adjacent to D2 ribbon vein). Mafic lava is sulphide rich (opaque pyrite grains) and the grains show clear quartz pressure shadows parallel to long axis of the photo. Quartz veining is also clearly stretched and shows intrafolial folding. Scale disk = 5 mm diameter.

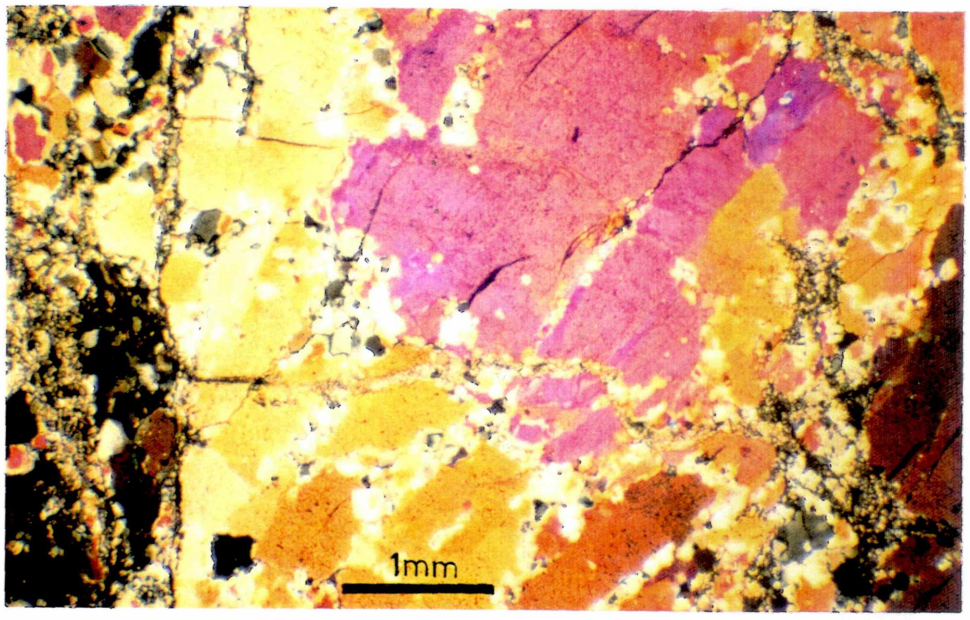


Figure 5.15 - Photomicrograph of rather thick section of D2 mineralised vein (Sample 30-2). Short axis of photo is parallel to the main trend of the vein. The large quartz grain in the field of view is partially recrystallised along planes running from top-right to bottom-left of the photo. Such dynamic recrystallisation to smaller sub-grains is indicative of sinistral shear, looking south perpendicular to dip of the Patchway vien as viewed on this photo (see Figure 5.6). This sense of shear supports reverse dip-slip.

suggestion that the domainal spacing in the phyllosilicate zones decreases closer to the vein indicative of higher strain by dynamic recrystallisation. The sub-ophitic texture of the mafic lavas is preserved further from the vein where a wider spaced continuous cleavage is evident.

Kinematic indicators are quite rare in the deformed mafic units as the cleavage seams are sub-parallel to anastomosing with no hard grains to behave as rotational or non-rotational porphyroclasts. The quartz laminae behave as micro-lithons during deformation in most cases, with plastic deformation limited to recrystallisation and suturing of grain boundaries developed (Figure 5.15). However, it is evident that later brittle deformation has occured in these domains, with brittle cracks infilled with mainly carbonate (Figure 5.16).

Some sections show evidence for development of the S-C fabric seen on a macroscopic scale. These are generally supportive of the reverse sense of shear suggested (Figure 5.17). Tentative examination of deformed felsite samples suggest the presence of rotated hard quartz porphyroclasts although in some cases interpretation is often equivocal.

Some of the best potential kinematic indicators are pyrite grains which are ubiquitous in the deformed vein wallrocks. Figures 3.3 and 5.14 show photographs of a number of these where a strong stretching lineation is indicated in the plane of deformation. Examination of vorticity in the fibres is often supportive of reverse shear sense, although conflicting grains are also seen. One problem in interpreting these indicators is the chronology of grain growth as the pyrite grains show a complex chronological history (Chapter 6) and the actual fibre trails may only document the last deformation event experienced by the grains.

D3 Deformation

The second major structural event during the development of the gold deposits in the region around Patchway is the development of a second major trend of structures striking approximately 070°. This trend is parallel to:

a) The "Central Shear Zone" at Patchway and similar zones at Golden Valley
b) The "Rouge Shear" and associated orebody
c) The Erin orebody.
(for locations see Figures 2.6 and 3.1)

D3 Effects on D2 Mineralisation

Figure 5.18 indicates the location of the detailed areas referred to in the following discussion.

The D3 deformation is marked by a second fabric at Patchway (S3) which is developed at variable intensity throughout the deposit within the vein hosting shear zone, but more importantly in discrete

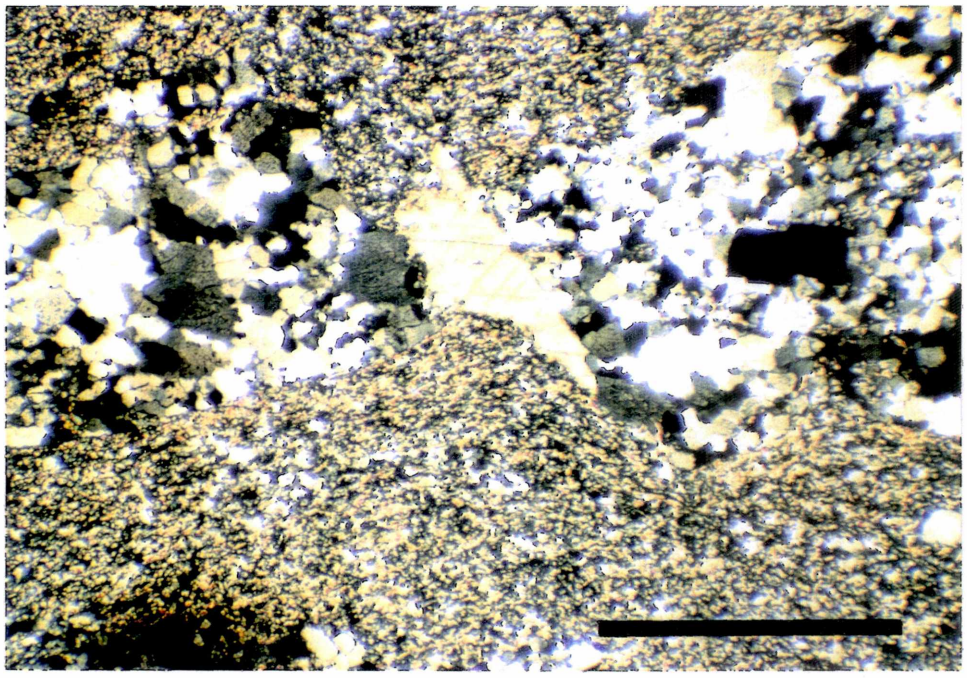


Figure 5.16 - Photomicrograph of highly deformed sheared felsic intrusive comprising quartz, phyllosilicate and carbonate with deformed quartz veining (Sample 10-34, immediately adjacent to D2 ribbon vein). Thin quartz veinlet at centre of field is boudinaged and finally fractured with the created dilatancy infilled with carbonate. Scale bar = 2 mm.

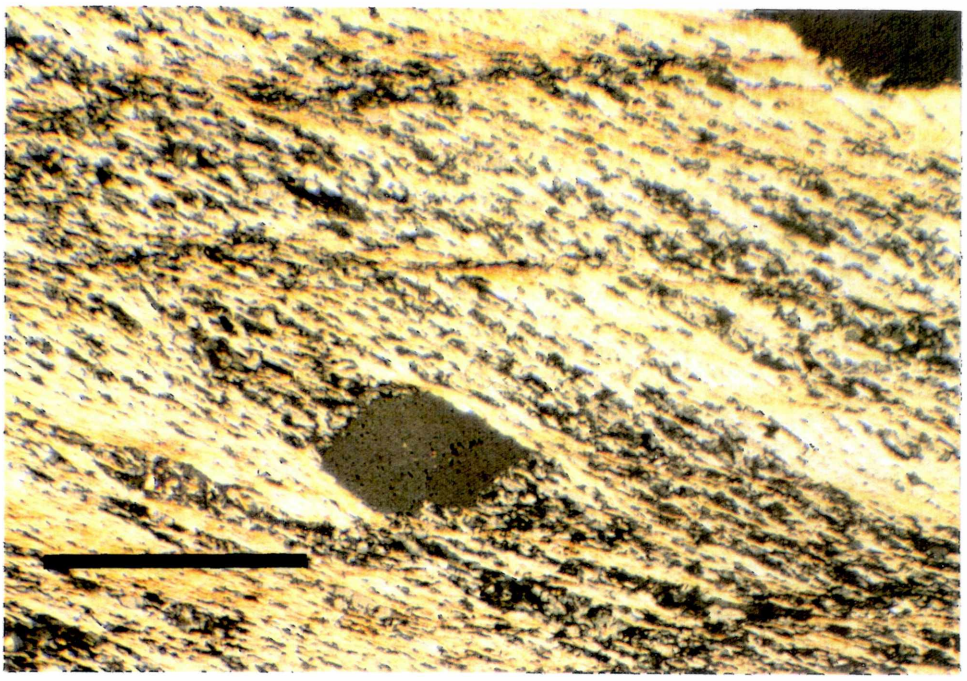


Figure 5.17 - Photomicrograph of highly deformed felsite (Sample 30-5). Central to the photograph is a quartz phenocryst around which is developed a strong S-C fabric in the mainly white mica and fine-grained quartz (see Figure 5.6). C fabric is parallel to long axis of photograph and again sample is viewed southwards perpendicular to vein dip, again supportive of reverse sense of shear.

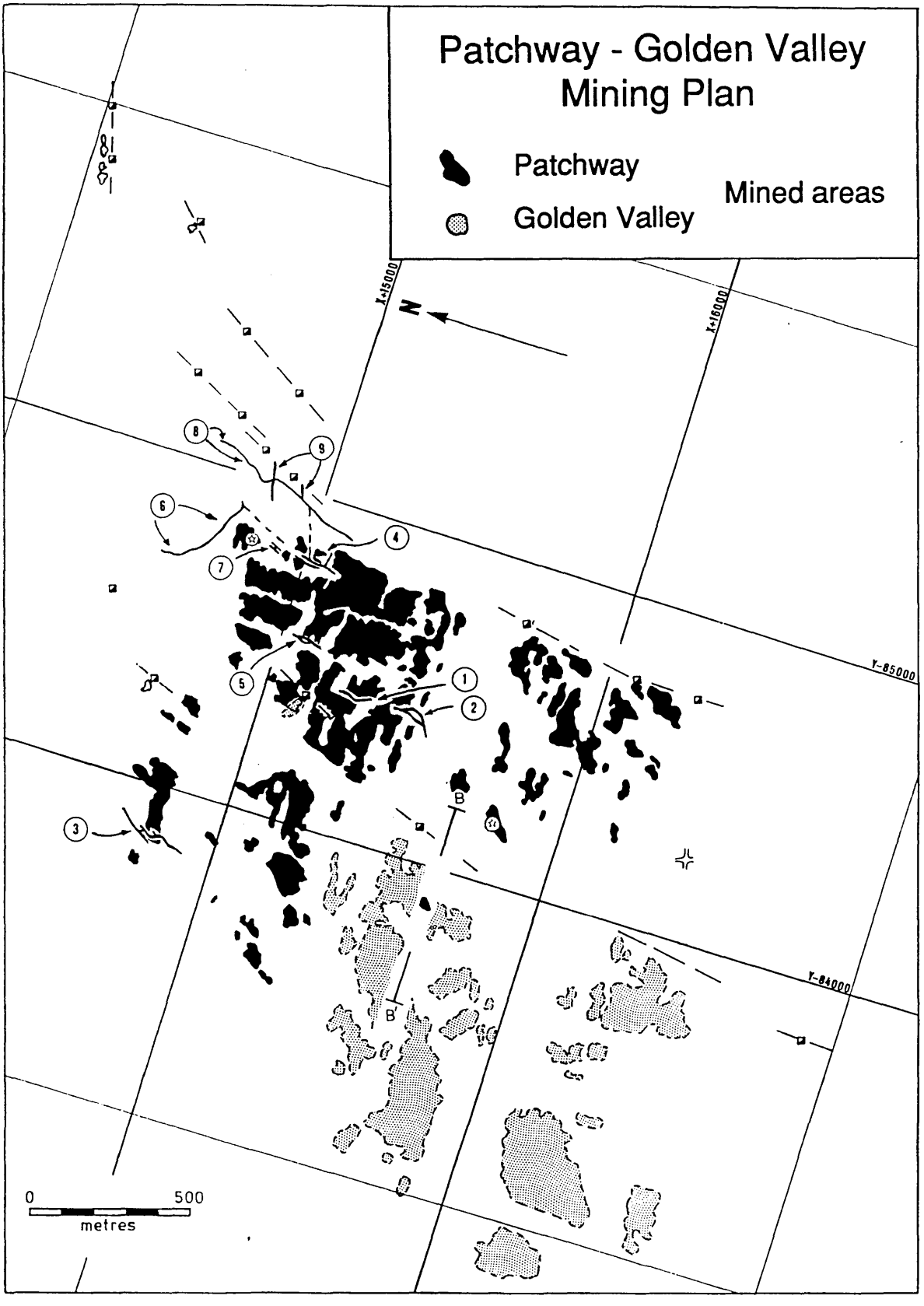


Figure 5.18 - Location plan of the Patchway mine (see Figure 2.7 for key) showing detailed areas described in the D3 and D4 deformation section. Numbers refer to detailed maps : 1 - Fig. 5.20, 2 - Fig. 5.22, 3 - Fig. 5.23, 4 - Fig. 5.24, 5 - Fig. 5.25, 6 - Area of D3 "Kabanga" veining, 7 - Fig. 5.42, 8 - Basil Reef, 9 - D3 cross-veins, B-B' - Raise section shown on Figs. 5.38 and 5.39.

cross cutting zones like the Rouge shear, Central shear zone and Erin structure (Figure 5.19). Figure 5.20 shows a section of the main vein on 10 level at Patchway ("1" on Figure 5.18) where some of the main D2 mineralisation has not been mined out. In this region the vein has suffered considerable attenuation due to D3 deformation. Here, D3 is largely characterised by boudinage and thinning of the vein. The boudinage is indicative of volume loss across the structures, again indicative of a compressive regime. Examination of both the ribbon quartz vein and the felsite intrusive body also caught in the later deformation zone indicates a duplication of these units at the northern part of the zone, consistent with a sinistral strike-slip component to shear. Parts of the vein shows minor folding, particularly in the more intensely deformed areas. Plunges of the axial traces of these minor folds is parallel to the plunge of boudin crests, consistent with formation during the same deformation event (Figure 5.21).

Figure 5.22 shows a plan of the 10 level at Patchway in the region of the Central Shear Zone. Here rotation of boudinaged gold bearing D2 veins, shown arrowed "A" on the figure, is consistent with this sinistral strike-slip movement. Mineralised vein loss in this zone is apparent and thin remnants of earlier mineralisation is present as boudinaged sections scattered throughout the Central Shear Zone, sometimes only present as thin lenses. The dolerite intrusives are much later as they clearly cross-cut both the D2 and D3 structures.

Figure 5.23 shows, in plan, an area of the D2 mineralisation on 28 level close to the northern limit of the current mine workings ("3" on Figure 5.18). In this area, D3 deformation is largely confined to discrete but intense cross-cutting zones which clearly disrupt mineralisation, complicating mining operations. Again there is clear evidence of sinistral strike-slip motion on these structures, which is accompanied by the apparent rotation of the faulted segments of the quartz-gold veins to closer parallelism with the strike of the D3 zones in this area. It is interesting to note that in this area that the down-dip extrapolation of the Rouge Shear lies close to the north of this section of the mine. The trend of both this and the shears on 28 level is 070° which suggests that these structures are linked.

Figures 5.24 and 5.25 show two sections of the mine on 4 and 9 levels respectively. Here thin felsite intrusive bodies are very closely associated with the early D2 shear structure and they themselves show clear D2 deformation features. The intrusives are also deformed by the D3 shearing event. The felsite on 9 level shows rotation consistent with sinistral strike slip motion, with thickening of the body in the inflections of rotation. The early quartz-gold mineralisation has been dramatically attenuated in zones of maximum D3 deformation, better preserved in the more extentional sites during shear folding during D3. The area on 4 level shows very clearly attenuation of both mineralisation and felsite intrusives by D3, with again good evidence of rotation of the felsite body by sinistral sense shearing. Minor folds in the D2 quartz veining and S-C relationships in the shear zone (shown in detail on Figure 5.24) would corroborate this. Interestingly, here the felsite and mineralisation have somewhat complex relationships, with partly divergent trends (complicated somewhat by deformation).

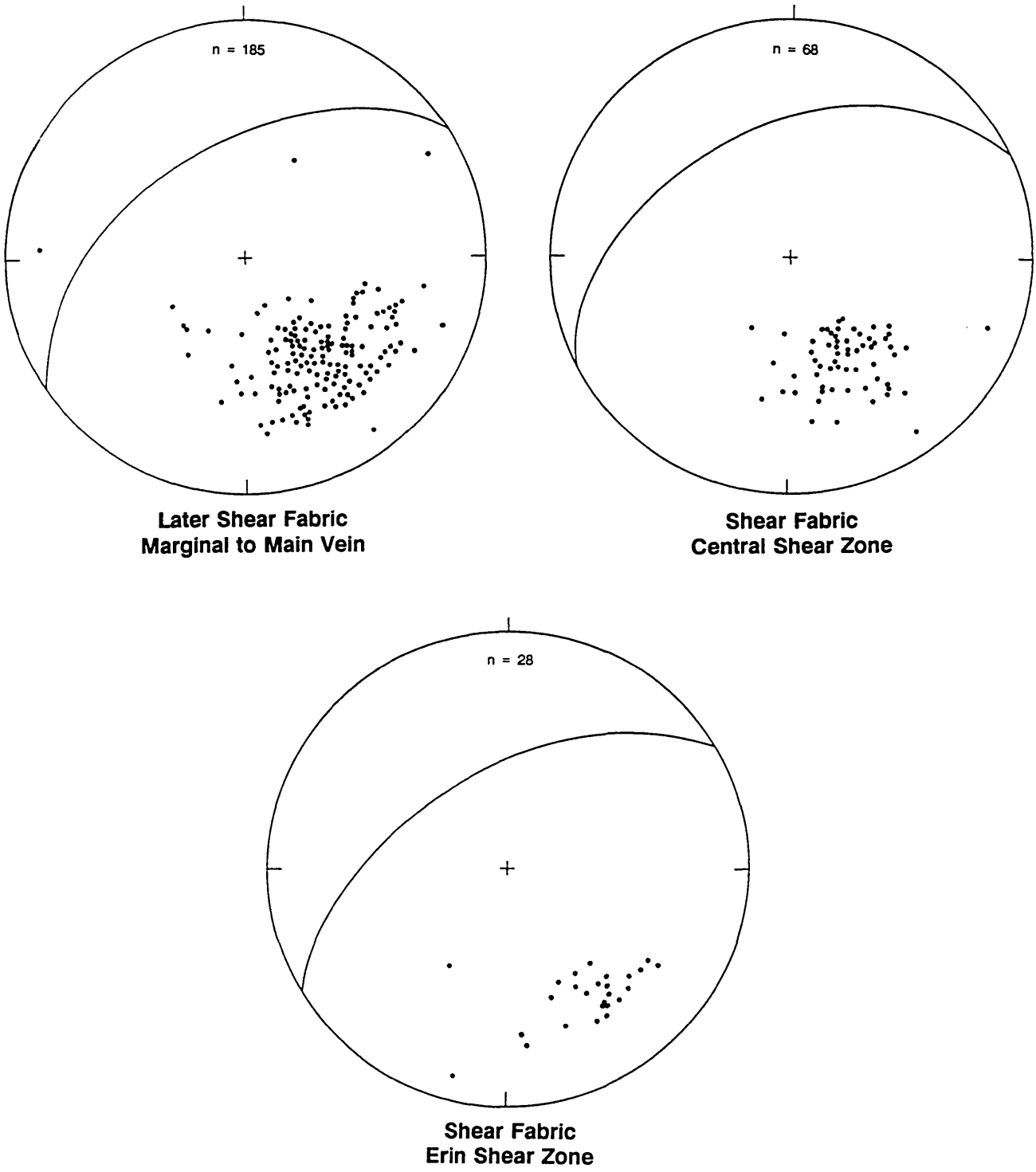


Figure 5.19 - Stereonet plot of poles to later shear fabric (S3), marginal to the D2 veins and in discrete cross-cutting structures. Average great circles for each data set are also plotted. Sources of data from the areas indicated.

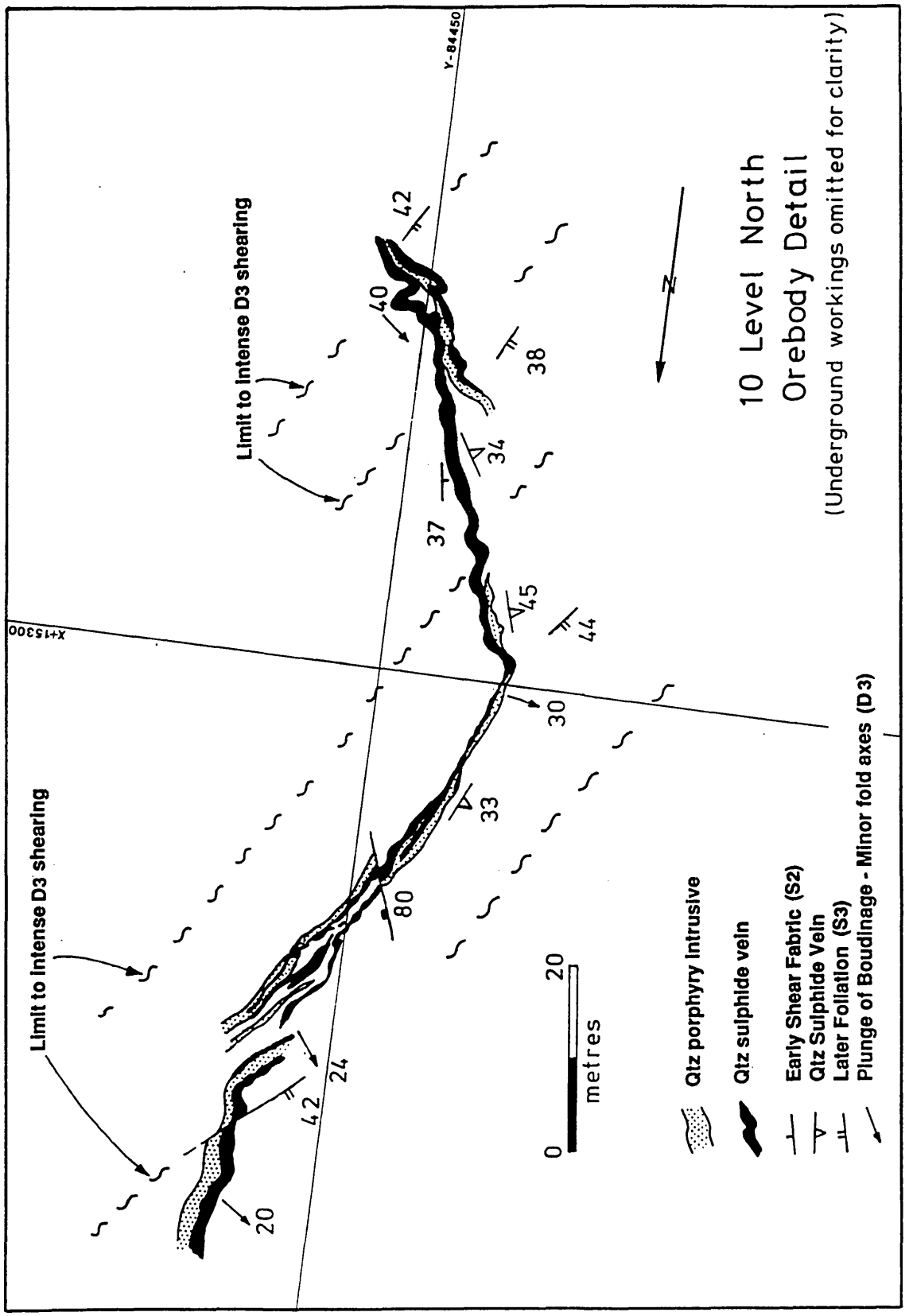
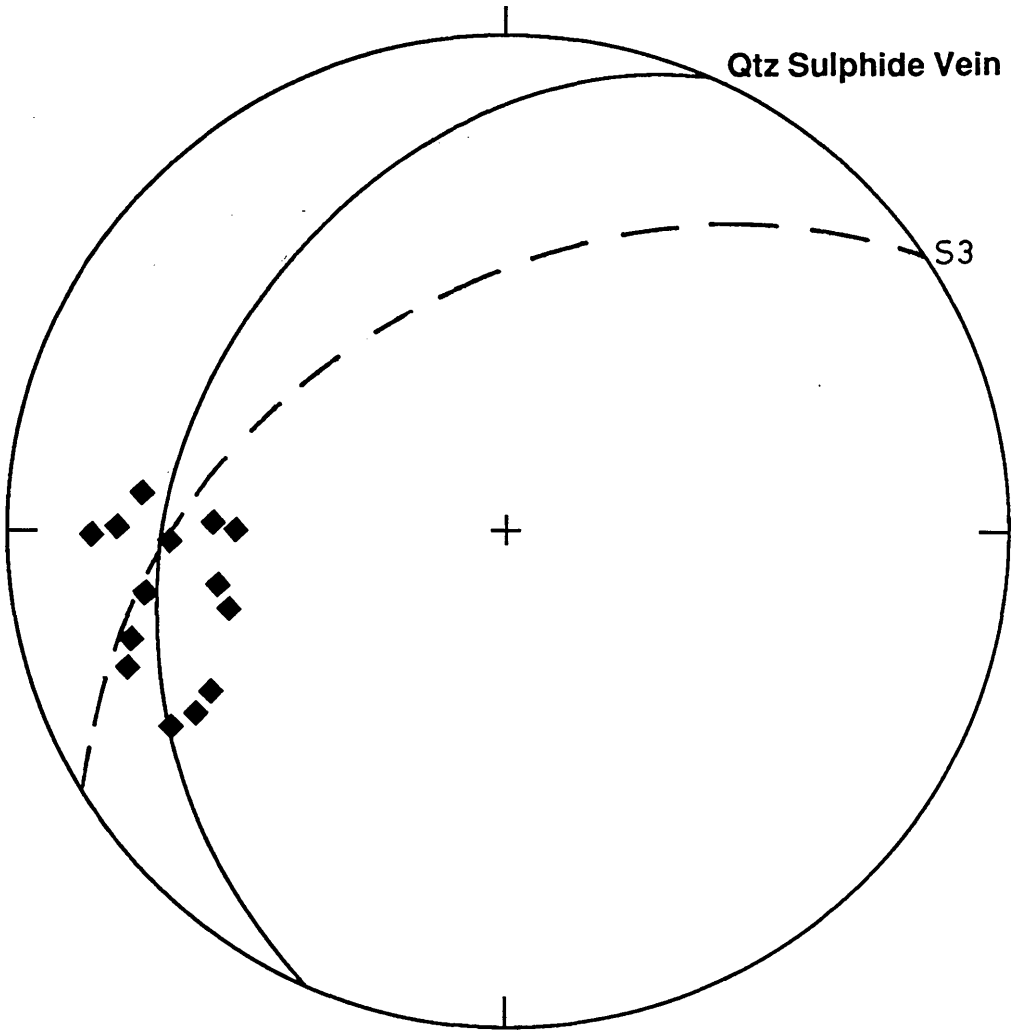


Figure 5.20 - Level plan 10 Level North (1 on Figure 5.18). Plan shows deformation effects of D3 on the D2 ribbon vein orebody.



◆ **Plunge of boudinage - minor fold axis**

Figure 5.21 - Stereonet plot of plunges of boudinage crests and minor fold axes of D3 deformation of D2 ribbon vein. Also plotted are average great circle of D2 ribbon vein and S3 shear fabric (from Figure 5.19).

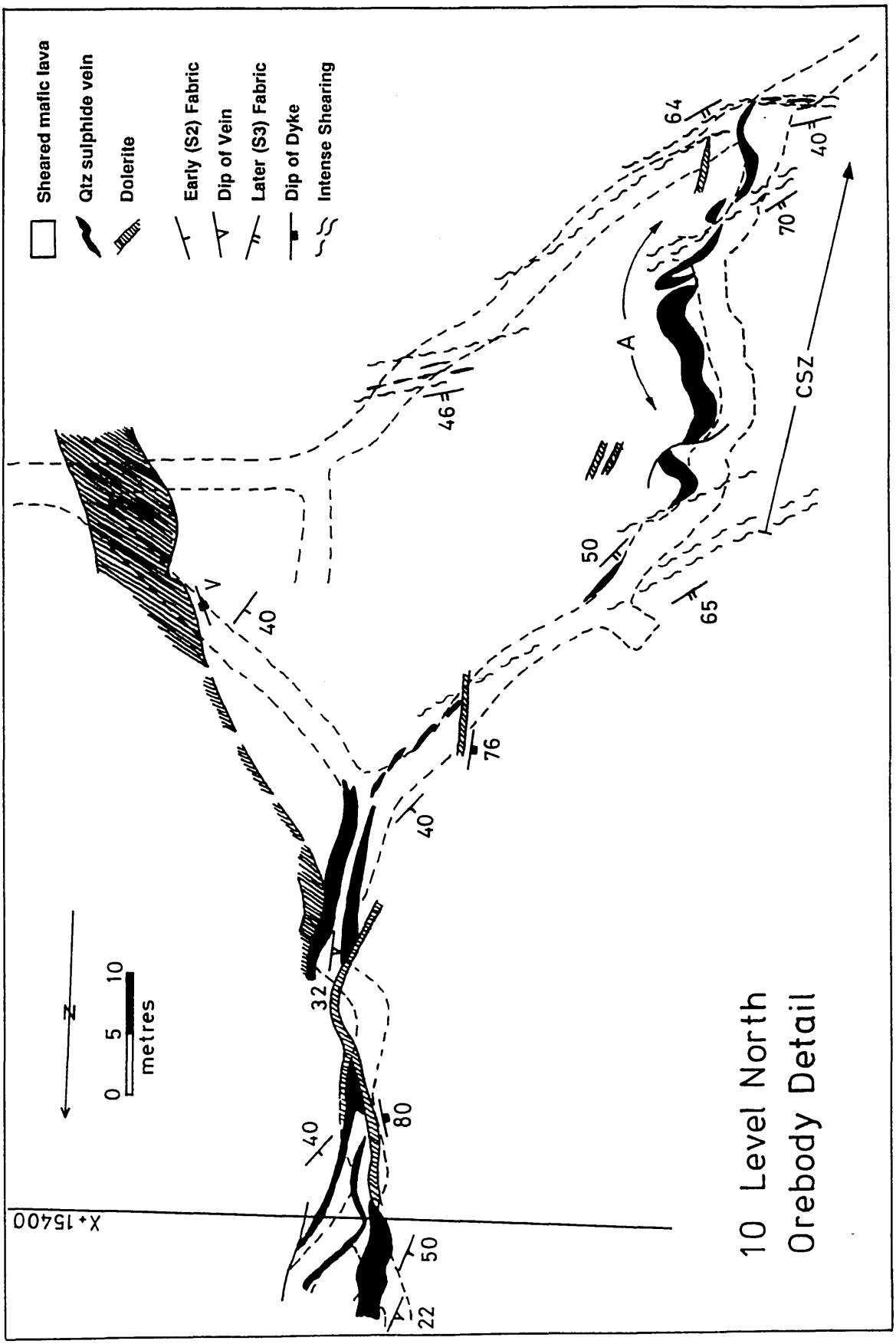


Figure 5.22 - Level plan 10 Level North (2 on Figure 5.18). Plan shows intense D3 deformation to the D2 ribbon veining close to the northern margin of the central shear zone (see Figure 2.7). Here, underground workings are indicated in dashed lines.

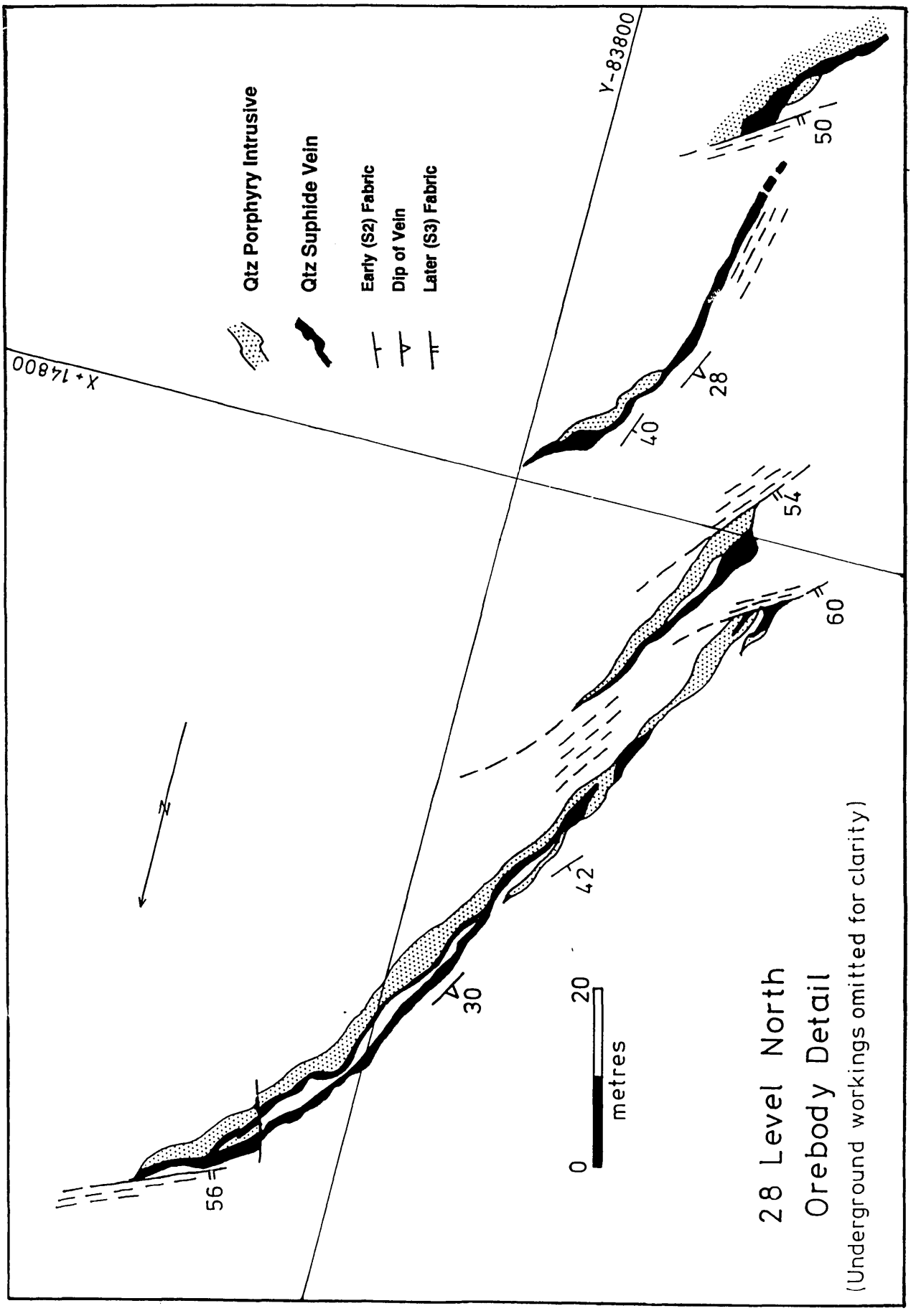


Figure 5.23 - Level plan 28 Level North (3 on Figure 5.18). Plan shows D3 fault repetition of the D2 ribbon veining close to the northern margin of current mine workings.

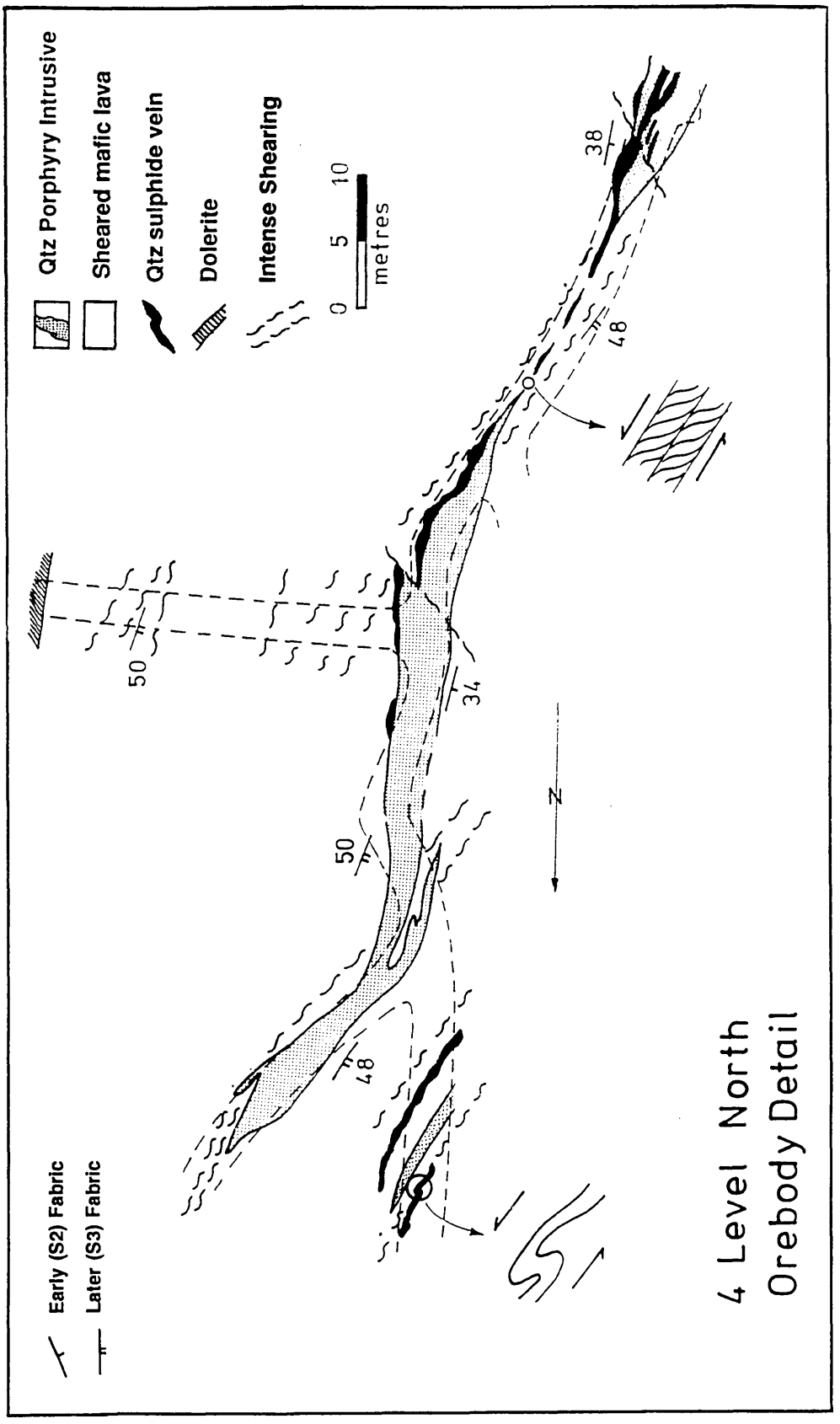


Figure 5.24 - Level plan 4 Level North (4 on Figure 5.18). Plan shows D3 deformation of both D2 ribbon veining and felsite intrusive. Minor structures arrowed on the plan support sinistral strike-slip movement on the D3 structures. Underground workings shown as dashed lines.

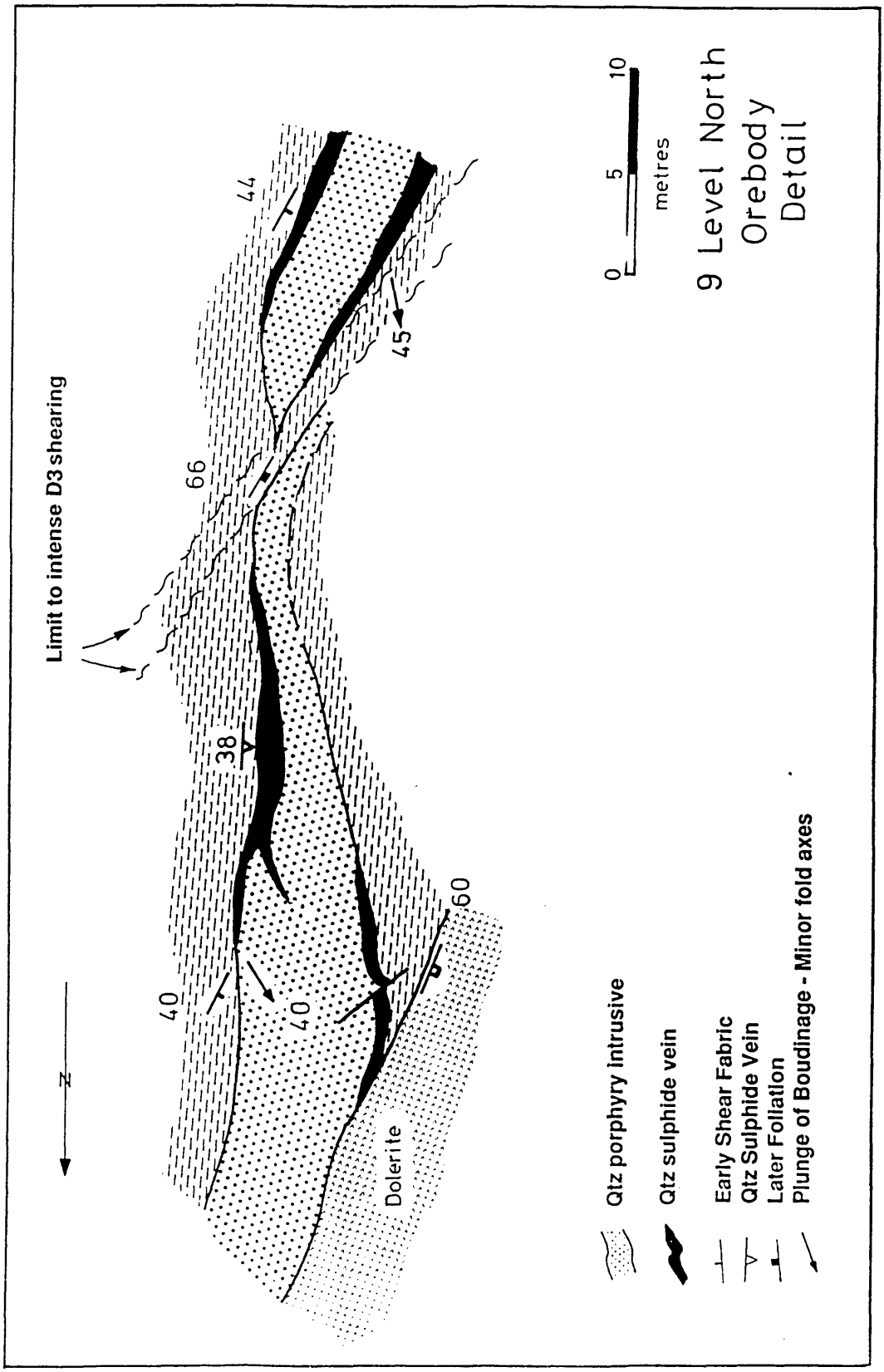


Figure 5.25 - Level plan 9 Level North (5 on Figure 5.18). Plan shows D3 deformation of both D2 ribbon veining and felsite intrusive. Sense of displacement on S3 shear and rotation of felsite mass is consistent with sinistral-sense slip. Underground workings shown as dashed lines.

During D3 it is evident that the main D2 vein suffered a variable degree of attenuation as was described earlier. Boudinage is common throughout the mine and leads to serious attenuation in many areas of the mine. During this boudinage event a new generation of quartz with tourmaline is seen infilling boudinage necks. Extension veins are similarly infilled even show strong post emplacement deformation by the D3 event probably responsible for their earlier formation (Figure 5.26).

The Erin Structure

The main host structure for mineralisation at Erin is clearly parallel to the main D3 structures mapped at Patchway (Figures 2.5 and 2.6). Immediately apparent is the deformation style of the Erin structure, which is quite different to that seen surrounding the main veins at Patchway and Golden Valley. Alteration takes the form of intense carbonate flooding of opened shear foliation lending the mineralised zone a characteristic striped appearance (Figure 5.27). Minor folds in the mineralised zone are common, strikingly open in form in some places (Figure 5.28). Mapping at Erin in this structure (Figure 5.29) indicates that a similar sense of shear can be deduced from all the kinematic indicator elements, showing dominantly sinistral strike-slip motion. Such a shear-sense supports the view that the Erin structure is a D3 structure, with similar sense of shear to the mapping at Patchway. Figure 5.30 shows minor structures supportive of the broadly mapped relationships. The highly deformed nature of the mineralisation at Erin also suggests that some of the mineralisation pre-dated a large part of the D3 deformation, suggesting either a long-lived D3 deformation event or that D3 at Erin may simply overprint an existing D2 style of mineralisation previously developed at Erin. Significantly, Erin lies at the intercept of an 020° and an 070° trending air-photo linear (Figure 5.2), which may support the idea of D3 deformation overprinting existing mineralisation formed during D2 in an 020° structure.

The Kabanga, Munya-Skati and Other Minor Veins

The so called Kabanga and Munya-Skati Reefs intercepted at the northwest end of 4 level at Patchway also appear to be located on D3 structures. Figure 5.31 shows a stereonet projection of the data collected from this area indicating its association with the D3 trend. The mineralised structures examined underground show some strong similarities with the alteration style at Erin. The striped appearance of the marginal alteration at Kabanga (Figure 5.32) is even more apparent here than the alteration at Erin. The veins themselves show deformation styles of a more brittle nature too; Figure 5.33 shows the vein breccias seen in the footwall of the Kabanga reef and the often chaotic nature to the vein and its included wallrock fragments.

Also exposed by cross-cutting to Basil Reef in the northern marginal areas of the mine on 4 level, cross-veins were discovered. These have been partially investigated by underground development. Gold contents of this mineralisation is negligible, and there are distinct mineralogical differences. Figure 5.34 shows the mineralisation exposed on 4 level. Despite the similar ribboned appearance of some of the veins, they are quite different from the main auriferous veins. Sulphides are notably absent and

Figure 5.26a - Quartz-tourmaline extension vein on 6 Level North. Vein clearly cross-cuts ribbon quartz-sulphide vein. Tourmaline forms the black phase in the vein, best developed where the extension vein cuts iron-rich parts of the vein and wallrock.

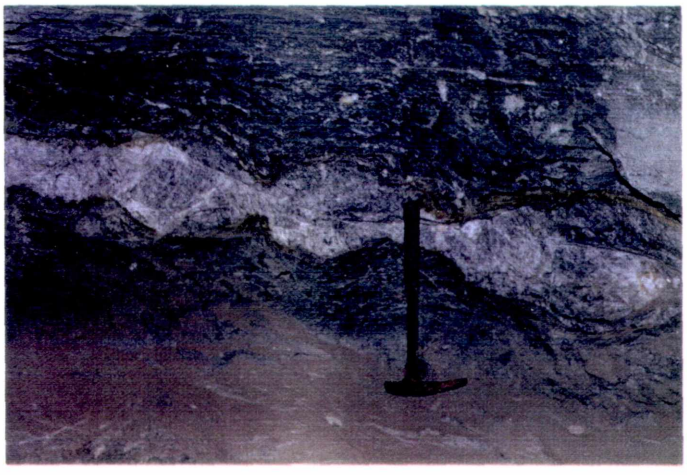
Figure 5.26b - Quartz-tourmaline veining infilling boudinage neck in ribbon quartz-sulphide vein on 10 Level North. Ribbon vein shows strong attenuation by D3 deformation with necks in boudins forming extensional sites. Quartz-tourmaline vein (Q) again shows black tourmaline nucleated in areas where the veining crosses iron-rich phases in the ribbon vein.

Figure 5.26c - Strong boudinage seen in ribbon quartz veins, 10 Level North. Quartz shows evidence of strong recrystallisation during boudinage caused by D3.

Figure 5.26d - Deformed quartz-tourmaline veining on 4 Level Kabanga vein. Quartz-tourmaline extension veins similar to those in Figure 5.26a are here clearly deformed by D3 deformation, indicating that they formed early in the D3 event.









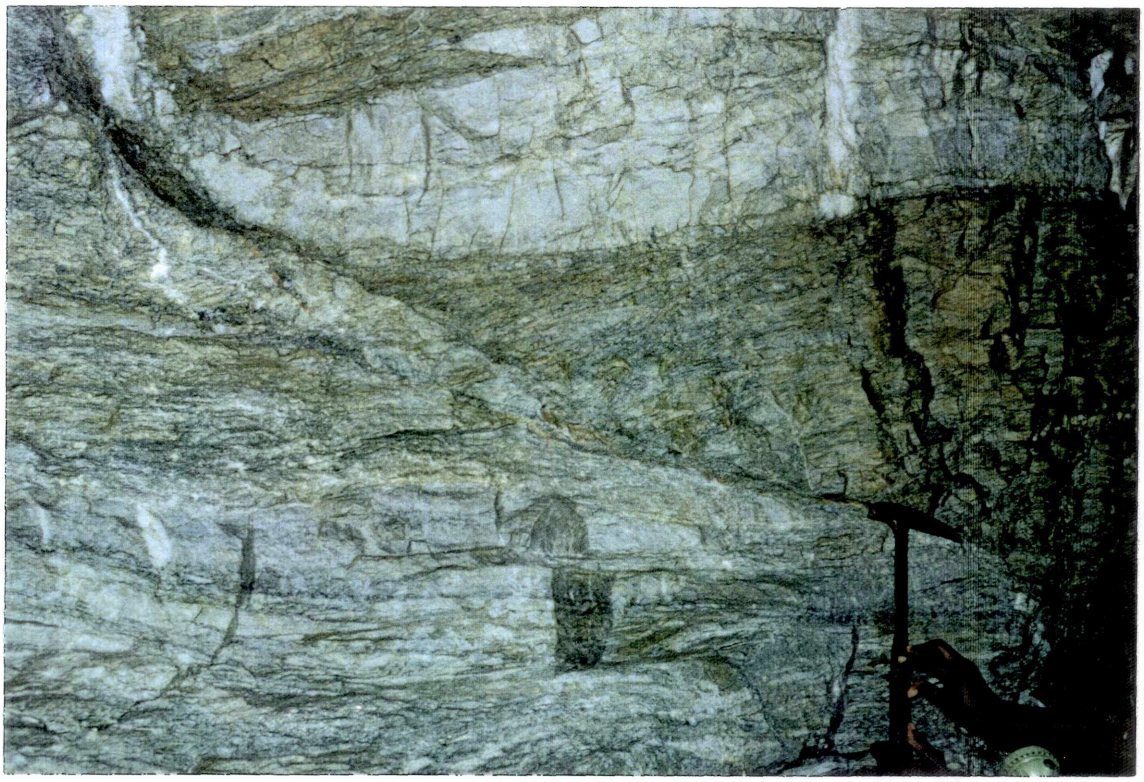


Figure 5.27 - Deformed rocks in the Erin shear zone, 90 Fathom Level. Distinctive stripy appearance of the host rocks to the Erin mineralisation is caused by the abundant white-buff carbonate laminae. Photograph shows a thin felsite intrusion (upper part of photo), in the dominantly mafic host rock, which is similarly deformed. At the base of the photograph a distinctive green mica gives an apple-green colouration to the phyllosilicate-rich zones.

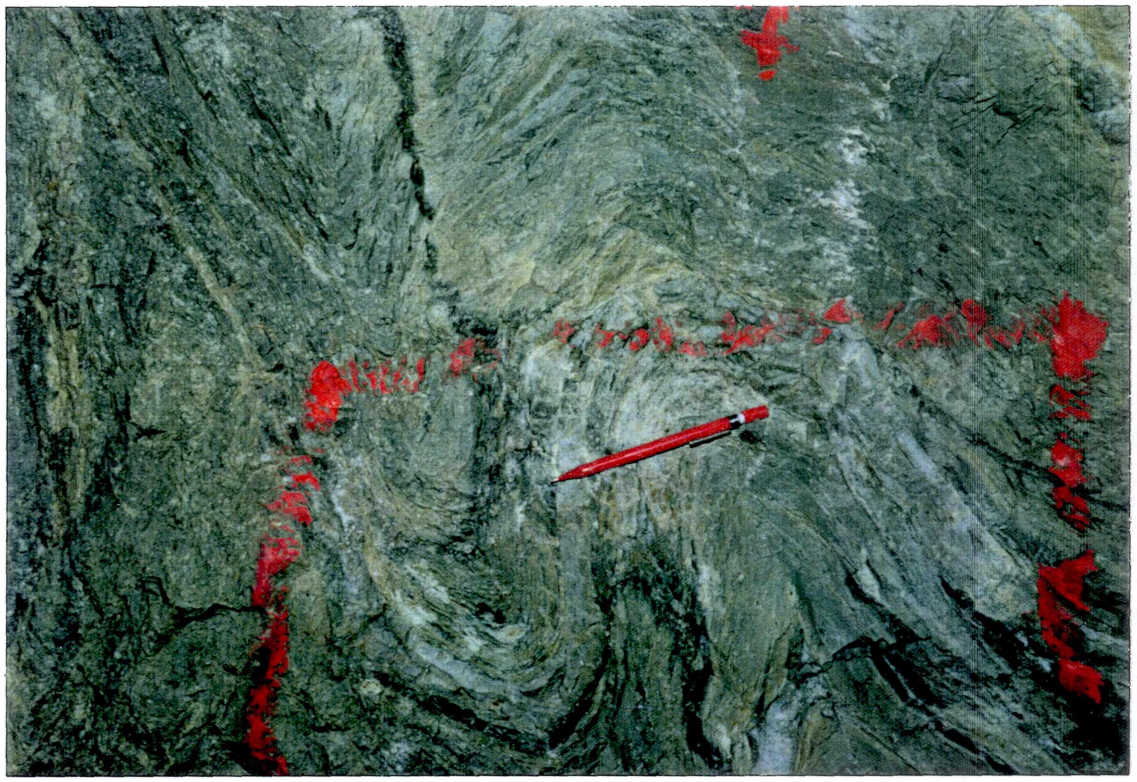


Figure 5.28 - Folded foliation (intrafolial fold) in the Erin shear zone, 90 Fathom Level. Foliated wallrock is deformed along with thin quartz vein seen at point of pencil. Pencil scale is 12 cm long.

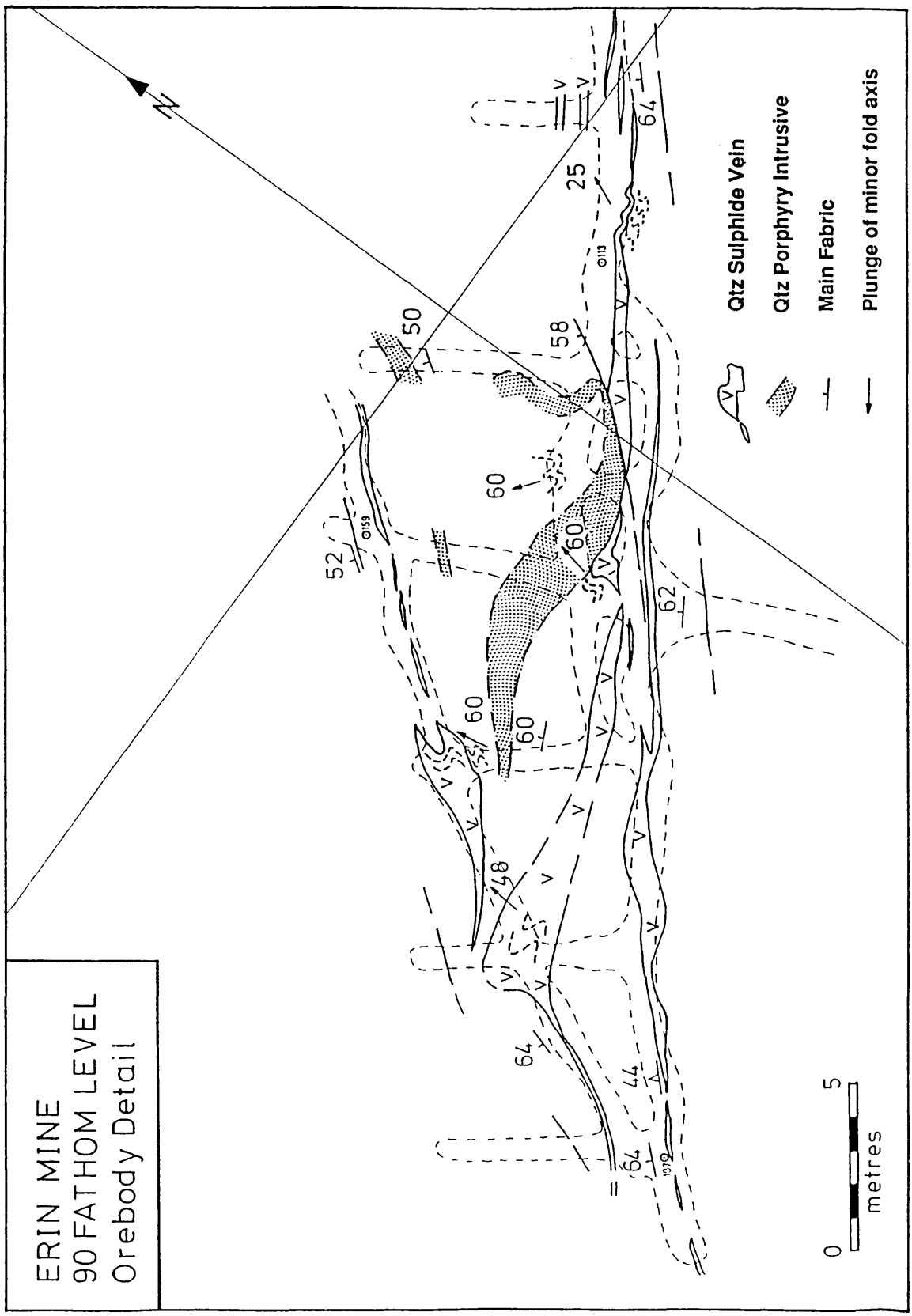


Figure 5.29 - Level plan 90 Fathom Level Erin mine (for location see Figure 2.5). Plan shows the complex, highly deformed geology of the Erin orebody.



Figure 5.30a - Minor folding in the Erin shear-zone, 60 Fathom Level. Thin quartz-sulphide veinlets are folded by shearing. Sense of shear is sinstral looking down-dip (dextral up-dip here), consistent with the shear sense during the main deformation at Erin. Minor fold axes plunge steeply north, perpendicular to slip-vector.

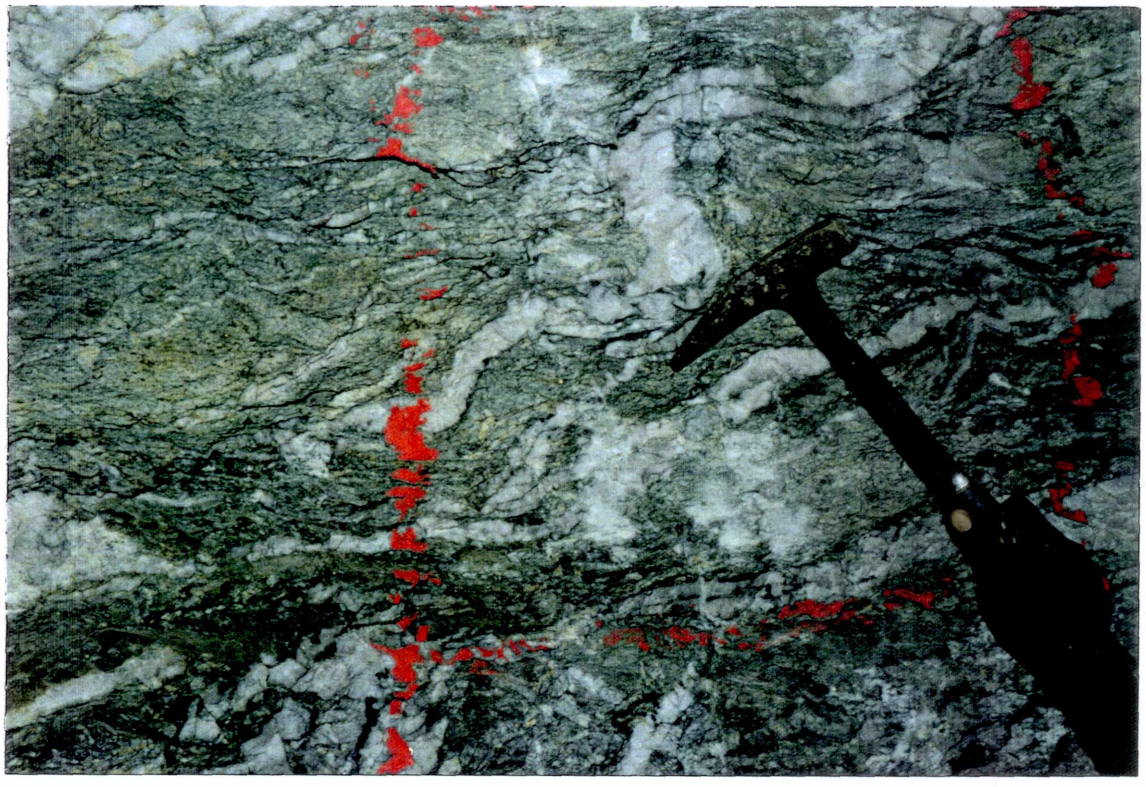


Figure 5.30b - Minor folding of Erin mineralisation, 90 Fathom Level. Thin quartz veining is folded during shearing. Photograph looking north, down-dip, indicates sinistral shear-sense.

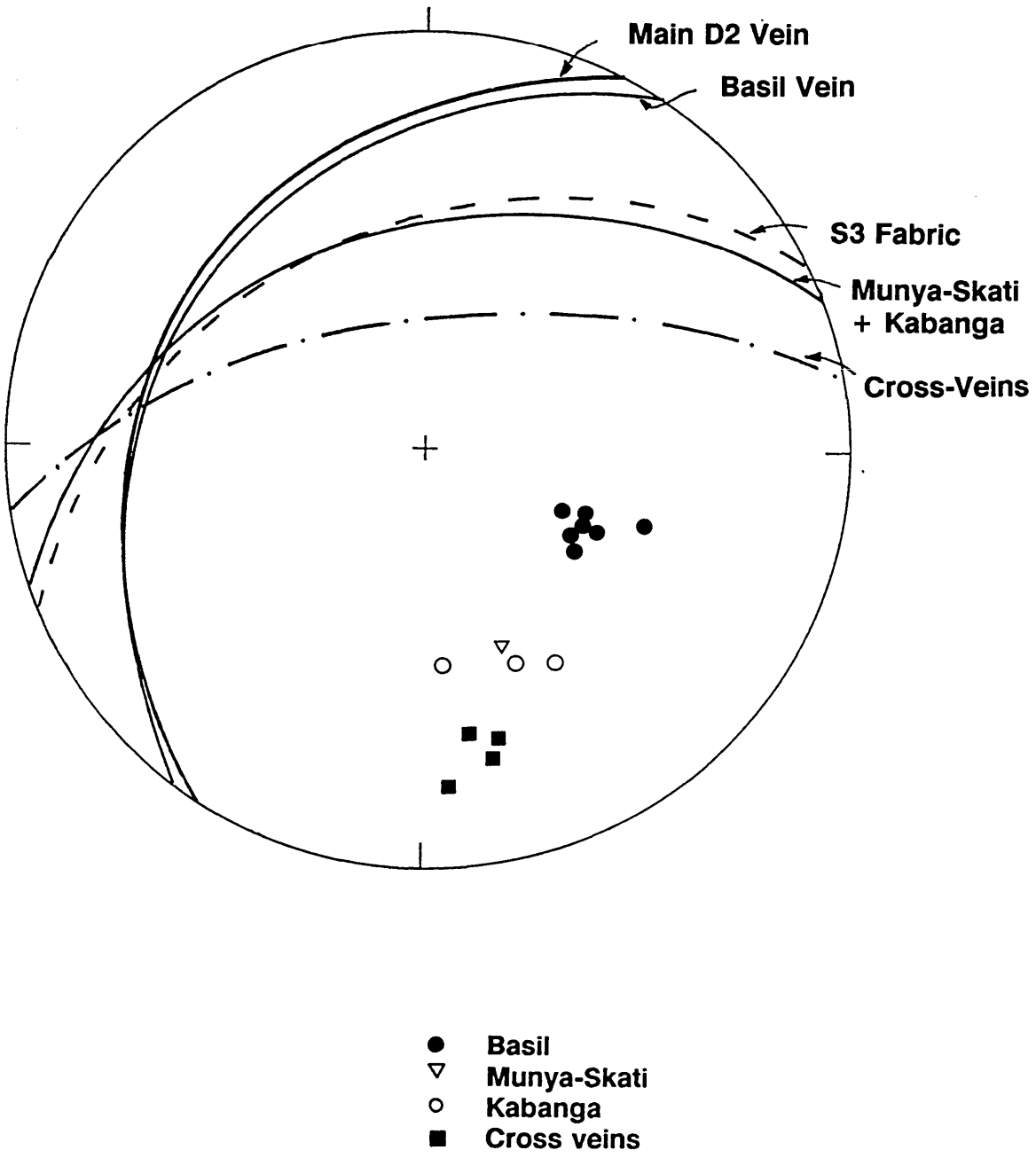


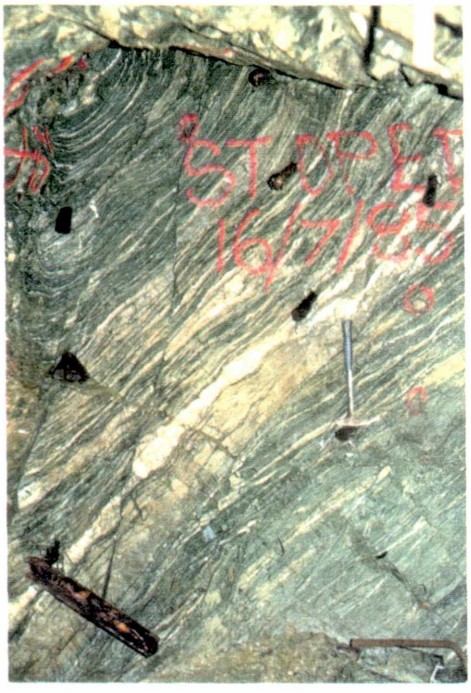
Figure 5.31 - Stereonet plot of poles to veining for minor veins underground at Patchway. Average great circles for each data set are also plotted. It is apparent that the Basil vein is sub-parallel to the main D2 ribbon vein and hence is probably D2 age. The Kabanga and Munya-Skati mineralisation is parallel to S3. The minor cross-veins are distinct but significantly all the vein trends have a common intercept. This suggests that all the mineralisaed structures may be fundamentally related, at least in their initiation.

Figure 5.32 - Distinctive alteration marginal to Kabanga mineralisation seen on Level 4 North. Characteristic striping caused by abundant buff carbonate laminae.

Figure 5.33a - Kabanga vein seen on Level 4 North. Vein shows some ribbon textures, but also clearly shows chaotic, brecciated textures at the base, with large incorporated wallrock fragments in the more central portions.

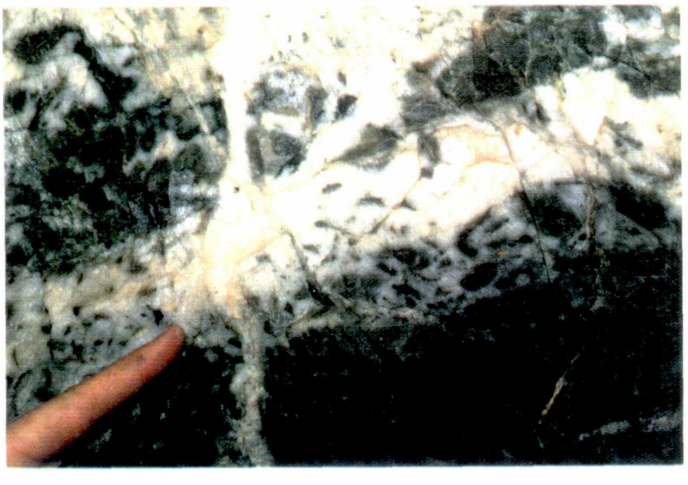
Figure 5.34 - Cross-vein seen on 4 Level North in the cross-cut to the Basil vein ("9" on Figure 5.18). Vein shows ribbon textures but is sulphide poor and barren of significant gold mineralisation. Cross-cutting quartz-tourmaline extension veins are seen cutting the ribbon vein.

Figure 5.33b - Close up of Kabanga vein on 4 Level. Chaotic wallrock fragments set in a quartz matrix are clearly visible.


STOPE
16/7/82







tourmaline is a common accessory within the ribbon septa which elsewhere at Patchway is only seen in the late, barren cross cutting D4 extension veinlets and as D3 an D4 boudinage neck infillings.

Relationship Between D2 and D3

The relationship is often seen where the S3 fabric is sometimes developed within the vein hosting shear zone without apparently cross-cutting into the undeformed margins of the D2 shear-zones, which perhaps indicates a linked initiation of the D2 and D3 type structures, with the S3 plane perhaps forming one of the Riedel set during D2 initiation. Further support is provided by the common intercept of the D2 veining, the S2 shear fabric and S3 on a stereonet (Figure 5.35). One geometric solution is that the main vein formed the "C" failure plane, S2 the shear fabric and S3 possible "P" shears to the early D2 event (Figure 5.36).

It is clear however, that a great deal of the deformation along the D3 structures post dates events on the D2 structures, as the main D2 gold mineralisation suffers thinning, truncation and even repetition. It is furthermore suggested that the association of gold bearing mineralisation and D3 is perhaps of minor significance compared to the D2 event. Such a hypothesis is perhaps supported by the general lack of ore grade gold-bearing mineralisation within D3 structures except where mineralisation is itself strongly seen to be also deformed by the D3 deformation event (as seen at Erin for example). Some of the D3 deformation was associated with similar vein-forming processes as D2, however. Veins such as the low-grade Kabanga and Munya-Skati mineralisation, together with the cross-veins show features common to both D2 and D3 type mineralisation (e.g. ribbon veins with tourmaline). Since the orientation of the D3 structure (approximately 070/60 N) is highly unfavourable for the reverse slip motion seen on the D2 plane, the main movement during D3 probably only occurred when the compressive stress field changed to allow dominantly strike-slip motion on the S3 plane.

There are thus two main trends of quartz veining where significant gold values are recorded. These two trends relate to the D2 and D3 deformation events respectively, with the D2 structures dominant as far as gold content. Figure 5.37 shows this graphically at Patchway, but the model extends to on at least a local regional scale (Patchway - Golden Valley - Hamburg - Erin) and a classification of two orebody types based on D2 and D3 shearing events can perhaps be suggested.

Good evidence for the later deformation on the D3 structures is provided from the literature. Bliss (1970) notes that the Rouge Shear, which has an identical trend to the Patchway Central Shear and the Erin structure, in fact truncates the late dolerite dyke intrusions. Although this cannot be seen at Patchway, a clearly more protracted period of deformation post dating mineralisation is recorded on the D3 structures.

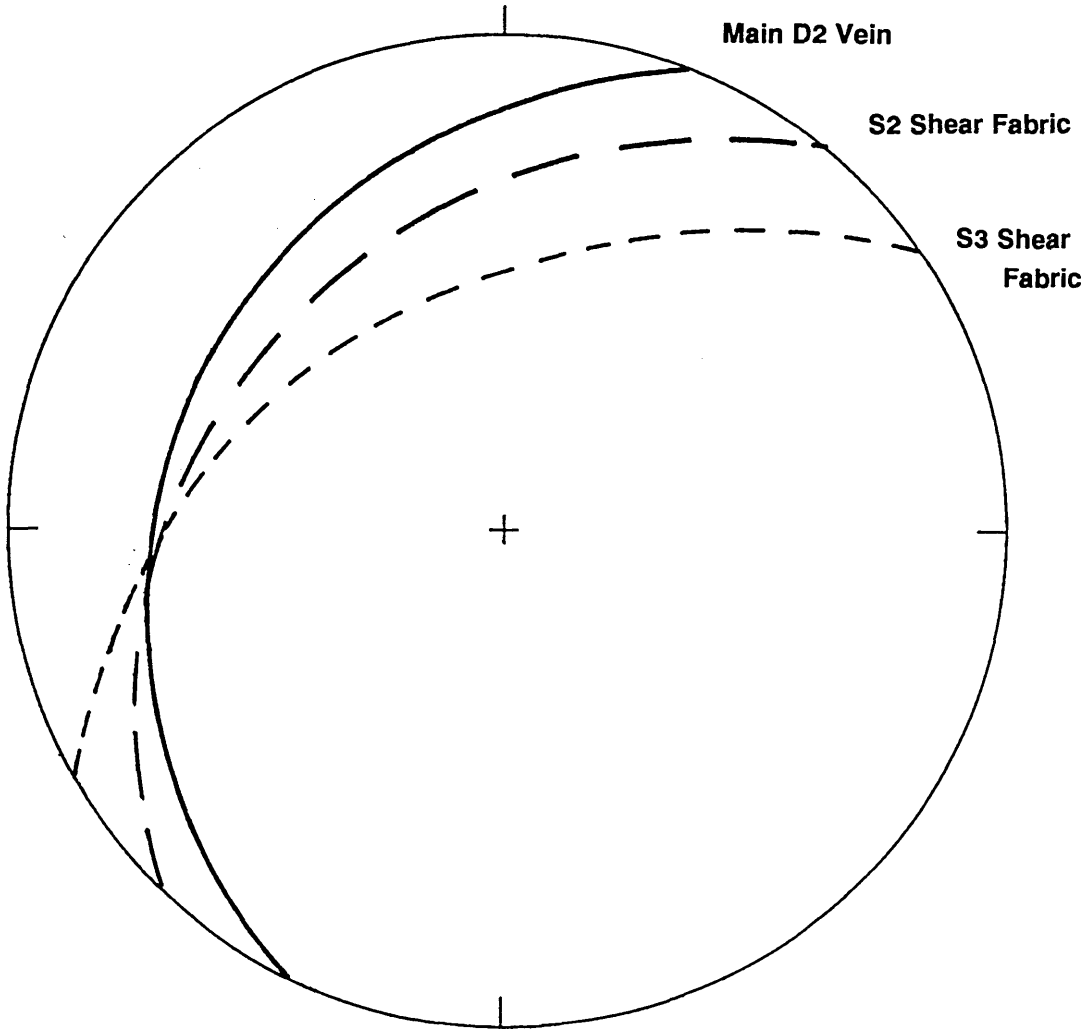


Figure 5.35 - Stereonet showing common intercept of D2 vein, S2 shear fabric and S3 shear fabric. This relationship suggests that all three planes may have initiated in the same deformation event.

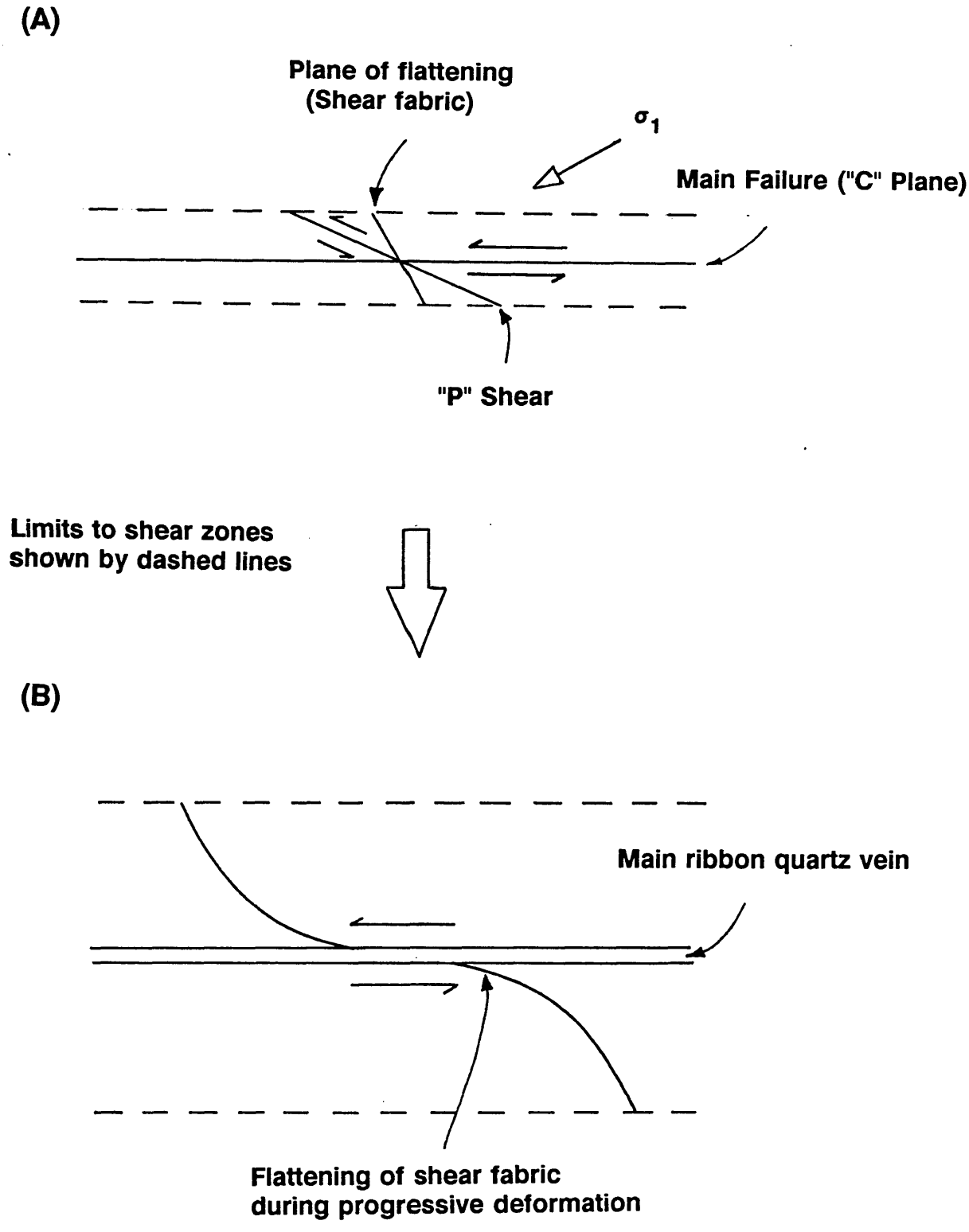


Figure 5.36 - Diagram showing possible initiation of D2 and D3 structures. (A) shows the initiation of D2, with development of the main failure plane (infilled by qtz-gold ribbon veining), early orientation of flattening (shear) fabric (S2) and "P" shears (later to become the S3 fabric). (B) shows evolution during continued D2 shearing as the zone of shearing broadens. The shear fabric becomes flattened into parallelism with, or low angle to, main failure plane. Early "P" shears initiated during (A) thus have a geometry at higher angle to the qtz-sulphide vein than the shear fabric due to the flattening of the latter. The early D2 "P" shears are later reactivated as strike-slip structures under D3.

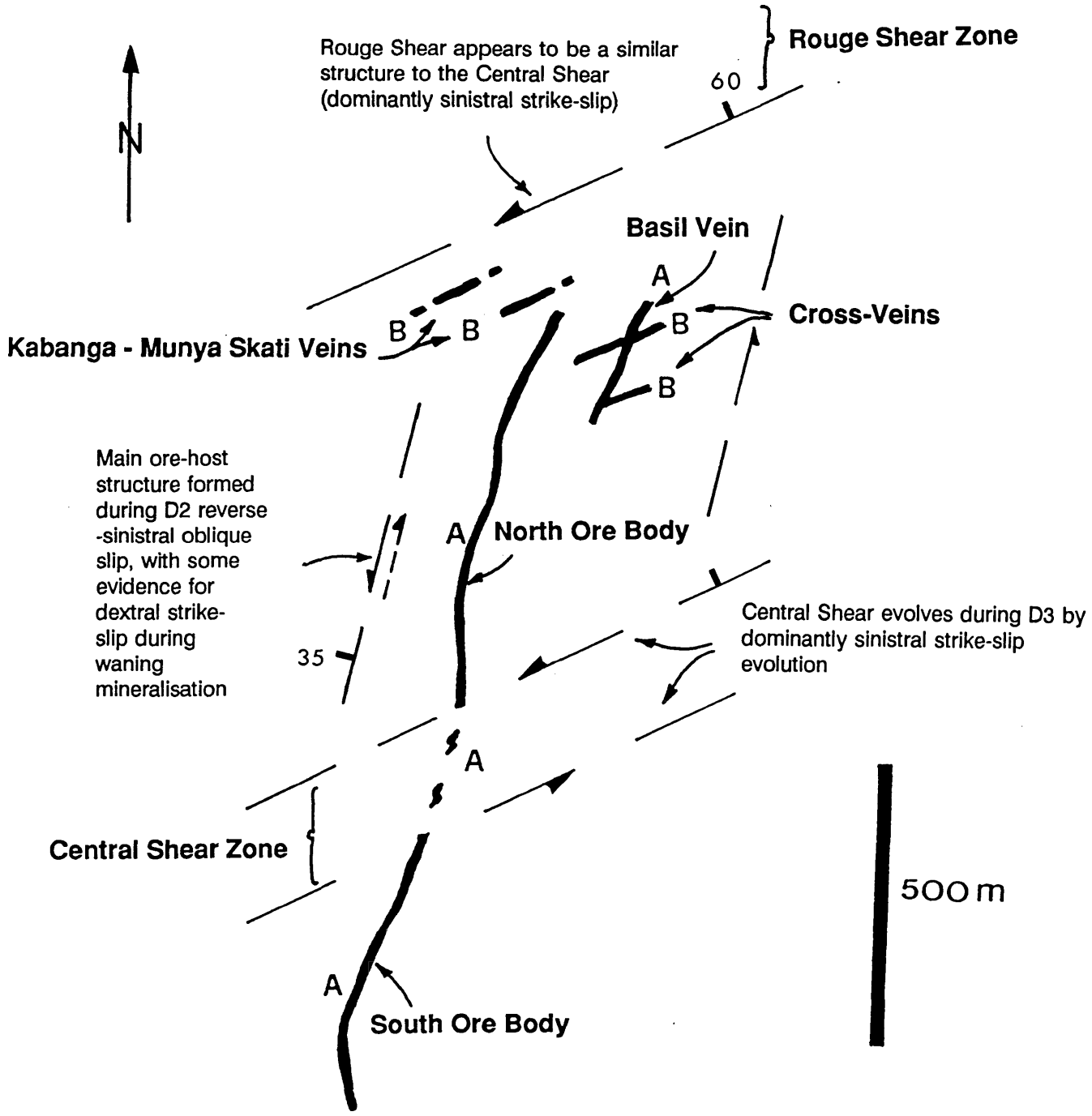


Figure 5.37 - Schematic representation of mineralised veins at Patchway showing their spatial relationships. The two main vein trends, "A" (≈020°) and "B" (≈070°) are clearly highlighted.

D4 Deformation

The latest major deformation event recorded at the Patchway mine is expressed as a major period of extension which was oriented in an almost east-west direction across the region. The deformation is largely manifest as a distinct event of normal dip-slip on the main vein, leading to another period of stretching and boudinage of mineralisation. Accompanying this normal faulting of the mineralisation is the intrusion of later dolerite dykes. This deformation event is responsible for the fault disruption and attenuation seen between the upper and lower sections of the mine at Patchway.

Mapping in the raise between 15 and 18 levels on the south orebody demonstrates the results of this deformation event very well (Figures 5.38 and 5.39) and each of the features can be seen. Asymmetric boudinage down-dip is common and the plot of the plunges of the crests of this boudinage data shows close coincidence with the intercept of the extension veins with the main vein, showing that this boudinage occurred during this early expression of stretching. The deformation later evolved to the more brittle normal faulting (Figure 5.40), and this seems to have been closely accompanied by the intrusion of the dolerite dykes. Stereonet projection of data shows the late faults, veining and dyke intrusions (Figure 5.41) which is again suggestive of a strong Riedel geometric control to the elements, supported by detailed mapping in other parts of the mine. Figure 5.42 shows a development face of 5 level, together with the possible Riedel analysis of the structures seen.

In summary, the main D4 failure planes are coincident with the most dilatant "R" and "T" planes of the Riedel geometry and, during the D4 event, were infilled with quartz and tourmaline, and in the case of some of the "T" planes, doleritic magma.

Late Regional Features

The veins hosted in the large tonalite bodies which have have produced scheelite during the second world war (Bliss 1970), at first appear unrelated to any of the events above. These veins probably post-date the D2 gold veins, since the Sesombi tonalite suite is seen to have a metamorphic aureole overprinting gold mineralisation in shear zones of ages presumed contemporaneous with D2 (Robertson 1976). Although not demonstrably related, the orientation of the veins (Figure 5.43) is consistent with them having formed in orientations favourable for extension with respect to the D3 deformation event. It is proposed that the veins formed late in the D3 deformation cycle, obviously after intrusion of the tonalite.

Finally late faults trending NW-SE are seen to cut all lithologies in the region (Bliss 1970). These faults are seen to host "barren" quartz mineralisation when striking 150 to 160° in the Patchway area (Figure 3.1). One such vein was sampled at Lion Hill and it is believed to represent very late deformation as the faults would appear to cross-cut all regional geological features.

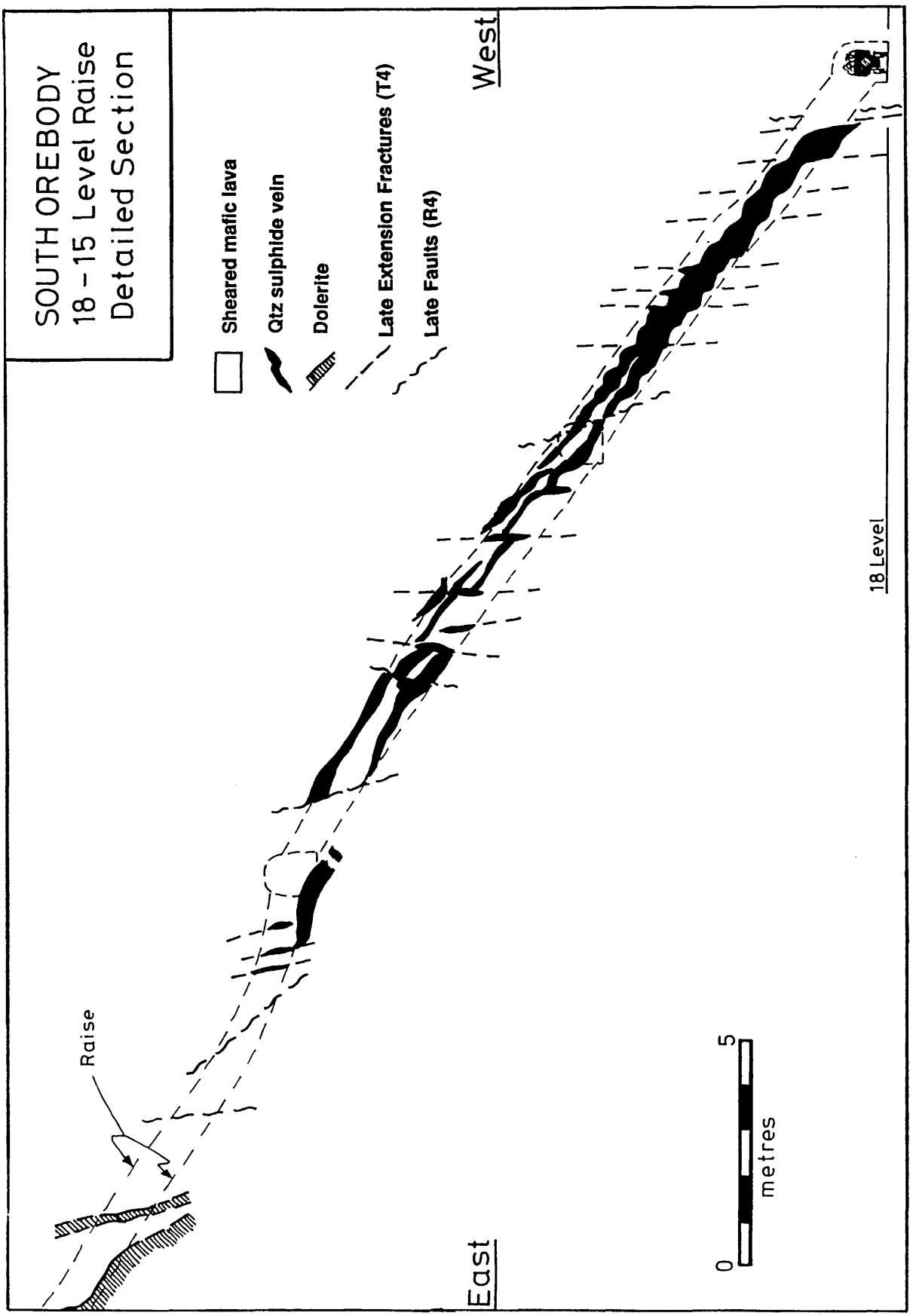


Figure 5.38 - Section through 18 Level to 15 Level Raise, South Orebody (B to B' on Figure 5.18). Section shows effects of late D4 deformation on the D2 ribbon vein orebody.



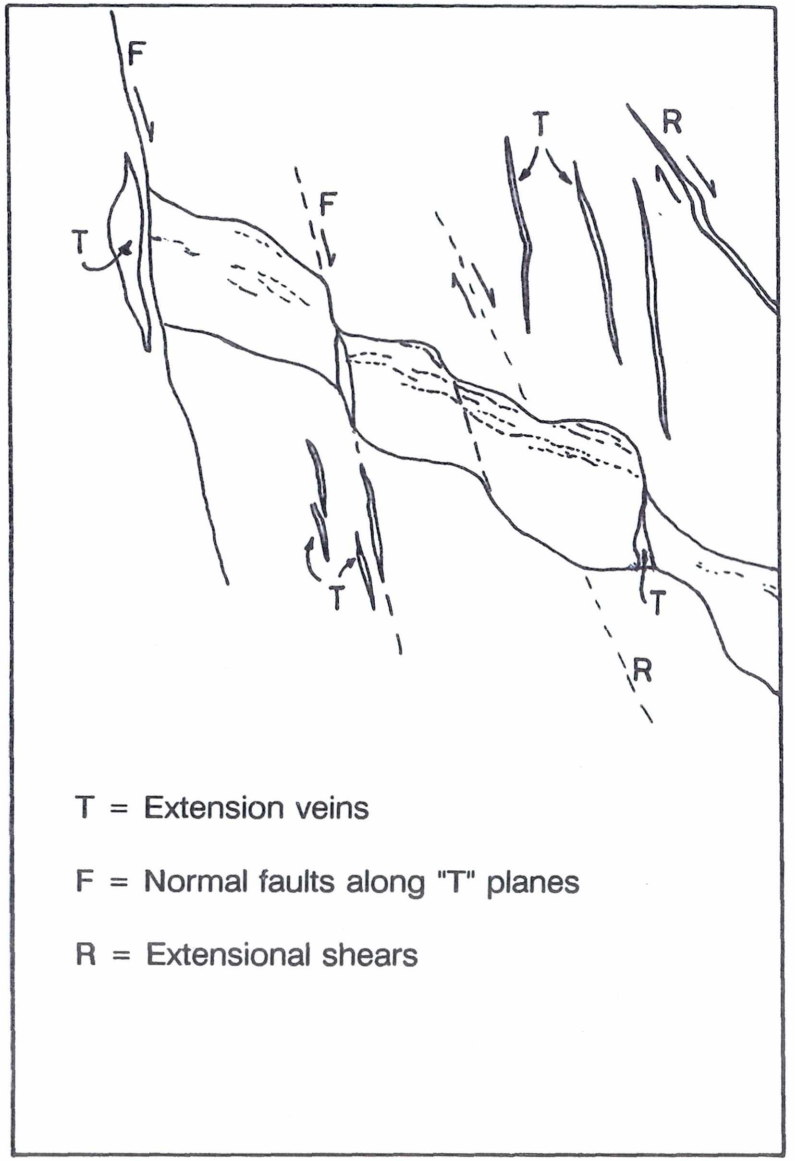


Figure 5.39 - Ribbon veining exposed in 18 Level to 15 Level Raise. Photograph shows asymmetric boudinage, normal faulting and extension veining related to D4. Annoted sketch on the right identifies the observed structures.

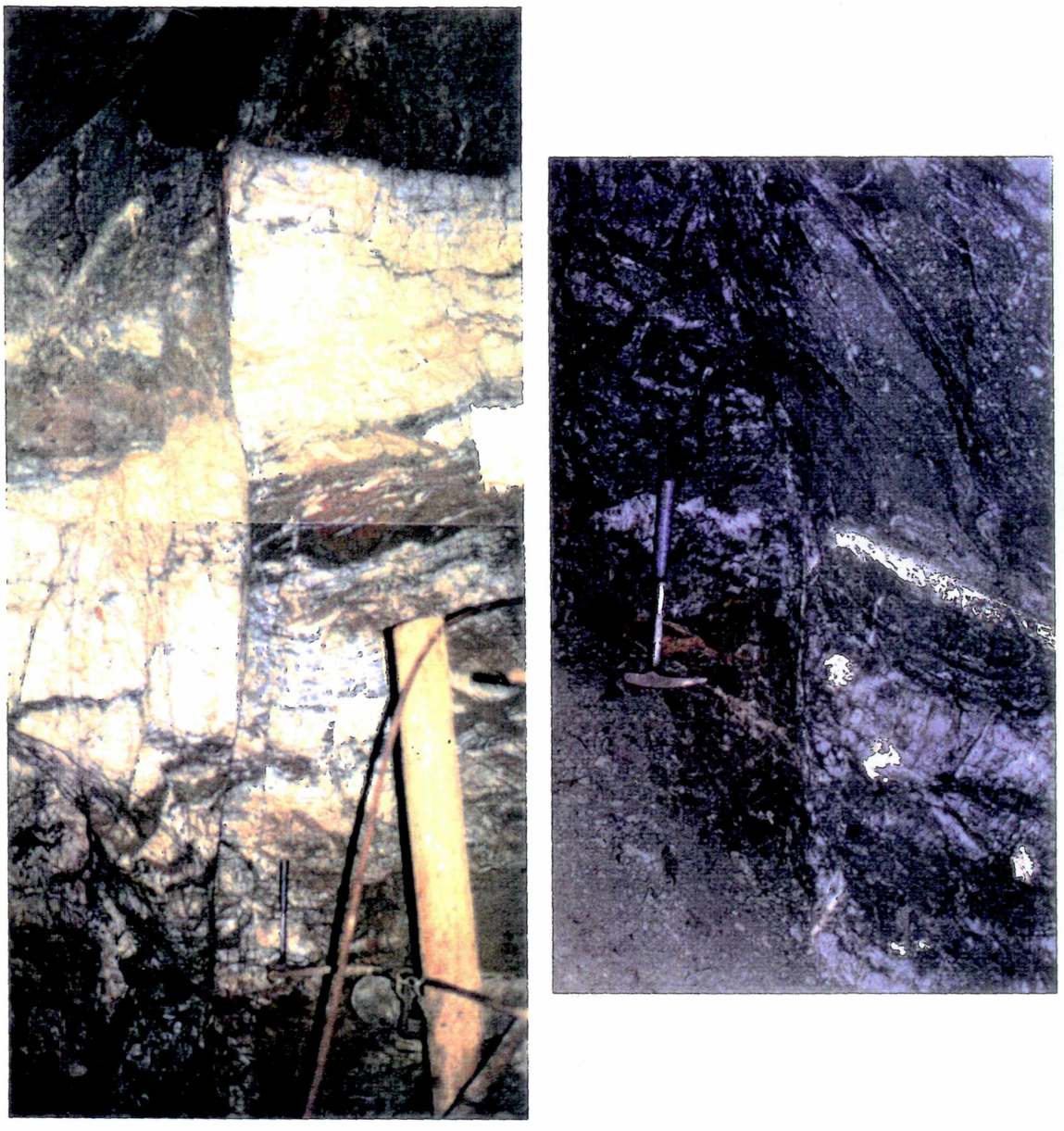


Figure 5.40 - Late normal faulting of mineralisation. Photograph on the left is at Golden Valley mine, 26 Level Raise, looking north; photograph on right is at Patchway 10 Level North looking south. Both faults trend 160°, roughly sub-vertical.

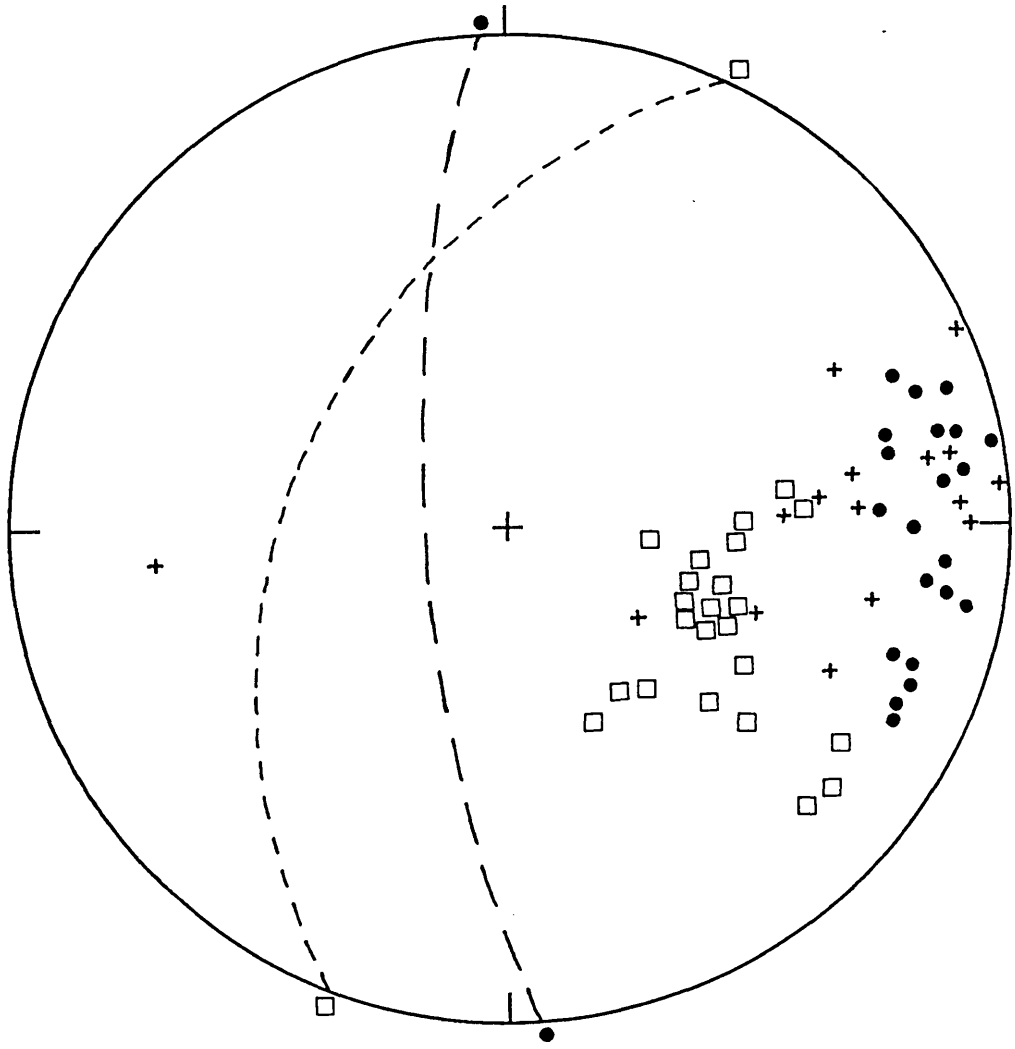
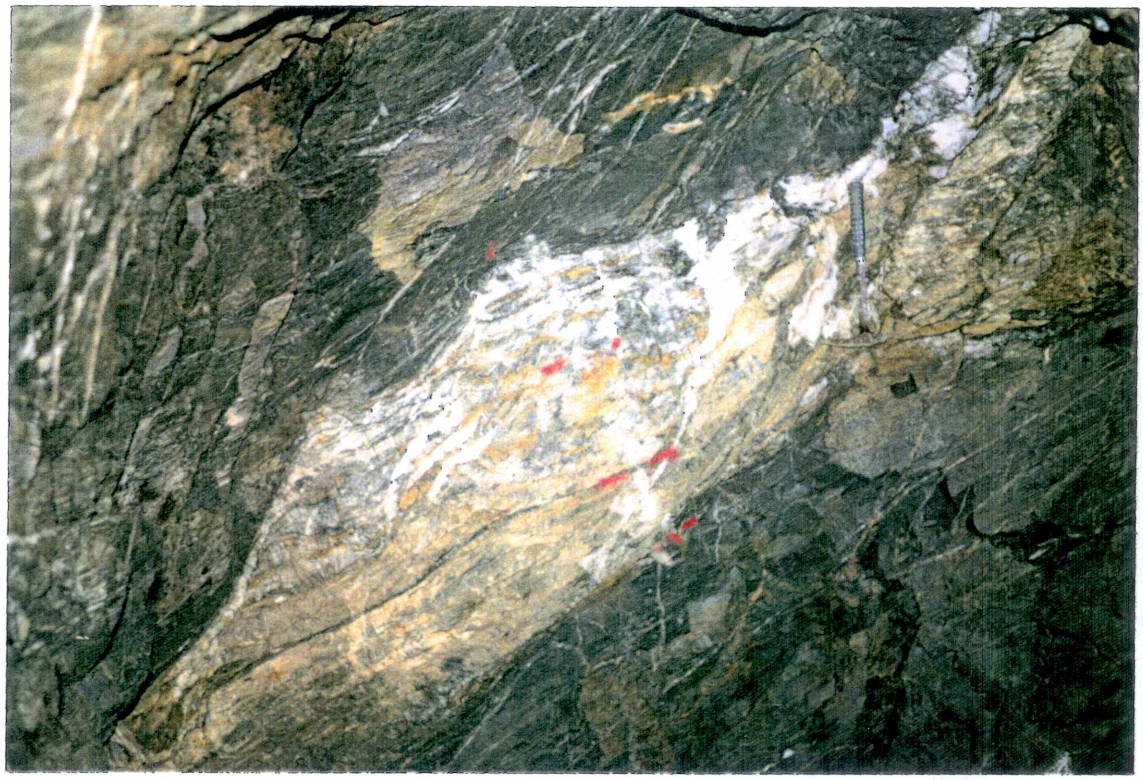


Figure 5.41 - Stereonet plot of poles to late faults, dolerite dykes and extension fractures related to D4. Average great circles for the late faults and extension fractures are shown. The intercept of these two trends is not coincident with the D2 and D3 features.



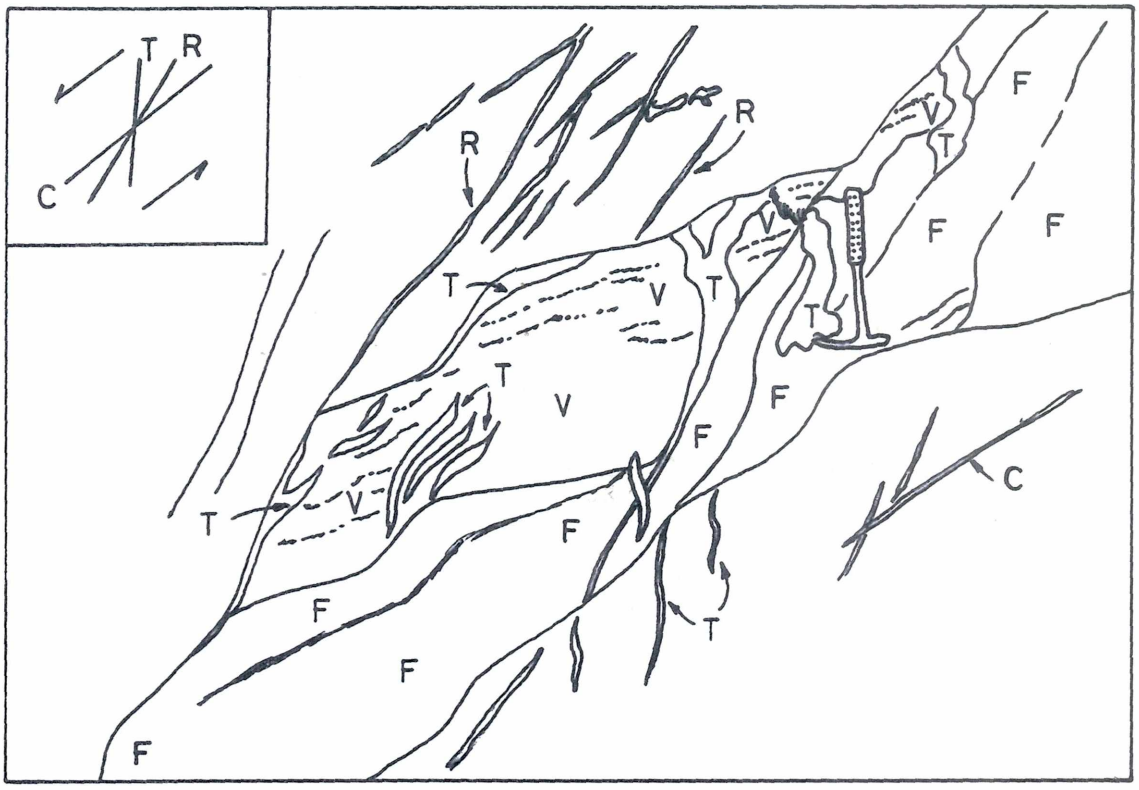


Figure 5.42 - Development face on 5 Level North ("7" on Figure 5.18), looking north. Annotated sketch below shows D4 features with inset Riedel analysis of major structural elements (see Figure 4.8). F = Felsite and V = Ribbon Quartz-Sulphide Vein (D2). Wallrock host is deformed mafic lava.

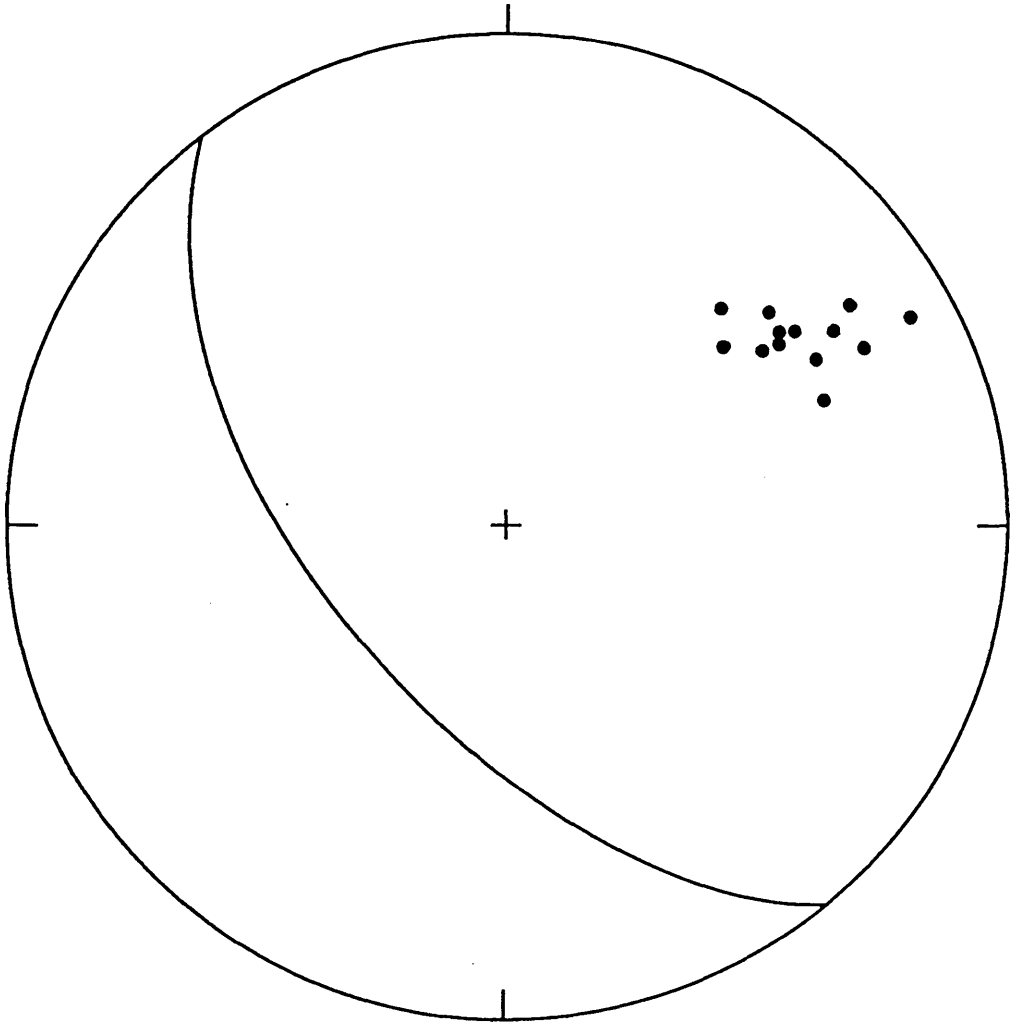


Figure 5.43 - Stereonet plot of poles to tonalite hosted quartz-scheelite veins at Lion Hill (see Figure 2.5). Great circle plotted for mean of data (140/60W).

On a deposit scale, these deformation events can be summarised graphically as shown on Figure 5.44. This three phase deformation model (phase 1 and phase 2 can be considered as the same event) can now be integrated into the regional framework.

5.5 Deformation Model for the Kadoma Region with Reference to Regional Events

The regional deformation events are summarised in Table 5.1 with an attempt to link them to the deposit scale structural model. The table also shows an outline of the observed mineral assemblages ascribed to each of the deformation events. These constrained vein assemblages form the basis for the mineralogical study in Chapter 6 and the detailed fluid study outlined in Chapter 7. The deformation model is shown graphically on Figure 5.45.

The first major event observed in the Kadoma region is the regional folding described by Bliss (1970), responsible for the Kadoma anticline and related structures. These structures resulted from shortening across the greenstone belt by NE-SW directed compression. Culmination of this event can probably be linked with initiation of the major terrain boundary structures, the Lily Fault and the Rhodesdale Shear Zone (see "1" on Figure 2.4). Stowe (1980) proposes that the latter at least initiated as a thrust fault, supporting this idea. This event, is shown graphically as Event 1 on Figure 5.45, also may have coincided with initiation of the Golden Valley, Patchway and other sub-parallel 020° structures. Field evidence suggests that mineralised structures paralleling or at low angle to the Lily fault are steeper the closer they are to the main Lily Fault (Bliss 1970). The Dalny shear (Carter & Foster 1990) would also have initiated during this event, although it too has a steeper dip of 70°. Figure 5.46 shows the proposed relationships between the early motion on the Lily Fault and the mineralised shears of Patchway, Golden Valley and Dalny. The gravity profile (Figure 5.3) allows the suggestion that the Golden Valley and Patchway main vein structures could merge as a thrust duplex at depth overlying basement rocks. Naylor *et al.* (1986) suggest that in conditions where oblique slip (strike-slip plus dip-slip) motion on steeply dipping basement faults (such as the Lily Fault), complex, convex-upward, "flower"-type fault splays may result. Many similar systems are described in the literature, notably in "transpressive" (Sanderson & Marchini 1984) terrains such as California (Wilcox *et al.* 1973, Sylvester & Smith 1976). If this were the case, such structures would be anticipated to show a steepening toward the main structure as shown in Figure 5.46. Such a phenomenon is confirmed by the field observation, where veins steepen with increasing proximity to the Lily Fault (Bliss 1970). The Lily Fault would now appear to form a sub-vertical to steeply dipping structure (Bliss 1970). Regionally Event 1 can be linked to the proposed model of NW to SE directed compression discussed in Chapter 2 and a component of strike-slip together with reverse sense movement would be likely on the major structures in the region.

The main part of the D2 deformation at Patchway is shown to be dominantly reverse plus a component of sinistral strike-slip (see 1 and 2 on Figure 5.44). Such a movement sense suggests continued

1 - Initiation of main 020° and 070° structures under roughly N-S compression. (1) is the main D2 ribbon vein trend, (2) is the Basil vein and (3) is the Rouge-Erin-Central Shear trend. The intercept of (1) and (3) is shown as the dashed line which is perpendicular to the maximum principal stress, assuming contemporaneous initiation.

2 - Continued reverse oblique-slip on 020° structures during D2 results in the main period of gold mineralisation. Limited kinematic indicators show a likely slip vector towards 175° for the hanging wall. Slip on the 020° structures was cyclic allowing development of ribbon veining. Unfavourable orientation of the 070° structures meant that these are poorly mineralised during this main gold-bearing mineralisation event.

3 - Maximum principal stress field apparently reorientates to NNE-SSW during the bulk of D3 deformation. Deformation changes to dominantly dextral strike-slip on 070° structures, particularly the Central shear zone (4) and the Rouge shear (7). The main ribbon vein is deformed and boudinaged in places (5) and even fault offset (6). Waning fluid flow results in the Munya-Skati and Kabanga veins (7) as well as the Cross veins (8). The footwall extension veining to the 020° ribbon vein may have formed at this time during minor dextral slip on the 020° structure.

4 - Broadly E-W extension across the deposit results in the normal faulting (9) and dolerite intrusion (10) during D4. Maximum principal stress is again probably N-S.

Figure 5.44 - Summary of deformation events at Patchway with respect to mineralisation events. Interpreted applied stress field shown as large black arrows.

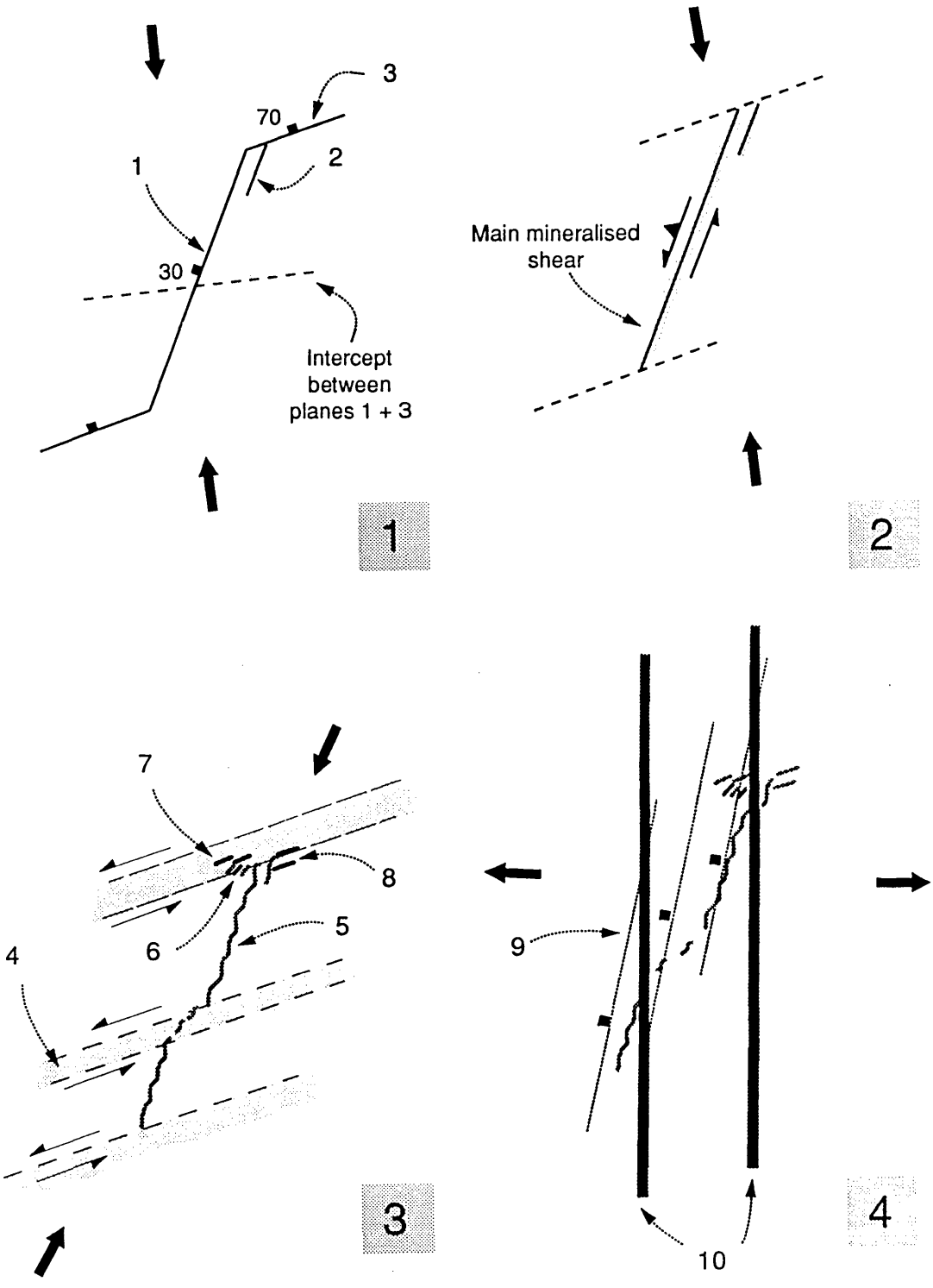

3
70
1
2
30
Intercept
between
planes 1 + 3
1
Main mineralised
shear
2
7
8
6
5
4
3
9
10
4

Table 5.1 - Summary of regional deformation events and mineralisation in the Patchway region.

DEFORMATION EVENT				MINERALISATION	
STAGE	REGIONAL SCALE	**STAGE**	DEPOSIT SCALE	**STAGE**	ASSEMBLAGE
Early 1	Early NNW-SSE compression, major folds, initiation of main faults	**Early D1**	Diagenesis-Metamorphism in greenstone sequence, large scale folding.	**Q1**	Pillow infilling quartz-epidote
2	Continued NNW-SSE compression, reverse plus strike-slip motion on first-order structures modified by expulsion of Rhodesdale block westwards	**D2**	Reverse (+strike-slip) faulting on first and second-order structures. Gold-quartz mineralisation in 020° ribbon quartz veins (also 045° structures - Dalny).	**Q2**	Quartz-sulphide-gold veins
3	Intrusion of tonalite diapirs, during strike-slip motion on structures in greenstone belts under NE-SW? stress	**D3**	Strike-slip motion on 070° structures, attenuation of D2 gold-bearing veins. Some gold-quartz veining.	**Q3**	Later quartz-sulphide-tourmaline(±gold) veins
4	Compression N-S with stress direction leading to Great Dyke intrusion, same regime culminating in dolerite dyke emplacement	**D4**	East-west extension, N-S normal faults, extension veins and lastly dolerite dykes.	**Q4**	Quartz-tourmaline extension veins, remobilised sulphides
		Late D3	Brittle fractures in tonalite diapirs.	**Q5**	Quartz-scheelite veins
		Post D4	Late brittle fractures, dominantly 150 to 160°	**Q6**	"Barren" quartz veins

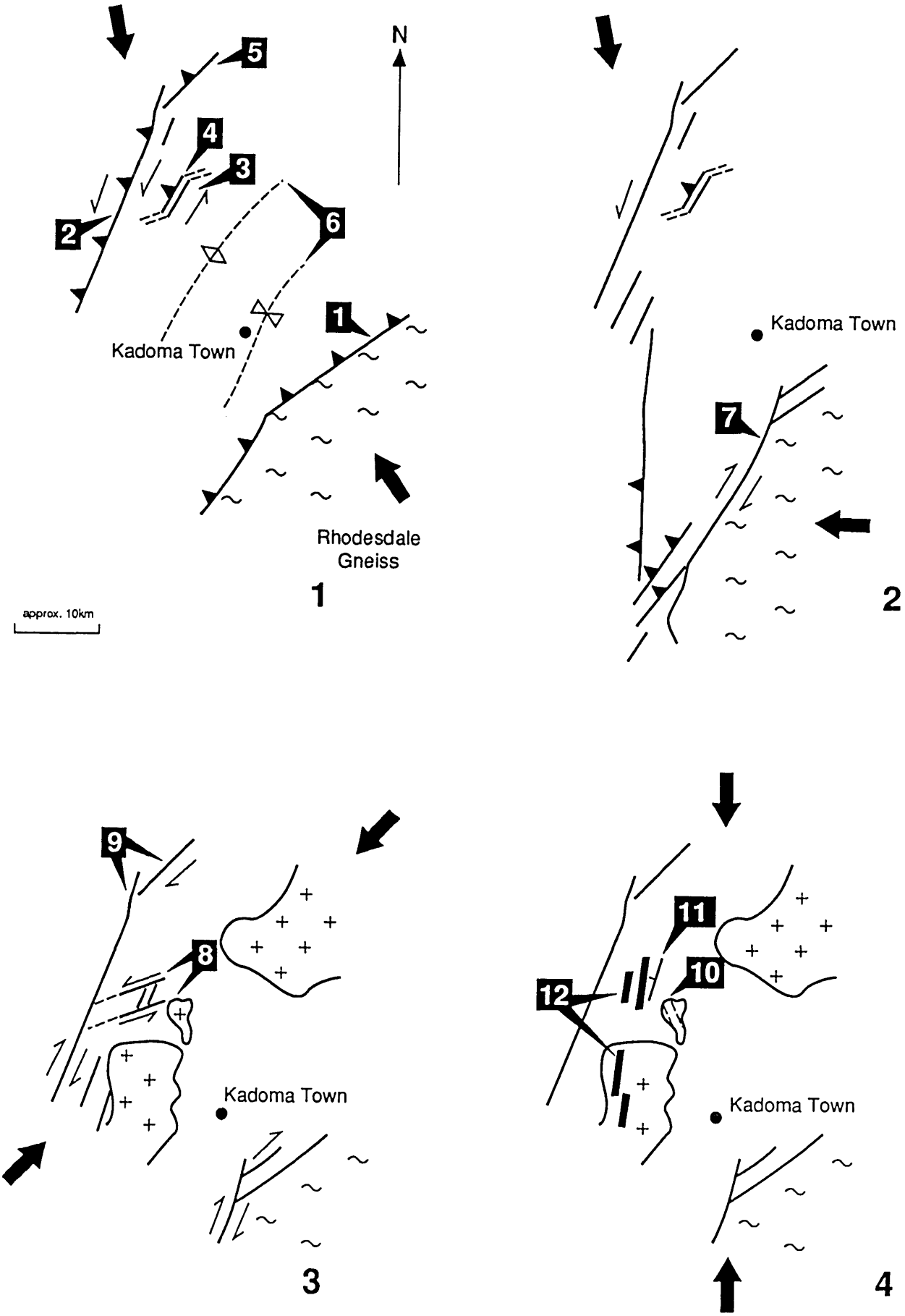
1 - Initiation of major structures (1 to 5) at culmination of early folding (6) during roughly N-S compression. This coincides with the beginning of Limpopo deformation due to movement of Kaapvaal craton northwards (Coward 1980). Features are: 1 - Rhodesdale boundary shear, 2 - Lily fault, 3 - Patchway structure, 4 - Golden Valley structure, 5 - Dalny shear, 6 - Main fold axes.

2 - Continued reverse oblique-slip on Patchway and Golden Valley structures during mineralisation. Evolution of major structures to strike-slip motion, particularly the Rhodesdale boundary shear system (7), in response to lateral expulsion of Rhodesdale Gneiss block.

3 - Reorientation of stress field to NNE-SSW in response to motion of Rhodesdale block, focus of deformation onto cross-structures at Patchway and Golden Valley (8) synchronous with major strike-slip motion on the Lily fault system (9). Large tonalite diapirs intrude roughly parallel to stress field.

4 - Stress field oriented roughly N-S during intrusion of 2.5 Ba Great Dyke continues for intrusion of late, Proterozoic (Wilson *et al.* 1987) dykes in Kadoma region (12). Late normal faulting accompanies this at Patchway (11). Stress field compatible for formation of brittle veins in the small Lion Hill tonalite diapir (10).

Figure 5.45 - Provisional timetable of deformation events in the Kadoma region with respect to deposit scale deformation events. Interpreted regional applied stress field shown as large black arrows.


N
5
4
3
2
6
1
Kadoma Town
Rhodesdale
Gneiss
1
approx. 10km
Kadoma Town
7
2
9
8
Kadoma Town
3
11
10
12
Kadoma Town
4

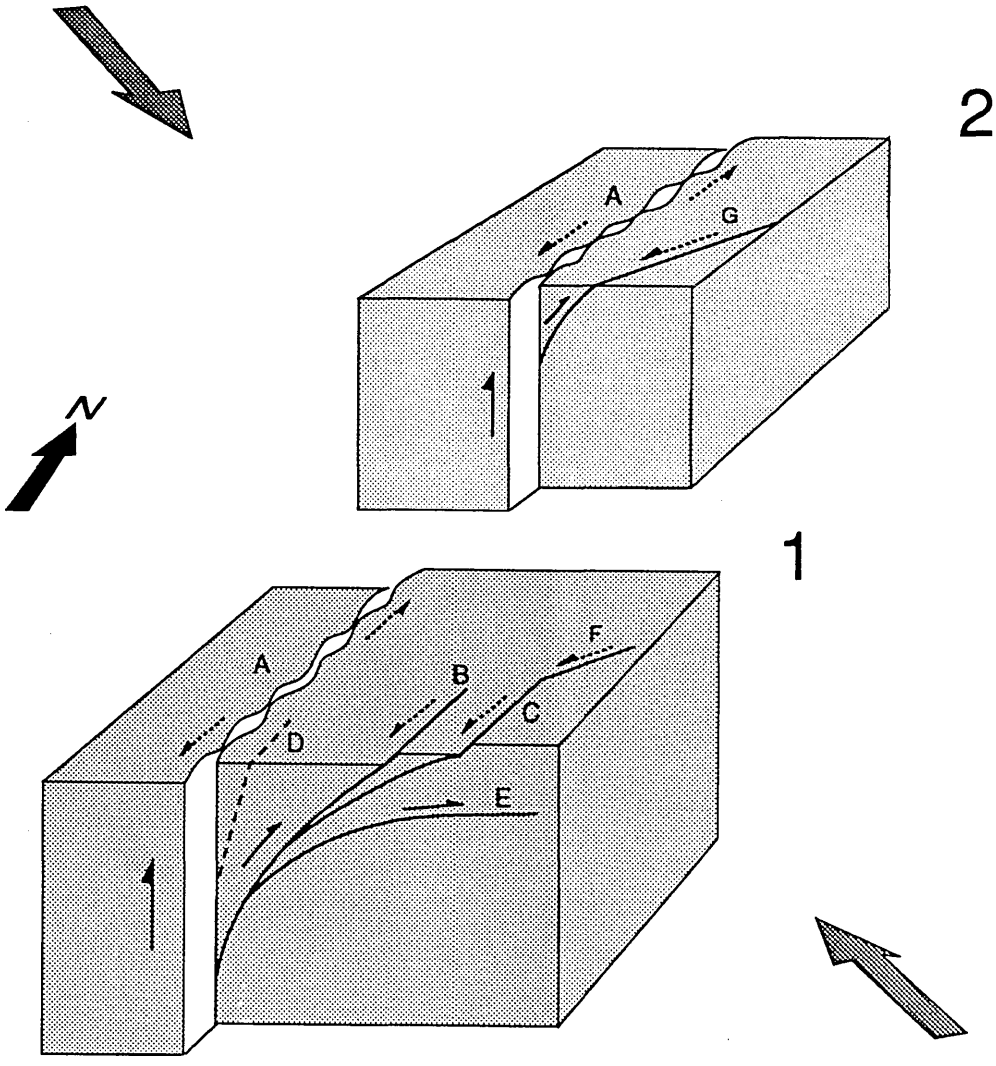


Figure 5.46 - Block diagram model (not to scale) for initiation and evolution of the gold-bearing structures in the Patchway region under NW-SE compression (signified by large grey arrows). Main Lily fault "A" forms the major regional, first-order, structure from which the "B", Golden Valley shear, "C" Patchway shear and "G" Dalny shear form second-order splays. Structure "E", is a schematic representation of the style of possible low-angle thrust faulting (see Figures 5.3 and 5.4 for possible evidence). "D" represents the veins seen close to the Lily fault (Figure 2.5) and "F" represents the Rouge (or Erin) - type shear zones. The structures evolved under "transpression" (Harland 1971) in response to NNW-SSE regional compression (arrows). In such a stress regime convex-up, "flower-fault" splays are expected (Naylor *et al.* 1986). The splays in such a system would be expected to show similar movement sense to the main structure (Ramsay & Huber 1987).

compression, probably from the north-west (Event 2 Figure 5.45). Carter & Foster (1990) concludes a similar slip vector for the Dalny structure during the bulk of the deformation during mineralisation. Pitfield & Campbell (1989) note stretching lineations on the Rhodesdale boundary shear-zone pitching to the NE, again consistent with the movement sense on the Lily Fault associated structures. These authors further suggest mineralisation in the Battlefields area may be related to this early thrust plus strike-slip faulting. Nutt *et al.* (1988) report on deposits in the KweKwe region farther south where high angle reverse faulting accompanies mineralisation. Since the mineralisation is likely to be of similar age to that in the Kadoma region, it supports the proposed lateral secretion of the Rhodesdale block westwards at this time (see lower arrow, Event 2 on Figure 2.4). If this event occurred at the same time as the generally applied NE-SW compression, as seems likely, then rather complex displacement relationships might be expected.

The felsite intrusive bodies seen close to mineralisation underground show variable age relationships to the deformation events. Almost invaribly the intrusives have been intruded sub-parallel to the main D2 deformation. In some cases the intrusives occur within the mineralised D2 structures and in this case the bodies have often suffered the same deformation and alteration. Some of the intrusives actually show syntectonic relationships, whilst others clearly cross-cut at least the D2 structures. The balance of data suggests at least a broad temporal relationship between the felsite intrusives and the deformation.

Deformation then appears to have evolved in response to an apparent reorientation of principal stress to an ENE to WSW direction, possibly as a result of the expulsion of the Rhodesdale Block westwards (see 2 on Figure 2.4). Deformation on a mine scale evolved to principally sinistral strike-slip shearing focussed on the the 070° D3 structures (see "3" on Figure 5.44). The stereonet plot of the combined D2 and D3 structures shown in Figure 5.35 suggested that both structures may have initiated under the same stress field and it is possible that the D3 structures (proposed to have initiated as "P" shears to the D2 event) accomodated most of the strain after the change in applied stress field shift (Event 3 on Figure 5.45). The Lily Fault itself would be subject to different applied stress on either side of the structure and it might behave as a dextral strike-slip fault at this time simply because the block to the southeast is being forced east. The D2 structures do show evidence of some post ribbon-veining dextral strike-slip motion (Figure 5.12 and 5.13) and this may have occurred at this time. Bliss (1970) records up to 40 Km of dextral displacement on the Lily fault and very strong displacement of the Shamvian sediments is also indicated in the Battlefields area on the Munyati-Rhodesdale Boundary Shear (Pitfield & Campbell 1989), also with a dextral sense. The change in focus of deformation onto the D3 structures was accompanied by the waning mineralisation events of Kabanga, Erin, Rouge and associated veins, coupled with deformation of existing D2 mineralisation.

Event 3 was probably accompanied by the intrusion of the larger tonalite bodies such as the Whitewaters stock (and regionally the Sesombi tonalite suite). Orientation of the stress field in the Kadoma region

into an ENE-WSW direction would be conducive to intrusion of these bodies parallel to the local $\sigma 1$ at this time. The strong geochemical affinity of these tonalite diapirs and the mine felsite intrusives is quite clear, and the intrusion of the diapirs would be a logical result of the large body of magma rising higher into the upper crust. These tonalites show that they have also suffered some deformation, particularly in the marginal zones, which is strong evidence for a syntectonic intrusion event. At the end of this event the tonalite hosted scheelite-bearing veins probably formed.

Any regional model must take account of the similar, but easterly dipping structures are seen to the east of Lion Hill (Figure 2.5) which are host to small gold deposits (Bliss 1970). Annhausser (1976) shows how these deposits are distributed in arcuate fashion around the tonalite intrusives and thus alludes to a genetic relationship between the veins and the tonalites. However, initiation of the host structures to these deposits can be explained if these initiated as the conjugate thrusts to the Patchway-Golden Valley veins (see Figure 5.4) and later structural modification by the forceful emplacement of the Whitewaters tonalite could explain the observed arcuate distribution.

The latest major deformation event, Event 4 on Figure 5.45, is the late extension seen on a deposit and regional scale. The late normal faulting at the mine with barren quartz-tourmaline extension veins is followed by intrusion of dolerite dykes (4 on Figure 5.44). A relationship between this event and the orientation of the circa 2500 Ma Great Dyke intrusion (see 3 on Figure 2.4) an interesting possibility. As indicated during Event 4 on Figure 2.4 , the same stress regime could lead to brittle extension fracturing oriented parallel to maximum principal stress. This late event might be linked to reactivation of structures parallel to the Great Dyke coupled with late dyke intrusion.

Very late brittle faulting is probably a result of relaxation of the stress field in the region, resulting in the barren quartz veins seen close to Lion Hill (Figure 2.5).

CHAPTER SIX - MINERALISATION

6.1 Introduction

This chapter outlines the mineralogy of the gold bearing stage of the paragenesis at Patchway, the D2 deformation-mineralisation event and presents the mineral chemistry of the principal phases. Mineralisation is essentially confined to veins and peripheral narrow alteration zones, with quartz dominant in the gangue mineral assemblage in association with chlorite, sericite and scheelite. Later quartz veining contains abundant tourmaline, which distinguishes it from the earlier gold-bearing phases. Gold is intimately associated with a distinct sulphide assemblage dominated by pyrite together with minor arsenopyrite, pyrrhotite, sphalerite and galena.

Examination of the mineralised assemblages was made using standard optical microscopy techniques in association with SEM and EPMA. Operating conditions for the latter, which included study by both energy dispersive (EDS) and wavelength dispersive (WDS) analysis methods, is outlined in Appendix II.

6.2 Mineralisation predating gold bearing veins

Veining which pre-dates the main gold-bearing ribbon veins is essentially confined to irregular segregation of quartz-epidote-carbonate seen developed marginal to pillows in the undeformed mafic flow rocks (Figure 3.2). No gold or sulphides were seen in this veining, but some coarse chlorite aggregates occur within the quartz.

6.3 Gold-bearing (D2) mineralisation

Mineralisation associated with the D2 ribbon-quartz veins show some distinct differences to the other stages of mineralisation, apart from the obvious absence of gold. A distinct sulphide assemblage dominated by pyrite is demonstrably associated with the gold. In addition an important gangue mineralogy includes scheelite, common in both the Patchway and Golden Valley deposits, fine grained sericite and chemically distinct chlorite.

6.3.1 Gangue mineralogy

Scheelite

Scheelite occurs within the ribbon quartz veins, often directly associated with the white "barren" central portions of the veins as well as intergrown with sulphide grains in phyllosilicate septa. It appears to form idiomorphic grains, generally less than 1mm across, although coarse aggregates are recorded, particularly

at Golden Valley (Figure 6.1). Idiomorphic grains are often disseminated along carbonate, pyrite bearing fractures (Figure 6.2). Texturally, it is clear that much of the scheelite is related to the main quartz precipitation. The scheelite, which is translucent in thin section, is also seen to contain fluid inclusions of identical composition to those in the co-existing quartz grains (see Chapter 7). The chemistry of the scheelite (Table 6.1) indicates very little substitution by Mo.

Muscovite

White mica is ubiquitous in the phyllosilicate septa and wallrock inclusions. It is intergrown with chlorite, sometimes as alternating layers (Figure 6.3). Probe analysis shows composition of the mica co-existing with both pyrite-gold and scheelite is fairly similar (Table 6.2), also very similar to the muscovite associated with the alteration (i.e. close to end member K-muscovite).

Chlorite

Chlorite, like sericite, is associated with the septa and wallrock bands where the sulphides and gold are concentrated. The chlorite in the vein itself is fine grained, generally less than 100 microns in length, often intergrown with white mica and carbonate. Chlorite also forms in pressure shadows to the pyrite grains as well as solid inclusions. In one case gold is seen totally enclosed within a chlorite grain.

The chlorite, which occurred within the main D2 vein assemblage, showed a clearly different chemistry to the bulk of the wallrock chlorite. Table 6.2 outlines data from both gold-intimate chlorite grains and chlorite grains associated with scheelite grains in the main ribbon vein. Comparative analyses of grains in deformed wallrock and undeformed lava are shown in Table 3.1.

6.3.2 Gold and sulphide mineralogy

The vein sulphide mineralogy is dominated by pyrite which forms well over 90% of the sulphide minerals. Other sulphides in order of decreasing abundance are pyrrhotite, chalcopyrite, galena, arsenopyrite, sphalerite. Tiny included grains of probably stibnite and tetrahedrite were identified from qualitative probe analyses, although small size precludes accurate identification.

Gold is apparently present mainly in the native state as separate grains. The current study suggests that gold grains actually occur in three distinct associations in the main D2 gold-bearing veins. Gold is seen as a) Tiny grains encapsulated in complex pyrite grains, b) Infillings along cracks in earlier formed pyrite grains and c) Discrete grains adjacent to, or isolated from, sulphide grains, sometimes encapsulated in quartz grains. These three associations are illustrated in Figure 6.4. EPMA analyses of gold in all associations demonstrates it to be electrum, with up to 20 wt% Ag (Table 6.3).



Figure 6.1 - Ribbon-quartz vein at Golden Valley mine. Bright pink aggregates are coarse scheelite, clearly visible above hammer handle.

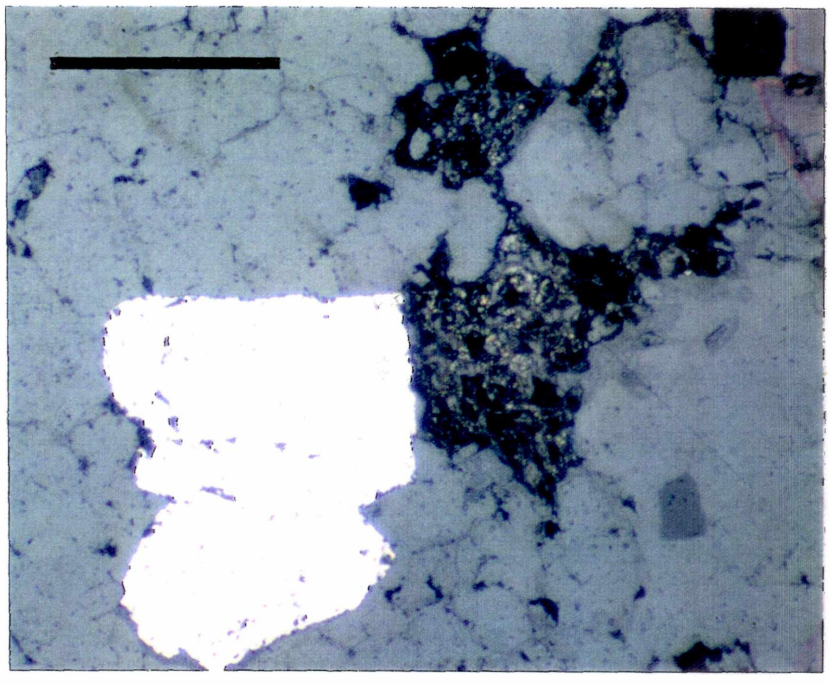


Figure 6.2 - Reflected light photomicrograph of scheelite with pyrite in ribbon-quartz veining at Patchway (Sample 20-12). Scale bar = 0.5 mm

Sample	20-12 (n=6)
CaO	19.87
WO_3	79.46
MgO	0.12
MO_3	0.37
Total	99.82

Table 6.1 -
EPMA analyses of scheelite. Sample 20-12 grains are in ribbon quartz, associated with pyrite grains (see Figure 6.2).

Sample	10-25 (n=10) (A)	20-14 (n=8) (B)
wt% oxide		
SiO_2	24.49	24.21
TiO_2	0.01	0.01
Al_2O_3	21.26	23.53
Fe_2O_3	0.00	0.00
FeO	35.81	25.79
MnO	0.31	0.27
MgO	7.57	13.87
CaO	0.08	0.00
Na_2O	0.21	0.17
K_2O	1.48	0.04
H_2O	10.83	12.04
Total	102.04	99.90
no. of atoms		
Si(IV)	2.65	2.55
Al(IV)	1.35	1.48
Al(VI)	1.36	1.48
Ti	0.00	0.00
Fe^{3+}	0.00	0.00
Fe^{2+}	3.25	2.27
Mn^{2+}	0.03	0.02
Mg	1.21	2.18
Ca	0.00	0.01
Na	0.04	0.03
K	0.20	0.00
O	10.00	10.00
OH	8.00	8.00

Sample	10-25 (n=5) (A)	20-12 (n=5) (B)
wt% oxide		
SiO_2	46.26	47.61
TiO_2	0.39	0.37
Al_2O_3	32.33	33.90
Fe_2O_3	0.00	0.00
FeO	2.51	1.81
MnO	0.00	0.00
MgO	0.89	1.19
CaO	1.52	0.18
Na_2O	0.31	0.34
K_2O	10.56	11.14
H_2O	4.48	4.49
Total	98.51	101.03
no. of atoms		
Si(IV)	6.31	6.29
Al(IV)	1.69	1.72
Al(VI)	3.51	3.57
Ti	0.04	0.03
Fe^{3+}	0.00	0.00
Fe^{2+}	0.29	0.20
Mg	0.18	0.24
Ca	0.08	0.02
Na	0.08	0.09
K	1.84	1.89
O	20.00	20.00
OH	4.00	4.00

Table 6.2 - EPMA analyses of chlorite and sericite grains associated with gold and sulphides in ribbon-quartz veins. Table left for chlorite, table right for sericite. 10-25 grains are intimate with gold grains, 20-12 and 20-14 grains are intimate with stylolite sulphides.

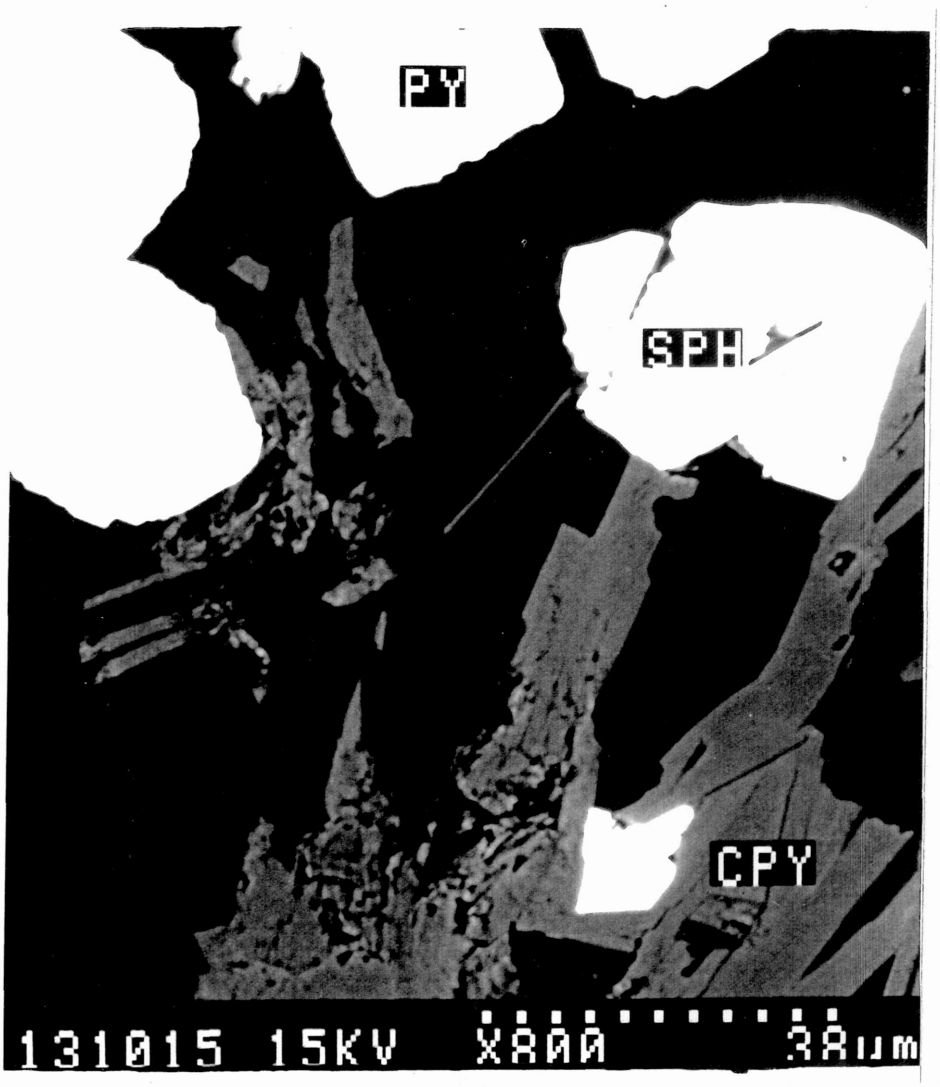


Figure 6.3 - High-contrast backscattered electron image of vein material at Patchway (sample 10-25). Due to high contrast, all sulphides appear white. Other minerals seen are chlorite (light grey), sericite (dark grey) and quartz (black). Note the interlayered chlorite and sericite seen centre left of photograph beneath bright sulphide grain.

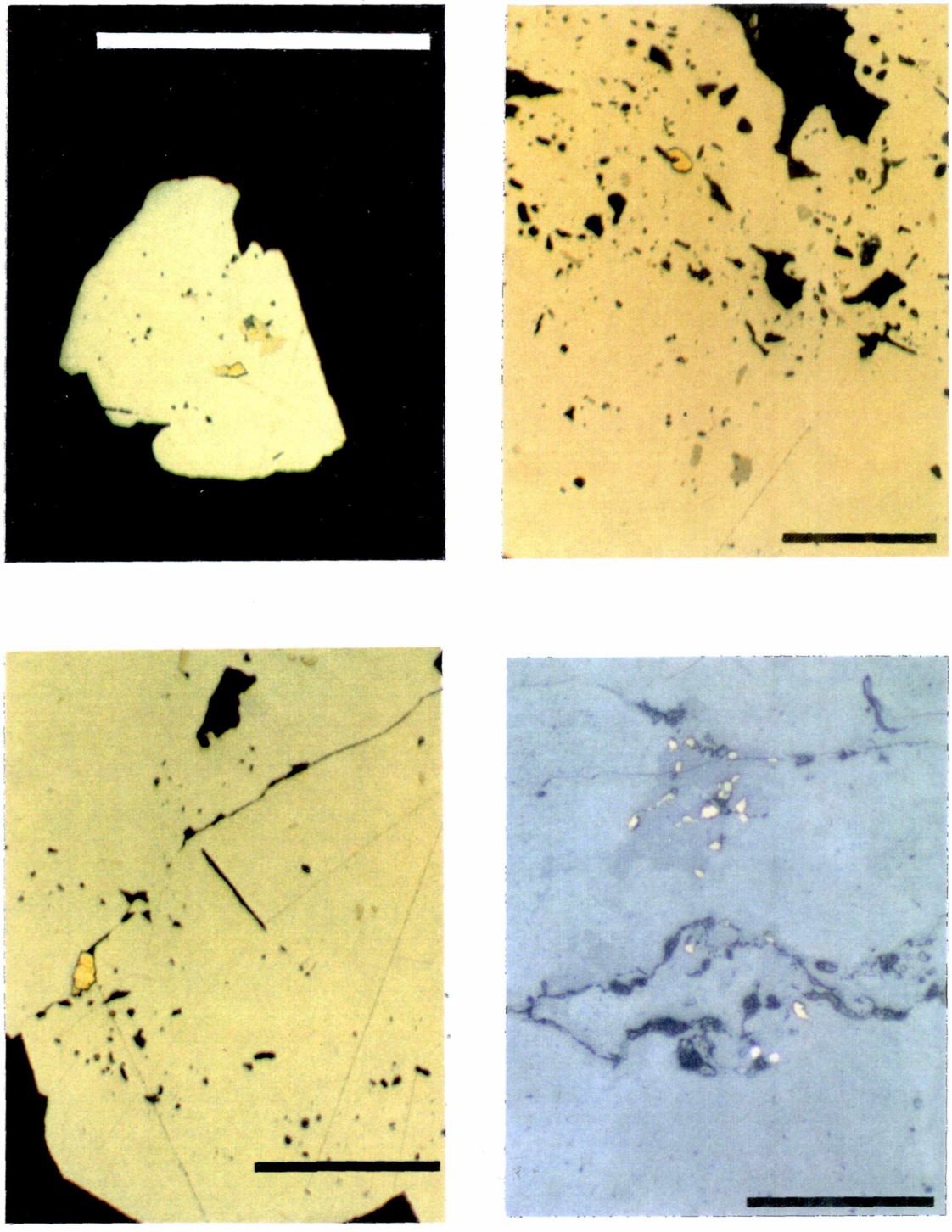


Figure 6.4 - Photomicrographs indicating association of gold in the ribbon-quartz veins at Patchway mine. A - Sample 19HG1 : Gold encapsulated in pyrite, pyrite also contains duller yellow chalcopyrite grains (Scale bar = 0.5 mm). B - Sample 30-2 : Gold encapsulated in pyrite, pyrite also contains dark silicate inclusions and buff-brown pyrrhotite grains (Scale bar = 0.5 mm). C - Sample 30-2 : Gold located along crack in pyrite grain, again pyrite contains silicates and tiny buff-brown pyrrhotite (Scale bar = 0.2 mm). D - Sample 19HG1 : Isolated gold (electrum) grains located along vein stylolite and also within grey-green quartz grain. No sulphides are seen in field of view (Scale bar = 0.5 mm).

Pyrite, the most dominant sulphide in the D2 veins, can often be demonstrated to be intergrown with the gold itself. Pyrite is not only present in the veins, but, as discussed earlier, commonly occurs as strong disseminations in the wallrock, up to 50 cm from the vein margin. Texture of the grains is quite variable, but are generally seen to be idioblastic cube forms in the veins and as both cubes and pyritohedra in the wallrock. Irregular, lenticular aggregates are common in the wallrock.

All pyrite is interpreted as being formed as a result of hydrothermal precipitation, but there textures suggest that much of the wallrock pyrite is formed largely as a result of sulphidation of existing oxides or silicates (see Figure 6.5). Some of the vein pyrite may also have nucleated around an initial grain of altered Fe bearing oxide or phyllosilicate, as these grains often contain tiny solid inclusions.

Sulphides in the Fe-S system are dominated by pyrite. The pyrite in the vein, within the phyllosilicate septa and wallrock slivers showed clear differences *both* compared to pyrite from the wallrock alteration distal to the vein *and* sulphide from within "barren" white ribbon areas of the vein itself. Only pyrite from the vein septa and wallrock bands close to the quartz veining contained inclusions of any other phases, the pyrite in the "barren" regions forms generally homogeneous grains. Inclusions in the vein pyrite grains include chlorite and sericite, as well as all the other sulphide phases (Figures 6.6 and 6.7), particularly pyrrhotite, together with occasional gold grains and tiny minor telluride phases. Some evidence of growth banding is seen in the pyrite (Figure 6.8). Gold, sulphides and tellurides were also seen in fractures within pyrite grains. Pyrrhotite is present in certain parts of the vein assemblage, particularly as generally tiny (< 30 micron) inclusions within the pyrite (Figure 6.7). Only rarely does it occur in isolation from pyrite. The other iron sulphide present, pyrrhotite, normally occurs in the central portions of pyrite grains, with evidence for later overgrowth of pyrite only enclosing the core areas. Discrete pyrrhotite grains are only recorded in one sample examined from the deformed mafic wallrock.

Of the other sulphide phases, chalcopyrite commonly occurs associated with pyrite in the vein assemblage and commonly forms inclusions within pyrite grains, often in pyrrhotite bearing grains (Figure 6.9). Galena is present in the gold bearing assemblage, particularly as tiny inclusions in pyrite which also contains gold grains. Arsenopyrite is seen only as inclusions within pyrite and generally occurs in the grains which contain appreciable sulphide inclusions. Arsenopyrite is thus interpreted as being cogenetic with the enclosing pyrite which makes it useful as a potential mineral geothermometer. Although the arsenopyrite is not seen directly in contact with gold grains, it occurs enclosed in the same pyrite grains which host gold and can thus be considered contemporaneous. Finally, although rare, sphalerite also occurs as minor inclusions within pyrite. Grains are generally tiny, and were confirmed by electron microprobe examination. Occasional free grains are associated with other sulphide phases (Figures 6.3, 6.8 and Table 6.4).

Grain type	1 (n=6)	2 (n=9)	3 (n=2)
Au	79.18	78.49	71.58
Ag	19.50	19.62	24.51
Fe		0.71	3.06
Cu	0.59		
Total	99.27	98.82	99.15

Table 6.3 - EPMA analyses of gold grains. Type 1 grains are free gold grains, type 2 are encapsulated by pyrite and type 3 are located along cracks in pyrite grains.

Sample	18-1 (n=7)	20-14 (n=3)	10-29 (n=5)
Fe	4.84	1.52	10.60
S	48.66	48.11	36.70
Zn	46.28	50.16	52.31
Total	99.78	99.80	99.61
Mole% ZnS	9.66	3.07	21.03

EPMA analyses of sphalerite. Sample 18-1 is from ribbon-vein stylolite and the grains are hosted in pyrite grains, associated with pyrrhotite. Grains in sample 10-29, from wallrock lava, are free, isolated grains in thin quartz veinlets.

Sample	30-2 (n=4)	10-29 (n=7)
Fe	47.52	46.93
S	52.34	52.14
Ni	0.21	0.53
Total	100.07	99.60

EPMA analyses of pyrrhotite grains. All grains are included within pyrite grains. Sample 30-2 is from ribbon-vein stylolite pyrite, sample 10-29 is from vein margin wallrock lava which contains thin quartz veinlets.

Table 6.4 - Microprobe analyses of sulphides associated with mineralised ribbon-quartz veins.



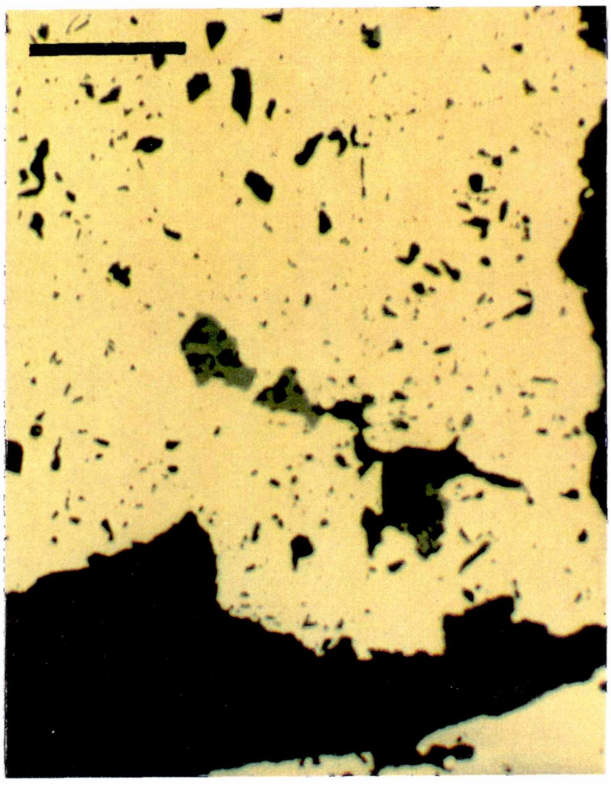
Figure 6.5 - High-contrast backscattered electron image of vein wallrock material at Patchway (sample 10-29). Due to high contrast, all sulphides appear white. Other minerals seen are rutile (light grey), sphene (dark grey) and quartz (black). Note the intimate relationship between sphene and rutile and close association of bright (white) pyrite grain.

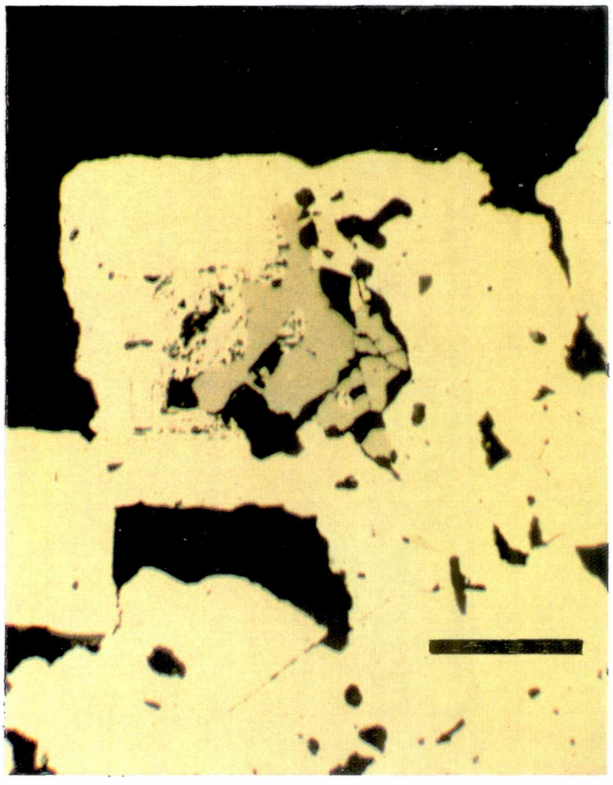
Figure 6.6 - Pyrite grain enclosing grey ilmenite grains at the core (Sample 10-26). Scale bar = 0.5 mm. Reflected normal light image

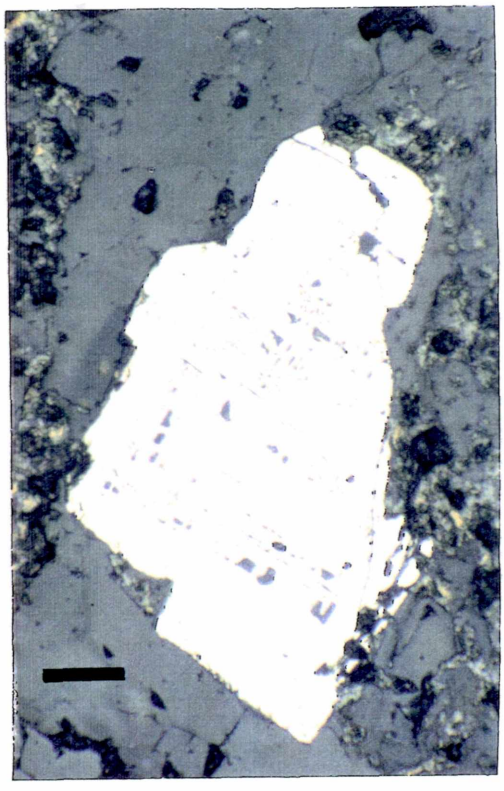
Figure 6.7 - Pyrite grain enclosing darker buff-brown pyrrhotite at the core (Sample 19HG1). Scale bar = 0.5 mm. Reflected normal light image.

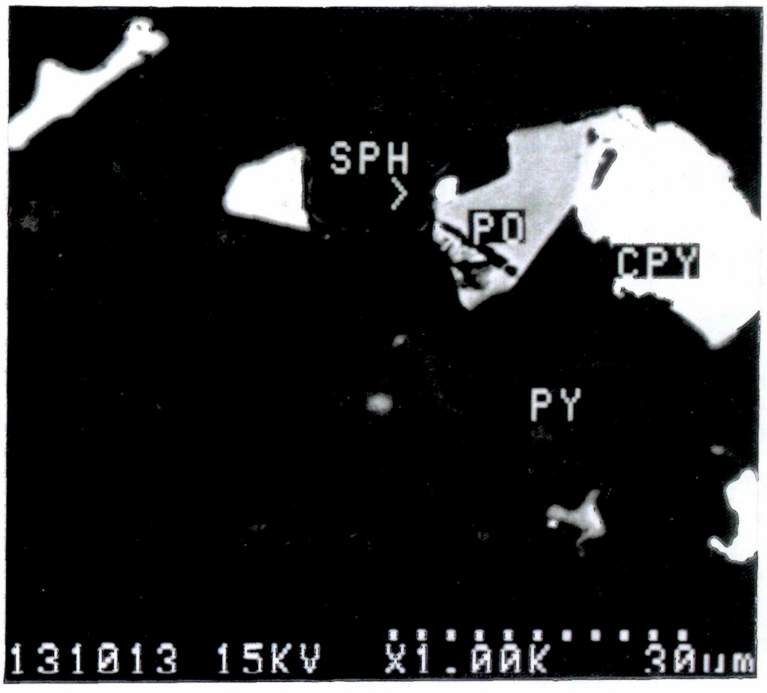
Figure 6.8 - Pyrite grain showing evidence of complex internal growth banding (Sample 10-29). Scale bar = 0.5 mm. Reflected normal light image.

Figure 6.9 - High-contrast backscattered SEM image of pyrite grain (dark area of entire field). Tiny enclosed sulphide grains can be distinguished under backscattered imaging (Sample 10-29).








SPH
PO
CPY
PY
131013 15KV X1.00K 30µm

Hessite, the silver telluride, has been found as isolated inclusions in pyrite together with more complex gold-bearing tellurium phases. Traces of stibnite and tetrahedrite are suspected as sub-microscopic inclusions in pyrite close to chalcopyrite. In at least one section löllingite is indicated as a phase within the complex pyrite grain.

6.3.3 Detailed electron microprobe study of sulphides

Gold and its associated grains were examined by SEM and analysed by quantitative EPMA X-Ray EDS analysis. In addition pyrite was examined in more detail by high contrast back-scattered electron imaging together with WDS mapping to study trace element substitution.

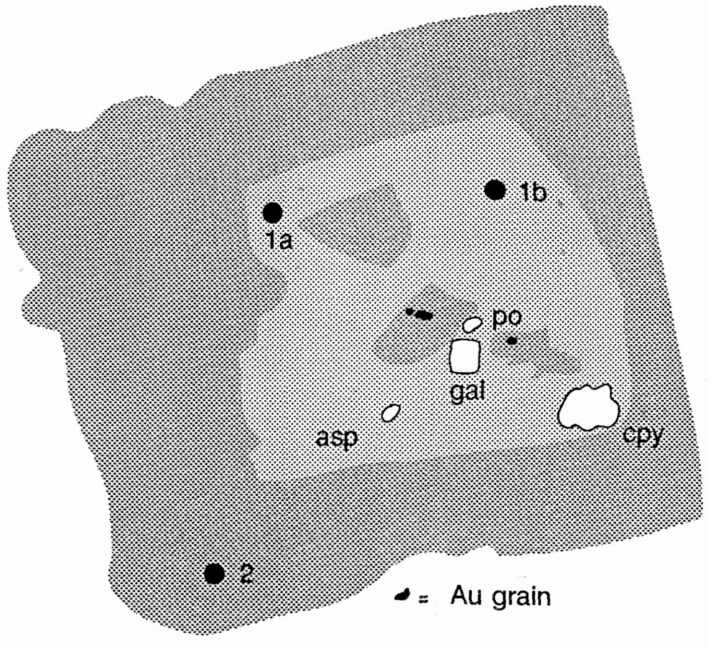
Simple high contrast back-scattered electron imaging of the pyrite grains highlighted some interesting textures. Figure 6.10 shows typical pyrite grains in the phyllosilicate septa zones in vein samples. Apart from the evident tiny inclusions which include tiny gold grains, the pyrite is evidently zoned.

There is definition of different domains within the grain. Generally, a dark inclusion free core is surrounded by a complex area of dark and lighter pyrite areas with up to 30% bright inclusions of differing compositions. Surrounding this is lighter pyrite (higher molecular weight than the dark areas) with relatively no inclusions. Lastly, an area of darker, inclusion free pyrite rims the whole grain. Imaging of other grains showed similar patterns, some of which suggested concentric zoning and accretionary textures. Point analysis of the brighter imaging areas pointed to the presence of significant As content in the pyrite. Figure 6.11 shows a grain where there is a clear subdivision of the pyrite grain into a dark core, inner bright zone and outer dark zone. The very bright included grains are shown to be galena, chalcopyrite and arsenopyrite. The probe traverses across the grain are shown below the high contrast backscattered image with the analysis results. It is clear that the bright areas are again due to substitution of As in the pyrite for S, effectively raising the molecular weight of the pyrite, hence the image contrast.

Some X-Ray WDS mapping of the grains was undertaken to study distribution of other elements at low concentration (<0.1%) in the pyrite grains. SEM operating conditions were adopted as outlined in Appendix II.

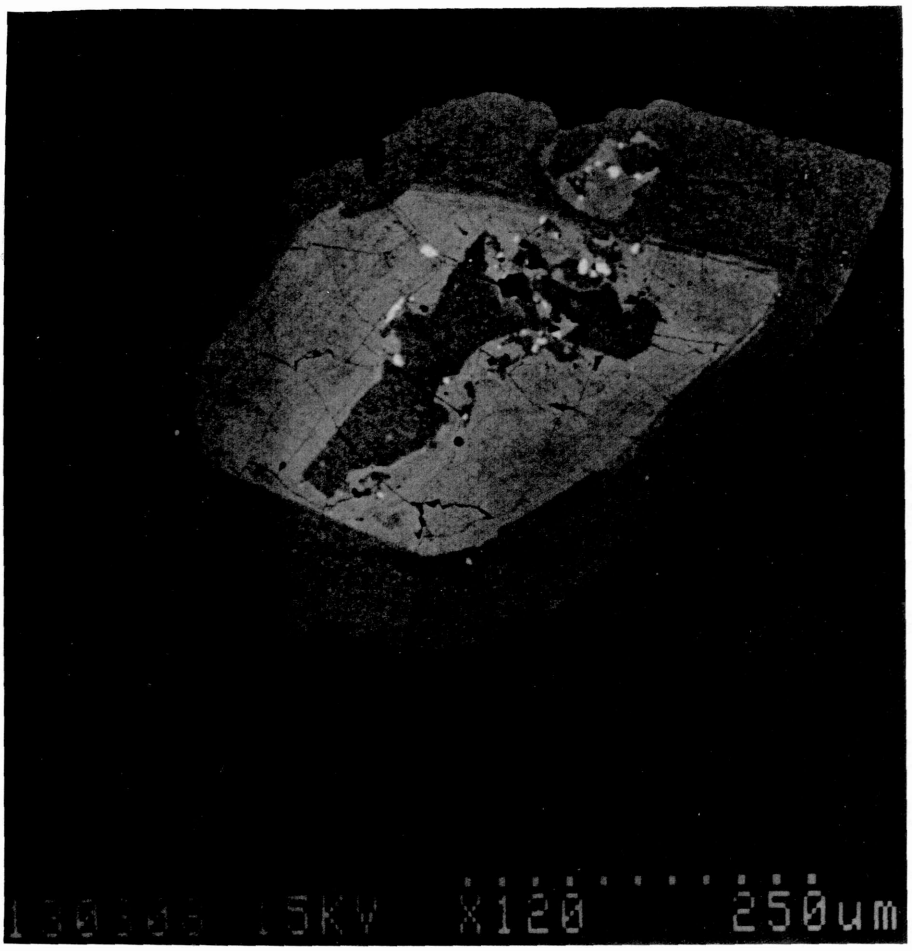
The pyrite grains studied were from two distinct areas within the vein. The first area comprised grains from the vein septa which were closely associated with gold and other sulphide phases. The second areas studied were from within the white quartz ribbon areas themselves where isolated sulphide grains occur. It became clear that the only elements showing systematic variations within the pyrite grains themselves were arsenic and nickel. The other elements sought showed no systematic variation in the pyrite itself, but served to highlight included phases containing that element (e.g. Cu and Pb which

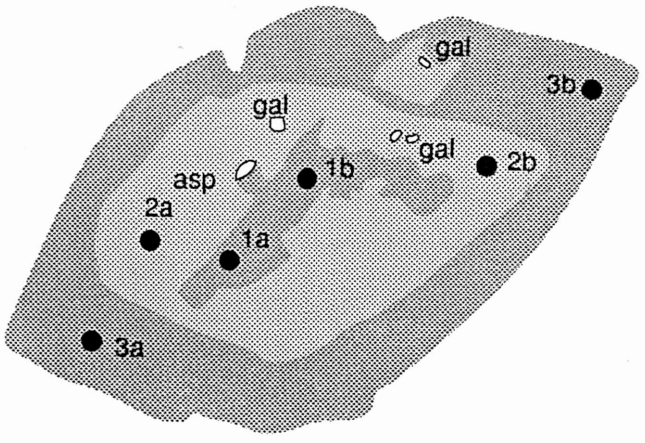




Point	Fe	S	As
	atomic%		
1a	33.99	64.74	1.07
1b	34.19	64.54	1.20
2	33.84	65.26	0.12

Figure 6.10 - High-contrast backscattered SEM image of pyrite grain (Sample 18-1). Points on sketch below show microprobe analyses of pyrite, indicating major As substitution in bright areas of the grain. Minute gold grains are present in the pyrite core.





Point	Fe	atomic% S	As
1a	34.56	65.04	0.00
1b	34.48	65.10	0.00
2a	34.84	64.45	0.54
2b	34.89	64.44	0.59
3a	34.96	65.00	0.00
3b	34.62	65.21	0.00
asp	33.95	41.32	24.60

Figure 6.11 - High-contrast backscattered SEM image of pyrite grain (Sample 18-1). Points on sketch show microprobe analyses of pyrite, again indicating major As substitution in bright areas of the grain. Arsenopyrite and galena grains are also present in the grain.

highlighted tiny inclusions of chalcopyrite and galena). Several grains were also mapped for gold to examine if any gold may be present in solid solution.

Figure 6.12 shows a pyrite grain from sheared sulphidised lava included within the main ribbon quartz vein at Patchway. Distinct zonation of the grain is demonstrated by the WDS maps for Ni and As. A central As and Ni poor zone is surrounded by tiny arsenopyrite and pyrrhotite grains (bright spots on the As and Ni maps respectively). The As-rich and Ni-rich zones in the pyrite are generally mutually exclusive, the late pyrite overgrowth clearly Ni-bearing.

Figure 6.13 is a pyrite grain in a vein ribbon stylolitic septum. The grain shows clear growth banding of both Ni and As bearing areas. The grain also shows truncated banding, indicative of possible grain corrosion. The outer zone in the pyrite is again Ni-bearing.

Figure 6.14 shows a pyrite grain from the immediate vein margin to quartz hosting coarse native gold grains. The map for Au shows the discrete gold grains in the As-poor core of the pyrite. The gold clearly contains Ni. The Ni map confirms the co-existence of pyrite and pyrrhotite close to the gold grains. Surrounding the As-poor pyrite is a complex As-rich zone. Finally, the outermost zone contains significant Ni, a similar pattern to the other grains.

Figure 6.15 is a pyrite grain in a ribbon vein stylolite. Gold grains occur in the As-poor grain core, and the WDS map for Au shows evidence for some Au substitution into the pyrite itself.

Lastly, pyrite from the "barren" white quartz central portions of the ribbon veins show little evidence of trace element zonation (Figure 6.16). No gold was detected in pyrite from this association.

6.3.4 Discussion

The occurrence of the highly zoned complex pyrite grains in the vein septa and wallrock inclusion areas of the vein clearly documents changing physiochemical conditions during crystallisation. Almost identical textures have recently been described from the Agnico-Eagle deposit, Canada (Fleet *et al.* 1989), where complex, arsenic poor and arsenic bearing areas of pyrite grains are surrounded by concentrically banded arsenic bearing pyrite. Some of the grains also show later, dark arsenic poor overgrowths.

They conclude that the arsenic is present as a metastable solid solution in the form of $Fe(S,As)_2$ or as discrete bands of arsenopyrite (FeAsS) within the grain. Clark (1960) showed that under laboratory conditions, which are assumed to represent equilibrium, arsenic does not substitute into pyrite. The same authors show that even at 600° C, uptake is less than 0.53 weight%. Fleet *et al.* (1989) suggest that surface chemistry may control the substitution of As into the pyrite lattice.

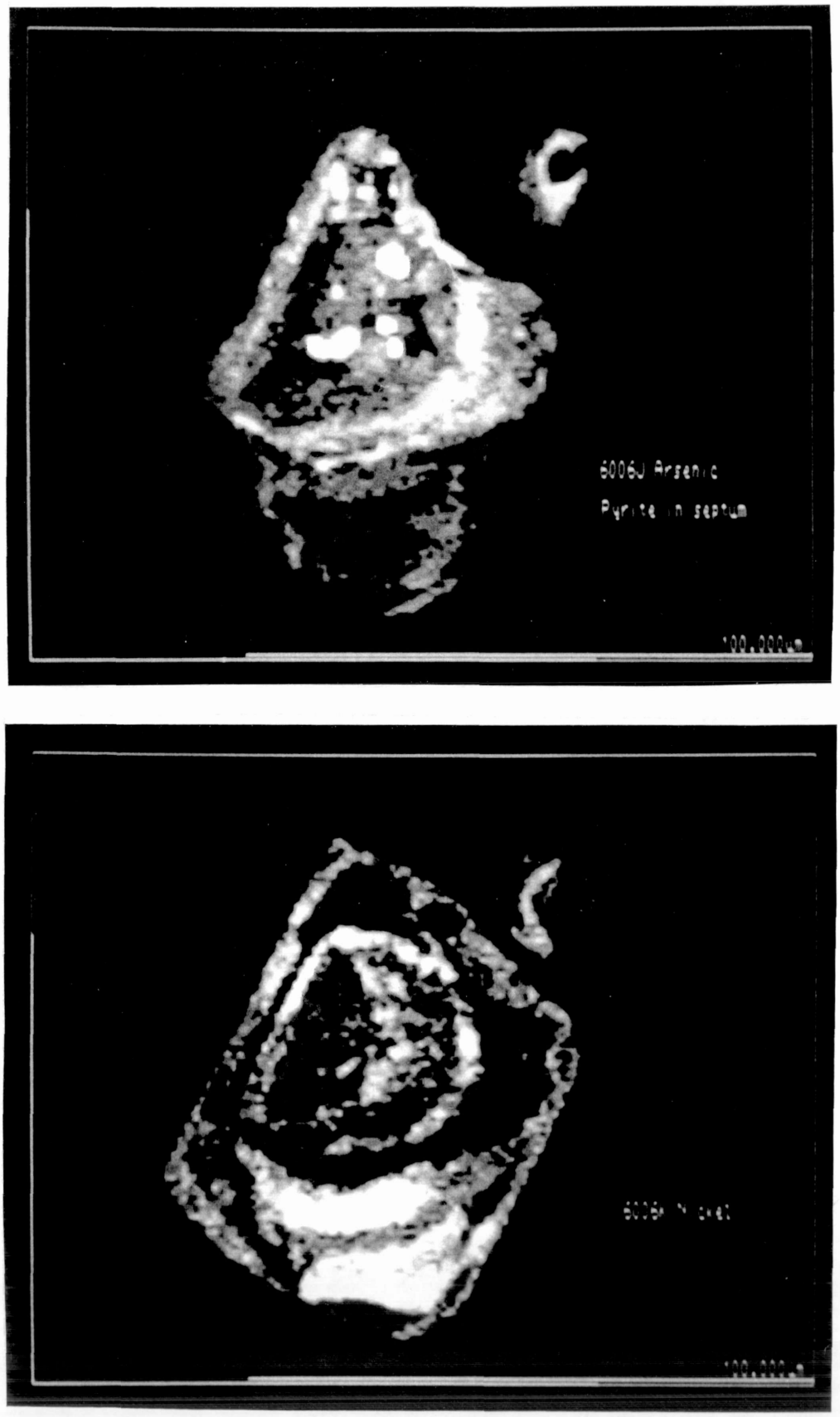


Figure 6.12 - WDS maps of pyrite grains in gold-bearing sample 6006b from 6 Level pillar (Fig. 4.16). Upper image shows As map, lower image Ni map. Central core shows small arsenopyrite grains (white areas, top image) and concentric zonation for both elements indicates quite different substitution behaviour.

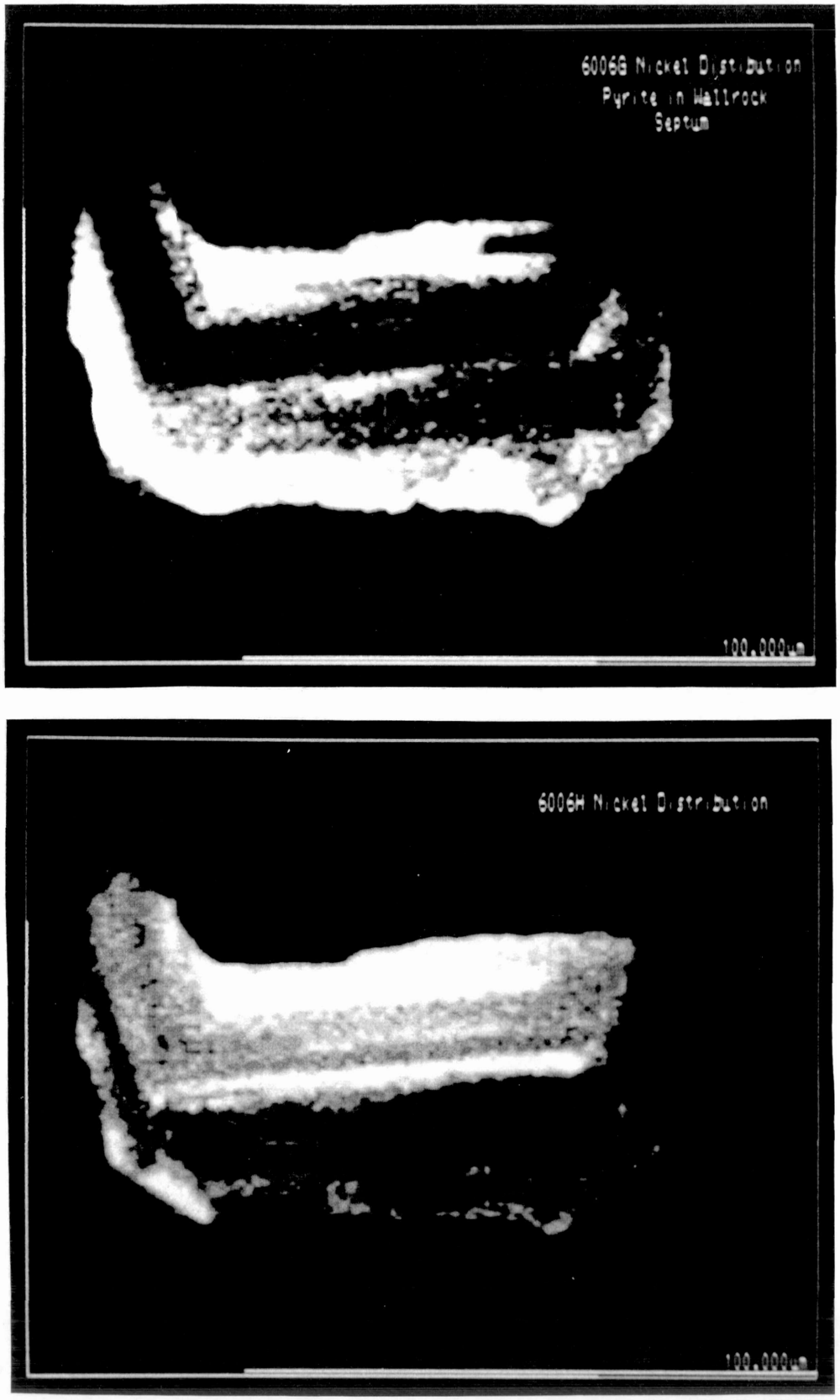


Figure 6.13 - WDS maps of pyrite grains within stylolitic phyllosilicate zone in gold-bearing sample 6006b from 6 Level pillar (Fig. 4.16). Upper image shows As map, lower image Ni map. Concentric zonation is indicated with different substitution behaviour for the two elements. Grain shows some evidence for corrosion (truncated banding), perhaps during pressure solution.

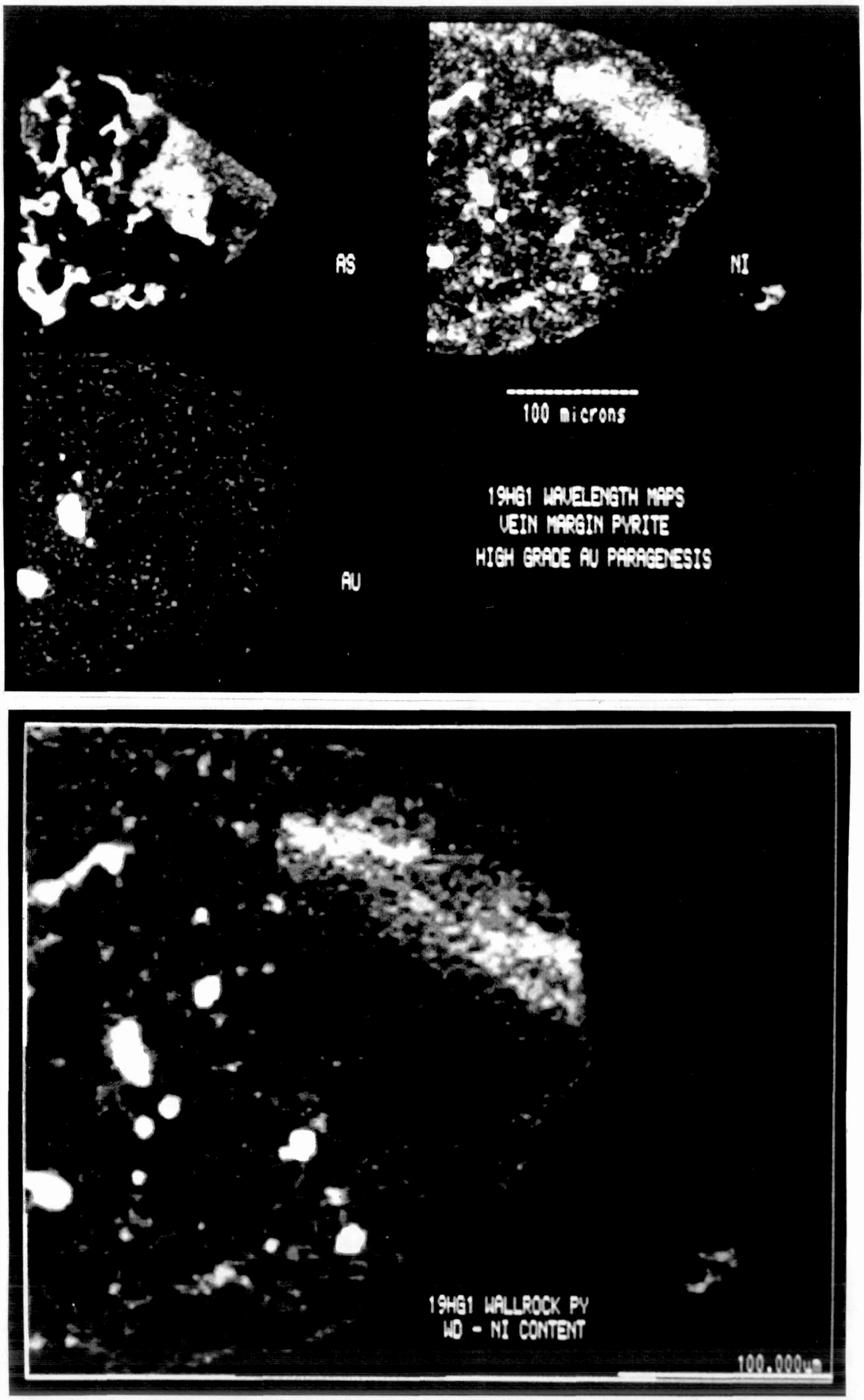


Figure 6.14 - WDS maps of pyrite grain containing included gold grains (sample 19HG1). Upper image shows composite As, Ni and Au map, lower image close up of Ni map. Complex zonation is indicated with different substitution behaviour for Ni and As. Discrete gold grains clearly contain Ni and seem to be located at the complex cores of the pyrite grains.

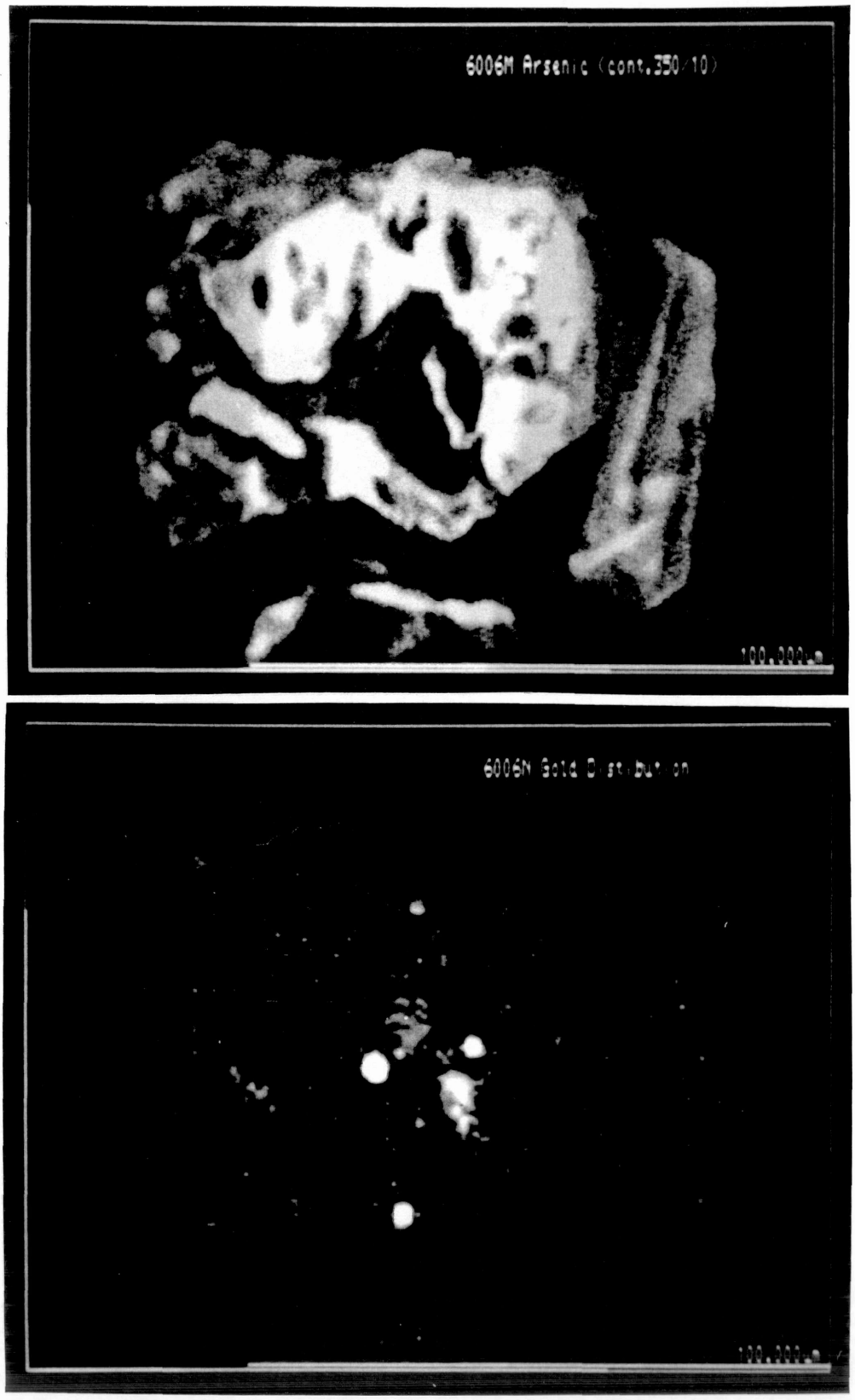


Figure 6.15 - WDS maps of pyrite grain containing included gold grains (sample 6006b). Upper image shows As map, lower image Au map. Complex zonation is indicated for As and the gold grains are the very bright areas on the lower image. Discrete gold grains seem to be located at the complex cores of the pyrite grains and there is some evidence for gold substitution in the pyrite (grey areas on lower image).

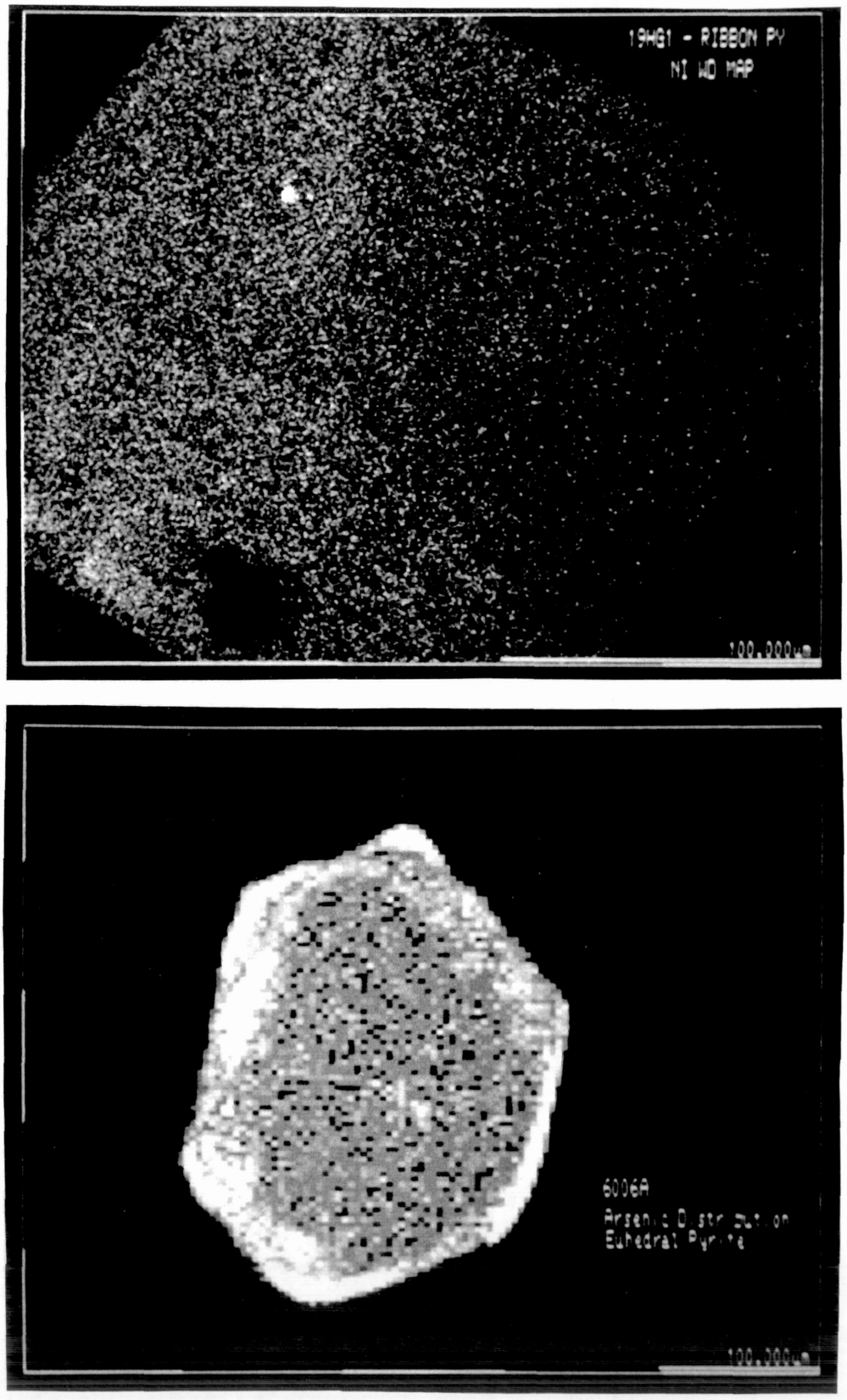


Figure 6.16 - WDS maps of pyrite grains in "barren" quartz ribbons (Area type "A" discussed in Chapter 4.9 (sample 19HG1 above and sample 6006b below). Upper image shows Ni map, lower image As map. No real zonation patterns are indicated for either element in the central areas of the grains. No gold grains were located in this pyrite association.

One interesting observation at Patchway is the general absence of arsenopyrite from the arsenic rich portions of the pyrite grains. This seems to suggest that during formation of the arsenic rich bands in the pyrite, arsenopyrite was precluded from forming. Figure 6.17 from Kretschmar & Scott (1976) indicates the stability fields for the Fe-As-S species as a function of temperature and sulphur activity. Area "A" on the figure, indicates the field within which arsenopyrite is no longer stable, i.e. high sulphur activity. The concentric banding of these arsenic bearing zones in the pyrite might suggest fluctuating sulphur activity during formation of this pyrite. The central As-poor pyrite core which contains arsenopyrite may possibly represent a zone where exsolution has resulted in discrete arsenopyrite and As-poor pyrite grains. The latest pyrite growth on the outer parts of the grains is arsenic poor, and may well represent a later event of mineralisation.

Arsenopyrite was first recognised as a potential geothermometer by Clark (1960). Kretschmar & Scott (1976) followed this up experimentally and this work was further refined to accommodate the effect of pressure by the work of Sharp *et al.* (1985). For arsenopyrite to be suitable as a geothermometer it must be buffered by the sulphide phases pyrrhotite and pyrite, contain minor trace elements less than 1% (Sundblad *et al.* (1984) suggest less than 0.2%) and the formation conditions must be less than amphibolite facies. The gold bearing mineralised samples analysed have arsenopyrite seen as inclusions within pyrite grains which also contain cores of pyrrhotite. The range of As values from 28.62 to 31.00 atomic% As for 19HG1, and 30.25 to 31.05 atomic% As for 26-14d, give a range of temperatures from below 300° C to 380° C when plotted in the py-po field on Figure 6.17. The mean value of 29.90 atomic% As gives a value of 330° C. The same Figure 6.17, can be further utilised to estimate the range in sulphur activity for the system at an assumed fixed temperature. If the assumption of the system lying on the pyrite-pyrrhotite buffer is made, then the mean value for arsenic gives a value for log aS_2 of -7.8. As suggested above the presence of As in the pyrite suggests that aS_2 may actually be higher than that calculated by assuming pyrite-pyrrhotite buffering. In contrast, the rare presence of small included grains of löllingite in the centre of some pyrite grains points to somewhat lower sulphur fugacity conditions than conditions for the formation of coexisting arsenopyrite-pyrite-pyrrhotite. Gold grains, when included in pyrite, generally occurs in the pyrite-pyrrhotite-arsenopyrite sections of the grains, so the calculated aS_2 of -7.8 is reasonable for conditions during part of the gold mineralisation. Later As rich pyrite overgrows these zones, indicative of higher aS_2. The latest pyrite growth is As poor but cannot be constrained by other sulphur-bearing species.

The use of the Zn-Fe-S system as a geobarometer at temperatures in excess of 300° C has been proposed based on the FeS content of sphalerite where sulphur activity is buffered by pyrite, pyrrhotite and sphalerite (Scott & Barnes 1971, Scott 1973). The presence of other trace elements are considered unlikely to have any effect on such a system. This sphalerite barometer is thus suitable when applied to the pyrite hosted sphalerite grain analyses reported in Table 6.4. The mean value of 9.8 atomic% Fe calculates to a molar% FeS of 20%. Figure 6.18 is the diagram from Scott (1973) and from this a

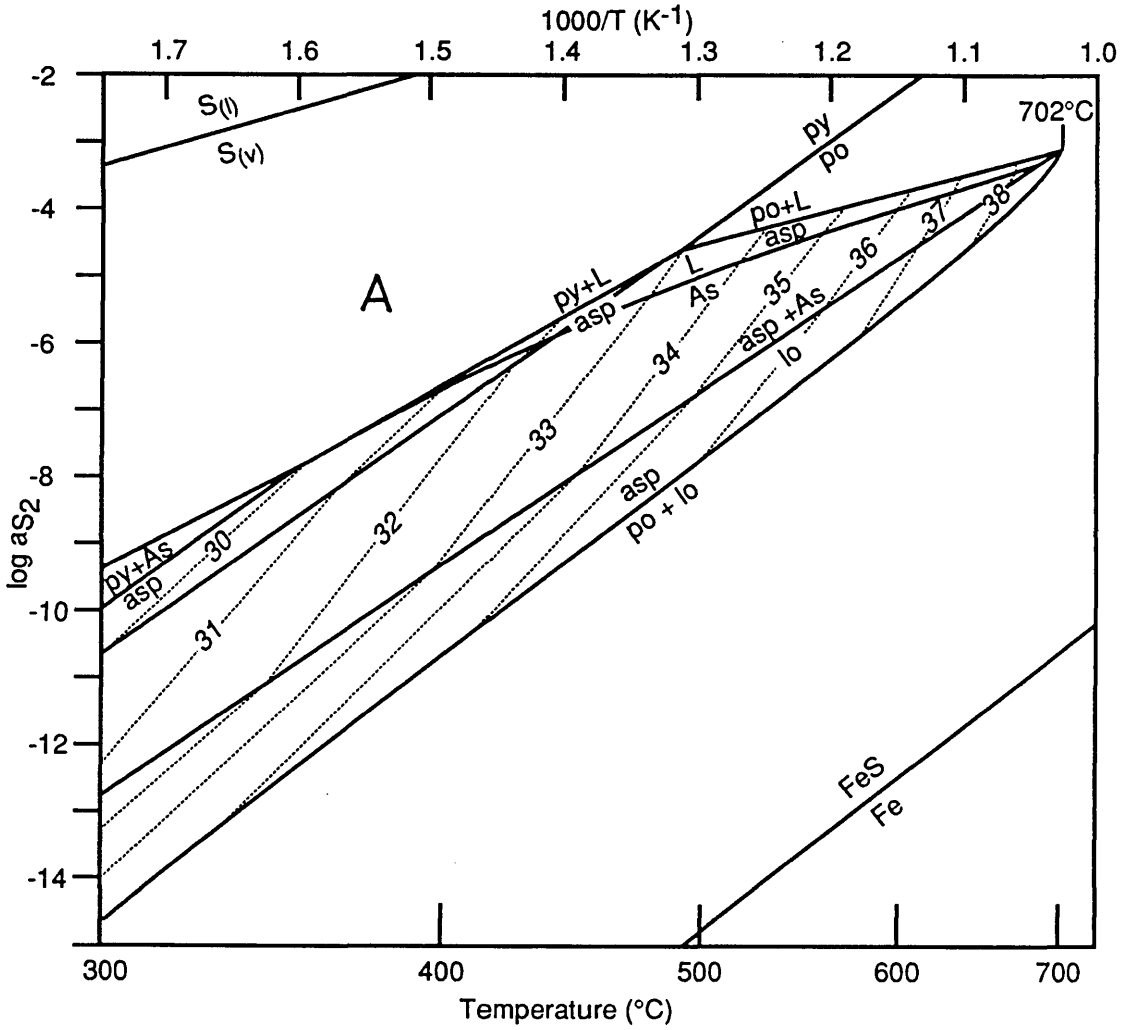


Figure 6.17 - S_2 activity-temperature projection of the stability field of arsenopyrite, contoured in atomic % arsenic (from Kretschmar & Scott 1976).

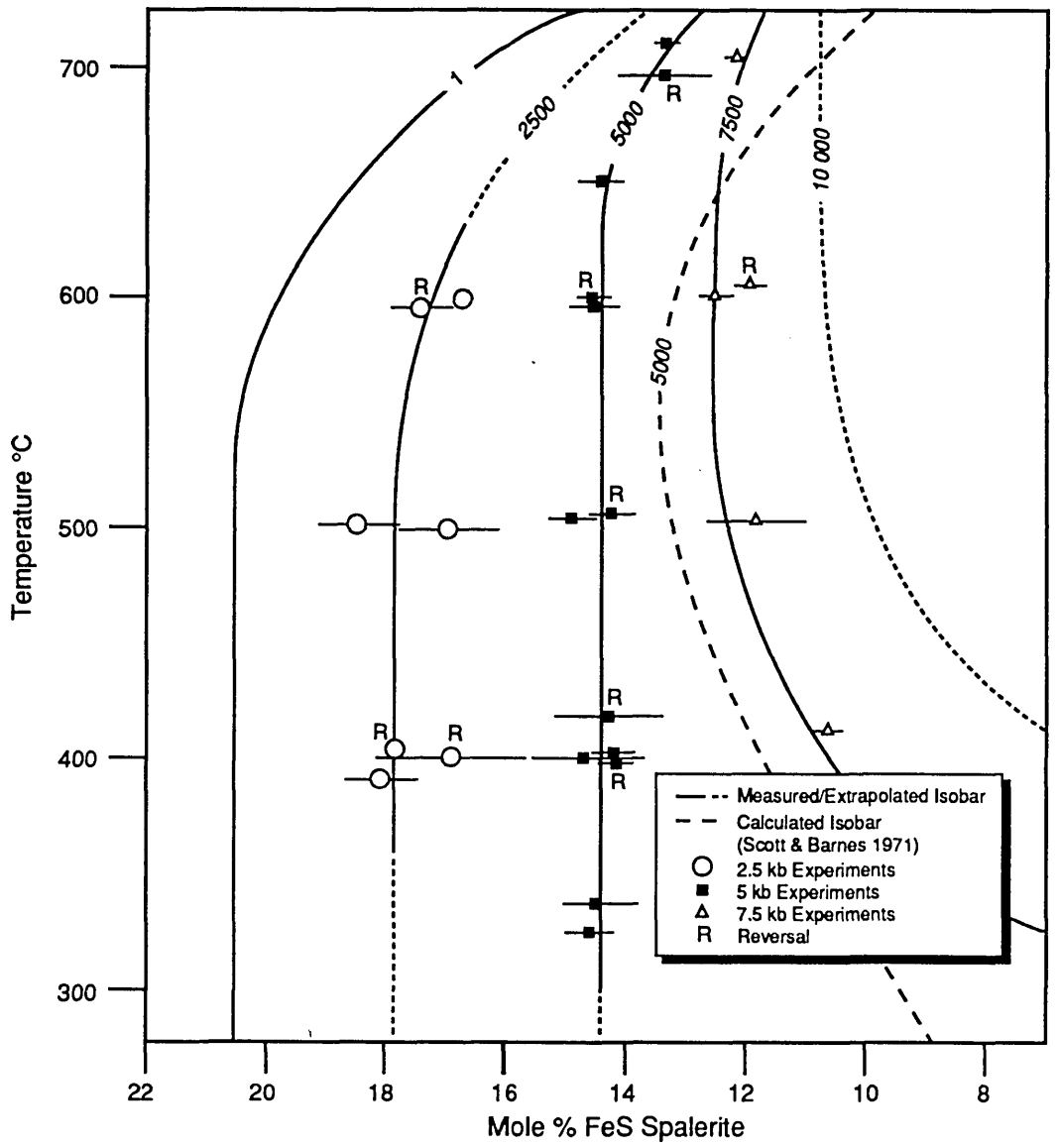


Figure 6.18 - T-X projection of the sphalerite + pyrite + hexagonal pyrrhotite solvus isobars. Pressure measurements are in bars (from Scott 1973).

formation pressure of considerably less than 2.5 kbars in the temperature range 500 to 300°C is indicated. Microprobe data from the free sphalerite grains (3 to 5 mol% FeS), where buffering by the other sulphide phases cannot be demonstrated, not surprisingly gives totally unrealistic pressure estimates using Figure 6.18. The work of Scott (1983) indicates that, at low pressures, sphalerite with very low FeS content is consistent with aS_2 much higher than the pyrite-pyrrhotite buffer. Although pressure affects this quite dramatically, ambient pressures for the two sphalerite types are not considered to be greatly different so it is suggested that the ambient aS_2 during formation of the free sphalerite grains was much higher.

Barton & Skinner (1967) showed that iron content of pyrrhotite below the pyrite buffer is governed by sulphur activity and furthermore is pressure independent (Craig & Scott 1976). Figure 6.19 is from this work and from the average analysis of 47 atomic% Fe, a value for aS_2 at the pyrite-pyrrhotite buffer can be interpolated of log aS_2 of -7 at 410°C. Since the arsenopyrite geothermometer indicates temperatures lower than this, later, lower temperature equilibrium is suggested and the activity value above may reflect a possible maximum figure.

6.4 Later mineralisation

Later veining at Patchway is related to D3 and D4. Mineralisation associated with the D3 structures (Munya-Skati, Erin and Kabanga) is very similar to the gold-bearing mineralisation discussed in section 6.3 except for the presence of tourmaline in some structures. Sulphide contents of the veins themselves are generally lower (negligible in the cases of the cross-reefs) and gold was not observed in the few sections studied. The D4 assemblage comprises almost entirely quartz-tourmaline-carbonate, with local remobilistion of sulphides when the extension veins cut the D2 ribboned veins.

Tourmaline

This mineral is absent from the D2, but present in the D3 vein assemblages, and this is the key mineralogical difference between the stages, observed macroscopically, at Patchway. Tourmaline is also the main phase apart from quartz in the D4 assemblage. Tourmaline occurs generally as aggregates of prismatic crystals in the D3 veins, sometimes the main silicate phase in the dark ribbon inclusions. In the D4 veining, the tourmaline is generally coarser, forming crystals up to 3mm in length, mainly as aggregates nucleated on the walls of the veins. Where D4 veins cut the earlier D2 ribbon veins, tourmaline often nucleates close to phyllosilicate-rich inclusion bands and Figure 6.20 shows the situation where a D4 vein cuts such a region. The conclusion is that tourmaline may well form after chlorite, resulting from the reaction of the boron-bearing D4 fluid with the phyllosilicate bands.

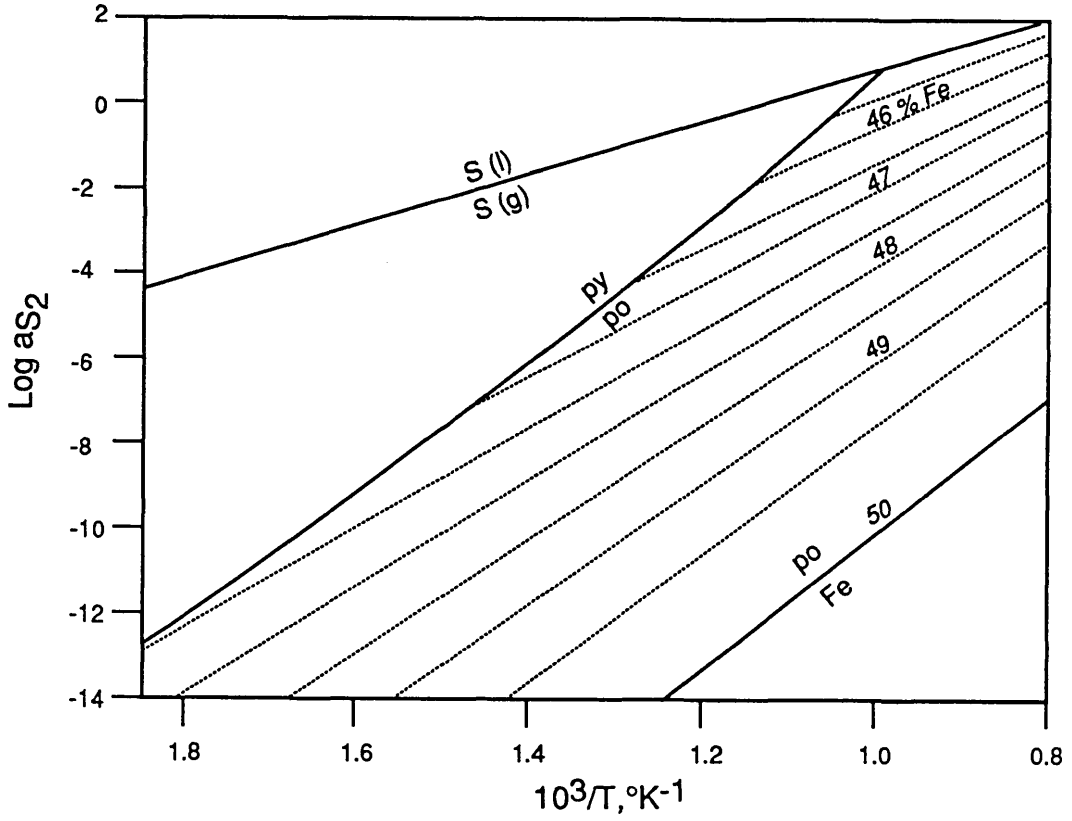


Figure 6.19 - Composition of pyrrhotite in atomic % Fe as a function of S_2 activity and temperature (from Barton & Skinner 1967).

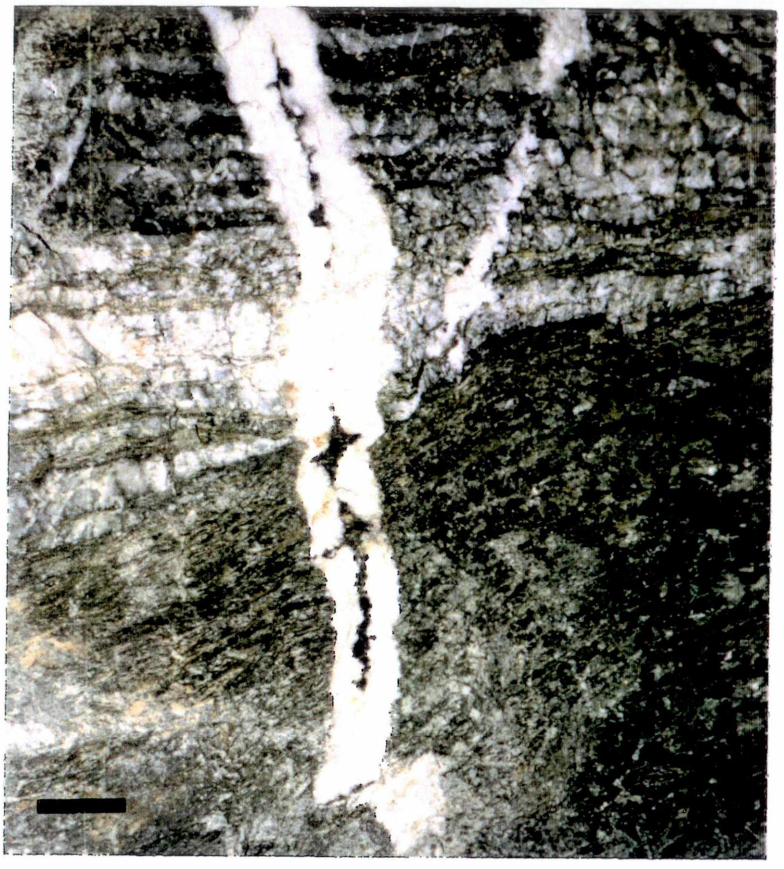


Figure 6.20 - Late D4 quartz-tourmaline vein, clearly cross-cutting earlier D2 ribbon-quartz veins. Note how black tourmaline aggregates are best developed where the late vein crosses phyllosilicate-rich (± sulphides) zones (Black scale = 5cm).

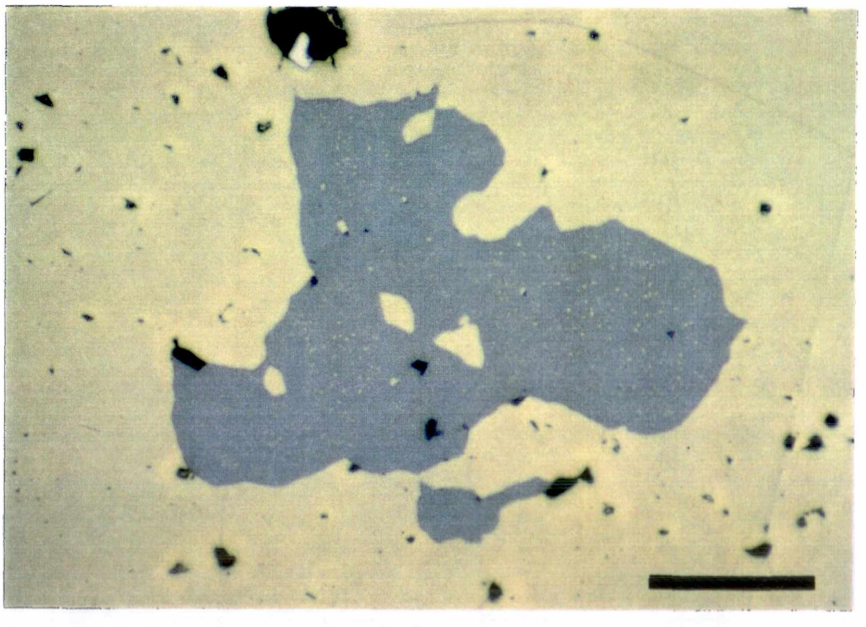


Figure 6.21 - Coarse chalcopyrite segregation in D4 veining (Sample 1800-6). Chalcopyrite is seen encapsulating grey sphalerite which shows "chalcopyrite disease" (Black scale = 0.5 mm).

Sample	18-23 (n=8) (A)	30-7 (n=10) (B)
SiO_2	37.15	36.96
TiO_2	0.59	0.37
Al_2O_3	31.24	31.96
FeO	7.75	7.92
MnO	-	0.05
MgO	8.09	7.52
CaO	0.70	0.14
Na_2O	2.67	2.42
K_2O	-	-
B_2O_3	8.95	9.01
Total	97.14	96.35

Tourmaline analyses:

A - Late vein segregation
B - Late extension vein

Table 6.5 - EPMA Tourmaline analyses from late veining. Calculation of B_2O_3 values is made assuming a stoichiometry of 29 oxygens.

In thin section the tourmaline is green-yellow in colour, suggestive of a dravitic composition and Table 6.5 shows microprobe analyses of tourmaline in both D3 and D4 veins, where the composition is clearly shown to be in the schorlite-dravite series (after Gallagher 1987).

Sulphides

Sulphides are less common than in the D2 ribbon-vein assemblage. In the D3 veins only pyrite and minor chalcopyrite was detected. Gold was not seen in the D3 veins studied and the D3 veins encountered underground at Patchway have not supported sustained mining operations, although assays record gold grades may reach several grammes per tonne locally. D4 veins rarely contain sulphides, except where the D4 vein cuts sulphide-rich D2 veining. Figure 6.21 shows coarse sphalerite and chalcopyrite in such a vein. The sphalerite is suffering from "chalcopyrite disease", which may indicate later exsolution or the reaction of FeS within sphalerite with Cu in solution (Scott 1983).

6.5 Summary

The phyllosilicates in the D2 vein assemblage are generally very similar to the wallrock alteration phyllosilicates. Chlorite intimately associated with gold does show very high iron enrichment, however, which may have sulphur or oxygen fugacity implications.

The sulphide phases in the gold-bearing vein are dominated by pyrite together with included grains of pyrrhotite, arsenopyrite, chalcopyrite, galena, sphalerite and some more minor telluride phases. Gold and silver are largely contained within electrum grains which occur *either* within pyrite as inclusions or crack infills *or* as discrete native grains. Gold clearly coprecipitates with the sulphide phases pointing to introduction of gold, silver and arsenic together with some copper, zinc, lead and traces of tellurium from the hydrothermal fluid. Most significantly, gold grains are seen in some cases to be totally enclosed within single quartz grains. Since these quartz grains appear to contain primary fluid inclusions, direct evidence for the conditions of gold precipitation may be obtained from inclusion study. Chapter 7 describes fluid inclusion study of the gold-bearing quartz in detail.

The dominant sulphide phase, pyrite, is seen forming in 3 distinct paragenetic associations : 1) wallrock alteration, 2) vein septa pyrite and 3) vein quartz ribbon pyrite. Type 1) pyrite forms largely as a result of sulphidation of existing iron bearing phases (e.g. ilmenite), perhaps by interaction with sulphur bearing species mobilised into the wallrock, whilst types 3) and probably the bulk of type 2) forms by direct precipitation from the hydrothermal fluid. Type 2) grains are complex, containing multiple inclusions of other phases including gold. These grains also show concentric zonation in arsenic bearing pyrite overgrowths, pointing to fluctuation in fluid conditions during precipitation of these sulphides. Pyrite types 1) and 3) conversely show no complex internal structure and indicate stable conditions during formation.

Good constraint on formation temperature for both phyllosilicate and sulphide phases co-existing with the gold mineralisation is possible from chlorite and arsenopyrite phase chemistry. Chlorite grains intergrown with gold grains, indicate formation temperatures of between 350 and 370° C, whilst the arsenopyrite analyses indicate formation temperatures in the range 300 to 380°C. Chlorite analyses from the wallrock alteration (Chapter 3) indicate slightly higher temperatures between 380 and 400°C, indicating that the vein formation may have occurred at slightly lower than peak deformation and alteration temperatures. "Metamorphic" chlorite analyses from outside the alteration zone give typical greenschist values of between 350 and 360 °C.

Some estimate of ambient pressures during mineralisation is potentially possible from probe analyses of sphalerite. Sphalerite analyses from grains in equilibrium with pyrite and pyrrhotite indicate formation pressures of somewhat less than 2.5 kbars.

Sulphur is an important component of the introduced fluid and the stable sulphide assemblage allows some rough estimates of sulphur activity (fugacity) to be predicted from this. The FeS contents of both pyrrhotite and arsenopyrite are a function of temperature *and* sulphur fugacity. Microprobe analyses of the pyrite-included arsenopyrite grains (formed close to the pyrite-pyrrhotite buffer) suggest a log aS_2 values of between -7 and -7.8. Sulphur activity probably increases during formation of the arsenic bearing zoned overgrowths on type 2) pyrite, which fits with the restriction of pyrrhotite and arsenopyrite to the core areas of such grains. The possibility of gold being transported as a sulphur complex (Seward 1973) becomes an important consideration when fluctuations in sulphur activity might be linked to sulphide and contemporaneous gold precipitation.

The later mineralisation D3 is associated with a similar assemblage to that of the D2 veins with the exception of tourmaline. Tourmaline is common in both the D3 and D4 veins and appears to be the result of reaction between boron-bearing fluids with chlorite to form a dravite-schorl tourmaline. No introduction of sulphides is indicated during D4, but local remobilisation of existing sulphides in the D2 veins is indicated during the later event.

CHAPTER SEVEN - FLUID INCLUSION STUDIES

7.1 Introduction

Fluid inclusions are trapped parts of the fluid medium from which the host mineral phases grew. Such fluid inclusions are of two distinct associations (Roedder 1984), either a) primary, where the inclusions formed during the initial growth of the host crystal or, b) secondary, where the inclusions are situated on fractures or imperfections created and healed subsequent to the formation of the host crystal. It is quite evident that much information about the conditions during formation of the host mineral phases and subsequent events can be obtained from a study of these inclusions. Current techniques permit estimation of *P-V-T-X* from fluid inclusions, utilising experimental studies on hydrothermal fluid systems (Shepherd *et al.* 1985).

A major programme of fluid inclusion investigation was performed on quartz vein samples from the different mineralisation stages which are temporally constrained by the structural mapping and paragenetic studies. The main aim of the study was to define the possible provenance and behaviour of the hydrothermal fluid responsible for mineralisation related to the deformation events. Since quartz is ubiquitous in all the studied parageneses, this medium provided more than 95 % of the inclusions studied. Samples from the early gold bearing mineralising event also contained scheelite and this transparent mineral contained some inclusions suitable for study.

The fluid inclusion study particularly focussed on the D2 ribbon vein assemblage as this formed the most important stage for gold mineralisation. Fluids active during D2 are believed to have resulted in the discrete alteration envelope around the ribbon veins. Some definition of the D2 fluid chemistry could thus aid interpretation of the alteration assemblage discussed in Chapter 3. This study also allowed comparisons to be made between fluid inclusion populations in different spatial and paragenetic associations within the veins. Such a study would test the hypothesis presented in Chapter 4 which invoked cyclic fluid processes during vein formation.

7.2 Previous work

An increasing amount of microthermometric data collected from Archaean gold-quartz deposits has appeared in the literature (e.g. Smith *et al.* 1984, Ho *et al.* 1985, Santosh 1986, Robert & Kelly 1987, Teixeira *et al.* 1990 see also summary in Table 7.1).

Some consistent key features emerge from these studies that may point to a common model for, at least, broad fluid chemical parameters in gold-bearing Archaean structures. The presence of a low salinity (generally < 5 equiv. wt% NaCl), carbonic (up to 30 mole % CO_2), aqueous fluid of moderate

DEPOSIT	FLUID INCLUSION DATA	COMMENTS
CANADA		
Red Lake, Ontario *Brown & LaKind (1986)*	Primary, low salinity H_2O-CO_2; higher density CO_2, variable CO_2/H_2O contents T_{hom} = 110°C to 360°C	Authors interpret possible fluid unmixing during gold mineralisation
McIntyre-Hollinger Mine, Timmins, Ontario *Smith et al. (1984)*	Pseudo-secondary or primary H_2O-CO_2, T_{hom} = 220°C to 385°C, 3 to 24 mol% CO_2, CO_2 density 0.46 - 0.78 gcm^{-3}	Authors suggest possible fluid unmixing; fluids buffered by QFM; trapping conditions at 0.35 to 0.5 Kbars
Hollinger Mine, Timmins, Ontario *Wood et al. (1986)*	Primary H_2O-CO_2, variable phase proportions; 1 to 4 equiv wt% NaCl; 6 mol% CO_2; T_{hom} = 225°C to 355°C, mean 277°C; minor CH_4; CO_2 density 0.65 gcm^{-3}	Authors suggest phase separation during gold mineralisation
O'Brien Mine, Cadillac, Quebec *Krupka et al. (1977)*	Primary H_2O-CO_2 with constant phase proportions; T_{hom} = 210°C to 380°C	Homogeneous trapping of early fluid
Sigma Mine, Val d'Or, Quebec *Robert & Kelly (1987)*	Secondary H_2O-CO_2 inclusions with <10 equiv wt% NaCl, 15-30 mol% CO_2; T_{hom} = 285°C to 395°C	Authors suggest episodic fluid unmixing
AUSTRALIA		
Yilgarn Block, Western Australia *Ho et al. (1987)*	Primary H_2O-CO_2, some with variable phase proportions; 20 to 30 mol% CO_2; <2 equiv wt% NaCl; T_{hom} = 200°C to 390°C	Suggestion of unmixing during mineralisation
ZIMBABWE		
Golden Valley Mine, Zimbabwe *Foster (1990)*	Primary H_2O-CO_2; 0.1 to 5.9 equiv wt% NaCl; T_{hom} = 210°C to 320°C	Trapping estimated at 370°C to 440°C, 1.5 to 2 Kbars. Author suggests gold precipitation due to cooling and fluid-rock interaction.
Dalny Mine, Zimbabwe *Carter (1990)*	Primary H_2O-CO_2; 5-10 mol% CO_2; average 6.74 equiv wt% NaCl; T_{hom} ave. = 222°C	Trapping estimated at 390°C ± 20°C; 3.6 ± 0.3 Kbars. Gold precipitation due to sulphide precipitation and lowering of fS_2
INDIA		
Champion Reef, Kolar, South India *Santosh (1986)*	Secondary coexisting CO_2 rich and CO_2 poor CO_2-H_2O inclusions; 7 to 12 equiv wt% NaCl; CO_2 density 0.88 to 0.81 gcm^{-3}; 5 to 15 vol% CO_2; T_{hom} = 220°C to 260°C	Author suggests fluids trapped at solvus during unmixing
BRAZIL		
Fazenda Brasileiro, Bahia, Brazil *Teixeira et al. (1990)*	Primary H_2O-CO_2-CH_4; ave 60 mol% CO_2; ave density 0.83 to 0.88; T_{hom} = 255°C to 390°C; <10 equiv wt% NaCl	Trapping estimated at 400°C and 3 Kbars by authors. Gold precipitated by fluid-wallrock interaction

Table 7.1 - Published fluid inclusion studies for selected Archaean gold deposits

density (0.7 to 1.0 g cm^{-3}), is ubiquitous. The very strong cluster of proposed formation temperature between 250° and 350°C is apparent. Pressure estimates for entrapment are less well confined with ranges of 700 bars (Spooner *et al.* 1987) to 4000 bars (Safonov *et al.* 1984).

Chemical studies of dissolved ionic species in fluid inclusions from Archaean deposits are even rarer (e.g. Ho 1987, Robert & Kelly 1987) and these data are summarised in Table 7.2. The data obtained by Robert & Kelly (1987), and Ho (1987) are from the analysis of leachate from quartz crushed and leached in deionised water. Alternative bulk analytical methods such as lanthanum-doped crush-leach (Bottrell *et al.* 1988 or D-ICP (Thompson *et al.* 1980) are applicable having been used in other ore-environments. It sees that perhaps the latter technique is preferable in cases of complex paragenetic relationships with, for example, abundant solid inclusions in the inclusion-bearing phase (Rankin *et al.* 1990). Since the presence of significant CO_2 in fluid inclusions from Archaean vein gold deposits is ubiquitous, volatile analyses from Archaean ore fluids are more common (e.g. Burrows & Spooner 1986, Spooner *et al.* 1987, Walshe *et al.*1988). Bulk analysis is by decrepitation and gas chromatography-mass spectrometry yields measurements of H_2O, CO_2, CH_4 and N_2 together with qualitative measurements of other species (Shepherd & Miller 1988, Spooner *et al.* 1987). Microscope mounted Laser-Raman spectroscopy (Wopenka & Pasteris 1986, Dubessy *et al.* 1989) allows point analysis on individual inclusions. Published data from Archaean deposits is shown summarised in Table 7.3. Common features are highlighted, namely the presence of strongly carbonic fluids which contain in many cases detectable levels of CH_4, H_2S and N_2.

7.3 Methodology

From the selected vein-quartz samples, doubly polished fluid inclusion wafers of 100μm or less were prepared according to methods outlined in Shepherd *et al.* (1985). Some of the wafers were mounted on glass slides using lakeside, to enable them to be examined by electron-microscopy prior to microthermometry. The contained fluid inclusions were examined and classified using a normal optical microscope. This was complemented by a brief SEM cathodoluminescence study of the complex ribbon-vein quartz.

Techniques employed to study the fluid characteristics of the inclusions are described in detail in Appendix IV. Methods utilised included classic microthermometry on the prepared fluid inclusion wafers (Shepherd *et al.* 1985) Other techniques employed include decrepitation-ICP (after Thompson *et al.* 1980), crush-leach-ICP (after Roedder 1984, Bottrell *et al.* 1988) and bulk volatile analysis of fluid inclusions (after Shepherd & Miller 1988) from carefully cleaned and selected quartz grains (see Appendix V for preparation technique). Finally, opened fluid inclusions were examined in the SEM (following the procedure for mounting broken polished wafers described in Shepherd *et al.* 1985), in order to examine decrepitates and possible daughter phases.

DEPOSIT	FLUID INCLUSION ANALYSIS	METHOD AND COMMENTS
Sigma Mine, Quebec *Robert & Kelly (1987)*	Atomic ratios Na/K = 7 to 82, Na/Ca = 0.4 to 6.2, K/Ca = 0.003 to 0.056	Crush leach (*after Roedder 1984*)
Pamour Mine, Ontario *Walsh et al. (1988)*	Atomic ratios Na/K = 3 to 10, Na/Ca = 0.3 to 50, K/Ca = 0.05 to 2	EDA analysis of inclusion decrepitates (*after Haynes & Kesler 1987*)
Red Hill, Australia *Ho et al. (1985)*	Atomic ratio Na/K = 7.8 to 14.9 (average 9)	Crush leach (*Ho 1986*)
O'Brien Mine, Cadillac, Quebec *Krupka et al. (1977)*	Atomic ratio Na/K ≈ 1 (post ore Na/K > 24)	Neutron activation of picked quartz

Table 7.2 - Published fluid inclusion fluid cation determinations for selected Archaean gold deposits.

DEPOSIT	VOLATILE ANALYSIS OF INCLUSIONS	ANALYTICAL METHOD
McIntyre-Hollinger Mine, Ontario *Smith et al. (1985)*	H_2O = 86-98 mol%, CO_2 = 1-13 mol%, CH_4 = 0.05-0.6 mol%, detectable CO and N_2	Gas chromatography, bulk analysis
Hollinger Mine *Spooner et al. (1987)*	H_2O = 93 mol%, CO_2 = 6 mol%, CH_4 = 0.5 to 1 mol%	Gas chromatography, bulk analysis
Sigma Mine, Quebec *Robert & Kelly (1987)*	H_2O = 75-95 mol%, CO_2 = 1-25 mol%, CH_4 = 0.1-1.5 mol%, traces CO and N_2	Gas chromatography, bulk analysis
Red Hill, Australia *Ho (1987)*	H_2O = 51-97 wt%, CO_2 = 8-49 wt%, CH_4 = trace	Raman spectroscopy, point analysis
Fazenda Brasileiro, Bahia, Brazil *Teixeira et al. (1990)*	H_2O = 39.5 mol%, CO_2 = 52.9 mol%, CH_4 = 6.1 mol%, N_2 = 1.3 mol%	Raman spectroscopy, point analysis

Table 7.3 - Published volatile analyses for selected Archaean gold deposits.

All the microscopy and microthermometry was carried out at Imperial College. Chemical analysis by ICP was also carried out at Imperial College, whilst the volatile analyses of fluid inclusions were obtained in conjunction with Dr. T. J. Shepherd at the British Geological Survey facility.

The data generated by these techniques was utilised to calculate likely *P-V-T-X* for the various fluid phases to be made, generally using the techniques of isochore construction described by Shepherd *et al.* (1985), together with calculated fluid alkali geothermometry and independent mineral geothermometers.

7.4 Optical Characterisation of Inclusion Types

Fluid inclusion wafers were cut from each of the vein assemblages outlined by the detailed structural and paragenetic study (summarised in Table 5.1 and in Table 7.4). The presence of quartz in all the stages of mineralisation made it a suitable choice for both microthermometric study and the chemical analysis of the fluid inclusions. The six distinct quartz stages, all contained primary inclusions (following the criteria of Roedder 1984) and many contained secondary inclusions. For the chemical analyses of inclusion fluids, it was obviously important to utilise material which contained inclusions primary to the paragenetic stage studied. A detailed optical study of fluid inclusion wafers, to characterise inclusion types prior to any analytical work, was crucial in this regard. The D2 assemblage study (Q2), included some electron microscope cathodoluminescence examination to assess the extent of recrystallisation in the Q2 quartz.

Quartz Stage 1 (Q1)

This quartz, taken from the pillow margin infillings (see Figure 3.2) probably represents what is considered to be the earliest quartz formed after lithification at Patchway. Inclusions in this quartz Stage are generally "pseudo-secondary" (following Roedder's criteria), showing a broad planar distribution to inclusions. Inclusions, which appear more secondary, are developed at mineral grain boundaries but the limited microthermometry data suggests that they are similar to the pseudo-secondary inclusions. Figure 7.1 shows typical inclusions, generally 3 to 10 microns long, two phase (liquid and bubble) inclusions. Inclusion "degrees of liquid fill" average 0.9 and Figure 7.2a suggests that there is no evidence for major variation in degrees of fill. Cross-cutting, tectonically-induced, trails of secondary fluid inclusions are generally absent from the samples collected, which in any event were deliberately chosen for their relatively undeformed nature. Quartz textures suggest that there has been no major recrystallisation subsequent to formation of the pseudo-secondary inclusions, which are termed Type 1 inclusions for this study.

Quartz Stage 2 (Q2)

Quartz from this paragenetic stage contains the most complex fluid inclusion assemblage, and forms the gold bearing paragenetic stage. The vein quartz forms characteristic "ribbons", region A in the detailed

Deformation Event	Mineralisation Assemblage	Quartz Stage	Fluid Inclusion Types
Regional Metamorphism ("D1")	Pillow margin infills, quartz-carbonate-epidote	Q1	Type 1 (P-L+V,aq)
D2	Ribbon quartz-sulphide-gold veins (020° trend)	Q2	Types 2A (P-L+L+V,carb), 2B (P-L+V,aq), 2C (S-L+V,aq)
D3	Quartz-sulphide (gold) veins (070° trend)	Q3	Types 3A (P-L+L+V,carb), 3B (S?-L+V,aq)
D4	Late quartz-tourmaline extension veins	Q4	Type 4 (P-L+V,aq)
D3/D4	Tonalite-hosted quartz-scheelite veins	Q5	Type 5 (P-L+L+V,carb)
Post D4	Late regional "barren" quartz veins	Q6	Type 6 (P-L+V,aq)

Table 7.4 - Summary of fluid inclusion types identified in the different vein assemblages.
Quartz stages are directly related to the deformation events discused in Chapter 5.
For the fluid inclusion types, P = primary, S = secondary, L = liquid, V = vapour, aq = aqueous (H_2O-Salts) and carb = carbonic-aqueous ($CO_2[\pm CH_4]$-H_2O-Salts).

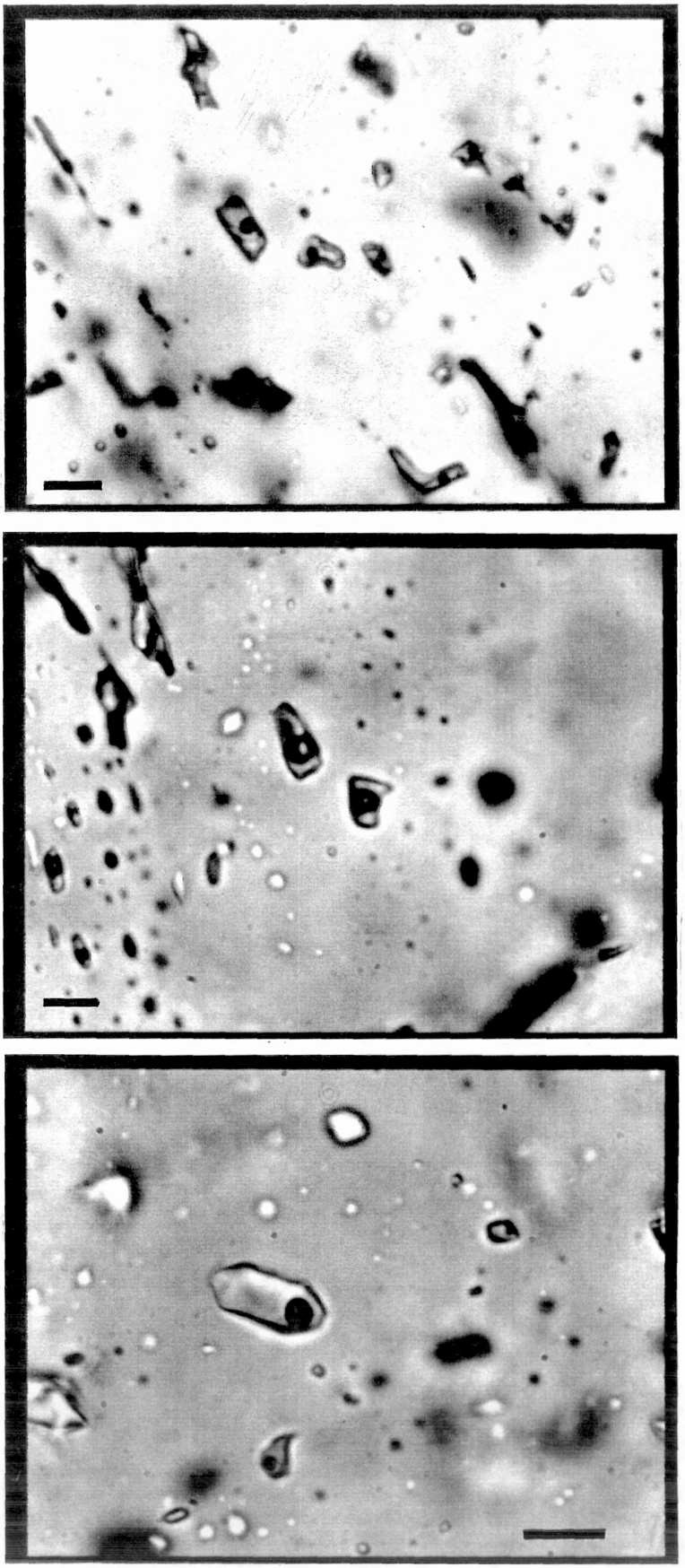


Figure 7.1 - Video images of Q1 fluid inclusions. One defined inclusion population is present, Type 1. Apparently planar groups of inclusions (see central image) appear to be primary and are crystallographically controlled. Scale bar in each case = 10 μm).

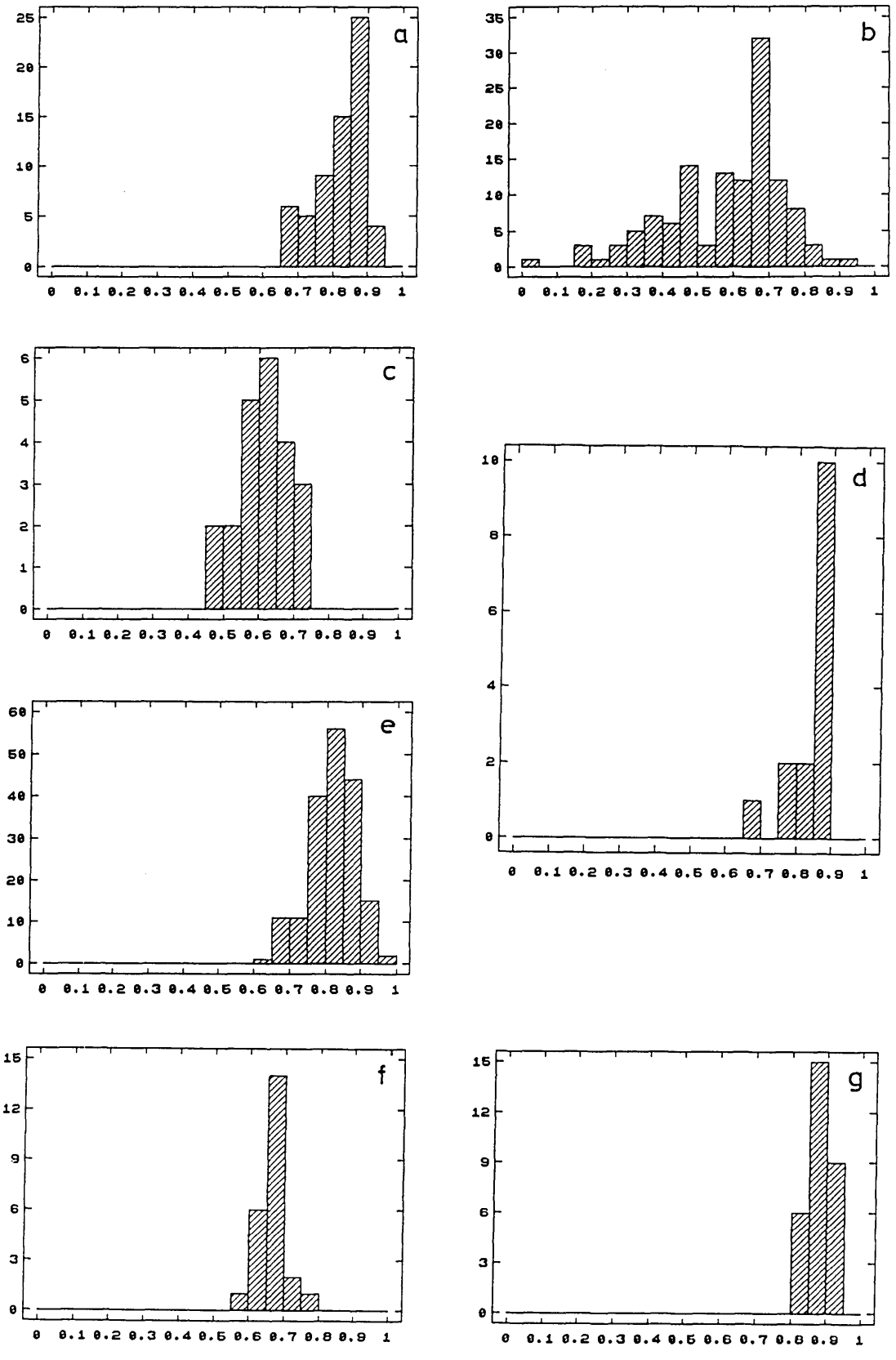


Figure 7.2 - Histograms showing degree of aqueous liquid fill of various fluid inclusion Types. On all graphs, x = degree of liquid fill and y = frequency. Key to graphs: a = Type 1, b = Type 2A, c = Type 3A, d = Type 3B, e = Type 4, f = Type 5 and g = Type 6 inclusions.

discussion in Chapter 4 as well as interstitial quartz in the B and C regions of the ribbon vein. Inclusions within these quartz ribbons comprise inclusions characteristically 2 to 10 μm in length which are clearly primary. These form ovoid to negative crystal shapes (Figure 7.3) and are best developed in the central portions of large quartz grains. The texture of the quartz in the ribbons is generally equigranular although grain size reduction through later plastic deformation is common. In these recrystallised areas inclusions are commonly absent.

Recrystallisation of host phases can affect the integrity of an inclusion, particularly with respect to volatile phases (Hollister 1990). One method of assessing this problem in quartz, which very often optically shows no sign of recrystallisation, is cathodoluminesence (CL). Most previous CL studies of quartz have focussed on identification of low temperature overgrowths on detrital quartz grains (Marshall 1988). However, studies of hydrothermal quartz using electron microscope-based, CL detectors also reveal subtle differences in CL response indicative of recrystallisation textures (Farmer & Herrington 1989, Poty *et al.* 1990), particularly pressure-solution features. The cause of the variations in the CL response of quartz is poorly understood, but may be the result of lattice defects or substitutions, particularly OH^- (Grant 1988). A limited investigation of the Q2 ribbon quartz at Patchway indicated the potential of such a technique.

Figure 7.4 shows a typical CL photomicrograph from a typical Q2 ribbon-vein. Early unpublished work (Grant *pers. comm.*) at Imperial College suggests that the darker luminescence may be due to incorporation of water into the quartz lattice during pressure solution. Improvement in emission intensity by use of a cold stage on the electron microscope based system (Marshall 1988, Kearsley & Wright 1988) could upgrade the usefulness of this tool in vein studies.

The conclusions from the Q2 vein CL study is that the core areas of most of the quartz grains studied are still intact and that primary inclusions should be preserved. The use of inclusions from areas close to grain boundaries can thus be avoided, as well as sections where pronounced recrystallisation is apparent.

"Secondary" inclusions close to and parallel to grain boundaries (see Figure 7.3b) are often present, although they are commonly modified by later deformation. This is particularly true in veins showing strong stylolitisation (evidence of grain boundary pressure solution). More common are secondary inclusion "trails" or healed tectonic discontinuities. This inclusion type is more common in quartz where strong later deformation events can be recorded in the wallrocks. These truly secondary inclusions are typically irregular in shape and of highly variable size from less than 2μm to over 30μm long. Very often the inclusions show necking down, indicative of continued recrystallisation along the trails. These inclusions can be shown to have similar thermometric properties to inclusions primary to the D4 event and are here termed Type 2C inclusions. A study was initiated with the aim of examining the inclusion

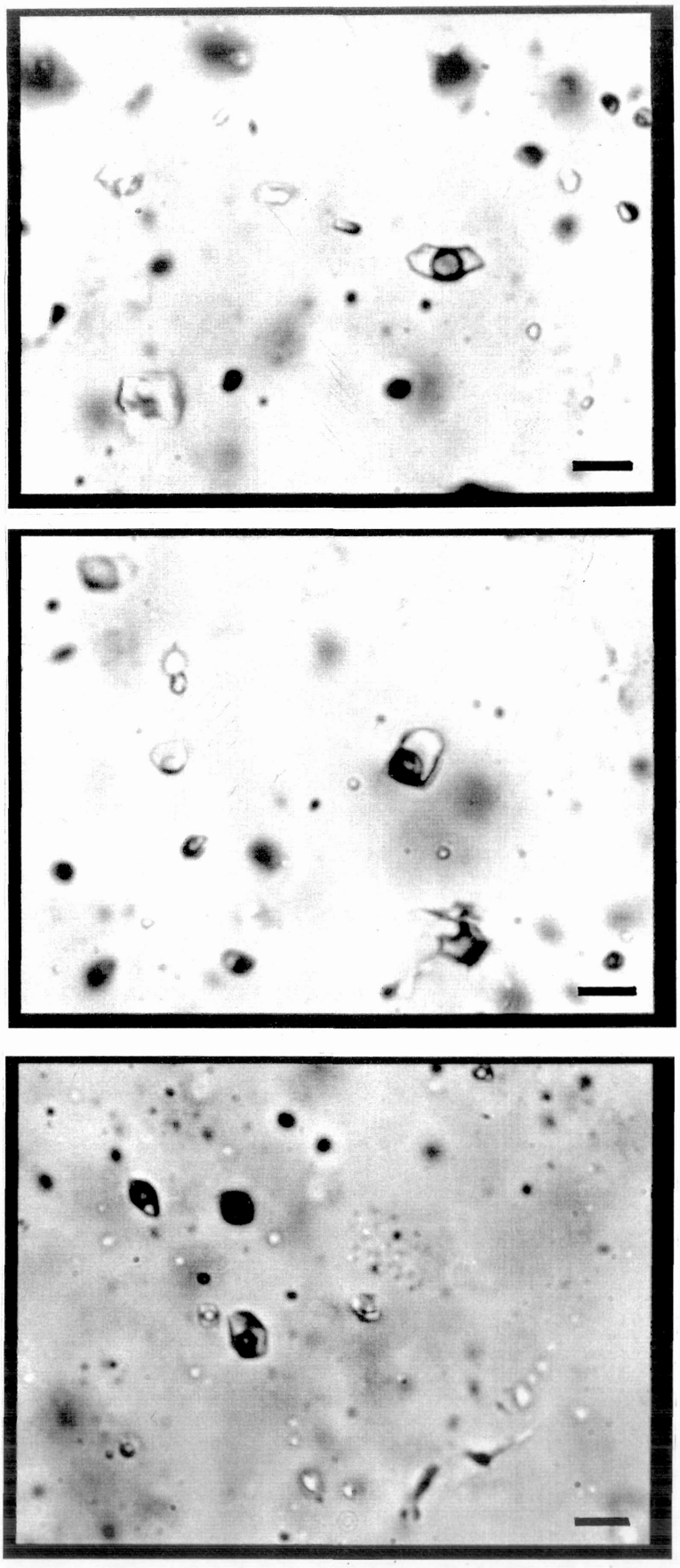


Figure 7.3a - Video images of Q2 fluid inclusions at 25 °C. Inclusions shown here are carbonic-aqueous, Type 2A primary inclusions. Upper image shows 2 phase liquid CO_2 (dark bubble)-aqueous liquid inclusion, middle image shows 3 phase vapour CO_2 (inner bubble)-liquid CO_2 (outer bubble)-aqueous liquid inclusion and lower image shows adjacent 2 phase inclusions with quite different degrees of aqueous fill. (Scale bar in each case = 10 μm).

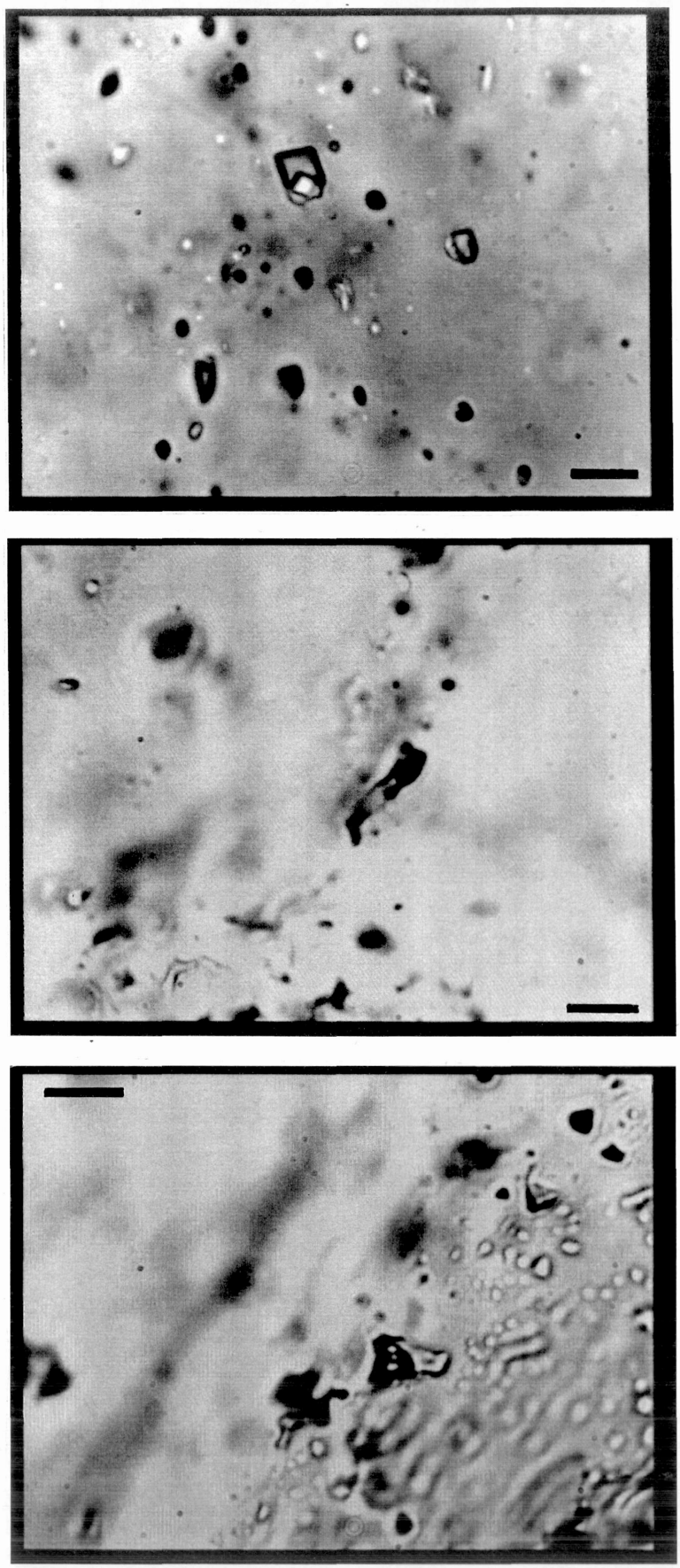


Figure 7.3b - Video images of Q2 fluid inclusions at 25 °C. Inclusions shown here are: upper image, carbonic-aqueous, Type 2A primary inclusion with included birefringent solid phase(white cube); middle and lower image, 2 phase aqueous liquid-vapour Type 2C inclusions located along fractures or grain boundaries. (Scale bar in each case = 10 μm).

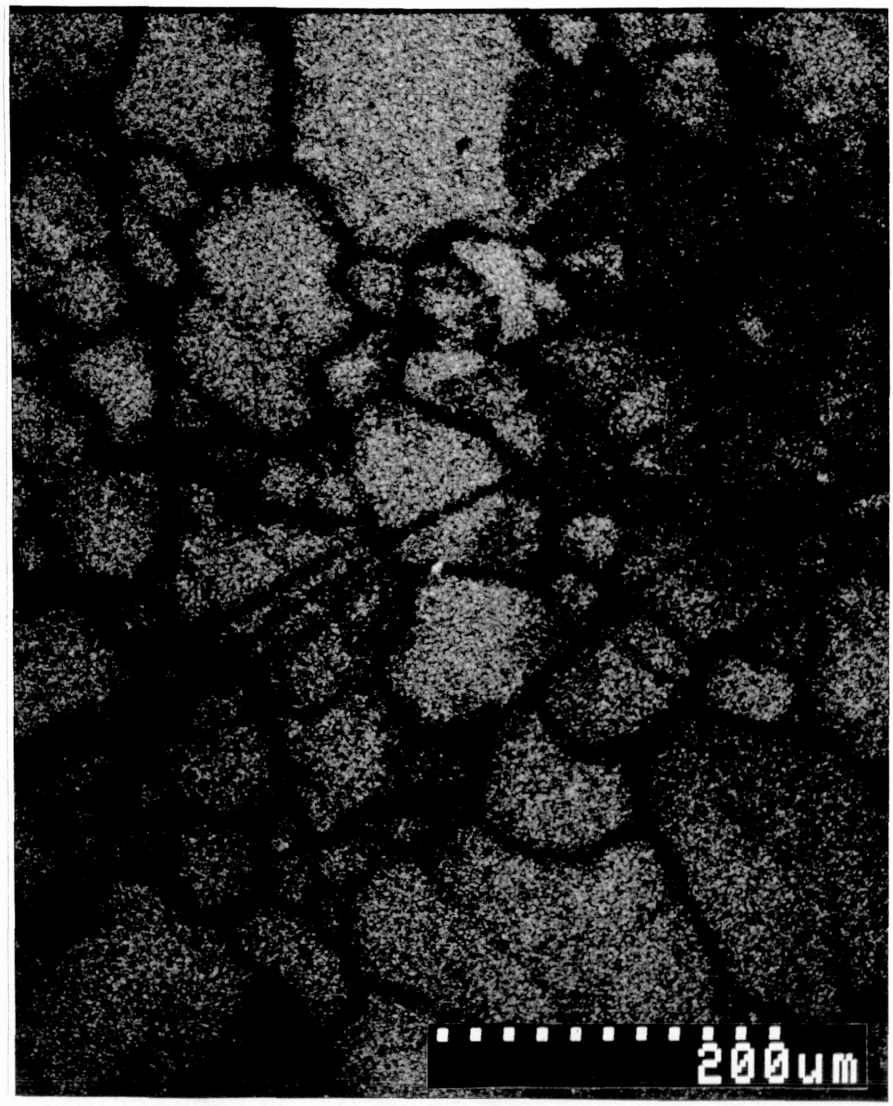


Figure 7.4 - SEM Cathodoluminescence (CL) image of Q2 quartz (sample 10-25). Image shows polycrystalline aggregate of quartz grains, typical of the white quartz ribbon areas of the vein. The grains show brighter luminescing cores with dark rims marking grain boundaries. Larger dark areas at grain boundaries mark areas of recrystallisation, core areas (containing Type 2A and 2B inclusions) are generally free from recrystallisation. Thin dark lines which cross the grains roughly east-west are tectonically induced cracks, healed by later quartz and containing secondary fluid inclusions (Type 2C).

trails for orientation (Tuttle 1949, Pecher *et al.* 1985). The aim was to see whether preferred trail directions could give new structural data. The preliminary results of this study were rather discouraging. Clearly defined secondary trails were only developed in Q2 quartz developed adjacent to extension veinlets containing Q4 quartz. However, the data collected did confirm that many of the inclusion trails in the Q2 quartz do contain identical fluid to the primary inclusions in Q4 quartz. Elsewhere, inclusion trails were poorly developed, cutting at best only one or two adjacent quartz grains. The inferred problem of any such study is the mechanical behaviour of a poly-crystalline quartz aggregate, such as the ribbon-quartz veins, during deformation. Mitra (1978) suggests that in the early stages of deformation in such an aggregate, cracks are developed largely in response to the orientation of crystal defects, rather than to the orientation of the applied stress field. Furthermore, failure of one of an aggregate of grains has the immediate effect of changing the local stress field for all adjacent grains. These effects are likely to result in very complex inclusion trail patterns. The simple patterns interpreted by Tuttle (1949) and Pecher *et al.* (1985) may have resulted from very specific stress conditions.

Gold and its associated sulphide mineralisation are clearly related to quartz containing abundant "primary" inclusions (Figure 7.5). *If the gold and its host quartz grains can be considered contemporaneous, then a constraint on the nature of the gold-bearing hydrothermal fluid by detailed fluid inclusion study is possible.* The CL study suggests that the quartz grain boundaries may well have suffered a protracted history of formation and recrystallisation, unlike the grain cores which are interpreted as being largely unaffected. Because of this, inclusions located close to the margins of quartz grains were not included in the microthermometry analysis due to recrystallisation problems. Truly "secondary" inclusions located in trails were measured however, as these inclusions are likely to be representative of fluid active during later deformation events. Q2 quartz was also contained scheelite which, as a transparent mineral, can also be used for microthermometric fluid inclusion study. This scheelite contains numerous small negative crystal primary inclusions (Figure 7.6). Secondary inclusions were not seen in the scheelite grains studied, although some empty primary inclusions were seen, the contents perhaps lost through brittle fracturing of the inclusion wall during later deformation.

The primary inclusions in both the quartz and co-existing scheelite grains of the D2 assemblage are generally quite similar. They appear to be CO_2-bearing aqueous inclusions which show either two (L+V or L+L) or three (L+V+L) phases at room temperature (Type 2A inclusions). The degree of aqueous fill is highly variable (Figure 7.2b), perhaps indicative of trapping of immiscible fluids during crystallisation of the quartz (Ramboz *et al.* 1982). This observation is considered to be highly significant, particularly as some of the most extreme cases of variable fill are seen in quartz grains directly associated with gold or gold bearing phases (Figure 7.7). Some of the inclusions in this region where fluid unmixing was suspected during entrapment, are aqueous-only inclusions and were shown to contain solid "daughter" phases (Type 2C inclusions). Although prismatic with square or rectangular cross-section, the minerals are birefringent (Figure 7.8). Electron microscopy and qualitative X-ray analysis

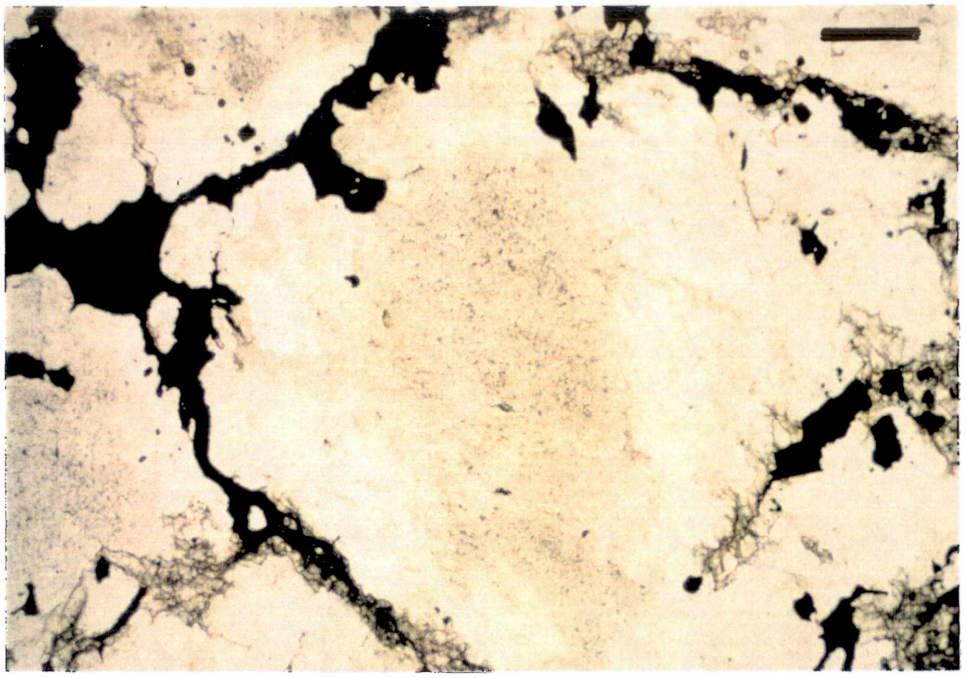


Figure 7.5a - Coarse gold and pyrite surrounding central quartz grain. Turbid central area of quartz contains abundant tiny (5 μm) carbonic-aqueous inclusions. (Scale bar 1 mm)

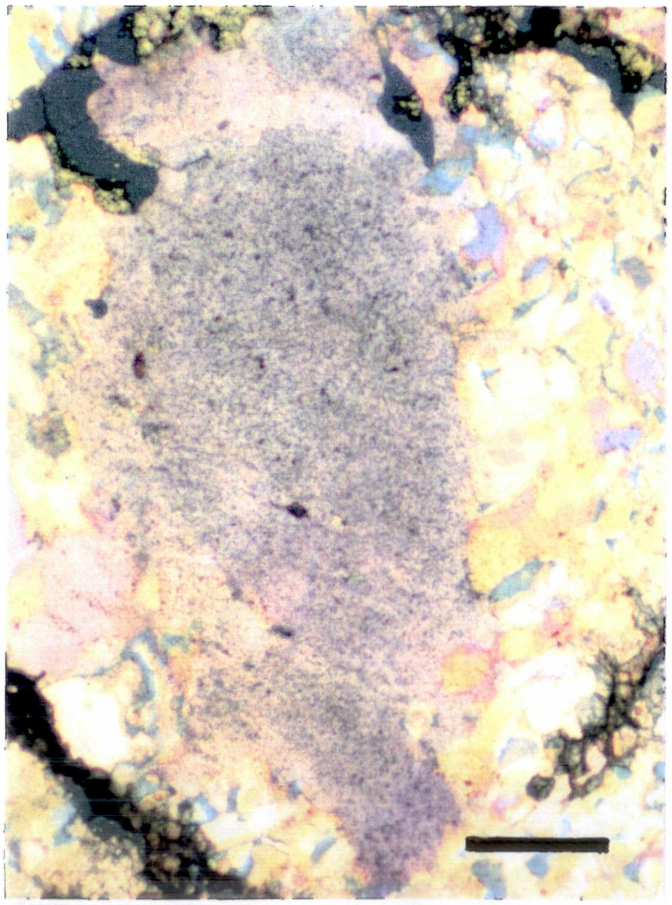


Figure 7.5b - Same view as above in crossed polars. Inclusion-rich turbid area clearly forms one large remnant quartz grain not recrystallised. Clear, inclusion-free areas are recrystallised to smaller sub-grains and no primary inclusions remain. (Scale bar 1 mm)

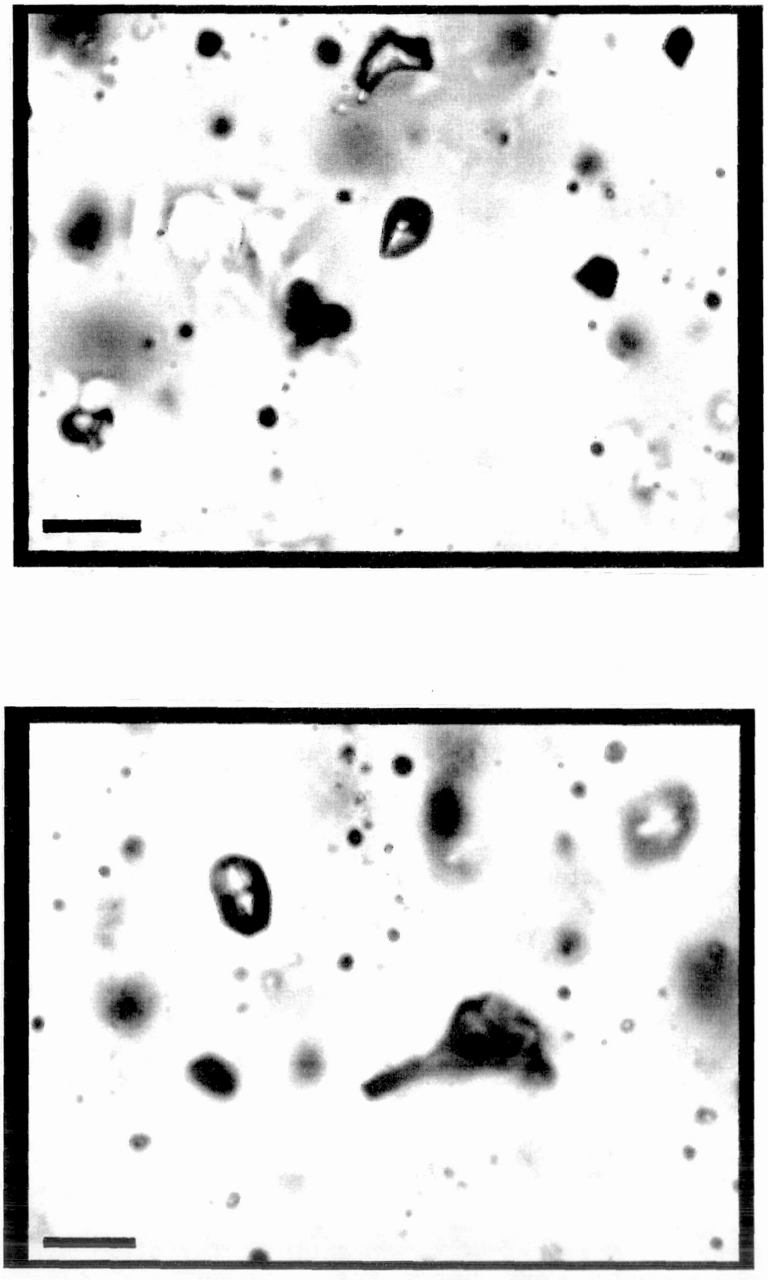


Figure 7.6 - Video images of fluid inclusions in scheelite from the Q2 assemblage at 25 °C. Inclusions shown here are 2 phase, carbonic-aqueous primary inclusions. (Scale bar in each case = 10 μm).

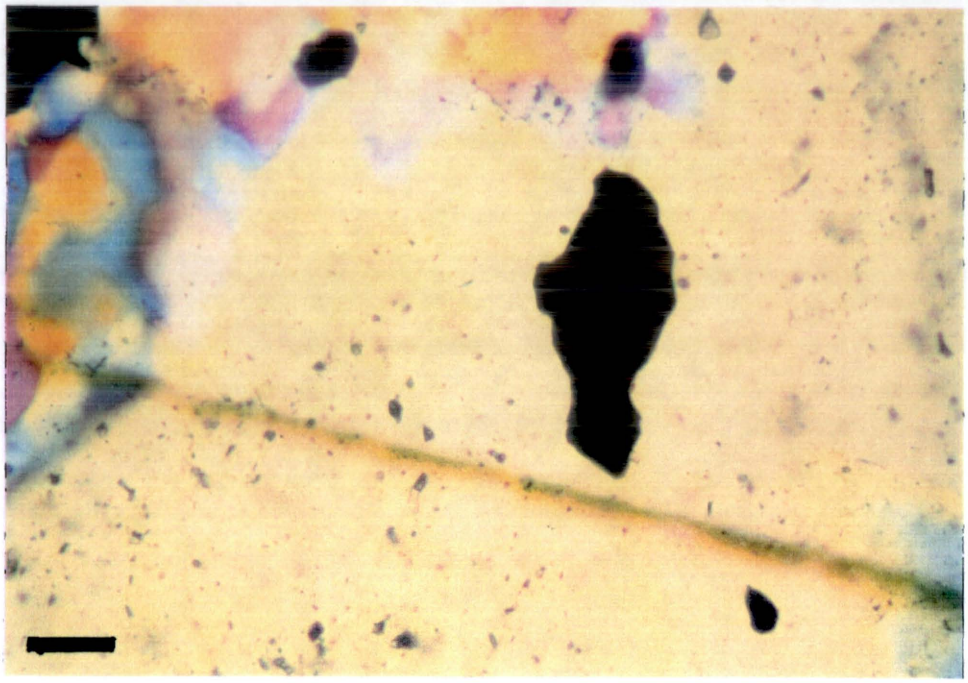


Figure 7.7a - Gold grain entirely hosted within single quartz grain which contains primary carbonic-aqueous inclusions. Crossed polars show grain boundary lies top left of field. Sub-horizontal line is etch mark on slide mount below lakeside mounted fluid-inclusion wafer. Mounting wafers on slides with lakeside permits thinner wafers to be made (<60 μm) and also allows SEM examination before microthermometry. (Scale bar 50 μm)

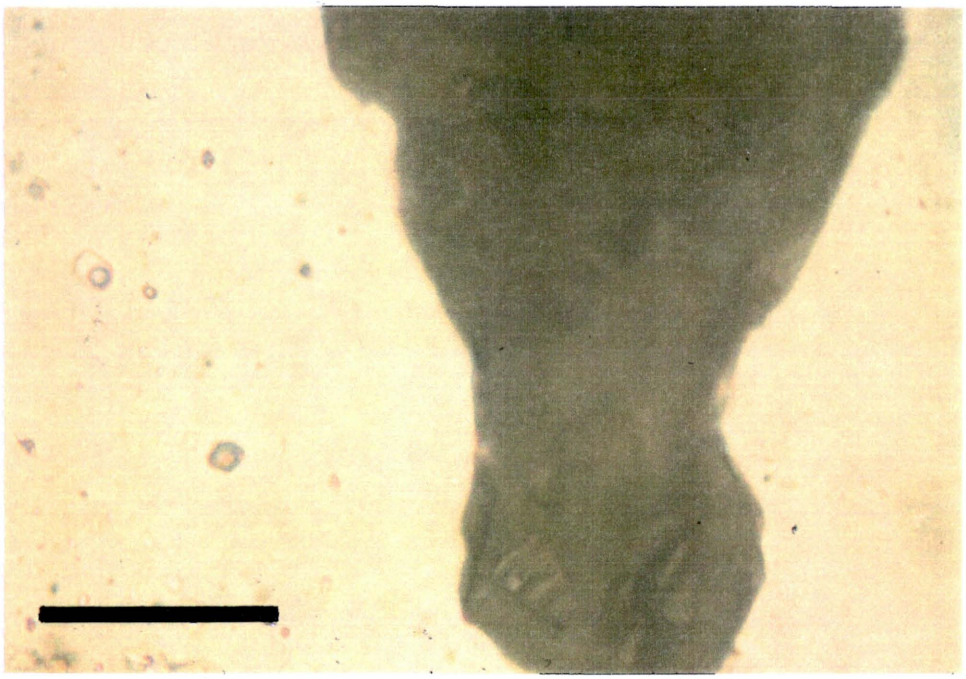


Figure 7.7b - Close up of view above showing fluid inclusion detail. Carbonic-aqueous inclusions, primary with respect to the quartz grain encapsulating gold, show extreme ranges in degree of fill. Two larger inclusions to the left of the gold grain (centre) show the upper inclusion to be aqueous dominant whilst the lower inclusion is clearly more carbonic (darker bubble in both cases). (Scale bar 50 μm)

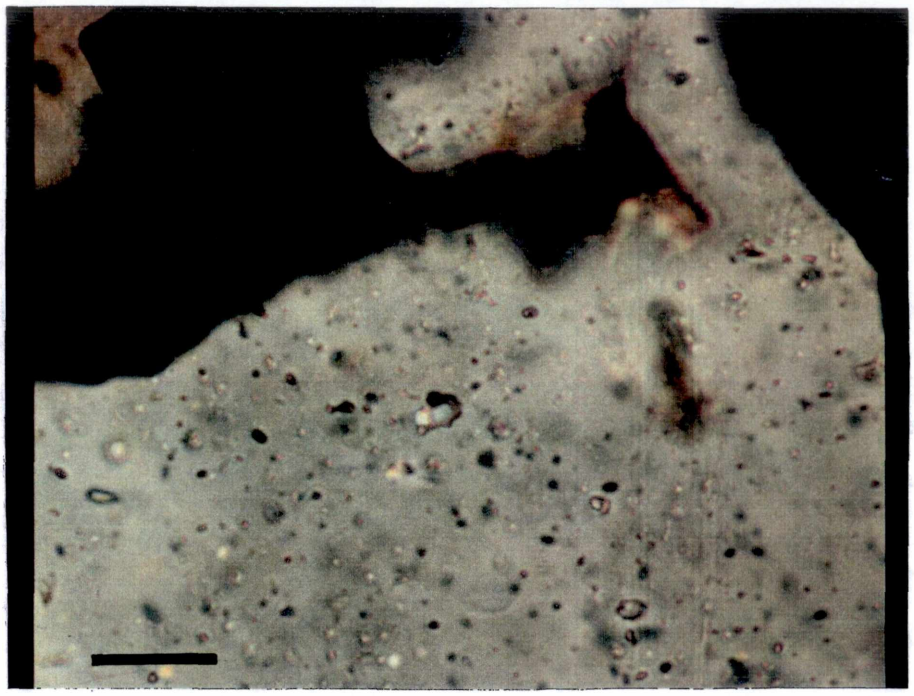


Figure 7.8a - Fluid inclusion (centre field) in quartz containing birefringent solid viewed under crossed polars (Sample 10-25). Dark phase above is pyrite (cubic habit) which contains tiny gold inclusions. (Scale bar 50 μm)



Figure 7.8b - Secondary electron image of opened fluid inclusion from sample shown above. Small (5 μm) carbonic-aqueous inclusions, primary with respect to the host quartz grain occasionally show solid phases. Here a tiny rectoid phase is seen inside the opened inclusion.

suggests that the mineral may be anhydrite.

The inferred "unmixing" phenomenon, suggested above, was studied on the scale of a single grain in a high-grade, gold bearing sample. In this sample, a thin quartz ribbon cuts highly sulphidised wall rock, and coarse visible gold is associated with minor sulphides, hosted entirely within a single quartz grain (Figure 7.5). From this textural evidence it appears that gold was formed during early quartz growth (perhaps trapped as a solid phase). Therefore during the growth of a single quartz grain, the unmixing of a CO_2 bearing hydrothermal fluid and the precipitation of gold may be linked.

In summary, three broad inclusion types are identified in the Q2 quartz and scheelite. Co-existing primary carbonic-aqueous (Type 2A) and aqueous (Type 2B) inclusions are common in the unstrained cores of quartz grains which have suffered no apparent recrystallisation. Late, cross-cutting, healed fractures host aqueous inclusions (Type 2C) which are clearly secondary.

Quartz Stage 3 (Q3)

The inclusions found in this quartz Stage are generally tiny (< 5μm long axis) and poorly developed. The quartz in the Munya-Skati vein (for location see Figure 5.18) particularly has suffered some degree of recrystallisation and hence microthermometric data from this quartz are much less easy to obtain. Typical inclusions are shown in Figure 7.9. The types comprise co-existing CO_2-bearing aqueous inclusions (Type 3A) together with aqueous inclusions (Type 3B). Unlike the Type 2A inclusions, the Type 3A inclusions show a more consistent degree of fill (Figure 7.2c). The Type 3B inclusions also show a very consistent degree of aqueous fill (Figure 7.2d). Although the Type 3A and Type 3B inclusions look co-genetic, the general lack of inclusions and suspicions of quartz recrystallisation make this observation tentative.

Quartz Stage 4 (Q4)

Fluid inclusions identified as primary are typically 5 to 12 μm in length, but never exceed 20 μm in length (Figure 7.10). These, Type 4, inclusions are often irregular to sub-negative crystal shapes with a degree of fill around 0.85 (Figure 7.2e). As outlined above, there is strong evidence that the Type 2C, secondary inclusions, seen as cross-cutting trails in the Q2 quartz may also contain the same fluid as the Type 4 inclusions. The thermometric data from both the Type 4, primary, and Type 2C, secondary, inclusions is therefore discussed together.

Quartz Stage 5 (Q5)

Inclusions in this quartz are comparatively large, often 10 to 15 μm in length (Figure 7.11). They occur as commonly irregular, and often negative-crystal shapes, and would appear to be generally primary in character. Most inclusions are CO_2-bearing aqueous (Type 5) inclusions, showing fairly consistent degrees of aqueous fill (Figure 7.2f). Some secondary aqueous inclusions were also seen, particularly

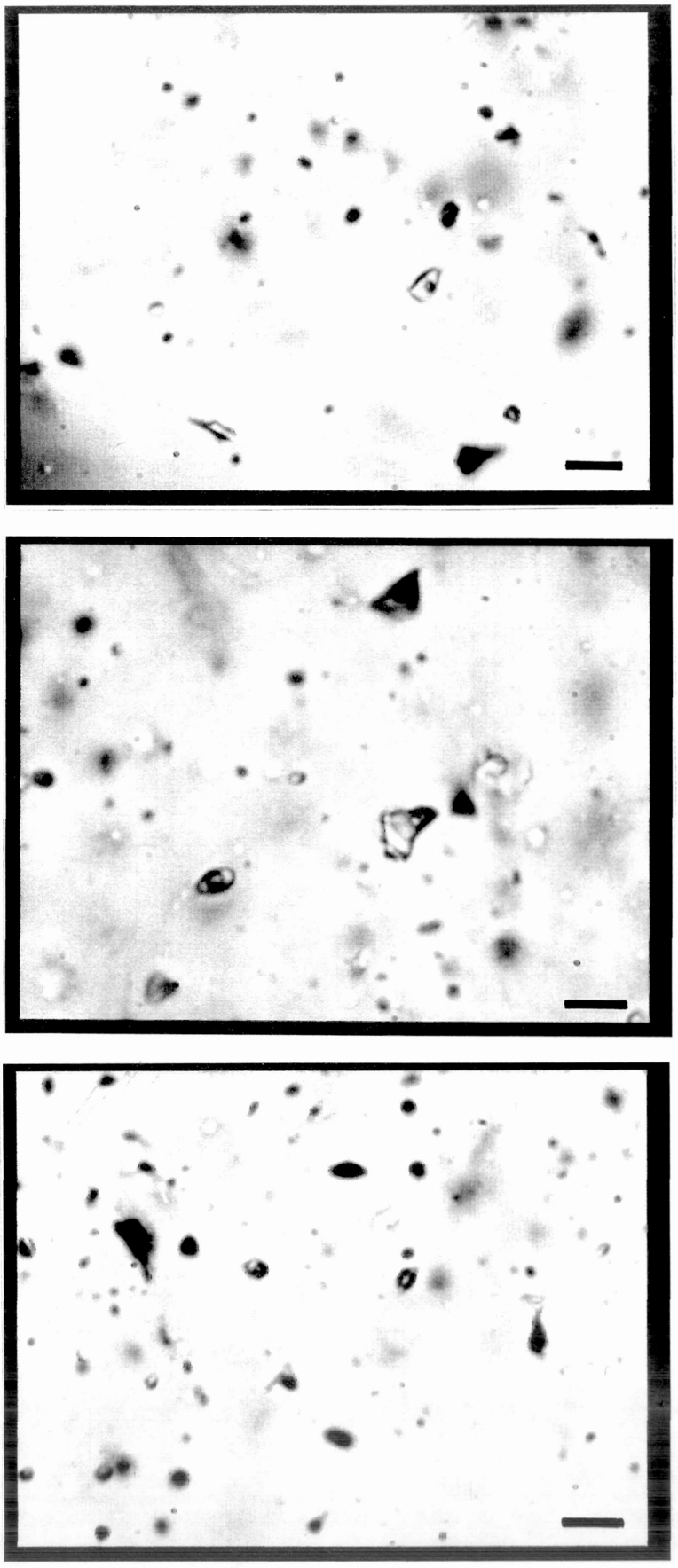


Figure 7.9 - Video images of Q3 fluid inclusions at 25 °C. Inclusions shown here are: A - 2 phase, aqueous-vapour primary? Type 3B inclusions, B - 2 and 3 phase carbonic-aqueous Type 3A primary inclusions and C - mixed inclusions (A and B above). (Scale bar in each case = 10 μm).

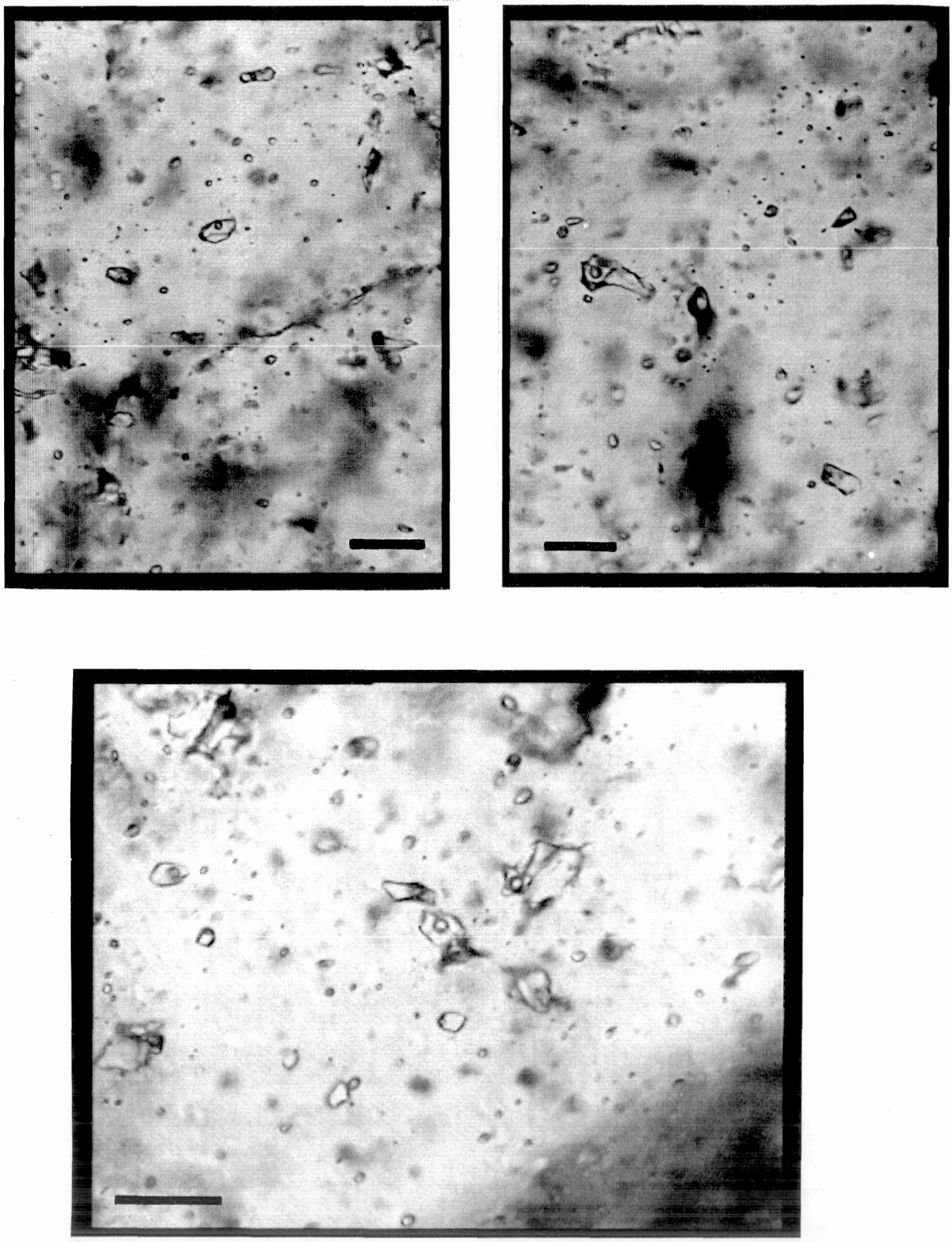


Figure 7.10 - Video images of Q4 fluid inclusions at 25 °C. All inclusions shown here are 2 phase, aqueous-vapour primary Type 4 inclusions. (Scale bar in each case = 10 μm).

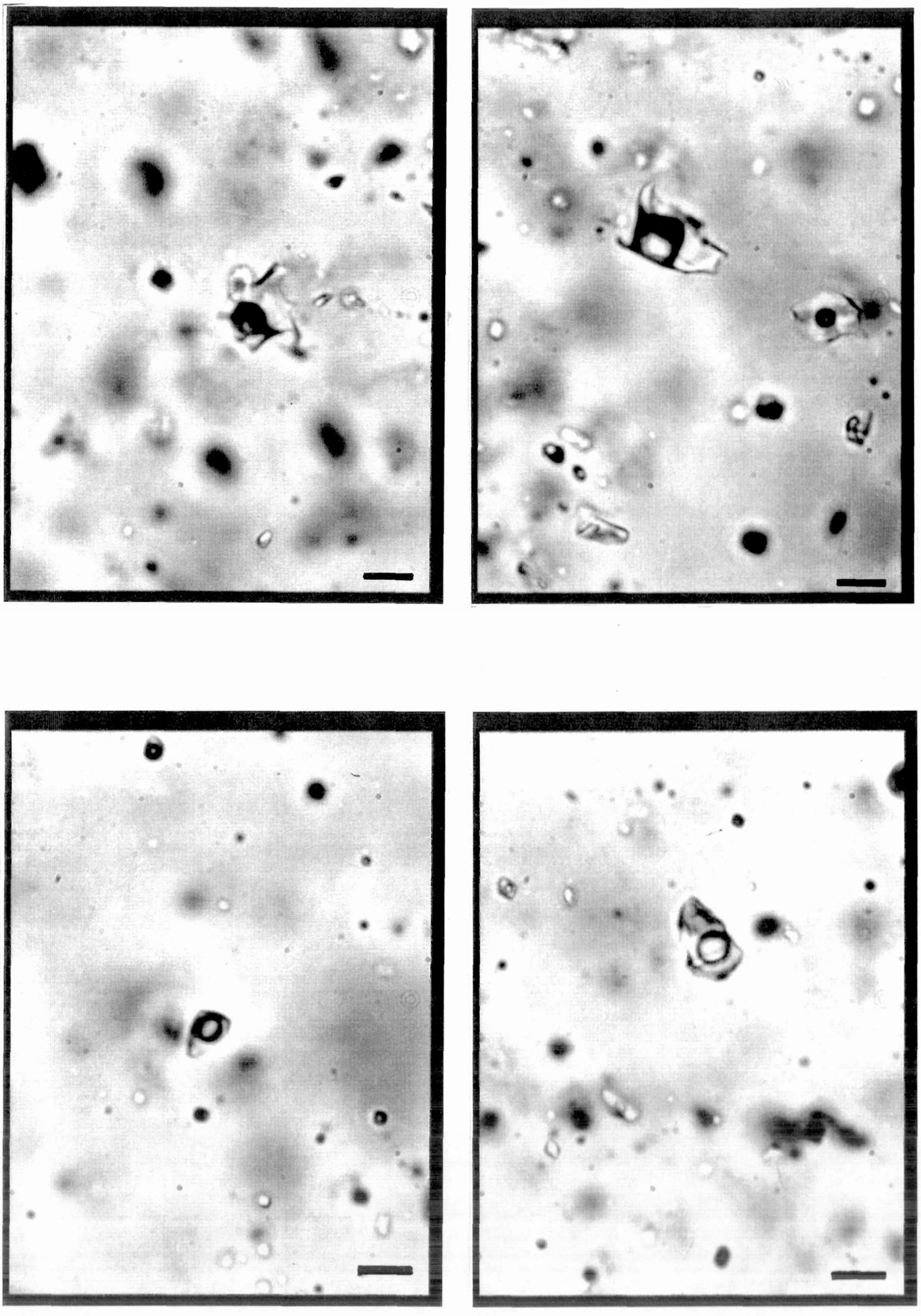


Figure 7.11 - Video images of Q5 fluid inclusions at 25 °C. All inclusions shown here are 2 phase, carbonic-aqueous, primary Type 5 inclusions. (Scale bar in each case = 10 μm).

at quartz grain boundaries, and these are generally less than 5 μm in size. The carbonic-aqueous primary inclusions are here termed Type 5 inclusions.

Quartz Stage 6 (Q6)

Inclusions in this quartz stage are very small (generally < 5 μm), apparently primary inclusions (Figure 7.12). They are aqueous type with degrees of fill greater than 0.8 (Figure 7.2g) and are termed Type 6 inclusions.

Figure 7.13 is a synoptic sketch of the inclusion types discussed in this section. The figure also indicates the broad spatial distribution of the inclusions within the quartz studied. Table 7.4 summarises the various quartz generations, Q1 to Q6, discriminated by the structural study, and links the fluid inclusion types to quartz stage, and thus deformation event.

7.5 Microthermometric Study

The following table summarises the abbreviations for phase changes recorded during the fluid inclusion microthermometry study. Equipment calibration gives accuracies of the phase changes measured of: ± 0.2°C in the range -65°C to 30°C, ± 0.5° between 30°C and 150°C and ± 2°C between 150°C and 350°C.

T_e	= Eutectic temperature or first appearance of melt in aqueous only (H_2O-NaCl) inclusions.
T_{mI}	= Last ice melt temperature in aqueous only (H_2O-NaCl) inclusions.
T_{mCO2}	= Melt temperature of solid CO_2 phase in carbonic (CO_2-H_2O-NaCl) inclusions.
T_{mClath}	= Melt temperature of solid clathrate phase in carbonic inclusions.
T_{hCO2}	= Homogenisation temperature (to liquid or vapour) for CO_2 phase in carbonic inclusions.
T_{htot}	= Homogenisation temperature of all phases in any inclusion type to liquid or vapour.

All corrected data from the inclusion microthermometry are detailed in Appendix IV with data presented here in summary, graphic, form. Tables 7.5 to 7.7 show tabulated summary statistics for the microthermometric data for all the inclusion types.

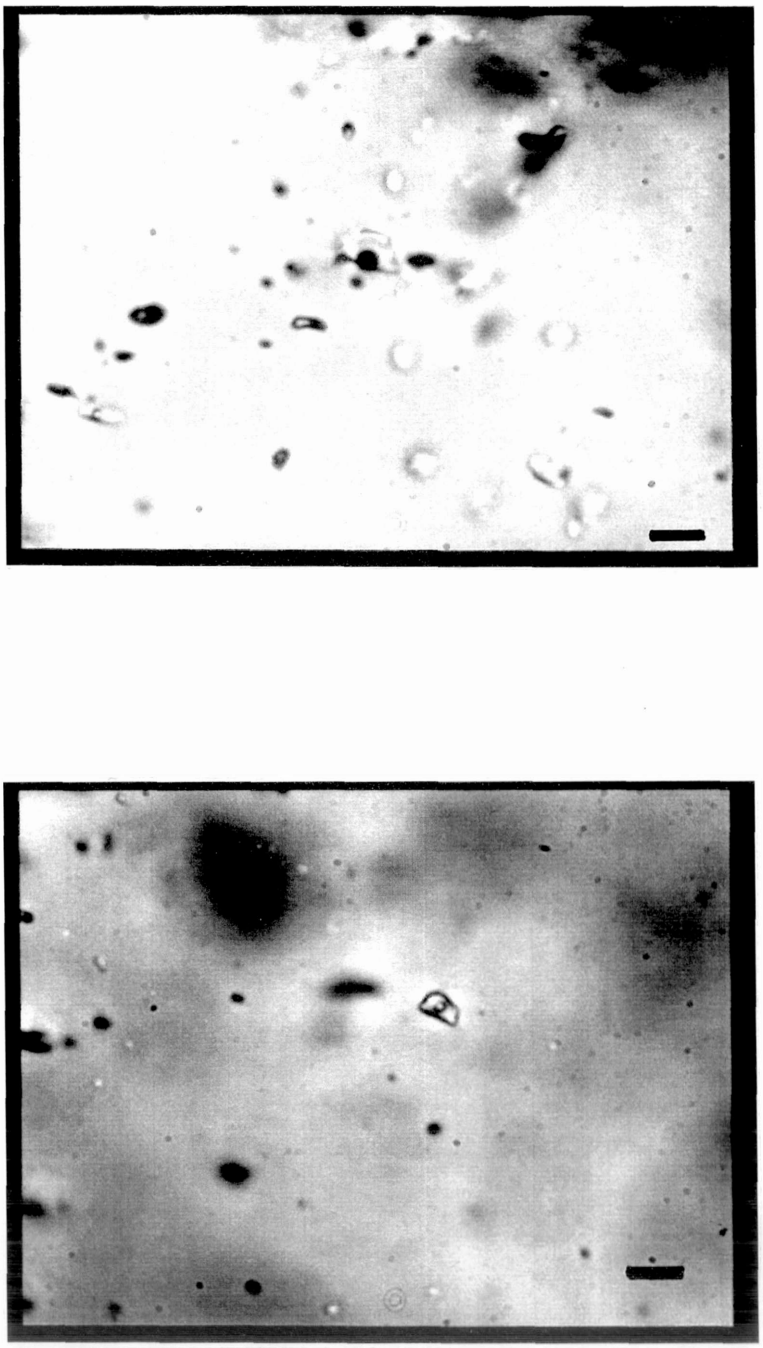


Figure 7.12 - Video images of Q6 fluid inclusions at 25 °C. All inclusions shown here are 2 phase, aqueous liquid-vapour, primary Type 6 inclusions. (Scale bar in each case = 10 μm).

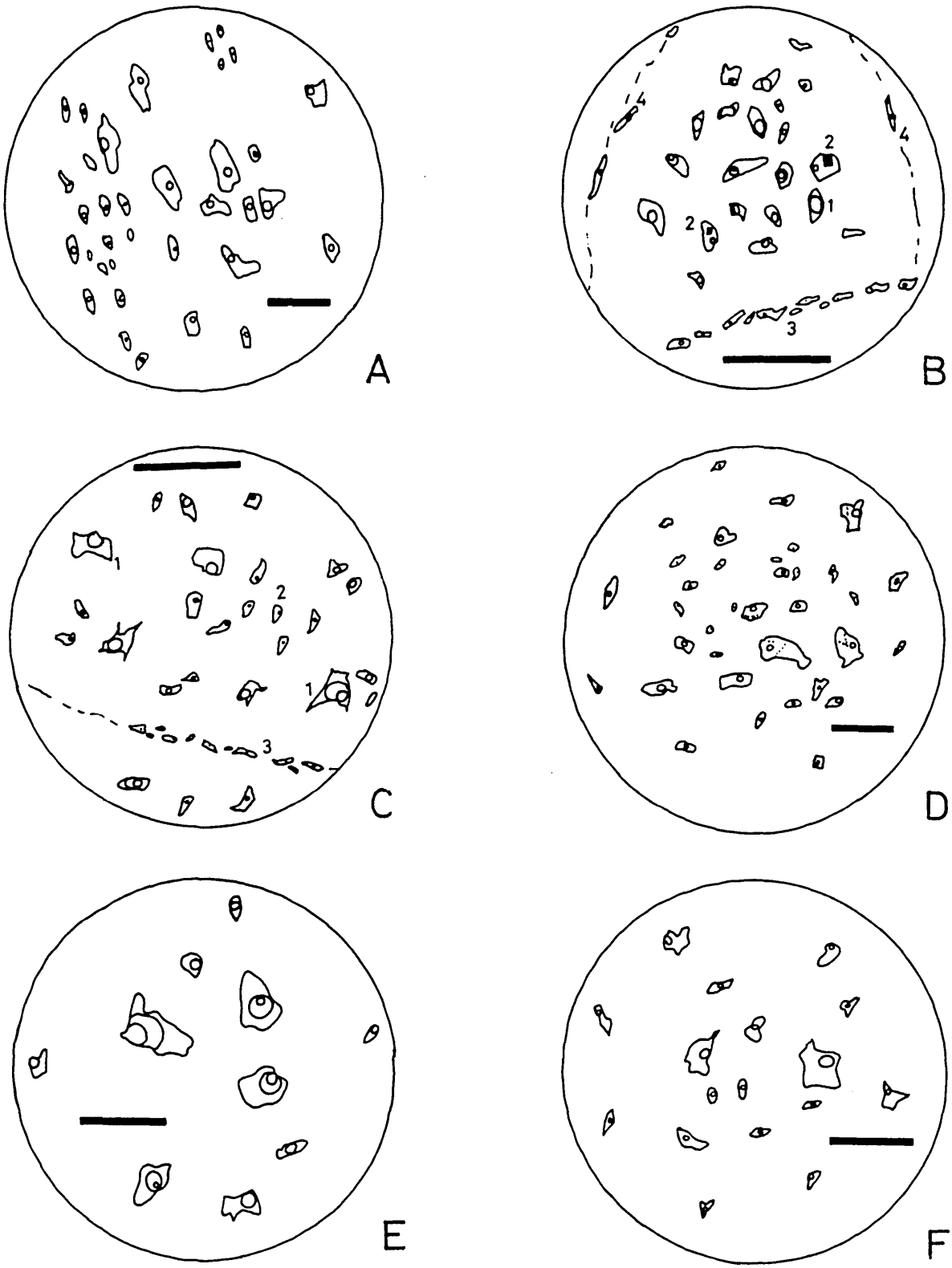


Figure 7.13 - Synoptic sketch of typical fields of view for different quartz stages. Field A = Q1, H_2O-NaCl (Type 1) inclusions (Bar = 10 μm). Field B = Q2, "1" are CO_2-H_2O-NaCl (Type 2A), "2" are H_2O-NaCl (Type 2B)," 3" are H_2O-NaCl (Type 2C) and "4" are H_2O-NaCl inclusions, too small to measure phase changes (Bar = 20 μm). Field C = Q3, "1" are CO_2-H_2O-NaCl (Type 3A), "2" are H_2O-NaCl (Type 3B) and "3" are H_2O-NaCl inclusions, too small to measure phase changes (Bar = 20 μm). Field D = Q4, H_2O-NaCl (Type 4) inclusions (Bar = 10 μm). Field E = Q5, CO_2-H_2O-NaCl (Type 5) inclusions (Bar = 10 μm). Field F = Q6, H_2O-NaCl (Type 6) inclusions (Bar = 10 μm).

Type 1 inclusion microthermometry statistics

	Degree of Aqueous Fill	Te (n=1)	Tml (n=63)	Thtot (n=24)
Mean	0.85	-38.1	-2.7	158
Mode	0.90	-	-1.9	152
Std. Deviation	0.07	-	1.45	13.8
Minimum	0.70	-	-7.9	132
Maximum	0.95	-	-0.5	188

Type 2B inclusion microthermometry statistics

	Degree of Aqueous Fill	Te (n=3)	Tml (n=20)	Thtot (n=27)
Mean	0.82	-41.5	-3.5	299
Mode	0.90	-	-3.2	236
Std. Deviation	0.10	-	2.8	46.0
Minimum	0.70	-	-12.5	235
Maximum	0.90	-	-0.5	403

Type 3B inclusion microthermometry statistics

	Degree of Aqueous Fill	Te (n=2)	Tml (n=15)	Thtot (n=18)
Mean	0.86	-51.0	-8.5	162
Mode	0.90	-	-9.1	147
Std. Deviation	0.06	-	0.8	22.7
Minimum	0.70	-53.1	-10.1	134
Maximum	0.90	-49.0	-7.5	227

Table 7.5 - Summary microthermometry statistics for Type 1, 2B and 3B, aqueous inclusions.

Type 2A inclusion microthermometry statistics

	Degree of Aqueous Fill	$TmCO_2$ (n=125)	TmClath (n=125)	$ThCO_2$ (n=128)	Thtot (n=48)
Mean	0.60	-58.7	8.5	16.3	284
Mode	0.70	-57.1	8.5	27.9	301
Std. Deviation	0.17	2.60	3.3	23.7	26.5
Minimum	0.05	-68.5	-3.5	-85.7	220
Maximum	0.95	-54.4	18.9	32.6	352

Type 3A inclusion microthermometry statistics

	Degree of Aqueous Fill	$TmCO_2$ (n=22)	TmClath (n=17)	$ThCO_2$ (n=22)	Thtot (n=7)
Mean	0.64	-57.3	7.95	26.0	285
Mode	0.65	-57.1	10.5	29.9	275
Std. Deviation	0.07	0.75	1.7	5.26	21.7
Minimum	0.50	-60.4	5.9	12.9	258
Maximum	0.75	-56.7	10.7	31.3	325

Type 5 inclusion microthermometry statistics

	Degree of Aqueous Fill	$TmCO_2$ (n=24)	TmClath (n=24)	$ThCO_2$ (n=24)	Thtot (n=24)
Mean	0.70	-57.0	10.4	26.0	258
Mode	0.70	-56.9	10.7	26.7	260
Std. Deviation	0.04	0.43	0.75	1.72	12.5
Minimum	0.60	-58.2	8.7	22	238
Maximum	0.80	-56.6	12.2	29.9	267

Table 7.6 - Summary microthermometry statistics for Type 2A, 3A and 5, carbonic-aqueous inclusions.

Type 2C inclusion microthermometry statistics

	Degree of Aqueous Fill	Te (n=19)	Tml (n=84)	Thtot (n=83)
Mean	0.88	-42.2	-12.6	147
Mode	0.90	-47.9	-9.8	129
Std. Deviation	0.06	10.2	6.4	29.7
Minimum	0.80	-59.1	-30.6	93
Maximum	0.95	-24.5	-1.6	294

Type 4 inclusion microthermometry statistics

	Degree of Aqueous Fill	Te (n=13)	Tmh (n=7)	Tml (n=117)	Thtot (n=115)
Mean	0.86	-47.2	-22.4	-8.5	162
Mode	0.90	-49.1	-22.4	-9.1	147
Std. Deviation	0.05	8.3	0.5	0.8	22.7
Minimum	0.80	-50.9	-23.2	-10.1	134
Maximum	0.90	-41.0	-21.8	-7.5	227

Type 6 inclusion microthermometry statistics

	Degree of Aqueous Fill	Te (n=0)	Tml (n=30)	Thtot (n=30)
Mean	0.91	-	-6.13	157
Mode	0.90	-	-6.5	139
Std. Deviation	0.04	-	2.0	17.0
Minimum	0.85	-	-10.5	127
Maximum	0.95	-	-3.4	187

Table 7.7 - Summary microthermometry statistics for Type 2C, 4 and 6, aqueous inclusions

7.5.1 Microthermometry Results

Q1 Quartz Inclusions

Cooling these inclusions to -196°C produced only one phase change (formation of ice) in this inclusion type, Type 1. It is concluded, therefore, that the inclusions contain negligible phases apart from water and dissolved salts. On heating from frozen, a single eutectic measurement was recorded in a larger inclusion at -38.1°C. This suggests a more complex solute than simple NaCl-water. Possible causes of such a eutectic are H_2O-Na_2CO_3-K_2CO_3 or H_2O-NaCl-$FeCl_2$ (Borisenko 1977). On further heating, the last ice-melt temperature was recorded. The histogram of data from the Type 1 inclusions for T_{mI} (Figure 7.14a) shows a skewed, but nevertheless, relatively normal distribution, indicative of a single population of inclusions and hence fluid type. The mean temperature of -2.8°C equates to a 4.7 equivalent wt% NaCl salinity for the fluid (after Potter *et al.* 1978 and Hall *et al.* 1988), ignoring the effect of other solutes apart from NaCl. The expression of salinity as equivalent wt% NaCl is in line with current practice in the literature (Shepherd *et al.* 1985) The data for heating to homogenisation, T_{htot}, are all homogenisations to the liquid state (L+V = L). These data produce a similar shaped histogram for the Type 1 inclusions (Figure 7.14b), with a mean value of 160°C.

Q2 Quartz and Scheelite Inclusions

This stage of quartz formed during the development of the ribbon-quartz veins and associated gold mineralisation. Inclusion types in this quartz belong to the three groups discussed before: 1) Type 2A, primary CO_2-H_2O-NaCl, 2) Type 2B, primary H_2O-NaCl and 3) Type 2C, secondary H_2O-NaCl. Types 2A and 2B would appear to be co-genetic, since the same unstrained quartz grains can be shown to contain both inclusion types. Some of the microthermometric data have been obtained from scheelite, where small, primary, Type 2A inclusions are found. No Type 2B or 2C inclusions could be found in this mineral.

Cooling of these inclusion types down to -196°C highlighted the clearly different nature of the Type 2A inclusions compared to Types 2B and 2C. Type 2A inclusions all nucleated a third phase on cooling (L+L+V). The three phases were confirmed as aqueous liquid, carbonic liquid and gas after successive formation of ice and solid CO_2 during further cooling. Some inclusions formed no solid CO_2 phase even at -196°C (the limit to liquid nitrogen cooling), and the presence of another dissolved gas in the carbonic phase was suspected. Inclusion Types 2B and 2C showed similar phase changes on cooling to those of Type 1, and are thus aqueous (water + salts).

The Type 2B inclusions appear to co-exist with Type 2A, but are two phase inclusions with no sign of a major carbonic component in them. Isolated examples show possible evidence for a CO_2 melt, but this was not conclusive. A few T_e indicate temperatures around -41°C. Such a eutectic indicates other salts apart from NaCl, and the presence of $CaCl_2$ or carbonate species is suspected (after Borisenko

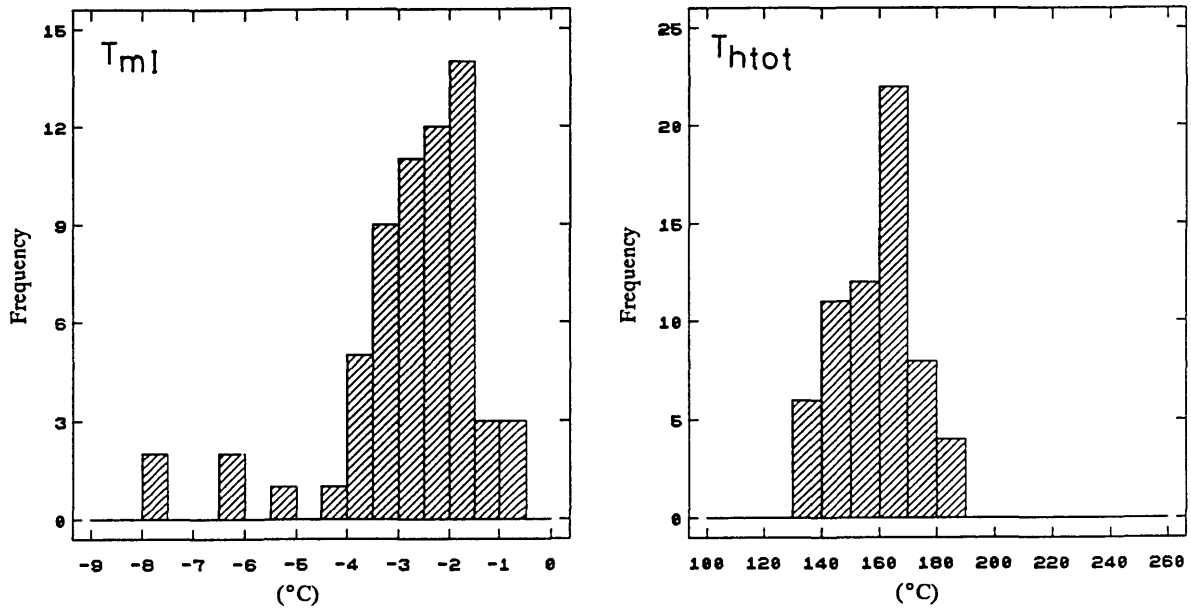


Figure 7.14 - Histograms of microthermometry of Type 1 inclusions.

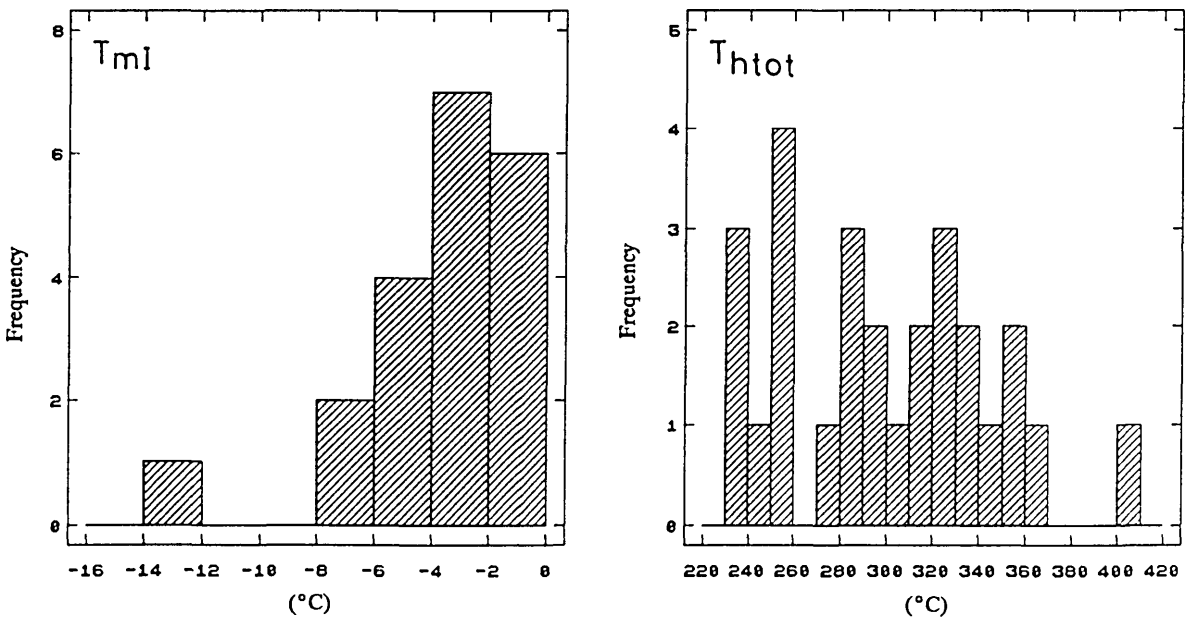


Figure 7.15 - Histograms of microthermometry of Type 2B inclusions.

1977). The T_{mI} data, measured on heating from frozen, is shown on Figure 7.15a. The data shows a rather skewed population, but has a mean of -3.5°C. This equates to a salinity of 5.5 equivalent wt% NaCl. Homogenisation (T_{htot}) data for the Type 2B inclusions are shown on Figure 7.15b. There is a very broad spread of data from 235°C to 403°C with a mean of 299°C. However, no clear normal distribution of the data is demonstrated.

Type 2A are the dominant primary inclusions in Q2 quartz. For such carbonic-aqueous inclusions, four main phase changes pertinent to interpreting *P-V-T-X* of the fluid can be recorded. These phase changes, T_{mCO2}, T_{mClath}, T_{hCO2} and T_{htot}, are all generally recorded during a heating run from the CO_2-phase freezing point, usually below -110°C. However, in some Type 2A inclusions, the CO_2 phase failed to freeze even at liquid nitrogen temperatures (-196°C). In addition, for certain inclusions, T_{hCO2} was measured during cycled cooling-heating, as the T_{hCO2} was lower than the T_{mClath}. Measurement of Th_{CO2} in the presence of clathrate produces errors in CO_2 phase density calculations. These four phase changes for the Type 2A data set are plotted as a series of histograms on Figure 7.16. Although broad peaks are clearly shown in all data sets, much of the data is spread away from the modal value in each case.

The data for T_{mCO2} (Figure 7.16a) shows a peak at the modal value of -57.1°C, with strong skewness towards values as low as -69°C (some inclusion data are missing where the CO_2-phase failed to freeze even at -196°C). There is, perhaps, suggestion of a second population of data centred on -62°C. Since the triple point for pure CO_2 at 1 atmosphere is -56.6°C, then the melt depression below this temperature is a clear indication of the presence of other miscible gases such as CH_4, N_2, Ar or other hydrocarbon gases (Shepherd *et al.*, 1985). T_{mClath}, in carbonic inclusions, is the melting temperature of CO_2 dominated gas hydrates (generally $CO_2 \cdot 5.75H_2O$, Van der Waals & Platteeuw 1959) formed during freezing of mixed carbonic-aqueous inclusions. The melting temperature of this relates directly to the salinity of the aqueous fraction of the inclusion in the case of a CO_2-H_2O-Salt system (Collins 1979). Again, assuming a pure NaCl solute, the CO_2 clathrate melts at 10.0°C above that for T_{lm} of a similar salinity H_2O-NaCl only fluid. No systematic, published experimental work on mixed cation salt systems is generally available, although the effect of other cations on clathrate melt would be expected to be similar to Na. Of more importance is the effect of the significant raising of the clathrate melt due to the presence of methane and higher hydrocarbons which form their own clathrates, so a measure of both miscible gas levels and possibly cation ratios in the aqueous phase is necessary to fully interpret clathrate melt temperature, in terms of dissolved salts. However, for inclusions where fairly pure CO_2 is indicated from the T_{mCO2}, "equivalent wt% NaCl values" are an adequate interpretation.

Figure 7.16b shows T_{mClath} plotted as a histogram for the Type 2A inclusions. Again a peak is defined by this data with quite a spread away from the modal value of 8.5°C. There is also suggestion of a second population centred on a modal value of around 12°C. Assuming the aqueous phase to be

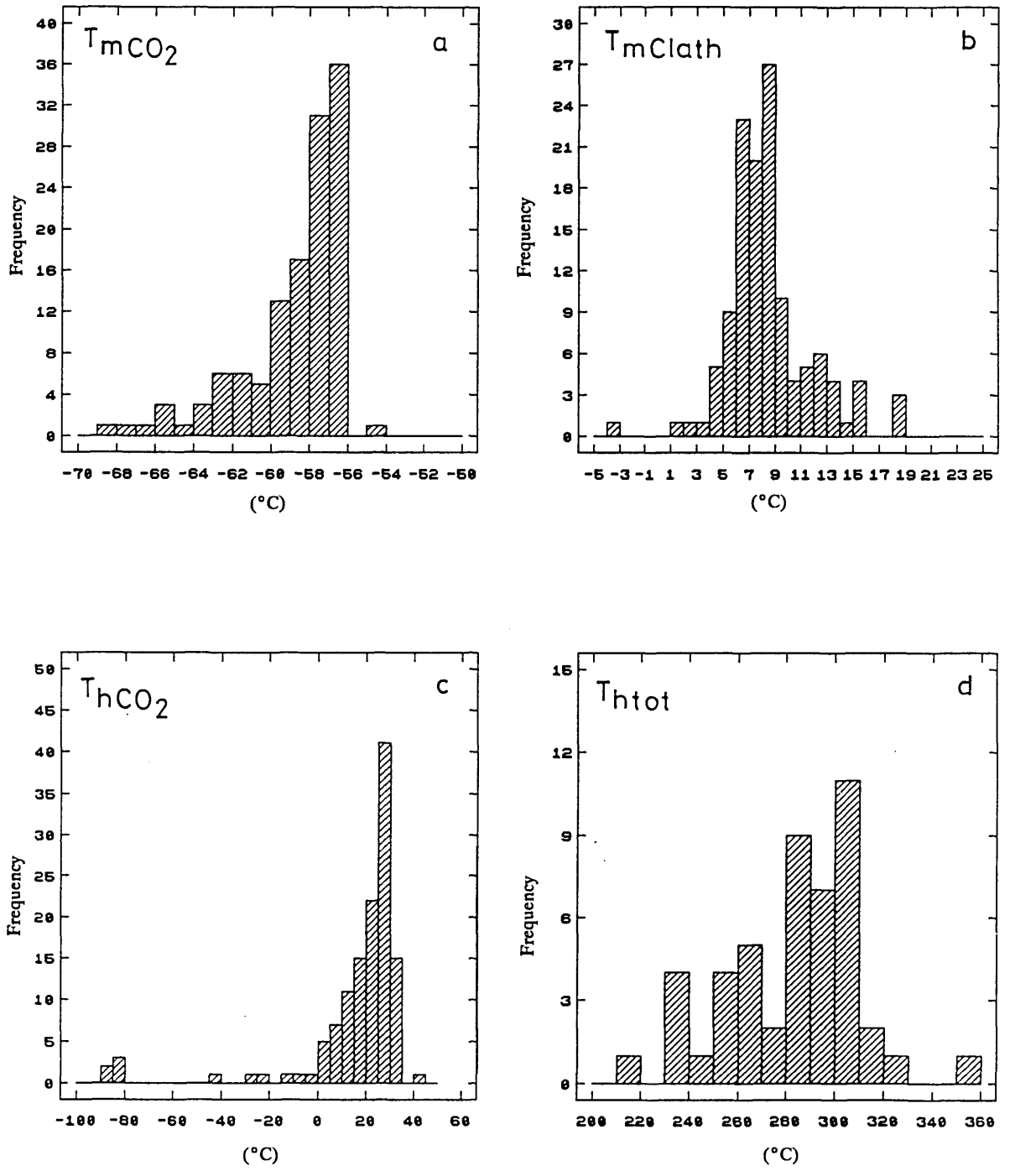


Figure 7.16 - Histograms of microthermometry of Type 2A inclusions.

dominated by NaCl as solute and a CO_2 dominated clathrate, then the value of 8.5°C gives a salinity of 3.5 wt% equivalent NaCl for the aqueous phase (after Collins 1979). The value of 12°C is above the melting temperature of pure CO_2-water clathrate and another clathrate must be present in these inclusions. Some inclusions are clearly more saline, and there are a significant number of inclusions with T_{mClath} above that for a pure H_2O-CO_2 clathrate. This effect is likely to be caused by the presence of other clathrates formed by other gases, notably methane (Shepherd *et al.* 1985). This raising of clathrate melt by other gases, leads to the conclusion that the estimate of 3.5 wt% NaCl equivalent is a minimum figure as other gases raise clathrate melt and thus lowers the interpreted apparent salinity.

Measurement of T_{hCO2} is taken when the CO_2 phase homogenises from L+V to either L or V. This value relates to the density of the CO_2 phase in a pure CO_2 system (Valakovich & Altunin 1968), and hence is an important thermodynamic measurement. Data plotted for T_{hCO2} also shows a distinct skewness from the modal value (Figure 7.16c). The mode of the data is close to the critical point for CO_2 of +31.1°C. Most of this homogenisation data is into the liquid phase, which suggests a minimum density of the CO_2 phase of 0.5 g cm^{-3} (Valakovich & Altunin 1968). The skewness of the data, down as low as 25°C below the melting temperature of pure CO_2, is again supportive of other miscible gases in the CO_2 phase. The possible other species which may depress this triple point are shown in Table 7.8.

If the data for T_{hCO2} versus T_{mCO2} and T_{mClath} versus T_{mCO2} are plotted (Figure 7.17), very interesting trends are indicated. The broadly linear correlation (regression line plotted), suggests that the cause of the melt of the CO_2 phase depression, is also causing a concomitant decrease in the CO_2 homogenisation temperature and increase in the clathrate melt temperature. This decrease in CO_2 homogenisation temperature leads to an apparent increase in the calculated density of the CO_2 phase (Valakovich & Altunin 1968). Methane is one of the obvious possible causes of this effect (Heyen *et al.* 1982). The clathrate melt evidence could also be explained by the presence of methane. If this is the case then the presence of variable methane in the inclusions has important implications for fluid behaviour (e.g. fO_2).

Finally, the data for T_{htot} is shown on Figure 7.16d. The number of data is significantly smaller than for the other phase changes, due to the habit of overpressured CO_2 bearing inclusions explosively decrepitating below homogenisation temperature. The data has a mean of 279°C with the modal value somewhat higher at 285°C. There is a fair spread around two peak values of around 300°C and 260°C. Homogenisation occurs both to the vapour and to the liquid phase (Appendix V), supportive of possible immiscible trapping. The spread of data may be due to the small number of data collected, but they should be considered in conjunction with the data from the co-existing Type 2B inclusions, which were presented earlier. The plot of T_{htot} versus T_{mCO2}, Figure 7.17, shows that there is a suggestion that the

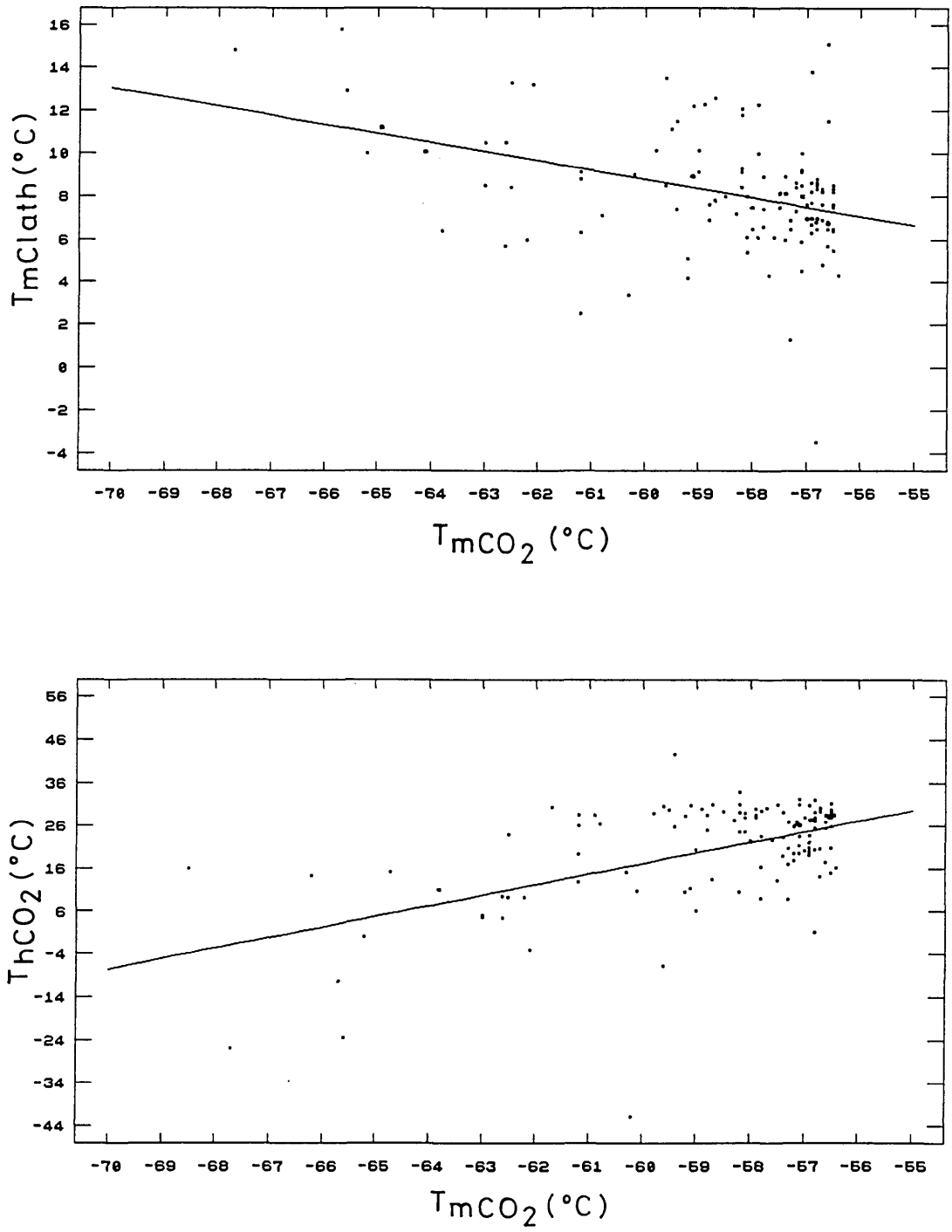


Figure 7.17 - Scatter plots of T_{mClath} vs. T_{mCO2} and T_{hCO2} vs. T_{mCO2} for Type 2A inclusions.

inclusions with lower CO_2 melts might also have lower total homogenisation temperatures. The T_{mCO2} and T_{htot} data both indicate the possibility of two inclusion populations, and suggests the low CO_2 melt population group and the low T_{htot} population group might be the same inclusion population.

Type 2C inclusions are always seen lying along, or close to, healed fractures and trails. T_e for these inclusions is shown to have a mean of -42.2°C. The phase change is quite clear in this inclusion type, comprising a distinct darkening of the ice phase together with development of a granular ice-aggregate. This very low T_e for this inclusion type could be highly significant with regard to cation types present in the fluids. One suggestion is $CaCl_2$ is present, the eutectic for this species in water is -49.5°C or in the $CaCl_2$-NaCl-H_2O system is -55°C (Borisenko 1977). The effect of a mixed carbonate-chloride system on this eutectic is unknown. The T_{mI} data for Type 2C inclusions is shown on Figure 7.18a, where a fairly well defined, slightly skewed population is shown. The mean of the T_{mI}, indicates a salinity of 16.5 equivalent wt% NaCl. The T_{htot} data shows a clear, single population, with a mean of 137°C (Figure 7.18b).

Q3 Quartz Inclusions

Data generated from quartz taken from the D3 cross veins, is fairly sparse due to the tiny size of most of the inclusions. However, from the data collected, it is clear that discrimination can be made between the two major inclusion types present, Type 3A and Type 3B.

Two measurements of T_e for the Type 3B aqueous inclusions indicate a eutectic of around -51°C, close to either the H_2O-KCl-$CaCl_2$ system eutectic of -50.5°C or the H_2O-NaCl-$CaCl_2$ (Borisenko 1977). The T_{mI} values (Figure 7.18c) have a mean of -8.5°C, indicating a salinity of 12.2 equivalent wt% NaCl. Values of T_{htot} (Figure 7.18d), all to the liquid phase, are rather spread out, but a modal value of 147°C is indicated.

The Type 3A inclusions are carbonic-aqueous and hence show the same four main phase changes seen in Type 2A inclusions. Figure 7.19a shows the T_{mCO2} data indicating a fairly restricted data range with a mean of -57.3°C. T_{mClath} data is more widely spread around a mean of 8.0°C (Figure 7.19b). The mean value points to a salinity of 3.8 equivalent wt% NaCl assuming pure CO_2. T_{hCO2} is always to the liquid, except for a few inclusions showing critical behaviour close to 30°C (Figure 7.19c). The range of data points to a CO_2 density between 0.5 and 0.8 gcm^{-3} with a mean value of 0.7 gcm^{-3}. Finally the data for T_{htot} is shown on Figure 7.19d, all inclusions homogenising to the liquid phase. The few data are generally clustered around a modal value of 275°C.

Q4 Quartz Inclusions

Type 4 primary inclusions are generally larger than the other inclusion types which makes microthermometry easier. Freezing to liquid nitrogen temperatures indicates the inclusions are aqueous

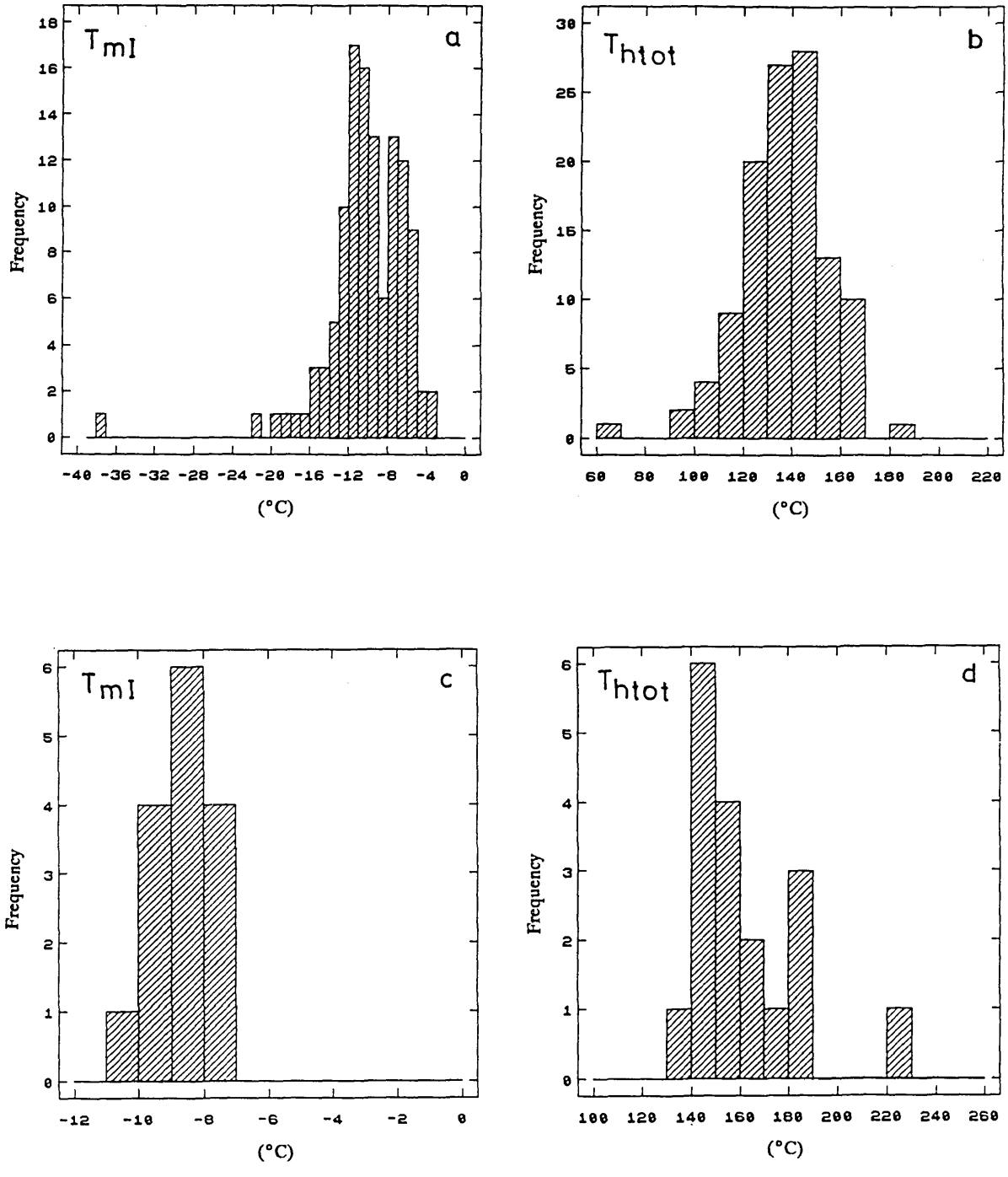


Figure 7.18 - Histograms of microthermometry of: a & b, Type 2C inclusions and c & d, Type 3B inclusions.

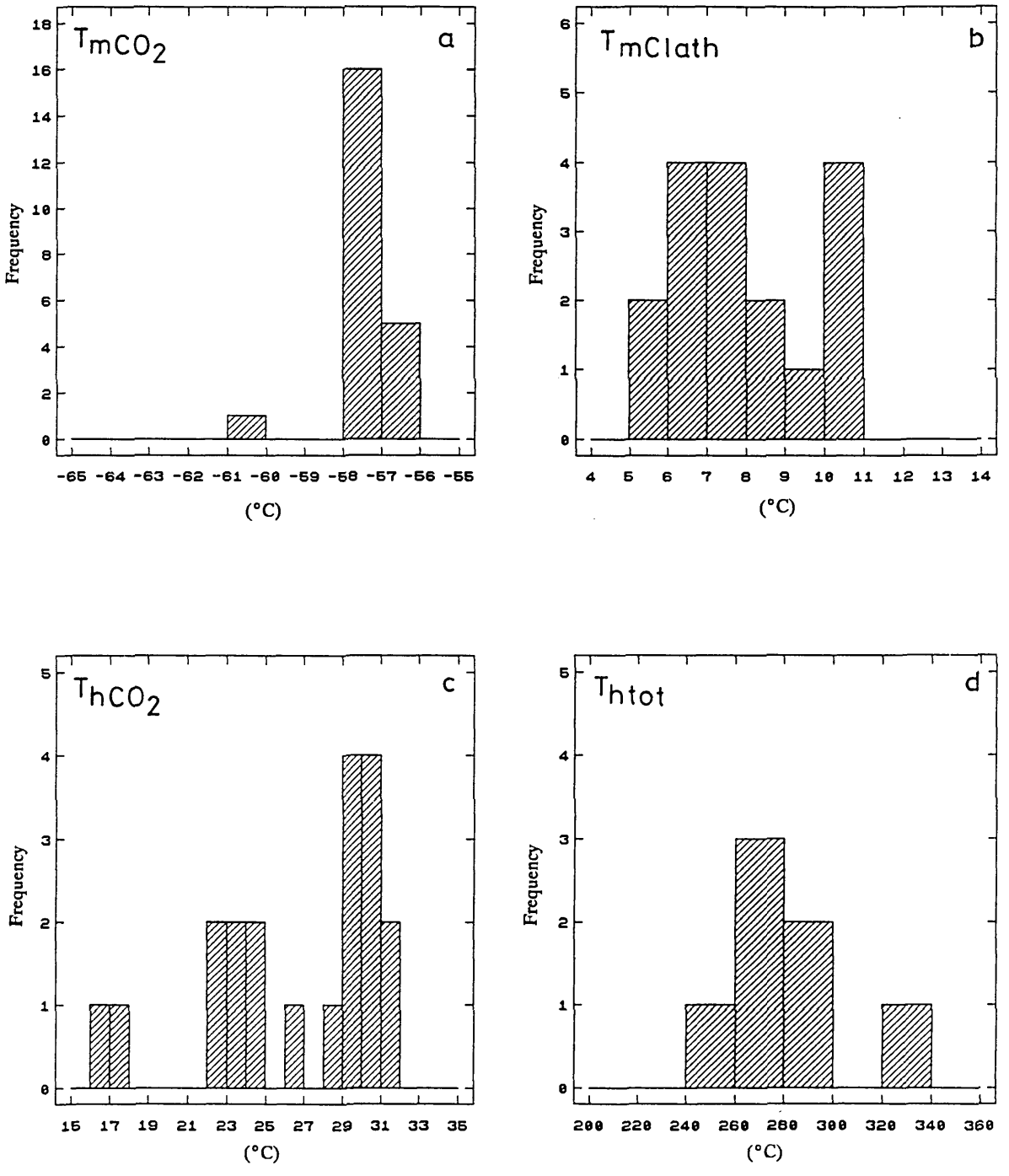


Figure 7.19 - Histograms of microthermometry of Type 3A inclusions.

only. On heating, the eutectic melt was clearly noted in many inclusions with a range from -51 to -47°C and a modal value of -49.1°C. This points to a complex solute (possibly containing one or more of Ca, K and Mg). The size of inclusions and moderately high salinity permit measurement of hydrohalite melt (T_{mh}). The values of T_{mh} are well constrained between -23.2°C and -21.8°C. The most likely solute system for the Type 4 fluid is domination of the species NaCl-$CaCl_2$-H_2O (supported by the T_e values). In this case, hydrohalite melt can be used as a measure of the NaCl:$CaCl_2$ ratio. Figure 7.20a shows a ternary plot of the system H_2O-NaCl-$CaCl_2$ with isotherms for ice melt superimposed (Borisenko 1977). Seven measurements from Type 4 inclusions are plotted and, even though a range of salinities is indicated (13 to 20 equivalent wt% NaCl), a narrow range of NaCl:$CaCl_2$ ratios (xNaCl = 0.8 to 0.9) is suggested. T_{mI} data for the inclusions shows a range of temperatures forming a large skewed peak around the mode of -12.1°C (Figure 7.20b). The mean of -10.1°C equates to a salinity of 14.1 equivalent wt% NaCl. Figure 7.20c shows the data for T_{htot}, all inclusions homogenising to the liquid phase.

Q5 Quartz Inclusions

The Type 5 inclusions in quartz from the tonalite hosted veins are shown to be aqueous-carbonic on freezing. Heating from below the temperature of freezing of the CO_2 phase indicates a narrow range of T_{mCO2}. The inclusions record values slightly lower than the pure CO_2 melt temperature, with the modal value at -56.9°C (Figure 7.21a). The T_{mClath} data also indicates a narrow range around a modal value of 10.7°C (Figure 7.21b). Since the melt temperature for a CO_2 clathrate in pure H_2O is 10.1°C (Collins 1979), this clathrate melt modal value is consistent with the presence of another miscible gas, probably methane, in the carbonic phase. A low salinity is likely, although impossible to quantify. Figure 7.21c shows the T_{hCO2} data plotted, with a well defined modal peak at 26.7°C. All homogenisations are to the liquid phase and thus a CO_2 density of 0.7 gcm^{-3} is indicated, within a data range of 0.65-0.75 gcm^{-3}. The T_{htot} data cluster around a mode of 254°C (Figure 7.21d).

Q6 Quartz Inclusions

Freezing the Type 6 inclusions in this quartz shows the inclusions to be aqueous only. The T_{mI} data from the inclusions have a mode of -6.5°C and a mean of -6.1 (Figure 7.22a). The modal value is equivalent to a salinity of 9.8 equivalent wt% NaCl. The T_{htot} data, all homogenising to the liquid, have a mean of 157°C and mode of 139°C (Figure 7.22b).

7.5.2 Discussion of Microthermometry Results

Shepherd *et al.* (1985) conclude that most hydrothermal fluids are multi-component systems dominated by dissolved, chloride-complexed ions, particularly Na, Ca, K, Mg and Fe. All these dissolved ions depress the melting point of any solution below that for pure water. The work of Potter *et al.* (1978) and Hall *et al.* (1988) has experimentally derived the freezing point depression as a function of NaCl and

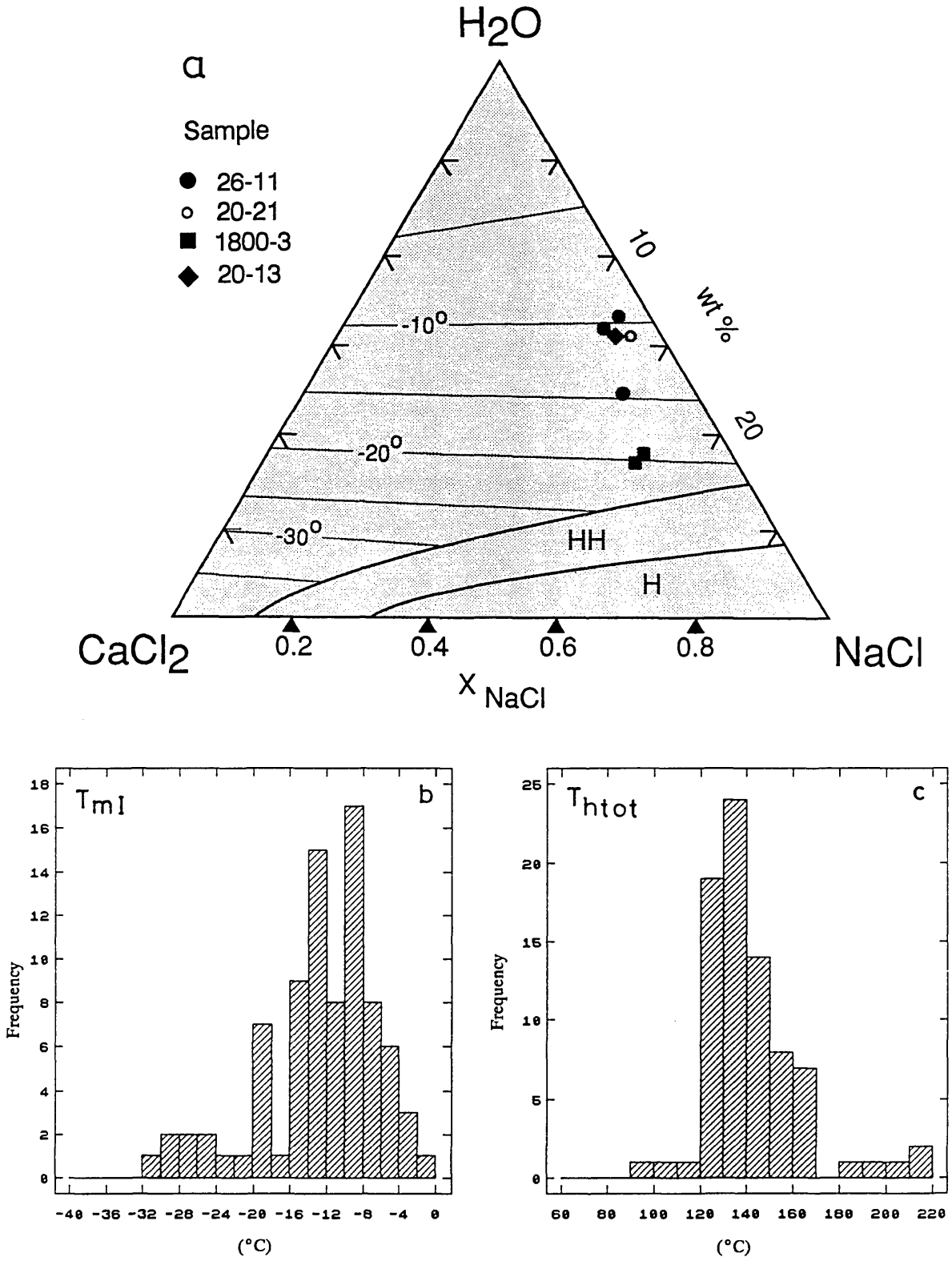


Figure 7.20 - Histograms of microthermometry of Type 4 inclusions (b & c) and ternary plot of H_2O-NaCl-$CaCl_2$ system with hydrohalite melt isotherms (a) [after Borisenko (1977)].

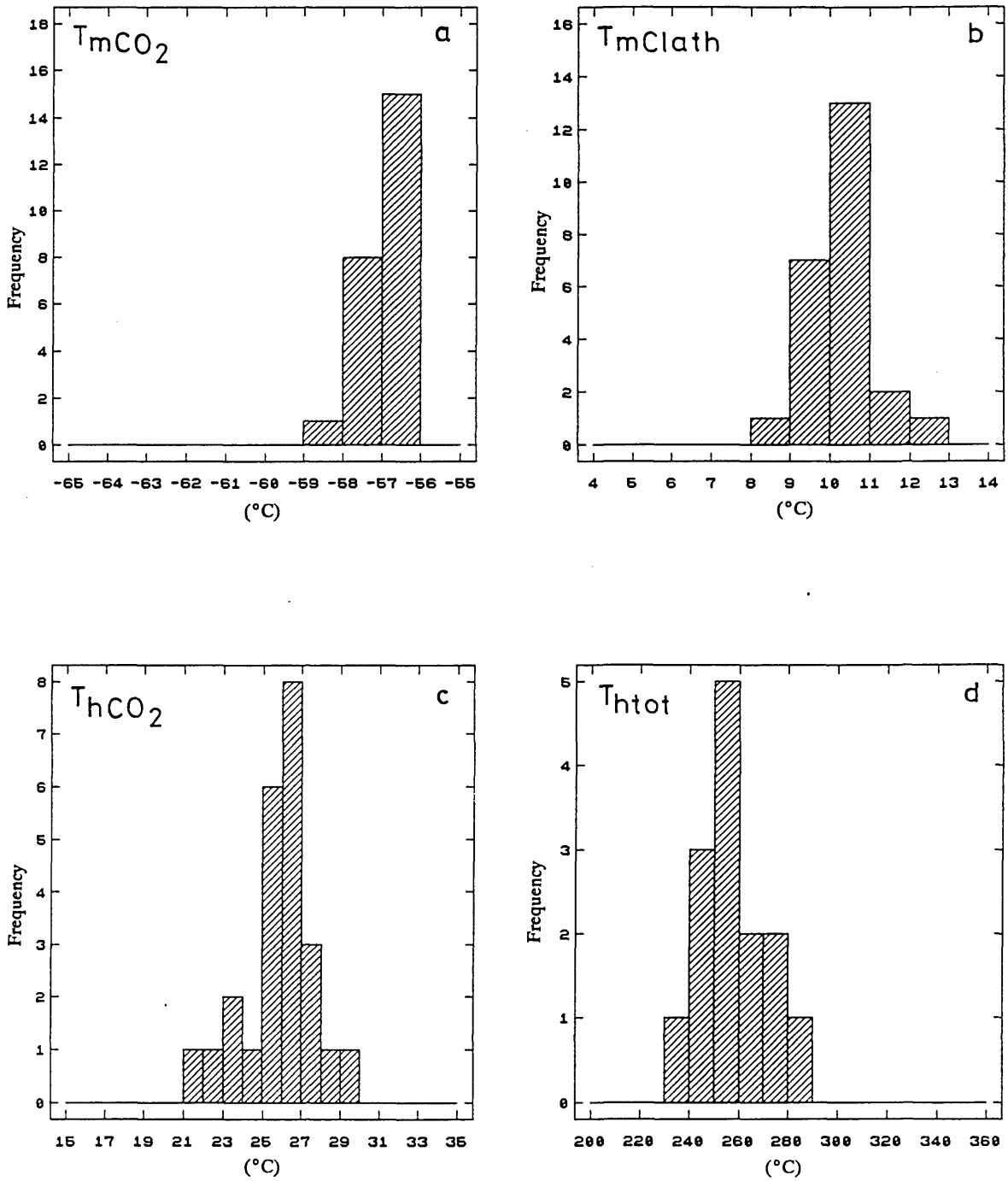


Figure 7.21 - Histograms of microthermometry of Type 5 inclusions.

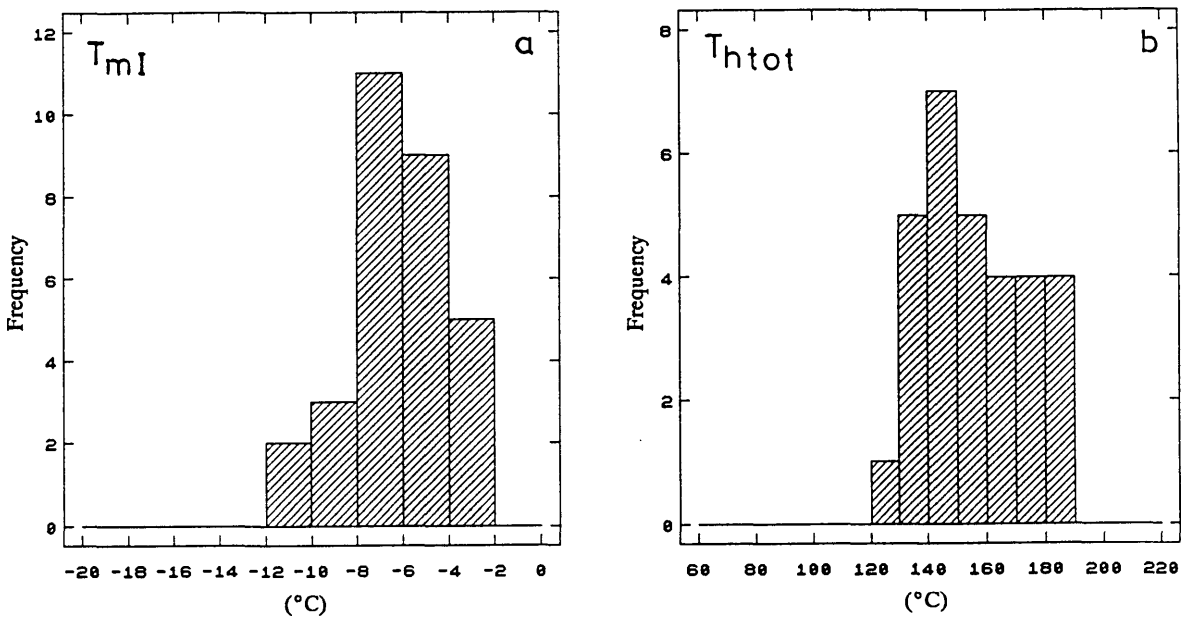


Figure 7.22 - Histograms of microthermometry of Type 6 inclusions.

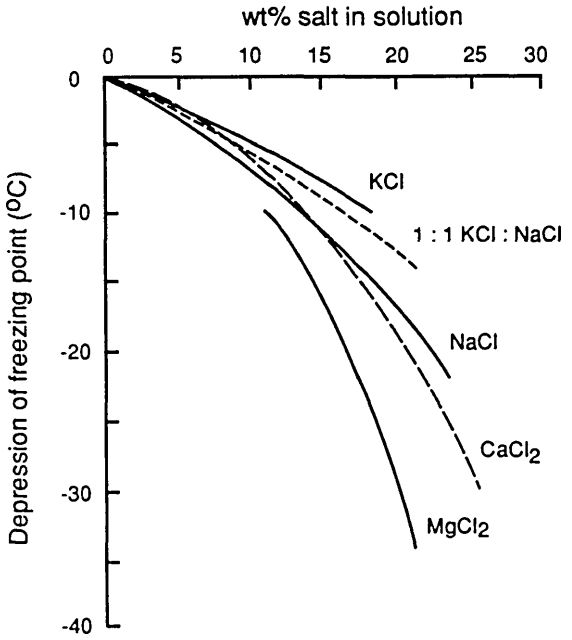


Figure 7.23 - Graph showing the depression of the freezing point of water caused by the addition of various salts to water (from Borisenko 1977).

KCl concentration, data not readily available for the other species. In reality, the effect of the other ions is small in NaCl dominated systems, leading to total error, assuming pure NaCl of less than 5% (Clynne & Potter 1977). The work of Ho *et al.* (1985) estimates a freezing point depression of 0.46°C and 0.44°C respectively for 1 wt% KCl and $CaCl_2$ as compared to 0.30°C for 1 wt% NaCl. Figure 7.23 shows graphically the effect of the addition of these major salts to the melting point of ice. The graph demonstrates the small errors likely by assuming pure NaCl-water in the range 0 to 5 wt% total dissolved salt.

In the microthermometric study of inclusions containing a carbonic phase, the measured phase changes can be used to detect the presence of other gases. The triple point of CO_2 (-56.6°C) is lowered by the presence of both CH_4, N_2 and probably Ar amongst other gases. The second major phase change to be observed in such inclusions is the homogenisation of the carbonic phases (L+V to V *or* L). The temperature of this phase change is primarily related to density of the carbonic phase, but it is also significantly affected by the presence of CH_4 (Heyen *et al.* 1982). Other miscible gases such as H_2S and SO_2, which have been detected in hydrothermal fluids by Raman spectroscopy and volatile analysis (Boiron *et al.* 1989, Bottrell *et al.* 1989), would be expected to alter both the triple point and the critical point of the carbonic species (Table 7.8). In estimates of salinity from T_{mClath}, it must be borne in mind, however, that clathrate melts are raised by the presence of CH_4 and higher order alkanes (Shepherd *et al.* 1985). Salinities can be calculated from Collins (1979), but must be considered minimum values when the presence of CH_4 is suspected. The effect of other electrolytes on clathrate melting temperatures has not been systematically studied. However, similar limitations for clathrate derived salinities as those made for low salinity, aqueous fluids is expected. For the present study, it was necessary to model the fluids assuming a pure NaCl electrolyte in the aqueous phase, although from ICP analyses (presented later) K, Ca, Sr, B, Fe and Li are also present in some inclusions. This practice is in line with most studies to date (Shepherd *et al.* 1985) due to the lack of experimental studies. Errors in assuming this should be ±2 equivalent wt% NaCl in the samples studied where Na, K and Ca are the dominant cations. The salinity estimates from CO_2 bearing inclusions are based on a CO_2-water-NaCl system, avoiding the use of inclusions where other miscible gases, such as CH_4, which raise clathrate melt temperatures, are demonstrated.

Type 1 Inclusions

The fluid in this inclusion population is clearly aqueous (water + salts). T_e suggests that it may be dominantly NaCl with possible Fe and K species present. The T_{mI} indicates an average fluid salinity of 4.7% NaCl. T_{htot} indicates homogeneous trapping and thus isochoric projection of the data to trapping conditions is necessary.

Species	Triple Point (°C) (S+L+V)	Critical Temperature (°C)
H_2O	+0.015	+374
CO_2	-56.6	+31.1
H_2S	-85.5	+100.4
CH_4	-185.5	-82.1

Table 7.8 - Physical properties of one-component fluids likely to be present in hydrothermal systems (after Shepherd *et al.* 1985).

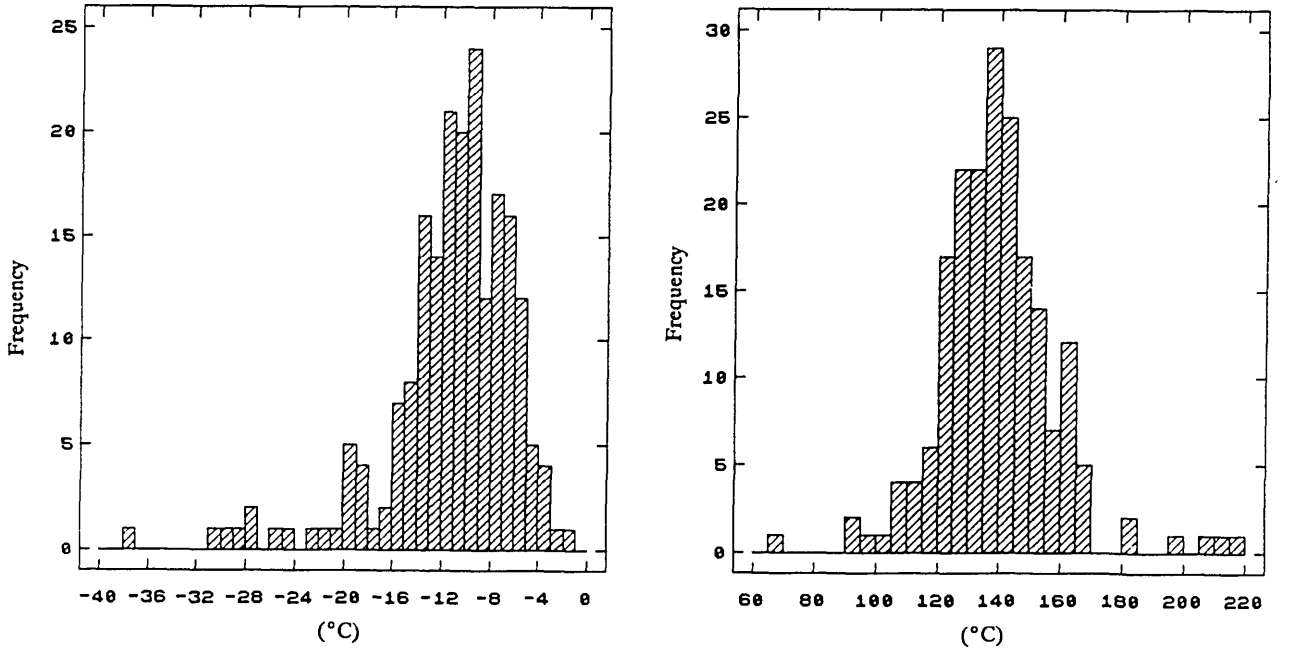


Figure 7.24 - Histograms of microthermometry of combined Type 2C & Type 4 inclusion groups.

Type 2A and 2B Inclusions

The presence of co-existing Type 2A and 2B inclusions in the ribbon quartz, Q2, could be due to the trapping of two immiscible fluids during quartz precipitation. The model of vein formation presented in Chapter 4 implies probable major fluid pressure fluctuation, a process capable of inducing phase separation in a carbonic fluid. Such unmixing leads to partition into an aqueous dominated, and a carbonic dominated, phase.

The fluid trapped in Type 2A inclusions is carbonic-aqueous with a salinity of around 3.5 equivalent wt% NaCl. There is suggestion that CH_4 (and/or N_2, H_2S, Ar) is present which makes this figure a minimum value. The fluid trapped in Type 2B inclusions is aqueous (sometimes with minor CO_2) and has a salinity of 5.5 equivalent wt% NaCl. Te suggests that the fluid may be in the NaCl-$CaCl_2$ system.

T_{hCO2} of the Type 2A inclusions indicates a variable CO_2 density, although some of this apparent variability may be due to the presence of CH_4. An average CO_2 density of 0.67 gcm^{-3} is suggested. Given the degree of fill, and salinity of the aqueous part of the inclusion, a bulk density in the order of 0.9gcm^{-3} is indicated.

The T_{htot} for both Type 2A and 2B inclusions is comparable. The average values of 284°C and 299°C are close, and the range of values for both inclusion types is similar. Some of the data collected from the Type 2A inclusions indicates inhomogeneous trapping, probably during fluid unmixing. In such a case, trapping is likely to occur at the fluid solvus and hence homogenisation temperature and trapping temperature are the same.

The Type 2B inclusions appear to be more saline than Type 2A. This salinity difference is consistent with the unmixing model, since the loss of a more carbonic phase during unmixing would leave the remnant aqueous fluid more saline. It is therefore not unreasonable to estimate an original composition of the D2 hydrothermal fluid lying between the 3.5 equivalent wt% NaCl derived from Type 2A inclusions and the 5.5 equivalent wt% NaCl for the Type 2B inclusions. However, it is still possible to invoke a model of fluid mixing to explain the co-existing Type 2A and Type 2B inclusions. A more saline aqueous fluid mixing with a lower salinity carbonic fluid would result in precisely the same inclusion distribution as the unmixing model.

The data generated from the study of Type 2A and Type 2B inclusions also clearly indicates that there are also potentially significant variations in miscible gas contents (other than CO_2), within this single Q2 quartz generation. The physical process of fluid mixing, or more particularly unmixing, would be expected to cause major variations in miscible gas species. Since such gases have different partition co-efficients for different fluid phases (Drummond & Ohmoto 1985, Naden & Shepherd 1990), individual

species will report to the two fluid phases in rather different proportions during any mixing or unmixing event.

The observation of possible mixing or unmixing during gold-quartz precipitation needed further detailed study as it could be a key process in the mineralisation event. It was decided therefore to study the volatile contents of fluid inclusions in the main ribbon vein (Q2) in detail at two localities. This study is presented later in this chapter in section 7.11.

The very close similarites between all the phase changes measured in Type 2C and Type 4 inclusions during the microthermometry suggests that the fluids may be the same. The Type 2C and Type 4 inclusion types are therefore discussed together below.

Type 3A and 3B Inclusions

Type 3A and Type 3B inclusions also appear to occur in the same quartz generation. However, despite initial similarities with the Type 2A and Type 2B inclusions, it seems likely that the Type 3A and Type 3B fluids are quite different.

The Type 3A inclusions show T_{mCO2} values indicative of minor amounts of CH_4 or N_2, corroborated by some T_{mClath} values above 10.1°C. The salinity of 3.8 equivalent wt% NaCl is very similar to the Type 2A fluid. The T_{hCO2} values are closer spread than the Type 2A fluid, and give a tighter range of CO_2 densities, close to the modal value of the Type 2A fluid. The calculated bulk density from the average values, 0.91 gcm^{-3}, is also close to the Type 2A fluid.

The average salinity, of 12.2 equivalent wt% NaCl, calculated from the Type 3B inclusions is much higher than the Type 3A inclusions. The T_{htot} values for both groups are also very different. The mean T_{htot} for Type 3A is 285°C, whilst the figure for Type 3B is 162°C. These two differences suggest that two different fluids are trapped in quartz stage Q3.

Type 2C and Type 4 Inclusions

Microthermometry shows these inclusion types to be very similar (Table 7.7). Figure 7.24 shows the result of combining both data sets into one. T_{mI} shows a clearer modal value of -10°C, or a salinity of 14 equivalent wt% NaCl. T_{htot} shows a very well formed single population, with a mode of 137°C. The very similar T_e ranges indicate that a more complex salt system, possibly NaCl-KCl-$CaCl_2$, is present in the aqueous fluid. Since homogeneous trapping is suggested, temperatures must be extrapolated, isochorically, to trapping conditions.

Type 5 Inclusions

Accurate salinity estimates from the Type 5 inclusions is not possible due to the suspected presence of methane. A salinity lower than 5 equivalent wt% NaCl is likely, however. Homogeneous trapping is interpreted and thus trapping temperature must be isochorically extrapolated from the T_{htot} mode of 264°C. The bulk density calculated is around 0.9 gcm^{-3}, assuming a salinity <2 equivalent wt% NaCl, similar to both the Type 2A and 3A fluids.

Type 6 Inclusions

Type 6 inclusions have very similar microthermometric characteristics to the Type 2C and Type 4 inclusions. A fluid with a salinity of 9.8 equivalent wt% NaCl is indicated, which homogeneously trapped. No reliable eutectic measurements were recorded in the tiny inclusions so no conclusions about salt species can be made from the microthermometry.

7.6 Bulk Volatile Analysis of Fluid Inclusions

At Patchway, the presence of aqueous inclusions with significant amounts of other gases was demonstrated. The most common of these volatiles in the hydrothermal environment is CO_2, but significant amounts of CH_4 and N_2 may also be present in the carbonic phase. Since these gases show very limited solubilty in water at room temperatures they partition into a distinctly separate "carbonic" phase in the inclusion. The presence of these species is suspected from microthermometry and their presence affects the phase relationships of the fluid.

The understanding of the effects of these gases on the behaviour of hydrothermal fluids at elevated pressures and temperatures is currently limited. To date, only the systems CO_2-H_2O-NaCl (Takenouchi & Kennedy 1964, 1965, Jacobs & Kerrick, 1981a, Bowers & Helgeson 1983, Brown & Lamb 1989) CO_2-CH_4-H_2O (Haas 1978, Jacobs & Kerrick 1981b, Krader & Franck 1986) and N_2-CH_4-CO_2 (van der Kerkhof 1988) have been adequately modelled to date. However, extrapolation between these modelled systems is possible to some degree, and thus accurate analysis of the volatile species can aid the interpretation of fluid inclusions.

7.6.1 Bulk Volatile Analysis Results

A programme of bulk volatile analysis was undertaken on carefully prepared quartz separates. The quartz was chosen after fluid inclusion microthermometry had ensured, as well as physically possible, that the inclusion types in the sample were predominantly primary inclusions. 19 samples were run on the BGS gas extraction line after careful grain picking and cleaning. 12 samples were from Q2 quartz, which was chosen after microthermometry in order than it might contain predominantly Type 2A and Type 2B primary inclusions. The other samples comprised 2 samples from Q2 quartz containing mainly

Type 2C secondary inclusions, 1 sample from Q3 quartz with Type 3A and 3B inclusions, 1 sample from Q4 quartz with Type 4 inclusions, 2 samples from Q5 containing Type 5 inclusions and finally 1 sample from Q6 containing Type 6 inclusions.

The results are tabulated in Table 7.9 where consistent differences can be seen. The Q2 quartz, which was chosen to contain largely Type 2A and 2B inclusions, contains up to 10 mole% CO_2 and 2.5 mole% CH_4. There is detectable N_2, particularly in inclusions containing methane. Other reduced species, H_2 and CO, are only detected in the Q2 samples. From these results, it is concluded that the depression of T_{mCO2} and anomalously high T_{mClath} are caused by methane. From the other samples, the analyses of the Q2 quartz containing mainly Type 2C secondary inclusions confirm the low carbonic component of the fluid. The CO_2 and CH_4 detected is believed to be contributed by remaining Type 2A inclusions. The result from Q3 quartz confirms the presence of CO_2 in the inclusion Type 3A. No CH_4 is detected, supporting the observed T_{mCO2} values lying close to the value for pure CO_2. Very low CO_2 values are recorded for both Q4, Type 4 inclusions and Q6, Type 6 inclusions. This confirms the microthermometry results. Lastly the analysis of Q5 quartz shows that the Type 5 inclusions are indeed carbonic, and moreover they contain significant CH_4.

7.6.2 Discussion of Bulk Volatile Analysis Results

The interpretation of these volatile analysis and microthermometric results from the fluid inclusions, must be made in light of recent work on volatile loss from inclusions after trapping. Hall & Bodnar (1990) suggest that hydrogen diffusion can occur, resulting in enhanced CH_4 levels in the inclusions. Hollister (1990) also records loss of H_2O from carbonic inclusions, due to the greater ability of water to migrate from the inclusion during recrystallisation of host quartz grains.

Both of these phenomena are thought to be unimportant in the Q2 quartz studied, because the host grains can be demonstrated to show recrystallisation limited to grain boundaries. It is possible that CO_2 loss may have occurred in the quartz containing Type 2C inclusions to account for the low volatile contents, although the similarity with the Type 4 inclusions suggests that the fluid was originally aqueous only. Recrystallisation in the other quartz stages is not considered to be significant.

Of note in the analyses of the Q2 and Q5 veins is the detected presence of CH_4, indicated from the microthermometry. Carbonaceous wallrocks have been suggested to account for the presence of CH_4 in inclusions at other gold deposits (Ho *et al.* 1985, Bottrell *et al.* 1988, Naden & Shepherd 1990). No carbonaceous rocks are recorded anywhere in the Patchway area, which probably excludes this as a local reduced carbon source.

Sample	Quartz Stage (Inclusion Types)	xH_2O	xCO_2	xCH_4	xN_2	xH_2	xCO
6007b	2 (2a,2b)	91.60	7.94	0.21	0.06	0.11	0.08
6006c	2 (2a,2b)	93.26	6.53	0.06	0.04	0.06	0.05
6006e	2 (2a,2b)	93.38	6.62	-	-	-	-
6008f	2 (2a,2b)	95.51	4.47	-	-	-	-
6006b	2 (2a,2b)	94.15	5.32	0.17	0.10	0.12	0.14
19HG1	2 (2a,2b)	86.80	9.55	2.59	0.33	0.43	0.30
A10/20D	2 (2a,2b)	92.60	6.02	0.29	0.22	0.73	0.14
10-21	2 (2a,2b)	94.60	5.33	-	0.07	-	-
10-32a	2 (2a,2b)	90.82	8.04	0.61	0.14	0.19	0.20
10-35b	2 (2a,2b)	95.05	4.47	1.15	0.09	0.24	-
26/3	2 (2a,2b)	95.03	4.55	0.21	0.11	0.09	0.05
30-3	2 (2a,2b)	95.83	2.95	0.87	0.18	0.17	-
30-7	2 (2c,2a,2b)	98.97	0.67	0.27	0.05	0.04	-
26-2	2 (2c,2a,2b)	98.69	1.10	0.13	0.04	0.04	-
400-24	3 (3a,3b)	94.03	5.97	-	-	-	-
26-14	4 (4)	98.75	1.19	0.06	-	-	-
TQ-2	5 (5)	95.49	4.18	0.35	0.05	-	-
TQ-3	5 (5)	95.76	3.95	0.29	-	-	-
LH7	6 (6)	99.90	0.10	-	-		-

Table 7.9 - Volatile analyses for picked quartz samples. Dashes indicate values below detection limit. (H_2 and CO analyses *qualitative* only)

Deep sources of hydrocarbons, possibly from the mantle, are the subject of much debate (Gold 1987). Recent work (Abrajano *et al.* 1988, Welham 1988) suggest that methane may form from metamorphic reactions such as serpentinisation and reduced carbon is predicted as a result of granulitisation (Skippen 1990). Since the structures that contain the gold mineralisation, such as Patchway, probably extend deep into the crust, access of the Patchway mineralised system to fluids containing abiogenic, reduced carbon species is quite feasible.

The methane in the Patchway D2 fluid (Type 2A plus Type 2B inclusions) is therefore proposed to form part of the the original, internally equilibrated fluid C-O-H bearing fluid from which the Q2 quartz crystallised. Further support for an exotic methane source, is the presence of the gas in the Type 5 inclusions from Q5. This quartz occurs in veins hosted entirely within the large Whitewaters tonalite pluton where a local reduced carbon source is excluded.

The other main conclusion from the volatile analysis is that other dissolved gases are of minor importance compared to CO_2 and CH_4. All the Patchway fluids can thus be broadly modelled in the H_2O-CO_2-CH_4-Mixed Salts system.

7.7 Fluid Inclusion Bulk Analysis by ICP-AES

Bulk analysis of fluid inclusions by ICP-AES from the different quartz generations can provide information about the important cation species in the aqueous components of the fluid inclusions. The nature of the fluid solvents in the Patchway system had been confirmed by the volatile analyses. A program of bulk ICP analysis was therefore carried out on the various quartz generations at Patchway, in order to provide information about the dissolved ionic species.

Ratios of the major alkali metals in the fluid can be used as fluid geothermometers in certain instances (Truesdell 1984), and their use in fossil hydrothermal systems is increasingly common. The use of these geothermometers was recently reviewed by Rankin & Graham (1988). Both decrepitation-linked ICP analysis (D-ICP) (Thompson *et al.* 1980), and traditional and modified crush-leach methods (CL-ICP) (Bottrell *et al.* 1988), all generate suitable data for calculation of these values. Certain limitations pertain to both D-ICP and CL-ICP techniques (Rankin *et al.* 1990), so both methods were carried out for comparative purposes during this study. The CL-ICP method can also allow measurement of Cl^- using a specific ion electrode, which is not possible by the D-ICP method.

The D-ICP technique, although well tested, must be used with caution (Rankin *et al.* 1990). Particularly important is the study of the decrepitation event itself, and in this regard a series of time-resolved D-ICP analyses were made prior to the main study, so as to optimise the furnace temperature and ICP integration times, suitable for all the different quartz generations. This time-resolved D-ICP work is

included in Appendix V, which allowed an optimum selection of pre-heat and integration times for the later D-ICP work. In this study, a pre-heat time of 30 seconds, followed by an integration time of 90 seconds was shown to be the most suitable for the range of Patchway quartz samples.

7.7.1 Comparison of ICP Techniques

In total 48 analyses were performed by D-ICP, selected after the time-resolved D-ICP study, 20 analyses by traditional (Roedder 1984) CL-ICP and 8 by modified CL-ICP (modified from the method of Bottrell *et al.* 1988). The raw data blank corrected is presented in Appendix V. Excellent reproducibility is obtained by D-ICP and this technique is particularly sensitive to Li and B analysis of low salinity solutes. CL-ICP permitted an attempt at ion balance (Na^+, Ca^{2+} etc. against Cl^-). However, CL-ICP did show limitations when analysing low salinity leachates, due to the dilution of element concentration by the DDIW leachate, below the detection limit of the ICP-AES analysis technique.

Comparison between the various techniques was an important part of this study, since very few comprehensive analytical studies have been attempted on low salinity (< 5 wt% NaCl equivalent) solutions. Because of the detection limit problems in low volume, low salinity solutions, comparison of selected, major cations only, where the ICP is particularly sensitive, were made.

Analytical procedures for the comparative studies are detailed in Appendix V. Briefly, the quartz samples were all prepared in identical fashion, washing in nitric acid and double de-ionised water (DDIW) only, careful grain picking under binocular microscope before either leaching or decrepitation. D-ICP was carried out in identical fashion to the test work with an integration time of 90 seconds. "Normal" CL-ICP was done in pure DDIW compared to the use of ≈2,000 ppm La $(NO_3)_3$ solution, containing <0.2 ppm of any other cations, in the modified technique. A nitrate solution was chosen to allow Cl^- analysis of the same solution. Previous work (Poty *et al.* 1974, Bottrell *et al.* 1988) has pointed to the problems of adsorbtion of polyvalent ions (particularly), on the surface of fractured host mineral (quartz). The use of La^{3+} doped DDIW for a leach solute helps avoid this problem.

Weight ratios of major elements of interest (K, Ca, B and Li) with respect to Na, the major cation, are shown in Table 7.10 for identical samples analysed by the three techniques. It is clear that major differences for some of the elements, particularly the polyvalent ions, are shown between the techniques. D-ICP should not suffer the surface adsorption effects seen for the CL-ICP method, because the inclusion contents are released instantaneously, upon decrepitation, in the form of an aerosol. This event is supported by the very sharply defined decrepitation events demonstrated by the time-resolved D-ICP test work. Comparitive data for the Na : Ca : K ratio determined by all three methods is shown for Q2 and Q2 quartz stages on Figure 7.25. Q2 and Q4 quartz was chosen for the comparative study as this comprised the bulk of the quartz studied. It is clear that there is at least one order of magnitude

	Elemental Weight (ppm) Ratios from ICP Analysis														
	K/Na Ratio			Li/Na Ratio x 1000			Ca/Na Ratio			B/Na Ratio x 100			Sr/Na Ratio x 100		
Sample	DICP	CLICP	DCLICP	DICP	CLICP	DCLICP	DICP	CLICP	DCLICP	DICP	CLICP	DCLICP	DICP	CLICP	DCLICP
PMQ-1	0.16	0.15	NR	4.40	4.41	NR	0.57	0.83	NR	2.04	2.32	NR	1.29	1.77	NR
26-3	0.10-0.13	0.11	NR	6.60-6.81	5.24	NR	0.08-0.59	0.85	NR	0.64-0.80	0.92	NR	1.44	2.10	NR
A10-21b	0.35	0.27	0.47-0.50	6.39	7.89	3.18-4.41	0.02	0.04	0.89	0.68	3.77	4.0-4.16	0.40	0.38	1.05-1.46
26-14	0.11-0.12	0.13-0.14	0.14-0.16	5.84-6.03	3.79-6.01	5.13-5.66	0.16-0.20	0.13-0.14	0.91-0.94	0.19-0.22	0.94-2.39	0.96-1.42	1.28-1.35	1.83-1.85	2.12-2.50
30-7	0.10-0.12	0.09-0.17	0.12-0.13	6.62-6.72	6.18-6.93	5.65-6.38	0.08-0.13	0.35-0.48	0.72	0.30-0.41	1.82-2.03	2.34	0.77-0.97	1.38-1.54	1.55-1.68
26-2	0.11-0.12	0.13-0.32	0.33-0.34	6.81-7.57	7.28-7.70	5.82-5.87	0.06-0.08	0.28-0.45	1.08-1.10	0.14-0.51	1.38-1.53	1.49-1.77	0.49-0.59	0.76-1.17	1.36-1.37

Table 7.10 - Comparison of cation ratios with respect to Na for comparitive ICP analysis techniques.
Ranges of data for samples with replicate analyses shown except for single analyses. NR = No result.

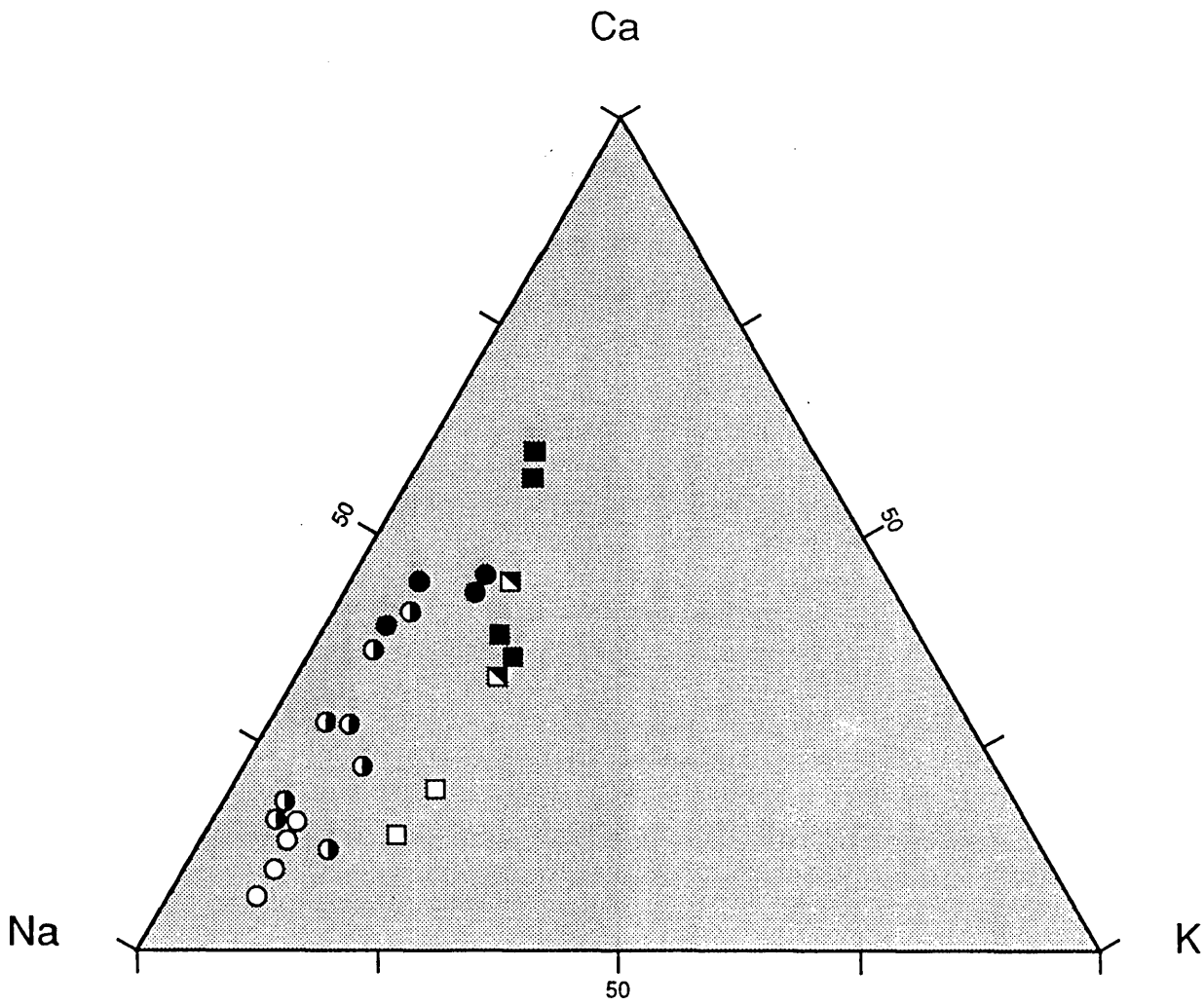


Figure 7.25 - Ternary diagram showing Ca:Na:K ratios for the inclusion fluids from Q2 and Q4 quartz samples measured by D-ICP, CL-ICP and modified CL-ICP. Circles show Q2 quartz, squares Q4 quartz. Open symbols represent samples analysed by D-ICP, half-filled symbols represent deionised water CL-ICP and filled symbols represent La-solution CL-ICP.

decrease in the Na : Ca weight ratio between the D-ICP and CL-ICP methods for the Q2 quartz stage, and in one case a decrease by two orders of magnitude. The difference is less extreme for the Q4 quartz samples (0.5 to 1 order of magnitude). Significantly, the Na : K ratio shows very little variation between methods.

The chloride content of the CL-ICP solutions was measured utilising a specific ion electrode, by the technique described in Appendix V. Measurement of the chloride ion is not possible by the D-ICP technique. Results of the study are tabulated in Table 7.11, where an attempt to balance ionic charge is shown. Boron is assumed to be present as the common $H_2BO_3^-$ complex (Truesdell 1984), but in any event is of negligible importance. Values for each element are calculated from the ICP results, which are quoted in ppm (μg/l), by dividing the value by the element atomic weight to derive molality (moles/litre). Tabulated values are all in moles/litre (m).

Discussion

This major differences in Na : Ca ratios can perhaps be explained, however, from the microscopy of the host quartz. Calcite is a ubiquitous part of the Q2 quartz vein assemblage and is present as both coarse grains and as microscopic to sub-microscopic (2 to 3 μm) solid inclusions in the quartz. Calcite and possibly anhydrite are also seen to form solid phases within the fluid inclusions themselves (Figure 7.9). It thus becomes impossible to include the calcite as a true "daughter" phase and it is probable that the Ca values obtained by CL-ICP are far too high, reflecting contamination from these solid phases. The Q4 quartz is also associated with calcite, and again although the carefully picked quartz was washed in concentrated nitric acid, tiny solid inclusions are almost bound to remain encapsulated in the quartz grains. This hypothesis is substantiated by the charge balance calculations. It can be seen that the total cations figure is far too high in all cases, although the balance is much closer for samples from the Q4 quartz. One possible reason for the imbalance is the omission from the analyses of other possible anion complexes (carbon or sulphur species), not included in the balance calculations. Another possible reason is the presence of small solid particles of carbonate, liberated as solid inclusions from the quartz during crushing, in the leachate not forming part of the fluid solute. Interestingly, if the Na : Ca ratio generated by the D-ICP analysis is used to correct the CL-ICP Ca data, then a much better balance is obtained. The balance is not exact, however, which probably truly reflects the presence of sulphur and carbon anion complexes in the fluids.

Most significantly, for the monovalent cations like K^+ and Li^+, ratios are reasonably consistent between techniques. Data for the Q2 quartz samples is shown on Figure 7.26. There is a good correlation between the Na : K ratio using D-ICP and both CL-ICP methods. Similarly, the data for Na : Li ratio also shows very little change with technique (less than a 0.2 order of magnitude variation). The data for the Q4 quartz is equally as good, with only relatively minor discrepancy between techniques (Figure 7.27).

Sample	Li^+	Na^+	K^+	Mg^{2+}	Ca^{2+}	Total $^+$ Charge	Total $^-$ Charge	Cl^-	$H_2BO_3^-$
De-ionised Water Leachate									
30-7	0.010	0.610	0.051	-	0.038	0.279	0.234	0.226	0.008
A10/21B	0.002	0.150	0.024	0.001	0.013	0.183	0.116	0.104	0.012
26/2	0.011	0.444	0.083	0.005	0.071	0.672	0.651	0.538	0.013
26/14	0.014	0.719	0.060	0.004	0.167	1.117	1.002	0.988	0.014
26/2A	0.010	0.406	0.076	0.020	0.136	0.636	0.483	0.471	0.012
La^{3+} Treated Leachate									
30-7	0.008	0.439	0.030	0.001	0.181	0.819	0.704	0.683	0.021
A10/21B	0.002	0.158	0.046	0.017	0.074	0.387	0.156	0.143	0.013
A10/21B	0.002	0.164	0.045	0.017	0.084	0.399	0.190	0.176	0.014
26/2	0.009	0.489	0.096	0.009	0.310	1.217	0.835	0.820	0.015
26/14	0.010	0.610	0.051	-	0.320	1.299	0.947	0.935	0.012
26/2A	0.013	0.628	0.122	0.007	0.390	1.533	1.045	1.021	0.024

Table 7.11 - Charge balance calculations for CLICP samples. Total positive charges are weighted for the charge of the ion (i.e. bi-valent Ca provides double the positive charge for a given concentration compared to mono-valent Na). Balance of the cations is provided by Cl^- (from electrode measurements) and B as $H_2BO_3^-$ (from ICP analysis). Dash represents analysis below detection limit.

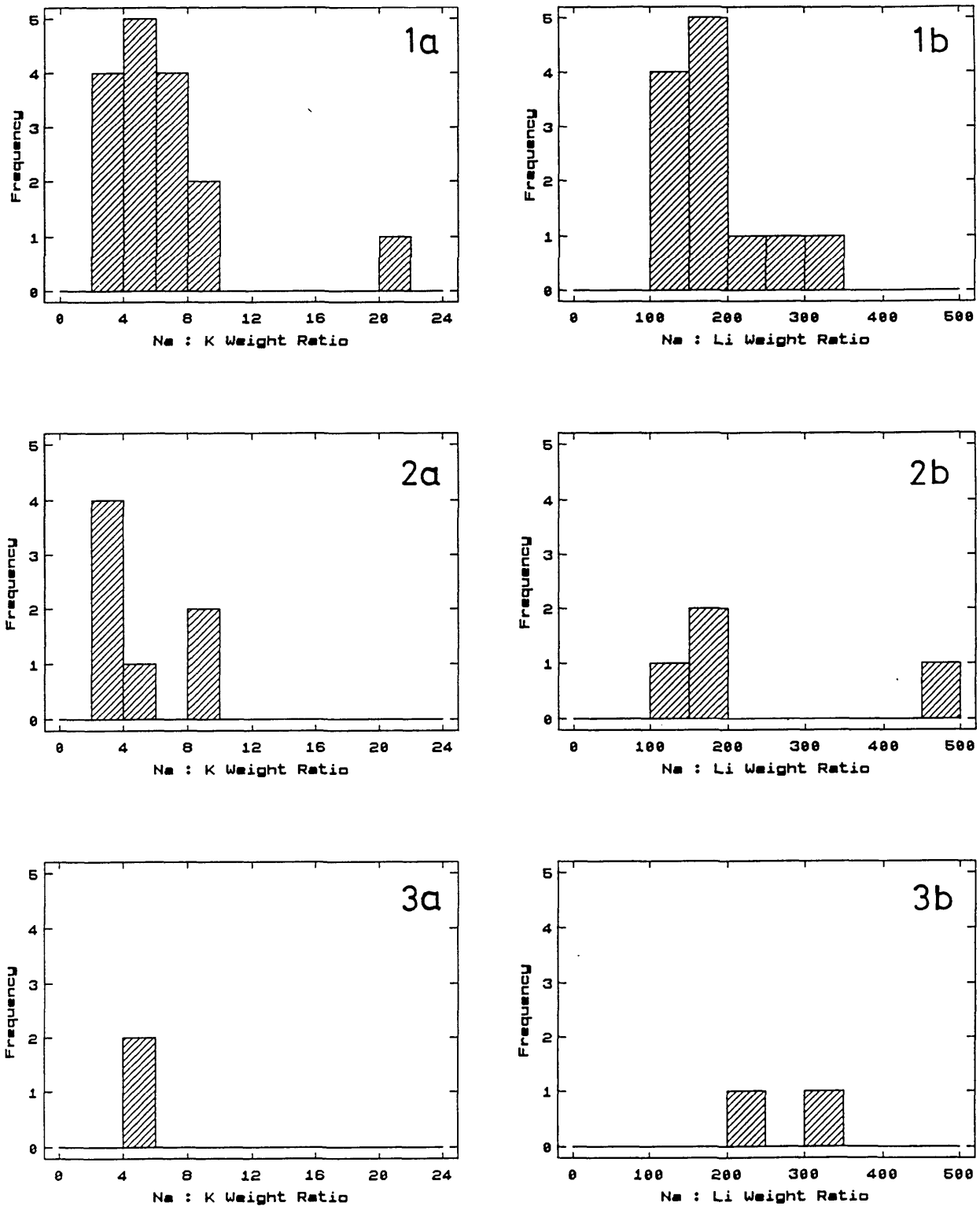


Figure 7.26 - Histograms showing derived Na:K and Na:Li ratios for the inclusion fluids from Q2 measured by D-ICP, CL-ICP and modified CL-ICP. Graphs suffixed "a" show Na:K weight ratios, "b" show Na:Li weight ratios. Graphs 1 are for D-ICP, 2 are for CL-ICP in deionised water and 3 are for CL-ICP in La-solution.

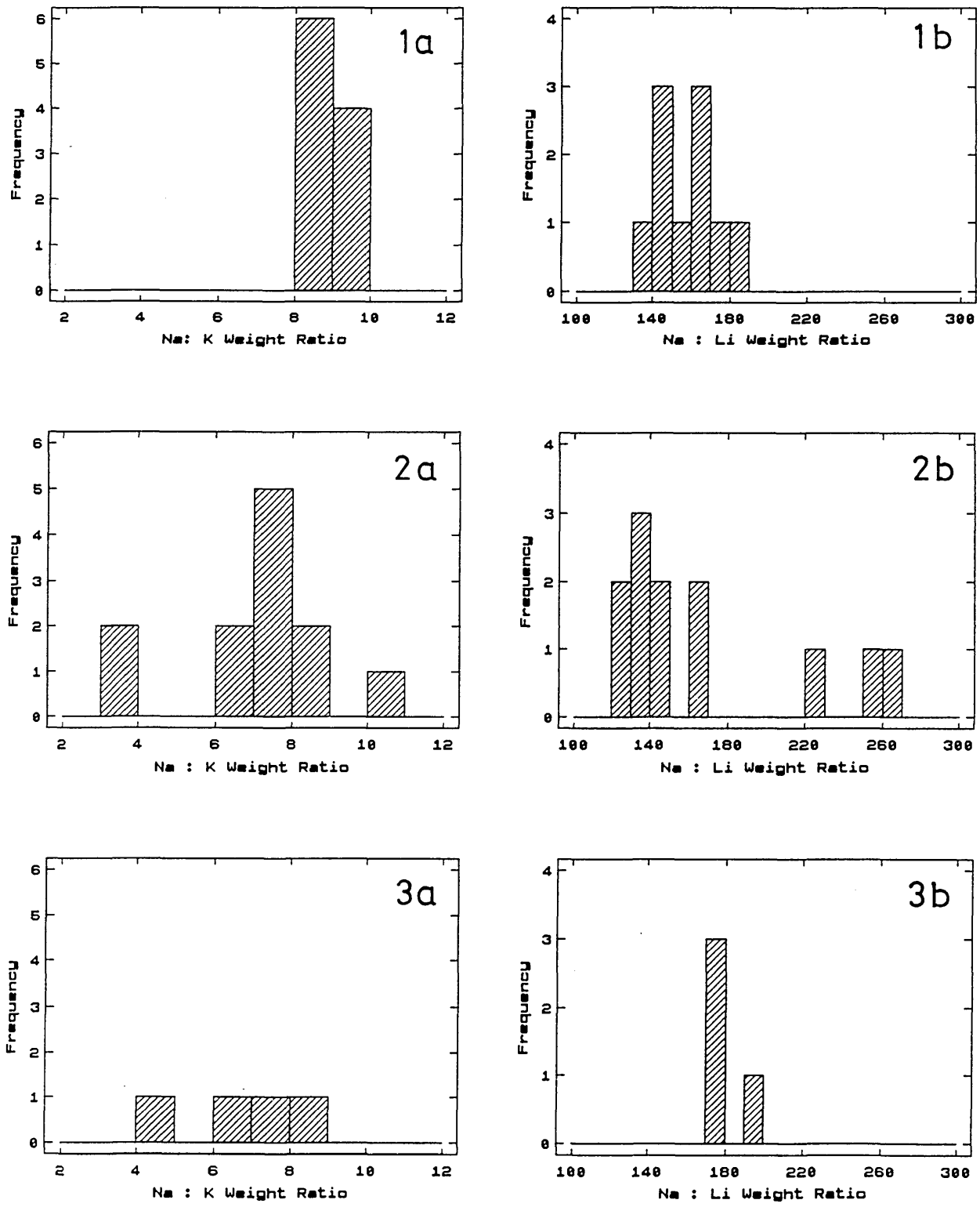


Figure 7.27 - Histograms showing derived Na:K and Na:Li ratios for the inclusion fluids from Q4 measured by D-ICP, CL-ICP and modified CL-ICP. Graphs suffixed "a" show Na:K weight ratios, "b" show Na:Li weight ratios. Graphs 1 are for D-ICP, 2 are for CL-ICP in deionised water and 3 are for CL-ICP in La-solution.

The observed problem of microscopic solid phases, containing polyvalent ions such as Ca^{2+} and perhaps Sr^{2+}, within some of the quartz generations disadvantages the CL-ICP techniques. The D-ICP data is considered to be the most accurate in these circumstances since release of solid phases from the quartz by this technique seems unlikely. Since D-ICP gives comparable monovalent ion results, and since all ions are simultaneously released to the ICP plasma during decrepitation, the values for polyvalent ions should be as accurate. The chloride ion electrode data would also seem to permit a better charge balance when the CL-ICP Ca data are corrected using the D-ICP generated Na : Ca ratio. Discussion of fluid chemistry and application of alkali geothermometry was confined to the D-ICP generated data.

7.7.2 D-ICP Fluid Chemistry Results

Samples from each of the six quartz stages, Q1 to Q6 where predominantly primary fluid inclusions are present, have been subject to D-ICP analysis. This means for the quartz stages with different inclusion types present (Q2 and Q3), the analyses are a composite of all inclusions present. However, for Q2, samples were selected with dominantly Type 2A and 2B inclusions, which microthermometry suggests may represent one original fluid unmixed. Only elements where the concentrations are well above detection limit, are considered (see Appendix V). The fluids in the inclusions of the quartz stages Q1, Q2 and Q5 show salinities calculated from microthermometry in the range 2 to 5 equivalent wt% NaCl. In this case, for most of the 40 calibrated elements on the ICP spectrometers, concentrations are either close to, or below, the detection limits, and only the elements Na, K, Ca, Li, B and Sr are considered adequate. Furthermore, the precision of the ICP technique results in significant analytical variation. The range for the major element ratios are comparable with the D-ICP data reported by Rankin & Graham (1988) for fluid inclusions in fluorite from the South Pennine orefield.

These data are presented in Table 7.12 for all the D-ICP results. Since the fluid salinity has been established by microthermometry, a fairly accurate estimate of absolute concentrations of the various ionic species in the aqueous portions of the fluid can be calculated from these ratios. True concentrations of the major cations in solution can be estimated using the Na to element ratio, in conjunction with the equivalent wt% NaCl, derived from microthermometry. In the case of the Q2 quartz, the D-ICP results are obviously a combination of fluid from Type 2A and Type 2B inclusions. However, the microthermometry suggests that the two inclusion types may have resulted from the unmixing of a single fluid during Q2 mineralisation. In this case, the combined response from Type 2A and Type 2B inclusions may more accurately reflect initial fluid chemistry.

The fluid compositions estimated in this manner are summarised in Table 7.13. Major differences between the fluids from different quartz stages are apparent. Such differences are likely to reflect differences in equilibrated mineral assemblage, salinity and temperature (Bischoff *et al.* 1981, Eugster 1982). Of these factors, temperature is probably the most significant with regard to the major

Fluid Inclusions - Decrepitation ICP Analysis Derived Weight Ratios						
Sample	Type	K/Na	Ca/Na	100Sr/Na	100B/Na	1000Li/Na
PMQ-1	1	0.16	0.57	1.29	2.04	4.40
26-3	2	0.13	0.59	1.44	0.64	6.60
26-3	2	0.10	0.08	0.00	0.80	6.81
A10-21b	2	0.35	0.02	0.40	0.68	6.39
26-14	4	0.11	0.19	1.28	0.19	5.96
26-14	4	0.11	0.20	1.31	0.19	6.03
30-7	4	0.11	0.13	0.97	0.41	6.72
26-2	4	0.12	0.08	0.59	0.51	7.57
26-14	4	0.11	0.16	1.32	0.19	5.84
26-14	4	0.12	0.16	1.35	0.22	6.02
30-7	4	0.10	0.08	0.77	0.30	6.62
26-2	4	0.11	0.06	0.49	0.14	6.96
26-2	4	0.11	0.06	0.50	0.15	6.81
Fluid Inclusions - De-ionised Water Crush-Leach ICP Analysis Derived Weight Ratios						
Sample	Type	K/Na	Ca/Na	100Sr/Na	100B/Na	1000Li/Na
PMQ-1	1	0.15	0.83	1.77	2.32	4.41
26-3	2	0.11	0.85	2.10	0.92	5.24
A10-21b	2	0.27	0.04	0.38	3.77	7.89
26-2	4	0.12	0.42	1.05	1.46	7.81
26-2	4	0.13	0.45	1.15	1.53	7.64
30-7	4	0.09	0.42	1.38	1.82	6.18
30-7	4	0.11	0.48	1.54	1.88	6.89
26-14	4	0.14	1.03	1.84	2.29	4.49
26-2	4	0.13	0.45	1.03	1.53	7.70
26-14	4	0.14	0.85	1.83	2.39	3.79
26-14	4	0.13	0.94	1.90	2.37	3.98
30-7	4	0.17	0.35	1.43	2.03	6.93
26-2	4	0.32	0.28	0.76	1.38	7.28
26-14	4	0.14	0.41	1.85	0.94	6.01
26-2	4	0.32	0.59	1.17	1.40	7.52
Fluid Inclusions - Lanthanum Solution Crush-Leach ICP Analysis Derived Weight Ratios						
Sample	Type	K/Na	Ca/Na	100Sr/Na	100B/Na	1000Li/Na
A10-21b	2	0.50	0.82	1.05	4.00	4.41
A10-21b	2	0.47	0.89	1.46	4.16	3.18
26-14	4	0.14	0.91	2.12	0.96	5.13
26-14	4	0.16	0.94	2.50	1.42	5.66
26-2	4	0.34	1.10	1.37	1.49	5.87
30-7	4	0.13	0.72	1.55	2.34	6.38
30-7	4	0.12	0.72	1.68	2.34	5.65
26-2	4	0.33	1.08	1.36	1.77	5.82

Table 7.12 - Derived weight ratios (Cation:Na) from ICP analysis of inclusion fluids.

Mean weight ratios (derived from D-ICP analyses)											
Quartz Stage	Na/K	Na/Ca	Na/Li	Na/B	Na/Ba	Na/Sr	Na/Fe	Na/As	Na/Cu	Na/Zn	mole% "Na" (from salinity)
1 (n=2)	6.68	1.21	226.61	43.02	317.25	56.65	105.75			507.60	0.71
2 (n=17)	9.33	16.70	130.85	101.44	549.03	405.14	163.95	42.74	302.64	324.49	0.41
3 (n=3)	25.59	6.95	576.64	331.76	442.11	70.70	479.57	201.17	765.71	199.34	0.45
4 (n=11)	8.94	9.37	157.64	470.56	488.97	118.55	287.57	269.73	1600.17	3425.66	2.40
5 (n=6)	6.87	25.41	31.52	79.93	618.89	378.25	120.69	9.49	176.99	1086.65	0.32
6 (n=2)	27.75	0.54	532.98	18.66	118.84	19.22					1.55
Mole fractions of elements in fluids (assuming total cation mole fraction is equivalent to the "equivalent Na" mole fraction derived from the salinity measurement). Hence mole % "Na"(below), is found from microthermometry "xNaCl" x 100/2). All values below as mole %											
Quartz Stage	Na	K	Ca	Li	B	Ba	Sr	Fe	As	Cu	Zn
1	0.251	0.064	0.360	<0.001	0.003	0.006	0.018	0.007			0.001
2	0.284	0.054	0.031	0.001	0.002	0.003	0.003	0.005	0.022	0.003	0.002
3	0.316	0.021	0.079	<0.001	0.001	0.005	0.016	0.001	0.005	0.002	0.004
4	1.659	0.315	0.312	0.003	0.002	0.019	0.053	0.013	0.019	0.004	0.001
5	0.177	0.044	0.013	0.002	0.001	0.003	0.002	<0.001	0.060	0.005	0.001
6	0.340	0.021	1.091	<0.001	0.009	0.017	0.018				

Table 7.13 - Tabulation of element weight ratios with respect to Na, for inclusion fluids from the various quartz generations, Q1 to Q6. Calculated below are the approximate molalities for the various elements in the fluids. These calculations are performed assuming the total cation molality is equivalent to the molality for Na, a figure calculated from the "equivalent weight% NaCl" value derived from microthermometry freezing measurements. The calculated molalities are approximate, since the presence of significant Ca and K will result in an error of salinity estimate assuming a pure NaCl system.

monovalent species, when the hydrothermal fluid has some degree of equilibration with a wallrock silicate assemblage (Giggenbach 1988). The fluid composition is, therefore, firstly discussed in terms of fluid geothermometry.

Use of alkali geothermometry

Empirically derived geothermometers based on the Na, K and Ca contents of modern geothermal waters have been shown to be useful in determining fluid temperatures (Truesdell 1984). Variation in the alkali ratios appear to be temperature dependent when fluid equilibrium with a limited number of common silicate assemblages can be demonstrated. Suitable assemblages are albite - K-feldspar - K-mica - paragonite, K-feldspar - albite etc., but also involving calcite. The theoretical basis for validity of these techniques will not be discussed here, but field evidence suggests that the Na : K geothermometers of Fournier (1981), Giggenbach (1988) and Truesdell (1984) are useful at temperatures above 180°C in cases where the presence of a feldspar - quartz - mica assemblage can be considered in equilibrium with the fluid. These thermometers have been shown to be independent of pressure (Truesdell 1984) and are thus particularly useful in the study of dynamic geological systems. Use of any of these geothermometers is based on two assumptions, that the fluid is in chemical equilibrium with the rock and that Na, K, Ca, Li bearing phases other than the assemblage outlined above are of minor importance in the rock. Fouillac & Michard (1981) have proposed a geothermometer based on fluid Na : Li ratios and the fluid Na : Ca : K ratio is used in the geothermometer of Fournier & Truesdell (1973). Giggenbach (1988) has recently highlighted the use of fluid geothermometers to assess the degree of equilibration between an aqueous fluid and a given mineral assemblage. Giggenbach (1988) suggests that Na/K ratios in geothermal fluids may actually reflect fluid reservoir temperatures and rapidly ascending fluids may not rapidly re-equilibrate with the local mineral assemblage. However, given caution, the recent use of alkali geothermometers (Rankin & Graham 1988, Yucheng 1989, Wilkinson 1990) has demonstrated their use in examining fluid P-T conditions. They show that the use of these geothermometers is relevant in fossil systems, where the two key assumptions described can be demonstrated at least in broad terms.

The use of alkali geothermometry in the study of gold deposits is to date limited to a few studies (Hubert 1986, Robert & Kelley 1987). These studies suggest that a reasonable correlation of derived temperatures and proposed fluid temperatures can be demonstrated.

Table 7.14 summarises the geothermometers proposed by various authors in the system Na - Ca - K - Li. These elements have all been analysed in the Patchway fluid inclusion fluids and have been used to calculate fluid temperatures for the various parageneses. In the case of Na : K geothermometers there is a discrepancy in derived temperatures for a given Na : K ratio between the three methods. This discrepancy is shown in graphic form on Figure 7.28. In the range of ratios derived from this study, this

Geothermometer	Equation	Units
Na-K *(Fournier 1981)*	$T = \frac{1217}{\log(Na/K) + 1.483} - 273.15$	mg/kg
Na-K *(Truesdell 1984)*	$T = \frac{855.6}{\log(Na/K) + 0.8573} - 273.15$	mg/kg
Na-K *(Giggenbach 1988)*	$T = \frac{1390}{1.75 - \log(Na/K)} - 273.15$	mg/kg
Na-K-Ca *(Fournier & Truesdell 1973)*	$T = \frac{1647}{\log(Na/K) + \beta[\log\sqrt{(Ca/Na)} + 2.06] + 2.47} - 273.15$ $\beta = 1.33$ if $T < 100°C$ or 0.33 if $T > 100°C$	mg/kg
Na-Li *(Fouillac & Michard 1981)*	$T = \frac{1000}{\log(Na/Li) + \gamma} - 273.15$ $\gamma = +0.38$ if $[Cl^-] < 0.3m$ or -0.19 if $[Cl^-] > 0.3m$	mole/l

Table 7.14 - Empirical equations used to determine fluid temperatures from alkali ratios derived from inclusion ICP analysis results.
(Temperatures are expressed in °C)

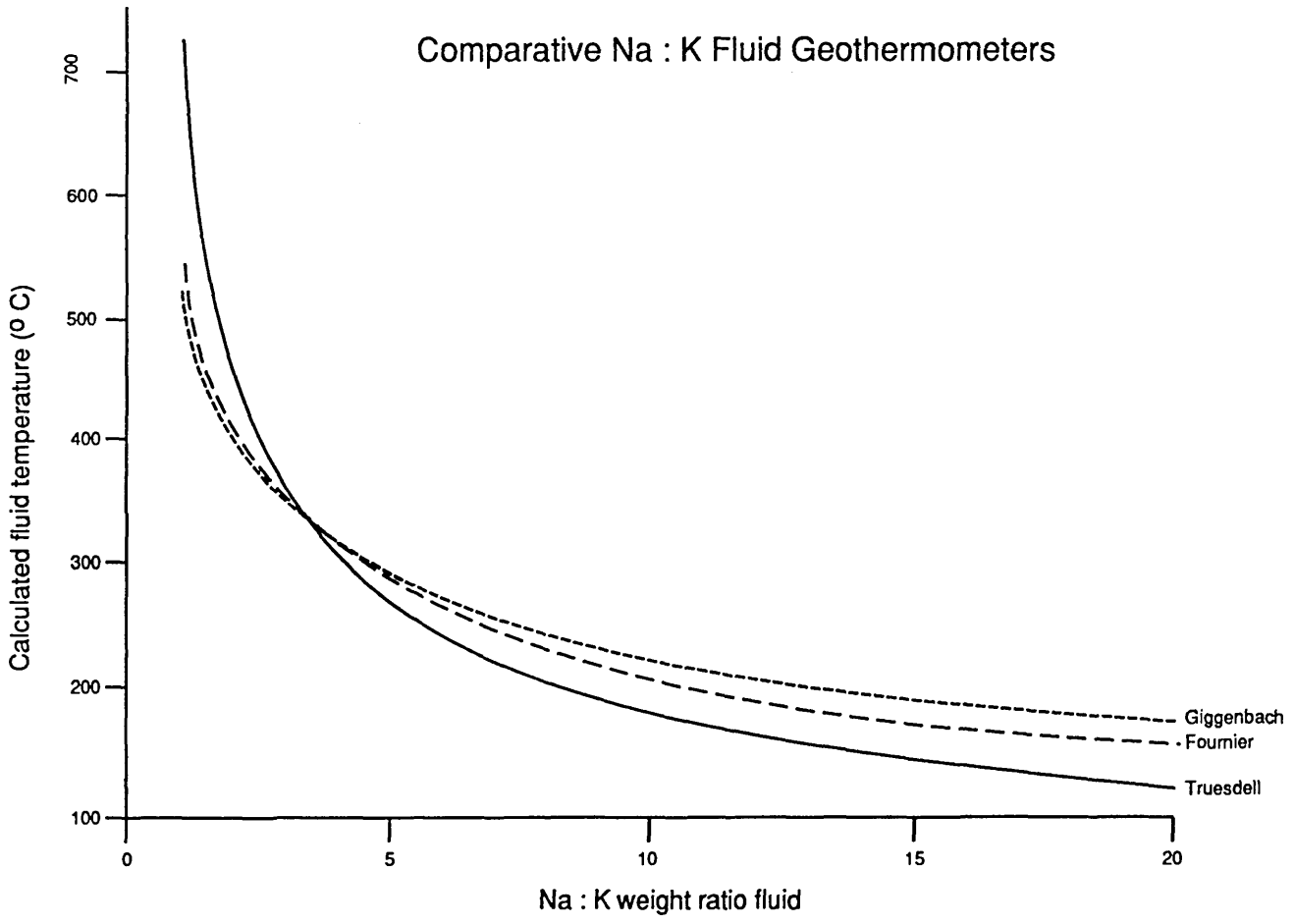


Figure 7.28 - Plot of comparative Na:K fluid geothermometers calculated from the equations in Table 7.14.

difference is less than 50°C, and in the case of the fluid responsible for gold mineralisation, amounts to less than 20°C.

7.7.3 Discussion of D-ICP Results

Fluid Geothermometry

The results for the samples analysed are shown in Tables 7.15 to 7.20. The calculated values for all the geothermometers is shown. In many cases, the calculated values are inconsistent with the observed microthermometry (i.e. values are lower than fluid inclusion homogenisation temperatures).

The Na : K ratio data is considered to be more reliable, particularly for the Q2 quartz stage, where fluid buffering with the Na-K silicate rich wallrock might be expected. The calculated range of temperatures for the Q2 samples show a mean of 279°C and mode of 285°C, very close to the mean of the homogenisation temperatures for the Type 2A inclusions. Since solvus trapping (during phase separation or unmixing) is suspected in many of the Type 2A inclusions, the Na : K derived geothermometry may be quite reasonable for trapping conditions. The Na : K values for the Q4 and Q5 fluids also derive geologically reasonable temperatures, and again buffering between the fluid and a wallrock silicate assemblage might be expected.

Major problems are anticipated with calculations involving Ca, due to the presence of Ca-bearing phases not considered in the fluid buffered assemblage modelled for the geothermometers (e.g. epidote, scheelite and tourmaline). In addition discrepencies in Na : Li derived fluid temperature values are described in data from Cornwall (Alderton & Sheppard 1977 and Edmunds *et al.* 1984), where the breakdown of Li-bearing micas in host granitic phases is suggested as the reason for abnormally high Li values. Such abnormal values are recorded for the Q4 and Q5 fluids, and may reflect an exotic Li-enriched fluid in these cases, particularly as the Q5 veins are hosted in the large tonalite intrusives.

The Na : Li ratios for the Q1 and Q2 fluid give much higher values than the Na : K derived temperatures and might possibly reflect the fluid source temperatures. In the case of Q1, the value of 330°C is close to the chlorite geothermometry value derived from EPMA analysis, consistent with lower-greenschist metamorphic facies conditions observed in the host rock assemblage. The values of 313°C to 458°C for the Q2 samples are also in the range for greenschist to amphibolite metamorphic facies conditions, and could represent the higher temperature at which the fluid was introduced into the structure. This is proposed since the separate chlorite and arsenopyrite mineral geothermometers indicate values between 300°C and 380°C for ambient temperatures at the time of sulphide and gold precipitation.

Sample Number	T Na-K[1] (°C)	T Na-K[2] (°C)	T Na-K[3] (°C)	T Na-Li[4] (°C)	T Na-K-Ca[5] (°C)
PMQ1	254	267	236	333	162

Table 7.15 - Calculated alkali fluid geothermometers for Q1 quartz sample.
Equations for calculation of individual geothermomters are from:
1 - Fournier 1981, 2 - Giggenbach 1988, 3 - Truesdell 1984,
4 - Fouillac & Michard 1981, 5 - Fournier *et al.* 1973.

Sample Number	T Na-K[1] Fournier (°C)	T Na-K[2] Giggenbach (°C)	T Na-K[3] Truesdell (°C)	T Na-Li[4] (°C)	T Na-K-Ca[5] (°C)
s26-3	317	324	323	385	211
s26-3a	293	302	289	412	222
s30-3	307	315	309	355	197
s30-3a	292	301	287	313	184
s20-12	284	294	276	---	160
s26-11	219	234	190	273	160
s10-32a	261	273	244	342	223
a10/20/d	235	249	210	458	166
a10/21/b	250	263	230	399	193
a600/6/b	371	372	404	413	217
a10/20/d	334	338	347	370	225
a10/21/d	255	268	237	402	199
a10/21/d1	245	259	224	430	185
a600/6/e	308	316	310	---	194
a600/8/f	164	182	123	---	127
a600/6/b	327	332	337	---	227
a10/21/b3	399	396	449	---	214

Table 7.16 - Calculated alkali fluid geothermometers for Q2 quartz samples.
For key to equations 1 to 5 see Table 7.16.

Sample Number	T Na-K[1] (°C)	T Na-K[2] (°C)	T Na-K[3] (°C)	T Na-Li[4] (°C)	T Na-K-Ca[5] (°C)
s400/24	146	165	102	227	110
s400/24a	150	169	107	202	118

Table 7.17 - Calculated alkali fluid geothermometry for Q3 quartz samples. Equations as for Table 7.15.

Sample Number	T Na-K[2] (°C)	T Na-K[3] (°C)	T Na-Li[4] (°C)	T Na-K-Ca[5] (°C)
s30-7	243	202	409	183
s26-2	249	210	434	185
s20-13b	241	200	370	184
s26-14	240	198	385	188
s26-14a	240	198	388	186
s26-14b	243	202	382	179
s26-14c	245	205	387	180
s30-7	233	189	406	177
s26-2a	241	200	416	193
s26-b	240	197	412	191

Table 7.18 - Calculated selected alkali fluid geothermometers for Q4 quartz samples. Equations as for Table 7.15.

Sample Number	T Na-K[1] (°C)	T Na-K[2] (°C)	T Na-K[3] (°C)	T Na-Li[4] (°C)	T Na-K-Ca[5] (°C)
TQ3	243	256	220	982	194
TQ2	316	323	321	1016	198
TQ2a	299	308	297	987	209
TQ3a	225	240	198	962	180
TQ3b	221	236	193	1002	181

Table 7.19 - Calculated alkali geothermometers for Q5 quartz samples.
Equations as for Table 7.15.

Sample Number	T Na-K[1] (°C)	T Na-K[2] (°C)	T Na-K[3] (°C)	T Na-Li[4] (°C)	T Na-K-Ca[5] (°C)
LH7a	107	128	60	183	67
LH7b	235	249	210	303	129

Table 7.20 - Calculated alkali geothermometers for Q6 quartz samples.
Equations as for Table 7.15.

Chemical Evolution of the Fluids

As outlined in the previous section, most of the major cation ratios defined by the ICP analyses, can be explained in terms of fluid temperature variation, when equilibration with a silicate assemblage can be demonstrated. However, fluid concentration of other elements such as boron and the transition metals, for which fluid-mineral element interchange is unlikely, could reflect differences in fluid source chemistry.

Data for the Na:B ratio are shown on Figure 7.29a for the different fluids. What is very apparent is, that despite some variability within sample groups, very clear differences between the groups can be demonstrated. Relatively high boron levels are associated with the fluids released from Q1, 2, 5 and 6. At first this is surprising since the vein parageneses containing tourmaline are Q3 and 4. It is clear that fluids in Q3 and 4 are depleted in boron precisely because tourmaline has precipitated due to particular ambient conditions.

It is interesting to note that the fluid from Q4 has Na:Li ratios indicative of a more exotic, possibly "granitic" source. This "exotic" Na:Li ratio is also indicated by the Q5 fluid despite the much higher salinity and lack of CO_2 in the fluid from Q4.

The Q3 fluid is enigmatic but if it does represent a composite of two mixing fluids then a complex chemical signature might be expected. One of the fluid inclusion types is quite clearly similar to Type 2A inclusions, being carbonic and with fairly high homogenisation temperatures. If there is mixing with another fluid, then it has caused the Na:B and Na:Li levels in particular to be quite different from the Q2 fluid. The other possibility is that the Q3 fluid may result from a Q2 fluid which shows extreme evolution through unmixing. Barium, shown on Figure 7.29b, shows a fairly consistent ratio with Na for all the quartz stages, except for Q6. The enhanced barium levels in Q6 is enigmatic, but may be testament to a different fluid source.

Transition metals, Fe, Cu and Zn are shown on Figures 7.29c to 7.29e. Zn:Na ratios are quite variable with highest Zn in Q3. Cu and Fe show very similar patterns, with higher Cu:Na and Fe:Na ratios indicated in the carbonic Q2 and Q5 fluids. Since chalcopyrite and pyrite are common in the D2 veins, the Q2 values are not unexpected. The enhanced Cu and Fe ratios in the Q5 fluid is further support

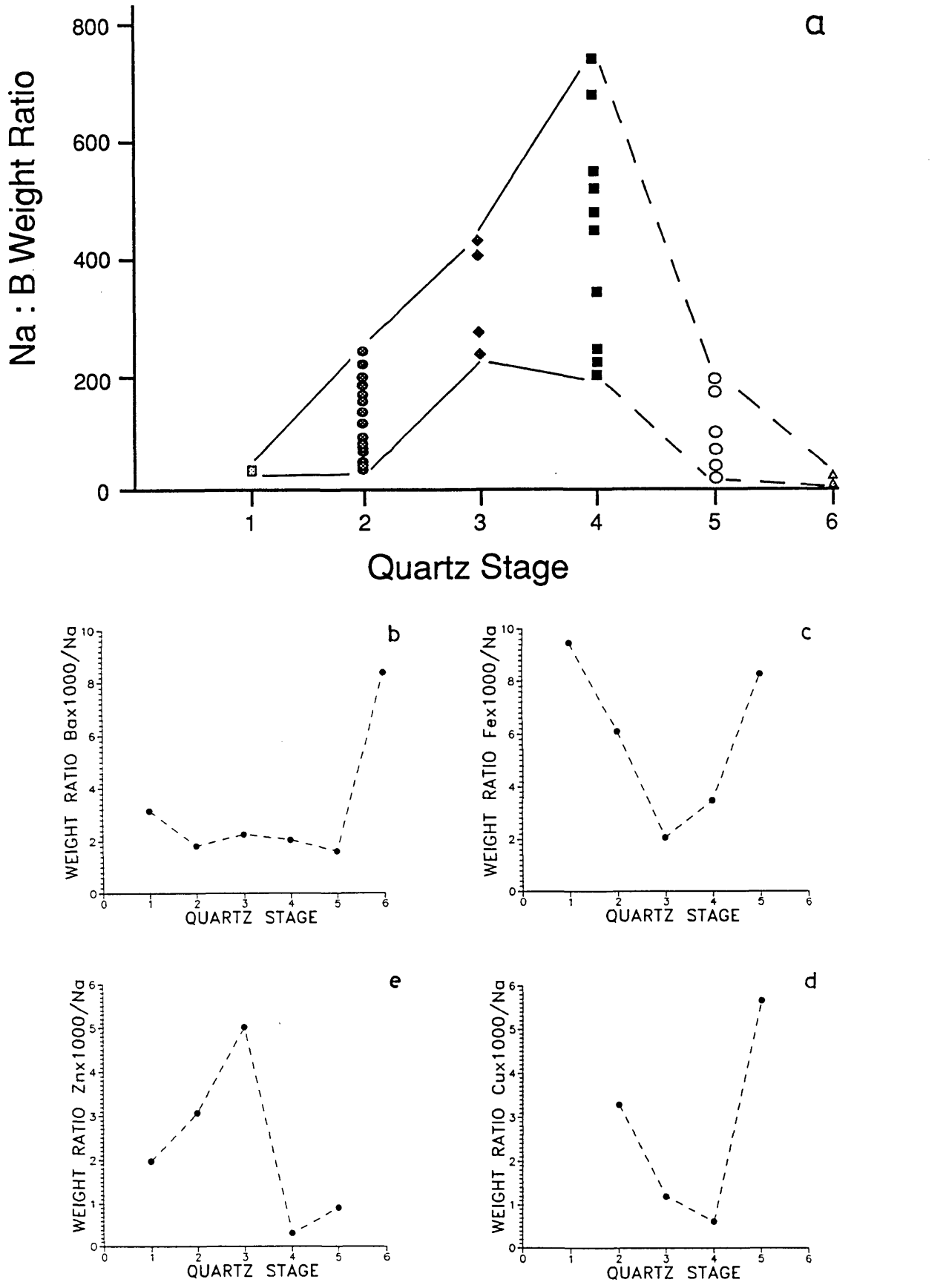


Figure 7.29 - Graphs showing variations in trace element:Na ratios for the inclusion fluids from Q1 to Q6, measured by D-ICP. Graph "a" shows B:Na, "b" shows Ba:Na, "c" shows Fe:Na, "d" shows Cu: Na and "e" shows Zn:Na. Where no points are shown, element values were below detection limit.

for a very similar chemistry to the Q2 carbonic-aqueous fluid, although the Zn:Na ratios of the two fluids are rather different.

The fluid in Q2 and Q5 primary inclusions (Type 2A and Type 5 inclusions respectively), show quite similar patterns for the dissolved, temperature independent fluid species. This is highly supportive of a common chemistry and probably source. The fluid from Q3 shows chemical evidence for affinity with both the Type 2A and Q4 primary (Type 4 inclusions) fluids. The B:Na ratio of Q3 supports a high input of the Type 4 fluid, whilst the carbonic fluid inclusions are similar to the Type 2A inclusions.

Lastly the Q6 fluid (Type 6 inclusions), although quite similar in microthermometric characteristics to the Q4 fluid, is quite different in Ba:Na ratio to all other quartz types.

7.8 Calculated Trapping Temperatures and Pressures

7.8.1 Fluid Inclusions as P-T Indicators

The temperatures and pressures for trapping conditions of the various fluid phases at Patchway can now be calculated utilising the defined parameters of fluid inclusion homogenisation temperatures, fluid compositions and the various independent geothermometry calculations. Extrapolation of the fluid inclusion homogenisation data to the established fluid temperature at the time of trapping by the process of isochore construction is necessary in some cases. In certain conditions such as boiling or phase separation, homogenisation temperature of the inclusion actually reflects the true trapping temperature, since trapping occurs on the solvus. Since in the case of the carbonic inclusions of Q2, phase separation is suspected during formation of some of the inclusions, this must be borne in mind. However, inclusions in the other quartz types show no clear signs of phase immiscibility, or indeed boiling. These inclusions trapped above the solvus, and hence an isochoric extrapolation to a higher trapping pressure and temperature is necessary.

In the case of the simple aqueous inclusions, calculations of bulk density must be calculated on the simple H_2O-NaCl system since necessary experimental data for more complex systems is not available. Utilising these bulk density calculations from the microthermometry data it is possible to extrapolate the homogenisation temperature to the trapping temperature and pressure by having an independent measurement of either trapping temperature or pressure conditions. In the case of Patchway, this is provided by the established independent geothermometry.

For the carbonic fluid phases at Patchway, the situation is a little more complex. Although the H_2O-NaCl-CO_2 system has been modelled (Bowers & Helgeson 1983, Brown & Lamb 1989), more complex fluids are indicated at Patchway. The Q2 fluids contain other species such as KCl and $CaCl_2$ and these

together with the detected miscible gases such as CH_4 have an poorly defined effect on fluid behaviour. Pure H_2O-CH_4 fluids have been modelled (Krader & Franck 1986, Haas 1978) and some degree of extrapolation of this data to the system is possible (Naden & Shepherd 1990). Again for the purposes of calculations for the Patchway fluid, approximation to a H_2O-NaCl-CO_2 fluid must therefore be assumed. However the effect of significant CH_4 in the carbonic phase must be considered. In general, at a fixed pressure and temperature, the addition of CH_4 to a single phase, mixed carbonic-aqueous fluid, close to the solvus curve, would serve to induce fluid unmixing. As a corollary, a single phase carbonic-aqueous fluid containing methane, will unmix at both higher pressures and temperatures than a similar fluid, not containing methane.

Density of the CO_2 phase can be estimated from the graphic presentation of Valakovich & Altunin (1968)'s data presented in Shepherd *et al.* (1985). The density of the aqueous phase can be defined from the salinity (hence mole fraction salts and water). These densities, together with the degree of fill of the carbonic versus aqueous phases, allows a bulk density to be calculated. In the modelling of these carbonic fluids which may have undergone phase separation during trapping, a combination of isochoric projection based on bulk density calculations (Bowers & Helgeson (1983) and Brown & Lamb (1989)), together with the experimental P-T immiscibility volume data generated by Gehrig *et al.* (1979), permits an approximation of trapping conditions to be made. The general effect of CH_4 on this system can be demonstrated from the data of Haas (1978) and Krader & Franck (1986).

Inherent in the bulk density calculations for fluid inclusions is the big error induced by poorly estimating the degrees of fill. This is critical when calculating densities of carbonic inclusions. This can be avoided by using the method proposed by Guenther (1989) which does not rely on the degree of fill estimate. However, in practice a degree of fill error of 10% at the degrees of fill indicated for the carbonic inclusions, for any given inclusion results in only a pressure estimate variation of a few hundred bars. By constructing individual isochore projections for all the fluid inclusion data using the FLINCOR programme developed by Brown *et al.* (1989) and then estimating an average isochore, this source of error can be largely avoided.

7.8.2 Calculated Conditions of Trapping

Q1

Since the Type 1 inclusions are entirely aqueous-vapour, trapped above the solvus, a simple isochore based on the average bulk density has been constructed from the microthermometry data (Table 7.21). This isochore is shown on Figure 7.30 together with the calculated Na:Li and chlorite geothermometer data which are considered robust. These lead to an estimate of 330 to 360°C and 3 to 3.5 Kbars as the ambient conditions during formation of Q1 quartz. This is roughly equivalent to a depth of burial of

Fluid (inclusion population)	Type	xH_2O,xCO_2,xNaCl	Bulk Density	Thtot mean
1 (Type 1)	H_2O-NaCl	0.986,0,0.014	0.786	158
2 (Type 2A +2B)	H_2O-CO_2-NaCl	0.839,0.153,0.008	0.869	284
3 (Type 3A)	H_2O-CO_2-NaCl	0.896,0.095,0.009	0.886	285
4 (Type 2C + 4)	H_2O-NaCl	0.952,0,0.048	1.030	137
5 (Type 5)	H_2O-CO_2-NaCl	0.954,0.040,0.006	0.870	258
6 (Type 6)	H_2O-NaCl	0.969,0,0.031	0.979	157

Table 7.21 - Summary of fluid parameters used in isochore construction. Mole fractions calculated from microthermometry. For Type 2A fluid, bulk volatile analysis confirms the estimate from fluid inclusion study. For Type 3A fluid, dilution by Type 3B inclusions makes the bulk analysis xH_2O far too high (0.940). Bulk analysis of Type 5 fluid confirms microthermometry estimate of molar fractions, NaCl content is an estimate here due to the problem of CH_4 effect on salinity estimate from clathrate melt.

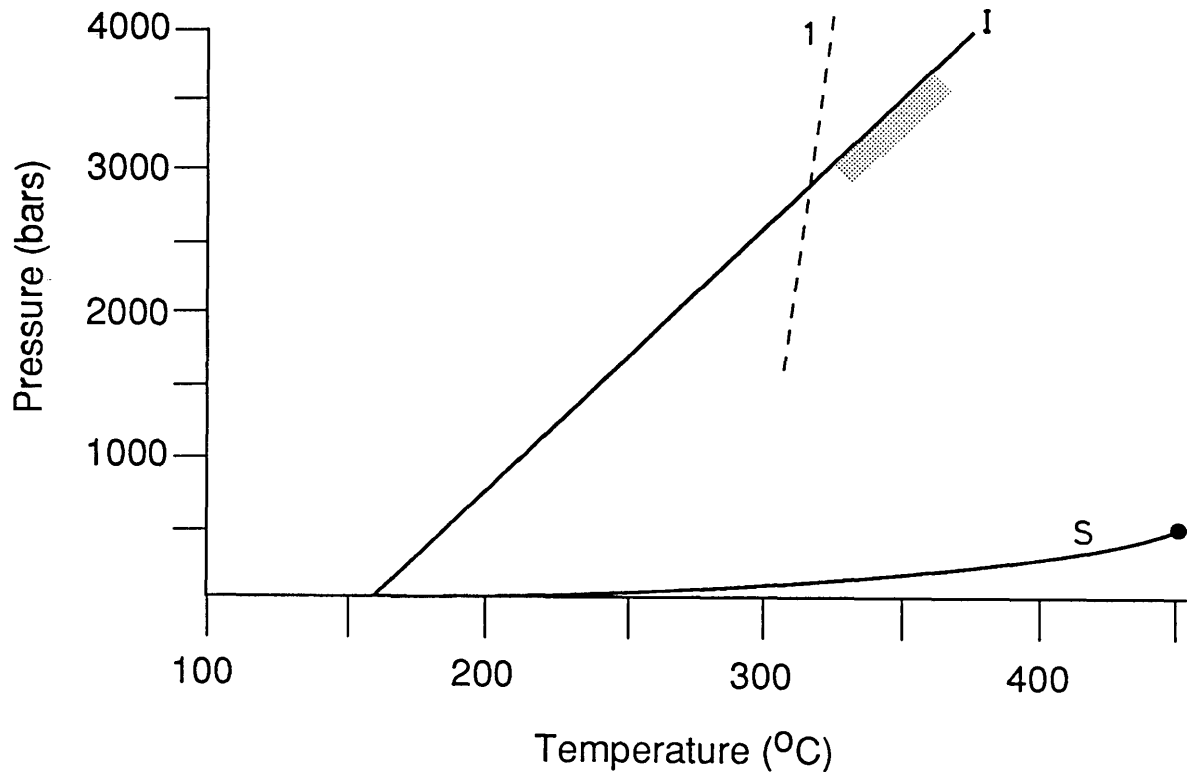


Figure 7.30 - Calculated isochore for Type 1 primary inclusions, extrapolated to trapping conditions during formation of Q1. I = calculated isochore, S = solvus curve for Type 1 fluid. 1 = curve showing lower stability field for chlorite-quartz-pumpelleyite (after Liou *et al.* 1985) and shaded box indicates temperature range indicated by chlorite mineral and Na:Li fluid geothermometry.

around 13 km assuming lithostatic load. This compares well to the likely prevailing conditions at the time of shear-zone initiation during regional metamorphism at Patchway.

Q2

Establishing the trapping conditions for inclusions during the formation of this mineralisation stage is the most problematic. The Q2 quartz is seen to contain both Type 2A and 2B co-existing, primary, inclusions. Primary, Type 2A inclusions show strong evidence of fluid unmixing during trapping and thus inclusions trapped at the solvus. For trapping at the solvus, isochoric projection is unwarranted since T_{htot} = T trapping. The unmixing phenomenon could also help to explain the very large variation in CO_2 homogenisation temperatures coupled with variable degrees of fill. Utilising the full range of microthermometric data would lead to a wide range of bulk densities calculated for individual inclusions. However, some of the inclusions containing methane are believed to represent the fluid before the unmixing event. Obviously isochores constructed from these inclusions would be more valid.

Microthermometry results from a range of individual Type 2A inclusions were processed using the FLINCOR (Brown 1988) software package. A range of bulk densities between 0.66 to 0.95 gcm^{-3} are indicated, with most of data lying in the 0.85 to 0.95 gcm^{-3} range.

Since construction of individual isochores from these inclusions gave a wide range of possible trapping conditions (to be expected if unmixing occurred during trapping), construction of an "average" isochore, representative of the Q2 fluid before mixing, would give a better estimate of bulk fluid characteristics. The "average" fluid was derived from the modal CO_2 homogenisation, clathrate melt and degree of fill measurements. The composition of this "average" fluid is further constrained by the bulk volatile analysis data, where mole fractions of H_2O, CO_2 and CH_4 were accurately known.

The "average" isochore for a density of 0.869 (from Table 7.21) is shown on Figure 7.31 which also shows the construction of the solvus line (separating the one-phase region above the line from the two phase region below). This solvus curve is constructed from the data of Gehrig *et al.* (1979) and Bowers and Helgeson (1983a), assuming no CH_4, since no experimental data for the mixed H_2O-CO_2-CH_4-NaCl system is available. This diagram defines the lower limit for possible trapping conditions, where the isochore intercepts the solvus line. This intercept condition is at 278°C at a pressure of 1.45 Kbars. If the estimate of the average fluid is reasonable, then all the fluid inclusion data for Q2 should be extrapolated isochorically above this if trapping is not at the solvus. The alkali geothermometry shows that extrapolation to higher temperature is likely to be necessary for some of the samples.

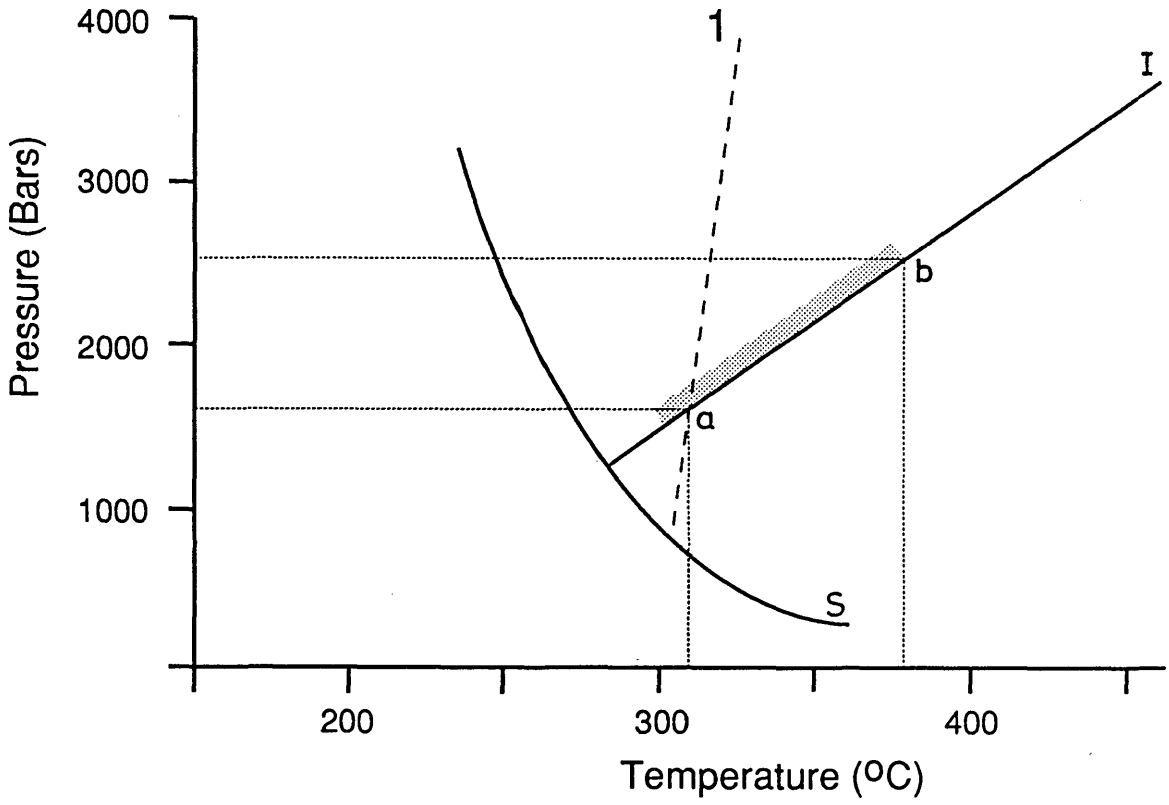


Figure 7.31 - Calculated "average" isochore for Type 2A primary inclusions, extrapolated to trapping conditions during formation of Q2. I = calculated isochore, S = solvus curve for Type 2A fluid (extrapolated from Gehrig *et al.* 1979). 1 = curve showing lower stability field for chlorite-quartz-pumpelleyite (after Liou *et al.* 1985) and shaded box indicates temperature range indicated by chlorite and arsenopyrite mineral geothermometry, and by Na:K fluid geothermometry. Estimates of the minimum and maximum of the "average" conditions are shown by a and b respectively.

The construction for the "average" fluid on Figure 7.31 is quite a valid approximation for the Q2 fluid, since the lowest homogenisation temperatures from the Type 2A and 2B inclusions is very close to the solvus-isochore intercept of 278°C. It is also apparent that the trapping temperatures and pressures for the fluid, defined from the various geothermometers ranges from a possible 2.1 to 2.8 Kbars at 330°C to 380°C. However, since unmixing is suspected, these trapping pressures are a maximum figure and significant variation below this might be expected. Further support of the unmixing model, which is invoked to explain the variable miscible gas content and degree of fill in Type 2A inclusions, together with the co-existing Type 2B inclusions, is provided by a plot of the T-X diagram for the H_2O-CO_2-NaCl system. Figure 7.32 shows this system plotted for the Type 2 fluid composition before unmixing. One curve is plotted at 3 wt% NaCl and 2 Kbars (solid line), which approximates the composition of the original fluid (constructed from Bowers & Helgeson 1983, Gehrig 1980). The other dashed curves is a 3 wt% NaCl at 0.35 Kbars, interpolated from the data of Gehrig (1980).

The shaded box shows the range of trapping temperatures, estimated from the Na:K alkali geothermometry, and the dashed extension shows the homogenisation temperature range for the Type 2A inclusions. The box is plotted at the "average" bulk fluid composition for H_2O-CO_2, shown on the X-axis. This diagram clearly shows that with the fluid composition indicated by the fluid inclusions, unmixing is inevitable if confining fluid pressure drops suddenly. Since the vein formation model hypotheses just such a fluid pressure drop, unmixing and trapping at the solvus is highly likely during vein formation. Furthermore, the result of such unmixing results in an H_2O liquid containing virtually no CO_2 (trapped as the Type 2B inclusions), and a CO_2-rich vapour (likely to be highly mobile).

Q3

Thermometric data from Type 3A carbonic inclusions measured in wafers from the Q3 quartz is plotted on Figure 7.33. The calculated bulk density of 0.886 is very similar to the Q2 carbonic fluid (Table 7.21). Two solvus curves are plotted on Figure 7.33, one drawn from the bulk volatile analysis result from Q3 quartz, the other curve plotted for the composition of the Q2 fluid. The Type 3A homogenisation temperatures have a mean around 285°C, and thus the solvus curve drawn, from the volatile analysis data must be in error. The mean point lies directly on the average Q2 fluid solvus curve, and thus may be a better estimate of Type 3A composition. The bulk volatile analysis result is affected by addition of H_2O to the analysis from the Type 3B inclusions, abundant in the Q3 quartz. It is therefore suggested that the carbonic phase of Q3 represents the final involvement of the type Q2 auriferous fluid in the structures, perhaps slightly more saline in the Type 3A inclusions.

The fluid in Type 3B inclusions is a more saline aqueous-only fluid, showing closer similarities with the Type 4 inclusion fluid. This difference suggests that the Type 3B inclusions may in fact be a late overprint on the Q3 quartz. The Type 3B inclusion isochore is very similar to the Type 4 inclusion isochore presented below.

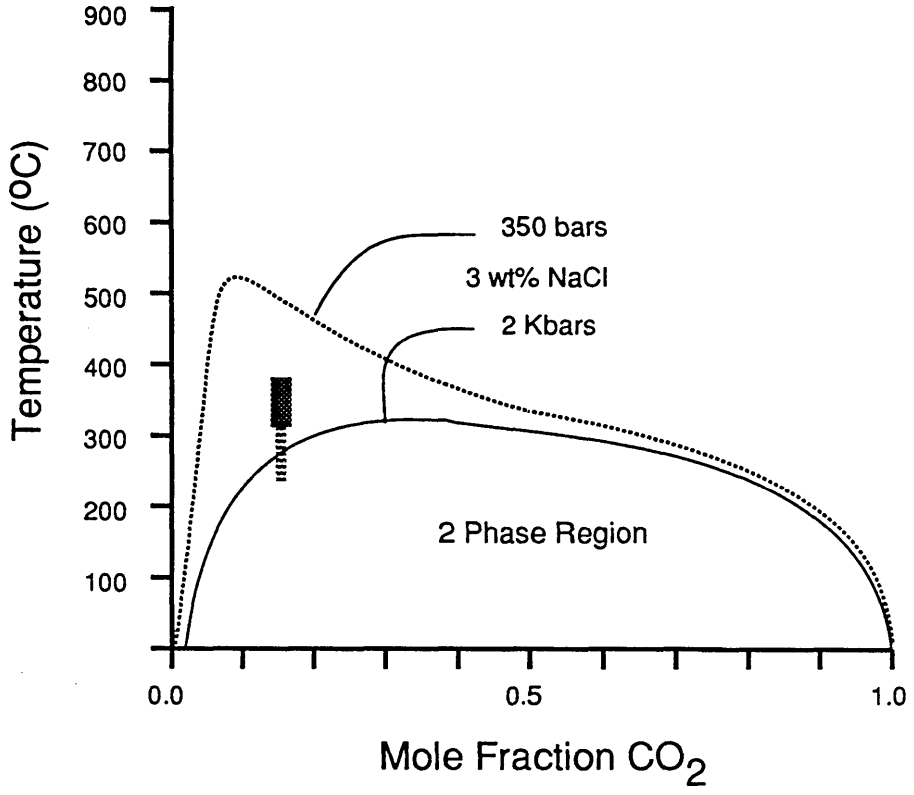


Figure 7.32 - *T-X* plot for the H_2O-CO_2-NaCl system. Solvus curves are plotted (extrapolated from Bowers & Helgeson 1983a and Gehrig 1980) for a 3 wt% NaCl fluid at 2000 and 350 bars (solid and dashed line respectively). Such a fluid approximates the composition of the Type 2 carbonic fluid (inclusions Types 2A plus 2B), before unmixing. I = calculated isochore, S = solvus curve for Type 2A fluid (extrapolated from Gehrig *et al.* 1979). The shaded box shows the probable composition and range in temperature of the Patchway fluid, which lies in the one-phase field (liquid) at 2 Kbars pressure. The dashed tail to the box shows the possible low range of temperatures estimated for the Type 2 fluid during trapping, if some of the inclusions which show unmixing reflect solvus trapping. In any event, such a fluid is highly sensitive to pressure drop shown by the shift in the solvus position at 350 bars. Large pressure drop in the system will undoubtedly initiate fluid unmixing.

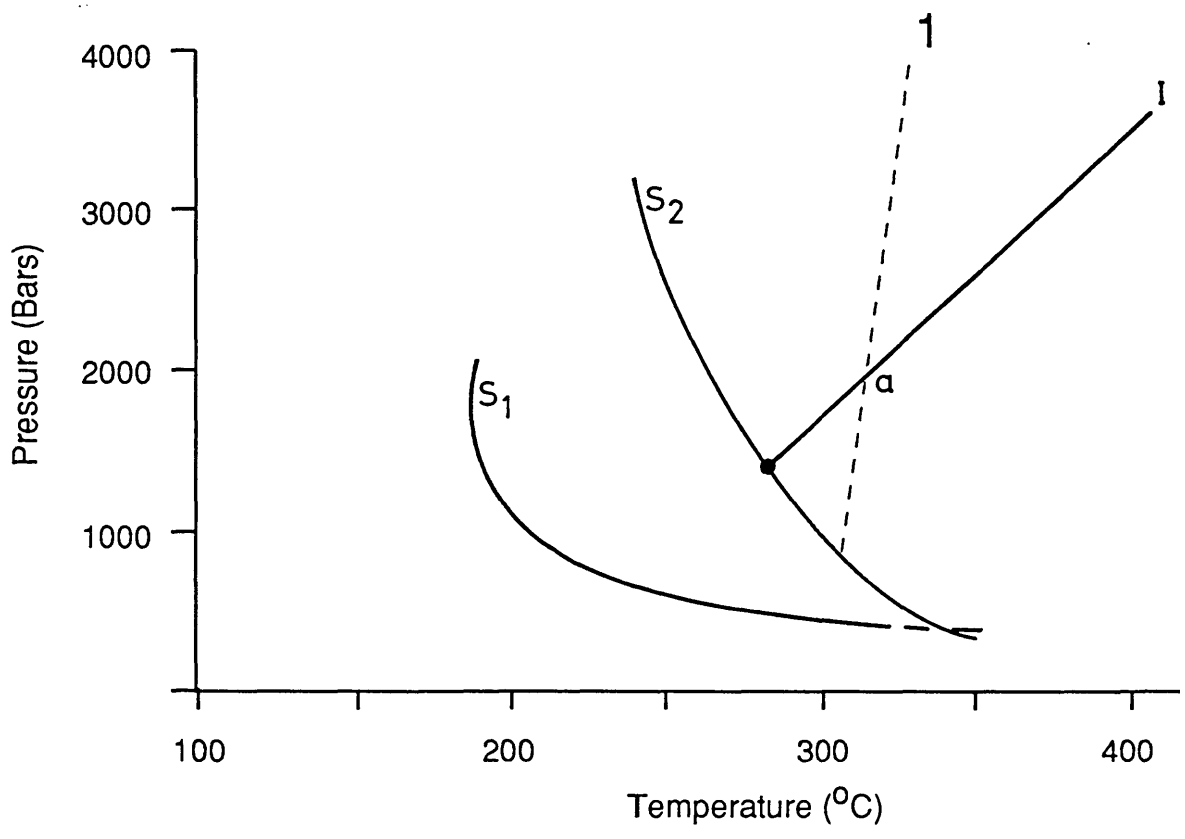


Figure 7.33 - Calculated isochore for Type 3A primary inclusions, extrapolated to trapping conditions during formation of Q3. I = calculated isochore, S_1 = solvus curve for Type 3 fluid (Type 3A plus Type 3B inclusions) from bulk volatile analysis, S_2 = solvus for Type 2 fluid from Fig. 7.31 (extrapolated from Gehrig *et al.* 1979). 1 = curve showing lower stability field for chlorite-quartz-pumpelleyite (after Liou *et al.* 1985) and point "a" indicates the minimum trapping temperature and pressure assuming chlorite-quartz stability.

Q4

This fluid is also represented by aqueous-vapour inclusions only, trapped above the solvus and again a simple isochore can be constructed. The mean of the data from the microthermometry is used to calculate bulk density for both the "primary", Type 4, and "secondary", Type 2C, inclusion populations (Table 7.21). When plotted, the isochores are parallel and almost co-incident, further support for them being the same fluid (Figure 7.34).

The conflicting geothermometers are plotted, and it becomes apparent that the Na:K values lead to the more credible conditions of a maximum of 250°C and 2 Kbars for trapping conditions. The Na:Li value of >380°C leads to a pressure estimate of more than 4 Kbars, giving a depth estimate below that for the more ductile deformation phase during D2 for the proposed deformation and metamorphic regime, since much of the deformation during D4 is brittle extensional fracturing. The high lithium values would therefore appear to reflect a rather more Li enriched fluid source than would be normally buffered at this temperature.

Q5

Since fluid inclusions in Q5 did not show any evidence for phase separation, a simple average isochore was constructed using the mean of the microthermometric data. The fluids are of very low apparent salinity (< 1 wt% NaCl), and this together with the CO_2 homogenisation temperature leads to a bulk density calculation of approximately 0.87 (Table 7.21). This density is quite similar to the Q2 fluid and thus a similar isochore can be constructed.

The chemical composition of the fluid is somewhat different and thus a different solvus line is to be expected. The isochore and calculated solvus line are plotted on Figure 7.35, where the two lines are seen to intercept at around 235° and 700 bars. Alkali geothermometry suggests a temperature close to the mean homogenisation temperature is likely for trapping, around 265°C. This implies a pressure of around 1 Kbar, significantly shallower than conditions demonstrated for D2. This concurs with the obviously brittle fracture style to the veining.

Q6

The highly variable independent geothermometry data available suggests a maximum trapping temperature of around 200°C. Bulk density data calculated from the microthermometric measurements (Table 7.21) can be used to construct a simple isochore (Figure 7.36). From this it can be assumed that the maximum trapping temperature of less than 180°C equates to a pressure less than 800 bars.

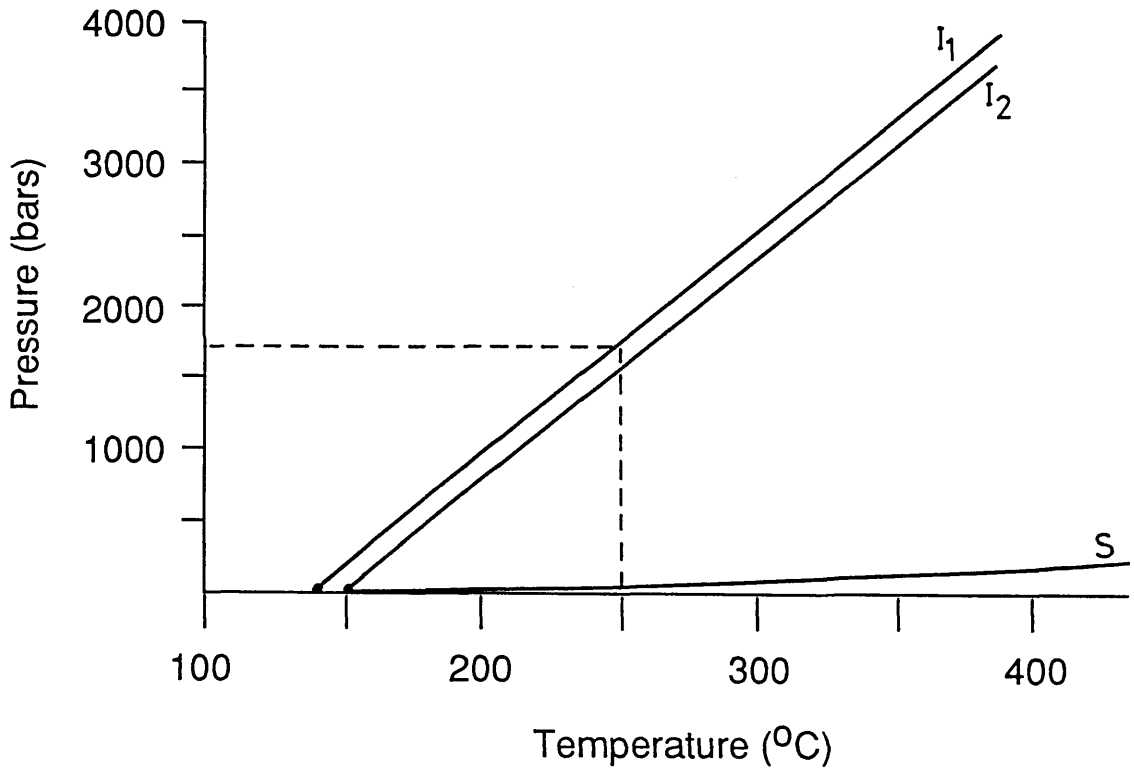


Figure 7.34 - Calculated isochore for Type 4 primary and Type 2C secondary inclusions, extrapolated to trapping conditions during formation of Q4. I_1 and I_2 = calculated isochores from Type 4 and Type 2C inclusions respectively, S = solvus curve for Type 4 fluid. Dashed line indicates maximum trapping temperature estimated from fluid geothermometry.

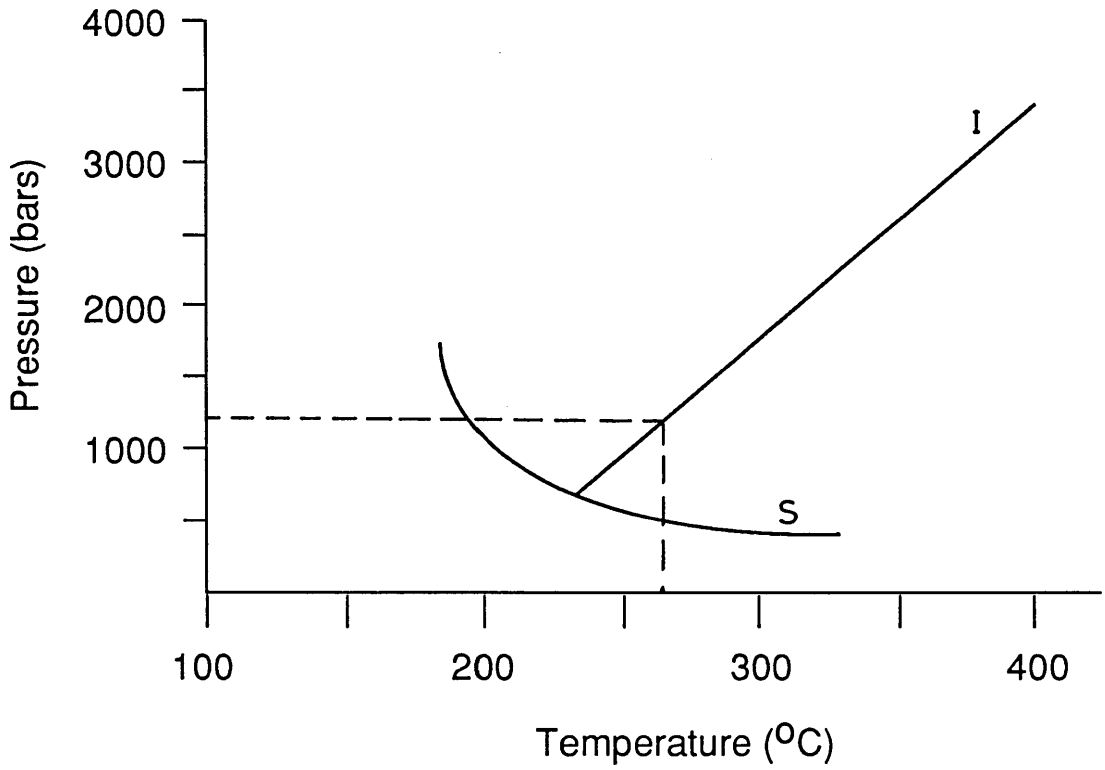


Figure 7.35 - Calculated isochore for Type 5 primary inclusions, extrapolated to trapping conditions during formation of Q5. I = calculated isochore from Type 5 inclusions, S = solvus curve for Type 5 fluid (extrapolated from Gehrig *et al.* 1979). Dashed line indicates maximum trapping temperature estimated from fluid geothermometry.

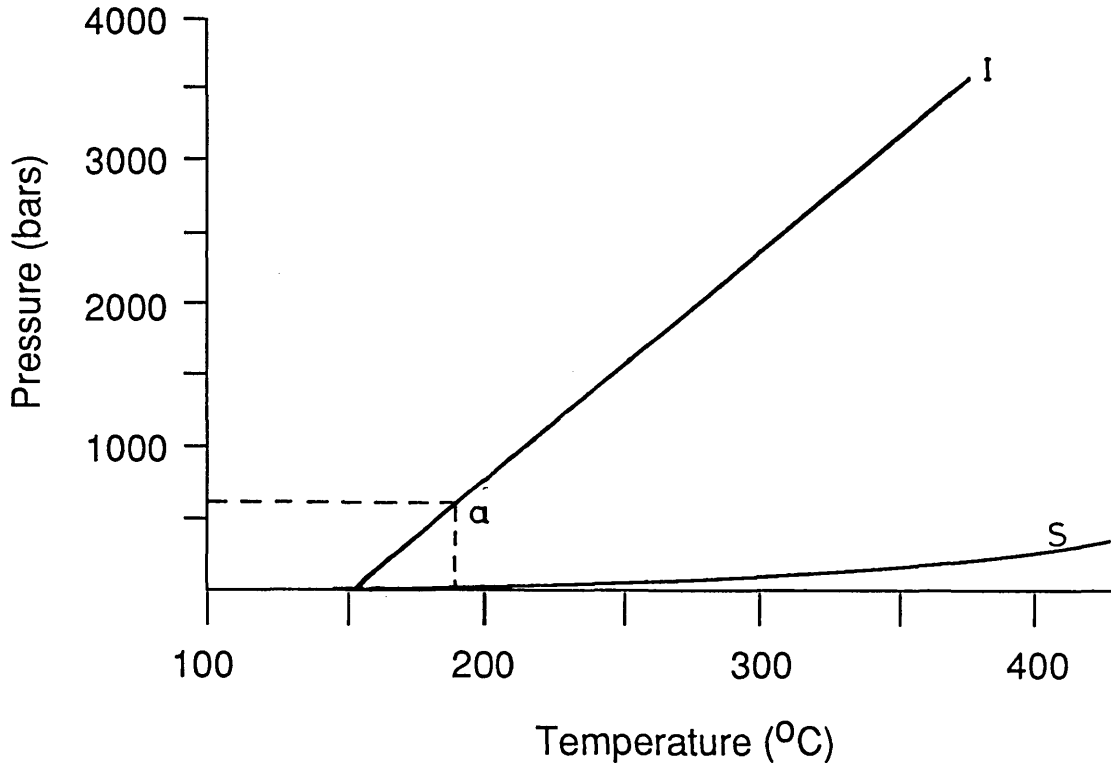


Figure 7.36 - Calculated isochore for Type 6 primary inclusions, extrapolated to trapping conditions during formation of Q6. I = calculated isochore from Type 6 inclusions, S = solvus curve for Type 6 fluid. Dashed line indicates maximum trapping temperature estimated from fluid geothermometry.

7.9 Detailed Study of D2 Ribbon Quartz Veins

Detailed fluid inclusion studies were carried out on the main ribbon vein at the two localities indicated by stars in Figure 5.18. The inclusion wafers were cut from vein pillars which are shown in the photographs in Figure 4.16. The aim was to document the variation in fluid inclusion characteristics with respect to sample position and paragenetic association within the vein. This was initiated from the study of quartz where undeformed grains were host to gold grains. The sample showed strong evidence for i) primary methane in the fluid trapped close to the gold grains (Type 2A CO_2 and CH_4-bearing inclusions), ii) strong evidence for fluid unmixing during gold precipitation and iii) evidence that later quartz trapped methane poor fluids, perhaps even containing sulphate minerals indicative of more oxidising conditions (Type 2B inclusions, some containing solid, birefringent phases). This change, if it could be demonstrated, has important implications for CO_2, CH_4 and H_2O ratios, hence likely fO_2. The studied vein profiles are shown in Figure 7.37, where sampling was made with regard to the three distinct types of region (A, B and C - see Chapter 4), within the ribbon vein. These different regions might have formed at different times during the vein dilatancy, fluid infilling and mineral precipitation cycle predicted by the vein formation mechanism outlined in Chapter 4.

7.9.1 Microthermometry and Volatile Analysis Results

Sample locations for the 6 Level vein are shown on Figure 7.37a. Measurements of T_{mCO2}, T_{mClath}, T_{hCO2} and T_{htot} were made on the inclusions. Only data directly pertinent to the estimates of dissolved volatiles are presented here (CO_2 and clathrate melts), as the study of the relative CO_2, H_2O and CH_4 contents of the inclusions could be indicated from this data. These data are shown on Figure 7.38 where distinct, consistent differences are observed of the melting point of the CO_2 phase , approximately consistent with a rise in clathrate melt temperature. The plot on Figure 7.39, from comparative microthermometric versus bulk volatile analysis data, indicates that the depression of the CO_2 melting temperature away from the pure CO_2 triple point of -56.6 Celsius is a direct indicator of the methane content of the fluid since the levels of nitrogen (the only other likely possible cause of significant melting point depression) is shown to be generally low (Table 7.9). From Figure 7.38, it is apparent that the higher CH_4 : CO_2 ratios are associated with the wallrock septa and included slivers of wallrock (region types A and B) whilst the barren, quartz only ribbons (region A) have low CH_4 : CO_2 ratios, with, in some cases, less than detectable methane.

The vein on 10 Level has the same ribbon appearance (Figure 7.37b), although the "A" (quartz only) areas are much broader, and significantly gold grades are lower than the 6 Level pillar (Patchway Mine Records). Fluid inclusion wafers were again cut from different areas of the vein and carefully-selected, clean, quartz samples from contrasting areas of the vein were taken for comparative volatile analysis.

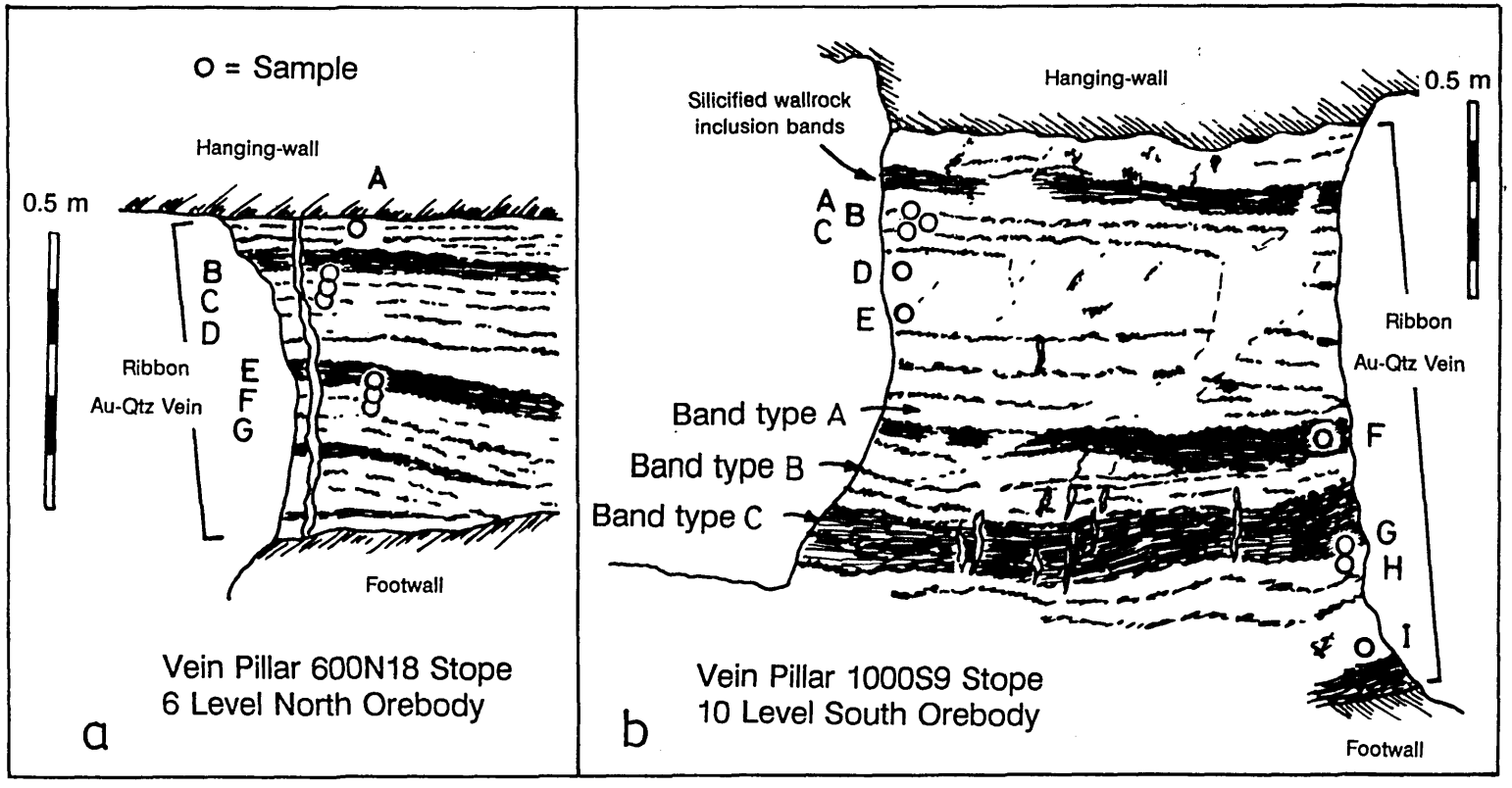


Figure 7.37 - Sample location sketch of detailed fluid inclusion study on 6 and 10 Levels. For location see starred localities on Figure 5.18. Sample letters shown on the sketches are consistent through Figures 7.37, 7.38 and 7.40. They refer to samples collected as follows:

6 Level : A = 6006e, B = 6006d, C = 6006c, D = 6006b, E = 6007b, F = 6008d, G = 6008f

10 Level : A = A/10/20b, B = A/10/20c, C = A/10/20d, D = A/10/20e, E = A/10/21b, F = A/10/27A, G = A/10/28a, H = A/10/30e, I = A/10/31a

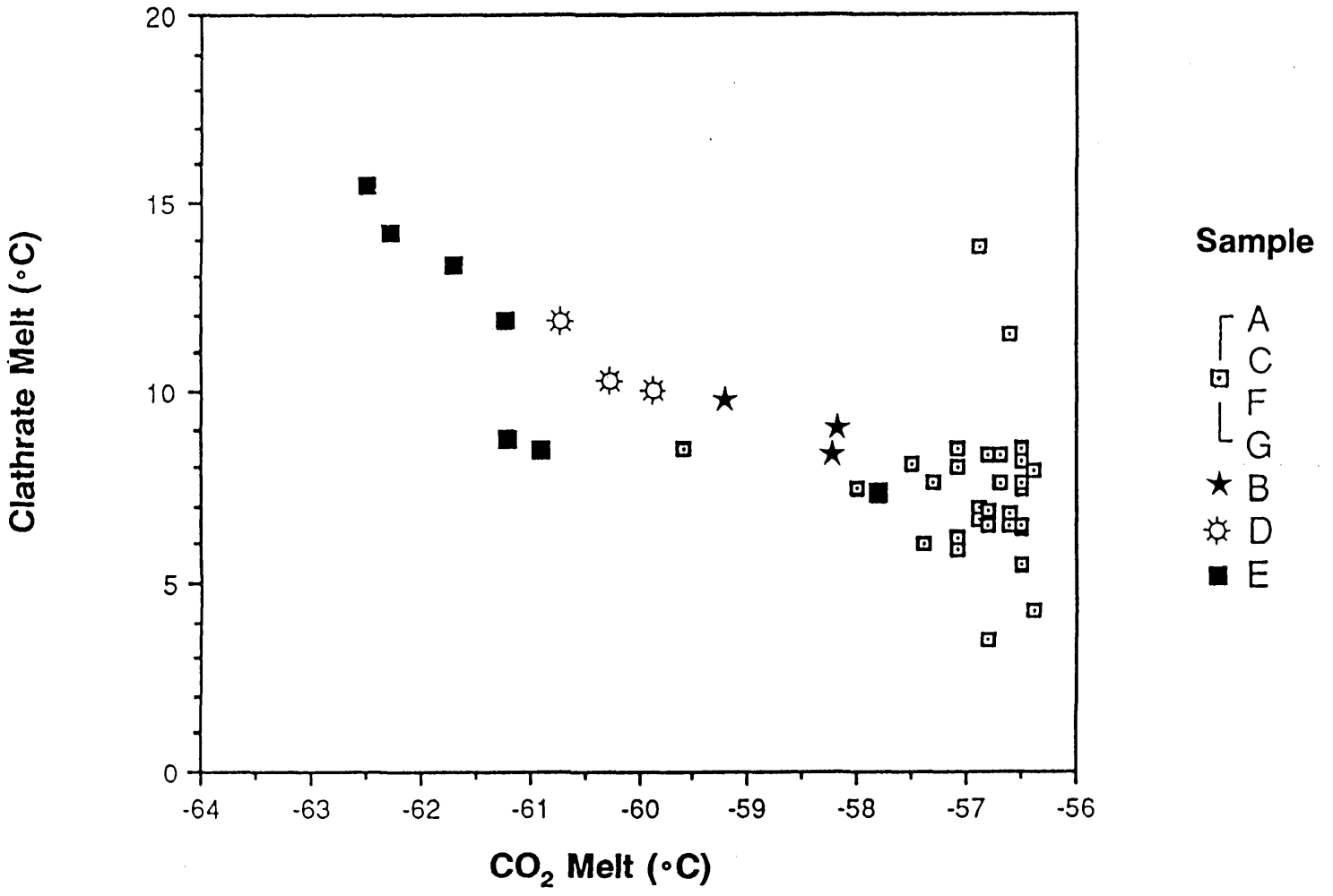


Figure 7.38 - Microthermometry from Type 2A primary fluid inclusions in 6 Level pillar (Fig. 7.37a). Sample letters shown are explained on Figure 7.37.

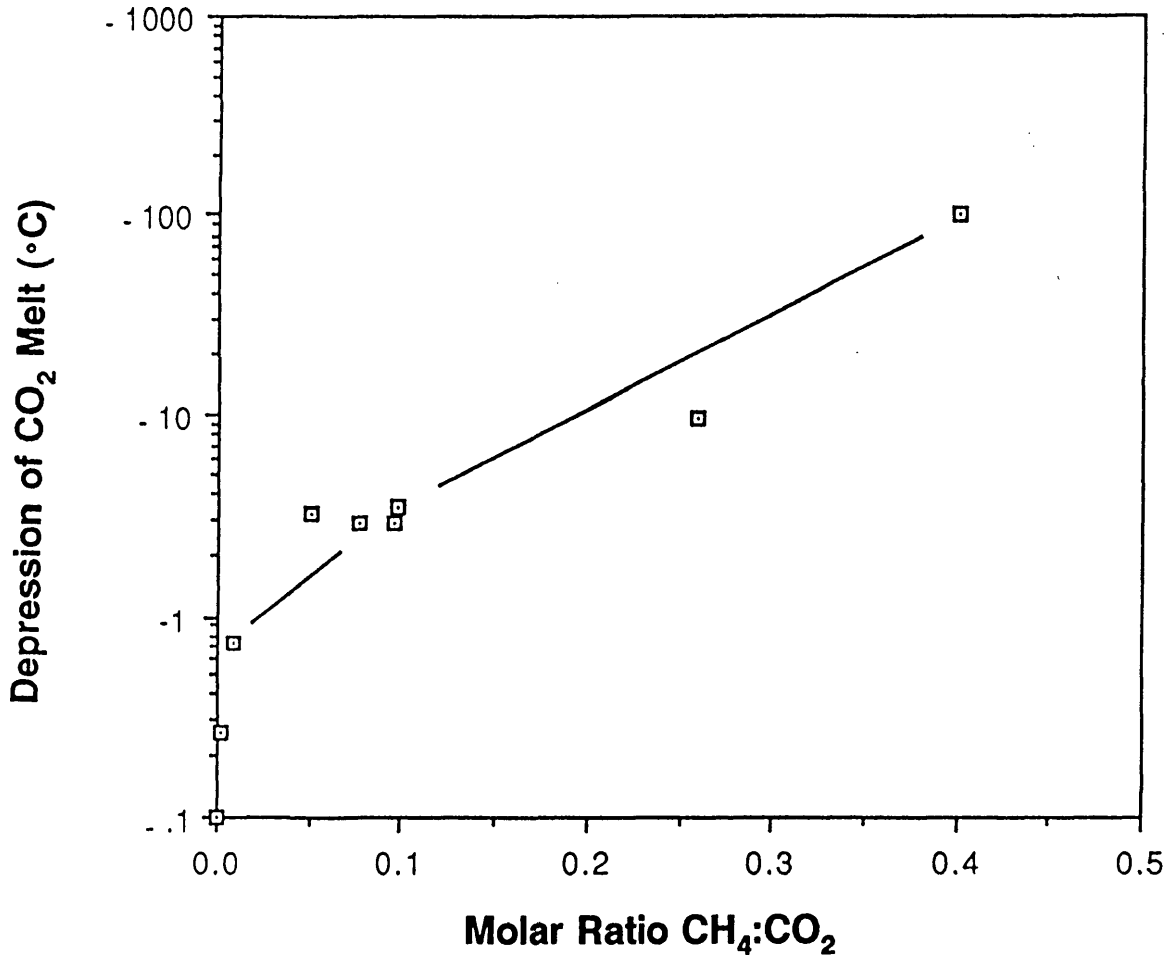


Figure 7.39 - Comparison of observed depression of CO_2 melt temperature and CH_4:CO_2 ratios determined by bulk analysis for samples studied. Depression of CO_2 melt is evidently a function of CH_4 content.

Wafers cut from all region types of the vein (A, B and C) contain dominantly Type 2A inclusions, with some Type 2B inclusions. Type 2C inclusions, where observed, were ignored as they formed after development of the ribbon-veins. Microthermometric results are shown on Figure 7.40 and the main conclusions are again that depresssion of CO_2 melting temperatures, reflecting methane levels, is greatest in the wallrock-inclusion and phyllosilicate regions (B and C). "Barren" quartz, from region A, shows negligible CH_4 with the data forming a cluster close to the pure CO_2 value of -56.6°C.

Data from both areas points to the strong association in the veins between regions A and B (where sulphides and gold almost always occur) and the presence of significant methane in the inclusion fluid.

7.9.2 Discussion

The presence of methane in fluid inclusions associated with shear-hosted gold veins has generally been interpreted in terms of fluid-wallrock interaction (e.g. Ho 1987). However, methane is reported from gold deposits where the sediment association is unclear (e.g. Spooner *et al.* 1987). This is particularly true at Patchway where the host rocks contain no carbonaceous matter and are almost entirely dominated by mafic volcanics and acid intrusives. Analysis of fluids from later, but associated, veins transecting the large regional tonalite intrusives show up to 0.2 molar% methane (Table 7.9) where a host-rock source of reduced carbon can be almost completely excluded. The gold bearing fluid was probably introduced into the vein fracture, containing up to 3 mole% CH_4 in solution prior to the mineralisation event, with a composition close to the composition of the fluid inclusions in the quartz wafers examined which are seen to host gold grains.

Data from both vein areas studied points to the strong association between the ribbon margins (where sulphides and gold almost always occur) and the presence of significant methane in the inclusion fluid. The quartz in the barren central portions contains less (or often negligible) methane. This difference between methane bearing and methane poor fluid has important implications for fluid fO_2.

Numerous studies cite phase separation in a gold bearing carbonic fluid as an effective mechanism for gold precipitation from a sulphur complex (e.g. Spooner *et al.* 1987). This effectively allows the reduced species such as H_2S, H_2 and CH_4 which have high vapour partition coefficients (Drummond & Ohmoto 1985) to pass into the vapour phase. Phase separation in this case is analogous to boiling, but here is the condition when the carbonic fluid separates into a dominantly carbonic vapour phase leaving a residual more aqueous enriched liquid phase. "Boiling" has an even more profound effect to destabilise and hence precipitate soluble gold dissolved as a chloride complex (Seward 1990). Such an event is also shown to have a major effect on the solubility of silica at the ambient pressures and temperatures likely for the Patchway system (see Chapter 4). The implications for such a fluid model on the hydrothermal system are addressed in Chapter 9.

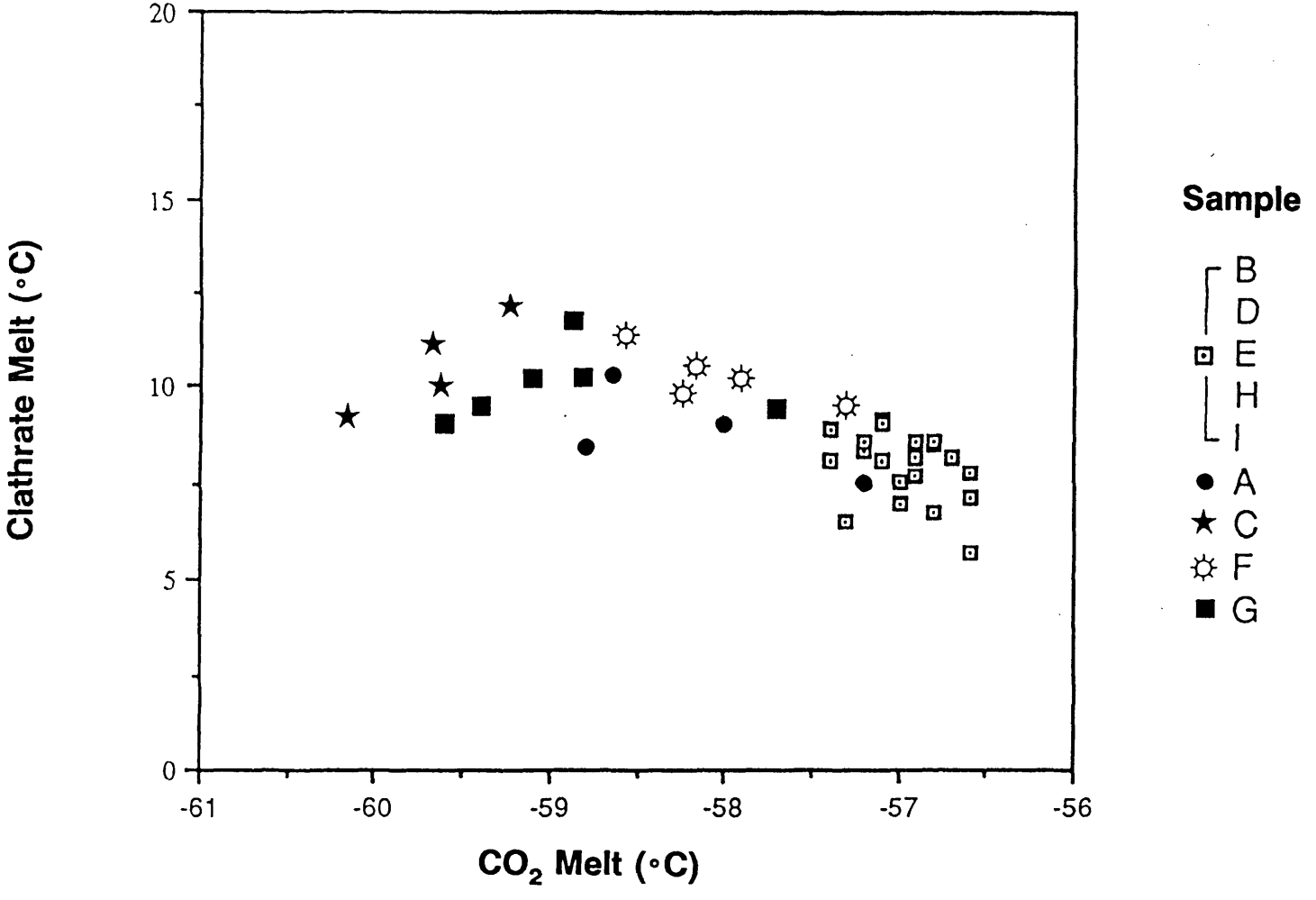


Figure 7.40 - Microthermometry from Type 2A primary fluid inclusions in 10 Level pillar (Fig. 7.37b). Sample letters shown are explained on Figure 7.37.

The data collected at Patchway points to a phase separation model, as the likely mechanism for fluid evolution during the D2 mineralisation event. The hydrothermal fluid carrying gold was introduced as a carbonic-aqueous low salinity fluid where CO_2 and methane were in equilibrium. Inducing phase separation in such a fluid leads to the partitioning of species referred to earlier. The necessary trigger for phase separation in the case of Patchway is caused by the rapid fluid pressure drop likely after the catastrophic hydraulic fracturing which opened the incremental ribbon.

7.10 Summary of Fluid Characteristics of the Evolving Mineralised System

Fluid inclusion study has highlighted the differences between the quartz generations identified during the structural mapping. There are clear differences in ambient P-T conditions of formation and distinct chemical changes in fluid chemistry between generations.

The earliest, Q1, quartz contains primary aqueous only fluid inclusions of 9.8 equivalent wt% NaCl. Trapping conditions of 330 to 360°C at 3 to 3.5 Kbars are indicated, equivalent to a maximum burial depth of 13 km, assuming lithostatic load. This is consistent with the peak of lower greenscist facies metamorphism. The Q1 fluid has low dissolved transition metal levels but high boron levels, and is fairly consistent with a locally derived, metamorphic fluid.

The gold-bearing ribbon-vein quartz, Q2, contains primary inclusions suggestive of fluid unmixing during trapping. Carbonic-aqueous inclusions containing some methane are believed to represent the original fluid before unmixing. The indicated salinity of the aqueous phase is 3.5 equivalent wt% NaCl, and the fluid contained around 13 mole% CO_2 and 2.2 mole % CH_4. Fluid unmixing results in formation of aqueous-only inclusions and loss of the miscible gas phases. Trapping conditions are estimated to lie in the range 300 to 330°C and 1.8 to 2.2 Kbars fluid pressure, although much lower pressures might be anticipated during the mineralisation event itself. Assuming that fluid pressures may approximate lithostatic load, depths of some 9 km might be expected. This is consistent with some degree of uplift after peak metamorphism during formation of Q1. Alternatively fluid pressure may be somewhat lower than lithostatic load, and in this case, 9 km is a minimum depth estimate. The chemistry of the Q2 fluid, from representative analyses, indicates elevated base metal levels, consistent with the observed base metal sulphides within the veins, particularly chalcopyrite.

The inclusions in Q3 show evidence for being of two fluid sources. Some inclusions contain a fluid very similar to the Q2 carbonic fluid. The other aqueous-only inclusion type is similar to secondary inclusions in the Q2 quartz and primary inclusions in the Q4 quartz. The Q3 carbonic fluid shows many characteristics of the Q2 primary fluid, evidently low salinity (3.8 equiv. wt% NaCl). Trapping conditions for the Q3 carbonic inclusions are similar to those of the Q2 inclusions. The aqueous only inclusions have a salinity of 12 equivalent wt% NaCl, but trapping conditions are poorly constrained. Chemical

analysis of the Q3 quartz is somewhat meaningless, since two different fluids are in the same quartz. However, the chemical results suggest much different levels of B, and perhaps Zn, to that of the Q2 fluid.

The Q4 quartz contains predominantly one population of aqueous-only inclusions. A moderate salinity of 14 equivalent wt% NaCl is indicated, with significant Ca present in the fluid. Trapping conditions for the inclusions are interpreted as 250°C and 2 Kbars ambient pressure. This equates to a depth of around 9 km if assuming lithostatic load, a similar burial depth to the Q2 quartz, at significantly lower temperature. Chemically the fluid is quite different to the Q2 fluid, with much lower base metal to Na ratios. This fits with the general lack of significant mineralisation associated with the Q4 veining. The B:Na ratio is very low, despite the clear association of tourmaline with the Q4 quartz. Perhaps the low boron is in fact due to its precipitation from the fluid.

The Q5 quartz contains carbonic-aqueous inclusions with very similar characteristics to those in the Q2 quartz. Q5 inclusions show no sign of fluid unmixing however and the salinity appears lower, although difficult to quantify due to the presence of methane in the inclusions. However, a similar salinity to the Q2 carbonic-aqueous inclusions is suggested (3.5 wt%). Trapping conditions are estimated at 265°C and 1 Kbar, significantly lower than the Q2 inclusions. This equates to a depth of 4.5 km assuming lithostatic load, consistent with the brittle style to the veining. The base metal ratios of the fluid are similar to the Q2 fluid. Without strict constraint on salinity, the validity of these ratios is difficult to assess.

Lastly, Q6 quartz contains primary, aqueous only, inclusions. The fluid has a salinity of 9.8 equivalent wt% NaCl. Trapping conditions poorly constrained by fluid geothermometers, but are estimated to be less than 200°C at a pressure of around 800 bars. Again, this is consistent with the observed brittle style to the veining. The base metal levels in the fluid are very low (generally below detection limit), but the Ba:Na value is extremely high, unlike any of the other fluid types.

Possible sources and provenance for these fluids are further discussed in light of the thermodynamic calculations and stable isotope study presented in Chapter 8.

CHAPTER EIGHT - HYDROTHERMAL FLUID MODELLING

8.1 Introduction

The gold-bearing quartz vein mineralisation and its associated alteration envelope developed marginal to the veins were formed during the introduction of a carbonic-hydrothermal fluid during the deformation events, D2 and D3. Strong K-metasomatism is evident with concomitant Na-depletion, similar to many Archaean gold deposits elsewhere (Colvine *et al.* 1988). Later mineralisation is largely confined to brittle structures and fluids show limited interaction with host rocks.

The broad chemical nature of this fluid has been determined in the preceeding chapters and one of the aims of this chapter is to try to characterise further the thermodynamic activities (a_i) of fluid species, particularly H^+, O_2, H_2S and SO_2. From the fluid inclusion volatile and cation analysis data presented in Chapter 7, thermodynamic calculation of activities of various species (including major cations, pH, fO_2 and fH_2S) can be made. Evolution of this fluid during the mineralisation event can be semi-quantified in terms of fO_2 and fS_2.

During the current study, oxygen isotopes in quartz from the various quartz generations were determined. In addition carbon and sulphur determinations were made from the gold-bearing mineralised zone and the associated marginal wallrocks. The isotopic study of quartz included analysis of samples from the vein pillars, where comparitive fluid inclusion microthermometry, volatile analyses and D-ICP analyses were available.

8.2 (D2) Gold Bearing Fluid Cation Activities and pH

From the fluid inclusion study in Chapter 7, the parameters for the gold bearing fluid are shown in Table 8.1. From these parameters it is possible to calculate the activities of the main ionic species involved. Activities of dissolved species (in this case ions) may be calculated from the equation:

$$a_i = \gamma_i \cdot x_i \qquad (8\text{-}1)$$

Here a_i is the activity of the species i, x_i is the molar fraction of i and γ_i is the activity co-efficient of i. The activity co-efficient can be calculated from a version of the expanded Debye-Hückel equation (Truesdell 1984) (see Figure 8.1). Confident use of this equation in systems with total molalities below 2 molal is to be expected at the indicated range of temperatures, 250°C to 400°C, of the Patchway system (Truesdell 1984). At high temperatures or low absolute concentrations dissociation is almost complete and $\gamma_i \rightarrow 1$.

From Table 8.1 the total ionic strength, I (which is effectively $\Sigma\, mNa^+ + mK^+ + mCa^{2+}$ for such a fluid) is equal to the chloride molality of 0.52m, indicated from the fluid inclusion microthermometry.

$$-\log \gamma_i = \frac{Az_i^2 . I^{1/2}}{1 + \mathring{a}_i B I^{1/2}} + bI$$

Figure 8.1 - Expanded Debye-Hückel equation for simple ionic solutions (after Truesdell 1984). Equation shows where, for a given species, i, z is the ionic charge and A, B, $\mathring{a}_i$ and b are constants. I, the ionic strength, in most geothermal systems, approximates the sum of $mNa^+ + mK^+ + mCa^{2+}$ (molalities). The constants A and B are related to solvent properties (assumed to be water here) and can be obtained from tables (Helgeson *et al.* 1981). Constant $\mathring{a}_i$ is the distance of closest approach between specific ions, again approximated from tables (Truedsdell & Jones 1974). Constant b is called the deviation function and here is approximated to 0.05 (after Helgeson 1969). Confident use of this equation in systems with total molalities below 2 molal is to be expected at the indicated temperatures less than 400°C, which is anticipated for the Patchway system (Truesdell 1984). At high temperatures or low absolute concentrations dissociation is almost complete and $\gamma_i \rightarrow 1$.

Fluid Salinity Equivalent wt% NaCl	Cl- Molality	Na : K Molar Ratio	Na : K Activity Ratio
3.5 wt%	0.52m	5.48	7.07

Table 8.1 - Calculated Na and K levels in the aqueous part of the D2, gold-bearing hydrothermal fluid.

This estimate assumes both a) a charge balance in the fluid and b) that the salinity estimate, based on pure NaCl-H_2O, is a best estimate to indicate Cl molality. The Na : K ratio derived from the DICP analyses in Chapter 7 thus permits calculation of activities for both Na^+ and K^+, using equation 8-1.

In order to establish pH of the system, the data set of the computer programme SUPCRT (Bowers *et al.* 1984) was used to calculate stability fields for Al-bearing phases known in the vein and wallrock assemblage at Patchway. The diagrams were checked using a similar programme PTA (Brown *et al.* 1985). Conditions chosen for calculating the fields were 350° C and 2.5 Kbars (approximated from the fluid inclusion and geothermometer data). The stability fields for the likely silicate assemblage are plotted on Figure 8.2, together with the line derived for the Na and K activities of the D2 fluid shown in Table 8.1. The other lines shown plotted are for fluid Na : K activity ratios of 1 and 10 in order to indicate system sensitivity to the Na : K ratio. Values at specific pH at 350° C are plotted as points on each fluid line which define other lines of constant hydrogen ion activity. From the studies in Chapter 3, the mineralogy of Al-bearing phases in the wallrock alteration and veining is dominated by K-rich muscovite. Albite is seen in deformed host rocks at the margins of the hydrothermally altered zone, but is evidently unstable in the fluid itself which constrains the fluid rather well to a pH lower than 6. The presence of pyrophyllite seen in some of the wallrock alteration marginal to the gold-bearing vein (Chapter 3) is perhaps indicative of slightly higher H^+ activities (lower pH), as albite breaks down in the presence of excess H^+ ions to form pyrophyllite, releasing Na^+ ions. An initial pH in the order of 5 to 5.5 is thus suggested for the D2 fluid.

8.3 (D2) Fluid C-O-H-S Species Activities

Modelling geological fluids in C-O-H systems at moderate to high temperatures (>300° C) is outlined by Holloway (1987). In this system the dominant species are shown to be dominated by H_2O, CO_2, CO, H_2 and CH_4. In such a system, reactions controlling activities of the various components can be defined. These are outlined below:

Reaction	*Equilibrium Constants*	
$C + O_2 = CO_2$	$K = fCO_2/(aC.fO_2)$	(8-2)
$C + ½O_2 = CO$	$K = fCO/(aC.fO_2^{½})$	(8-3)
$C + 2H_2 = CH_4$	$K = fCH_4/(aC.fH_2)$	(8-4)
$H_2 + ½O_2 = H_2O$	$K = fH_2/(fH_2O.fO_2^{½})$	(8-5)

In a closed system we also have the assumption that the sum of the mole fractions of the various species is 1. Since in practice O_2, H_2 and probably CO are present in negligible quantities the approximation of the system might be:

$$xCO_2 + xCH_4 + xH_2O = 1 \qquad (8\text{-}6)$$

(where xI is mole fraction of species I)

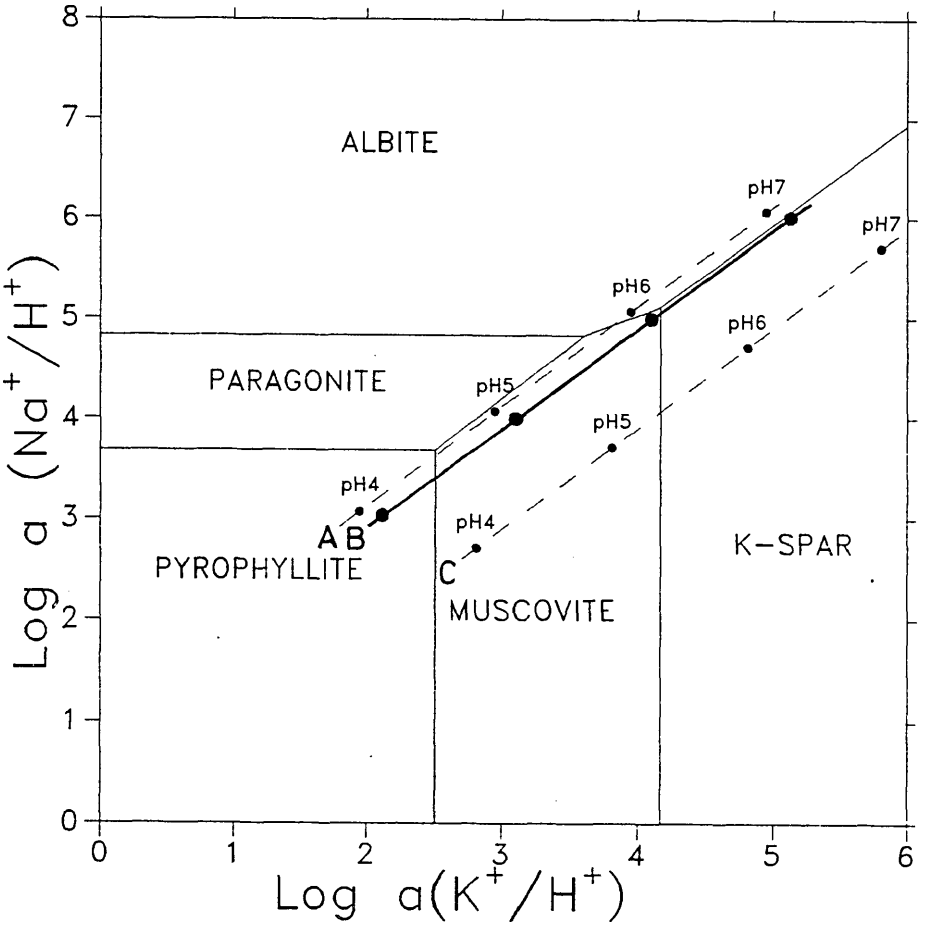


Figure 8.2 - Stability diagram for Na-K-silicate minerals as a function of Na and K ionic activity at 350°C and 2.5 Kbars. Fields calculated from Bowers *et al.* (1984) and Brown *et al.* (1985), [aH_2O] = 1, silica saturated. Lines plotted are for Na^+ : K^+ activity ratios of A = 10, B = 7.07 (Fluid D2 average, see Table 8.1) and C = 1. Points of equal pH plotted on each line.

In reality, sulphur must be added to the system as indicated by Eugster & Skippen (1967). The important sulphur-bearing species likely to be involved are controlled by the following reactions:

Reaction	*Equilibrium Constants*	
$H_2 + ½S_2 = H_2S$	$K = fH_2S/(fH_2.fS_2^{½})$	(8-7)
$O_2 + ½S_2 = SO_2$	$K = fSO_2/(fO_2.fS_2^{½})$	(8-8)

However, since these species are likely to be minor, albeit chemically important components in the type of hydrothermal fluid responsible for mesothermal gold deposits, the bulk composition is probably controlled by the species in equation (8-6).

8.3.1 Oxygen Fugacity

It is suggested then that the composition of the fluid is largely controlled by the three main C-O-H species and that in fact fO_2 might be mostly sensitive to changes in these. The gold bearing fluid responsible for mineralisation at Patchway is confirmed from the volatile analyses as a C-O-H bearing fluid dominated by H_2O, CO_2, CH_4 with only minor H_2 (Table 7.9).

From equations (8-2) to (8-5) the role of carbon activity, $[a_C]$, is crucial in establishing the fluid equilibria. The presence of graphite in the system would imply an activity of 1. At Patchway there is no clear demonstration of the presence of free carbon buffered by the hydrothermal fluid, so it must be assumed that $a_C < 1$ at Patchway. One way of calculating activities of the species involved is to make the assumption that the system is effectively closed and largely controlled by the reaction of the dominant fluid species (Dubessy *et al.* 1989, Polya 1989). The reaction between the dominant fluid species can be summarised:

$$CH_4 + 2O_2 = CO_2 + 2H_2O \qquad (8\text{-}9)$$

Of all the reactions in the C-O-H system, this is reasoned to be the slowest (Giggenbach 1987). However, this reaction can be used to construct a significant estimate of fO_2, provided the fluids measured are trapped at significantly high temperature. Sheppard (1981) shows that CH_4 and CO_2 equilibrate isotopically down to temperatures of 320°C. This implies that reactions involving the breaking of C-H and C-O bonds occur above this temperature, and that fO_2 could also be controlled by reaction 8-10 above this temperature. Giggenbach (1982) shows that chemical reaction proceeds 100 times faster than isotopic equilibrium between CO_2 and CH_4, thus at temperatures above 320°C, fluid chemical equilibration should be expected. From equation 8-10, it is clear that the volatile analysis data determined in Table 7.9 provides measurement of three of the four species in equilibrium with oxygen, and might be utilised to calculate an approximation of the fO_2 of the fluid. The initial assumption for

such a calculation is that the fluid is at least in internal equilibrium when it is introduced into the vein fracture. This is not unreasonable if the vein fluid model accepted approximates the model of Gold & Soter (1985), where a large volume of interconnected fluid in a fluid reservoir "domain" is episodically tapped, to "valve" into the vein dilatancy as proposed in the modified Sibson (1981) "fault valve" model (see Figure 4.18). Furthermore, Dubessy *et al.* (1989) demonstrate that the thermodynamic conditions of the fluid studied, although different to the conditions of trapping, have little effect on the calculations of ambient fugacity derived for time of trapping. The same authors suggest that other problems such as the loss of hydrogen by diffusion from the inclusions post-trapping are not considered to significantly affect the calculations.

It is apparent that a range of molar ratios for the various species is demonstrated from these analyses (Table 7.9). Given this range of values, it was decided to calculate fO_2 for each of the samples, since distinct differences in paragenetic association could be linked to systematic changes in the volatile contents from the inclusion study, and hence the differences in calculated fugacity could be significant to the mineralisation process. The fluid inclusion study from the detailed sampling on 6 and 10 levels indicated that the fluid initially contained substantial CH_4 when introduced into the vein fracture. Furthermore, the fluid probably unmixed in the fracture immediately after introduction into the fracture, losing the contained CH_4. This event is linked to gold precipitation and hence chemical differences between the early methanoic and later non-methanoic fluid may give some clue to the gold transport and precipitation mechanism.

The equilibrium constant for reaction (8-9), which can be termed K_r is defined as:

$$K_r = \frac{[fCO_2].[fH_2O]^2}{[fCH_4].[fO_2]^2}$$

and by rearranging:

$$[fO_2]^2 = \frac{[fCO_2].[fH_2O]^2}{[fCH_4].K_r} \qquad (8\text{-}10)$$

The equilibrium constant, K, for any given reaction is directly related to the Gibbs Free Energy coefficient ΔG by:

$$\Delta G = -2.303.RT.\log K \qquad (8\text{-}11)$$

and can be utilised in composite reactions by:

$$\Delta G\text{Reaction}_{P,T} = \Delta G\text{Products}_{P,T} - \Delta G\text{Reactants}_{P,T} \qquad (8\text{-}12)$$

The constituent reactions from the elemental species (which by definition have ΔG values themselves equal to zero) together with their experimentally derived equilibrium constants for these reactions are tabulated in Table 8.2. For the purposes of the calculations the conditions of the hydrothermal fluid are taken to be T = 350 °C and P = 2.5 Kbars, which is derived from the foregoing fluid inclusion study.

The tabulated log K values for the molecular species in the constituent reactions can be substituted in each case into a relevant form of equation (8-11). The ΔG values so calculated can be then substituted into a form of equation (8-12) for equilibrium reaction (8-9) to calculate the ΔG for the reaction. By substituting this derived value into equation (8-10), log K_r can be determined. From this calculation log K_r(8-10) is found to be 62.98 at 350° C, and thus $K_r = 9.55 \times 10^{62}$.

In order to calculate fO_2 from equation (8-10) we must also find the fugacities of the other species in the equation. We know molar ratios from the gas analysis data, and we can calculate fugacities, utilising the fugacity equation of Redlich & Kwong (1949):

$$\phi_i = f_i/(x_i.P_f) \qquad (8\text{-}13)$$

(where ϕ_i is the fugacity coefficient of species, i, at pressure P_f and temperature T(ϕ_i), x_i is the molar fraction of i and f_i is the fugacity of component i at those conditions).

This equation ignores any non-ideal mixing but, the work of Poulsen & Ohmoto (1989) suggests that, at 350° C this phenomenon should not be important. Using this we can now rewrite equation (8-10):

$$fO_2 = \sqrt{\frac{(xCO_2.\phi CO_2.P_f).([xH_2O]^2.[\phi H_2O]^2.[Pf]^2)}{xCH_4.\phi CH_4.K_r}}$$

Values for ϕ for the species involved are available from published tables of Ryzhenko & Malinin (1971), Ryzhenko & Volkov (1971) and Burnham *et al.* (1969) for the relevant temperatures and pressures. These values for the relevant conditions are shown in Table 8.2. Using the values for molar fractions of the species from the gas analyses, the calculated K_r value and the pressure estimate, fO_2 at 350° C and 2.5 Kbars can now be calculated for each bulk sample. The calculated fO_2 results are shown in Table 8.3.

By way of comparison with the modelling of a closed, internally equilibrated carbonic fluid, fO_2 can also be estimated assuming the presence of carbon. Such a calculation is much simpler utilising equation (8-2) together with suitable forms of the Redlich-Kwong equation (8-13). This method of calculation was also applied to the Patchway D2 fluid, assuming two different carbon activities. The presence of graphite assumes a carbon activity [aC] equal to 1 (Holloway 1977), so fO_2 values were calculated for [aC] = 1

Reaction	log K @ 350°C
$C + 2H_2 + = CH_4$	1.71
$C + O_2 = CO_2$	33.13
$H_2 + ½O_2 = H_2O$	15.78

Species	Fugacity Co-efficient (ϕ) @ 350°C
CO_2	3.990
CH_4	2.303
H_2O	0.018

Table 8.2 - Tabulated thermodynamic constants used in fugacity calculations. Data taken from Helgeson (1978) in the case of the equilibrium constants (log K values) and from Ryzhenko & Malinin (1971) and Ryzhenko *et al.* (1971) in the case of the fugacity co-efficients.

Sample	Molar % Methane	Log fO_2 Calculated at 350°C and 2.5 Kbars		
		Internal Fluid Equilibrium	Graphite Buffering {aC} =1	{aC} = 0.1
6007b	0.21	-28.97	-27.70	-28.70
6006c	0.06	-28.73	-27.14	-28.18
6006e	0.01	-28.34	-26.36	-27.36
6008f	0.01	-28.42	-26.34	-27.34
6006b	0.15	-28.96	-27.53	-28.53
10/21	0.01	-28.38	-26.35	-27.35
A10/20/D	0.29	-29.09	-27.83	-28.83
26/3	0.21	-29.07	-27.67	-28.67
Samples below show intimate association with Au-bearing phases				
10/32a	0.61	-29.20	-28.17	-29.17
30/3	0.86	-29.47	-28.28	-29.28
10/35b	1.13	-29.45	-28.41	-29.41
19HG1	2.59	-29.49	-28.84	-29.84

Table 8.3 - Calculated oxygen fugacities generated from the volatile analysis data (Table 7.9). Method of calculation is after Holloway (1977) and Dubessy *et al.* (1989). "Internal Fluid Equilibrium" considers the C-O-H system controlled by equilibrium between CH_4, CO_2, O_2 and H_2O with oxygen fugacity assumed to be controlled by equation (8-10). "Graphite Buffering" assumes carbon activity = 1, and final column is calculated assuming a carbon activity = 0.1, in both cases, oxygen fugacity calculated in terms of equations 8-5 and 8-6.

and one order of magnitude lower, [aC] = 0.1. These calculated figures are shown for comparitive purposes in Table 8.3. As stated before, no carbon has been seen at Patchway and so [aC] would be expected to be <1. Assuming [aC] = 1 gives a constraining maximum estimate of fO_2.

Figure 8.3 shows the data from Table 8.3 in graphic form where the relationship between fluid methane content and fO_2 are evident.

Discussion

The calculated fugacities for the equilibrated fluid (circles), show a range from approximately 10^{-30} to 10^{-28} at 350° C and 2.5 Kbars, implying variation of over one order of magnitude. The methanoic fluid, not surprisingly, has the lowest value of fO_2 (samples 19HG1 and 10-35b) and the fluid with no methane shows a substantial increase in fO_2 (e.g. samples 600f and 10-21). This variability in fO_2 is highly significant, particularly with regard to stability of reduced versus oxidised sulphur species within the system. The most significant feature is that although the figures of oxygen fugacity may be slightly in error based on the assumptions, the clear difference in relative fO_2 between the methanoic and non-methanoic inclusions is marked by all the calculation methods and reflects a real change in fO_2.

As discussed earlier the fluid is likely to be in internal equilibrium when introduced, so the fO_2 values calculated for the more methanoic fluid of ± 10^{-30} are believed to be quite valid, since this is interpreted as the early introduced fluid before unmixing. Disequilibrium might be expected during an instantaneous unmixing event, but since the unmixing process only serves to increase fO_2, then the later fugacity estimates of ± 10^{-28} may well be conservatively low and thus the actual fO_2 shift may be greater.

8.3.2 Sulphur Species Fugacities

Bulk volatile analyses did not include any of the sulphur gases, so estimates of the activities of sulphur species must be made indirectly. Leading on from the calculations of estimated oxygen fugacity, it is possible to make similar estimates for the major sulphur species likely to be present in the hydrothermal fluid system. These estimates rely on a figure for fluid sulphur fugacity derived by assuming fluid equilibrium with the sulphide phases which were precipitated from it. From the equation of Poulsen & Ohmoto (1989) and substituting the ambient P-T conditions of 350° C and 2.5 Kbars, the derived fS_2 for the Patchway fluid, buffered by pyrite-pyrrhotite, is 1.35×10^{-9} bars.

Calculation of fH_2S activity is governed by the reaction (8-7). Hence:

$$[fH_2S] = [fS_2]^{½}.[fH_2].K_{(8\text{-}8)}$$

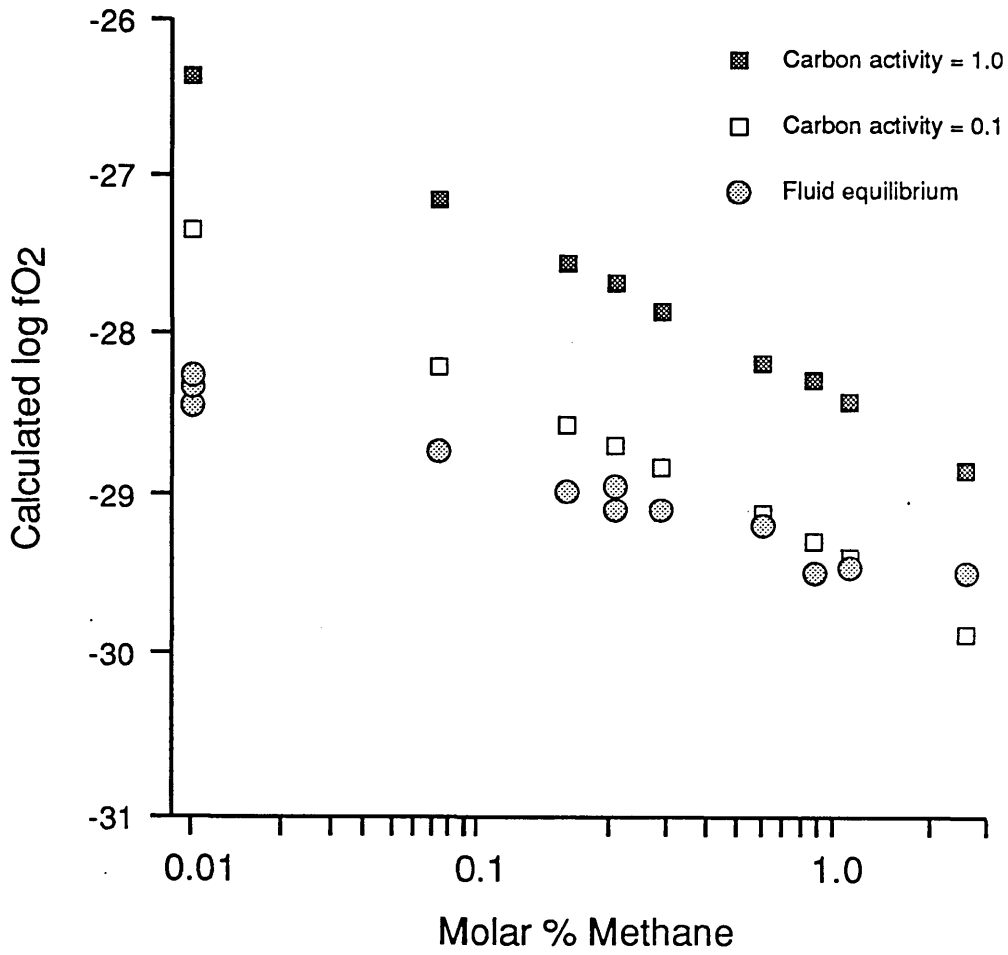


Figure 8.3 - Graphic representation of fO_2 values calculated in Table 8.3 as a function of molar% methane from the volatile analyses. The shaded circles represent the values calculated assuming an internally equilibrated H_2O-CO_2-CH_4-O_2 fluid.

The log K value for reaction (8-7) is 3.50 at 350°C and the sulphur fugacity from co-existing sulphides is already suggested to be in the order of 10^{-9} bars. The value of fH_2 can be found from equation (8-5) again utilising the volatile analysis data of the fluid inclusions. The volatile data used is from 19HG1, where gold grains are demonstrated to be totally enclosed within quartz grains containing primary inclusions (Figure 7.6) which the analysis represents. Significantly this fluid is shown to be the most methanoic in the previous sections and, hence, has the lowest calculated fO_2. The analysis of the fluid from these inclusions is considered to most closely represent the the introduced gold bearing fluid composition.

From the analysis of 19HG1, xH_2O is 0.87 and this can be substituted, together with the fugacity coefficient ϕH_2O = 0.018 and equilibrium constant, log K = 15.78 (Table 8.2) at 350° C and the previously calculated fO_2 value at 350° C and 2.5 Kbars (log fO_2 = -29.49) into a rearranged form of equation (8-5) to calculate fH_2 :

$$fH_2 = \frac{fH_2O}{[fO_2]^{\frac{1}{2}}.K} = \frac{[0.87 \,.\, \phi H_2O \,.\, P_f]}{[3.23\times10^{-30}]^{\frac{1}{2}} \,.\, 6.03\times10^{15}} = \frac{[0.93 \,.\, 0.018 \,.\, 2500]}{10.85}$$

$$= 2.33 \text{ bars}$$

This value of fH_2 = 2.33 bars can be substituted into equation (8-7):

$$fH_2S = (1.35\times10^{-9})^{\frac{1}{2}} \times 2.33 \times 3162$$
$$= 0.27 \text{ bars}$$

From this figure, the absolute concentration of H_2S in solution can be calculated from the Redlich-Kwong equation (8-12). The fugacity coeffficient can be calculated from the equation of Rhyzenko & Volkov (1971) which for H_2S is as follows :

$$\begin{aligned}\phi H_2S = {} & 1 + 1.240\times10^{-2}(P_f/P_{crit}) + 2.540\times10^{-4}(T/T_{crit})(P_f/P_{crit}) - \\ & 5.104\times10^{-5}(T/T_{crit})^2(P_f/P_{crit})^2 + 1.109\times10^{-3}(P_f/P_{crit})^2 - \\ & 1.998\times10^{-4}(T/T_{crit})^2(P_f/P_{crit}) + 9.393\times10^{-5}(T/T_{crit})^2(P_f/P_{crit})^2\end{aligned}$$

From this equation, at 350° C and 2.5 Kbars, ϕH_2S is calculated at 1.85 and thus:

$$\begin{aligned}xH_2S &= 0.27/(1.85 \times 2500) \\ &= 5.84\times10^{-5} \\ &= \text{equivalent to } 1.96\times10^{-3} \text{g/mole fluid}\end{aligned}$$

This mole fraction is in a fluid where xH_2O = 0.87, xCO_2 = 0.10 and xCH_4 = 0.03. One mole of such a fluid has a mass of 20.06g, therefore ($1.96x10^{-3}/20.06$) x 100 wt % of the fluid is H_2S. This is equivalent to a possible concentration of 98 ppm H_2S in the fluid within the constraints of the data.

It is clear from the mineralogy that a pyrite-pyrrhotite buffered assemblage was likely only during the early precipitation of sulphides and gold. After this time, pyrite is the dominant iron-bearing sulphide and conditions may have been much different. However, from Figure 8.4 the stability field of pyrite + chalcopyrite and pyrite + bornite can give a possible upper limit to fS_2, as bornite is unknown in the sulphide assemblage at Patchway. Maximum fS_2 in this case is around $5.5x10^{-6}$ which can perhaps be used as a maximum constraining value. Similarly because fS_2 is clearly linked to fH_2 and hence fO_2, calculation must be made for both the upper and lower fO_2 values to define the possible range.

Assuming the highest fO_2 value and a calculated minimum fS_2 value (sample 6008f with pyrite-pyrrhotite buffering), xH_2S is around $3x10^{-5}$ which is equivalent to less than 50 ppm H_2S. Assuming the lowest fO_2 and highest fS_2 (sample 19HG1 and chalcopyrite-bornite buffering), xH_2S is $3.9x10^{-3}$ which is equivalent to over 6000 ppm H_2S.

The calculations can be further extended to obtain a figure for fSO_2 by using equation (8-9). The log K value for this reaction at 350° C is 26.0, thus fugacity can be calculated thus:

$$fSO_2 = [fS_2]^{½}.[fO_2].1x10^{26}$$

So calculating the extremes again, for sample (19HG1) fSO_2 is $2.81x10^{-9}$ bars and for sample (6008f) fSO_2 is $2.51x10^{-7}$ bars assuming respectively pyrite-pyrrhotite and chalcopyrite-bornite buffering. These figures are both much lower than the fH_2S values calculated for both samples, but the decrease in fH_2S seen in 6008f is accompanied by a two order of magnitude increase in fSO_2, clearly indicating that oxidised sulphur ligands might be expected after unmixing which seems to accompany gold precipitation. This makes the observation of small grains of possibly anhydrite within opened inclusions examined in the microprobe, in gold-bearing quartz grains where fluid unmixing is likely, particularly significant.

Discussion

The maximum figure of 6000 ppm H_2S seems unusually high given the published values from the Hunt Mine, Kambalda Australia (Neall & Phillips 1987). These values were calculated from mass action relationships of the iron bearing silicate, oxide and sulphide phases. At Kambalda, levels of between 95 and 325 ppm H_2S are indicated in the fluid from a similar Archaean shear-hosted deposit. This might suggest that the possible limiting upper value of fS_2 at the chalcopyrite-bornite buffer is far too high. Indeed there is no indication of bornite in the gold bearing paragenesis, at Patchway, and a lower figure might be expected. Although the experimental work on sphalerite composition with respect to fS_2 is only quantitatively valid to 1 Kbar as stated before, it would be anticipated that at fS_2 levels close to the cpy-bn buffer, FeS levels in sphalerite would be expected to be low (< 1 mole%). However from probe

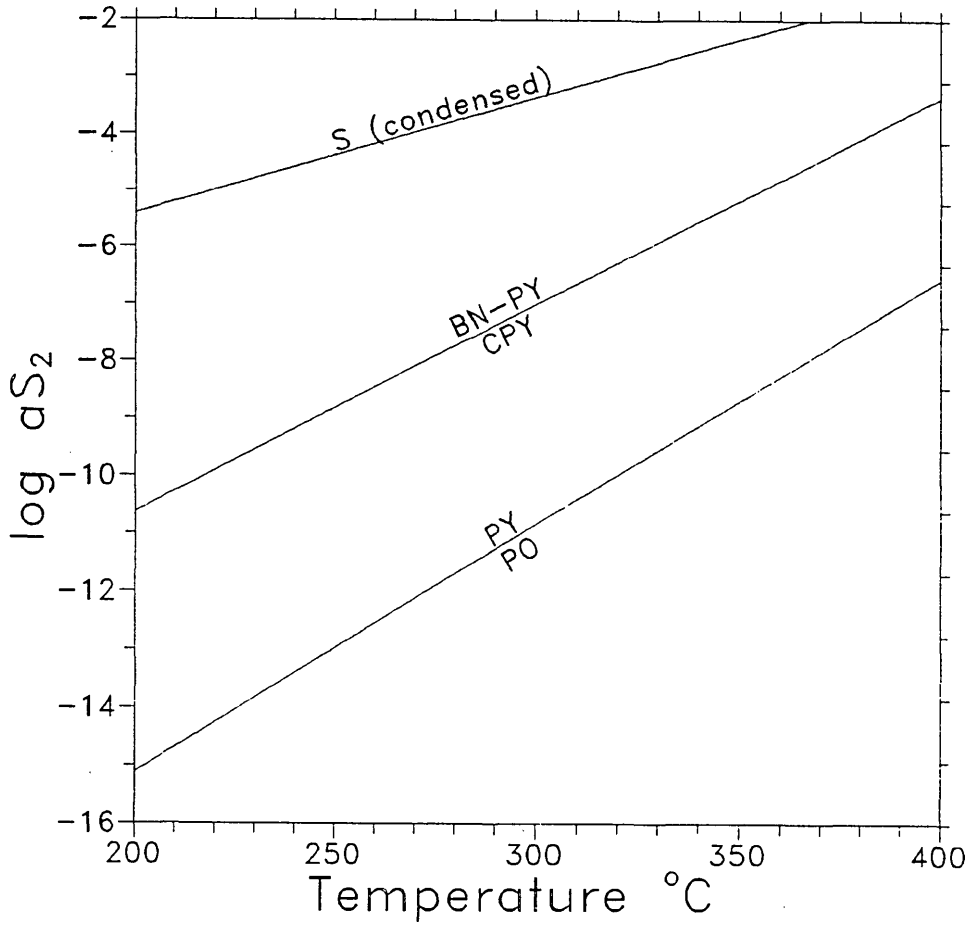


Figure 8.4 - Log aS_2 -temperature plot for major species in the Cu-Fe-S system (after Barton 1973).

analyses of sphalerite close to gold bearing sulphide grains values of 7 to 8 mole% FeS are obtained. This tentatively suggests a more conservative upper estimate for fS_2 of perhaps 10^{-8} bars, closer to the pyrite-pyrrhotite buffer. This leads to a maximum calculated xH_2S of $2.51x10^{-4}$, equivalent to around 400 ppm in the fluid.

In conclusion then, the possible range of fluid compositon would appear to lie between 50 and 400 ppm H_2S, with one fairly well constrained value of 98 ppm H_2S during the precipitation of early gold in the complex pyrite grains, where pyrite-pyrrhotite buffering is demonstrated (Chapter 6). The process of proposed unmixing and consequent loss of methane is seen to both increase fO_2 and decrease fS_2, hence H_2S is seen to be lost from the fluid. This loss would undoubtedly affect any sulphur-bearing ligands in solution.

The corresponding change in fSO_2 indicates that oxidised sulphur species may become important as the fluid evolves and the tentative presence of anhydrite in unmixed fluid inclusions tends to support this.

8.4 Stable Isotope Study

8.4.1 Introduction

The fluid studies have constrained the fluid nature in regard to bulk composition and the more detailed investigation of the gold-bearing D2 fluid permits an estimate of the activities of the major components to be made. In order to study further the behaviour of the mineralising fluids throughout the evolution of the deposits, and make some predictions about the possible fluid sources, a programme of stable isotopic study of major mineral phases was carried out. The ubiquitous presence of quartz at every mineralised stage meant a study of $\delta^{18}O$ in quartz could be made, particularly as the quartz chosen for analysis was already well constrained by fluid inclusion microthermometry and geothermometry data which showed quite major diffences between fluids. Determination of $\delta^{34}S$ in pyrite from both the gold-bearing sulphide assemblage and the deformed and altered wallrock was made to study the behaviour of fluid sulphur species. Lastly, preliminary determination of $\delta^{13}C$ in calcite from a) the D2 veining, b) deformed and altered wallrock and c) undeformed wallrock was made.

8.4.2 Experimental Methods

Stable isotopic ratios for the minerals chosen were determined at the NIGL Stable Isotope Unit under the guidance of Dr. B. Spiro. Procedures for oxygen determinations are detailed in Appendix VI, method after Clayton & Mayeda (1963), whilst the carbon analyses of calcite were made using the method of McCrea (1950) and the sulphur analyses in pyrite after Robinson & Kusakabe (1975).

8.4.3 Oxygen Isotope Study

Published Studies

Studies of $\delta^{18}O$ for quartz in Archaean gold deposits are numerous. Data for the Australian deposits is discussed in Golding & Wilson (1987) where ranges of +11.4 to +13.4 ‰ are indicated. Colvine *et al.* (1988) in their review of data for the Canadian Shield quotes values of between +10.8 and +15.4 ‰. Interpreted fluid compositions range from +6 ‰ to around +10 ‰. This data is presented in Table 8.4. Limited data published from the adjacent Golden Valley deposit (Foster *et al.* 1979), shows a range from +11.5 to +13 ‰, from which an estimate of fluid composition +8 ‰ at 400° C is estimated. They note a decrease in $\delta^{18}O$ from the margin to the centre of the vein, although the sample points are not located in detail. No systematic study integrated with detailed fluid inclusion microthermometry and alkali geothermometry has been previously published on this type of quartz vein.

Calculation of results

Quartz samples deposited from water-dominated hydrothermal solutions are relatively straight forward to interpret with respect to the fluid from which they formed. Using the equation of Matsushisa *et al.* (1979), $10^3 \ln\alpha$, the quartz-water fractionation factor can be derived:

$$10^3 \ln\alpha = 3.34(10^6/T^2) - 3.31 \qquad (8\text{-}14)$$

From this equation, the $\delta^{18}O$ fluid can be calculated if the temperature of formation in °K is known from the following equation:

$$\delta^{18}O_{fluid} = \delta^{18}O_{quartz} - 10^3 \ln\alpha \qquad (8\text{-}15)$$

Results

Table 8.5 shows the results recorded for the total sample set of 23 Patchway quartz separates analysed. 1 sample was taken from the Q1 quartz, 13 were taken from the gold bearing Q2 quartz, 1 sample from Q3, 3 samples from Q4, 2 samples from Q5 and 3 samples of quartz phenocrysts from various intrusive phases from the mine. Reliability of reported values is estimated to be better than ±0.1 ‰.

Table 8.5 shows the fluid geothermometer values or fluid inclusion homogenisation data which was presented in Chapter 7. This data is plotted in graphic form on Figure 8.5 and clearly shows that the isotopic signatures of Q2, Q4 and Q5 show quite different patterns.

The Q1 result, although a single point, stands clearly apart from the other groups. The calculated $\delta^{18}O_{fluid}$ for this stage, calculated from equations (8-14) and (8-15) is +5.98 ‰, formed at a temperature of 330° C as indicated by the chlorite geothermometer (Chapter 3).

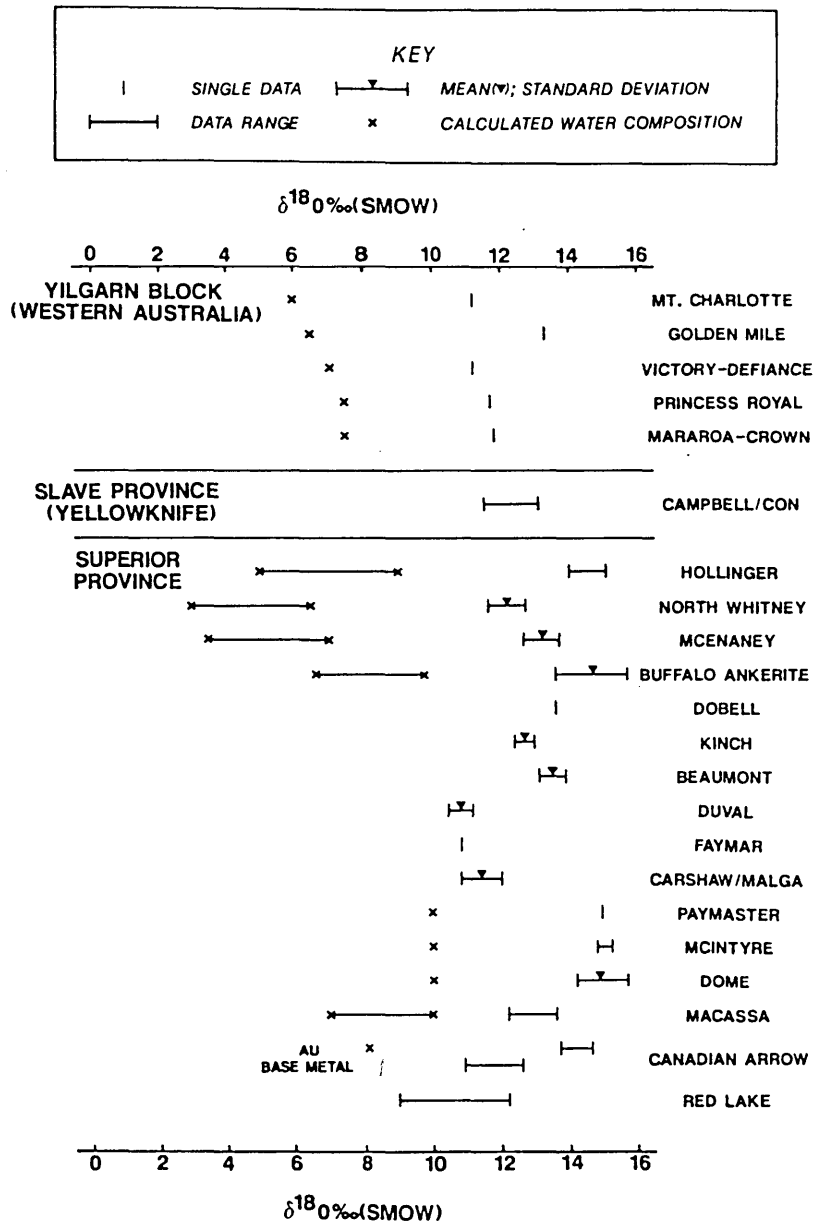


Table 8.4 - Compilation of $\delta^{18}O$ vein quartz values in Archaean gold deposits (from Colvine *et al.* 1988).

Sample	Quartz Generation	$\delta^{18}O$ Quartz	Independent Geothermometer (°C)
PMQ-1	1	+11.7	330 Chlorite
26-3	2	+10.4	312 Alkali Na:K
30-3	2	+10.8	310 Alkali Na:K
19HG1	2	+11.8	295 (Homogenisation)
20-12	2	+11.3 +11.3	294 Alkali Na:K
A10/21/B	2	+11.5	263 Alkali Na:K
A10/20/D	2	+11.8	268 Alkali Na:K
A10/20/C	2	+12.7	249 Alkali Na:K
30-6	2	+11.2 +11.2	<350 Chlorite
26-11	2	+11.0	<350 Chlorite
20-4	2	+11.2	<350 Chlorite
30-7	2	+11.2	<350 Chlorite
400-24	3	+12.7	255 (Homogenisation)
26-14	4	+11.3	<350 Chlorite
20-13	4	+11.3 +11.0 +11.0	241 Alkali Na:K
26-2	4	+10.9	249 Alkali Na:K
30L7	4	+10.8	233 Alkali Na:K
TQ2	5	+10.2 +10.4	310 Alkali Na:K
TQ3	5	+10.7	250 Alkali Na:K
18-12	Fresh Felsite Phenocryst	+9.9 +9.7	
LH5	Tonalite Phenocryst	+10.0	
10-5	Altered Felsite Phenocryst	+11.3	

Table 8.5 - Tabulated $\delta^{18}O$ quartz values for Patchway samples analysed (replicates shown). Independent geothermometers shown are alkali fluid geothermometers, where considered robust (see Tables 7.9 to 7.14). In the absence of this, chlorite geothermometry or fluid inclusion homogenisation temperatures are shown (this latter method provides a minimum temperature figure only).

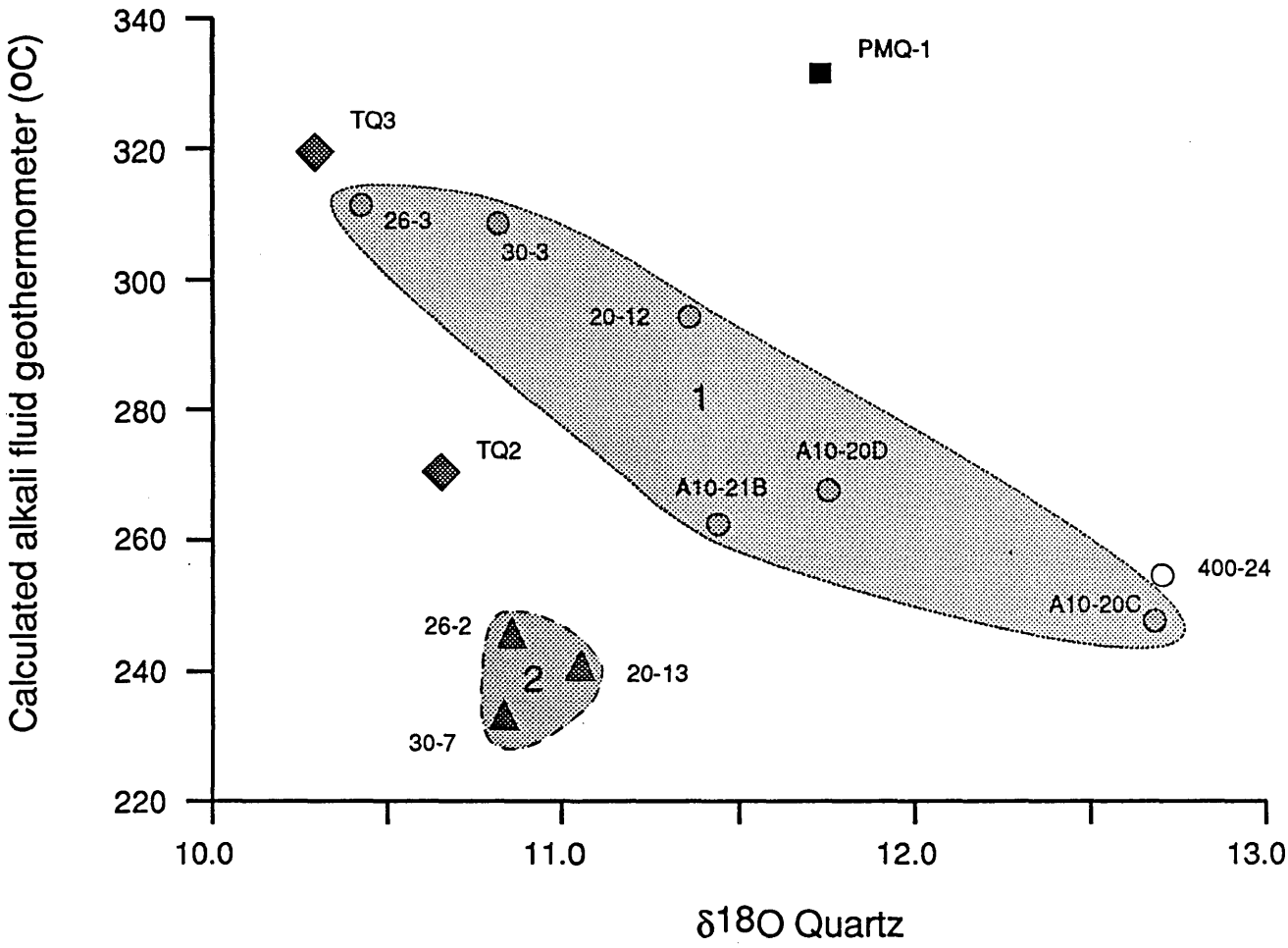


Figure 8.5 - Plot of $\delta^{18}O$ quartz versus Na:K alkali geothermometer for fluid inclusion fluids calculated from D-ICP analyses. Group 1, circles, are samples from Q2 ribbon-vein quartz. Group 2, triangles, are samples from Q4 late quartz-tourmaline veins. PMQ-1 is a sample of Q1, pillow margin infill quartz, 400-24 is from the Q3 Kabanga mineralisation and TQ2, TQ3 are from the tonalite-hosted Q5 quartz-scheelite veins.

The Q2 fluid data is the most interesting, as although the results indicate a range in quartz $\delta^{18}O$ values of nearly 3 ‰, the $\delta^{18}O_{fluid}$, calculated using the fluid geothermometer temperature, shows a range of only 0.5 ‰. The result for sample 26-3, which has the lowest $\delta^{18}O$ and highest fluid geothermometry, calculates to a fluid composition of around +4.3 ‰ at the temperature indicated at 310° C. The data is plotted on Figure 8.6 together with the curve indicating the predicted signatures for quartz forming from an infinite volume fluid (oxygen) reservoir, cooling from initial conditions of 350° C with a $\delta^{18}O_{fluid}$ signature of +4.1 ‰. This curve is calculated using (8-14) and (8-15), and it is striking how closely the data for the Q2 vein quartz lies to this curve.

Another very striking feature of the results is the fact that there is a clear distiction between the samples from the north orebody and the south orebody (Figure 8.7). The north orebody is of notably higher grade than the south orebody (the latter is only mined in restricted areas at present). It does appear on this data that the calculated fluid geothermometer temperature, quartz $\delta^{18}O$ value and the gold grade of the vein might be related. This is further supported by the result of the sample from the Q3 quartz (Figure 8.5), which carries only traces of gold, and which plots in the same field as the low grade south orebody, however temperature constraint for this sample is based on fluid inclusion homogenisation data and hence must be taken as a *minimum* temperature figure.

The fluid responsible for precipitation of Q4 quartz appears quite different, with a consistent quartz signature for the paragenesis consistent with a fairly restricted mineralisation event responsible. The $\delta^{18}O$ calculated value of +1.76 ‰ for the fluid is much lower than that for the Q2 quartz, indicative of a different oxygen reservoir. No evidence for evolution of the fluid is indicated in the tightly clustered (both fluid geothermometer and $\delta^{18}0$) data.

The $\delta^{18}O$ results for the Q5 quartz plots close within the range of the lighter Q2 quartz values. The constraining temperature is poorly defined, however, by highly variable fluid inclusion geothermometer temperatures which must be treated with some caution.

Data from the quartz phenocrysts analysed from the three intrusives indicate a whole rock signature of 7.3 to 7.9 ‰ for the fresh "felsite" and tonalite analysed, as a roughly 2 ‰ difference between the quartz phases and whole rock is to be expected (Valley *et al.* 1986). Sample B10/5 is taken from deformed "felsite" immediately adjacent to the vein on 10 Level, north orebody. It has a signature closer to that of the mineralised quartz than the "fresh" intrusives, and thus isotopic "resetting" of the quartz phenocryst oxygen during the deformation and mineralisation event is likely.

Discussion

The Patchway quartz data shows a comparatively small spread of data (± 3 ‰), well within the published ranges of Archaean hydrothermal quartz. In this case, however, the availability of the independently

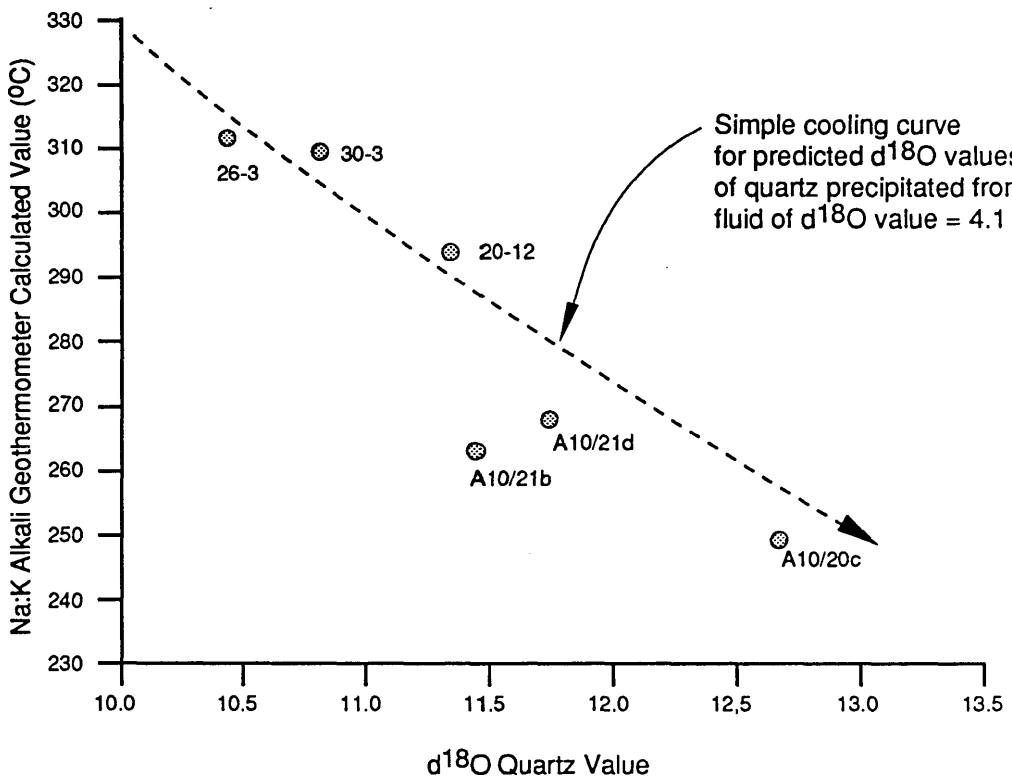


Figure 8.6 - Replot of $\delta^{18}O$ quartz versus calculated Na:K alkali geothermometer for Q2 samples only. Also plotted is the temperature fractionation curve, representing the expected $\delta^{18}O$ quartz values, forming from an infinite oxygen reservoir with a $\delta^{18}O$ value of 4.1 ‰ (using the equation of Matsushisa *et al.* 1979).

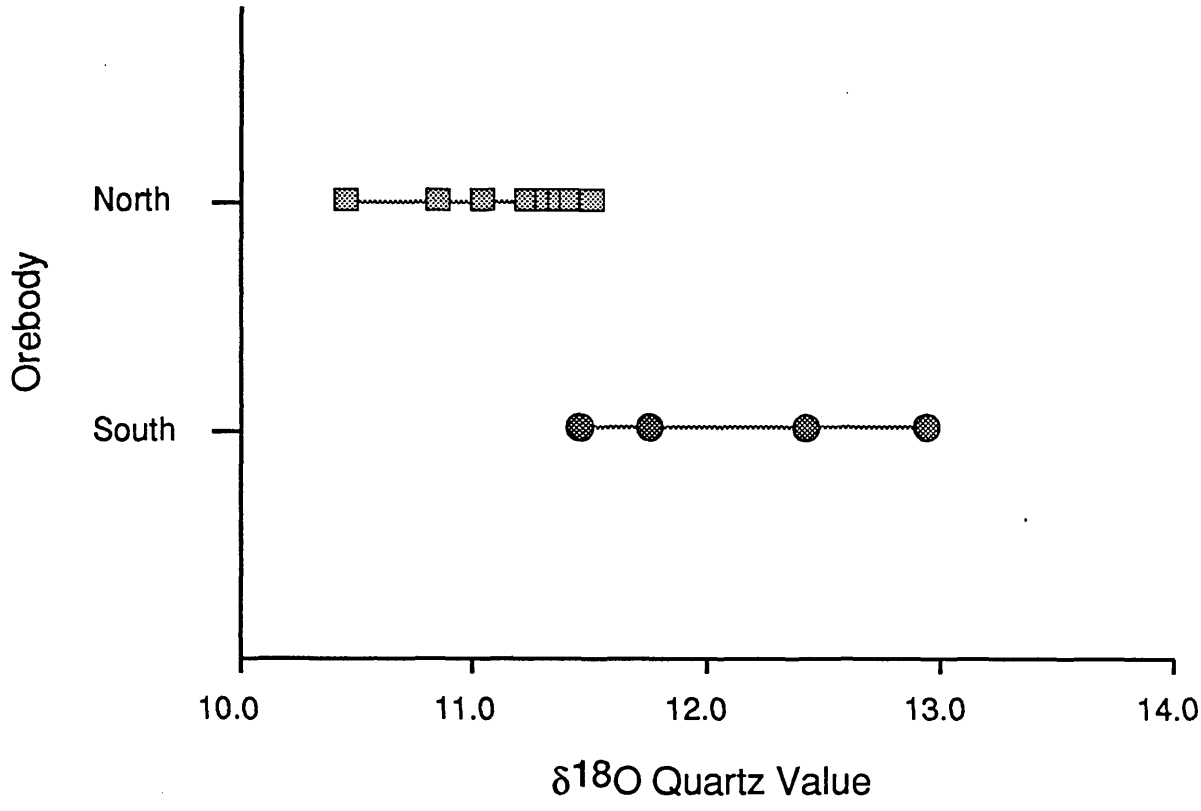


Figure 8.7 - Graphic representation of $\delta^{18}O$ quartz values for Q2, ribbon-vein quartz, from the Patchway mine. Samples shown as squares are from the more extensively mined North Orebody (see minined area on Figure 2.7). Samples shown as circles are from the South Orebody.

determined alkali fluid geothermometry determined directly from primary fluid inclusions allows further constraint on the values. Calculations of initial $\delta^{18}O$ fluid can be made utilising the Na:K alkali geothermometer as a measure of ambient fluid temperature. When this is done, at least three populations of quartz can be discriminated.

Calculation of fluid isotopic compositions for the Q1, Q2 and Q4 quartz indicate potential differences in initial fluid reservoir isotopic ratios. Q1 formed from a fluid with a $\delta^{18}O$ ratio of around 6 ‰, Q2 formed from a fluid with a composition of around +4 ‰, whilst the Q4 quartz formed from a fluid with a composition of around +2 ‰.

The oxygen data for the Q2 quartz data is the most interesting, since the spread of data generated lies quite close to the temperature fractionation curve (quartz-water) for a fluid initially having a $\delta^{18}O$ composition of +4 ‰. This pattern suggests that a single fluid source (reservoir) was responsible for the range of actual $\delta^{18}O$ quartz values generated. The measured isotopic differences probably result from variation in the temperature at which each quartz sample formed from the fluid. This has very profound consequences for the interpretation of the mineralising events during D2.

The dynamic structural-fluid model for the vein formation proposes a large, well buffered reservoir of hydrothermal fluid which is episodically "valved" into the structure, precipitating quartz, sulphides and gold. The $\delta^{18}O$ of such a fluid reservoir in a crustal-scale structure (which could possibly be considered of infinite volume), would be expected to remain fairly consistent through successive "valving" events. The quartz results appear to be compatible with such a model, if the change in $\delta^{18}O$ values between samples can be ascribed to formation temperature differences. The limited data from Q3 indicates that this quartz too may have the same fluid oxygen signature as the Q2 quartz.

Furthermore, the Q2 data suggests that isotopic differences between quartz related to high-grade gold-bearing mineralisation and that from lower-grade veins may be present. If this is a function of different fluid temperatures at the time of mineralisation, then a fluid temperature above 270° C (calculated from 8-14 and 8-15), appears more favourable for gold mineralisation.

The Q4 quartz data forms a fairly tight cluster, indicative of formation from a fluid with a $\delta^{18}O$ value of around +2 ‰. The cluster suggests very little temperature range for quartz formation and a single fluid source, distinct from either the fluid responsible for Q1 or Q2.

Since the Q5 veins are hosted within the large tonalite bodies, it is tempting to invoke a magmatic oxygen source for these veins. The veins are hosted within brittle fractures cutting the tonalite, however, which may not imply a direct genetic link. The data is somewhat erratic (due to the small data set), but there is an indication that the fluid oxygen source may be of similar composition to that for Q2.

In light of the results from the Patchway veins it is suggested that some of the range of $\delta^{18}O$ values reported in the literature (Table 8.4) may not reflect variation in fluid source but may actually be due to differences in temperatures of formation for the quartz analysed. Without strict control on the actual temperature of quartz formation (through fluid inclusion data), an observed data range for quartz of 3 ‰, as seen at Patchway, may actually reflect quartz formed from the same fluid over a temperature range of ± 100° C.

8.4.4 Carbon Isotope Study

Published Studies

Typical carbon isotope data for Archaean gold deposits is reviewed by Colvine *et al.* (1988) and shown in Table 8.6. Values for the mineralising fluid itself are estimated at around -5 ‰ $\delta^{13}C$ for the Abitibi lode deposits (Colvine *et al.* 1988). This is very similar to the estimate for the Yilgarn deposits of Western Australia (Golding *et al.* 1987). Many of these deposits show zoned patterns over distances of several metres for $\delta^{13}C$ in the alteration marginal to mineralisation, and this may be linked partly to intensity of alteration. Carbonate mineralogy also changes with intensity of alteration with the general trend of dolomitic-ankeritic zones close to mineralisation with calcitic marginal zones. Typical zonation patterns of $\delta^{13}C$ vary from -4 ‰ for carbonate close to ore to 0 ‰ in the marginal wallrock alteration (Fyon *et al.* 1983, Fyon 1986).

This trend in the isotopic signature was interpreted largely in terms of Rayleigh fractionation during wallrock interaction (Fyon 1986). This implies a finite carbon reservoir which evolves by precipitation of carbonate depleted in $\delta^{13}C$ to minerals of increasingly isotopically heavier. This trend was demonstrated at the Lawlers gold deposit in Western Australia (Kassidy *et al.* 1988) where the trend of increasing $\delta^{13}C$ in carbonate away from the mineralised vein is matched by decreasing total carbonate.

The presence of carbon bearing species in the wallrock (particularly sediments with reduced carbon species) is a potentially major cause of variation in isotopic composition due to fluid-wallrock interaction. Since carbonaceous sediments are not present in the wallrocks at the Patchway deposit, it is not necessary to consider this in the interpretation of the values obtained.

Carbon isotopes are particularly applicable in Archaean gold deposits where the mineralising fluid contains up to 20 mole% CO_2 (+ CH_4) and large volumes of carbon may be introduced into the vein and wallrock with the fluid. In such a fluid, in the absence of graphite, reaction between the various carbon species is largely dominated by reaction (8-9). The two stable carbon isotopes, ^{12}C and ^{13}C, fractionate very strongly between the two species CO_2 and CH_4 (Bottinga 1968). This reaction is clearly affected by fO_2 and this parameter is a major control on CO_2 carbon isotopic composition.

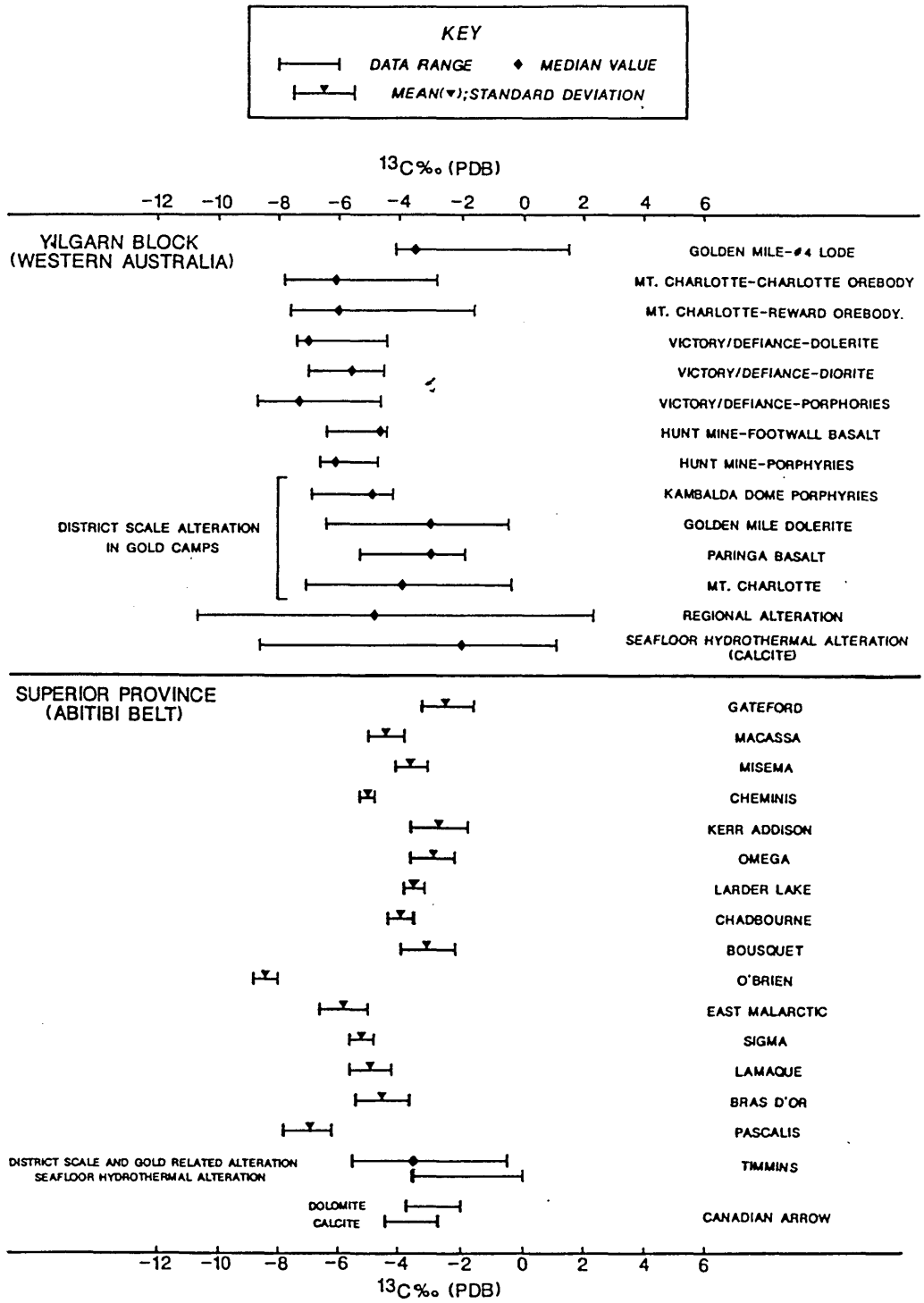


Table 8.6 - Compilation of $\delta^{13}C$ hydrothermal carbonate values in Archaean gold deposits (from Colvine *et al.* 1988).

Calculation of results

Isotopic fractionation between calcite and the CO_2 from which it formed must also be considered in interpreting the isotopic signature obtained from the carbonate. The fractionation factor, α, is temperature dependent according to the equation:

$$\delta^{13}C \text{ fluid } (CO_2) = \delta^{13}C \text{ carbonate (calcite)} - 10^3 \ln\alpha$$

Values for $10^3 \ln\alpha$ have been determined as a function of temperature both empirically and by calculation and these are shown graphically on Figure 8.8. It is apparent that at temperatures between 350 and 250° C, the likely temperature range for the Patchway deposit, the fractionation is not particularly sensitive to temperature with a difference of only 2 ‰ over the whole range. Therefore changes in $\delta^{13}C$ are likely to be functions of fO_2 and Rayleigh fractionation effects in the current study.

The $\delta^{13}C$ signature of the carbonate should thus enable the original hydrothermal fluid composition to be determined, when the fluid temperature and fO_2 are known. Any variation in the values determined for carbonates related to the mineralisation event may give clues to fluid behaviour during mineralisation.

Results

A total of 7 samples were run from the Patchway deposit. Results are shown in Table 8.7. Five of the samples run were from the wallrock alteration around the vein, taken from varying distances from the vein itself. The remaining two samples comprised one representative of the gold bearing mineralisation itself and one from a sample of hydrothermally altered "felsite" intrusive, adjacent to mineralisation, which contained minor calcite. Table 8.7 also shows the loss on ignition determined for the wallrock alteration samples which were obtained during whole rock ICP analysis (see Chapter 5). This value roughly relates to the carbonate content of the sample (plus any water released from the phyllosilicate phases). Reproducibility of results is better than ± 0.05 ‰.

Figure 8.9 shows a plot of $\delta^{13}C$ versus distance from mineralisation for the samples taken marginal to mineralisation. It is suggested that the mineralised sample value of -5.0 ‰ is probably the likely value in equilibrium with the mineralising fluid at the proposed fluid temperature of around 350° C. From Figure 8.8, a fluid value of -7.0 ‰ is suggested, since the microprobe data suggests calcite is the dominant carbonate (see chapter 3).

Discussion

The figure of -7.0 ‰ is very close to the estimates from Canadian and Australian studies (Colvine *et al.* 1988, Golding *et al.* 1987). The hydrothermal fluid responsible for mineralisation at Patchway has a

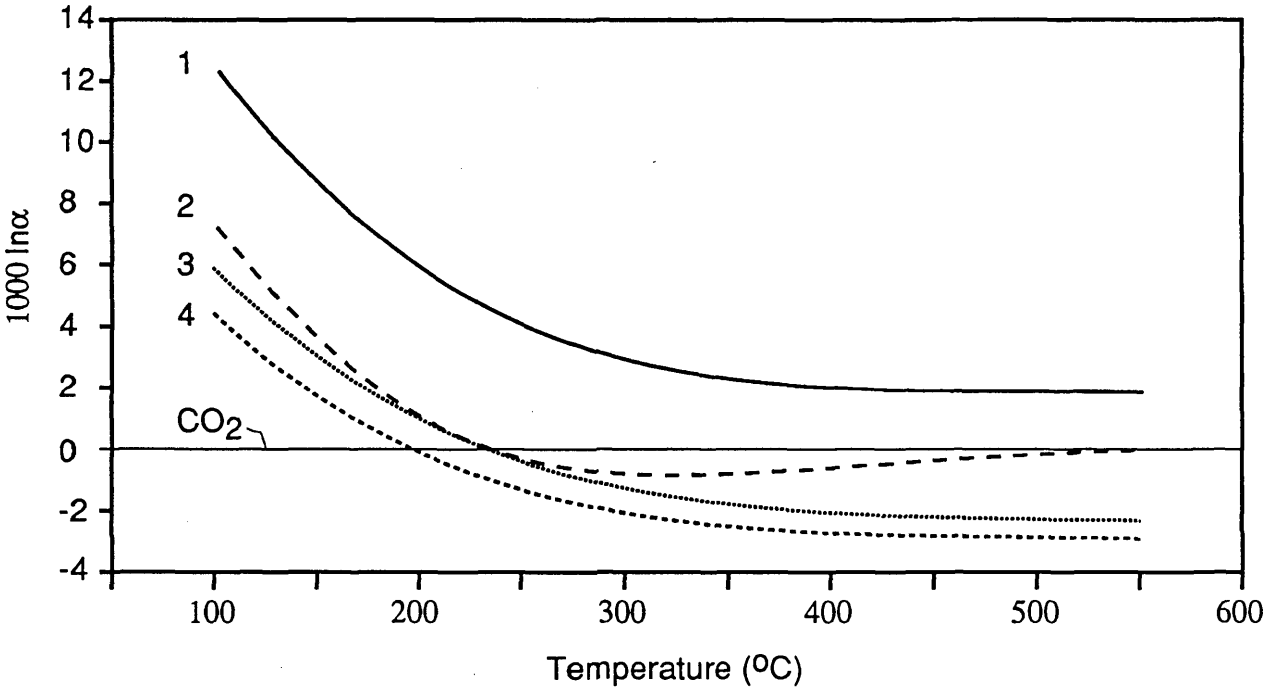


Figure 8.8 - Graph showing calcite-dolomite-magnesite-CO_2 fractionation factors vs. temperature (from Kassidy *et al.* 1988). Curves : 1 - Calcite-CO_2 (Bottinga 1968), 2 - Dolomite-CO_2 (Golyshev *et al.* 1981), 3 - Dolomite-CO_2 (Ohmoto & Rye 1979) and 4 - Magnesite-CO_2 (Golyshev *et al.* 1981).

Sample	Loss on ignition (wt%)	Distance from vein margin (m)	$\delta^{13}C$ calcite (duplicates)
15-1	3.21	+5	-2.85
1500/F	3.21	+1.2	-4.94 (-4.94)
1500/C	11.96	+0.6	-4.62 (-4.60)
1500/A	5.81	+0.2	-5.48
1500/V	1.08	0 (Vein)	-5.04
10-36	2.75	+0.5 (Felsite)	-5.21

Table 8.7 - Carbon isotope determinations from calcite in samples peripheral to mineralised (D2) ribbon-quartz veins.

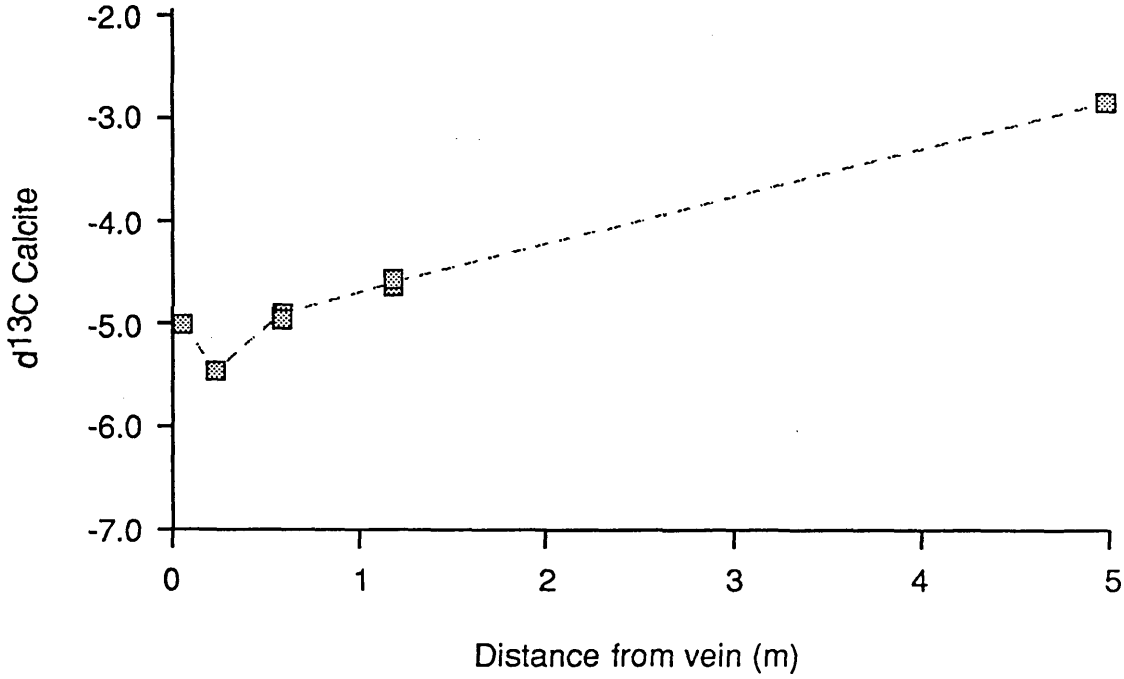


Figure 8.9 - Plot of $\delta^{13}C$ calcite versus distance from the Q2 ribbon-quartz vein on 15 Level. Replicate analyses shown as separate squares.

suggested log fO_2 in the range -30 to -28 (see previous section). At the suggested temperature of 350° C, the sensitivity of $\delta^{13}C$ to minor changes in fO_2 is negligible (see Figure 8.10). A change in oxygen fugacity does not therefore seem likely to explain the observed change in $\delta^{13}C$ in the altered wallrock. The observed trend of increasing $\delta^{13}C$ away from the mineralisation into the wallrock can therefore be interpreted in similar fashion to the "fractionation" patterns seen by Fyon (1986), away from the increasingly consumed CO_2 bearing fluid reservoir in the vein fracture. This explanantion supports the whole rock geochemistry of the wallrocks marginal to the vein, where strong K-metasomatism (Chapter 3) is testament to interaction between the hydrothermal fluid introduced during D2 and the wallrocks. The single sample from the altered "felsite" shows a value very close to that for the mineralisation itself, further evidence that least some of the intruded bodies having suffered intense alteration by the gold-bearing hydrothermal fluid.

The fluid value for carbon isotopic composition could support either a magmatic or mantle CO_2 source (Mattey 1987, Kerrich 1989), which tends to strengthen support for models invoking these fluid sources.

8.4.5 Sulphur Isotope Study

Previous studies

Studies of sulphur isotopes in sulphides from Archaean deposits are generally preliminary based on a few "representative" samples. More recent studies however (Schwarcz & Rees 1985 and Cameron & Hattori 1987) have begun to tackle the significance of the data generated. Redox seems to be the most important factor in the interpretation of sulphur isotopic variation (Cameron & Hattori 1987). However fractionation is a function of temperature and in low total sulphur systems Rayleigh fractionation may be important.

The data from published studies shows a range of sulphide $\delta^{34}S$ from +10 to -4 (Colvine et al. 1988), with a large cluster of data in the range 0 to +4. The negative values have been interpreted as largely resulting from sulphide precipitation from relatively oxidised fluids (Cameron & Hattori 1987).

Calculation of results

The principles of interpreting sulphur isotopes are essentially similar to that of carbon (Ohmoto 1972). Isotopic equilibrium is primarily a function of temperature, relative proportions and degree of equilibrium between the various sulphur species. In a similar fashion to carbon, sulphur fractionation becomes highly sensitive to changes in fO_2 in certain conditions. For the mineralising fluid in the Patchway system, sulphur is likely to be dominantly present as the species $H_2S_{(aq)}$ in equilibrium with $SO_4^{2-}{}_{(aq)}$ and so $\delta^{34}S$ of each species is controlled by:

$$H_2{}^{34}S_{(aq)} + {}^{32}SO_4{}^{2-}{}_{(aq)} \rightleftharpoons {}^{32}H_2S_{(aq)} + {}^{34}SO_4{}^{2-}{}_{(aq)}$$

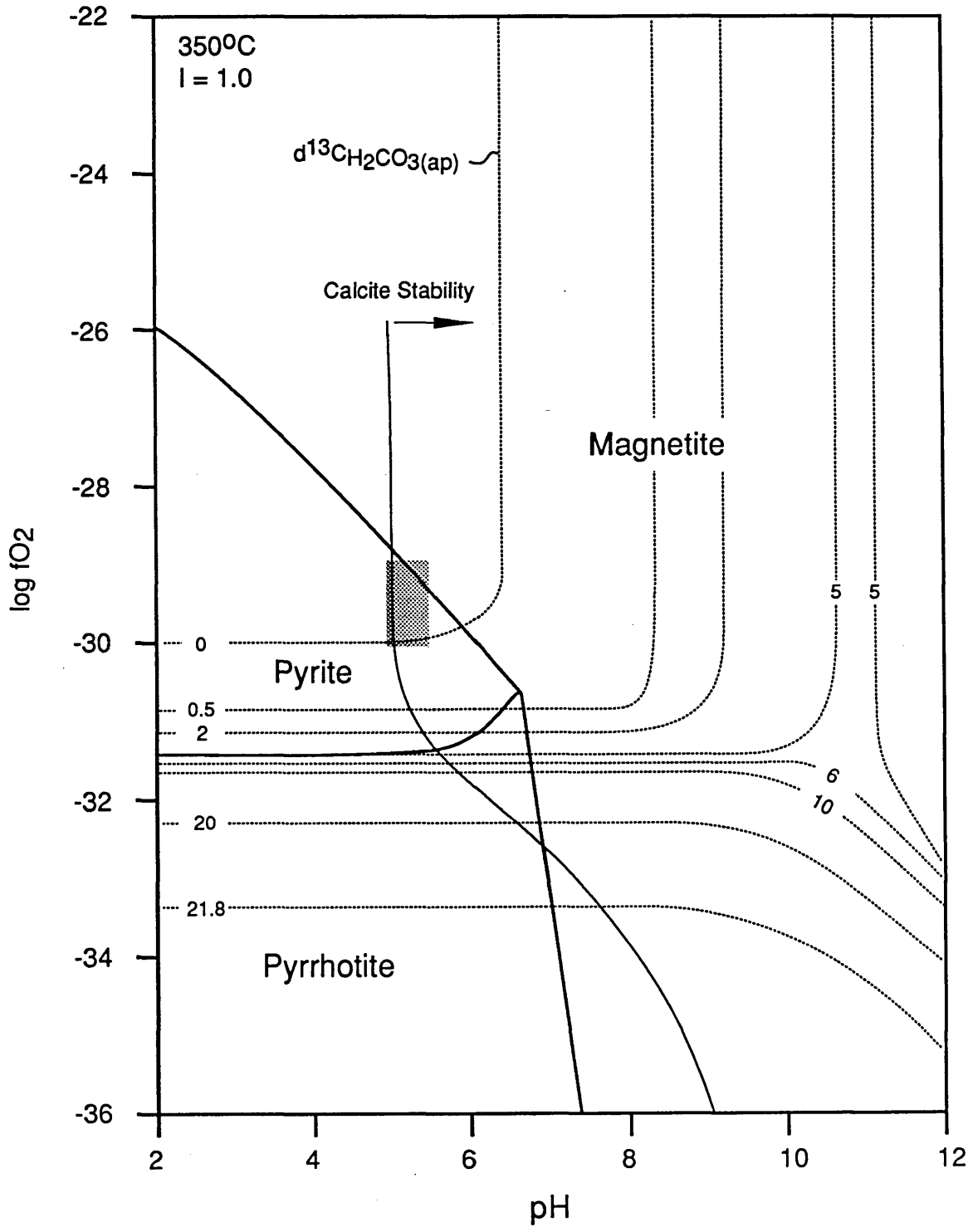


Figure 8.10 - Graph showing positions of $\delta^{13}C$ contours fluid vs. calcite as a function of fO_2 and pH (from Ohmoto 1972). Dashed line indicates stability fields for calcite. $\delta^{13}C$ contours are for $H_2CO_{3(ap)}$ at $\delta^{13}C$ = 0‰. Patchway fluid conditions shown as shaded box.

The equilibrium constant for this reaction is temperature dependent, lying between 1.02 and 1.03 between 250 and 250° C (Stanton 1972), which leads to a 2 to 3% enrichment in ^{34}S in the sulphates over this range. This can lead to large fractionation effects in co-existing reduced and oxidised species. Since any pyrite forming has a sulphur signature very close to that for H_2S (Ohmoto 1972), the ratio H_2S : SO_4^{2-} becomes critical in defining fractionation.

This phenomenon is summarised on the log fO_2 vs. pH plot on Figure 8.11. At 350° C, near neutral pH and at the range of log fO_2 likely for the Patchway fluid (-28 to -30), fractionation is highly sensitive to small changes in fO_2. A one order of magnitude increase in log fO_2 from -30 at pH 5.5 can theoretically cause a shift of 11 ‰ in the $\delta^{34}S$ of the precipitating pyrite. These contours are highly temperature sensitive however, and for the same conditions at 300° C, the fractionation effect is negligible for the same change in the fO_2 value.

In summary then, the sulphur isotope signature of precipitating pyrite is largely dependent upon temperature and fO_2 and a good constraint of these two parameters is necessary when interpreting $\delta^{34}S$ differences.

Results

Determination of $\delta^{34}S$ values were made for 11 pyrite separates. The sample set comprised 5 samples from the vein mineralisation itself, 5 samples from sulphidised altered wallrock and 1 sample from one of the felsite intrusive bodies. The results are shown in Table 8.8, and indicate a small range of values from +1.9 to +3.1 and reproducability is better than 0.05 ‰.

The compositions of the vein sulphide show a range of values between +2.5 to +3.1. If we assume equilibrium conditions at the time of precipitation and the dominance of H_2S as the sulphur species in the fluid (demonstrated in section 8.3), it is possible to calculate $\delta^{34}S$ for the mineralising fluid using the fractionation factor presented by Ohmoto & Rye (1979). This is shown below:

$$10^3 \ln\alpha = (0.4/T^2 \times 10^6) \times 1000$$

At the estimate of the fluid temperature at time of sulphide precipitation of 350 °C, a calculation of $\delta^{34}S_{fluid}$ between +2.9 and +3.5 is made.

The wallrock sulphide samples have a distinctly lighter signature with values of $\delta^{34}S$ falling between +1.6 and +2.6. The sample set did not allow a truly systematic study of variation in $\delta^{34}S$ away from the central vein, however those samples taken immediately adjacent to the ribbon vein have the values closest to the vein itself.

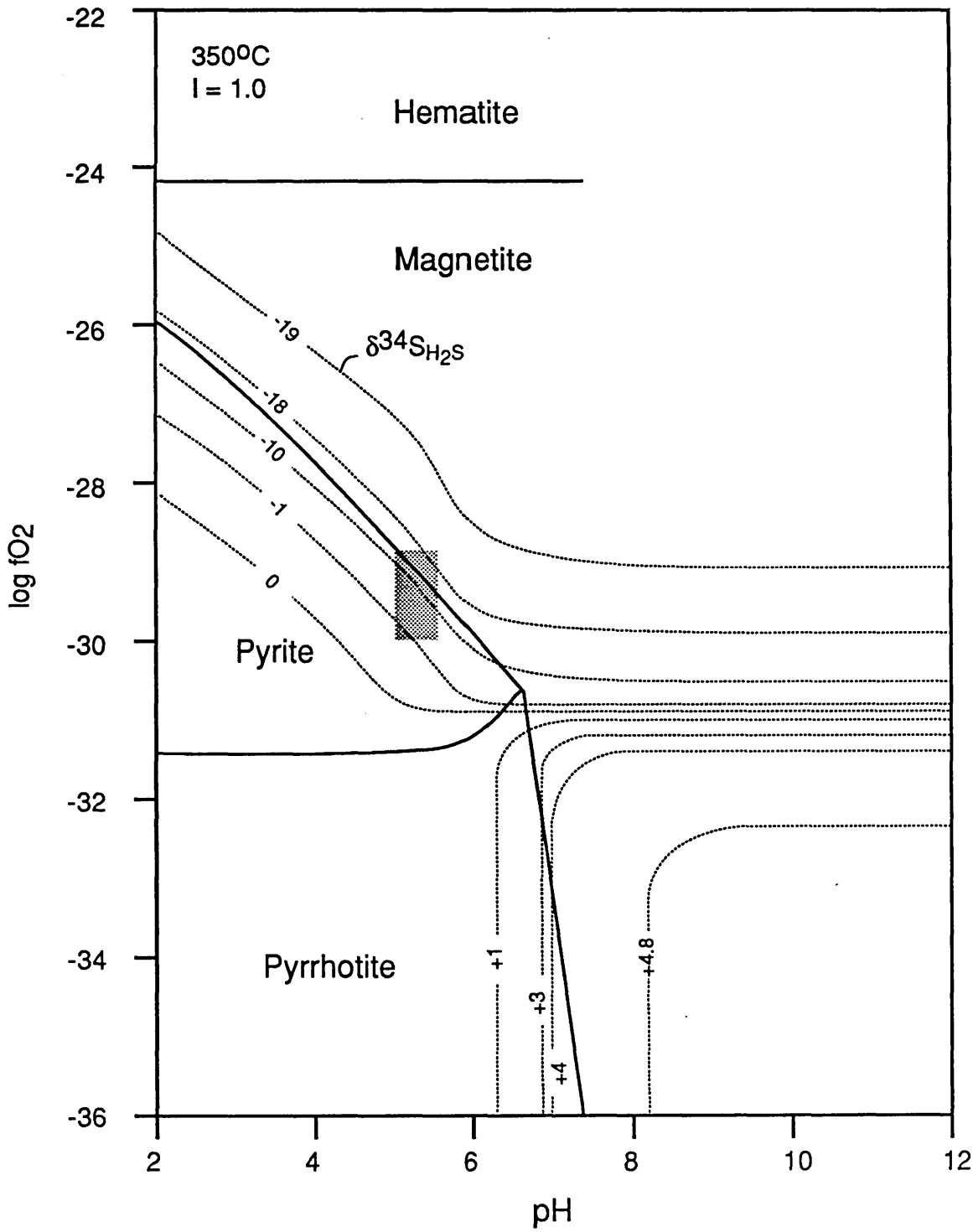


Figure 8.11 - Graph showing positions of $\delta^{34}S$ contours H_2S vs. fluid as a function of fO_2 and pH (from Ohmoto 1972). Stability fields for Fe minerals assuming ΣS = 0.01m shown. $\delta^{34}S$ contours are for H_2S at $\delta^{34}S$ = 0‰. Patchway fluid conditions shown as shaded box.

Sample	Location	$\delta^{34}S$
2400/N/8	Main Q2 Vein	3.07
2200/1	Main Q2 Vein	2.67
30-6	Main Q2 Vein	2.70
30-2	Main Q2 Vein	2.46
26-11	Main Q2 Vein	2.63
10-36	H/W Vein + 0.8m	2.45
10-29	H/W Vein + 0.2m	2.33
19HG-1	Main Q2 Vein (+Au)	2.40
600/1	F/W Vein - 0.8m	1.89
20-9	F/W Vein - 0.8m	1.59

Table 8.8 - Sulphur isotope determinations from pyrite. Samples are all taken from mineralised Q2 ribbon-quartz veins or from deformed rocks marginal to such veins.

Discussion

The shift of $\delta^{34}S$ away from the vein would therefore imply either a temperature change or a change in fO_2. Simple Rayleigh fractionation would not cause this trend, since H_2S is very slightly ^{34}S enriched with regard to pyrite at the suggested temperatures and hence residual H_2S would tend to get increasingly heavier. The fall in $\delta^{34}S$ seen away from the vein would imply a temperature rise away from the mineralisation. This is not likely as the speculated ore-fluid temperature is close to the highest recorded metamorphic temperatures in the host lithologies. A change in fO_2 could thus be the cause of this change.

The implication from the mineralising fluid evolution model is that phase separation during mineralisation releases H_2S into the vapour phase (section 8.3.2). As H_2S gets locally consumed to form pyrite in the vein, the resultant fluid becomes more oxidising. This has the effect of lowering the $\delta^{34}S$ of the residual H_2S. The wallrock pyrite, which probably precipitated after this oxidation event, is thus likely to have a lower $\delta^{34}S$. It was predicted above (Figure 8.11) that such a change might be up to 11 ‰. However this effect is likely to be counteracted by the changes induced by *both* the likely temperature drop during mineralisation *and* the strong Rayleigh fractionation effects likely in a low total sulphur system like this. The results indicate that the $\delta^{34}S$ of the wallrock sulphides are indeed lower, however the effect is opposed by the temperature drop and consumption of ΣS.

The original value for the fluid of between +2.9 ‰ and +3.5 ‰ is fairly equivocal for distinguishing the ultimate source between magmatic and metamorphic sulphur. Lambert *et al.* (1984) suggest values between -4 and +4 ‰ are typical of mantle derived, magmatic S, whereas Ohmoto (1986) suggests a more restricted range of 0 ± 0.5 ‰. Reduced metamorphic fluids of low total S have indistinguishable signatures from magmatic fluids (Kerrich 1989). The one sample taken from the felsite containing accessory pyrite shows a value of 2.70 ‰, very close to the vein pyrite values. It is difficult to be sure that this value truly represents original magmatic S, despite the apparently unaltered nature of the sampled intrusion, the result does not contradict a possible magmatically derived S component to the mineralised system.

Finally the data generated from this study are quite consistent with published values from Archaean gold deposits (Colvine *et al.* 1988, Groves 1989). These authors allow either magmatic or metamorphic remobilisation of magmatic sulphur as a source for sulphur. The figures would appear to exclude a highly oxidised fluid at the time of mineralisation.

8.5 Discussion

Excellent constraint on the nature of the D2 hydrothermal fluid is now possible from the fluid inclusion and stable isotope studies, together with the thermodynamic calculations. The fluid is shown to be a

relatively K-rich (aNa+ : aK+ = 7.07) carbonic-aqueous, low-salinity fluid buffered by a silicate wallrock and vein assemblage. From this assemblage and the fluid composition, a pH of 5 to 5.5 is indicated for the fluid at 350°C and 2.5 Kbars. Further thermodynamic calculations from the volatile analyses of fluid inclusions suggest an initial fluid fO_2 in the order of 10^{-30} bars, with distinct changes during a proposed unmixing event to a later fO_2 more than one magnitude greater. Further calculations permit an estimate of H_2S concentration in the fluid between 400 and 100ppm initially. After the unmixing, loss of H_2S is demonstrated as well as a potentially dramatic increase in the SO_2 : H_2S ratio in the more oxidised residual fluid. This change in sulphur species is in addition to any loss of sulphur to precipitating sulphides.

Oxygen isotopes of the Q2 quartz indicate precipitation from a fluid with a $\delta^{18}O$ signature of close to +4 ‰ at 350°C, consistent with a magmatic or metamorphic fluid source. Fluid alkali geothermometry from the individual samples suggest that the spread of over 3 ‰ in the samples mainly reflects the formation of the quartzes at different temperatures from an identical fluid. This supports the proposed model of a large fluid (oxygen-rich) reservoir, episodically tapped into the fracture. Cooling of the fluid during quartz precipitation is evident, and there is some suggestion that the higher temperature quartz is related to better gold values.

Sulphur isotopes are believed to show a combination of fO_2 change and Rayleigh fractionation during precipitation, accounting for a small decrease in $\delta^{34}S$ between the vein and wallrock. Carbon isotopes suggest simple Rayleigh fractionation effects to account for increasing $\delta^{13}C$ away from the vein. The implied Rayleigh fractionation implies a finite, introduced source of both sulphur and carbon, from the hydrothermal fluid itself with little local derivation of either species.

The carbon isotope signature of the fluid, $\delta^{13}C$ = -7‰, is consistent with a magmatic or mantle CO_2 source. The fluid sulphur value of $\delta^{34}S$ = +2.8 to +3.5 is consistent with either magmatic or metamorphic sulphur source.

The oxygen isotope values from quartz belonging to other generations, helps further discriminate fluids responsible for their formation. The Q1 quartz is distinct, formed from a fluid having a $\delta^{18}O$ of around +6 ‰ at 330°C. The Q5 quartz probably formed from a similar oxygen reservoir to Q2, although the data is not very well constrained. Q3 appears to have formed from the same reservoir as Q2, but more data is probably needed. The fluid responsible for Q4 is very distinct, however. The quartz formed at a very consistent temperature from an isotopically light fluid source with $\delta^{18}O$ of +1.8 ‰.

In conclusion, the fluid modelling is consistent with the ribbon-quartz veins formed during cyclic hydrothermal fluid introduction into the vein fracture. This event was accompanied by fluid phase separation or unmixing, methane and H_2S loss into the CO_2 rich vapour. The remaining fluid became

more oxidised, gold and quartz precipited from the fluid, the latter probably over more protracted periods of fluid cooling. Sulphides were formed by sulphidation reactions from H_2S in the more mobile vapour phase, generally in the wallrock and wallrock inclusion bands. The model of fluid "valving" from a large buffered, equilibrated source reservoir is supported by the fluid alkali geothermometer and isotopic study. This fluid appears to have carried the introduced carbon and sulphur into the vein and alteration assemblage.

CHAPTER NINE - DEPOSIT MODEL

9.1 Introduction

This chapter discusses the results presented in the preceeding chapters and aims to develop a model for the chronology and evolution of the gold deposits in the Patchway region. The possible mode of transport and deposition of gold are addressed, together with isotopic evidence for fluid behaviour during mineralisation. The source of the mineralising fluids is briefly discussed and the possible fluid evolution through the deformation-mineralisation cycle is outlined. The model developed has implications for regional metallogenesis and these are highlighted.

9.2 Timing of Gold Mineralisation

Absolute age constraint of the mineralisation event is not possible without specific age dating of alteration and mineralisation assemblages. The age of the mineralisation can, however, be linked to a regional geological evolution model which can be chronologically defined.

The maximum age for the deposits is derived from the age of the greenstones themselves, 2700 Ma (Hawkesworth *et al.* 1975) or 2800 Ma (Moorbath *et al.* 1987). Lead isotope study (Kramers & Foster 1984) suggests an age of around 2650 Ma for the Zimbabwian Archaean gold deposits. Possible minimum age constraint is provide by the clearly later mafic dykes. If they are indeed part of the Mashonaland dyke swarm then a minimum age of 2150 Ma (Wilson *et al.* 1987), can be inferred.

The closely associated tonalite intrusive bodies in the Kadoma region have been dated at 2554 +- 128 Ma (Jap.Int.Co.Ag. & Min.Met.Ag.Jap.1987). If all the mine felsites are related, which geochemistry suggests, then mineralisation may be almost contemporaneous, since mineralisation is seen to both pre and post-date some of the felsites. There is evidence that some of the large Sesombi diapirs may have metamorphic aureoles overprinting mineralisation (Robertson 1976), which further supports this idea.

Gold mineralisation is closely related to the craton deformation history which is itself linked to the major events seen in the Limpopo belt (Coward 1980). N-S crustal shortening at the beginning of this event, led to develpoment of major folding in the Kadoma region with axes directed NE-SW. This folding probably accompanied peak metamorphism, which from fluid inclusion evidence in pre-mineralisation, metamorphic quartz suggests conditions of around 360°C and 3.5 Kbars for the Patchway deposit area (13 km burial depth).

This N-S directed compression also probably initiated the major first-order terrain boundary structures (Lily and Rhodesdale faults). The Patchway, Golden Valley and Dalny shear systems are probably

linked to the major Lily Fault system and initiated at this time. During the main mineralisation event, movement was dominantly reverse-slip with a sinistral strike-slip component. A strongly foliated and altered wallrock assemblage developed during episodic, "stick-slip" fault failure. Later deformation was focussed onto 070° trending, cross-structures, such as the Erin, Rouge and Central shears. Lower grade, patchy mineralisation formed in these structures, indicative of waning auriferous hydrothermal fluid-flow. Deformation along these D3 structures has caused attenuation and faulting of the gold-bearing D2 vein structure. The Dalny vein system has this same orientation, but is significantly better mineralised. This may be testament to a switch of fluid flow to the Dalny region, or different deformation histories for the two regions.

9.3 Detailed Mechanical Controls to Mineralisation

Gold mineralisation at Patchway, and the other related deposits, is located within discrete structural sites. Mineralisation generally follows the main central shear failure ("C" plane plane on the Riedel diagram, Figure 4.8). Two distinct trends, 020/35W and 070/60N are indicated, and these are demonstrated to perhaps have initiated as conjugates or Riedel pairs. These two structural trends probably form part of the major terrain boundary Lily fault complex. The Lily fault system can be traced for at least 50 km north-south, and is seen to join with the more complex Munyati shear zone further south. Early mineralisation, in the Patchway region, favoured the shallow dipping 020/35W D2 structure, probably due to the more favourable "Andersonian" orientation for reverse slip under compression. The steeper 070/60N structures seemed to be poorly mineralised in the Patchway region and show a more protracted deformation history post-dating gold mineralisation. This indicates a shift from reverse-slip on the D2 structures to dominantly strike-slip on the D3 structures. It is interesting to speculate on the history of the Dalny structure, some 15 km north of Patchway. This structure is oriented approximately 070/60N, yet is very well mineralised. Carter & Foster (1990) proposes early reverse-slip with later sinistral strike-slip for this structure, in line with the chronology of the Patchway deformation. Mineralisation at Dalny therefore probably either occurred during D2, accompanied by high fluid pressures ($P_f = P_{lith}$), or alternatively much of the mineralisation may relate to the D3 event recorded at Patchway. If the latter explanation is correct, this may indicate a shift in hydrothermal activity from the Patchway structures to the Dalny region further north.

Since much of the gold mineralisation is present as distinctive ribbon-quartz veins, it is apparent that mineralisation evolved as a cyclic, episodic brittle deformation event, invoking a strong mechanical role for the gold-transporting hydrothermal fluid. Such brittle deformation implies volumatic inflation and is thus a highly pressure sensitive event, implying major changes in fluid pressure during deformation.

Later deformation, D3 and D4, resulted in serious attenuation to the early D2 gold bearing ribbon veins. This later deformation is summarised in the synoptic sketch of the Patchway North Orebody shown on Figure 9.1.

During D3, the D2 orebody suffered boudinage, thinnning and in some cases fault disruption. The central shear zone is the most intense of these zones seen at Patchway, and mineralisation is now absent in this zone, apart from isolated folded pods and thin stringers. Faulting is more evident in the northern parts of the north orebody, where repetition of the main D2 vein is caused by sinistral sense strike-slip motion. The D2 veining has also suffered a flattening rotation into the plane of the D3 shear, and hence assumes a more oblique strike and steeper dip. The clearly defined 30-35° westerly plunging payshoot trend at the mine is caused by the D2-D3 intersection. This trend is repeated at the neighbouring Golden Valley deposit.

The later D4 deformation has resulted in an east-west stretching across the area, with susequent stretching and faulting on a mine scale. A second asymmetric boudinage is developed down-dip, and down dip normal faulting is common. The D4 deformation is particularly focussed between 15 and 18 levels on the north orebody and betwen 11 and 18 levels on the south orebody, where large areas of fault omission of the mineralisation occur. Also related to D4 are the intrusion of dolerite dykes, which are seen to generally intrude normal faults, consistent in orientation to other D4 normal faults. The intersection of D4/D2 leads to the second main payshoot trend, approximately horizontal with a north-south orientation to the boudinage and a 015° to 020° orientation to the dolerite-vein and fault-vein intercepts.

The mineralisation hosted in the tonalites occurs in simple, brittle veins which post date the host diapirs. Scheelite is the only ore-mineral recorded in significant amounts in these deposits and the later (Sesombi) tonalite bodies in general do not host significant gold deposits. Fluid inclusions suggest the fluid has some similarities with the fluid responsible for the gold mineralisation, although P-T conditions of vein formation are calculated to be much lower. Later extension veins, like that seen close to Lion Hill, contain no economic mineralisation. Fluid inclusions show them to have formed in relatively shallow, low-temperature conditions, unlikely to host any gold mineralisation. The fluid responsible is quite unlike that responsible for the gold veins.

Mineralisation in the Kadoma region in general is focussed in the mafic lavas of the Mafic formation rocks (Foster & Wilson 1984). Whole rock geochemistry shows these lavas to be Fe-rich tholeiites, generally a highly competent lithology when unaltered. The structural system related to the main Lily fault transects felsic volcanics of the Bimodal unit, but this terrain is poorly mineralised. The Bimodal unit contains a series of meta-sediments and tuffs and would have quite different rheological characteristics to the mainly massive basaltic rocks of the Mafic formation. It is proposed that the more

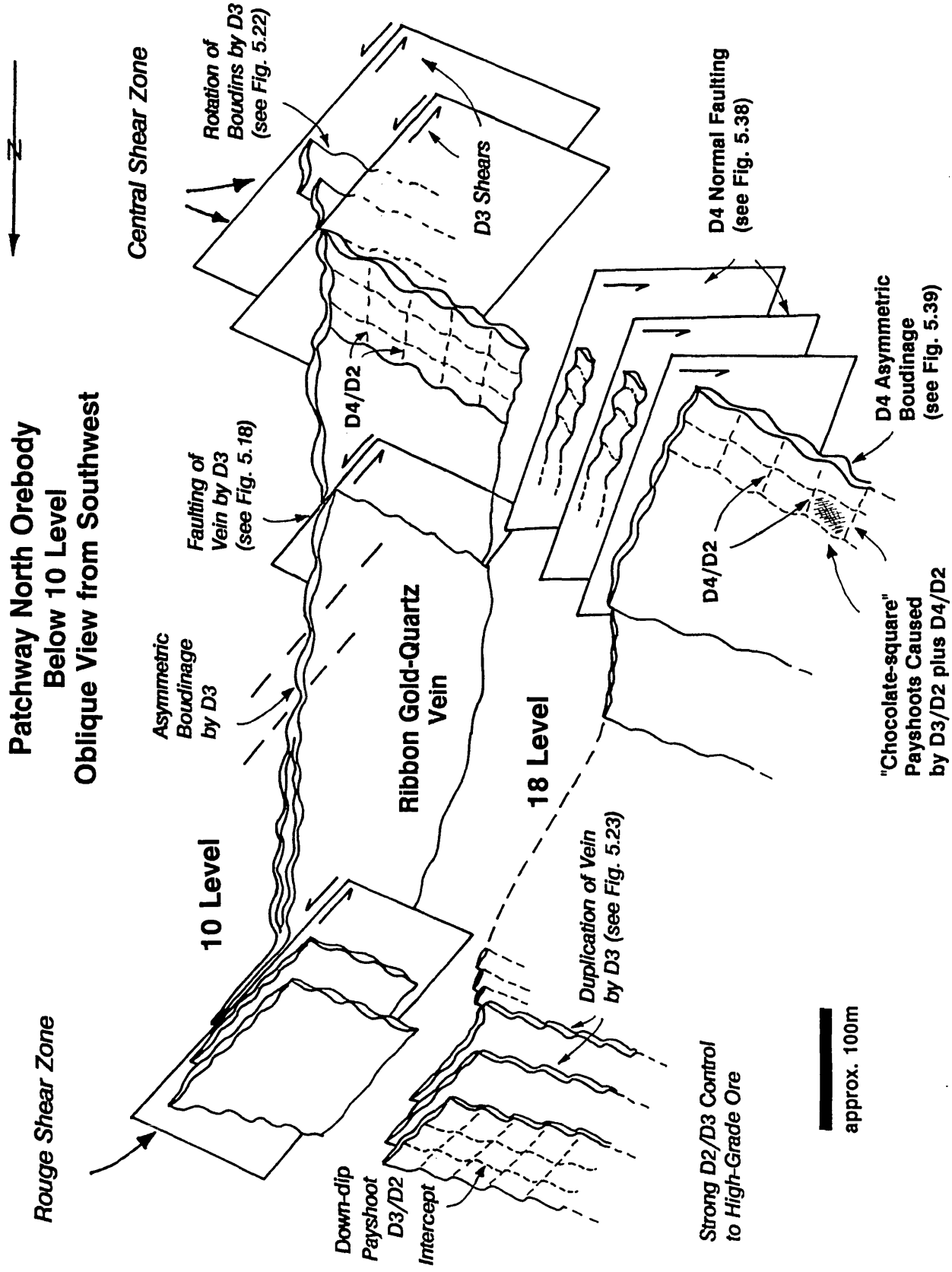


Figure 9.1- Schematic representation of post-mineralisation deformation on the D2 gold-quartz ribbon vein of Patchway North Orebody. Orebody is viewed from the southwest, above. D3 and D4 features are shown, leading to distinct "payshoot" directions at the mine. The intercept of D3 on D2 leads to a roughly E-W plunging definition to ore-lenses, with faulting and boudinage parallel to this. D4 on D2 leads to a roughly N-S horizontal "payshoot"present as boudinage and commonly as faulting, often intruded by dolerite dykes.

competent basalts hosted discrete vein arrays which may well pinch out into the less competent Bimodal units. The main Lily fault is also poorly mineralised, but since the zone has suffered high-strain, suitable deposition sites may not be present for gold deposition. The first order structure is poorly mineralised in most productive greenstone terrains (Colvine *et al.* 1984).

9.4 Nature of the Gold-Bearing Hydrothermal Fluid

The fluid inclusion study allows very accurate constraint to be placed on the nature of the hydrothermal fluid responsible for the ribbon-quartz-gold veins. Mesothermal gold deposits worldwide are associated with CO_2-bearing, low salinity fluids (Kerrich 1989) and the Patchway and Golden Valley deposits indicate the role of similar fluids.

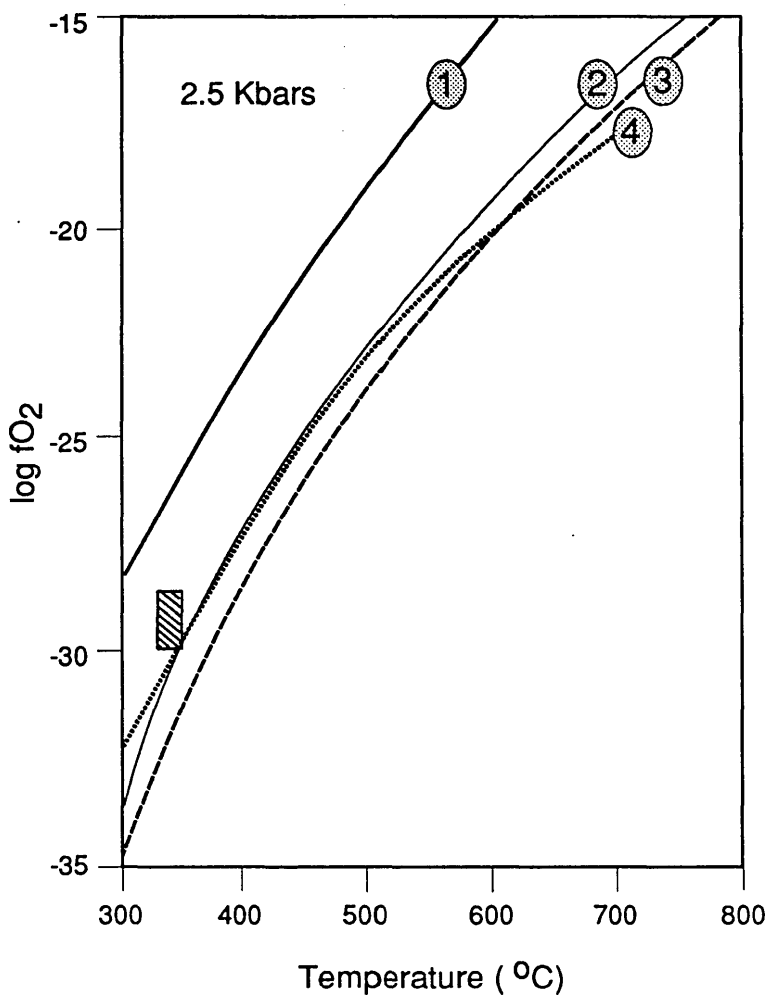
The fluid responsible for the gold mineralisation is introduced CO_2 and sulphur as dissolved species, together with a complex solute containing K and Ba. This fluid interacted with the deformed mafic lava wallrock, resulting in a carbonated, hydrated, sulphidised, phyllosilicate rich assemblage. The wallrock shows signs of intense K metasomatism, testament to fluid-wallrock interaction. The bulk fluid composition is shown in Table 9.1. Levels of the various cations are calculated by utilising the salinity estimates which assume pure NaCl. The Cl^- activity is calculated from the NaCl molality and the various cations are then weighted, using the DICP generated element/Na ratio.

Quartz was the major phase precipitated from the fluid, and the fluid would be expected to be mostly saturated with respect to quartz, buffered by the quartz previously precipitated in the vein. Neglecting the role of CO_2 (addition of which both decreases water activity, and decreases the fluid static dielectric constant, which have opposing effects on silica solubility), quartz content of the fluid would be expected to be in excess of 1800 mg/kg at 2.5 kbars.

The fO_2 of the fluid is fairly well constrained from the volatile analyses, indicating a figure of 3.24×10^{-30} bars. The range of fO_2 values calculated for the Patchway fluid are shown diagrammatically on Figure 9.2. The fluid plots just above the maximum stability field for graphite, in line with the observed absence of graphite from the wallrock or vein assemblage, very close to the QFM buffer (line 3). The fluid, when introduced, is interpreted as having an fO_2 at the bottom of the shaded box.

9.5 Fluid Source

Four main sources for gold-bearing hydrothermal fluids are proposed for the Archaean (Kyser & Kerrich 1990). The possible sources are meteoric fluid circulation, orthomagmatic fluid, metamorphic dehydration fluid and mantle degassed fluid.



BUFFERS SHOWN ABOVE (assemblage to left below stable above the curve plotted) :

1 - Hem-Mag
2 - NO-Ni
3 - QM-F
4 - Max. stability graphite

Figure 9.2 - Fugacity buffers plotted at 2.5 kbars from 300 to 800 °C. Conditions calculated for Patchway fluid shown as a box.

xH_2O	xCO_2	xCH_4	x"NaCl"	xH_2S	Na	K mol%	Ca	Temperature (°C)	pH	$\delta^{18}O$	$\delta^{13}C$	fO_2
0.840	0.130	0.022	0.008	$2.51x10^{-4}$	0.28	0.05	0.03	330-350	5.5	4.1	-7.0	$3.24x10^{-30}$

Table 9.1 - Table shows a summary of calculated fluid chemistry of the D2, gold-bearing hydrothermal fluid rsponsible for the ribbon-quartz veins (+gold +sulphides) at Patchway. Mole fractions are calculated from volatile analyses, microthermometry and D-ICP analyses, except for xH_2S which is calculated thermodynamically from the stable sulphide mineral assemblage (see Chapter 8). Temperature is estimated from fluid and mineral geothermometry. The pH value is an estimate from mineral stabilities and fluid Na:K ratio. The oxygen and carbon isotopic ratios are calculated from mineral isotopic analysis and oxygen fugacity is calculated from measured volatile analyses of C-O-H fluid species and sulphide-mineral sulphur buffering.

Meteoric water

This model, proposed in various forms as recirculated seawater (Hutchinson & Burlington 1984) or downward circulating meteoric water (Nesbitt *et al.* 1986) would appear generally implausible as a source for the Archaean gold deposits. The generally low chloride and high carbon-dioxide contents would appear to exclude seawater. Reaction between seawater and volcanics would be expected to result in loss of CO_2 from the fluid to form calcite (Thompson 1981). Furthermore seawater has a salinity of 3.5% NaCl initially which would undoubtedly rise after fluid-rock interaction. Connate brines have much higher salinities. Nesbitt *et al.* (1986) suggest that δD values of fluids from decrepitated inclusions are consistent with meteoric water source. Pickthorn *et al.* (1987) discount these results concluding that later, secondary inclusion fluids, post-dating gold mineralisation, were measured by this technique.

At Patchway, the model for vein formation implies high fluid pressures, perhaps where $P_f \approx P_{lith}$. In such a case, circulation of meteoric water to depths necesssary to access the host shear system seems highly unlikely.

Oxygen isotopes at Patchway further discount this model. The late D4 fluid is shown to have a $\delta^{18}O$ of +1.8 whilst the D2 fluid shows a $\delta^{18}O$ of around +4. The lower value for D4 is more compatible with a meteoric source (Bischoff & Dickson 1975), whilst the D2 fluid appears to have a different origin.

Orthomagmatic source

This model gained much support in Canada (Hodgson & MacGeehan 1982, Wood *et al.* 1984, Burrows *et al.* 1986, Hattori 1987), where the ubiquitous presence of syn-tectonic tonalite-granodiorite intrusives was well known (Boyle 1979, Colvine *et al.* 1984, 1988). Wood *et al.* (1984) demonstrated the presence of CO_2 in many orthomagmatic ore deposits, whilst Burrows & Spooner (1984) demonstrated the very restricted range of $\delta^{13}C$ carbonate values in the gold veins, identical to that in alteration related to felsic intrusions at Mink Lake. The values are compatible with Hoefs (1980) value for a magmatic C reservoir.

Hattori (1987) showed that some Canadian gold deposits are related to I-type granites, which were potential oxidised fluid sources (Cameron & Hattori 1987). From the literature, fluids responsible for many gold deposits are not generally oxidised (Kyser & Kerrich 1990), and in the case of Patchway rather reduced conditions are calculated for the initial gold-bearing fluid.

Geochronology in Canada now suggests intrusion and mineralisation may not be strictly linked (Colvine *et al.* 1988) and furthermore, isotope studies also suggest there may be inconsistencies in this model. $\delta^{18}O$ values show either too much enrichment or depletion collectively to have a magmatic source (Kyser & Kerrich 1990). Furthermore the vein radiogenic isotope signatures are often very different to the associated intrusion (Franklin *et al.* 1983, Kerrich *et al.* 1987).

In the Patchway region the main tonalite diapirs are generally barren of economic gold mineralisation. However, some of the mine felsites, which have a strong geochemical affinity with the main tonalite diapirs, show evidence for intrusion before mineralisation. Other felsites cut the mineralisation, so the timing of mineralisation and felsite intrusion may be closely linked. The D2 fluid at Patchway is also boron rich, although so is the pillow-margin infill.

Metamorphic dehydration

Metamorphic fluids show much similarity with the fluids seen in fluid inclusions within Archaean gold deposits. During greenschist to amphibolite metamorphism, 5 wt% of the rock is released in the form of water and volatiles, and these fluids tend to be low salinity, moderately CO_2-rich fluids (Crawford 1981). Carbon isotopes for the mineralised assemblages suggest values incompatible with CO_2 formation from metamorphic carbonate (Kerrich 1983). The ore-fluids have a carbon signature more suggestive of a juvenile carbon source (Golding *et al.* 1987). Mineralisation timing may also exclude the metamorphic model. Alteration associated with mineralisation appears to be retrogressive, occurring syn-post peak metamorphism (Perring *et al.* 1987).

Mantle degassing

A juvenile source of hydrothermal fluid by the granulitisation of the lower crust via mantle degassing is a model put forward by Colvine *et al.* (1984) and Cameron (1988). The model of formation is one of mantle CO_2 advection causing granulitisation in the model of Newton *et al.* (1980). Supporting evidence includes the K, Rb enrichment typical in such hydrothermal systems, with some evidence for depleted granulite terrains near gold deposits, despite some more recent work (O'Nions & Oxburgh 1988) which suggests that mantle CO_2 flux in tectonic zones is inadequate to produce granulites on a regional scale. Mantle heat flow and fluid flux rates may have been quite different in the late Archaean (Watson 1978).

The presence of lamprophyric intrusions in similar structures to those hosting gold deposits is testament to access of some of these gold-bearing structures to the lower crust and deeper. Although lamprophyres are not seen in the vicinity of the Patchway deposit, there is a close gold-lamprophyre association in some gold deposits in Canada and Australia (Rock *et al.* 1987, Wyman & Kerrich 1988). Carbon isotopes are further supportive of a lower-crust or mantle fluid CO_2 source (Perring *et al.* 1987), although Ohmoto & Rye (1979) suggest that $\delta^{13}C$ values around -5 are difficult to interpret, precisely because mantle, average igneous, metamorphic and sedimentary carbon all have $\delta^{13}C$ within this range.

Quite pertinent to this model is the two-stage model proposed by Tarney & Weaver (1987). They link an early mantle CO_2 flux with generation of depleted granulite which then produces a depleted, tonalitic magma. Skippen & Marshall (1990) show that at the depths and temperatures of granulisation, generated gas pressures will exceed lithostatic pressure at the QFM buffer, which results in the forcible

expulsion of the fluid phase to higher parts of the crust. The Tarney & Weaver model may be applicable to the Kadoma region where a clear temporal and spatial relationship between the mineralised shear zones and late tonalite diapirism, of the Sesombi suite, is demonstrated. The lack of alteration around the large tonalites is possible evidence for the forcible expulsion of volatiles, suggested by Skippen & Marshall (1990), before generation of the melt.

Proposed fluid source

The preferred model for the generation of the gold-bearing hydrothermal fluids at Patchway follows the model proposed by Tarney & Weaver (1987). The hydrothermal fluids are proposed to have been generated by granulitisation of deeply buried, earlier formed crust. This fluid accessed the upper crust via the major Lily and Rhodesdale fault systems. Although the Lily fault is poorly mineralised, the high strain of this zone made it a poor host for mineralising fluids which accessed the second and third order structures. The major Rhodesdale and Munyati fault systems show evidence for major fluid flux, with regional carbonatisation, particularly in the Battlefields area (Robertson 1976, Pitfield & Campbell 1990). The Patchway stable isotope data is consistent with such a common fluid source. Granulites are not exposed in the belt, but might be speculated at depth, and are the proposed source material for generation of the tonalite magma responsible for the Sesombi tonalite suite.

9.6 Gold Transport and Deposition

The gold bearing hydrothermal fluid was also a multi-component carbonic-aqueous electrolyte introduced under high pressure and moderately high temperature (2.5 Kbars, 350°C). In such a solution, it is possible for gold to be transported in a variety of complexes as indicated by Seward (1990). Gold commonly forms ions of $^{+1}$ and $^{+3}$ oxidation states, however, in hydrothermal solutions in the earths crust, low oxidation states are the general rule (Henley *et al.* 1984). In such hydrothermal solutions, the $^{+1}$ oxidation state of gold, Au^+, is the dominant gold species.

The Au^+ ion, due to electron configuration of its d^{10} shell, means it prefers co-ordination with more polarisable 'soft' Lewis bases of electron donor complexes. This preference is shown by the increased stability of the covalent bonded AuI_2- (I^- is considered a 'soft' polarisable ion) over the $AuCl_2^-$ complex (Table 9.2). Even more support is provided by comparison of equilibrium constants for Au^+ with sulphur-bearing ligands in Table 9.2. The $Au(HS)_2^-$ complex is nearly 21 orders of magnitude more stable than $AuCl_2^-$. Not all sulphur bearing species form good gold complexes, however. For example Au^+ does not form a stable sulphate complex.

In considering hydrothermal systems, this simple consideration of stabilities must be considered in conjunction with actual ligand availability (a function of species molality). From Table 9.2, the $Au(CN)_2^-$

Ligand	log β_2	Ligand	log β_2
$Au(CN)_2^-$	38.7	$Au_2S_2^{2-}$	41.1
AuI_2^-	19.0	$Au(HS)_2^-$	30.1
$AuBr_2^-$	12.4	$Au(SCN)_2^-$	16.8
$AuCl_2^-$	9.2	$Au(S_2O_3)_2^{3-}$	26.0

Table 9.2 - Equilibrium constants for the formation of aqueous Au (I) complexes at 25 °C (from Seward 1989).

appears the most stable, but has not been demonstrated as a major component of hydrothermal fluids. Obvious choices are chlorine and sulphur complexes, given the demonstrated presence of around 3 equivalent wt% NaCl and up to 400 ppm H_2S in the Patchway D2 fluid. Although no high temperature stability data is available, tellurium complexes may also possibly transport gold (e.g. Te_2^{2-}, TeS_2^-). Evidence for tellurium complexing comes from Smith (1944), where gold telluride was formed from a sulphide-polysulphide solution containing tellurium, at 250°C. In addition, tellurides are found associated with many gold deposits, including Patchway. As and Sb bearing sulphur complexes ($As_3S_6^{3-}$, $Sb_3S_6^{3-}$) are also suggested as possible ligands (Seward 1989), and the presence of detectable As ions in the D2 hydrothermal fluid (0.02m from Table 7.13), may support such complexing in the Patchway system. However, in the absence of experimental data on more exotic complexes, Seward (1989) concludes that Cl^- and HS^- are the most likely ligands for gold complexing and transport in hydrothermal solutions, but more experimental data on other complexes is needed to confirm this.

Calculations made for natural fluids found in low-salinity, near-neutral, precious metal-dominated hydrothermal systems are fairly consistent in their conclusions. Seward (1989) has calculated for the Broadlands geothermal system in New Zealand (P_f > 250 bars, T = 290 °C, pH = 6.2, Cl^- = 0.04 m, H_2S = 0.004 m), that $Au(HS)_2^-$ is 8 orders of magnitude more abundant than $AuCl_2^-$. Böhlke (1989) describes a mesothermal gold deposit, (P_f = 2 Kbars, T = 325 °C, pH = 6, Cl^- = 0.7 m, H_2S = 0.01 mole%, CO_2 = 10 mole%) and calculates that the $Au(HS)_2^-$ species is up to 6 orders of magnitude more abundant than $AuCl_2^-$ in this case. Recent theoretical work by Segalstad & Berg (1990) suggests that such calculations may be somewhat over simplified and that the effects of the co-existing equilibrium assemblage (e.g. metal sulphides, oxides and carbonates), on the fluid gold-complexing ligands, needs more careful study.

However, in the absence of a better approximation, calculations made for the Patchway gold-bearing fluid suggest very similar fluid parameters to those of Böhlke's calculation above. For Patchway, xH_2S is calculated to be at least $3x10^{-5}$, but more likely $2.51x10^{-4}$ or 400ppm H_2S (Table 9.1). Since the Cl^- activity is only 0.52 m, a similar dominance of the $Au(HS)_2^-$ species in the hydrothermal fluid is anticipated. However, $AuHS^0$ may be even more stable at the pH and temperature proposed for the Patchway fluid (Figure 9.3). This is based an extrapolation from low temperature work, however, and more experimental work appears neccessary.

The role of dissolved CO_2 in such fluids is not considered in these calculations. Dubessy *et al.* (1989), indicate that the static dielectric constant of an aqueous fluid is likely to be decreased by the addition of CO_2. Decreasing this constant has the effect of increasing the stability of ligands such as Cl^-. Such an effect means that gold-chloride complexing may be more important than the above calculations suggest. Despite this, further circumstantial evidence supports sulphur complexing in precious metal

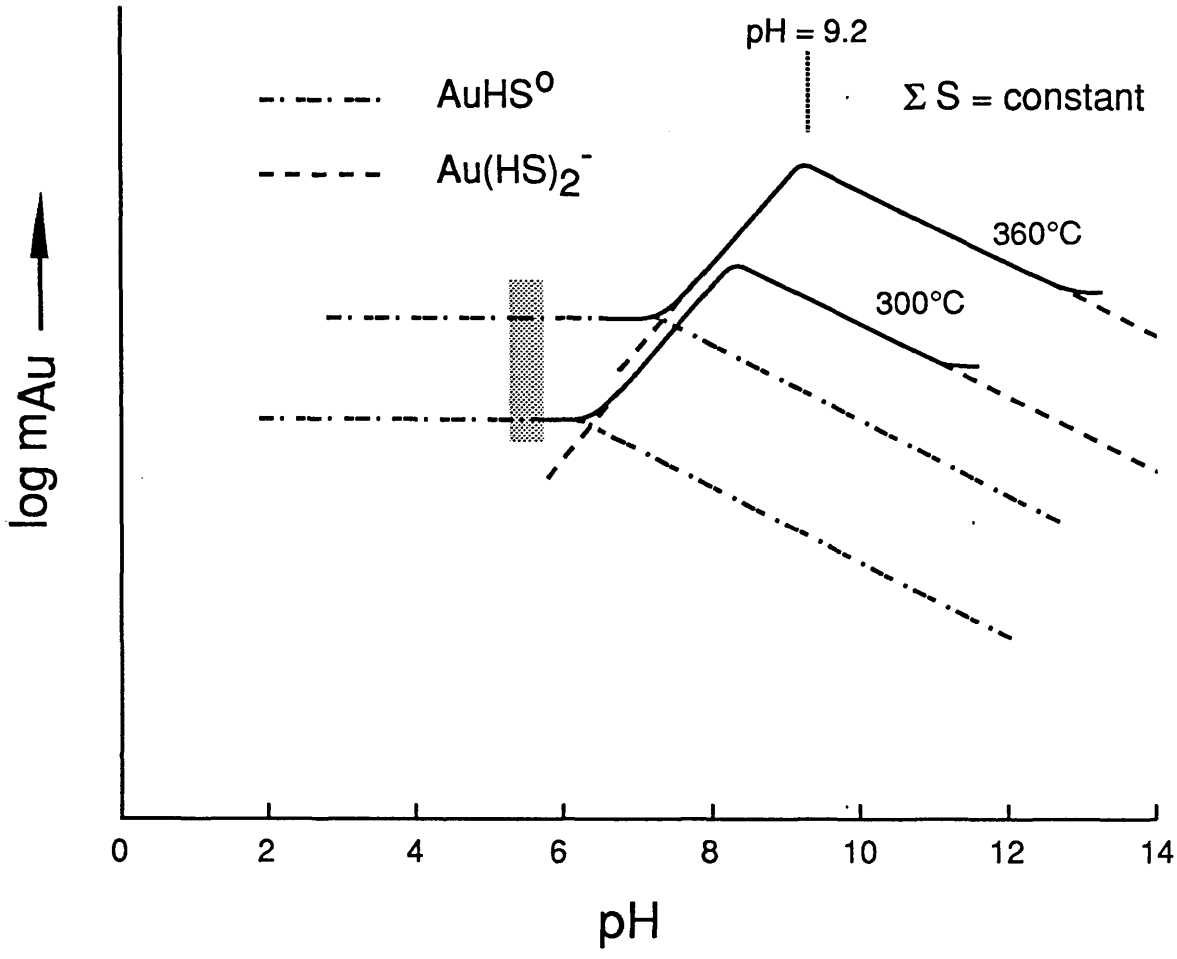


Figure 9.3 - Curves showing relative gold solubility with respect pH at various temperatures for gold-sulphur complexes commonly present in hydrothermal systems (from Seward 1990). Stippled region shows pH range indicated for the Patchway D2 fluid across the temperature range predicted for the fluid. It is clear that $AuHS^{o}$ is likely to be the dominant complex present.

systems, namely the general lack of base metals in gold-bearing vein systems (Hodgson & MacGeehan 1982), as base metals are likely to favour chloride complexing.

Gold deposition from hydrothermal systems obviously largely depends on how the gold was initially complexed. Gold solubility as both chloride and sulphur complexes generally increases with temperature (Henley 1973, Seward 1973), hence simple cooling preciptates gold from either complex.

Fluid phase separation (unmixing or "boiling"), thermodynamically modelled by Drummond & Ohmoto (1985), induces major chemical change in a hydrothermal fluid. Chloride complexed cations are deposited as a result of increased proton concentration due to loss of CO_2. Bisulphide complexes are destabilised due to loss of H_2S to the vapour phase. In addition, CO_2 is lost, pH and salinity rises and the fluid may adiabatically cool. Fluid-rock interaction may be important, where such a process results in destabilisation of the gold complex. Sulphidation reactions effectively remove total sulphur from the fluid, destabilising bisulphide complexed gold. This mechanism may be particularly important in BIF hosted deposits or high Fe-wallrocks. Gold precipitation directly onto the surface of previously formed phases is another possible mechanism. Starling *et al.* (1989) have shown the potential importance of pyrite surfaces as suitable gold precipitation sites. This observation is supported by the observation of gold grains hosted along fractures in pyrite in the Patchway veins.

For the Patchway vein system, the mechanical model of vein formation invokes cyclic fluid pressure to explain the multiple, episodic mode of ribbon formation. Catastrophic fluid pressure drop would be predicted from the model and would result in phase separation of the type modelled by Drummond & Ohmoto (1985). Figure 7.33 demonstrates the effect of pressure drop on the H_2O-CO_2-NaCl solvus for for a similar fluid to the gold-bearing hydrothermal fluid at Patchway. The effect is to force the fluid into the two phase field where phase separation occurs. The effect on the fluid is loss of gases with high partition co-efficients ($CH_4 > CO_2 > H_2S$ Figure 9.4). This loss results in destabilisation of bisulphide complexed ions, decreased stability of chloride complexes due to a rise in static dielectric co-efficient, pH rise due to partial loss of CO_2, and finally fO_2 rise due to the loss of CH_4. Recent work (Brown 1989) suggests that initial phase separation may increase gold solubility due to the initially increased pH and hence increased bisulphide stability (Seward 1990), however volatile loss soon counteracts this together with H_2S loss. Multiple phase separation of the type proposed for the Patchway fault system would undoubtedly cause bisulphide instability. Of note is the fO_2 increase resulting from CH_4 loss. This pushes the fluid toward the hematite-magnetite buffer which increases SO_4:H_2S ratio of the fluid. This further serves to dramatically decrease bisulphide stability. Since the sulphate ligand does not form a stable gold complex (Seward 1990), gold is no longer soluble. Support for the precipitation of gold directly from a bisulphide complex due to volatile loss of H_2S is perhaps provided by the occurrence of native gold grains totally encapsulated in co-precipitated quartz (Figure 7.6). This model of vein

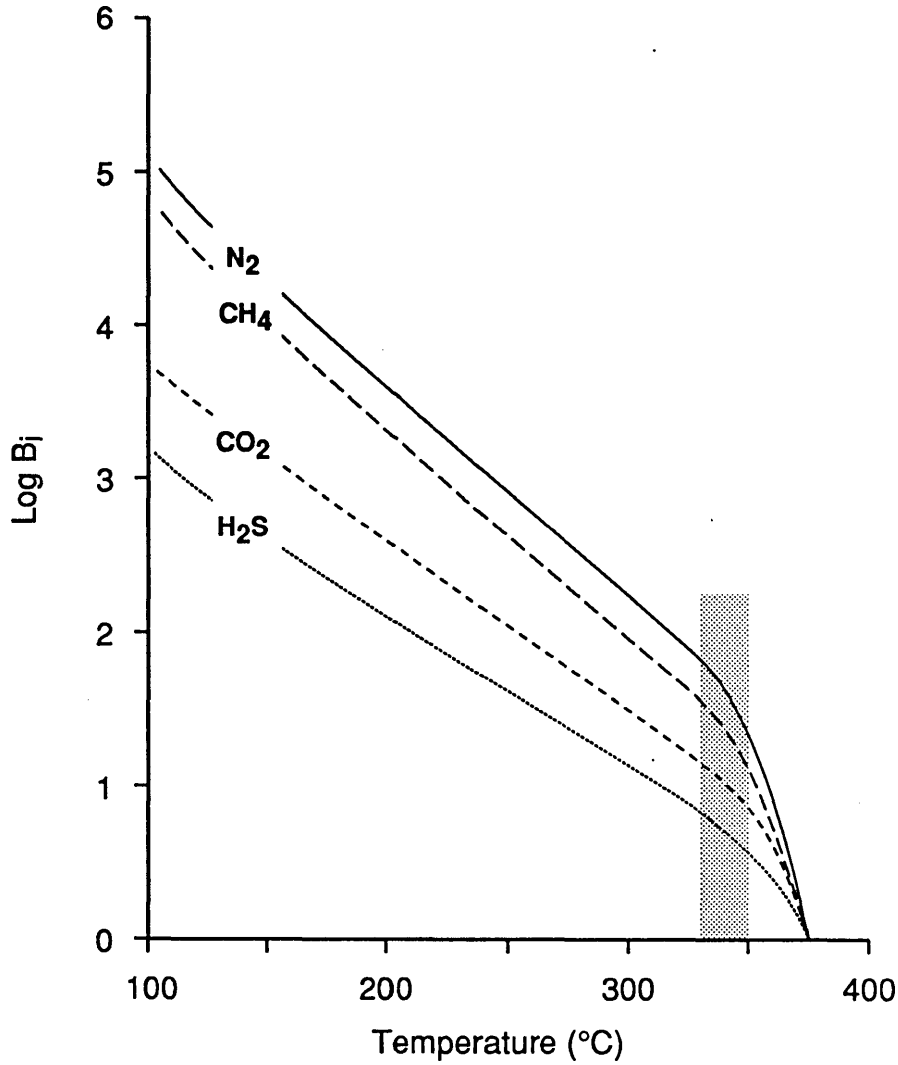


Figure 9.4 - Figure showing the variation in gas : liquid partition coefficients in pure water for major miscible gas species present in hydrothermal systems. Variable Bi is the ratio of molal concentration of the species i in the gas phase to the liquid phase at the vapour pressure of water. Curves are plotted for i = CH_4, N_2, CO_2 and H_2S (from Naden & Shepherd 1989). The shaded area on the diagram is the proposed range of temperature for the D2 gold-bearing hydrothermal fluid, indicating the range in partition coeffficients, all gases strongly favouring partition into the vapour phase.

evolution is summarised in Figure 9.5. Co-precipitation of gold and sulphides on wallrock septa is predicted, as well as direct precipitation of gold from solution to form discrete grains.

Most of the previous studies of chemical changes related to unmixing (Drummond & Ohmoto 1985) have examined the behaviour of more minor components of the system (metal ions). The hydrothermal fluid is, however, likely to be silica saturated and silica thus forms the major dissolved species. Above 300°C, the solubility of quartz is clearly pressure related. Major fluid pressure decrease induced by the failure of the vein structure would rapidly cause super-saturation of the fluid with regard to silica. The fluid pH is also shown to significantly rise due to the loss of CO_2 (> 0.5 pH unit expected) and thus a slightly alkaline (pH 6 to 6.5) residual fluid results from unmixing.

Fournier (1985) suggests that rapid quartz super-saturation induced by such a pressure drop is likely to result in precipitation of amorphous silica, probably initially as a colloid. Frondel (1938) shows that if a gold compound is reduced in the presence of silica sol (colloid), the formation of a gold sol is favoured. Furthermore, gold sols are shown to be protected by silica sols in experiments containing no electrolyte, at temperatures up to 410°C. Alkaline solutions are shown, by Frondel, to protect gold sols from coagulation by NaCl, supporting Lindgren's (1936) conclusion, that under alkaline conditions, gold probably only exists as a sol, protected by silica. This raises the interesting possibility of formation of a gold sol distributed in a silica saturated fluid. Such gold remains mobile in the fluid phase as a protected sol. The formation and transport of a protected gold sol is the model proposed by Saunders (1990) to explain the disseminated gold-silica textures seen at the Sleeper epithermal gold deposit.

In the Patchway situation, as the vein catastrophically fails and the "valved" hydrothermal fluid undergoes phase separation, silica super-saturation is likely to occur almost instantaneously. This favours silica precipitation in amorphous form and formation of silica colloid in any remaining hydrothermal fluid. Since gold is released from both chloride and sulphur complexes at the same time, colloidal gold may also form. In a vein system such as Patchway, further long-distance transport of gold as a colloid seems unlikely. However, a gold colloid suspended in amorphous silica gel may aggregate by diffusion (Boydell 1924), perhaps as a result of annealing. Such a process noted in the commercial production of gold-bearing "ruby glass". Coarse gold grains might therefore result and coarse gold grains are common in Archaean ribbon vein deposits (see Chapter 4).

The generally equigranular nature of the Patchway ribbon quartz veins is striking. Classic syntaxial and epitaxial quartz textures are the likely result of crack-seal quartz vein formation (Ramsay 1980), which might be expected in multiple vein failure and seal systems, where quartz is the dominant phase precipitating. It is suggested that the Patchway vein textures could be explained by the possible precipitation of silica initially in an amorphous form, which was suggested earlier. The silica later "restructures" to form the equigranular quartz texture now seen. Textures demonstrating such a

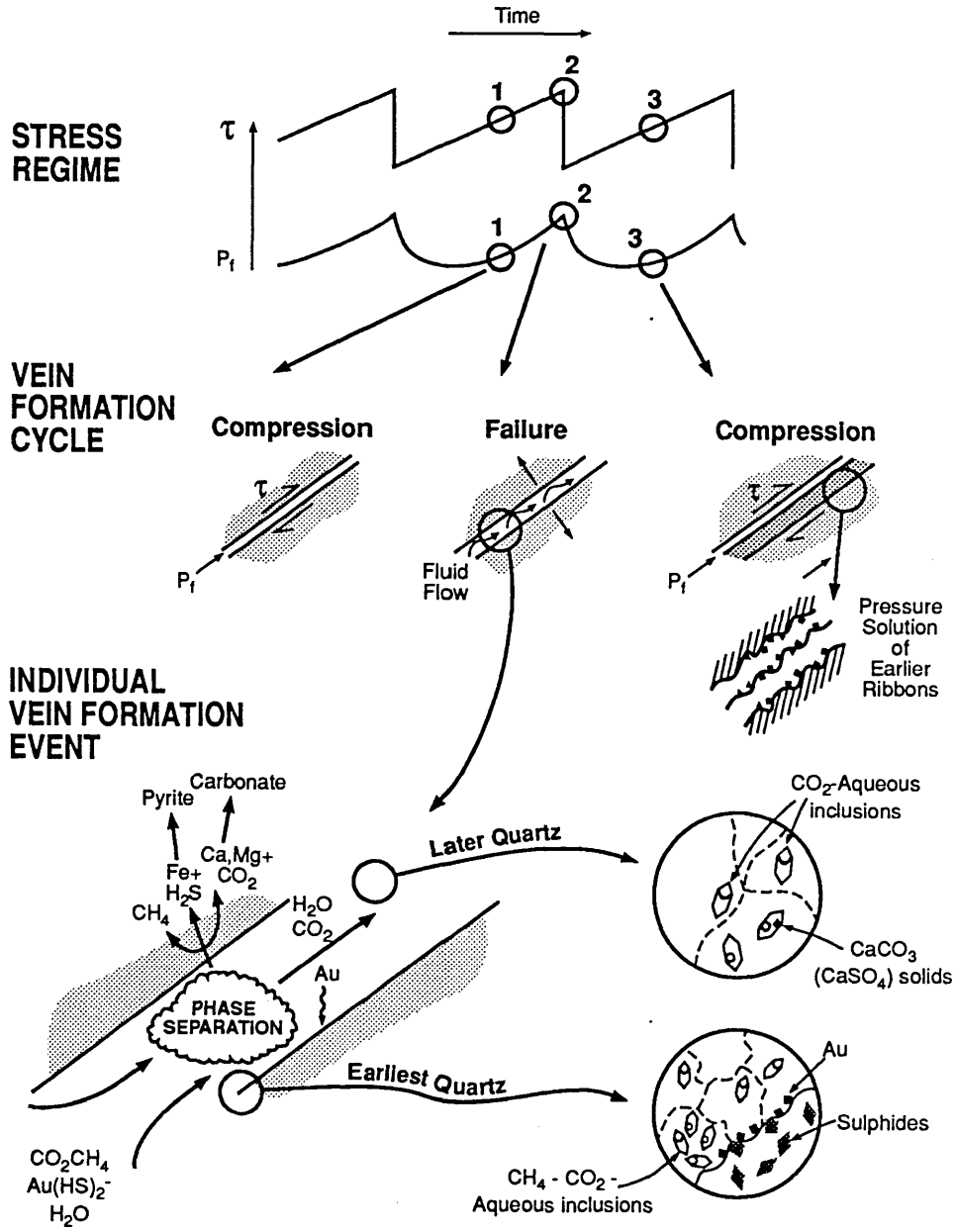


Figure 9.5 - Synoptic model for vein formation and gold-sulphide precipitation at Patchway during D2 deformation.

Upper sequence shows cycling of shear stress and fluid pressure during seismic slip (as proposed by Sibson 1981). The centre sequence shows the vein formation cycle, with massive fluid flow and precipitation during failure. The key texture, stylolitic banding in the inclusion bands, is evidence for a return to a compressive regime after failure and vein formation. The lower sequence documents the events on a fluid inclusion scale. The fluid, as introduced, carries significant CO_2 and CH_4 together with dissolved chloride and sulphur species (including gold as a bisulphide complex). Phase separation induced by the massive fluid pressure drop causes loss of volatiles (CH_4, CO_2 and H_2S) and undoubtedly leads to silica super-saturation and precipitation of silica, perhaps initially in a poorly crystalline amorphous form. Gold thus precipitates due to loss of H_2S, sulphides precipitate largely as pyrite, due to sulphidation of existing wallrock minerals (ilmenite and chlorite). Fluid inclusions document the evolution of the fluid from a reduced CH_4-bearing fluid to a more oxidised CH_4-poor fluid during this event. Possible anhydrite grains trapped in CH_4 poor fluid inclusions, in quartz formed after phase separation, are testament to this redox shift.

phenomenon are apparent in epithermal quartz veins studied from the Beowawe hot-spring system in Nevada, USA (unpublished observations). In these veins equigranular quartz forms pseudomorphing clearly aggregate spherular colloidal silica textures. The suggestion of such processes in the Patchway mesothermal veins could have rather profound implications for fluid inclusion study in such systems, although the transition from poorly structures silica to quartz may still preserve the fluid trapped during primary growth. The need for further textural and experimental investigation in this field is strongly indicated.

9.7 Fluid Evolution During Regional Deformation

The study of the various stages of mineralisation has defined six distinct quartz stages (Q1 to Q6) which can be linked to the four deformation events (D1 to D4) defined in Chapter 5. The fluid studies permit reasonable definition of fluid compositions during formation of the various quartz stages and estimates of possible ambient formation conditions. This data is summarised in Table 9.3 where a distinct evolution is indicated.

Peak metamorphic conditions appear linked to D1 at 360°C and 3.5 Kbars for the Patchway rocks (Greenschist facies). Development of the gold-mineralised structures during D2 occurred under probably reduced ambient pressure (indicative of possible uplift during transpressive strike-slip shearing). During D2, the shear zones formed a conduit for an exotic, low salinity, slightly acidic, reduced, gold-bearing carbonic-methanoic fluid which reacted with the wallrocks and precipitated quartz, sulphides and gold during cyclic stick-slip. This fluid was still active as deformation evolved to focus on D3 structures which marked the culmination of gold mineralisation. It is probable that the final stage of this event was the late, brittle scheelite-quartz veins of Lion Hill (Q5).

Later than this, late D4 deformation was accompanied by a more saline, aqueous fluid, resulting in quartz-tourmaline precipitation and local remobilisation of mineralisation. The ambient pressure and temperature suggests waning metamorphic conditions and some uplift between the D2 and D4 events. During D4, secondary fluid inclusions were developed in Q2 and Q3 (Type 2C and Type 3B inclusions) which confirms the overprint of this deformation event on the existing mineralisation.

Lastly, the late barren Q6 veins are testament to movement of a late formational brine through brittle faults in the region.

Deformation Event	Quartz Stage	Inclusion Type	Fluid Characteristics				Trapping Conditions	
			Equivalent wt% NaCl (Aqueous Fraction)	xH_2O, xCO_2, xCH_4	Na:Ca, Na:K (weight ratio aqueous fraction)	Fluid Bulk Density (gcm^{-3})	Temperature (°C)	Pressure (Kbars)
D1	Q1	1	4.5	Aqueous	1.21, 6.68	0.79	330-360	3.0-3.5
D2	Q2	2A	3.5	0.87, 0.10, 0.30	16.7, 9.33	0.87	330-380	2.1-2.8
		2B	5.5	Aqueous		0.78		
D4		2C	16.5	Aqueous	see Type 4 below	1.05	250	2.0
D2/3	Q3	3A	3.8	0.94, 0.06, <0.001	6.95, 25.59	0.89	min. 285	min. 1.5
D4?		3B	12.3	Aqueous		1.01	est. 250	est. 2.0
D4	Q4	4	14.1	Aqueous	9.37, 8.94	1.03	250	2.0
D3?	Q5	5	<2.0	0.945, 0.04, 0.005	25.41, 6.87	0.87	265	1.0
post D4	Q6	6	9.3	Aqueous	0.54, 27.75	0.98	<200	<0.8

Table 9.3 - Summary of characteristics of hydrothermal fluids active during deformation

9.8 Exploration Significance

Important gold deposits in the Kadoma region are clearly related to structure. The key elements in the structural framework are the *Lily, Rhodesdale and Munyati shear systems. Although often poorly* mineralised themselves, second and lower order splays off these faults are often well mineralised.

From the work in the Patchway region, two major trends of lower order structures are identified to control major gold deposits. In order of importance these are 020/35W and 070/60N. Air photo study around Patchway highlights these trends as suitable exploration targets (Figure 9.6). Interestingly the strong ENE-WSW lineament lying south of Patchway which follows one of the Umsweswe river tributaries, forms a clear structural boundary as shown by the different lineament trends south of the river. The area south of the lineament is dominated by structures which also cross-cut the tonalite, which are not known to host gold deposits.

On a regional scale the Golden Valley-Patchway, Dalny and Cam & Motor deposits all relate to probable splays from the main Lily and extrapolated Rhodesdale Boundary faults (Figure 9.6), all occurring within 5km of the main structure. At Cam & Motor, a strong magnetic lineament joins the deposit to the Rhodesdale structure northward extrapolation, which is interpreted as a probable second-order splay from the main structure.

If the distribution of the late tonalite intrusions and trend of major fold axes is noted, then a distinct swing from generally N-S orientation to NNE-SSE orientation occurs from south to north across the region. The splay structures mimic this swing (Figures 5.5 and 9.6). Since much of the motion on both the Lily and Munyati-Rhodesdale shear systems is interpreted as having a dextral shear component, the NNE splay structures probably represent more favourable dilational "jog" structures (Sibson 1985), where hydrothermal fluid-flow and hence mineralisation is likely to be focussed.

Selection of target areas should initially focus on the favourable structural trends, developed from the deformation model, located by a combination of air photo study, aeromagnetic interpretation and ground follow-up. Screening of any target areas where veining is located, particularly if geochemical sampling is not conclusive, could be aided by reasonably simple examination of any quartz float or outcrop material. The study at Patchway indicates the presence of significant CH_4 together with CO_2 in the gold-bearing hydrothermal fluid. The catastrophic unmixing of this fluid is linked to gold precipitation with a loss of CH_4. It therefore follows that vein material where both CH_4-bearing and CH_4-poor carbonic fluid inclusions are indicated, may be related to gold-bearing mineralisation. Preparation of a fluid inclusion wafer together with simple microthermometry would test this possibility.

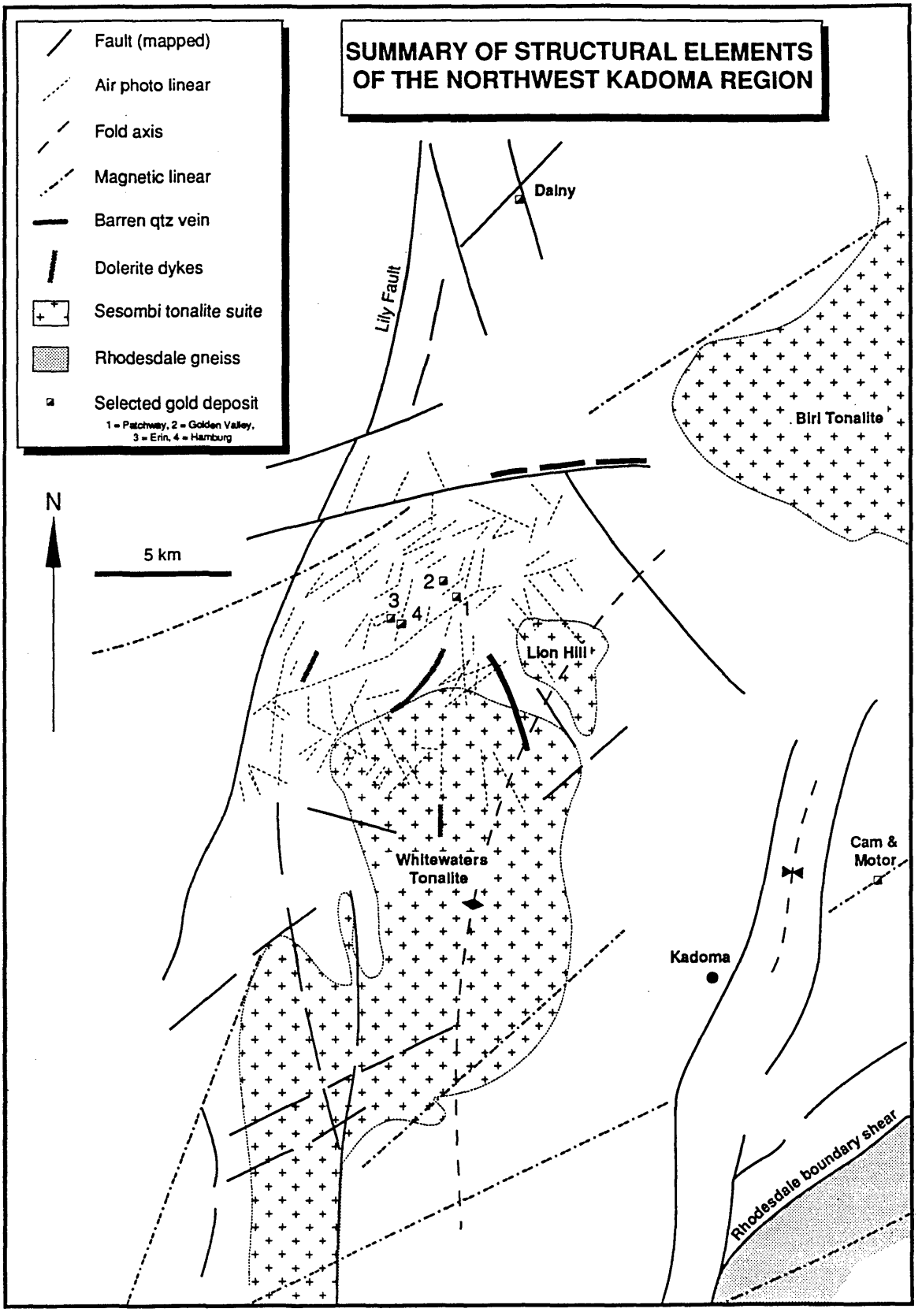


Figure 9.6- Summary of the key regional structural elements in the northwest Kadoma region (compilation from Bliss 1970, Pitfield & Campbell 1990 and this study).

More sophisticated techniques might include volatile analysis of the inclusions in such quartz to detect the gases present, together with D-ICP analysis of the solute to determine the fluid chemical fingerprint. Stable isotopic analysis of the $\delta^{18}O$ value of the quartz might be also be considered, particularly if the D-ICP data was robust enough to provide a possible fluid geothermometer. These techniques coupled with the microthermometry would permit a better prediction of the fluid type present in the quartz.

9.9 Suggestions for Future Research

The structural mapping and integration with the regional geology has established a reasonably accurate relative age constraint to mineralisation. Further structural assessment of the Kadoma region should be made by study of selected areas, particularly the boundary between the greenstone belt and the Rhodesdale Gneiss and the area around the major Cam and Motor gold deposit (> 100 tonnes Au produced). The use of remote sensing and detailed magnetic data would compliment such studies.

Absolute age determination of either stratigraphy or mineralisation was outside the scope of this project, but remains a key area for further work. High-precision (± 2 Ma) U-Pb dating of zircon as well as hydrothermal rutile, titanite and monazite is possible (Davis *et al.* 1990). The felsite intrusives and tonalites, which show variable age relationships with respect to mineralisation, in the Patchway region are highly amenable to such age-dating, and hydrothermal rutile is demonstrated in the altered vein wallrock assemblage. A programme of U-Pb age-dating is thus proposed to further constrain the mineralisation event.

The stable isotope geochemistry has highlighted the benefit of interpreting derived ratios in light of independent mineral and fluid geothermometry together with calculated fluid component fugacities. It is suggested that the apparent variability in isotopic ratios demonstrated in many published studies, in similar deposits, could well be due to the lack of understanding of hydrothermal fluid conditions at different times in the paragenetic sequence. Further research into the linking of stable isotope and detailed fluid inclusion study in complex vein systems is suggested. Such a study should also examine the stable isotopic characteristics of the fluid components of the inclusion fluids in the minerals studied.

This study has suggested that the role of colloids in mesothermal vein systems is a neglected aspect to petrogenetic modelling. Most published studies of fluid-mineral equilibria ignore the surface chemistry effects of mineral species which may be extremely important in some hydrothermal systems. The ability of amorphous silica colloids to protect gold as a suspended sol is demonstrated in the historical literature (Frondel 1938) but is largely neglected in more modern treatises (e.g. Seward 1990). In complex hydrothermal regimes, particularly those where ore-minerals are precipitated in concentration, massive fluctuations in physico-chemical conditions result in super-saturated, near critical fluids. In such conditions, fluid-mineral equilibrium is less likely, and surface chemical effects may be very important.

In the field of mesothermal quartz vein mineralisation, experimental modelling of complex C-O-H-S-Salts-Silica fluids under geological conditions is proposed. Simulation of the proposed mode of fluid pressure cycling under laboratory conditions would allow the examination of the products of such systems. Artificially created fluid inclusions would hopefully provide clues to the fluid behaviour during such events. Furthermore the validity of the concept of a "silica gel" precursor to vein quartz could also be assessed, and the role of such a gel on the behaviour of gold transport could be tested.

REFERENCES

ABRAJANO T.A., STURCHIO N.C., BOHLKE J.K., LYAN G.L., POREDA R.J. & STEVENS C.M., 1988, Methane hydrogen gas seeps, Tambales Ophiolite, Philippines : Deep or shallow origin?: Chem. Geology 71 pp 211-222.

AFFIFI, A.M & ESSENE, E.J., 1988, MINFILE: a microcomputer program for storage and manipulation of chemical data of minerals: Amer. Mineral., 73, 446-448.

AGRICOLA G., 1546, De Ortu et Causis Subterraneorum: Froben, Basel.

ALDERTON, D.H.M. & SHEPPARD, S.M.F., 1977, Chemistry and origin of thermal waters from sothwest England: Trans. Instn. Min. Metall. (Sect. B: Appl. earth sci.), 86, B191-194.

ALLISON, I. & KERRICH, R., 1980, History of deformation and fluid transport in shear zones at Yellowknife: in MORTON, R.D. (ed.), Proceedings of Gold Workshop, Yellowknife, Northwest Territories, 201-222.

ALLMAN-WARD, P., HALLS, C., RANKIN, A.H. & BRISTOW, C.M., 1982, An intrusive hydrothermal breccia body at Wheal Remfry in the western part of the St. Austell granite pluton, Cornwall: *in* EVANS, A.M. (ed.), Metallization associated with acid magmatism, Wiley, 1-28.

AMBRASEYS, N.N., 1969, Maximum intensity of ground movements caused by faulting: Proc. 4th World Conf. Earthquake Eng., 1, 154-171.

ANHAEUSSER, C.R., 1976, The nature and distribution of Archaean gold mineralisation in southern Africa: Minerals Sci. Eng., v.3, 46-84.

ATKINSON, B.K., 1982, Subcritical crack propagation in rocks: theory, experimental results and applications: J. Struct. Geol., 4, 41-56.

BARLEY, M. E & GROVES, D.I., 1987, Hydrothermal alteration of Archaean supracrustal sequences in the central Norseman-Wiluna belt, Western Australia: a review: in HO, S.E. & GROVES, D.I. (eds.), Recent advances in understanding Precambrian gold deposits, Vol. 1, Univ. West. Australia Publ., 11, 51-66.

BARLEY, M.E., DUNLOP. J.S.R., GLOVER, J.E. & GROVES, D.I., 1979, Sedimentary evidence for an Archaean shallow-water volcanic-sedimentary facies, eastern Pilbara block, Western Australia. Earth Plan. Sci. Letts. 43, 74-84.

BARLEY, M.E., EISENLOHR, B.N., GROVES, D.I., PERRING, C.S. & VEARNCOMBE, J.R., 1989. Late Archaean convergent margin tectonics and gold mineralisation : A new look at the Norseman-Wiluna belt, Western Australia. Geology, 17, 826-829.

BARTON, P.B. & SKINNER, B.J., 1967, Sulfide mineral stabilities: *in* BARNES, H.L. (ed.), Geochemistry of Hydrothermal Ore Deposits, Holt-Rinehart & Winston, New York, 236-333.

BARTON, J.M. Jr. & KEY, R.M., 1981, The tectonic development of the Limpopo mobile belt and the evolution of the Archaean cratons of southern Africa: *in* KRONER, A. (ed.), Precambrian Plate Tectonics, Elsevier, Amsterdam, 185-212.

BELL, T.H. & ETHERIDGE, M.A., 1973, Microstructures of mylonites and their descriptive terminology: Lithos, v.6, 337-348.

BELLAMY, R., 1975, Unpubl. Rept.

BERTHÉ, D., CHOUKROUNE, P. & JEGOUZO, P., 1979, Orthogneiss mylonite, and co-axial deformation of granites: the example of the South Armorican Shear Zone: J. Struct. Geol., 1, 31-42.

BISCHOFF, J.L & DICKSON, F.W., 1975, Seawater-basalt interaction at 200°C and 500 bars: implications for origin of sea-floor heavy-metal deposits and regulation of seawater chemistry: Earth Planet. Sci. Lett., 25, 385-397.

BISCHOFF, J.L., RADTKE, A.S. & ROSENBAUER, R.J., 1981, Hydrothermal alteration of graywackes by brine and seawater: roles of alteration and chloride complexing on metal solubilisation at 200°C and 350°C: Econ. Geol., 76, 659-676.

BJORNERUD, M., 1989, Toward a unified conceptual framework for shear-sense indicators: J. Struct. Geol., 11, no.8, 1045-1049.

BLISS N.W., 1970, The geology of the country around Gatooma, Rhodesia: Rhod. Geol. Surv. Bull. No. 64.

BÖHLKE, J.K., 1989, Comparison of metasomatic reactions between a common CO2-rich vein fluid and diverse wallrocks: Intensive variables, mass transfers, and Au mineralization at Alleghany, California: Econ. Geol., 84, 291-327.

BOIRON, M.C., CATHELINEAU, M., DUBESSY, J., KIBONZI, B., TOLLON, F. & NORMAND, M., 1989, Terra Abstracts, 1, 28.

BORISENKO, A.S., 1977, Study of the salt composition of solutions in gas-liquid inclusions in minerals by the cryometric method: Soviet Geol. & Geophys., 18, 11-19.

BOTTINGA, Y., 1968, Calculation of fractionation factors for carbon and oxygen exchange in the system calcite-carbon dioxide-water: J. Chem. Phys., 72, 800-808.

BOTTRELL, S.H., BRAND, N. & MILLER, M.F., 1989, Analytical evidence for sulphur species as gold ligands in metamorphic fluids: in ECROFI X, Program with Abstr., 10, London 1989, p.15.

BOTTRELL S.H., SHEPHERD T.J., YARDLEY B.W.P. & DUBESSY J., 1988. A fluid inclusion model for the genesis of the ores of the Dolgellau gold belt, North Wales. : J. Geol. Soc. London 145 pp 139-145.

BOWERS, T.S. & HELGESON, H.C., 1983a Calculation of the thermodynamic and geochemical consequences of non-ideal mixing in the system H2O-CO2-NaCl on phase relations in geological systems : equation of state for H2O-CO2-NaCl fluids at high pressures and temperatures. Geochim. Cosmochim. Acta, 47, 1247-1275.

BOWERS, T.S. & HELGESON, H.C., 1983b Calculations of the thermodynamic and geochemical consequences of non-ideal mixing in the system H2O-CO2-NaCl on phase relations in geologic systems ; metamorphic equilibria at high pressures and temperatures: Am. Mineral., 68, 1059-1075.

BOWERS, T.S., JACKSON, K.J. and HELGESON, H.C., 1984, Equilibrium activity diagrams for coexisting minerals and aqueous solutions at pressures and temperatures to 5 kb and 600°C : Springer Verlag, New York, 397p.

BOYER, S.E. & ELLIOTT, D., 1982, Thrust systems: Bull. Amer. Ass. Petrol. Geol., 66, 1196-1230.

BOYLE, R.W., 1961, The geology, chemistry and origin of the gold deposits of the Yellowknife district: Geol. Surv. Can. Mem. 310.

BOYLE, R.W., 1979, The geochemistry of gold and its deposits: Geol. Surv. Can. Bull. 280, 584p.

BROWN, K.L., 1989, Kinetics of gold precipitation from experimental hydrothermal sulphide solutions: Econ. Geol. Mon., 6, 320-327.

BROWN, P.E., 1989, FLINCOR: A fluid inclusion data reduction and exploration program (abstr.): Second Biennial PACROFI Prog. with Abstr., 14.

BROWN, P.E. & LAMB, W.M., 1989, P-V-T properties of fluids in the system H2O-CO2-NaCl: New graphical presentations and implications for fluid inclusion studies: Geochim. Cosmochim. Acta, 53.

BROWN, T.H., BERMAN, R.G. & PERKINS, E.H., 1988, GEO-CALC: Software package for calculation and display of pressure-temperature-composition phase diagrams using an IBM or compatible personal computer. Computers & Geosciences, v. 14, no. 3, pp 279-289.

BROWN, T.H., BERMAN, R.G. & PERKINS, E.H., 1989, PTA-SYSTEM: A GeO-Calc software for calculation and display of pressure-temperature-activity phase diagrams. Amer. Min., v. 74, pp 485-487.

BYERLEE, J.D., 1978, Friction of rocks: Pure Appl. Geophys., 116, 615-626.

BRYNDZIA, L.T. & SCOTT, S.D., 1987, The composition of chlorite as a function of sulphur and oxygen fugacity: An experimental study:

BURNHAM, C.W., HOLLOWAY, J.R. & DAVIS, N.F., Thermodynamic properties of water to 1000°C and 10,000 bars: Geol. Soc. Am. Spec. Paper 132.

BURROWS, D.R. & SPOONER, E.T.C., 1984, Low-$\delta^{13}C$ carbonate alteration associated with magmatically derived MoS_2 mineralization within a post-tectonic Archaean granodiorite/tonalite intrusion, Mink Lake, N.W. Ontario: *in* GAC-MAC Program with Abstracts, 9, 50.

BURROWS, D.R. & SPOONER, E.T.C., 1986, The McIntyre Cu-Au deposit, Timmins, Ontario, Canada. In: MACDONALD, A.J. (ed.) Proceedings of Gold '86, an International Symposium on the geology of gold. Konsult International Inc., Toronto, 23-39.

BURROWS, D.R. & SPOONER, E.T.C., 1988, Generation of a magmatic H_2O-CO_2 fluid enriched in Mo, Au and W within an Archaean sodic granodiorite stock, Mink Lake, northwestern Ontario: Econ. Geol. 82, 1931-1957.

BURROWS, D.R., WOOD, P.C. & SPOONER, E.T.C, 1986, Carbon isotope evidence for a magmatic origin for Archaean gold-quartz vein ore deposits: Nature, 321, 851-854.

BURNHAM, W., HOLLOWAY, J.R. & DAVIS, N. F., 1969, Properties of water to 1000°C and 10,000 bars: Geol. Soc. Am. Spec. Pap. 132.

CAMERON, E.M., 1989, Derivation of gold by oxidative metamorphism of a deep ductile shear zone : Part 1, Conceptual model. J. Geochem. Expl., 31, 135-147.

CAMERON, E.M. & HATTORI, K., 1987, Archaean gold mineralisation and oxidised hydrothermal fluids. Econ. Geol., 82, 1177-1191.

CARR, R.M. & FYFE, W.S., 1958, Some observations on the crystallisation of amorphous silica: Amer. Mineral., 43, 908-916.

CARTER, A.C. & FOSTER, R.P, 1990, Tectonic, thermal and chemical evolution of a late Archaean auriferous shear zone, Dalny mine, Zimbabwe: GAC-MAC Annual Meeting, Program with Abstr., A22.

CASEY, M., 1980, The mechanics of shear in isotropic dilatant materials: J. Struct. Geol., 2, 143-147.

CATHELINEAU C., 1988 Cation site occupancy in chlorites and illites as a function of temperature: Clay Minerals 23, 471-485.

CHACE, F.M., 1949, Origin of the Bendigo saddle reefs with comments on the formation of ribbon quartz: Econ. Geol., 44, 561-597.

CHAPPELL, B.W. & WHITE, A.J.R., 1974, Two contrasting granite types: Pacific Geology, 8, 173-174.

CLAYTON, R.N. & MAYEDA, T.K., 1963, The use of bromine penta-fluoride in the extraction of oxygen from oxides and silicates for isotopic analysis: Geochim. Cosmochim. Acta, 27, 43-52.

CLARK, L.A., 1960, The Fe-As-S system: Phase relations and applications. Econ. Geol., 55, 1345-1381.

CLYNNE, M.A. & POTTER, R.W.II, Freezing point depression of synthetic brines: Geol. Soc. Am. Abs. with Programs, 9, 930.

COLLINS, P.L.F., 1979, Gas hydrates in CO2-bearing fluid inclusions and the use of freezing data for the estimation of salinity. Econ. Geol., 74, 1435-1444.

COLLINS, W.J, BEARNS, S.D., WHITE, A.J.R. & CHAPPELL, B.W., 1982, Nature and origin of A-type granites with particular reference to southeastern Australia: Contr. Miner. Petrol., 10, 189-200.

COLVINE A.C, ANDREWS A.J., CHERRY M.E., DUROCHER M.E., FYON A.J., LAVIGNE M.J., MACDONALD A.J., MARMONT S., POULSEN K.H., SPRINGER J.S. & TROOP D.G., 1984, An integrated model for the origin of Archean lode gold deposits. : Ont. Geol. Surv. Open File Rep. No. 5524 98pp.

COLVINE, A.C., FYON, J.A., HEATHER, K.B., MARMONT, S., SMITH, P.M. & TROOP, D.G., 1988, Archaean Lode Gold Deposits in Ontario. Mines and Minerals division, Ontario Geological Survey, Misc. Paper 139, 136pp.

CONDIE, K.C., 1981, Archaean Greenstone Belts. Elsevier, Amsterdam, Netherlands, 434pp.

CONDIE, K.C. & HARRISON, N.M., 1976, Geochemistry of the Archaean Bulawayan Group, Midlands greenstone belt, Rhodesia. Precamb. Res., 3, 253-271.

COWARD, M.P., 1976, Archaean deformation patterens in South Africa. Phil. Trans. R. Soc. Lond., A283, 313-331.

COWARD, M.P., 1980, Shear zones in the Precambrian crust of southern Africa. J. Struct. Geol., 2, 19-27.

COWARD, M.P. & DALY, M.C., 1984, Crustal lineaments and shear zones in Africa : their relationship to plate movements. Precamb. Res., 24, 27-45.

COWARD, M.P. & FAIRHEAD, D., 1980, Gravity and structural evidence for the deep structure of the Limpopo belt, southern Africa: Tectonophysics, 68, 31-43.

COWARD, M.P., JAMES, P.R. & WRIGHT, L.I., 1976, The movement pattern across the northern margin of the Limpopo mobile belt, southern Africa. Bull. Geol. Soc. Am., 87, 601-611.

COX, S.F., 1987, Antitaxial crack-seal microstructures and their relationship to displacement paths. J. Struct. Geol., 9, 779-787.

COX, S.F. & ETHERIDGE, M.A, 1983, Crack-seal fibre growth mechanisms and their significance in the development of oriented layer silicate microstructures. Tectonophysics, 92,147-170.

COX, S.F., ETHERIDGE M.A., WALL V.J. & POTTER T.F, 1985, Hydrofracture dilatancy and the development of quartz vein arrays in the Wattle Gully Fault Zone, Victoria : (abstract). J.Struct.Geol.7,491.

CRAIG, J.R. & SCOTT, S.D, 1976, Sulfide phase equilibria: in RIBBE, P.H. (ed.), Sulfide Mineralogy, Rev. in Mineral., 1, Min. Soc. Amer., CS1-CS110.

CRERAR, D.A. & BARNES, H.L., 1976, Ore solution chemistry; V, Solubilities of chalcopyrite and chalcocite assemblages in hydrothermal solution at 200°C to 350°C. Econ. Geol. Vol. 71, pp772-794.

CRAWFORD, M.L., 1981, Fluid inclusions in metamorphic rocks - low and medium grade: in HOLLISTER, L.S. & CRAWFORD, M.L. (eds.), Fluid Inclusions: Applications to Petrology, Mineral. Assoc. Canada Short Course Handbook, 6, 157-181.

CURTI, E., 1987, Lead and oxygen isotope evidence for the origin of the Monte Rosa gold lode deposits (Western Alps, Italy): a comparison with Archaean lode deposits: Econ. Geol., 87, 2115-2140.

DAVIS, D.W, CORFU, F., JEMIELITA, R.A., KROGH, T.E & WONG, L., 1990, Contrasting age relationships between Archaean lode gold development in the Superior Province, 8th IAGOD Symposium, Prog. Abstr., A36.

DEER, W.A., HOWIE, R.A. & ZUSSMAN, J, 1966, An introduction to the rock-forming minerals. Longman, London.

DIETRICH, D. & GRANT, P.R,, 1985, Cathodoluminescence petrography of syntectonic quartz fibres. J.Struct. Geol., 7, 541-553.

DODSON, M.H., COMPSTON, W., WILLIAMS, I.S. & WILSON, J.F, 1988. A search for ancient detrital zircons in Zimbabwean sediments. Jour. geol. Soc. Lon., 145, 97-983.

DRUMMOND S.E. & OHMOTO H., 1985 Chemical evolution and mineral deposition in boiling hydrothermal systems: Econ. Geol., 80, 126-147.

DUBESSY, J., 1984, Simulation des equilibres chimiques dans le systéme C-O-H. Consequences methodologiques pour les inclusions fluides: Bull. Mineral., 107, 155-168.

DUBESSY, J., POTY, B. & RAMBOZ, C., 1989, Advances in C-O-H-N-S fluid geochemistry based on micro-Raman spectrometric analysis of fluid inclusions: J. Eur. Mineral.

DURNEY, D.W. & RAMSAY, J.G., 1973, Incremental strains measured by syntectonic crystal growths: *in* Gravity and Tectonics, John Wiley, New York, 67-96.

EDMUNDS, W.M. et al, 1984, The evolution of saline and thermal groundwaters of the Carnmenellis granite: Mineralog. Mag., 48, 407-424.

EISENLOHR, B.N., GROVES, D. & PARTINGTON, G.A, 1989. Crustal-scale shear zones and their significance to Archaean gold mineralisation in Western Australia. Mineral. Deposita., 24,1-8.

ETHERIDGE, M.A., 1983, Differential stress magnitudes during regional deformation and metamorphism: upper boundary imposed by tensile fracturing: Geology, 1, 231-234.

ETHERIDGE, M.A., WALL, V.J. & VERNON, R.H., 1983, The role of the fluid phase during regional metamorphism and deformation: J. Metamorph. Geol., 1, 205-226.

ETHERIDGE, M.A., WALL, V.J. & COX, S.F, 1984, High fluid pressures during regional metamorphism and deformation. Jour. Geophys. Res., 89B, 4344-4358.

EUGSTER, H.P. & SKIPPEN, G.B., 1967, Igneous and metamorphic equilibria involving gas equilibria: in ABELSON, P.H. (ed.), Researches in Geochemistry, vol.2, J. Wiley, New York, 492-520.

FARMER, C.B. & HERRINGTON, R.J., 1989, Cathodoluminescence studies related to fluid pathways in hydrothermal quartz veins: BSRG Workshop Meeting Abstracts Volume, Manchester University, p25.

FARMIN, R., 1941, Host-rock inflation by veins and dikes at Grass Valley, California: Econ. Geol., 38, 143-174.

FERGUSON, H.G. & GANNETT, R.W., 1932, Gold quartz veins of the Alleghany district, California: U.S. Geol. Surv. No. 172, 139p.

FERGUSON, S.A., AND ASSOCIATED GEOLOGISTS, 1968, Geology and ore deposits of the Tisdale Township: Ont. Dep. Mines, Geol. Rept., 58, 177p.

FLEET, M.E., MACLEAN, P.J. & BARBIER, J., 1989, Oscillatory-zoned As-bearing pyrite from strata-bound and stratiform gold deposits: An indicator of ore fluid evolution: Econ. Geol. Monograph 6, 356-362.

FOSTER, R.P., 1977, Solubility of scheelite in hydrothermal chloride solutions: Chem. Geology, v.20, 27-43.

FOSTER, R.P, 1979, The genesis of Archaean gold deposits - Golden Valley Mine. 10th A. Rep., Inst. Min. Res. Rep. Univ. Rhodesia, Salisbury, 24-27.

FOSTER, R.P., 1982, *in* VIEWING, K.A., Institute of Mining Research, 13th Annual Report, no.42, Univ. Zimbabwe.

FOSTER, R.P., 1983, Project 152, *in* VIEWING, K.A., Institute of Mining Research, 14th Annual Report, no. 46, Univ. Zimbabwe, 38.

FOSTER, R.P, 1985, Major controls of Archaean gold mineralisation in Zimbabwe. Trans. geol. Soc. S.Afr., 5, 25-38.

FOSTER, R.P., 1989, Archaean gold mineralisation in Zimbabwe: Implications for metallogenesis and exploration: Econ. Geol. Monograph No.6, 54-70

FOSTER, R.P., MANN, A.G., MILLER, R.G. & SMITH, P.J.R., 1979 Genesis of Archaean gold mineralisation with reference to three deposits in the Gatooma area, Rhodesia. : Spec.Publ. Geol. S. Afr. 5 pp25-38.

FOSTER, R.P., FURBER, F.M.W., GILLIGAN, J.H. & GREEN, D., 1986a, Shamva gold mine, Zimbabwe: A product of calc-alkaline linked exhalative, volcaniclastic and epiclastic sedimentation in the late Archaean: Geol. Assoc. Canada Spec. Paper 21, 41-66.

FOSTER, R.P., MANN, A.G., STOWE, C.W. & WILSON, J.F, 1986b, Archaean gold mineralisation in Zimbabwe: *in* ANHAEUSSER, C.R. & MASKE, S. (eds.). Mineral Deposits of Southern Africa, Johannesburg, Geol. Soc. S. Afr., Vol. 1, 43-112.

FOSTER R.P. & WILSON J.F., 1979, Geological setting of Archaean deposits in Zimbabwe. : IN: Gold 82,Geol.Soc.Zim.Spec.Rep.No.1 pp521-551.

FOSTER, R.P. & WILSON, J.F, 1984, Geological setting of Archaean gold deposits in Zimbabwe: *in* FOSTER, R.P. (ed.) Gold'82: Geology, geochemistgry and genesis of gold deposits. A.A. Balkema, Rotterdam, 521-551.

FOUILLAC, C., & MICHARD, G., 1981, Sodium/lithium ratio in water applied to the geochemistry of geothermal groundwaters: Geothermics, 10, 55-70

FOURNIER, R.O., 1981, Application of water geochemistry to geothermal exploration and reservoir engineering: *in* RYBACH, L. & MUFFLER, L.J.P. (eds.) Geothermal systems: principles and case histories. Wliey, Chichester, 109-143.

FOURNIER, R.O., 1985, The behaviour of silica in hydrothermal solutions: *in* BERGER, B.R. & BETHKE, P.M. eds., Reviews in Economic Geology Volume 2, Geology and Geochemistry of Epithermal Systems, 45-62.

FOURNIER, R.O. & POTTER, R.W., II, 1982, An equation correlating the solubility of quartz in water from 25° to 900°C at pressures up to 10,000 bars: Geochimica et Cosmochimica Acta, v.46, 1969-1973.

FOURNIER, R.O & TRUESDELL, A.H., 1973, An empirical Na-K-Ca geothermometer for natural waters: Geochim. Cosmochim. Acta., 37, 1255-1275.

FRANKLIN, J.M., ROSCOE, S.M., LOVERIDGE, W.D. & SANGSTER, D.L., 1983, Lead isotope studies in the Superior and Southern provinces: Geol. Surv. Canada Bull., 351, 60.

FRIPP, R.E.P., 1976, Stratabound mineral deposits in Archaean banded-iron formation, Rhodesia: Econ. Geol., 71, 58-78.

FRIPP, R.E.P., 1982, The Precambrian geology of the area around the Sand River, near Messina, N. Transvaal: Unpubl. PhD Thesis, Univ. Wits., Johannesburg, 251p.

FRONDEL, C., 1938, Stability of colloidal gold under hydrothermal conditions: Econ. Geol., 33, 1-20.

FUCHTER, W.A.H. & HODGSON, C.J, 1986, Gold deposits in the North-Western Mining Camp, Gwanda greenstone belt. In: MACDONALD, A.J. (ed.) Proceedings of Gold'86, an international Symposium on tthe Geology of Gold, Konsult International Inc., Toronto, 255-269.

FYFE, W.S., PRICE, N.J. & THOMPSON, A.B., 1978, Fluids in the earth's crust: Elsevier, Amsterdam, 383p.

FYFE, W.S. & KERRICH, R., 1984, Gold: Natural concentration processes: in FOSTER, R.P., (ed.), Gold '82, The geology, geochemistry and genesis of gold deposits, Geol. Soc. Zim. Spec. Publ. No.1, 99-128.

FYFE, W.S. & KERRICH, R., 1985, Fluids and thrusting: Chem. Geol., 49, 353-362.

FYON, J.A., 1986, Field and stable isotope characteristics of carbonate alteration zones, Timmins area: Unpubl. PhD Thesis, McMaster Univ., Hamilton, Canada, 399p.

FYON, J.A. & CROCKETT, J.H., 1981, Volcanic environment of carbonate alteration and stratiform gold mineralisation, Timmins area, Ontario: Ont. Geol. Surv. Misc. Pap. 97, 47-58.

FYON, J.A., CROCKET, J.C. & SCHWARCZ, H.P, 1983, Application of stable isotope studies to gold metallogeny in the Timmins-Porcupine camp. Ontario Geol.Surv., Open file report, 5464.

GALLAGHER, V., 1987, Tourmaline-bearing rocks and granite related to metallogenesis in S.E. Ireland: Unpubl. PhD Thesis, Nat. Univ. of Ireland.

GAMOND, J.F., 1983, Displacement fractures associated with fault zones; a comparison between observed examples and experimental models: J. Struct. Geol., 5, 33-45.

GEE, R.D, 1979, Structure and tectonic style of the Western Australian Shield: Tectonophysics, 58, 327-369.

GEHRIG, M., LENTZ, H. & FRANCK, E.U, 1979, Thermodynamic properties of water-carbon dioxide-sodium chloride mixtures at high temperatures and pressures. In: TIMMERHAUS, K.D. & BARBER, M.S. (eds.) International conference on high pressure science and technology (6th, 1977, Univ. of Colorado): Vol. 1, Physical properties and material synthesis. Plenum Press, New York, 539-542.

GEHRIG, M., LENTZ, H., FRANCK, E.U., 1986, Ber. Bunsen-Ges. Phys. Chem. 90, 525-533.

GILLIGAN, J.M. & FOSTER, R.P., 1987, Gold mineralisation in iron-formation: The importance of contrasting modes of deformation at the Lennox mine, Zimbabwe: in African Mining: London, Inst. Mining Metall., 127-138.

GIGGENBACH, W.F., 1982, Carbon 13 exchange between CO_2 and CH_4 under geothermal conditions: Geochim. Cosmochim. Acta, 46, 159-165.

GIGGENBACH, W.F., 1987, Redox processes governing the chemistry of fumarolic gas discharges from White Island, New Zealand: Appl. Geochem., 2, 193-201.

GIGGENBACH, W.F., 1988, Geothermal solute equilibria. Derivation of Na-K-Mg-Ca geoindicators. Geochim. Cosmochim. Acta, 52, 2749-2765.

GOLD, T., 1987, Power from the Earth: Deep Earth Gas-Energy for the Future: Dent., London.

GOLD, T. & SOTER, S., 1985, Fluid ascent through the solid lithosphere and its relation to earthquakes: Pure & Appl. Geophys. 122,

GOLDING, S.D., GROVES, D.I., MCNAUGHTON, N.J., BARLEY, M.E. & ROCK, N.M.S, 1987, Carbon isotopic compositions of carbonates from contrasting alteration styles and gold deposits in supracrustal rocks of the Norseman-Wiluna, Yilgarn block, Western Australia. In: HO, S.E. & GROVES, D.J. (eds.) Recent advances in understanding Precambrian gold deposits, Vol. 1, Univ. West.Australia Publ.,11, 215-213.

GOLDING, S.D. & WILSON, A.F, 1987, Oxygen and hydrogen isotope relationships in Archaean gold deposits in the Eastern Goldfields Province, Western Australia. In: HO, S.E. & GROVES, D.I. (eds.) Recent advances in understanding Precambrian gold deposits, Vol.1, Univ.West.Australia Publ.,11, 203-214.

GOODWIN, A.M. & RIDLER, R., 1970, The Abitibi orogenic belt: in BAER, A.J. (ed.), Symposium on Basins and Geosynclines of the Canadian Shield, Geol. Surv. Canada, Paper 70-40, 1-30.

GOLYSHEV, S.I., PADALKO, N.L. & PECHENKIN, S.A., 1981, Fractionation of stable oxygen and carbon isotopes in carbonate systems: Geochem. Internat., 18, 85-99.

GRANT, J.A, 1986, The isocon diagram - A simple solution to Gresens' equation for metasomatic alteration. Econ. Geol., 81, 1976-1982.

GRANT, P.R., 1988, Crystal chemistry of cathodoluminescence in quartz, and its implications for quartz cathodoluminescence petrography: BSRG Workshop Meeting Abstracts, Manchester University, p5.

GRANT, P.R. & WHITE, S.H., 1978, Cathodoluminescence and microstructure of quartz overgrowths : *in* JOHARI, O. (ed.), Scanning Electron Microscopy, 1978/1, Chicago, 789-794.

GRESENS, R.L, 1967, Composition-volume relationships of metasomatism. Chem. Geol.,2, 47-65.

GRIGGS, D.T., 1967, Hydrolytic weakening of quartz and other silicates: Geophys. J. Roy. Astron. Soc. 14, 19-31.

GROVES, D.I. & BATT, W.D, 1984, Spatial and temporal variations of Archaean metallogenic associations in terms of evolution of granite-greenstone terrains with particular reference to the Western Australian Shield. In: KRONER, A., HANSON, G.N. & GOODWIN, K.M. (eds) Archaean Geochemistry, Springer-Verlag, Berlin.

GROVES, D.I., & FOSTER, R.P, 1990, *in* FOSTER, R.P. (ed.), Gold Metallogeny and Exploration, Blackie, London.

GROVES, D.I., PHILLIPS, G.N., HO, S.E., HENDERSON, C.A., CLARK, M.E. & WOAD, G.M., 1984, Controls on the distribution of Archaean hydrothermal gold deposits in Western Australia: in FOSTER, R.P. (ed.), Gold '82, The geology, geochemistry and genesis of gold deposits, Geol. Soc. Zim. Spec. Publ. No.1, 99-128.

GROVES, D.I., HO, S.E., MCNAUGHTON, N.J., MUELLER, A.G., PERRING, C.S., ROCK, N.M.S. & SKWARNECKI, M.S, 1988, Genetic models for Archaean lode-gold deposits in Western Australia. In: HO, S.E. & GROVES, D.I. (eds.) Recent advances in understanding Precambrian gold deposits, Vol.2, Univ.West.Australia Publ.,12, 1-22.

GROVES, D.I., PHILLIPS, G.N., HO, S.E., HOUSTON, S.M. & STANDING, C.A., 1987, Craton-scale distribution of Archaean greenstone gold deposits: Predictive capacity of the metamorphic model. Econ. Geol., 81, 2045-2058.

GROVES, D.I. & PHILLIPS, G.N, 1987, The genesis and tectonic control on Archaean gold deposits of the West Australian shield - a metamorphic replacement model. Ore Geology Reviews, 2, 287-322.

GROVES, D.I., PHILLIPS, G.N., HO, S.E., HOUSTON, S.M. & STANDING, C.A, 1987, Craton-scale distribution of Archaean greenstone gold deposits: predictive capacity of the metamorphic model: Econ. Geol., 82, 2045-2058.

GUENTHER, M.A., 1989, V-X Projection of the pseudobinary H2O-CO2-(6wt%)NaCl system. (A practical method avoiding visual degree of fill estimation): Unpublished paper, Dept. of Geol., Tech. Univ. Braunschweig, Germany.

GUHA, J., ARCHAMBAULT, G. & LEROY, J., 1983, A correlation between the evolution of mineralisation, fluids and the geomechanical development of a shear zone, as illustrated by the Henderson 2 mine, Quebec: Econ. Geol., 78, 1605-1618.

GUNNING, H.C. & AMBROSE, J.W., 1937, Cadillac-Malartic area, Quebec: Can. Inst. Min. Metall. Trans., v.40, 341-362.

HAAS, J.L, 1978, An empirical equation with tables of smoothed solubilities of methane in water and aqueous sodium chloride solutions up to 25 weight percent, 360°C and 138 MPa: U.S.G.S. Open File Report No. 78-1004.

HALLBERG, J.A., 1985, The geology and mineral deposits of the Leonora-Laverton area, northeast Yilgarn Block, Western Australia, Hesperian Press, Perth, 140p.

HALL, D.L & BODNAR, R.J., 1990, Methane in fluid inclusions from granulites: A product of hydrogen diffusion?: Geochim. Cosmochim. Acta, 54, 641-651

HALL, D.L., STERNER, S.M. & BODNAR, R.J., 1988, Freezing point depression of NaCl-KCl-H_2O solutions: Econ. Geol., 83, 197-202.

HALLS, C. 1987, A mechanistic approach to the paragenetic interpretation of mineral lodes in Cornwall: Proc. Ussher Soc., 6, 548-554.

HANMER, S., 1986, Asymmetrical pull-aparts and foliation fish as kinematic indicators: J. Struct. Geol., 8, 111-122.

HARRIS, L.B., 1987, A tectonic framework for the Western Australian Shield and its significance to gold mineralisation: a personal view: in HO, S.E. & GROVES, D.J. (eds.) Recent advances in understanding Precambrian gold deposits, Vol. 1, Univ. West. Australia Publ., 11, 1-28.

HARRISON, N.M, 1970, The geology of the country around Que Que. Bull.Geol.Surv.Rhod., 65, 125.

HATTORI, K., 1987, Magnetic felsic intrusions associated with Canadian Archaean gold deposits: Geology, 15, 1107-1111.

HAWKESWORTH C.J. & BICKLE M.J., 1976, Rhodesian Rb-Sr geochronology from 3.6 to 2.0 b.a. a brief review. : 20th A. Rep. res. Inst. Afr. Geol. Univ. Leeds.

HAWKESWORTH, C.J., BICKLE, M.J., GLEDHILL, A.R., WILSON, J.F. & ORPEN, J.L, 1977, A 2.9 b.y. event in the Rhodesian Archaean: Earth Planet. Sci. Lett., 43, 285-297.

HAWKESWORTH, C.J., MOORBATH, S., O'NIONS, R.K. & WILSON, J.F, 1975, Age relationships between greenstone belts and 'granites' in the Rhodesian Archaean craton. Earth Plan.Sci.Letts., 25, 251-262.

HELGESON, H.C., 1969, Thermodynamics of hydrothermal systems at elevated temperatures and pressures. Am.J.Sci., 267, 729- 804.

HELGESON, H.C., KIRKHAM, D.H. & FLOWERS, G.C., 1981, Theoretical prediction of the thermodynamic behaviour of aqueous electrolytes at high pressures and temperatures: IV. Calculation of activity coefficients, osmotic coefficients and apparent molal and standard and relative partial molal properties to 600°C and 5 kb. Amer. J. Sci., v. 281, 1249-1516.

HENLEY, R.W., 1973, Solubility of gold in hydrothermal chloride solutions: Chem. Geol., 11, 73-87.

HENLEY, R.W., 1984, Metals in hydrothermal systems: in ROBERTSON, J.M. (ed.), Reviews in Economic Geology Vol.1, Fluid Mineral Equilibria in Hydrothermal Systems, 115-127

HENLEY, R.W. & BROWN, K.L., 1985, A practical guide to the thermodynamics of geothermal fluids and hydrothermal ore deposits: in BERGER, B.R. & BETHKE, P.M. (eds.), Reviews in Economic Geology Vol.2, Geology and Geochemistry of Epithermal Systems, 25-44.

HENLEY, R.W., TRUESDELL, A.H., BARTON, P.B. Jr. & WHITNEY, J.A., 1984, Fluid Mineral Equilibria in Hydrothermal Systems: Rev. in Econ. Geol. vol.1, 267p.

HEYEN, G., RAMBOZ, C. & DUBESSY, A., 1982, Simulation des équilibres de phases dans le systéme CO_2-CH_4 en dessous de 50°C et de 100 bar. Application aux inclusions fluides: C. R. Acad. Sci. Paris, 294, 203-206.

HICKMAN, M.H., 1974, Geochronological study of the Rhodesian Craton and the Limpopo Belt: Univ. Leeds Res. Inst. Afr. Geol. Ann. Rep., 18, 61-62.

HICKMAN, M.H., 1978, Isotopic evidence for crustal reworking in the Rhodesian Archaean craton, southern Africa. Geology, 6, 214-216.

HO, S., 1987. Fluid inclusions as exploration tools for Archaean gold deposits in Recent Advances in Understanding Pre-Cambrian Gold Deposits. : *in* HO, S. & GROVES, D.I. (eds.), U.W.A. Publ. No. 11 pp 239-264.

.HO, S.E, 1987, A fluid inclusion study of Archaean gold deposits in the Yilgarn Block, Western Australia: Unpubl. Ph.D Thesis, Univ. of Western Australia.

HO, S.E., GROVES, D.I. & PHILLIPS, G.N, 1985, Fluid inclusions as indicators of the nature and source of ore fluids and depositional conditions for Archaean gold deposits of the Yilgarn Block, Western Australia: Trans. Geol. Soc. S. Afr., 86, 149-158.

HODGSON, C.J., 1989, The structure of shear-hosted vein-type gold deposits: a review: Ore Geology Reviews, 4, 231-273.

HODGSON, C.J. & HAMILTON, J.V., 1989, Gold mineralisation in the Abitibi Greenstone Belt: End-stage results of Archaean collisional tectonics?: Econ. Geol. Mon., 6, 86-100.

HODGSON C.J. & MACGEEHAN, P.J., 1982, Geological characteristics of gold deposits in the Superior Province of the Canadian Shield: Canadian Inst. Min. Metall. Spec. Vol., 24, 211-229.

HOEFS, J., 1980, Stable Isotope Geochemistry: 2nd Edition, Springer Verlag, Berlin, 208p.

HOLLISTER, L.S., 1990, Enrichment of CO_2 in fluid inclusions in quartz by removal of H2O during crystal-plastic deformation: J. Struct. Geol., 12, 895-901.

HOLLOWAY, J.R., 1977, Fugacity and activity of molecular species in supercritical fluids: *in* FRASER, D.G. (ed.), Thermodynamics in Geology, D. Reidel, Dordrecht, Holland, 161-181.

HOLLOWAY, J.R., 1987, Igneous Fluids: *in* CARMICHAEL, I.S.E. & EUGSTER, H.P.(eds.) Thermodynamic modelling of geological materials: minerals, fluids and melts. Reviews in Mineralogy, 17, Min. Soc. Am., Washington, 211-233.

HOLLOWAY, J.R., 1981, Compositions and volumes of supercritical fluids in the earth's crust: in HOLLISTER, L.S. & CRAWFORD, M.L. (eds.), A short course in fluid inclusions, Min. Assoc. Canada Short Course Handbook, 6, 75-100.

HUANG, S.S., LEU, A.D., NG, H.J. & ROBINSON, D.B, 1985, Fluid Phase Equil. 19, 21-32.

HUBBERT, M.K. & RUBEY, W.W., 1959, Role of fluid pressure in the mechanics of overthrust faulting: Bull. Geol. Soc. Am., 70, 115-205.

HUBERT, C., TRUDEL, P., & GELINAS, L, 1985 Archaean wrench fault tectonics and structural evolution of the Blake River Group, Abitibi Belt, Quebec, CanJour. Earth Sci., 21, 1024-1-32.

HUBERT, P., 1986, Textures et inclusions fluides des quartz aurifères: Document BRGM no. 114, 350p.

HUGHES, C.J., 1973, Spilites, keratophyres and the igneous spectrum: Geol. Mag., 109, 513-527.

HULIN, C.D., 1929, Structural control of ore deposition: Econ. Geol., 24, 15-49.

HURST, M.E., 1935, Vein formation at Porcupine: Econ. Geol., 30, 103-127.

HUSSEIN, A.A.A., ALI, M.M. & EL RAMLY, M.F., 1982, A proposed new classification of the granites of Egypt: J. Volc. & Geotherm. Res., 14, 187-198.

HUTCHINSON, R.W., 1986, Metallogeny of Precambrian gold deposits: space and time relationships: Terra Cognita, 6, 533.

HUTCHINSON, R.W. & BURLINGTON, J.L., 1984, Some broad characteristics of greenstone belt gold lodes: *in* FOSTER, R.P. (ed.), *Gold '82, The geology, geochemistry and genesis of gold* deposits, Geol. Soc. Zimbabwe Spec. Publ. 1, A.A. Balkema, Rotterdam, 339-372.

JACOBS, G.K. & KERRICK, D.M., 1981a, Devolatilisation equilibria in H_2O-CO_2 and H_2O-CO_2-NaCl fluids; an experimental and thermodynamic evaluation at elevated pressures and temperatures: Amer. Mineral., 66, 1135-1153.

JACOBS, G.K. & KERRICK, D.M., 1981b, Methane: an equation of state with application to the ternary system H_2O-CO_2-CH_4: Geochim. Cosmochim. Acta, 45, 607-614.

JAEGER, J.G. & COOK, N.G.W., 1979, Fundamentals of Rock Mechanics: 3rd edn., Chapman & Hall, London.

JAHN, B.M. & CONDIE, K.C., 1976 On the age of Rhodesian greenstone belts. : Contrib. Mineral. Petrol. 57 pp317-330.

JAMES, P.R., 1975, A deformation study of the northern margin of the Limpopo belt, Rhodesia: Unpubl. PhD Thesis, Univ. Leeds.

JAPAN INTERNATIONAL CO-OPERATION AGENCY AND THE METAL MINING AGENCY OF JAPAN, 1987, Report on the co-operative mineral exploration in the Kadoma area. Phase 1.

JEFFERYS, H., 1952, The Earth: Camb. Univ. Press, London, 392p.

JENSEN, L.S, 1976, A new method of classifying sub-alkalic volcanic rocks. Ontario Division of Mines, Misc. Paper, 66.

JENSEN, L.S. & LANGFORD, D.R., 1985, Geology and petrogenesis of the Archaean Abitibi belt in the Kikland Lake area, Ontario: Ont. Geol. Surv. Misc. Paper, 123, 130p.

JENSEN, L.S. & PYKE, D.R., 1981, Komatiites in the Ontario portion of the Abitibi belt: *in* ARNDT, N.T. & NISBET, E.G. (eds.), Komatiites, George Allen and Unwin, London, 53-79.

JOHNSTON, W.D., 1940, The gold-quartz veins of Grass Valley, California: U.S. Geol. Surv., No. 194, 101p.

JONES, M.J, 1986, Gold deposits in Zimbabwe. Anglo American Propecting Services, Int.Rep.,28p.

KASSIDY, K.F., McNAUGHTON, N.J. & TURNER, J.V., 1988, Preliminary carbonate stable-isotope data for the Lawlers gold deposit, Western Australia: *in* HO, S.E. & GROVES, D.I. (eds) Advances in understanding Precambrian gold deposits, Vol 2. Geol. Dept. & Univ. Extension, Univ Western Australia, Publ. 12, 185-194.

KENNEDY, G.C., 1950, A portion of the system SiO_2-H_2O: Econ. Geol., 45, 629-653.

KERRICH, R., 1983, Geochemistry of gold deposits in the Abitibi greenstone belt: Canadian Inst. Min. Spec. Paper, 27.

KERRICH, R., 1986, Fluid infiltration into fault zones: chemical, isotopic and mechanical effects. Pageoph.,124, 225-268.

KERRICH, R., 1987, The stable isotope geochemistry of Au-Ag vein deposits in metamorphic rocks: in KYSER, T.K. (ed.), Stable isotope geochemistry of low-temperature fluids: Min. Assoc. Can. Short Course, 13, 287-336.

KERRICH, R., 1989a, Shear zone hosted mesothermal gold deposits; a review of geochemical evidence on the sources of fluids and solutes: in BURSNALL, J.T. (ed.), Mineralisation and shear zones, Geol. Assoc. Can. Short Course Notes, 6, 129-197.

KERRICH, R., 1989b, Geodynamic setting and hydraulic regimes: shear zone hosted mesothermal gold deposits: in BURSNALL, J.T. (ed.), Mineralisation and shear zones, Geol. Assoc. Can. Short Course Notes, 6, 89-128.

KERRICH, R. & ALLISON, I., 1978, Vein geometry and hydrostatics during Yellowknife mineralisation: Can. J. Earth. Sci., 15, 1653-1660.

KERRICH, R. & FYFE, W.S, 1981, The gold carbonate association: Source of CO2 fixation reactions in Archaean lode gold deposits, Chem. Geol., 33, 265-294.

KERRICH, R., FRYER, B.J., KING, R.W., WILLMORE, L.M. & VAN HEES, E., 1987, Crustal outgassing and LILE enrichment in major lithosphere structures, Archaean Abitibi greenstone belt: evidence on the source reservoir from strontium and carbon isotope tracers: Contrib. Mineral. Pet., 97, 156-168.

KEY, R.M. & HUTTON, S.M., 1976, The tectonic generation of the Limpopo Mobile Belt, and a definition of its western extremity: Precamb. Res., 8, 375-413.

KING, R.W, 1988, Geochemical characteristics of tourmaline from Superior Province Archaean lode gold deposits: implications for source regions and processes: in Bicentennial Gold'88, Melbourne, Ext. Abstr., Poster Vol.2 116-118.

KRADER, T. & FRANCK, E.U., 1986, Physica B+C 139-140, 66-69.

KRAMERS, J.D & FOSTER, R.P., 1984, A reappraisal of lead isotope investigations of gold deposits in Zimbabwe: in FOSTER, R.P. (ed.), Gold '82, The geology, geochemistry and genesis of gold deposits in Zimbabwe, A.A. Balkema, Rotterdam, 569-582.

KRETSCHMAR, U. & SCOTT, S.D, 1976, Phase relations involving arsenopyrite in the system Fe-As-S and their application. Canadian Mineralogist, 14, 364-386.

KRONER, A. (ed.)1981, Precambrian plate tectonics. Amsterdam, Elsevier. 791p.

KRUPKA, K.M., OHMOTO, H. & WICKMAN, F.E., 1977, A new technique in neutron activation analysis of Na/K ratios of fluid inclusions and its application to the gold-quartz veins at the O'Brien mine, Quebec, Canada: Canadian J.Earth Sci., 14, 2760-2770.

KYSER, T.K. & KERRICH, R., 1990, Geochemistry of fluids in tectonically active crustal regions: in, NESBITT, D.E. (ed.), Fluids in tectonically active regimes of the continental crust, Min. Assoc. Can., 18, 133-230.

LAMBERT, I.B., PHILLIPS, G.N. & GROVES, D.I, 1984, Sulphur isotope compositions and genesis of Archaean gold mineralisation. In: FOSTER, R.P. (ed) Gold '82. Geological Society of Zimbabwe, Special Publication 1, 372-387.

LAMEYRE, J. & BOWDEN, P., 1982, Plutonic rock type series: Discrimination of various granitoid series and related rocks: J. Volc. & Geotherm. Res., 14 (1-2), 169-186

LEDRU, P. & AUTRON, A., 1987, Relationships between fluid circulation, ore deposition, and shear zones: new evidence from the Salau scheelite deposits (French Pyrenees): Econ. Geol., 82, 224-229.

LIGHT, M.P.R, 1982, The Limpopo mobile belt: a result of continental collision. Tectonics, 1, 325-342.

LIN, Y., 1989, Comparative aspects of pegmatitic and pneumatolytic evolution in Cornish granites: Unpubl. PhD Thesis, Univ. of London.

LINDGREN, W., 1936, Amer. Inst. Min. Metall. Eng., Tech. Paper, 713, 16.

LIOU, J.G., MARUYAMA, S. & CHO, M, 1985, Phase equilibria and mineral paragenesis of metabasites in low-grade metamorphism. Min. Mag., 49, 321-333.

LISTER, G.S. & SNOKE, A.W., 1984, S-C mylonites: J. Struct. Geol., 6, 617-638.

LOVERING, T., 1923, The leaching of iron protores: solution and precipitation of silica in cold waters: Econ. Geol., 18, 523-540.

LUDDEN, J.N, DAIGNEAULT, R., ROBERT, F. & TAYLOR, R.P., 1984, Trace element mobility in alteration zones associated with Archaean Au lode deposits: Econ. Geol., 79, 1131-1141.

MACGREGOR, A.M, 1930, The geology of the country between Gatooma and Battlefields. Bull.geol. Surv. S.Rhod., 38, 79p.

MACGREGOR, A.M, 1951, Some milestones in the Precambrian of Southern Rhodesia. Geol. Soc. S.Afr. Proc., 54, 27-71.

MADDOCK, R.H., 1986, The petrology and geological significance of some fault cemented pseudotachylytes, Unpubl. PhD Thesis, Univ. London, 423p.

MARSHALL, D.J., 1988, Cathodoluminescence of geological materials, Unwin-Hyman, Boston, 146p.

MARTIN, A., 1978, The geology of the Belingwe-Shabani schist belt: Bull. Geol. Surv. Rhod., 83, 220p.

MATSUHISHA, Y., GOLDSMITH, J.R. & CLAYTON, R.N., 1979, Oxygen isotope fractionation in the system quartz-albite-anorthite-water: Geochim. Cosmochim. Acta, 42, 1131-1140.

MATTEY, D.P., 1987, Carbon isotopes in the mantle: Terra Cognita, 7, 31-37.

MAWER C.K., 1987, Mechanics of formation of gold-bearing quartz veins, Nova Scotia, Canada: Tectonophysics, 135, 99-119.

McCLAY, K, 1977, Pressure solution and Coble creep in rocks and minerals: a review: J. Geol. Soc. Lond., 134, 57-70.

McCOURT, S. & VEARNCOMBE, J.R., 1987, Crustal-scale shear zones in the Limpopo belt, southern Africa: Geol. Soc. Can., Prog. Abstr., 12.

McKINSTRY H.E. & OHLE E.L., 1949. Ribbon structure in gold quartz veins.: Econ. Geol. 44, 87-109.

McCREA, J.M., 1950, The isotopic chemistry of carbonates and a palaeotemperature scale: Jour: Chem. Phys., 18, 849-857.

MEISSNER, R., 1986, The Continental Crust. A Geophysical Approach: Academic Press, Orlando, 426p.

MITRA, G., 1978, Ductile deformation zones and mylonites; the mechanical processes involved in the deformation of crystalline basement rocks: Amer. J. Sci., 278, 1057-1084.

MOORBATH *et al.*, 1987, Early Archaean age for the Sebakwian Group at Selukwe, Rhodesia: Nature, 264, 536-538.

MOORBATH, S.M., TAYLOR, P.N., ORPEN, J.L., TRELOAR, P.J. & WILSON, J.F., 1987, First direct dating of Archaean stromatolitic limestone: Nature, 326, 865-867.

MUROWCHICK, J.B. & BARNES, H.L, 1987, Effects of temperature and degree of supersaturation on pyrite morphology. Amer. Min., 72, 1241-1250.

NADEN J. & SHEPHERD T.J., 1990. Role of methane and carbon dioxide in gold depositions: Nature, 342, 793-795.

NAYLOR, M.A., MANDL, G. & SIJPESTEIJN, C.H.K., 1986, Fault geometries in basement-induced wrench faulting under different initial stress states: J. Struct. Geol., 8/7, 737-752.

NEALL, F.B. & PHILLIPS, G.N, 1987, Fluid-wall rock interaction in an Archaean hydrothermal gold deposit: A thermodynamic model for Hunt mine, Kambalda: Econ. Geol., 82, 1679-1694.

NESBITT, B.E., MUROWCHICK, J.B. & MUEHLENBACHS, K., 1986, Dual origin of lode gold deposits in the Canadian Cordillera: Geology, 14, 506-509.

NESBITT, B.E. & MUEHLENBACHS, K., 1989, Origins and movement of fluids during deformation and metamorphism in the Canadian Cordillera: Science, 245, 733-736.

NEWTON, R.C., SMITH, J.V. & WINDLEY, B.F., 1980, Carbonic metamorphism, granulites and crustal growth: Nature, 288, 45-50.

NISBET, E.G., BICKLE, M.J. & MARTIN, A, 1977, The mafic and ultramafic lavas of the Belingwe greenstone belt. J.Petrol.,18, 521-566.

NISBET, E.G., WILSON, J.F. & BICKLE, M.J, 1981, The evolution of the Rhodesian craton and adjacent Archaean tectonic terrain: tectonic models: *in* KRONER, A. (ed) Precambrian Plate Tectonics, Elsevier, Amsterdam, 161-183.

NUTT, T.H.C., MCCOURT, S. & VEARNCOMBER, J.R, 1988, Structure of some antimony-gold deposits from the Kaapvaal and Zimbabwe cratons: *in* HO, S.E. & GROVES, D.I. (eds) Advances in understanding Precambrian gold deposits, Vol 2. Geol. Dept. & Univ. Extension, Univ Western Australia, Publ. 12, 63-80.

OBEE, H.K., 1985, Fault rock and deformation studies of a major continental fault system: Unpubl. PhD Thesis, Univ. London, 238p.

OHMOTO, H., 1972, Systematics of sulfur and carbon isotopes in hydrothermal ore deposits: Econ. Geol., 72, 551-578.

OHMOTO, H, 1986, Stable isotope geochemistry of ore deposits: *in* VALLEY, J.W., TAYLOR, H.P. & O'NEIL, J.R. Stable isotopes in high temperature geological processes. Reviews in Mineralogy, 16, Min. Soc.Am., Washington, 491-560.

OHMOTO, H. & KERRICK, D., 1977, Devolatilization equilibria in graphitic systems: Amer. J. Sci., 277, 1013-1044.

OHMOTO, H. & RYE, R.O, 1979, Isotopes of sulphur and carbon: *in* BARNES, H.L. (ed) Geochemistry of hydrothermal ore deposits. John Wiley & Sons, New York, 509-567.

O'NIONS, R.K. & OXBURGH, E.R., 1988, Helium volatile fluxes and the development of continental crust: Earth Planet. Sci. Lett., 90, 331-347.

PASTERIS, J.D., WOPENKA, B. & SEITZ, J.C., 1987, Practical aspects of quantitative laser Raman spectroscopy for the study of fluid inclusions: Geochim. Cosmochim. Acta.

PEARCE, J.A, 1982, Trace element characteristics of lavas from destructive plate boundaries: *in* THORPE, R.S. (ed) Andesites, John Wiley & Sons, New York, 525-548.

PEARCE, J.A, 1987, A users guide to basalt discrimination diagrams: Internal report, Open University, Milton Keynes, 25p.

PEARCE, J.A., HARRIS, B.W. & TINDLE, A.G, 1984, Trace element discrimination diagrams fo the tectonic interpretation of granitic rocks. Jour. Petrol. 25, 956-983.

PEARCE, J.A. & NORRY, J.N, 1979, Petrogenetic implications of Ti, Zr, Y and Nb variations in volcanic rocks. Contrib. Min. Petrol. 69, 33-47.

PEARCE, T.H., GORMAN, B.E. & BIRKETT, T.C., 1977, The relationship between major element chemistry and tectonic environment of basic and intermediate volcanic rocks: Earth Planet. Sci. Lett., 36, 121-132.

PECHER, A., LESPINASSE, M. & LEROY, J., 1985, Relations between fluid inclusion trails and regional stress field: a tool for fluid chronology - An example of an intragranitic uranium ore deposit (northwest Massif Central, France): Lithos, 18, 229-237.

PERRING, C.S., GROVES, D.I. & HO, S.E, 1987, Constraints on the source of auriferous fluids for Archaean gold deposits: *in* HO, S.E. & GROVES, D.I. (eds) Recent advances in understanding Precambrian gold deposits, Vol, 1, Univ. West. Australia Publ. 11, 189-201.

PERRING, C.S., BARLEY, M.E., BETTENAY, L.F., GOLDING, S.D., GROVES, D.I., HALLBERG, J.A., McNAUGHTON & ROCK, N.M.S., 1988, The conjunction of linear mobile belts, mantle-crustal magmatism and gold mineralization in the Archaean greenstone belts of Western Australia: Bicentennial Gold extended abstracts, oral programme, Geol. Soc. Aust., Melbourne, 296-301.

PHAUP, A.E., 1964, Gold mines of Southern Rhodesia - Introduction: *in* HAUGHTON, S.H. (ed.), The Geology of some Ore Deposits in Southern Africa.

PHILLIPS, G.N., 1985, Interpretation of Big Bell/Hemlo - type gold deposits: precursors, metamorphism, melting and genetic constraints: Trans. Geol. Soc. S. Afr., 88, 159-173.

PHILLIPS, G.N. & GROVES, D.I, 1983, The nature of Archaean gold-bearing fluids as deduced from gold deposits of Western Australia: Geol. Soc. Aust. J., 30, 25-39.

PHILLIPS, G.N. & GROVES, D.I, 1984, Fluid access and fluid-wall rock interaction in the genesis of the Archaean gold-quartz vein deposit at Hunt mine, Kambalda, Western Australia: *in* FOSTER, R.P. (ed) Gold '82: The geology, geochemistry and genesis of gold depoists. A.A. Balkema, Rotterdam. 389-416.

PICKTHORN, W.J., GOLDFARB, R.J. & LEACH, D.L., 1987, Comment on "Dual origins of lode gold deposits in the Canadian Cordillera": Geology, 15, 471-472.

PITFIELD, P.E.J. & CAMPBELL, S.D.G., 1990, Integrated exploration, Midlands goldfield project: Preliminary results: *in* BAGLOW, N. (ed.), Annals of the Zim. Geol. Surv. Vol. XV, Harare, 21-33.

POLYA, D.A, 1989, Chemistry of the main-stage ore-forming fluids of the Panasqueira W-Cu(Ag)-Sn deposit, Portugal: Implications for models of ore genesis: Econ. Geol., 84, 1134-1152.

POTTER, R.W. & BROWN, D.L, 1977, The volumetric properties of aqueous sodium chloride solutiuons from 0 to 500 oC at pressures up to 200 bars based on a regresion of available data in the literature: U.S. Geol. Surv. Bull. 1421-C.

POTTER, R.W., CLYNNE, M.A. & BROWN, D.L, 1978, Freezing point depression of aqueous sodium chloride solutions: Econ. Geol., 73, 284-285.

POTY, B.P., STALDER, H.A. & WEISBROD, A.M., 1982, Fluid inclusion studies in quartz from fissures of Western and Central Alps: Schweiz. Mineral. Petr. Mitt., 54, 717-752.

POULSEN, K.H. & ROBERT, F., 1988, A comparison of structural style and gold endowment of three Archaean gold districts, Superior Province, Canada: *in* Extended abstracts poster programme, v.1, Bicentennial Gold '88, Melbourne, 36-38.

POULSEN, S.R. & OHMOTO, H., 1989, Devolatilization equilibria in graphite-pyrite-pyrrhotite bearing pelites with application to magma-pelite interaction: Contrib. Mineral. Petrol., 101, 418-425.

RAMBOZ, C., PICHAVANT, M. & WEISBROD, A., 1982, Fluid immiscibility in natural processes: use and misuse of fluid inclusion data. II. Interpretation of fluid inclusion data in terms of immiscibility: Chem. Geol., 37, 29-48.

RAMSAY, J.G., 1980, The crack-seal mechanism of rock deformation: Nature, 284, 135-139.

RANKIN, A.H. & GRAHAM, M.J, 1988, Na, K, and Li contents of mineralizing fluids in the Northern Pennine Orefield, England, and their genetic significance: Trans. Inst. Min. Metall. (Sect.B: Appl. earth sci.). 97, B99-B107.

RANKIN, A.H., FARMER, C.B., HERRINGTON, R.J., MOSER, M. & WILKINSON, J.J, 1990 Improved microthermometric measurements using a new cryogenic attachment to a conventional heating and cooling microscope stage : 3rd PACROFI meeting, Toronto, Abstracts volume, p72.

RANKIN, A.H., HERRINGTON, R.J., RAMSEY, M.H., COLES, B., CHRISTOULA, M. & JONES, E., (in press), Current developments and applications of ICP-AES techniques for the geochemical analysis of fluid inclusions in minerals: 8th IAGOD Symposium volume, Ottawa, Canada.

REDLICH, O. & KWONG, J.N.S., 1949, On the thermodynamics of solutions: Chem. Rev., 44, 233-244.

RIEDEL, W., 1929, Zur Mechanik geologischer Brucherscheinungen: Zent. Min. Geol. Pal., 1929, 354-368.

ROBERT, F. & BROWN, A.C, 1986a, Archaean gold-bearing quartz veins at the Sigma mine, Abitibi greenstone belt, Quebec: Part 1. Geologic relations and formation of the vein system. Econ. Geol., 81, 578-592.

ROBERT, F. & BROWN, A.C, 1986b, Archaean gold-bearing quartz veins at the Sigma mine, Abitibi greenstone belt, Quebec: Part 2, Vein paragenesis and hydrothermal alteration. Econ. Geol., 81, 578-592.

ROBERT, F. & KELLEY, W.C, 1987, Ore-forming fluids in Archaean gold-bearing quartz veins at the Sigma mine, Abitibi greenstone belt, Quebec, Canada. Econ. Geol., 82, 1464-1482.

ROBERTS, R.G, 1987, Ore deposits models, Number 11: Archaean lode gold deposits; Geoscience Canada, 14, 37-52.

ROBERTSON, I.D.M., 1973, Potash granites of the southern edge of the Rhodesian Craton and Northern Marginal Zone of the Limpopo Belt: Spec. Publ. Geol. Soc. S. Afr., 3, 265-276.

ROBERTSON, I.D.M., 1976, The geology of the country around Battlefields, Gatooma district: Bull. Geol. Surv. Rhod., 76, 258p.

ROBINSON, B.W. & KUSAKABE, M., 1975, Quantitative preparation of sulfur dioxide for 34S/32S analyses from sulfides by combustion with cuprous oxide: Anal. Chem., 47, 1179-1181.

ROCK, N.M.S., DULLER, P., HASZELDINE, R.S. & GROVES, D.I, 1987, Lamprophyres as potential gold exploration targets: some preliminary observations and speculations: *in* HO, S.E. & GROVES, D.I. (eds), Advances in understanding Precambrian gold deposits, Geol. Dept. & Univ. Extension, Univ. West. Austr., Publ. 11, 271-286.

ROEDDER, E., 1984, Fluid Inclusions: Reviews in Mineralogy, Vol. 12, Mineralogical Society of America, Washington, 646p.

RUTTER, E.H., 1983, Pressure solution in nature, theory and experiment: J. Struct. Geol., 140, 725-740.

RUTTER, E.H., 1986, On the nomenclature of mode of failure transitions in rocks: Tectonophysics, 122, 381-387.

RUTTER, E.H. & BRODIE, K.H., 1987, Experimental "syntectonic" dehydration of serpentinite under controlled pore-water pressure: A.G.U. EOS Trans., 67(16), 365.

RYZHENKO, B.N. & MALININ, S.D, 1971, The fugacity rule for the systems CO_2-H_2O, CO_2-CH_4, CO_2-N_2 and CO_2-H_2O: Geokhimiya No. 8, 899-913.

RYZHENKO, B.N. & VOLKOV, V.P, 1971, Fugacity co-efficients of some gases in a broad range of temperatures and pressures. : Geokhimiya No. 7, 760-773.

SAAGER, R. & MEYER, M., 1984, Gold deposits in Archaean granitoids and supracrustal rocks from southern Africa: a comparison: *in* FOSTER, R.P. (ed), Gold '82, Geol. Soc. of Zim., Spec. Publ., 1, 372-387.

SAFONOV, Y.G., GENKIN, A.D., VASUDEV, V.N., KRISHNA RAO, B. & ANANTHA IYER, G.V., 1984, Genetic features of gold ore deposit at Kolar, Dharwar craton, India: Geol. Soc. India Jour. v.25, 145-154.

SANDERSON, D.J. & MARCHINI, W.R.D, 1984, Transpression: J. Struct. Geol., 6, 449-458.

SANTOSH, M., 1986, Ore fluids in the auriferous Champion Reef of Kolar, south India: Econ Geol., 81, 1546-1552.

SAUNDERS, J.A., 1990, Colloidal transport of gold and silica in epithermal precious- metal systems: Evidence from the Sleeper deposit, Nevada: Geology, 18, 757-760.

SCOTT, S.D., 1973, Experimental calibration of the sphalerite geobarometer: Econ. Geol., 66, 653-669.

SCOTT, S.D., 1983, Chemical behaviour of sphalerite and arsenopyrite in hydrothermal and metamorphic environments. Mineralog. Mag., 47, 427-435.

SCOTT, S.D. & BARNES, H.L., 1971, Sphalerite geothermometry and geobarometry: Econ. Geol., 66, 653-669.

SCHWARCZ, H.P. & REES, C.E., 1985, Sulphur isotope studies of Archaean gold deposits, Grant 202: *in* MILNE, V.G. (ed.), Geoscience Research Grant Program, Summary of Research 1984-1985, Ont. Geol. Surv. Misc. Paper 127, 246p.

SEGALSTAD, T.V. & BERG, H-J., 1990, Geochemistry of gold in hydrothermal systems: 8th IAGOD Symposium, Program with Abstr., A178.

SEWARD, T.M., 1973, Thio-complexes of gold and the transport of gold in hydrothermal ore solutions: Geochim. Cosmochim. Acta., 37, 379-399.

SEWARD, T.M., 1989, The hydrothermal geochemistry of gold and its implications for ore formation: boiling and conductive cooling as examples: Econ. Geol. Mon., 6, 398-404.

SEWARD, T.M., 1990, The hydrothermal chemistry of gold: *in* FOSTER, R.P. (ed.), Gold Metallogeny and Exploration, Blackie, London.

SHARP, Z.D., ESSENE E.J. & KELLY W.C, 1985, A re-examination of the arsenopyrite geothermometer: pressure considerations amd application to natural assemblages: Canadian Mineralogist, 23, pp517-534.

SHENBERGER, D.M. & BARNES, H.L., 1989, Solubility of gold in aqueous sulfide solutions from 150 to 350°C: Geochim. Cosmochim. Acta., v.53, 269-278.

SHEPHERD, T.J. & MILLER, M.F., 1988, Fluid inclusion volatiles as a guide to tungsten deposits, southwest England: applications to other Sn-W provinces in western Europe: in BOISSONAS, J. (ed.), Mineral Deposits Within the European Community, Spec. Publ. Soc. for Geol. Applied to Min. Deps., 6, 29-52.

SHEPHERD, T.J., RANKIN, A.H., ALDERTON, D.H.M, 1985, A practical guide to fluid inclusion studies, Blackie and Sons Limited, London.

SHEPPARD, S.M.F., 1981, Stable isotope chemistry of fluids: in RICKARD, D. & WICKHAM, F.E. (eds.), Chemistry of solutions at high temperatures and pressures, Physics and Chemistry of the Earth, 13 & 14, Pergamon, 419-443.

SHETTEL, D.L., 1974, The solubility of quartz in supercritical H_2O-CO_2 fluids: Unpublished M.S. thesis, The Pennsylvania State University, 52pp.

SIBSON, R.H., 1977, Fault rocks and fault mechanisms: J. Geol. Soc. London, 133, 191-214.

SIBSON, R.H., 1981a, Fluid flow accompanying faulting: Field evidence and models. In : Simpson, D.W. and Richards, P.G.(eds.). Earthquake Prediction: American Geophysical Union, Maurice Ewing Series 4, p.593-603.

SIBSON, R.H., 1981b, Controls on low stress hydro-fracture dilatancy in thrust, wrench and normal fault terrains: Nature, v.289, 665-667.

SIBSON, R.H., 1983, Continental fault structure and the shallow earthquake source. J. Geol. Soc. London, 140, 741-767.

SIBSON, R.H., 1984, Roughness at the base of the seismogenic zone: J. Geophys. Res., 89, 5791-5799.

SIBSON, R.H., 1986, Earthquakes and lineament infrastructure: Phil. Trans. R. Soc. Lond., A317, 63-79.

SIBSON, R.H., 1987, Earthquake rupturing as a mineralising agent in hydrothermal systems: Geology, 15, 701-704.

SIBSON, R.H., 1990, Faulting and fluid flow: in NESBITT, D.E. (ed.), Fluids in tectonically active regimes of the continental crust: Min. Assoc. Can. Short Course, 18, 91-132.

SIBSON, R.H., MOORE, M.J. & RANKIN, A.H, 1975, Seismic pumping - a hydrothermal transport mechanism: J.Geol. Soc. London, 131, 653-659.

SIBSON, R.H., ROBERT, F. & POULSEN, K.H., 1988, High angle reverse faults, fluid pressure cycling and mesothermal gold deposits: Geology, 16, 551-555.

SIMPSON, C. & SCHMID, S.M., 1983, An evaluation of the criteria to deduce sense of movement in sheared rocks: Geol. Soc. Am. Bull., v.94, 1281-1288.

SKIPPEN, G.B. & MARSHALL, D.D., 1990, The generation of ore-forming fluids by metamorphism of the lower crust of the earth: 8th IAGOD Symposium, Program with Abstr., A241-242.

SMITH, F.G., 1944, The alkali sulphide theory of gold deposition: Econ. Geol., 38, 561-590

SMITH, H.S, 1986, Evidence from δC and δO isotopes in carbonate minerals for the origin of fluids in Archaean greenstone belt metamorphic and mineralisation processes: *in* Geocongress '86, Extended Abstracts Vol., Geol. Soc. S. Afr., Johannesburg, 314-348.

SMITH, T.J., CLOKE, P.L. & KESLER, S.E, 1984, Geochemistry of fluid inclusions from the McIntyre-Hollinger gold deposit, Timmins, Ontario, Canada: Econ. Geol. 79, 1265-1285.

SNOWDEN, P.A., 1984, Non-diapiric batholiths in the north of the Zimbabwe Shield: *in* KRONER, A. & GREILING, R. (eds.), Precambrian Tectonics Illustrated, Springer Verlag, Berlin, 135-145.

SNOWDEN, P.A. & BICKLE, M.J, 1976, The Chinamora batholith: diapiric intrusion or interference fold?: J. Geol. Soc. London, 132, 131-137.

SPOONER, E.T.C., BRAY, C.J., WOOD, P.C., BURROWS, D.R. & CALLAN, N.J, 1987, Au-quartz vein and Cu-Au-Ag-Mo-anhydrite mineralization, Hollinger-McIntyre mine, Timmins, Ontario: $d^{13}C$ values (McIntyre), Fluid inclusion gas geochemistry, pressure (depth) estimation, and H_2O-CO_2 phase separation as a precipitation and dilation mechanism: Ont. Geol. Surv. Misc. Paper 110, 35-56.

STAGMAN, J.G., 1978, An outline of the geology of Rhodesia: Bull. Geol. Surv. Rhod., 80, 126p.

STANTON, R.L., 1972, Ore Petrology: McGraw-Hill, New York, 713p.

STARLING, A., GILLLIGAN, J.M., CARTER, A.H.C., FOSTER, R.P & SAUNDERS, R.A., 1989, High-temperature hydrothermal precipitation of precious metals on the surfaces of pyrite: Nature, 340, 298-300.

STOWE, C.W., 1971, Summary of the tectonics of the Rhodesian Archaean craton: Spec. Publ. Geol. Soc. Aust. 3, 373-383.

STOWE, C.W, 1974, Alpine-type structures in the Rhodesian basement at Selukwe. J.Geol.Soc. London, 130, 411-425.

STOWE, C, 1980, Wrench tectonics in the Archaean Rhodesian Craton : Trans. Geol. Soc. S. Afr. 83 1980 pp. 193-205.

STRECKEISEN, A., 1976, To each plutonic rock its proper name: Earth Sci. Rev., 12, 1-33.

SUMMERS, R., 1969, Ancient mining in Rhodesia. Museum Memoir no. 3, Trustees of National Museums of Rhodesia, Salisbury, 236p.

SUNBLAD, K., ZACHRISSON, E., SMEDS, S., BERGLUND, S. & ÅLINDER, C., 1984, Sphalerite geobarometry and arsenopyrite geothermometry applied to metamorphosed massive sulphide ores in the Swedish Caledonides: Econ. Geol., 79, 1660-1668.

SVERJENSKY, D.A., 1987, Calculation of thermodynamic properties of aqueous species and the solubilities of minerals in supercritical electrolyte solutions. In: CARMICHAEL, I.S.E. & EUGSTER, H.P. (eds) Thermodynamic modelling of geologic materials: Minerals, fluids and melts. Reviews in Mineralogy, 17, Mineralogical Society of America, 177-209.

SWARNECKI, M.S., 1988, Alteration and deformation in a shear zone hosting gold mineralisation at Harbour Lights, Leonora, Western Australia. In: HO, S.E. & GROVES, D.I. (eds) Recent advances in understanding Precambrian gold deposits, Vol 2, Geol. Det. & Univ. Extension, Univ. West. Austr. Publc., 12, 111-129.

SYLVESTER, A.G. & SMITH, R.R., 1976, Tectonic transpression and basement-controlled deformation in the San Andreas fault zone, Salton Trough, California: Bull. AAPG, 57, 74-96.

TABEART, C.F., 1989, Structural and geochemical setting of gold mineralisation at Renco mine, Zimbabwe. PhD thesis, Royal School of Mines, Imperial College, London 265p.

TAKENOUCHI, S. & KENNEDY, G.C., 1964, The binary system H_2O-CO_2 at high temperatures and pressures: Amer. J. Sci., 262, 1055-1074.

TAKENOUCHI, S. & KENNEDY, G.C., 1965, The solubility of carbon dioxide in NaCl solutions at high temperatures and pressures: Amer. J. Sci., 263, 445-454.

TANKARD A.J., ERIKSSON, K.A., HUNTER, D.R., JACKSON, M.P.A., HOBDAY, D.K. & MINTER, W.E.L., 1982, Crustal evolution of southern Africa: 3.8 billion years of Earth history: Springer-Verlag, New York, 523p.

TARNEY, J. & WEAVER, B.L., 1987, Geochemistry of the Scourian complex: petrogenesis and tectonic models: *in* PARK, R.G. & TARNEY, J. (eds.), Evolution of the Lewisian and Comparable High Grade Terrains, Geol. Soc. Lond. Spec. Publ., 27, 45-56.

TAYLOR, H.P., 1979, Oxygen and hydrogen isotope relationships in hydrothermal mineral deposits: in, BARNES, H.L. (ed) Geochemistry of hydrothermal ore deposits, Wiley & Sons, New York, 236-277.

TCHALENKO, J.S., 1968 The evolution of kink bands and the development of compression textures in sheared clays: Tectonophysics, v.6, 159-174.

TEIXEIRA, J.B.G., KISHIDA, A., MARIMON, M.P.C., XAVIER, R.P. & McCREATH, I., 1990, The Fazenda Brasileiro gold deposit, Bahia: geology, hydrothermal alteration, and fluid inclusion characteristics: Econ. Geol., 85, 990-1009.

THOMPSON, M., RANKIN, A.H., WALTON, S.J., HALLS, C. & FOO, B.N., 1980, The analysis of fluid inclusion decrepitates by inductively coupled plasma atomic emission spectroscopy: an exploratory study: Chem. Geol., 30, 121-133.

TOULMIN, P. & BARTON, P.B, 1964, A thermodynamic study of pyrite and pyrrhotite. Geochim. Cosmochim. Acta., 28, 641-671.

TRUESDELL, A.H, 1984, Chemical geothermometers for geothermal exploration. : In : Reviews in Econ. Geol. vol.1, 31-44.

TUTTLE, O.F., 1949, Structural petrology of planes of liquid inclusions: J. Struct. Geol., 57, 331-356.

VALAKOVICH, M.P. & ALTUNIN, U.V., 1968, Thermophysical properties of carbon dioxide: Collets, London.

VALLEY, J.W., TAYLOR, H.P. Jr. & O'NEIL, J.R., 1986, Stable Isotopes in High Temperature Geological Processes: Min. Soc. Amer., Reviews in Mineralogy, 16, Bookcrafters Inc., Michigan.

VALLIANT, R.I & BRADBROOK, C.J., 1986, Relationship between stratigraphy, faults and gold deposits, Page-Williams mine, Hemlo, Ontario, Canada: *in* MACDONALD, A.J. (ed.), Proceedings of Gold '86, an international symposium on the geology of gold, Toronto, 355-361.

VAN DEN KERKOFF, A.M., 1988, The System CO_2-CH_4-N_2 in Fluid Inclusions: Theoretical Modelling and Geological Applications: Free University Press, Amsterdam.

VAN DER WAALS, J.H. & PLATTEEUW, J.C., 1959, Clathrate solutions: in PRIGOGINE, I. (ed.), Advances in Chemical Physics, Interscience, 2, New York, 1-57.

VAN REENAN, D.D., BARTON, J.M., ROERING, C., SMITH, C.A. & SCHALKURYK, J.F, 1987, Deep crustal response to continent collision: The Limpopo Belt of southern Africa:

VEARNCOMBE, J.R., 1988, Fibrous vein geometry and gold mineralisation: in HO,S.E. & GROVES, D.I. (eds.) Advances in understanding Precambrian gold deposits, Vol 2. Geol. Dept. & Univ. Extension, Univ. Western Australia, Publ. 12, 63-80.

VEARNCOMBE, J.R., BARLEY, M.E., EISENLOHR, B.N., GROVES, D.I., HOUSTON, S.M., SKWARNECKI, M.S., GRIGSON, M.W. & PARTINGTON, G.A., 1989, Structural controls on mesothermal gold mineralisation: Examples from the Archaean terranes of southern Africa and Western Australia: Econ. Geol. Mon., 6, 124-134.

WARD, J.W.H, 1968, Geological aspects of the Patchway gold mine, Rhodesia: Trans. Geol. Soc. S. Afr., 71, Annex., 147-158.

WALSH, J.F., KESLER, S.E., DUFF, D. & CLOKE, P.L, 1988, Fluid inclusion geochemistry of high-grade, vein-hosted gold ore at the Pamour mine, Porcupine camp, Ontario. Econ. Geol., 83, 1347-1367.

WALTHER, J.V. & HELGESON, H.C., 1977, Calculation of the thermodynamic properties of aqueous silica and the solubility of quartz and its polymorphs at high pressures and temperatures: Am. Jour. Sci., 277, 1315-1351.

WALTHER, J.V. & SCHOTT, J., 1988, The dielectric constant approach to speciation and ion pairing at high temperature and pressure: Nature, 332, 635-638.

WATSON, J.V, 1978, Precambrian thermal regimes. Phil. Trans. R. Soc. Lond., A288, 431-440.

WELHAN, J.A., 1988, Origins of methane in hydrothermal systems: Chemical Geology 17 pp. 183-198.

WHITE, A.J.R., 1979, Sources of granite magmas: Geol. Soc. Amer. Abstr. Programs, 11, no.7, 539.

WHITE, J.C. & WHITE, S.H, 1981, The structure of grain boundaries in tectonites: Tectonophysics, 78, 613-628.

WHITE, S.H, 1975, Estimation of strain rates from microstructures. J.Geol.Soc. London, 131, 577-583.

WHITE, S.H., 1990, Shear zone controls of gold mineralisation in the Yilgarn Craton, Western Australia: GAC-MAC Annual meeting, Program with abstracts, Vol. 15.

WHITE S.H. & BAXTER J.L. 1987. Gold mineralisation in shear zones. : Hermitage Holdings unpublished company report.

WHITE, S.H., BRETAN, P.G. & RUTTER, E.H, 1986, Fault-zone reactivation: kinematics and mechanisms. Phil.Trans.R.Soc. Lond., A317, 81-97.

WHITE, S.H., BURROWS, S.E., CARREGAS, J., SHAW, N.D. & HUMPHREYS, F.J., 1980, On mylonites in ductile shear zones: J. Struct. Geol., v.2, 175-188

WILCOX, R.E., HARDING, T.P. & SEELY, D.R., 1973, Basic wrench tectonics: Bull. AAPG, 57, 74-96.

WILKINSON, J.J., 1990, The origin and evolution of Hercynian crustal fluids: Unpubl. PhD Thesis, Univ. of Southampton.

WILSON, A.H. & PRENDEGAST, M.D., 1989, The Great Dyke of Zimbabwe - I: tectonic setting, stratigraphy, petrology structure, emplacement and crystallisation: *in* PRENDEGAST, M.D. & JONES, M.J. (eds.), Magmatic Sulphides - The Zimbabwe Volume, 1-20.

WILSON, J.F., 1973, Granites and gneisses of the area around Mashaba: Rhod. Geol. Surv. Bull. No. 62, 239p.

WILSON, J.F., 1979, A preliminary reapparaisal of the Rhodesian basement complex. Spec. Publ. Geol. Soc. S. Afr., 5, 1-23.

WILSON, J.F., 1981, The granitic-greenstone shield, Zimbabwe: *in* HUNTER, D.R. (ed.), Precambrian of the Southern Hemisphere, Elsevier, Amsterdam, 454-487.

WILSON, J.F., BICKLE, M.J., HAWKESWORTH, C.J., MARTIN, A., NISBET, E.G. & ORPEN, J.L., 1978, Granite-greenstone terrains of the Rhodesian Craton: Nature, 271, 23-27.

WILSON, J.F. JONES, D.L. & KRAMERS, J.D, 1987, Mafic dyke swarms in Zimbabwe: *in* HALLS, H.C. & FAHRIG, W.F. (eds). Mafic dyke swarms. Geol. Assoc. Canada, Spec. Pap. 34, 433-444.

WINCHESTER, J.A. & FLOYD, P.A, 1977, Geochemical discrimination of different magma series and their differentiation products using immobile elements. Chem.Geol.20, 325-343.

WINCHESTER, J.A. & MAX, 1984, The geochemistry and origins of the Precambrian rocks of the Rosslare Complex, S.E. Ireland: J. Geol. Soc. London, 139, 309-319.

WISE, D.U., DUNN, D.E., ENGELDER, J.T., GEISER, P.A., HATCHER, R.D., KISH, S.A., ODOM, A.L. & SCHAMEL, S., 1984, Fault-related rocks - suggestions for terminology: Geology, 12, 391-394.

WOOD, B.J. & WALTHER, J.V, 1986, Fluid flow during metamorphism and its implications for fluid:rock ratios. In WALTHER, J.V. & WOOD, B.J. (eds). Fluid-rock interactions during metamorphism. Advances in Physical Geochemistry, Vol.5, Springer-Verlag, New York, 89-108.

WOOD, P.C., THOMAS, A.V., BURROWS, D.R., MacDONALD, A.J, NOBLE, S.R. & SPOONER, E.T.C., 1984, CO2-bearing low-moderate salinity fluids in Archaean gold-quartz-carbonate-(W-Mo) vein deposits and magmatically derived Mo, W, Ta and Sn mineralization: *in* Geol. Soc. Amer. Abstr. with Programs, 16, no.6, 700.

WOOD, P.C., BURROWS. D.R., THOMAS, A.V. & SPOONER, E.T.C, 1986, The Hollinger-McIntyre Au-quartz vein system, Timmins, Ontario, Canada; Geologic characteristics, fluid properties and light stable isotope geochemistry. In: MACDONALD, A.J. (ed) Proceedings of Gold '86, an International Symposium on the geology of gold. Konsult International Inc., Toronto, 56-80.

WOPENKA, B. & PASTERIS, J.D., 1986, Limitations to quantitative analyses of fluid inclsions in geological samples by laser-Raman microprobe spectroscopy: Appl. Spect., 40, 144-151.

WYMAN, D. & KERRICH, R, 1988, Alkaline magmatism, major structures and gold deposits: Implications for greenstone belt metallogeny, Econ. Geol., 83, 454-461.

YERKES, R.F., LEVINE, P. & WENTWORTH. C.M., 1985, Abnormally high fluid pressures in the region of the Coalinga earthquakes - a preliminary report: U.S. Geol. Surv. Open-file Rept., 85-44, 344-375.

APPENDIX I

SAMPLE LOCATIONS

The following sample location table provides the location and a brief description of all samples collected during this study. In addition, Figures I.1 and I.2 (see insert) are plans showing locations of samples collected underground at Patchway. Many samples were not used in the study, but are included in the reference collection.

Sample Number	Location (Section, Level)	Brief Description	Orientation	Study
10-1	S15, 10 Level	massive felsite	338/48W-r	
10-2	S15	massive pillow lava	072/29N-u	
10-3	S15	dolerite	032/37W-u	
10-4	S13	sheared lava	026/46W-r	
10-5	S13	massive felsite	245/54W-u	
10-6	S12/13	massive pillow lava	130/49W-r	
10-7	S12	sheared lava (in contact with felsite)	049/51N-u	
10-8	S11	sheared lava (relict pillow fabric)	191/72W-u	
10-9	S11	massive felsite	250/52N-r	
10-10	S11	sheared lava (vein f/w)	144/62E-u	
10-11	S9	sheared lava (vein f/w)	216/24W-r	
10-12	S9	sheared lava (vein h/w)	030/22W-u	
10-13	S9	ribbon vein (Q2)	342/66E-u	
10-14	S8	dolerite	341/78W-u	
10-15	S8	sheared lava	074/40W-r	
10-16	S6	sheared lava (boudinaged vein f/w)	044/24W-r	
10-17	S6	sheared lava (vein h/w)	034/72E-u	
10-18	N13	sheared lava (relict pillow texture)	029/V	
10-19	N12	dolerite	350/60W-r	
10-20	N12	sheared felsite (vein f/w)	000/52W-r	
10-21	N13	massive felsite	018/40W-r	
10-22	N11	highly sheared lava	048/38W-u	
10-23	N11	highly sheared felsite	None	
10-24	N12	sheared lava (vein h/w)	354/V	
10-25	N12	ribbon vein (Q2)	358/72W-u	
10-26	N12	sheared felsite (vein f/w)	030/48W-r	
10-27	N10	sheared lava within sheared felsite unit	078/84W-r	
10-28	N10	sheared felsite (upper vein f/w)	213/56W-r	
10-29	N10	sheared lava (upper vein h/w)	032/58W-u	
10-30	N9	sheared lava (upper vein h/w)	050/50W-u	
10-31	N9	upper ribbon vein (Q2)	320/52W-u	
10-32	N9	sheared felsite (upper vein f/w)	033/82E-u	
10-33	N9	slightly sheared felsite (inter-vein)	015/48W-r	
10-34	N9	sheared felsite (lower vein h/w)	052/40W-u	
10-35	N9	lower ribbon vein (Q2)	033/40E-u	
10-36	N9	sheared lava (lower vein f/w)	042/40W-r	
10-37	N1	dolerite	240/V	
10-38	N1	sheared lava (vein f/w)	024/54W-r	
10-39	S2	sheared lava	058/48W-u	
10-40	S2	boudinaged quartz vein (Q2?)	020/74W-r	
10-41	S3	sheared lava	060/60W-u	
18-1	N4, 18 Level	sheared sulphidic lava (vein inclusion)	338/64W-r	
18-2	N4	ribbon vein	063/80S-u	
18-3	N4	sheared lava (vein h/w)	010/18W-u	
18-4	N3	sheared lava (vein f/w)	026/48W-r	
18-5	N3	vein boudin (Q2)	040/40W-u	
18-6	N3	vein boudin tip (Q2)	316/30S-u	
18-7	N3	sheared lava	048/40W-u	
18-8	N3	sheared lava	241/48W-u	
18-9	N3	deformed dolerite?	216/26W-r	
18-10	N2	massive pillow lava	None	
18-11	N2	dolerite	None	

Sample Number	Location (Section, Level)	Brief Description	Orientation	Study
18-12	N1 18 Level	massive felsite	040/60W-u	
18-13	N1	sheared lava	154/V	
18-14	S1	massive pillow lava	290/80N-u	
18-15	S1	highly sheared lava	051/34W-u	
18-16	S1	dolerite	118/60N-r	
18-17	N1	massive felsite at upper contact	136/72S-u	
18-18	N1	dolerite	005/54W-u	
18-19	N2	sheared lava	062/52N-u	
18-20	S6, 18-15 Level Raise	dolerite	251/36N-u	
18-21	S6	quartz segregation in sheared lava	237/32N-u	
18-22	S6	sheared lava	014/30W-u	
18-23	S6	quartz vein (Q2?)	000/32W-u	
18-24	S6	ribbon quartz vein (Q2)	330/38W-u	
18-25	S6	sheared lava	030/30W-u	
18-26	S6	sheared lava from steep D4 fault	204/40W-u	
18-27	S6	sheared lava (immediate vein h/w)	048/40W-u	
18-28	S6	late quartz-tourmaline vein (Q4)	None	
18-29	S6	sheared lava (immediate vein f/w)	210/45W-r	
18-30	S6	ribbon quartz vein (Q2)	132/V	
18-31	S6	sheared lava (vein f/w)	030/34W-r	
18-32	S6	sheared lava (immediate vein h/w)	030/40W-u	
7-1	S1, 7 Level	sheared dolerite	054/40W-u	
13-1	N10, 13 Level	massive pillow lava	None	
13-2	N10	brecciated pillow lava	None	
13-3	N10	sheared lava	None	
13-4	N10	sheared lava	None	
13-5	N10	sheared felsite	None	
13-6	N10	sheared sulphidic lava (vein f/w)	050/28W-r	
9-1	N7, 9 Level	kink-banded sheared lava (vein h/w)	None	
12PMQ-1	N13, 12 Level	pillow-infilling quartz-epidote (Q1)	None	
12LQ1	N13	late quartz-tourmaline veinlets (Q4)	None	
A/10/1	S8, 10 Level	highly sheared lava (vein f/w)	058/12W-u	
A/10/2	S7	sheared lava inclusion in ribbon vein	110/28N-u	
A/10/3	S6	sheared, silicified lava (vein h/w contact)	070/34N-u	
A/10/4	S4	quartz-tourmaline veinlet in felsite	None	
A/10/5 & 6	S2	quartz vein, central shear (Q3?)	None	
A/10/7	N3	upper quartz vein (Q2)	025/30W-u	
A/10/8	N3	lower quartz vein (Q2)	030/10W-r	
A/10/9	N2	ribbon quartz vein (Q2)	054/40N-r	
A/10/10	N2	ribbon quartz vein (Q2)	None	
A/10/11	N2/N3	silicified felsite	064/62N-r	
A/10/12	N3	felsite	060/52N-u	
A/10/13	N3	late quartz-tourmaline (Q4)	None	
A/10/14	N4	late quartz infilling (Q4)	None	
A/10/15	N5	boudinage neck quartz-tourmaline infilling (Q4)	None	
A/10/16	S9	brecciated sheared lava vein f/w, qtz matrix	None	
A/10/17	S9	late quartz-tourmaline vein (Q4)	None	
A/10/18 to 32	S9	detailed ribbon vein pillar samples (see Chapter 7)	None	
A/10/33	S9	sheared lava	None	
A/10/34	S9	late quartz-tourmaline veinlet (Q4)	None	
600-1	N19, 6 Level	sheared sulphidic lava, vein inclusion	070/44N-r	
600-2	N19	deformed ribbon quartz vein (Q2)	062/70N-r	
600-3	N19	ribbon quartz vein (Q2)	058/30W-r	
600-4	N20	end of ribbon quartz vein (Q2)	None	

Sample Number	Location (Section, Level)	Brief Description	Orientation	Study
600-5	N16	sheared sulphidic vein f/w lava	060/40N-u	
600-6 to 8	N16	detailed ribbon vein pillar samples (see Chapter 7)	None	
700-1	S18, 7 Level	sheared felsite, vein inclusion	None	
700-2	S16	porphyritic dolerite	None	
700-3	S18	sheared lava (immediate lower vein h/w)	174/28W-u	
700-4	S18, 7 Level	upper ribbon quartz vein (Q2)	None	
700-5	S18	boudin of ribbon quartz (Q2)	024/26W-r	
700-6	S18	sheared lava (immediate upper vein h/w)	018/28W-r	
800-1	N16, 8 Level	sheared sulphidic lava (vein f/w)	060/40N-u	
800-2	N16	highly sulphidic sheared lava (inter-vein)	054/42N-r	
800-3	N16	ditto	088/48N-r	
800-4	N16	upper ribbon quartz vein (Q2)	054/40N-r	
800-5 & 6	N16	main ribbon quartz vein (Q2)	None	
1800-1	N14, 18 Level	dolerite at sheared contact	None	
1800-2	N14	deformed dolerite	None	
1800-3	N17	late quartz veining + cpy, sphal (Q4)	None	
1800-4	N10	sheared felsite vein f/w	None	
1800-5	N10	main ribbon quartz vein (Q2)	None	
1800-6	N19	sheared lava	None	
2400-1	N21, 24 Level	massive felsite	None	
2400-2	N21	ditto	None	
2400-3	N21	flow top breccia, lava	None	
2400-4	N21	sheared felsite	018/72W-r	
2400-5	N21	sheared felsite, vein f/w	None	
2400-6	N21	sheared sulphidic lava	None	
2400-7	N21	sheared lava	036/70W-r	
2400-8	N21	ditto	006/V	
2400-9	N21	main ribbon quartz vein (Q2)	094/34N-r	
2400-10	N8	main ribbon vein (Q2)	None	
2400-11	N7	late quartz-tourmaline vein (Q4)	None	
2400-12	N5	carbonate segregation in dolerite	None	
2400-13	N21	massive felsite (drillcore from -20m into f/w)	None	
2400N8	N7	ribbon quartz vein (Q2)	None	
2000-1	N19, 20 Level	sheared lava (immed. vein f/w)	080/32N-r	
2000-2	N19	sheared lava (immed. vein h/w)	074/64N-u	
2000-3	N19	ribbon quartz vein with cross-cutting quartz tourmaline veinlet (Q2 + Q4)	None	
2000-4	N19	ribbon quartz vein (Q2)	None	
20-1	N19	sheared lava	070/64W-u	
20-2	N19	sheared lava (immed. vein h/w)	078/60W-u	
20-3	N19	late quartz-tourmaline (Q4)	none	
20-4	N19	ribbon quartz vein (Q2)	none	
20-5	N19	ribbon vein at contact (Q2)	032/38W-r	
20-6	N19	sheared lava (vein f/w)	080/47N-u	
20-7	N19	sheared lava (vein f/w)	068/48N-u	
20-8	N19	ribbon vein + late qtz-tour. (Q2+Q4)	none	
20-9	N18	sheared lava (vein f/w)	062/29N-r	
20-10	N18	ribbon quartz vein (Q2)	none	
20-11	N18	sheared lava (vein h/w)	058/28W-u	
20-12	N17	ribbon quartz vein (Q2)	none	
20-13	N17	late quartz veinlet (Q4)	none	
20-14	N17	ribbon quartz vein (Q2)	none	
20-15	N16	sheared lava (10m into vein f/w)	none	
20-16	N16	sheared lava (immed. vein f/w)	066/46W-r	
20-17	N16	sheared felsite (vein inclusion)	020/34W-u	

Sample Number	Location (Section, Level)	Brief Description	Orientation	Study
20-18	N15, 20 Level	sheared lava	058/56W-u	
20-19	N14	highly sheared lava	072/62N-u	
20-20	N11	ribbon quartz vein (Q2)	none	
20-21	N11	ribbon vein f/w contact	none	
20-22	N11	sheared sulphidic lava (0.3 m into f/w)	022/34W-r	
20-23	N11	late quartz vein (Q4)	none	
20-24	N5	sheared lava	056/40W-u	
20-25	N3/N4	brecciated pillow lava	none	
26-1	N9, 26 Level	massive pillow lava	046/20W-r	
26-2	N13	late quartz-tourmalin veining (Q4)	none	
26-3	N13	ribbon quartz vein (Q2)	none	
26-4	N16	sheared lava (vein f/w)	none	
26-5	N16	ribbon quartz vein (Q2)	none	
26-6	N16	sheared felsite (vein h/w)	none	
26-7	N17	ribbon quartz vein (Q2)	none	
26-8	N17	sheared lava (0.4m into vein f/w)	none	
26-9	N17	highly sheared lava (vein f/w)	none	
N.B. 26-10 to 26-16 collected from 30 Level				
26-10	N4, 30 Level	sheared lava (vein h/w)	none	
26-11	N4	ribbon quartz vein (Q2)	none	
26-12	N4	sheared lava (vein f/w)	none	
26-13	N4	ribbon quartz vein (Q2)	none	
26-14	N6	late quartz-tourmaline veinlet (Q4)	none	
26-15	N6	sheared lava (vein f/w)	none	
26-16	N6	sheared lava (vein h/w)	none	
30-1	N19, 30 Level	highly sheared lava	none	
30-2	N19	ribbon quartz vein (Q2)	none	
30-3	N18	ribbon quartz vein (Q2)	none	
30-4	N18	sheared sulphidic lava (0.4m into h/w)	none	
30-5	N18	sheared felsite (immed. f/w)	none	
30-6	N18	ribbon quartz vein (Q2)	none	
30-7	N18	late quartz-tourmaline vein (Q4)	none	
400-1	N12, 4 Level Basil	massive felsite	None	
400-2	N13/N14 Basil	quartz vein (Q3)	None	
400-3	N13/N14 Basil	sheared lava (vein f/w)	106/44N-r	
400-4	N13 Basil	quartz vein (Q3)	None	
400-5	N14 Basil	flow-top breccia, lava	None	
400-6	N16 Basil	quartz vein (Q3)	None	
400-7	N16 Basil	late quartz-tourmaline veinlet (Q4)	None	
400-8	N17 Basil	sheared felsite	None	
400-9	N17 Basil	lower quartz vein (Q2)	None	
400-10	N17 Basil	upper quartz vein (Q2)	None	
400-11				
400-12	N18	boudin of quartz vein (Q2?)	070/38N-r	
400-13	N18	sheared felsite	None	
400-14	N18	quartz vein (Munya-Skati) (Q3)	None	
400-15	N18	sheared sulphidic lava (vein h/w)	None	
400-16	N22 Kabanga	sheared sulphidic lava (vein h/w)	082/50N-r	
400-17	N22 Kabanga	sheared felsite	066/40W-r	
400-18	N22 Kabanga	sheared, carbonated ("stripy") lava (vein f/w)	None	
400-19	N22 Kabanga	quartz vein breccia (Q3)	None	
400-20	N22 Kabanga	ribbon quartz vein (Q3)	None	
400-21	N22 Kabanga	quartz veining (Q3)	None	
400-22	N19 Kabanga	sheared lava (vein h/w)	076/46W-r	
400-23	N18 Kabanga	ribbon quartz-tourmaline (Q3)	None	
400-24	N18 Kabanga	quartz veining (+ tourmaline) (Q3)	None	
400-25	N19 Kabanga	quartz-tourmaline veining (Q3)	None	
400-26	N19 Kabanga	ribbon quartz veining (Q3)	None	

Sample Number	Location (Section, Level)	Brief Description	Orientation	Study
500-1	N14, 5 Level	ribbon quartz vein (Q2)	None	
500-2	N14	late quartz veinlet (Q4)	None	
500-3	N14	late quartz veinlet (Q4)	None	
500-4	N14	ribbon quartz vein, upper contact (Q2)	None	
500-5	N14	ribbon quartz vein, lower contact (Q2)	None	
500-6	N14	lost in transit		
500-7	N14	lost in transit		
500-8	N14	lost in transit		
500-9	N14	lost in transit		
500-10	N14	lost in transit		
500-11	N9	lower ribbon quartz vein (Q2)	None	
500-12	N9	upper ribbon quartz vein (Q2)	None	
500/A to F	N14, 5 Level	sheared lava, samples at 0.2m intervals into footwall of upper (main) ribbon quartz vein (Q2)	none	
1500/H/1 to 6	N14, 5 Level	sheared lava, samples at 0.2m intervals into hangingwall of upper (main) ribbon quartz vein (Q2)	none	
15-1	N3, 15 Level	massive pillow lava	None	
15-2	N3	minor quartz veining	None	
15-3	N3	dolerite	None	
15-4	N3	deformed dolerite	None	
15-5	N3	quartz veining in 15-4	None	
15-6	N3	ditto	None	
1500-7	N3	sheared lava	None	
1500-8	N3	highly sheared lava	None	
1500-9	N3	carbonate segregation	none	
1500-11	N3	sheared lava with felsite stringers	none	
1500-12	N3	ditto	none	
1500/A to F	N1, 15 Level	sheared lava, samples at 0.2m intervals into the footwall of the ribbon quartz vein (Q2)	none	
1500/H/1 to 6	N1, 15 Level	sheared lava, samples at 0.2m intervals into the hangingwall of the ribbon quartz vein (Q2)	none	
19HG1	N7, 19 Level	ribbon quartz vein with visible coarse gold (Q2)	none	
TQ-1 to TQ4	Lion Hill scheelite mine	massive quartz veining	none	
LH-1	Lion Hill scheelite mine	altered tonalite (vein margin)	none	
LH-2	ditto	ditto	none	
LH-3	ditto	thin quartz stringer in tonalite	none	
LH-4	Lion Hill village	massive tonalite on margin of intrusive	none	
LH-5	Lion Hill quarry	massive fresh tonalite	none	
LH-6	ditto	ditto	none	
LH-7	Lion Hill roadside	massive barren quartz vein	none	

APPENDIX II - ELECTRON MICROSCOPY AND MICROPROBE OPERATING CONDITIONS

II.1 EDS Analysis

Analysis of silicates, oxides, carbonates and sulphides was performed on a JEOL 733 Superprobe with an accelerating voltage of 15 kV and a current of approximately 2 μA. Standardisation using Co was performed every 20 minutes or so, and reference minerals were analysed frequently to check totals. Detection limits for elements are calculated from the 2σ values determined by the Link Analytical ZAF4 software and values below detection limits are not quoted. Recorded EDS analyses follow later in this appendix.

Data reduction of the EDS analyses is performed on the AN10000 processor linked to the JEOL 733 and stoichiometric calculations of mineral chemistry were performed using MINFILE (Affifi & Essene 1988), checked following the procedure of Deer *et al.* (1966).

II.2 WD Mapping

This technique measures the intensity of the X-Rays produced at distinct wavelengths for an element excited by the incident electron beam in an SEM. Using a crystal spectrometer, raster maps of fields of view for a selected crystal setting (a discrete wavelength range, hence one particular element's emission wavelength) show signal strength proportional to concentration of that element. Although qualitative, the method allows the study of distribution of elements present in a mineral at only trace levels (< 0.1 wt%). Much higher accelerating voltages (25 kV) and beam currents (>20 μA) were used.

Crystals and spectrometer settings for characteristic X-Ray wavelengths are shown below:

CRYSTAL	SPECTROMETER SETTING	ELEMENT	X-RAY LINE
LIF	81.77	As	Kα1
LIF	115.28	Ni	Kα1
LIF	107.12	Cu	Kα1
LIF	88.76	Au	Lα1
PET	187.05	Au	Mα1

Typical maps were acquired in real-time mode, 256x256 pixels with a dwell time of 30 ms on each pixel. Better quality maps were obtained using disk-mode, 1024x1024 pixels with a dwell time of 15 ms, with the map acquisition running overnight.

EPMA Analyses - Chlorite - Mineralised vein association

Sample 20-14 associated with scheelite, 10-25 associated with Au grains

	20-14i	0-14ii	-14iii	0-14iv	20-14v	0-14vi	-14vii	14viii	10-25a	10-25b	10-25c	10-25i	0-25ii	-25iii	0-25iv	10-25v
SiO2	24.43	23.86	24.53	24.29	24.20	24.14	23.64	24.55	23.91	24.15	24.19	25.19	23.53	25.09	24.28	24.83
TiO2	-	0.06	0.12	-	0.23	0.08	0.12	-	-	0.00	0.00	-	-	-	0.05	-
Al2O3	23.63	23.96	23.55	24.17	23.30	23.63	23.77	22.23	20.34	20.53	20.76	23.01	20.42	22.13	20.85	21.73
Fe2O3	-	-	0.00	-	0.00	0.00	0.00	-	-	-	0.00	0.00	0.00	-	0.00	-
FeO	24.92	25.44	25.50	25.64	26.61	25.22	26.74	26.22	43.59	43.10	43.57	41.86	29.75	29.86	33.65	32.88
MnO	0.32	0.27	0.24	0.26	0.18	0.29	0.21	0.37	0.21	0.23	0.57	0.46	0.41	0.33	0.31	0.24
MgO	14.41	14.32	13.98	13.30	13.33	14.54	13.23	13.83	2.75	2.70	2.88	3.48	11.20	11.42	8.37	9.99
CaO	-	-	-	-	-	-	0.03	0.08	0.12	0.15	-	0.09	0.05	-	0.05	-
Na2O		-	0.18	0.04	0.34	0.22	0.19	0.21	0.18	0.14	0.11	0.02	0.28	0.24	0.28	0.00	0.46
K2O		-	0.02	0.01	0.07	0.04	0.07	-	0.11	0.23	-	1.77	-	3.48	2.15	4.17	1.55
H2O	12.29	11.89	12.02	11.92	11.89	11.84	12.05	12.44	10.49	10.54	10.43	10.70	10.93	11.12	10.76	10.99
F		-	-	-	-	-	-	-	-	-	-	-	-	-	-	-
Cl		-	-	-	-	-	-	-	-	-	-	-	-	-	-	-
O=F		-	-	-	-	-	-	-	-	-	-	-	-	-	-	-
O=Cl		-	-	-	-	-	-	-	-	-	-	-	-	-	-	-
Total	100.00	100.00	100.00	100.00	100.00	100.00	100.00	100.00	101.79	101.52	104.20	105.07	100.02	102.37	102.49	102.66
#Si IV	2.57	2.51	2.58	2.55	2.56	2.53	2.51	2.61	2.68	2.70	2.66	2.67	2.58	2.64	2.63	2.63
#Al IV	1.43	1.49	1.42	1.45	1.44	1.47	1.49	1.39	1.32	1.30	1.34	1.33	1.42	1.36	1.37	1.37
T site	4.00	4.00	4.00	4.00	4.00	4.00	4.00	4.00	4.00	4.00	4.00	4.00	4.00	4.00	4.00	4.00
#Al VI	1.49	1.48	1.49	1.55	1.46	1.46	1.48	1.40	1.37	1.41	1.34	1.55	1.22	1.38	1.30	1.35
#Ti	-	0.00	0.01	-	0.02	0.01	0.01	-	-	0.00	0.00	-	-	-	0.00	-
#Fe +3	-	-	0.00	-	0.00	0.00	0.00	-	-	-	0.00	0.00	0.00	-	0.00	-
#Fe +2	2.19	2.24	2.24	2.25	2.35	2.21	2.37	2.33	4.09	4.03	4.00	3.71	2.73	2.62	3.05	2.91
#Mn +2	0.03	0.02	0.02	0.02	0.02	0.03	0.02	0.03	0.02	0.02	0.05	0.04	0.04	0.03	0.03	0.02
#Mg	2.26	2.24	2.19	2.09	2.10	2.27	2.09	2.19	0.46	0.45	0.47	0.55	1.83	1.79	1.35	1.58
#Ca	-	-	-	-	-	-	0.00	0.01	0.01	0.02	-	0.01	0.01	-	0.01	-
#Na	-	0.04	0.01	0.07	0.04	0.04	0.04	0.04	0.03	0.02	0.00	0.06	0.05	0.06	0.00	0.09
#K	-	0.00	0.00	0.01	0.01	0.01	-	0.01	0.03	-	0.25	-	0.49	0.29	0.58	0.21
O site	5.97	6.02	5.96	5.99	6.00	6.02	6.02	6.02	6.01	5.96	6.12	5.92	6.37	6.16	6.32	6.16
#O	10.00	10.00	10.00	10.00	10.00	10.00	10.00	10.00	10.00	10.00	10.00	10.00	10.00	10.00	10.00	10.00
#OH	8.00	8.00	8.00	8.00	8.00	8.00	8.00	8.00	8.00	8.00	8.00	8.00	8.00	8.00	8.00	8.00
#F	-	-	-	-	-	-	-	-	-	-	-	-	-	-	-	-
#Cl	-	-	-	-	-	-	-	-	-	-	-	-	-	-	-	-

EPMA Analyses - Chlorite - Deformed vein margin association

Sample 18-26 and 10-29 marginal to D2 ribbon gold-quartz vein

	18-26c	18-26d	18-26e	18-26f	18-26g	18-26h	18-26i	18-26j	18-26k	18-26l	-29a14	0-29aD	0-29aE	0-29aF	18-26a	18-26b
SiO2	26.62	26.37	26.70	26.33	26.73	25.46	26.73	26.38	26.10	25.90	25.90	24.01	23.73	25.48	27.12	26.18
TiO2	0.27	-	-	0.02	0.05	0.27	0.10	0.12	-	-	0.23	-	0.02	-	-	0.10
Al2O3	21.59	21.60	22.11	22.32	21.65	20.80	21.77	21.92	21.94	21.07	23.47	21.41	20.36	22.60	21.96	23.00
Fe2O3	-	-	-	0.00	-	0.00	-	-	-	0.00	0.00	0.00	0.00	-	0.00	-
FeO	24.43	25.55	25.98	25.39	24.49	24.25	25.12	25.28	25.07	26.29	27.34	28.27	27.66	30.74	25.70	25.80
MnO	0.15	0.23	0.22	0.24	0.12	0.25	0.42	0.22	0.09	0.56	0.29	0.32	0.19	0.31	0.16	0.49
MgO	15.85	16.25	16.70	16.56	16.91	16.26	16.90	16.42	15.95	15.50	15.97	12.78	12.93	12.31	16.57	16.30
CaO	0.02	-	0.01	-	0.05	0.28	0.01	0.04	0.15	0.04	0.04	0.09	-	-	0.03	-
Na2O	0.38	0.36	0.38	0.49	0.32	0.50	0.24	0.42	0.41	0.49	0.54	0.53	0.49	0.17	0.28	0.46
K2O	-	-	3.48	-	2.31	2.75	-	-	-	-	-	4.73	-	-	-	-
H2O	11.57	11.50	11.28	11.51	11.42	11.32	11.53	11.52	11.52	11.41	11.42	10.96	11.26	11.24	11.53	11.49
F	-	-	-	-	-	-	-	-	-	-	-	-	-	-	-	-
Cl	-	-	-	-	-	-	-	-	-	-	-	-	-	-	-	-
O=F	-	-	-	-	-	-	-	-	-	-	-	-	-	-	-	-
O=Cl	-	-	-	-	-	-	-	-	-	-	-	-	-	-	-	-
Total	100.89	101.86	106.85	102.87	104.05	102.14	102.84	102.31	101.24	101.26	105.19	103.11	96.64	102.86	103.34	103.83
#Si IV	2.73	2.69	2.63	2.66	2.68	2.63	2.69	2.68	2.68	2.68	2.57	2.54	2.63	2.63	2.72	2.62
#Al IV	1.27	1.31	1.37	1.34	1.32	1.37	1.31	1.32	1.32	1.32	1.43	1.46	1.37	1.37	1.28	1.38
T site	4.00	4.00	4.00	4.00	4.00	4.00	4.00	4.00	4.00	4.00	4.00	4.00	4.00	4.00	4.00	4.00
#Al VI	1.34	1.29	1.21	1.31	1.25	1.17	1.28	1.30	1.33	1.26	1.31	1.20	1.28	1.39	1.31	1.33
#Ti	0.02	-	-	0.00	0.00	0.02	0.01	0.01	-	-	0.02	-	0.00	-	-	0.01
#Fe +3	-	-	-	0.00	-	0.00	-	-	-	0.00	0.00	0.00	0.00	-	0.00	-
#Fe +2	2.10	2.18	2.14	2.14	2.06	2.10	2.12	2.15	2.15	2.28	2.27	2.50	2.56	2.66	2.15	2.16
#Mn +2	0.01	0.02	0.02	0.02	0.01	0.02	0.04	0.02	0.01	0.05	0.02	0.03	0.02	0.03	0.01	0.04
#Mg	2.43	2.47	2.46	2.49	2.53	2.51	2.54	2.48	2.44	2.39	2.36	2.01	2.13	1.90	2.48	2.43
#Ca	0.00	-	0.00	-	0.01	0.03	0.00	0.00	0.02	0.00	0.00	0.01	-	-	0.00	-
#Na	0.08	0.07	0.07	0.10	0.06	0.10	0.05	0.08	0.08	0.10	0.10	0.11	0.11	0.03	0.06	0.09
#K	-	-	0.44	-	0.30	0.36	-	-	-	-	-	0.64	-	-	-	-
O site	5.98	6.04	6.33	6.06	6.21	6.31	6.03	6.04	6.03	6.08	6.09	6.50	6.10	6.01	6.01	6.06
#O	10.00	10.00	10.00	10.00	10.00	10.00	10.00	10.00	10.00	10.00	10.00	10.00	10.00	10.00	10.00	10.00
#OH	8.00	8.00	8.00	8.00	8.00	8.00	8.00	8.00	8.00	8.00	8.00	8.00	8.00	8.00	8.00	8.00
#F	-	-	-	-	-	-	-	-	-	-	-	-	-	-	-	-
#Cl	-	-	-	-	-	-	-	-	-	-	-	-	-	-	-	-

EPMA Analyses - Chlorite - Deformed vein margin and undeformed lava association

Sample 10-2 undeformed mafic lava, 10-29 marginal to D2 ribbon vein

	10-2-5	0-2-10	0-2-12	10-2-1	10-2-2	10-2-3	10-2-4	0-29a2	0-29a3	0-29a4	-29a10	-29a11	-29a12	-29a13
SiO2	26.73	26.27	27.48	26.67	26.90	25.71	28.13	26.41	24.20	25.25	24.37	24.46	24.40	23.67
TiO2	0.03	-	0.13	-	0.03	0.10	0.02	0.08	-	0.02	-	0.10	0.06	0.02
Al2O3	19.26	19.81	20.40	21.49	20.20	21.81	20.55	22.14	21.62	21.13	23.00	20.78	21.52	21.42
Fe2O3	0.00	-	0.00	0.00	0.00	-	-	-	0.00	0.00	0.00	-	0.00	0.00
FeO	21.32	21.89	22.42	23.68	21.07	22.27	22.26	25.15	28.55	28.48	26.57	26.61	28.19	29.85
MnO	0.33	0.45	0.19	0.38	0.41	0.56	0.14	0.04	0.19	0.19	0.11	0.12	0.16	0.06
MgO	19.22	18.77	19.82	16.68	17.75	17.46	18.51	12.32	13.48	14.03	15.11	14.05	13.46	12.06
CaO	0.13	0.06	0.07	0.45	0.25	0.40	0.15	0.12	0.08	-	0.03	0.06	-	0.06
Na2O	0.48	0.38	0.65	0.63	0.59	0.45	0.81	0.55	0.43	0.31	0.47	0.47	0.78	0.39
K2O	0.41	4.76	3.84	-	2.02	4.02	-	-	-	0.57	-	-	4.69	2.51
H2O	11.64	11.32	11.41	11.57	11.48	11.35	11.69	11.54	11.27	11.27	11.40	11.36	10.99	11.03
F	-	-	-	-	-	-	-	-	-	-	-	-	-	-
Cl	-	-	-	-	-	-	-	-	-	-	-	-	-	-
O=F	-	-	-	-	-	-	-	-	-	-	-	-	-	-
O=Cl	-	-	-	-	-	-	-	-	-	-	-	-	-	-
Total	99.56	103.71	106.42	101.56	100.70	104.13	102.26	98.35	99.81	101.27	101.07	98.01	104.25	101.08
#Si IV	2.77	2.67	2.69	2.72	2.78	2.60	2.82	2.80	2.58	2.65	2.53	2.64	2.54	2.54
#Al IV	1.23	1.33	1.31	1.28	1.22	1.40	1.18	1.20	1.42	1.35	1.47	1.36	1.46	1.46
T site	4.00	4.00	4.00	4.00	4.00	4.00	4.00	4.00	4.00	4.00	4.00	4.00	4.00	4.00
#Al VI	1.12	1.04	1.05	1.30	1.23	1.19	1.24	1.56	1.30	1.26	1.35	1.29	1.18	1.26
#Ti	0.00	-	0.01	-	0.00	0.01	0.00	0.01	-	0.00	-	0.01	0.00	0.00
#Fe +3	0.00	-	0.00	0.00	0.00	-	-	-	0.00	0.00	0.00	-	0.00	0.00
#Fe +2	1.85	1.86	1.84	2.02	1.82	1.88	1.86	2.23	2.55	2.50	2.31	2.40	2.45	2.68
#Mn +2	0.03	0.04	0.02	0.03	0.04	0.05	0.01	0.00	0.02	0.02	0.01	0.01	0.01	0.01
#Mg	2.97	2.84	2.90	2.53	2.73	2.63	2.76	1.95	2.14	2.19	2.34	2.26	2.09	1.93
#Ca	0.01	0.01	0.01	0.05	0.03	0.04	0.02	0.01	0.01	-	0.00	0.01	-	0.01
#Na	0.10	0.07	0.12	0.13	0.12	0.09	0.16	0.11	0.09	0.06	0.10	0.10	0.16	0.08
#K	0.05	0.62	0.48	-	0.27	0.52	-	-	-	0.08	-	-	0.62	0.34
O site	6.13	6.49	6.42	6.06	6.23	6.40	6.05	5.87	6.10	6.11	6.11	6.08	6.52	6.31
#O	10.00	10.00	10.00	10.00	10.10	10.00	10.00	10.00	10.00	10.00	10.00	10.00	10.00	10.00
#OH	8.00	8.00	8.00	8.00	7.90	8.00	8.00	8.00	8.00	8.00	8.00	8.00	8.00	8.00
#F	-	-	-	-	-	-	-	-	-	-	-	-	-	-
#Cl	-	-	-	-	-	-	-	-	-	-	-	-	-	-

EPMA Analyses - Chlorite - Deformed vein margin association

Sample 20-21 marginal to D2 ribbon vein

	20-21i	0-21ii	-12iii	10-25	20-21i	0-21ii	-21iii	0-21iv
SiO2	26.54	23.70	25.76	24.80	26.33	26.74	26.40	24.95
TiO2	0.38	-	0.19	0.09	-	-	0.11	-
Al2O3	23.56	20.87	22.42	21.50	23.34	24.34	23.44	25.01
Fe2O3	0.00	0.00	0.00	-	-	-	0.00	-
FeO	26.24	26.39	27.38	30.73	25.95	26.62	24.98	23.08
MnO	0.17	0.24	-	-	-	-	-	-
MgO	15.14	13.29	13.92	11.05	17.32	17.28	16.52	16.78
CaO	-	0.19	0.04	0.06	-	-	0.10	-
Na2O	0.61	0.63	0.53	0.14	0.04	0.00	0.06	0.01
K2O	-	-	-	-	-	-	-	-
H2O	11.50	11.33	11.41	11.20	11.53	11.53	11.58	11.66
F	-	-	-	-	-	-	-	-
Cl	-	-	-	-	-	-	-	-
O=F	-	-	-	-	-	-	-	-
O=Cl	-	-	-	-	-	-	-	-
Total	104.15	96.63	101.64	99.56	104.51	106.53	103.21	101.50
#Si IV	2.67	2.59	2.66	2.67	2.61	2.59	2.64	2.52
#Al IV	1.33	1.41	1.34	1.33	1.39	1.41	1.36	1.48
T site	4.00	4.00	4.00	4.00	4.00	4.00	4.00	4.00
#Al VI	1.46	1.27	1.39	1.39	1.33	1.37	1.40	1.50
#Ti	0.03	-	0.01	0.01	-	-	0.01	-
#Fe +3	0.00	0.00	0.00	-	-	-	0.00	-
#Fe +2	2.21	2.41	2.36	2.77	2.15	2.16	2.09	1.95
#Mn +2	0.01	0.02	-	-	-	-	-	-
#Mg	2.27	2.16	2.14	1.77	2.55	2.50	2.46	2.53
#Ca	-	0.02	0.00	0.01	-	-	0.01	-
#Na	0.12	0.13	0.11	0.03	0.01	0.00	0.01	0.00
#K	-	-	-	-	-	-	-	-
O site	6.10	6.02	6.02	5.98	6.04	6.02	5.98	5.99
#O	10.28	9.76	10.00	10.00	10.00	10.00	10.00	10.00
#OH	7.72	8.24	8.00	8.00	8.00	8.00	8.00	8.00
#F	-	-	-	-	-	-	-	-
#Cl	-	-	-	-	-	-	-	-

EPMA Analyses - Sericite - Mineralisation and deformed vein margin association

Sample 10-25 associated with Au grains, 18-26 marginal to D2 ribbon vein, mica1-4 from sample 10-29 marginal to D2 ribbon vein

	mica1	mica2	mica3	mica4	10-25i	0-25ii	-25iii	18-26i	8-26ii
SiO2	44.46	45.97	49.25	49.36	46.15	46.46	46.17	49.25	49.36
TiO2	0.36	0.29	0.45	0.33	0.45	0.25	0.48	0.45	0.33
Al2O3	30.92	33.33	34.48	32.38	30.99	34.20	31.81	34.48	32.38
Cr2O3	-	-	-	-	-	-	-	-	-
Fe2O3	-	0.00	0.00	0.00	0.00	0.00	0.00	0.00	-
FeO	6.99	1.31	2.31	1.76	2.20	1.68	3.66	2.31	1.76
MnO	-	-	-	-	-	-	-	-	-
MgO	4.33	1.17	1.20	1.71	1.52	0.95	0.21	1.20	1.71
Li2O	-	-	-	-	-	-	-	-	-
BaO	-	-	-	-	-	-	-	-	-
CaO	0.15	0.10	0.25	0.17	0.65	0.66	0.21	0.25	0.17
Na2O	0.52	0.14	0.53	0.08	0.33	0.34	-	0.53	0.34
K2O	8.79	11.09	11.19	11.74	12.01	9.89	9.78	11.19	11.74
Rb2O	-	-	-	-	-	-	-	-	-
Cs2O	-	-	-	-	-	-	-	-	-
H2O	4.39	4.50	4.49	4.49	4.43	4.52	4.49	4.49	4.49
F	-	-	-	-	-	-	-	-	-
Cl	-	-	-	-	-	-	-	-	-
O=F	-	-	-	-	-	-	-	-	-
O=Cl	-	-	-	-	-	-	-	-	-
Total	100.91	97.90	104.15	102.01	98.75	98.95	96.82	104.15	102.27
#Si IV	6.01	6.26	6.31	6.46	6.32	6.24	6.38	6.31	6.45
#Al IV	1.99	1.74	1.69	1.54	1.68	1.76	1.62	1.69	1.55
#Fe IV	-	-	-	-	-	-	-	-	-
#Ti IV	-	-	-	-	-	-	-	-	-
T site	8.00	8.00	8.00	8.00	8.00	8.00	8.00	8.00	8.00
#Al VI	2.94	3.62	3.51	3.45	3.33	3.64	3.57	3.51	3.43
#Ti VI	0.04	0.03	0.04	0.03	0.05	0.03	0.05	0.04	0.03
#Cr	-	-	-	-	-	-	-	-	-
#Fe +3	-	0.00	0.00	0.00	0.00	0.00	0.00	0.00	-
#Fe +2	0.79	0.15	0.25	0.19	0.25	0.19	0.42	0.25	0.19
#Mn +2	-	-	-	-	-	-	-	-	-
#Mg	0.87	0.24	0.23	0.33	0.31	0.19	0.04	0.23	0.33
#Li	-	-	-	-	-	-	-	-	-
O site	4.64	4.03	4.03	4.00	3.94	4.05	4.08	4.03	3.99
#Ba	-	-	-	-	-	-	-	-	-
#Ca	0.02	0.01	0.03	0.02	0.10	0.09	0.03	0.03	0.02
#Na	0.14	0.04	0.13	0.02	0.09	0.09	-	0.13	0.09
#K	1.52	1.93	1.83	1.96	2.10	1.69	1.73	1.83	1.96
#Rb	-	-	-	-	-	-	-	-	-
#Cs	-	-	-	-	-	-	-	-	-
A site	1.67	1.98	1.99	2.00	2.28	1.88	1.76	1.99	2.07
#O	20.00	20.00	20.00	20.00	20.00	20.00	20.00	20.00	20.00
#OH	4.00	4.00	4.00	4.00	4.00	4.00	4.00	4.00	4.00

EPMA Analyses - Epidote - Undeformed lava association

Sample 10-2 massive lava, 10-18 slightly foliated lava

	10-2i	10-2ii	0-2iii	10-2iv	10-2v	10-2vi	0-2vii	10-18i	0-18ii	-18iii	0-18iv	18-10i	8-10ii	-10iii
SiO2	39.69	39.00	39.29	38.80	40.45	39.77	39.32	36.77	38.39	38.39	39.08	38.76	40.32	40.44
TiO2	0.13	0.09	0.05	-	0.03	0.02	0.02	0.02	0.12	0.15	-	0.09	0.17	0.23
Al2O3	26.75	26.27	24.74	24.65	27.82	28.55	25.13	23.43	27.43	24.84	26.42	27.93	28.66	28.72
Fe2O3	8.97	8.64	11.93	12.41	8.77	6.46	12.56	11.14	9.13	10.39	9.15	6.67	6.98	7.03
Mn2O3	-	-	-	-	-	-	-	-	-	-	-	-	-	-
FeO	-	-	-	0.03	-	-	0.03	-	0.04	-	-	-	-	-
MnO	0.13	0.12	0.08	0.11	-	-	0.12	0.05	0.34	-	0.08	0.03	-	0.15
CaO	24.05	24.17	23.89	22.82	24.94	24.55	22.98	22.23	23.11	23.58	23.84	24.08	24.22	24.29
Na2O	0.17	0.06	0.12	-	0.02	0.15	0.07	-	0.12	-	0.03	-	0.04	-
H2O	1.95	1.92	1.94	1.91	2.00	1.96	1.94	1.82	1.93	1.89	1.93	1.92	1.98	1.99
TOTAL	101.82	100.28	102.03	100.73	104.03	101.47	102.17	95.45	100.62	99.24	100.52	99.49	102.38	102.85
	-	-	-	-	-	-	-	-	-	-	-	-	-	-
#Si IV	3.04	3.04	3.04	3.04	3.03	3.04	3.03	3.04	2.98	3.04	3.04	3.02	3.05	3.04
#Al IV	-	-	-	-	-	-	-	-	0.02	-	-	-	-	-
Z site	3.04	3.04	3.04	3.04	3.03	3.04	3.03	3.04	3.00	3.04	3.04	3.02	3.05	3.04
#Al VI	2.42	2.41	2.25	2.27	2.46	2.57	2.28	2.28	2.49	2.32	2.42	2.57	2.55	2.55
#Fe +3	0.52	0.51	0.69	0.73	0.49	0.37	0.73	0.69	0.53	0.62	0.53	0.39	0.40	0.40
#Mn +3	-	-	-	-	-	-	-	-	-	-	-	-	-	-
#Ti	0.01	0.01	0.00	-	0.00	0.00	0.00	0.00	0.01	0.01	-	0.01	0.01	0.01
#Fe +2	-	-	-	0.00	-	-	0.00	-	0.00	-	-	-	-	-
#Mn +2	0.01	0.01	0.00	0.00	-	-	0.00	0.00	0.01	-	0.00	0.00	-	0.01
Y site	2.95	2.93	2.96	3.01	2.95	2.94	3.02	2.98	3.04	2.95	2.96	2.96	2.96	2.97
#Mn +3	-	-	-	-	-	-	-	-	-	-	-	-	-	-
#Mn +2	0.00	0.00	0.00	0.00	-	-	0.00	0.00	0.01	-	0.00	0.00	-	0.00
#Fe +2	-	-	-	0.00	-	-	0.00	-	0.00	-	-	-	-	-
#Ca	1.98	2.02	1.98	1.91	2.00	2.01	1.90	1.97	1.92	2.00	1.98	2.01	1.96	1.96
#Na	0.02	0.01	0.02	-	0.00	0.02	0.01	-	0.02	-	0.00	-	0.01	-
X site	2.00	2.03	2.00	1.92	2.01	2.03	1.91	1.97	1.95	2.00	1.99	2.01	1.97	1.96
#O	12.00	12.00	12.00	12.00	12.00	12.00	12.00	12.00	12.00	12.00	12.00	12.00	12.00	12.00
#OH	1.00	1.00	1.00	1.00	1.00	1.00	1.00	1.00	1.00	1.00	1.00	1.00	1.00	1.00
Total*	20.99	21.00	20.99	20.96	20.99	21.00	20.96	20.98	20.99	20.98	20.99	21.00	20.97	20.97

Atomic %	19HG1 (1)						19HG1 (2)									30-2 (3)	
Au	79.20	79.01	80.01	78.70	79.10	78.95	79.52	78.21	79.70	77.88	78.91	78.50	78.72	79.12	76.94	71.70	71.46
Ag	19.60	20.01	19.82	19.92	19.80	20.20	18.81	19.01	19.70	21.00	19.01	19.61	19.70	18.20	19.92	24.32	24.70
Fe							0.35	0.92	1.01	0.65	0.71	0.82	0.76	0.65	2.55	3.20	2.82
Cu	0.60	0.35	0.75	1.01	0.75	0.48									0.76		
Total	99.40	99.37	100.58	99.63	99.65	99.63	98.68	98.14	100.41	99.53	98.63	98.93	99.18	97.97	100.17	99.22	98.98

Table 1 - Gold Grains (1 = free, 2 = py hosted, 3 = py fracture hosted)

At.%	20-14			18-1							10-29				
Fe	1.47	1.56	1.55	4.84	4.98	4.66	4.72	4.91	4.52	5.01	10.58	10.10	10.71	10.47	11.01
S	48.25	48.50	47.59	48.26	48.41	49.25	49.10	48.77	48.35	48.10	36.81	40.01	38.20	36.10	36.02
Zn	50.22	49.68	50.57	46.53	46.18	45.53	45.91	46.20	46.60	45.81	51.68	52.01	52.75	52.32	52.40
Total	99.94	98.74	99.71	99.63	99.57	99.44	99.73	99.88	99.47	98.92	97.57	102.12	101.66	98.89	99.43

Table 2 - Sphalerite grains (20-14 free grains, 18-1 py-po associated, 10-29 py-po associated)

At.%	30-2				10-29						
Fe	47.60	46.82	47.85	47.50	47.01	46.90	45.50	47.55	46.87	47.21	46.20
S	51.82	53.21	52.50	52.21	52.20	53.01	52.82	52.91	53.20	52.18	51.80
Ni	0.30	0.18	0.20	0.17	0.54	0.51	0.52	0.48	0.57	0.52	0.53
Total	98.72	100.21	100.55	99.88	99.75	100.42	98.84	100.94	100.64	99.91	97.03

At %	18-1		19HG1
Fe	1.75	1.72	2.01
S	14.97	15.01	14.81
Ag	1.17	1.20	1.72
Pb	82.10	81.70	82.51
Total	99.99	99.63	101.05

Table 3a (left) & 3b (right) - 3a shows pyrrhotite grains (30-2 vein, 10-29 wallrock), 3b shows galena grains (18-1 vein, 19HG1 enclosed in gold-bearing pyrite)

At.%	19HG1																	
As	29.88	30.92	30.38	29.27	29.40	29.47	28.97	30.12	29.00	30.17	26.05	30.38	30.26	30.79	31.00	28.62	30.77	29.78	28.41
S	35.88	34.96	35.08	36.30	36.25	36.32	37.56	35.98	36.62	35.52	40.52	35.39	35.77	35.06	34.80	37.79	35.54	36.45	37.39
Fe	34.01	33.82	33.96	33.66	33.96	33.88	33.37	33.79	33.73	33.89	33.12	33.96	33.70	33.83	33.96	33.43	33.19	33.57	33.93
Total	99.77	99.70	99.42	99.23	99.61	99.67	99.90	99.89	99.35	99.58	99.69	99.73	99.73	99.68	99.77	99.84	99.50	99.80	99.73

Table 4 - Arsenopyrite grains (19HG1 grains in pyrite which also hosts pyrrhotite and gold grains)

APPENDIX III

ANALYSIS OF WHOLEROCK SAMPLES BY ICP-AES

1. The moisture content (H_2O-) and loss on ignition (LOI) of samples were determined before fusion of the samples for ICP analysis.

2. % H_2O- is determined by heating the sample (about 4 gm, accurately weighed into a porcelain crucible) overnight at 110 °C.

3. After the % H_2O- has been determined, 0.2500 +/- 0.00-1 g of the dried sample is weighed into a clean porcelain crucible. This was then used for the ICP preparation.

4. The remainder of the dried powder was then reweighed and the % LOI was determined on this portion. The % LOI is determined by heating the dried sample from room temperature to 950 °C in a muffle furnace and keeping at 950 °C overnight.

5. Before weighing samples after drying and ignition they were allowed to cool to room temperature in a dessicator for at least 3 hours.

6. If the LOI of a sample was greater than 5%, it was fused for ICP analysis by inserting the graphite crucible containing the flux-powder mixture into a cold furnace which was then heated to 1000 °C. Fusion was at 1000 °C for 20 minutes.

7. Before any flux weighings were made, the Spectroflux 100B was dried at 450 °C for 4 hours. The dried Spectroflux 100B was then stored in an efficient dessicator.

8. Samples prepared for ICP analysis were numbered in a manner consistent with XRF preparation numbers. Each sample was given a four figure analysis number (A-No) which lay between 2000 and 7990 and ended with a zero. Duplicate preparations were given the same numbers as the original sample, but ending with a 3 instead of a zero; a second duplicate has the same number but ending with a 6.

9. In every set of 30 samples 4 in-house reference materials were included. A blank solution and five duplicate preparations were also be analysed together with the main batch of samples. (Total number of unknown solutions analysed = 40).

SAMPLE PREPARATION

Procedure
Weigh 0.2500 =/- 0.0001 g of dried (110 °C) sample, previously ground to pass a 200 mesh sieve, into a clean porcelain crucible and mix intimately with 0.7500 =/- 0/0003 g of Spectroflux 100B (80% $LiBO_2$, 20% $Li_2B_4O_7$) using a plastic stirring rod. Transfer the mixture completely, using a narrow spatula and a small brush, to a pre-ignited graphite crucible and fuse at 1000 °C in an electric muffle furnace for 20 minutes. Carefully remove the crucible from the furnace and rotate it slowly so that the molten bead swirls round inside the crucible combining with any smaller beads. Pour the red-hot bead into a 400 ml plastic beaker containing 25 ml of 2N HNO_3 and 150 ml water.

Dissolve the shattered bead by using a magnetic stirrer without any heat for 30 minutes. When the graphite crucible has cooled examine it carefully to see if any small beads are adhering to the internal surfaces. If any are found, which only rarely happens, dislodge then with a spatula and add them to the solution in the beaker. Transfer this solution, when the bead has completely dissolved, to a clean 250 ml volumetric flask. Rinse the beaker thoroughly with water and add the rinsings to the flask. Dilute to volume and shake well to mix. Filter the solution through a Whatman 12.5 cm No. 41 filter paper into a plastic bottle. Seal the bottle well with a piece of plastic placed under the cap.

NOTES

1. The prepared solutions were analysed by ICP for:-

SiO_2, Al_2O_3, Fe_2O_3T, MgO, CaO, Na_2O, K_2O, P_2O_5, TiO_2, MnO, Ba, Be, Co, Cr, Cu, La, Ni, Sr, V, Zn, Zr.

2. Data Reduction

The ICP programme will normalise each reading obtained to that of a particluar chosen drift value which is then used as the reference drift value. This means that all drift analyses will be identical in the printed output. This procedure in some way compensates for long-term fluctuations in the sensitivity of the machine. A calibration line is then set up using a group or groups of standards (run as the programme menu prompts). This will relate the mV intensity of a particular element to its recommended concentration. A measurement of the closeness to linearity of this line is its correlation coefficient, r. For the major elements (Si, Al, Fe, Mg, Ca, Na, K), r should be close to 0.9999. This calibration line is then used to calculate element concentrations in the sample from the corrected (or normalised) mV values.

3. Analytical results

The results obtained must be treated with caution, as a number of factors will affect their reliability and accuracy.

(i) Ferrous Iron

ICP analyses report iron as total iron expressed as Fe_2O_3.

(ii) Trace Elements

Precision of trace elements (ppm) is as follows:-

Ba - +/- 10	Be - +/- 0.2	Cu - +/- 15
Cr - +/- 15	La - +/- 10	Ni - +/- 20
Sr - +/- 10	V - +/- 15	Zn - +/- 15
Zr - +/- 20		

(iii) SiO_2 Analysis

Silica, being the major component of most samples, will be the most critical element in the analysis. Samples analysed in duplicate should have SiO_2 values within 0.5% absolute. Samples which have low totals <99.0% (after the inclusion of all significant trace elements) should be re-prepared and re-analysed. In these cases the SiO_2 value calculated will almost certainly be too low and be the main cause of the low total.

Patchway Lava Samples

	Ave. Mafic Formation[1]	15-1	15-2	10-18	10-6	18-8	10-2
%							
SiO_2	50.50	47.23	43.20	49.53	48.77	42.26	48.02
Al_2O_3	14.00	14.70	13.53	14.47	13.78	13.01	13.49
Fe_2O_3	11.50	14.24	11.29	12.03	11.79	11.47	11.09
MgO	7.34	9.42	7.59	7.73	7.81	7.75	6.71
CaO	11.60	7.94	9.29	9.01	10.33	11.00	13.98
Na_2O	2.05	1.82	1.54	2.54	2.69	2.01	0.79
K_2O	0.06	0.06	0.04	0.05	0.08	0.02	0.04
P_2O_5		0.09	0.06	0.07	0.07	0.07	0.07
TiO_2	0.65	0.73	0.66	0.71	0.67	0.63	0.64
MnO		0.20	0.17	0.18	0.18	0.18	0.17
LOI	2.15	4.35	8.89	3.60	3.06	11.73	4.62
Total	99.80	100.78	101.24	99.93	99.22	100.12	99.61
ppm							
Ba	110	11	10	13	23	19	12
Cr	338	405	366	391	379	359	365
Co	50	62	53	60	48	52	46
La	4	14	13	3	0	8	3
Ni	122	190	200	173	181	169	171
Sr	82	83	67	179	115	65	200
Zr	100	54	51	37	35	34	37

Table showing wholerock analyses of mafic lava samples from Patchway mine. For comparison, 1 is the published average analysis of the Mafic Formation of the Upper Bulawayan (from Condie & Harrison 1976)

wt%	SiO_2	Al_2O_3	Fe_2O_3	MgO	CaO	Na_2O	K_2O	P_2O_5	TiO_2	MnO	LOI	Total
18-11	52.27	12.71	15.02	3.80	8.94	2.18	0.80	0.21	1.87	0.21	1.82	99.82
10-3	47.59	12.83	16.77	5.18	8.12	1.32	0.06	0.28	2.57	0.24	4.65	99.60
10-37	47.82	14.22	15.93	6.07	4.71	2.28	0.07	0.26	2.60	0.21	5.33	99.51

ppm	Ba	Be	Cr	Cu	La	Ni	Sr	Zn	Zr	Co	V
18-11	240	1.7	37	94	22	29	255	118	164	41	352
10-3	24	1.6	69	191	<1	47	271	150	190	42	360
10-37	37	1.7	77	211	<1	40	114	140	196	40	363

Table showing whole-rock ICP analyses of late mafic dyke phases at Patchway.

ICPNO	Sample	SiO2	Al2O3	Fe2O3	MgO	CaO	Na2O	K2O	P2O5	TiO2	MnO	LOI	Total
2120	s15/1	47.23	14.7	14.24	9.42	7.94	1.82	0.06	0.09	0.73	0.2	4.35	100.78
2130	s15/2	43.2	13.53	11.29	7.59	9.29	1.54	0.04	0.06	0.66	0.17	8.89	101.24
2110	S1500/1	49.11	13.93	11.53	6.98	13.04	0.98	0.07	0.07	0.67	0.18	3.21	99.77
2280	S1500/H/1	39.9	11.71	8.98	7.08	14.55	0.02	1	0.08	0.53	0.12	14.39	98.81
2240	S1500/H/2	49.03	12.73	9.83	4.18	9.48	0.1	2.39	0.06	0.61	0.13	9.95	98.49
2190	S1500/H/3	61.99	8.33	11.04	3.45	6.91	0.02	0.67	0.06	0.4	0.12	7.39	100.4
2220	S1500/H/4	58.67	16.23	10.6	2.96	1.72	0.07	3.49	0.05	0.82	0.06	4.77	99.43
2140	S1500/H/6	45.97	13.07	10.94	6.8	9.85	0.33	1.16	0.06	0.63	0.14	8.89	101.24
2200	S1500/A	54.42	9.18	11.44	3.49	8.89	0.05	1.19	0.05	0.46	0.13	8.68	97.99
2260	S1500/B	44.28	14.01	11.11	4.82	10.81	0.07	2.02	0.05	0.68	0.2	11.76	99.82
2180	S1500/C	39.77	12.72	10.35	6.26	13.99	0.04	1.41	0.06	0.61	0.14	3.21	99.82
2270	S1500/D	43.51	13.64	10.55	7.99	10.34	0.05	1.24	0.05	0.64	0.14	12.21	100.36
2150	S1500/F	44.06	13.29	10.76	8.89	9.61	0.35	0.73	0.05	0.64	0.15	11.96	100.5
2170	S500/2	39.47	13.61	13.85	3.58	12.07	0.06	2.62	0.05	0.67	0.14	12.78	98.9
2250	S500/4	41.87	13.17	11.22	5.71	12.74	0.02	1.7	0.07	0.64	0.15	13.36	100.67
2160	S500/6	44.85	12.57	10.07	4.61	12.44	0.04	1.93	0.04	0.62	0.13	12.43	99.73
2300	S500/A	54.69	7.42	8.92	3.77	11.72	0.03	0.9	0.02	0.46	0.13	10.89	99.04
2290	S500/B	44.9	13.54	13.91	5.56	8.42	0.07	1.46	0.08	0.83	0.16	10.25	99.19
2230	S500/F	46.9	16.77	10.01	4.7	7.05	0.12	3.18	0.09	1.04	0.16	9.3	99.32

ICPNO	Sample	Ba	Be	Cr	Cu	La	Ni	Sr	V	Zn	Zr	Co	Distance from vein
2120	s15/1	11	0.6	405	105	14	190	83	266	125	54	62	-20
2130	s15/2	10	0.5	366	226	13	200	67	242	82	51	53	-10
2110	S1500/1	9	0.5	372	151	11	168	173	242	87	53	47	-5
2280	S1500/H/1	67	0.4	296	66	12	117	124	196	85	55	43	0.2
2240	S1500/H/2	158	0.7	340	117	14	131	75	228	61	47	44	0.4
2190	S1500/H/3	63	0.4	236	229	18	99	53	183	78	50	23	0.6
2220	S1500/H/4	225	0.8	445	91	10	188	30	286	59	48	84	0.8
2140	S1500/H/6	129	0.8	361	132	11	184	73	235	77	51	50	1.2
2200	S1500/A	93	0.6	261	122	12	108	71	182	72	44	33	-0.2
2260	S1500/B	136	0.6	374	188	7	148	80	245	83	47	41	-0.4
2180	S1500/C	134	0.5	343	176	13	154	96	224	127	50	48	-0.6
2270	S1500/D	112	0.6	360	134	11	160	76	243	121	47	51	-0.8
2150	S1500/F	135	0.5	384	144	16	293	75	227	137	50	54	-1.2
2170	S500/2	170	0.9	351	189	15	140	82	243	102	54	58	0.4
2250	S500/4	120	0.5	344	108	15	155	80	228	102	54	49	0.8
2160	S500/6	190	0.4	322	137	9	148	70	218	95	48	46	1.2
2300	S500/A	60	0.5	135	73	12	94	75	143	83	51	24	-0.2
2290	S500/B	105	0.6	265	121	9	177	56	264	84	60	45	-0.4
2230	S500/F	296	0.8	308	143	8	167	58	331	68	60	53	-1.2

Table showing whole-rock ICP geochemical analyses of deformed mafic lavas marginal to the D2 ribbon quartz vein at Patchway. The final column, bottom right, indicates the sample distance from the ribbon vein margin in metres.

ICPNO	Sample	SiO2	Al2O3	Fe2O3	MgO	CaO	Na2O	K2O	P2O5	TiO2	MnO	LOI	Total
2020	LH6	70.59	15.32	2.23	0.85	3.13	4.96	1.64	0.09	0.28	0.02	1.03	100.15
2010	LH4	74.67	14.19	1.04	0.33	0.96	4.47	4.28	0.04	0.18	0.01	0.64	100.82
2030	S400/8	75.94	13.23	0.97	0.34	1.8	0.59	3.95	0.05	0.08	0.01	2.78	99.74
2060	S400/1	71.41	14.09	1.89	0.72	2.72	4.42	2.08	0.09	0.27	0.02	2.59	100.29
2050	S400/13	73.92	13.83	1.08	0.35	1.07	4.49	2.26	0.05	0.13	0	1.68	98.87
2070	S2400/N/1	74.2	13.88	1.26	0.45	1.43	5.66	1.44	0.06	0.15	0.01	1.45	100
2080	EM1	64.48	16.68	1.24	0.93	2.82	1.14	3.34	0.08	0.25	0.03	5.16	100.15
2090	GV14	73.79	14.6	1.67	0.9	0.98	0.09	4.6	0.08	0.22	0	2.69	99.61
2100	S2400/1	75.26	11.68	1.36	0.37	2.97	4.07	1.61	0.04	0.07	0.02	2.69	100.15
2210	B10/2	75.61	14.36	1.16	0.53	1.12	0.55	4.41	0.05	0.08	0.01	2.51	100.37

ICPNO	Sample	Ba	Be	Cr	Cu	La	Ni	Sr	V	Zn	Zr	Co
2020	LH6	413	1.2	23	31	24	16	306	31	48	108	7
2010	LH4	553	2.1	12	33	41	12	177	20	66	100	9
2030	S400/8	371	0.8	7	94	10	0.2	30	11	66	65	6
2060	S400/1	367	1	17	40	30	15	130	34	72	122	9
2050	S400/13	353	0.7	9	16	21	7	57	14	21	85	4
2070	S2400/N/1	320	0.9	9	32	29	4	61	18	31	97	8
2080	EM1	239	0.7	15	15	18	3	100	31	17	113	7
2090	GV14	566	1.5	14	8	24	13	49	26	20	103	8
2100	S2400/1	231	0.7	11	34	21	3	73	12	20	63	7
2210	B10/2	366	1.5	9	42	25	6	35	30	28	76	5

wt%	SiO_2	Al_2O_3	Fe_2O_3	MgO	CaO	Na_2O	K_2O	P_2O_5	TiO_2	MnO	LOI	Total
10-5	69.37	14.40	2.13	0.80	2.94	3.91	2.11	0.10	0.26	0.02	3.12	99.38
10-1	68.86	14.51	2.42	0.90	3.15	4.14	1.98	0.15	0.32	0.03	3.18	99.62
18-12	69.12	14.26	2.04	0.92	3.09	3.71	2.24	0.12	0.29	0.02	3.30	99.09

ppm	Ba	Be	Cr	Cu	La	Ni	Sr	Zn	Zr	Co	V
10-5	256	0.8	18	12	11	6	137	50	110	5	15
10-1	232	0.9	14	15	20	36	143	51	124	9	20
18-12	207	0.9	17	19	10	32	135	42	114	9	14

Table showing whole-rock ICP geochemical analyses of both undeformed and deformed felsic intrusive rocks from Patchway. Samples marked with a circle are considered "undeformed" (see sample descriptions Appendix I)

British Geological Survey - Geochemistry Directorate

PW 1404/10 & PW1480/10 X-ray Fluorescence Analysis

Notes on XRF analysis:~

Lower limits of detection are shown in Table 1. They are theoretical values for the concentration equivalent to three standard deviations above the background count rate for the analyte in a silica matrix.

No value is shown where background subtraction is not used. High instrumental stability results in practical values for these materials approaching the theoretical. They may however be adversely affected to a considerable extent by line overlap and interelement effects in other matrices and may not be reported to the precision shown in Table 1. Maximum limits of calibration for each element are also shown in Table 1.

In any method in which random emission of electromagnetic energy is measured and in which background subtraction is employed, negative results should occur for zero (or close to zero) concentrations of an element. Removal of these values from a data set creates a positive bias. Very negative values may however be caused by other factors and they are normally removed or corrected after a repeated determination. Screening cannot be done in this way for values greater than zero and so a small positive bias may occur.
Printouts and computer files may contain negative codes which are explained in Table 2.

In the case of tungsten determinations certain lanthanides interfere and as a caution a cerium determination is provided as an indication of the presence of these elements.

For bismuth determinations an indication is given, on the printout only, of the equivalent apparent concentration of thorium.

M.N.I. & T.K.S. 16-Dec-87

Table 1.

Element	Lower Limit of Detection (ppmw)	Maximum Limit of Calibration (%w)
Ca		40
Ti		40
V	1	2.0
Cr	1	2.5
Mn		1
Fe		70
Co	1	2.0
Ni	1	1.0
Cu	1	1.0
Zn	1	1.0
Rb	1	1.0
Sr	1	1.0
Y	1	1.0
Zr	1	5.0
Nb	1	1.0
Mo	1	.15
Ag	2	1.0
Sn	2	1.0
Sb	2	1.0
Ba	5	69.0
La	2	2.5
Ce	7	20.0
Pb	3	1.0
Th	1	1.0
U	2	1.0
As	1	1.0
W	1	.3
Bi	2	.25

M.N.I. & T.K.S. 16-Dec-87

Table 2.

Code	Comment
-95	Not determined because of high concentration; exceeds calibration limit.
-96	Not determined because of interference; probably of high concentration.
-97	Not determined because of interference; probably of low concentration.
-98	Not determined because of interference; no estimate.
-99	Absent data e.g. not requested.

British Geological Survey

Geochemistry Directorate

PW1480 X-Ray Fluorescence Major Element Analysis (%)

Sample	SiO2 %	TiO2 %	Al2O3 %	Fe2O3t %	MnO %	MgO %	CaO %	Na2O %	K2O %	P2O5 %	Cr2O3 %	LOI %	Total %
JCRH1020	75.51	0.06	13.84	1.16	0.020	0.37	1.74	0.84	3.97	0.04	0.002	2.56	100.11
JCRH1021	75.37	0.06	13.53	1.35	0.026	0.46	2.17	1.36	3.45	0.04	0.000	2.85	100.67
JCRH1021A	95.81	0.03	1.56	1.27	0.013	0.07	0.94	0.00	0.47	0.02	0.007	0.96	101.15>
JCRH1026	74.38	0.08	12.93	1.80	0.031	0.34	2.52	0.45	3.85	0.05	0.000	3.28	99.71
JCRH1028	53.99	1.03	21.70	5.24	0.034	0.98	3.38	0.10	6.93	0.06	0.068	5.39	98.90<
JCRH1031	100.60	0.00	0.71	0.20	0.004	0.00	0.19	0.00	0.21	0.00	0.003	0.32	102.24>
JCRH1032A	97.24	0.00	1.60	0.39	0.011	0.02	0.70	0.00	0.46	0.00	0.003	0.78	101.20>
JCRH1033	73.92	0.17	12.95	1.63	0.026	0.58	2.66	0.10	3.96	0.05	0.002	3.53	99.58
JCRH1034	76.16	0.18	14.01	2.09	0.015	0.92	0.72	0.10	4.14	0.07	0.003	2.54	100.95
JCRH1812	69.93	0.30	14.50	1.99	0.026	0.91	3.07	3.68	2.20	0.09	0.001	3.40	100.10

16-OCT-89 10:09
File: JIM

British Geological Survey

Report list: TRACESA3

Geochemistry Directorate

PW 1404 & PW 1480 X-Ray Fluorescence Analysis

Jim's Specials

Sample	U ppm	Ti %	Mn %	Fe %	V ppm	Cr ppm	Co ppm	Ni ppm	Cu ppm	Zn ppm	Rb ppm	Sr ppm
JCRH1020	1	0.033	0.020	0.79	4	7	2	-1	2	22	130	32
JCRH1021	2	0.033	0.023	0.89	3	12	2	1	3	17	126	41
JCRH1021A	2	0.024	0.012	0.84	20	51	8	10	81	7	17	8
JCRH1026	4	0.039	0.030	1.18	7	14	5	4	65	31	116	36
JCRH1028	0	0.455	0.029	2.90	262	476	71	168	35	17	222	31
JCRH1031	1	0.006	0.003	0.12	6	15	2	-1	6	1	7	3
JCRH1032A	2	0.007	0.008	0.25	4	18	1	0	3	2	14	7
JCRH1033	1	0.087	0.026	1.11	11	12	5	3	7	28	115	31
JCRH1034	3	0.091	0.014	1.37	23	8	4	4	1	21	132	17
JCRH1812	2	0.145	0.025	1.39	19	21	6	3	7	42	69	139

Sample	Y ppm	Zr ppm	Nb ppm	Mo ppm	Ag ppm	Sn ppm	Sb ppm	Ba ppm	La ppm	Ce ppm	Pb ppm	Th ppm
JCRH1020	2	62	3	3	1	-1	0	342	9	17	9	2
JCRH1021	3	60	4	-1	-1	-1	2	310	10	14	12	4
JCRH1021A	1	2	1	-0	1	-2	1	30	1	1	9	0
JCRH1026	4	57	1	0	2	1	3	287	12	11	25	3
JCRH1028	6	49	2	4	5	-1	5	586	3	-13<	22	2
JCRH1031	0	-0	1	0	1	-0	4	14	-3	4	10	-1
JCRH1032A	-0	6	1	1	1	0	2	34	1	-3	15	-1
JCRH1033	3	96	2	0	-0	0	1	330	13	21	7	3
JCRH1034	2	98	2	1	0	-1	2	299	15	21	7	4
JCRH1812	3	127	3	0	1	-0	-2	159	10	18	5	1

Table showing whole-rock XRF analyses of mainly felsic rocks from Patchway. Sample numbers are here prefaced JCRH.

APPENDIX IV

THE LINKAM HEATING/FREEZING STAGE AND CALIBRATION

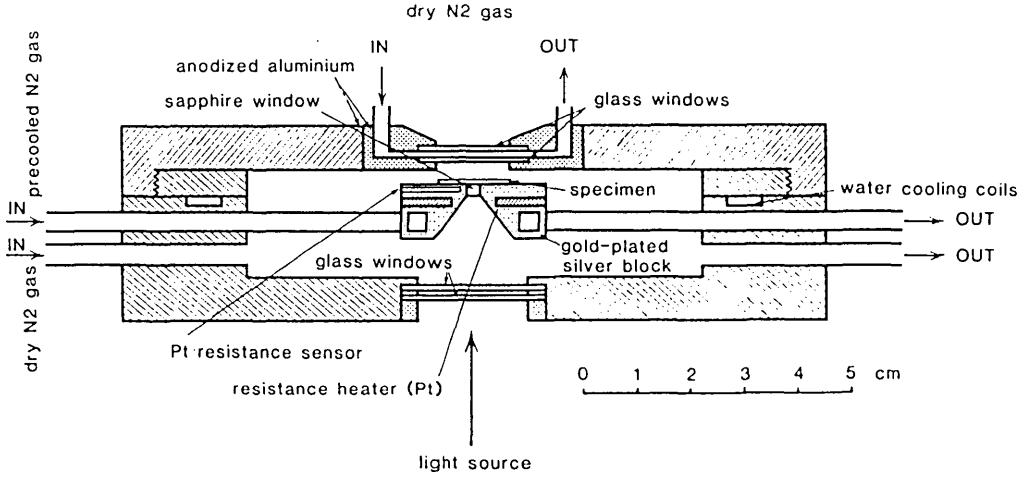
Microthermometry of fluid inclusions was performed on two heating and freezing stages, the Linkam TH600 and the Linkam THM600. These stages both have essentially the same components and differ only in the style of sample change procedure (Figure IV.1). The fluid inclusion wafer rests on a small silver block within a chamber in which an oxygen free atmosphere is maintained. The sample is heated by means of a platinum resistance heater within the silver block and cooled by N_2 gas. During the first phase of laboratory work the N_2 gas was cooled after flowing through a copper coil immersed in liquid nitrogen. In following experiments a cryogenic device was added (Rankin *et al.*, 1990) and this consists of a small pump which draws liquid nitrogen from a two litre dewar into the stage unit where it is vapourised. This adaption of standard equipment allows higher cooling to be obtained, reduces icing-up problems in the stage window and reduces the amount of liquid nitrogen used during an experimental session.

Temperatures are measured by a platinum resistance sensor mounted in the thermal block below the sample and as a consequence of this actual temperatures in the fluid inclusion will not equate with recorded temperature. This is due to several cumulative factors:-

i) temperature gradients exist across the sapphire window on which the sample sits. These gradients have been quantified at high temperature, e.g. at 400 °C errors are in the order of 4 °C, which is negligible for homogenization purposes.

ii) small thermal gradients exist within the thickness of the sample. Wafers in this study were prepared to 50-90 m thickness and slow heating rates were employed at critical temperatures to minimise any errors (estimated <0.1 °C) introduced as a consequence of this effect.

Calibration of each heating and freezing stage was done at regular intervals. Initially, the stage was calibrated by reference to the known melting points of chemical compounds. As a result the difference between the true melting point of a particular substance could be calibrated against the temperature recorded by the visual display on the control panel of the THM600. Towards the end of the study, synthetic inclusions made by Dr. J. Wilkinson provided more reliable and reproducible calibration points. Typical calibration curves are shown in Figure IV.2.



Cross-section of Linkam stage.

Fig IV.1

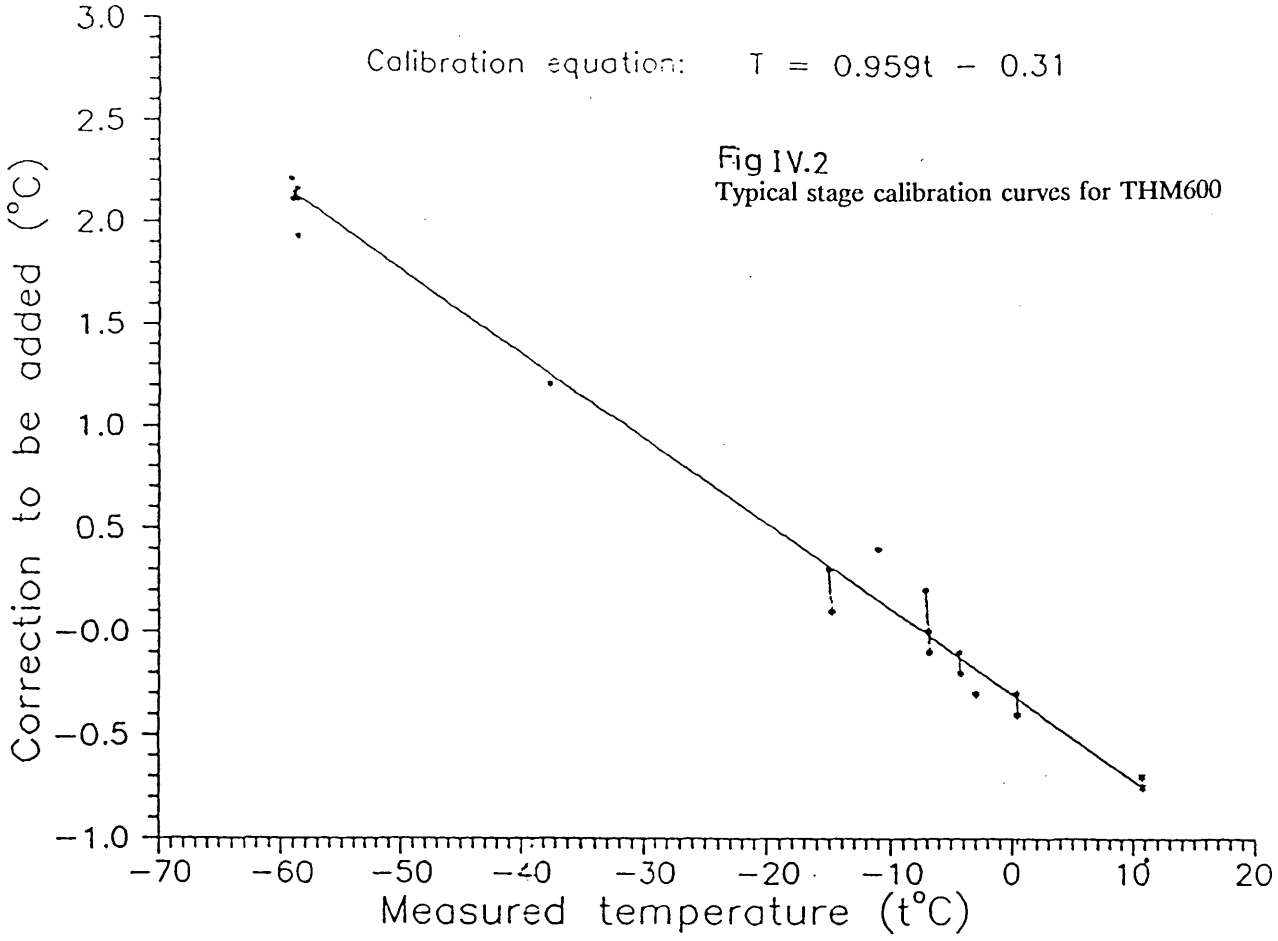
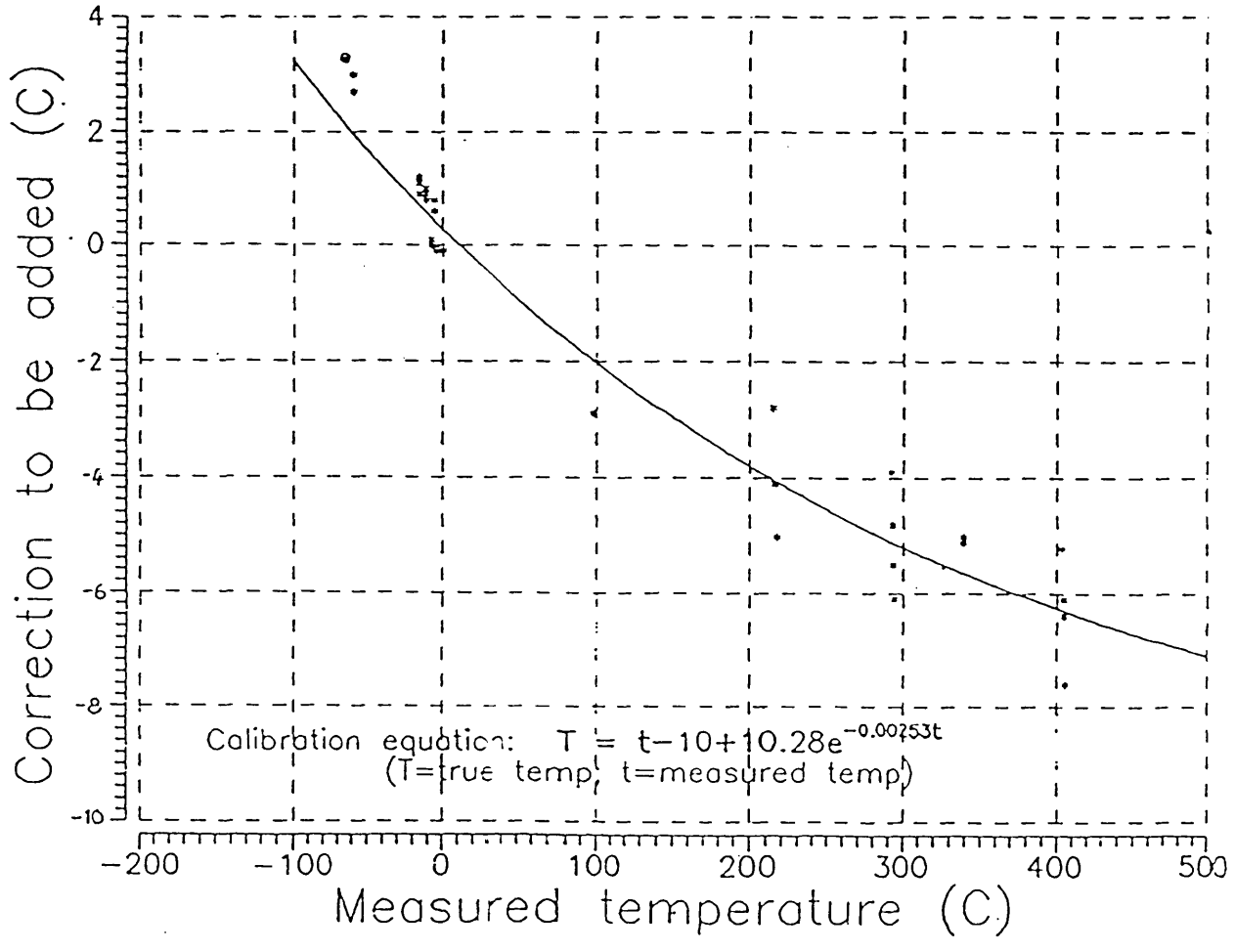


Fig IV.2
Typical stage calibration curves for THM600



CORRECTED MICROTHERMOMETRY RESULTS

TYPE 1 AQUEOUS INCLUSIONS - All total homogenisations to liquid phase

	Sample	TmI	Thtot	DegFill	Teut
1	s12l1	-7.9	184.3	0.70	
2		-3.0	133.9	0.75	
3		-2.3	141.8	0.80	
4		-1.7	177.2	0.80	
5		-1.9	152.3	0.75	
6		-1.5	153.0	0.80	
7		-1.2	163.9	0.80	
8		-3.4	146.9	0.85	
9		-2.5	143.6	0.90	
10		-2.0	169.0	0.85	
11		-1.9	151.6	0.80	
12		-7.9	184.3		
13		-3.0	133.9		
14		-2.3	141.8		
15		-1.7	177.2		
16		-1.9	152.3		
17		-1.5	153.0		
18		-1.2	163.9		
19		-3.4	146.9		
mx		-2.5	143.6		
21		-2.0	169.0		
22		-1.9	151.6		
23	s12q1	-3.6	156.8	0.90	-38.1
24		-2.7	188.3		
25		-2.3	180.2		
26		-1.9	159.4		
27		-3.3	161.5		
28		-3.1	160.9		
29		-2.9	162.6		
30		-2.9	163.3		
31		-2.6	175.0		
32		-2.7	171.4		
33		-2.6	162.0		
34		-2.2	162.8		
35		-1.6	134.7		
36		-5.1	137.5		
37		-3.7	142.2		
38		-2.7	150.0		
39		-2.1	158.0		
40	s12q3	-1.5	162.1		
41		-1.6	164.7		
42		-7.9	184.3	0.80	
43		-3.0	133.9	0.90	
44		-2.3	141.8	0.75	
45		-1.7	177.2	0.70	
46		-1.9	152.3	0.70	
47		-1.5	153.0	0.75	
48		-1.2	163.9	0.80	
49		-3.4	146.9	0.90	
50		-2.5	143.6	0.90	
51		-2.0	169.0	0.90	
52	s12q2	-1.9	151.6	0.85	
53		-3.6	156.8	0.85	
54		-2.7	188.3	0.90	
55		-2.3	180.2	0.85	
56		-1.9	159.4	0.90	
57		-3.3	161.5	0.95	
58		-3.1	160.9	0.90	
59		-2.9	162.6	0.85	
60		-2.9	163.3	0.85	
61		-2.6	175.0	0.90	
62		-2.7	171.4	0.90	

TYPE 1 AQUEOUS INCLUSIONS (cont.)

	Sample	TmI	Thtot	DegFill
63	s12q2	-2.6	162.0	0.90
64		-2.2	162.8	0.90
65		-1.6	134.7	0.85
66		-5.1	137.5	0.80
67		-3.7	142.2	0.90
68		-2.7	150.0	0.95
69		-2.1	158.0	0.95
70		-1.5	162.1	0.90
71		-1.6	164.7	0.90
72		-2.0	165.8	0.90
73		-2.5	162.5	0.90
74		-2.4	172.9	0.90
75		-2.1	165.9	0.85
76		-0.5	161.8	0.90
77		-3.5	162.1	0.85
78		-1.5	176.2	0.80
79		-1.4	165.4	0.90
80		-3.7	167.9	0.90
81		-3.1	170.9	0.95
82		-2.7	174.2	0.90
83		-6.4	141.2	0.85
84		-4.2	150.3	0.85
85		-6.0	142.6	0.90
86		-2.3	132.0	0.85
87		-3.1	151.0	0.85
88		-3.5	132.5	0.85
89		-0.5	165.0	0.90
90		-3.4	164.5	0.70
91		-2.1	162.4	0.75
92		-1.8	148.5	0.70
93		-0.7	159.2	0.70

TYPE 2B AQUEOUS INCLUSIONS - All total homogenisations to liquid phase

	Sample	DegFill	TmI	Thtot	Teut
1	s10-35a			350.	
2				359.	
3				311.	
4			-4.1	356.	
5				333.	
6				324.	
7				330.	
8	s10-21	0.70	-0.9	403	
9		0.85	-12.5	294.	
10		0.90	-6.0	272.	
11			-4.6	370.	
12			-3.6		
13			-3.2	309.	
14	s18-23	0.70	-4.8	255.	
15			-4.8	236.	-41.5
16	s10-35a	0.70	-3.2	258.	
17		0.85	-7.0	252.	
18	s20-21			314.	
19				333.	
20	s20-13	0.90	-0.6	294.	
21		0.90	-2.0	235.	
22	s19hg1	0.90	-2.5	282.	
23	6006/b	0.85	-3.5	321.	
24	6006/d	0.70	-0.8	286.	
25			-3.0	236.	
26	6006/a	0.80	-1.9	242.	
27	6007/b	0.95	-0.5	285.	
28	s8a1	0.80	-1.4	251.	

TYPE 2C AQUEOUS INCLUSIONS - All total homogenisations to liquid phase

	Sample	DegFill	TmI	Thtot	Teut
1	10-35a	0.80	-13.8	133.0	
2		0.90	-13.8	131.0	
3		0.90	-14.0	129.0	
4		0.90	-13.9	130.0	
5				136.0	
6	10-25a	0.90	-12.2	128.0	
7		0.90	-13.5	138.0	
8		0.80	-14.6	144.0	
9		0.95	-14.0	134.0	
10		0.80	-14.8	138.0	
11		0.90	-14.8	138.0	
12		0.80	-15.4	142.0	
13		0.90	-15.9	140.0	
14				124.0	
15	10-35	0.95	-7.0	145.0	
16			-16.1	104.0	
17		0.95	-12.8	139.0	
18		0.90	-13.1	141.0	-49.0
19		0.95	-13.6	134.0	
20		0.95	-13.2	140.0	
21	10-21	0.85	-12.5	294.0	
22		0.90	-8.4	158.0	
23		0.90	-8.5	166.0	
24		0.80	-9.8	183.0	
25		0.90	-10.8	213.0	
26	10-40		-2.3	164.0	
27	10-32b	0.95	-3.1	161.0	-41.0
28	10-21		-7.2	141.0	
29			-6.8	140.0	
30	18-24		-4.5	153.0	-36.8
31	10-21u		-8.1	92.9	
32		0.95	-6.5	127.0	
33	10-35a	0.98	-19.9	137.0	
34		0.95	-18.5	123.0	-57.0
35		0.95	-9.8	129.0	
36		0.97	-12.8	144.0	-31.9
37		0.98	-13.9	127.0	-38.3
38	10-31u		-6.5	127.0	
39	20-21b	0.95	-7.6	168.0	-27.6?
40		0.80	-11.7	167.0	
41		0.80	-9.9	219.0	
42		0.80	-7.5	200.0	
43		0.85	-11.9	155.0	-35.6
44			-13.9	149.0	
45	20-13a	0.85	-30.6	131.0	-48.5
46		0.80	-22.4	128.0	
47			-19.9	140.0	
48		0.90	-13.3	135.0	
49		0.80	-27.1	150.0	-47.9
50		0.85	-25.6	129.0	
51			-27.9	121.5	-53.0
52		0.90	-24.8	150.0	
53		0.85	-18.6	138.0	
54		0.80	-29.5	129.0	
55			-28.9	129.0	
56		0.90	-20.0		-56.5
57		0.80	-19.5		-47.9
58			-18.6	160.0	
59			-19.0		
60		0.80	-11.3	208.0	-41.3
61		0.90	-4.7	228.0	
62		0.80	-5.8	233.0	-32.5
63			-3.5	161.0	
64	30-2	0.95	-1.6	129.0	
65	10-25a		-5.5	148.0	

TYPE 2C AQUEOUS INCLUSIONS (cont.)

	Sample	DegFill	TmI	Thtot	Teut.
66	10-25a		-5.1	141.0	
67		0.90	-4.3	148.0	
68				149.0	
69	20-21	0.80	-11.3	158.0	-39.4
70			-10.2		
71	12q1	0.95	-9.8	120.0	-59.1?
72			-15.7	127.0	
73			-10.0	133.6	
74			-9.6	135.4	
75			-9.5	130.8	
76			-9.3	127.0	
77			-9.6	147.2	
78			-9.5	138.2	
79			-9.1	121.8	
80			-8.9	160.2	
81			-10.9	137.6	
82			-8.7	135.4	
83			-8.4	133.6	
84			-9.1	152.7	
85			-6.4	155.2	
86			-13.0	158.6	
87			-15.7	127.2	-34.5

TYPE 3B AQUEOUS INCLUSIONS - All total homogenisations to liquid phase

	Sample	DegFill	TmI	Thtot	Teut
1	400/14a	0.9	-8.2	188	-52
2		0.9	-8.4	227	
3		0.9	-7.5	147	
4		0.9	-7.8	183	
5		0.9	-10.1	148	
6		0.8	-9.8	152	-53
7		0.7	-9.2	155	
8		0.8	-9.1	178	
9		0.9	-8.3	134	
10		0.9	-8.2	146	
11		0.9	-9.1	153	
12		0.9	-8.1	149	
13		0.9	-7.9	190	
14		0.9	-8.3	162	
15		0.9	-7.9	147	
16				152	
17				147	
18				161	

TYPE 4 AQUEOUS INCLUSIONS - All total homogenisations to liquid phase

	Sample	DegFill	TmI	Thtot	Teut	Thm
1	26-11	0.8	-10.7	137		
2		0.9	-12.1			
3			-14.9	125	-48.9	
4			-12.3		-46.8	
5			-11.0			
6			-10.0	140		
7			-11.6			
8			-11.1			
9					-53.8	
10			-11.8	129		
11			-10.3	134	-50.9	
12			-10.6	131		
13			-8.7			

TYPE 4 AQUEOUS INCLUSIONS (cont.)

	Sample	DegFill	TmI	Thtot	Teut	Thm
14			-10.7			
15			-9.1	142		
16			-11.1			
17			-10.9			
18			-15.0	130		
19	20-13	0.9	-3.5	154		
20	26-11	0.9	-9.4	124		
21			-9.7	125		
22			-10.9	130		
23			-9.6	128		
24			-9.1	134		
25			-11.4	121		
26			-10.5	107		
27			-10.3	125		
28			-10.4	120	-49.1	
29			-11.2	126		
30			-16.7	112		
31			-11.9	127		
32			-11.4	111		
33			-37.2	108	-67.6?	
34			-10.0	66		
35			-9.2	124		
36	1800-3	0.8	-6.5	135		
37			-6.0	165		
38			-5.8	138		
39			-11.4	146		
40			-15.2	148		
41			-7.8	138		
42			-7.4	139		
43			-7.2	142		
44			-6.9	151		
45			-5.2	144		
46			-4.8	148		
47			-14.9	151		
48			-13.8	164		
49			-12.7	165		
50			-12.4	134		
51			-12.1	148		
52			-9.2	165		
53			-7.5	154		
54			-6.9	138		
55			-6.3	166		
56			-6.0	158		
57			-5.4	146		
58			-5.1	149		
59			-18.2	132		
60			-17.0	107		
61			-15.3	92		
62			-6.4	181		
63			-6.1	162		
64			-5.8	147		
65			-7.0	112		
66			-5.8	123		
67			-5.2	165		
68			-7.8	152		
69			-10.7	145		
70			-9.3	161		
71			-7.9	123		
72			-3.8	147		
73			-6.2	158		

TYPE 4 AQUEOUS INCLUSIONS (cont.)

	Sample	DegFill	TmI	Thtot	Teut	Thm
74	1800/3	0.8	-5.8	122		
75			-4.6	165		
76	26-14		-6.5	123		
77			-8.4	145		
78			-7.3	131		
79			-10.9	142		
80			-12.1	138		
81			-9.6	142		
82			-7.5	141		
83			-8.1	147		
84			-7.2	151		
85			-5.7	132		
86			-6.8	141		
87			-7.2	130		
88			-12.1	118		
89			-13.7	119		
90			-12.3	142		
91			-10.9	137		
92			-11.1	117		
93			-13.4	147		
94			-11.3	138		
95				121		
96				131		
97				154		
98				112		
99				144		
100				121		
101				132		
102	26-2		-12.1	142		
103			-6.8	99		
104			-9.1	110		
105			-9.5	137		
106			-7.2	168		
107			-8.7	153		
108			-9.5	133		
109			-11.2	145		
110			-8.1	137		
111			-7.5	131		
112			-8.2	138		
113			-11.8	152		
114			-12.1	141		
115			-10.9	152		
116			-13.1	142		
117			-11.0	118		
118			-13.2	137		
119	20-13	0.9	-21.1	136	-52.0	-23.2
120		0.9	-19.3	142	-50.3	-22.5
121	26-11	0.9	-9.5	131	-42.7	-22.0
122		0.8	-11.1	141	-38.2	-22.4
123		0.9	-14.8	154	-41.0	-22.8
124	20-21	0.9	-10.6	121	-37.5	-22.4
125	1800/3	0.8	-11.1	142	-38.0	-21.8

TYPE 6 AQUEOUS INCLUSIONS - All total homogenisations to liquid phase

	Sample	DegFill	TmI	Thtot
1	LH7	0.95	-10.5	160.0
2		0.90	-7.5	155.2
3		0.95	-6.5	147.6
4		0.85	-9.8	139.2
5		0.90	-10.1	150.1
6		0.90	-8.7	145.2
7		0.90	-3.5	144.0
8		0.90	-6.3	184.7

TYPE 6 AQUEOUS INCLUSIONS (cont.)

	Sample	DegFill	TmI	Thtot	Teut
9		0.90	-5.7	182.8	
10		0.90	-4.8	170.0	
11		0.90	-7.1	168.0	
12		0.95	-5.4	145.8	
13		0.95	-5.2	131.3	
14		0.95	-4.6	126.9	
15		0.85	-3.9	136.8	
16		0.85	-3.4	139.2	
17		0.90	-6.2	148.0	
18		0.95	-6.8	171.6	
19		0.95	-6.7	173.5	
20		0.90	-6.3	181.5	
21		0.90	-5.6	186.5	
22		0.95	-4.5	152.5	
23		0.85	-3.7	141.2	
24		0.90	-7.1	150.6	
25		0.85	-6.5	168.2	
26		0.85	-3.5	145.2	
27		0.95	-8.7	173.0	
28		0.90	-6.2	168.0	
29		0.90	-4.5	139.7	
30		0.90	-4.6	171.6	

AQUEOUS-CARBONIC INCLUSIONS (n.b. Homogenisations are given to L, liquid; V, vapour; and C, critical phase as shown by "Hom to" column following homogenisation temperature)

TYPE 2A AQUEOUS-CARBONIC INCLUSIONS

	Sample	DegAqFill	TmCO2	TmClath	ThCO2	Hom to	Thtot	Hom to
1	s10-40	0.50	-57.6	6.1	22.7	L		
2		0.60	-56.9	6.3	20.7	L	287	L
3		0.70	-56.7	4.8	22.9	L		
4		0.65	-56.7	6.9	14.0	L		
5		0.30	-57.8	6.6	23.5	L		
6	s18-23B	0.70	-59.0	9.1	20.3	L		
7		0.65		2.0	26.0	L		
8		0.70	-57.5	7.5	13.3	L		
9	S10-32B	0.70	-58.2	9.3	10.5	L		
10		0.50	-60.1	9.4	10.7	L		
11		0.65	-59.1	8.9	11.4	L		
12		0.40	-62.6	5.7	9.5	L		
13		0.35	-59.0	10.1	6.1	L		
14		0.60	-57.8	8.9	16.4	L		
15		0.50	-59.4	7.4	42.6	L		
16	S10-35B	0.70	-65.7	15.8	-10.4	L		
17		0.60	-65.6	12.9	-23.3	L		
18		0.50	-67.7	14.8	-25.8	L		
19	S20-21B	0.60	-65.2	10.0	0.1	L		
20		0.50	-63.0	10.5	5.1	L		
21		0.65	-62.6	10.5	4.5	L		
22		0.70	-59.2					
23		0.35	-61.1					

TYPE 2A (cont.)

	Sample	DegAqFill	TmCO2	TmClath	ThCO2	Hom to	Thtot	Hom to
24	S20-21B	0.70	-61.2	6.3	12.8	L		
25		0.60	-63.8	6.4	10.9	L		
26		0.80	-62.5	8.4	9.2	L		
27		0.75	-62.2	6.0	9.3	L		
28		0.45	-63.0	8.5	4.6	L		
29		0.50	-61.2	9.1	19.3	L		
30		0.65	-62.1	13.2	-3.0	L	240	D
31		0.60	-59.6	13.5	-6.9	L	285	L
32	S26-11	0.50	-58.0	6.5	22.3	L		
33		0.70	-58.1	6.1	24.5	L		
34		0.65	-58.7	7.8	13.5	L		
35	S19HG1	0.55		11.4	-85.4	L	290	L
36		0.50		18.9	-84.8	L	295	L
37		0.35		15.5	-85.7	L	285	V
38		0.30		18.6	-84.8	L	310	V
39		0.45		18.5	-83.2	L	317	L
40	S600/6	0.60	-57.1	10.0	26.3	L		
41		0.20	-57.3		17.0	L		
42	S600/7	0.40	-61.7		30.4	V		
43		0.70	-62.5	13.3	23.8	L		
44		0.60		15.5	23.6	L		
45		0.40	-61.2	2.5	25.9	L	235	L
46		0.40	-60.9	8.5	28.4	L	285	L
47		0.35	-61.2	8.8	28.5	V		
48		0.70	-57.1	8.0	32.2	V		
49		0.30	-58.0	7.5			220	L
50		0.60	-56.8	8.3	29.1	L	304	L
51		0.50	-60.8	7.1	26.4	L		
52		0.60	-59.8	10.1	28.8	L	240	L
53		0.70	-59.6	8.5	30.6	V	287	L
54	S600/6	0.70	-59.2	4.2	10.5	L		
55		0.45	-60.3	3.4	15.2	L		
56		0.75	-56.5	6.5	29.8	V		
57			-56.4	7.9	16.2	L		
58		0.60	-56.5	7.6	29.1	V		
59		0.50	-58.2	9.1	31.0	L		
60		0.85	-56.8	-3.5	1.2	L		
61		0.85		7.3	17.0	L		
62			-57.8		9.1	L		
63		0.40	-58.2	8.4	29.1	L		
64		0.45	-57.8	7.4	29.4	L		
65		0.45	-54.4	5.6	31.0	C	286	L
66			-56.6	15.1				
67		0.70	-57.1	8.5	30.9	C	247	L
68		0.70	-56.8	6.9	32.0	C	320	V
69		0.70	-56.9	6.7	30.8	C	302	L
70			-56.5	6.4	14.8	L		
71			-57.1	4.5				
72		0.65	-57.5	8.1	30.9	C		
73		0.75	-56.7	8.3	30.1	C	290	L
74		0.75	-56.6	11.5	28.5	L	235	L
75		0.80	-56.5	5.5	27.8	L	270	L
76			-56.9	13.8	22.0	L	256	L
77		0.80	-56.8	6.5	27.8	L	300	L
78		0.95	-56.5	8.2	4.8	L		
79		0.05	-56.5	8.3	20.8	L		
80			-57.3	1.3	8.9	L		
81		0.70	-56.5	8.5	25.8	L		
82		0.20	-56.4	4.3	23.4	L		
83	S600/8	0.20	-57.7	4.3	30.1	C		
84		0.70	-57.9	10.0	27.9	L		
85		0.70	-58.1	5.4	28.8	L		
86		0.85	-59.2	5.1	28.3	L	298	L
87		0.80	-58.1	8.0	27.9	L	305	L

TYPE 2A (cont.)

	Sample	DegAqFill	TmCO2	TmClath	ThCO2	Hom to	Thtot	Hom to
88	S600/8	0.75	-57.9	6.1	28.5	L		
89		0.25	-57.3	6.9	26.8	L	292	V
90		0.80	-56.9	7.0	27.2	L	260	L
91		0.55	-57.4	6.0	29.0	L	291	L
92		0.70	-57.1	5.9	23.5	L	298	L
93		0.60	-56.7	7.6	29.3	L	300	L
94		0.55	-56.6	6.8	26.8	L	302	V
95		0.70	-56.6	6.5	28.3	L		
96		0.50	-56.5	7.5	31.1	C		
97	S600/6	0.70	-58.8	6.9	28.4	L		
98		0.40	-58.3	7.2	27.3	L	320	V
99	A10/31	0.80	-56.8	8.8	25.3	L		
100		0.65	-60.2	9.0	-42.0	L		
101	S244/8	0.65	-68.5		16.0	L		
102		0.75	-66.2		14.2	L		
103		0.70	-64.7		15.2	L		
104	A10/23	0.75	-58.2	11.8	33.8	C		
105		0.70	-58.2	12.1	24.4	L		
106		0.70	-57.9	12.3	30.0	C	259	L
107	A10/27	0.65	-59.1	12.2	30.8	C	307	L
108		0.70	-58.9	12.3	30.0	C	309	L
109		0.65	-58.7	12.6	31.0	C	301	L
110		0.75	-59.5	11.1	29.8	L	301	L
111			-59.4	11.5	25.7	L	301	L
112	A10/30	0.70	-56.8	8.5	26.9	L	326	L
113		0.75	-57.4	8.9	23.3	L		
114		0.80	-56.9	8.6	19.8	L		
115		0.70	-57.1	8.1	19.4	L	275	L
116		0.75	-56.7	8.2	20.5	L	265	L
117		0.70	-57.1	9.2	26.0	L		
118		0.75	-56.9	7.7	23.7	L		
119		0.70	-57.3	6.5	20.7	L	265	L
120		0.50	-56.8	8.6	20.3	L	260	L
121		0.70	-56.6	7.9	25.3	L		
122		0.35	-56.6	5.7	17.3	L		
123		0.50	-57.0	7.0	20.1	L		
124		0.60	-57.1	9.1	21.4	L	304	D
125		0.70	-57.2	8.6	17.8	L		
126		0.65	-57.2	8.4	19.5	L	262	D
127		0.45	-56.9	8.2	19.0	L	270	D
128		0.50	-57.4	8.1	18.9	L	288	D
129		0.40	-57.0	7.6	27.9	L	352	L
130		0.70	-57.2	7.3	25.7	L		
131		0.75	-58.8	7.6	25.0	L		
132		0.80	-58.5	8.0	29.3	L	272	L
133		0.90	-56.8	6.8	29.0	L		

TYPE 3A AQUEOUS-CARBONIC INCLUSIONS

	Sample	DegAqFill	TmCO2	TmClath	ThCO2	Hom to	Thtot	Hom to	TmI
1	s400/14a	0.50	-57.0		29.8	L	280	L	-7.0
2		0.60	-57.3		17.4	L			
3		0.70	-57.0		12.9	L			-10.0
4	s400/21	0.70	-57.1	6.1	30.0	L			
5		0.65	-57.2	7.1	30.8	V			
6		0.65	-56.9	7.7	30.6	C	258	L	
7		0.70	-57.7	8.5	30.1	L			
8		0.65	-57.6	6.3	29.9	L			
9	s400/20	0.75	-56.9	10.7	31.3	L	325	L	
10		0.65	-60.4	10.1	26.7	L			
11		0.70	-57.8	6.7	24.9	L			
12		0.60	-57.1	10.5	28.1	L	290	L	
13		0.65	-57.1	10.5	31.1	L	295	L	

TYPE 3A (cont.)

	Sample	DegAqFill	TmCO2	TmClath	ThCO2	Hom to	Thtot	Hom to	TmI
14	400/14a	0.50	-57.0	16.1		L			-12.1
15		0.60	-57.1	23.4		L	275	L	-10.1
16		0.60	-56.8	7.2	22.7	L			
17		0.55	-56.7	6.5	24.6	L			
18		0.60	-57.0	8.8	25.2	L	269	L	
19		0.55	-56.9	5.9	23.8	L			
20		0.65	-57.2	7.6	22.2	L			
21	400/14	0.75	-57.2	9.1	30.1	V			
22		0.75	-57.1	5.9	29.9	V			

TYPE 5 AQUEOUS-CARBONIC INCLUSIONS

	Sample	DegAqFill	TmCO2	TmClath	ThCO2	Hom to	Thtot	Hom to
1	TQ3	0.7	-56.7	12.2	29.9	L	260	L
2		0.8	-56.6	9.8	25.6	L	257	L
3		0.7	-57.2	10.2	26.0	L	262	L
4		0.7	-56.8	11.0	26.1	L		
5		0.7	-56.9	9.9	27.0	L	271	L
6		0.7	-57.0	10.5	27.5	L	282	L
7		0.7	-56.6	11.0	22.0	L		
8		0.7	-57.1	10.7	26.7	L	267	L
9		0.7	-56.7	11.2	26.8	L	275	L
10		0.8	-56.8	11.3	25.7	L	242	L
11		0.7	-56.8	10.7	26.7	L		
12		0.7	-57.2	11.0	26.2	L		
13		0.7	-56.9	9.8	25.7	L	252	L
14		0.8	-57.5	10.2	25.8	L	248	L
15		0.7	-56.7	10.7	28.4	L	260	L
16		0.7	-56.8	9.7	26.3	L		
17		0.7	-56.9	10.2	27.1	L	249	L
18		0.7	-57.8	9.6	23.8	L		
19		0.7	-56.7	10.1	25.1	L		
20		0.7	-56.9	9.5	26.5	L	252	L
21		0.7	-58.2	8.7	23.6	L		
22		0.7	-57.6	10.8	27.2	L	238	L
23		0.7	-56.6	10.7	24.5	L		
24		0.6	-57.7	9.5	22.9	L		

APPENDIX V

ANALYSIS OF FLUID INCLUSION FLUIDS

V.1 Procedure for sample preparation of clean quartz chips for D-ICP, CL-ICP, stable isotope ($\delta^{18}O$) and bulk volatile analyses

Analyses of the inclusion fluids by the ICP and bulk volatile techniques required the preparation of clean quartz chips free from any contamination. The method was also employed for the preparation of quartz utilised for $\delta^{18}O$ analyses.

The samples were first crushed using a steel pestle and mortar which was cleaned after each run. The chips were then sieved and the 60 mesh to 2mm fraction retained. Approximately 5-10 grammes of this fraction was then hand picked under the binocular microscope in order to remove any contaminants such as carbonates, phyllosilicate phases and sulphides. Samples for D-ICP, stable isotope and bulk volatile analysis were then placed in concentrated Analar grade HCl at 60 °C for 8 hours. Samples for CL-ICP were washed in HNO_3 in place of HCl to avoid chloride contamination. The chips were subsequently washed in DDIW water several times and again picked under the binocular microscope. The quartz chips were then washed in 10 mol% acid (same acid as before), heated to 80 °C on a hotplate for a further 4 hours, before the chips were finally rinsed in DDIW several times. The samples were then dried overnight in an oven at 80 °C.

V.2 Time Resolved D-ICP Testwork

Time resolved D-ICP integrations were carried out with the aim of selecting the optimum spectrometer integration time for complete analysis of decrepitated inclusion fluids, liberated from the cleaned quartz chips. The furnace assembly connected to the ICP nebuliser and the special valve designed to prevent the plasma flame from extinguishing during sample change is fully described in Rankin *et al.* (1990).

Test profiles on samples selected from quartz Types 1,2 and 4 are shown on Figures V.1 to V.3 for Na and Si. Na is the dominant monovalent cation species in solution and Si should represent the quartz shards liberated during decrepitation. The x-axis shows time after introduction into the furnace, with the y-axis showing signal intensity ($\propto$ element concentration). It can be seen that a 90 second integration time is adequate to fully analyse the decrepitated aerosol from all the samples.

V.3 Crush-Leach ICP Analysis of Quartz Samples

Samples cleaned as described in V.1 were utilised for CL-ICP analysis. The procedure used is as follows:

A) Prior to use, clean agate mortar and pestle are soaked overnight in 10% Analar HNO_3.
B) Mortar is then 3x blank ground in DDIW, the third rinsing saved for analysis (procedure blank)

Then:

1) ± 2g quartz placed in mortar
2) Add 3ml DDIW
3) Grind quartz to ± 0.1mm
4) Allow to settle (20 seconds)
5) Decant leachate with disposable pipette to clean polythene tube - SOLUTION 1
6) Wash grains in further 3ml DDIW
7) Decant wash to clean polythene tube - SOLUTION 2
8) Wash grains to beaker for microscopic analysis
9) Blank grind 3x in DDIW, saving third rinse in a clean polythene tube - SOLUTION 3

Repeat steps 3) to 15) for subsequent samples

Solutions 1 to 3 are centrifuged and each solution is decanted to a new clean tube. Solution 1 is representative of the inclusion fluid, Solution 2 is taken as a check in case unexpected ICP results are recorded for Solution 1 and Solution 3 is taken to assess the "blank" response of the agate mortar.

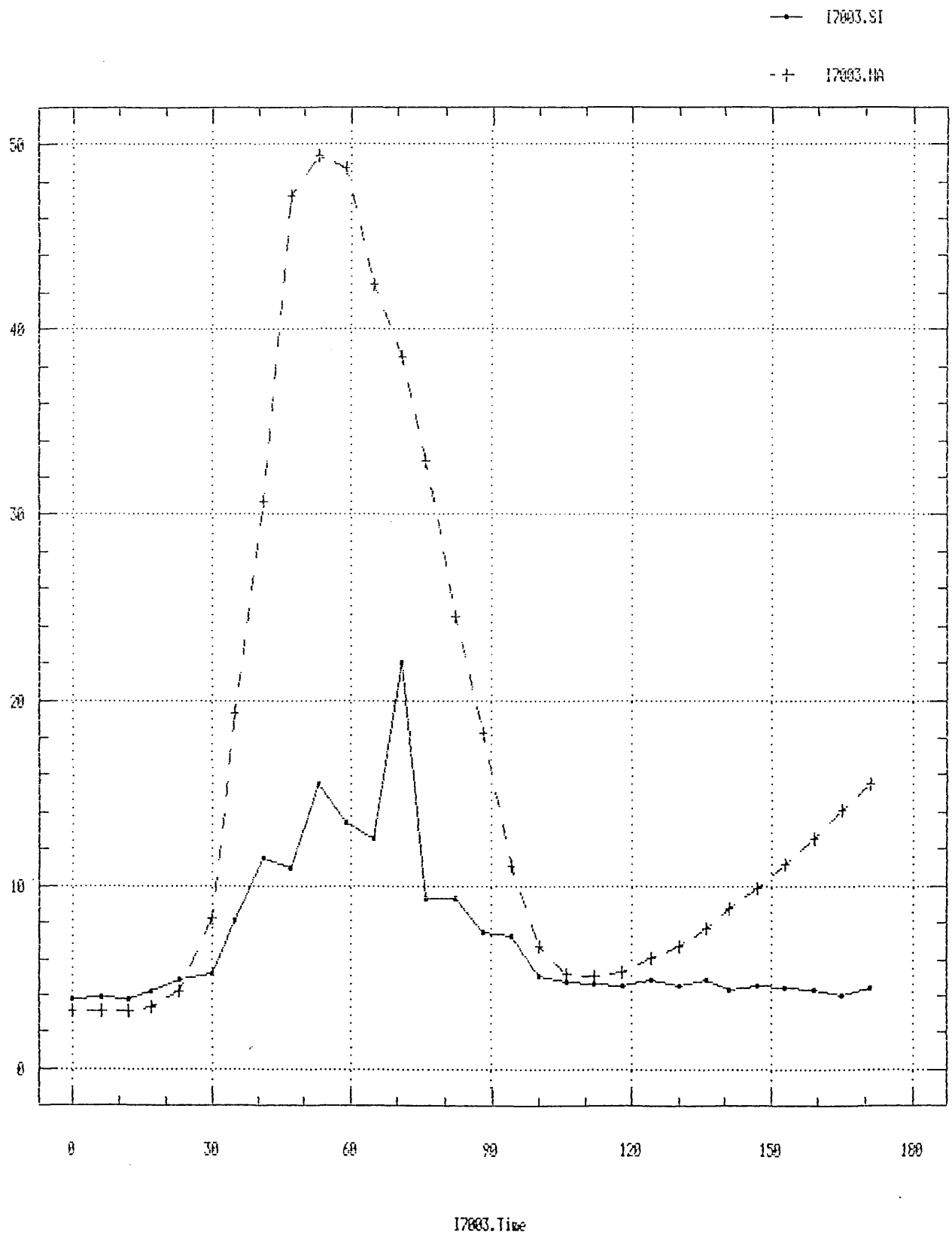
For standard CL-ICP the solutions are then acidified with 10% Analar HCl before analysing Solutions 1 and 3, together with suitable reagent "blanks" and duplicates. A series of low-concentration standard in-house solutions are also run to calibrate the ICP spectrometer.

VI.4 Chloride specific ion electrode

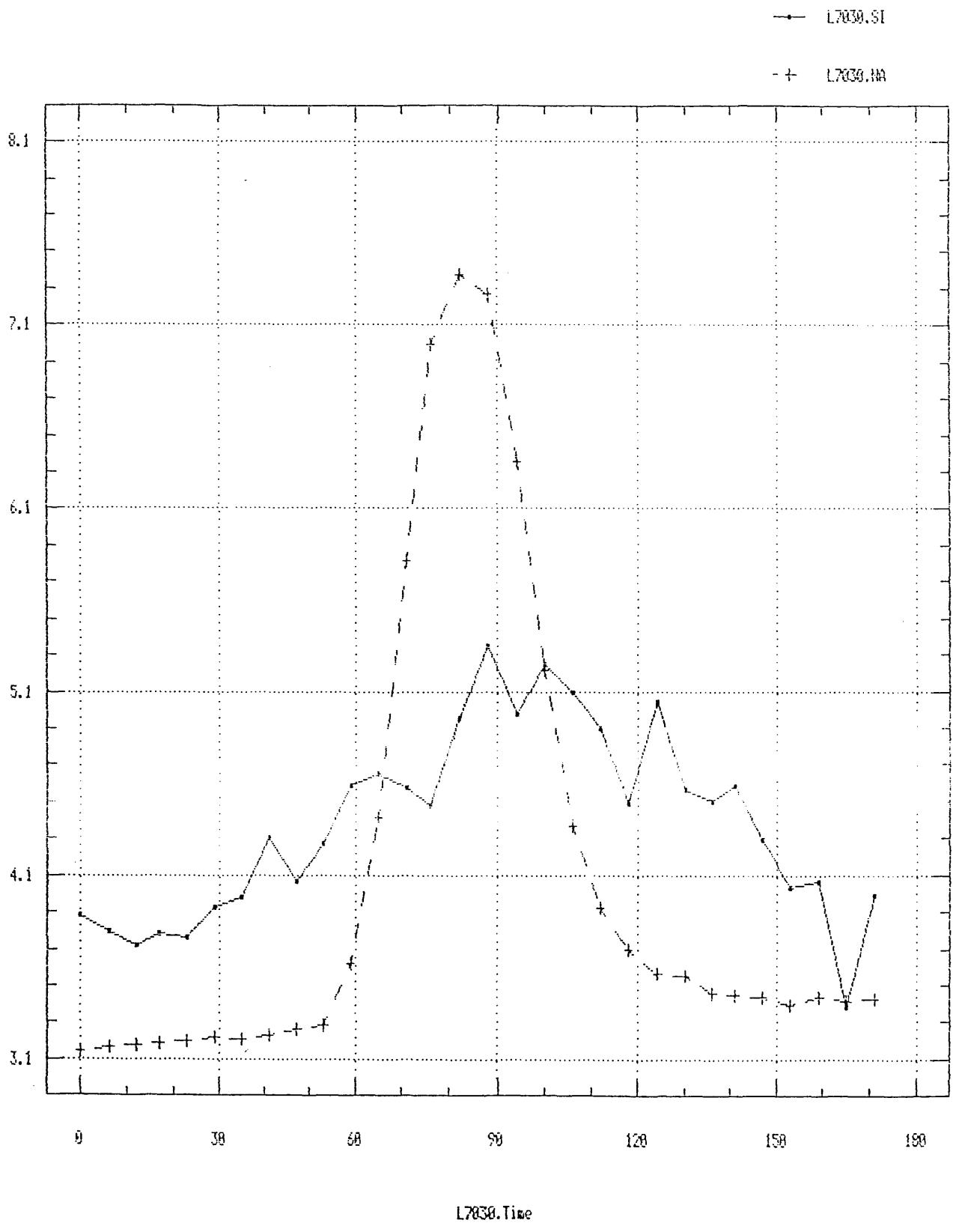
For specific ion electrode measurements of Cl^-, 4g of sample is ground in 6ml DDIW. After centrifuging, each solution is split; with only one of the splits acidified for ICP analysis, the other split used for Cl^- ion analysis. This permits an attempt at charge balancing the solution with respect to chloride. The calibration curve for the specific ion electrode determined during this study is shown in Figure V.4.

For the modified CL-ICP, 2,000ppm $La(NO_3)_3$ solution was substituted for DDIW during the crushing operation. This solution was prepared from Analar grade material and proved to contain < 0.5ppm combined Ca, Na, K. Since the leachates generally ran 8 to 20 ppm combined Ca, Na, K, the La-solution gave no contamination problems. The La-solution was also blank tested with the Cl^- ion electrode. A linear shift in the calibration curve showed the presence of trace Cl^-, but all results were corrected for this shift by a simple subtraction of the mV shift.

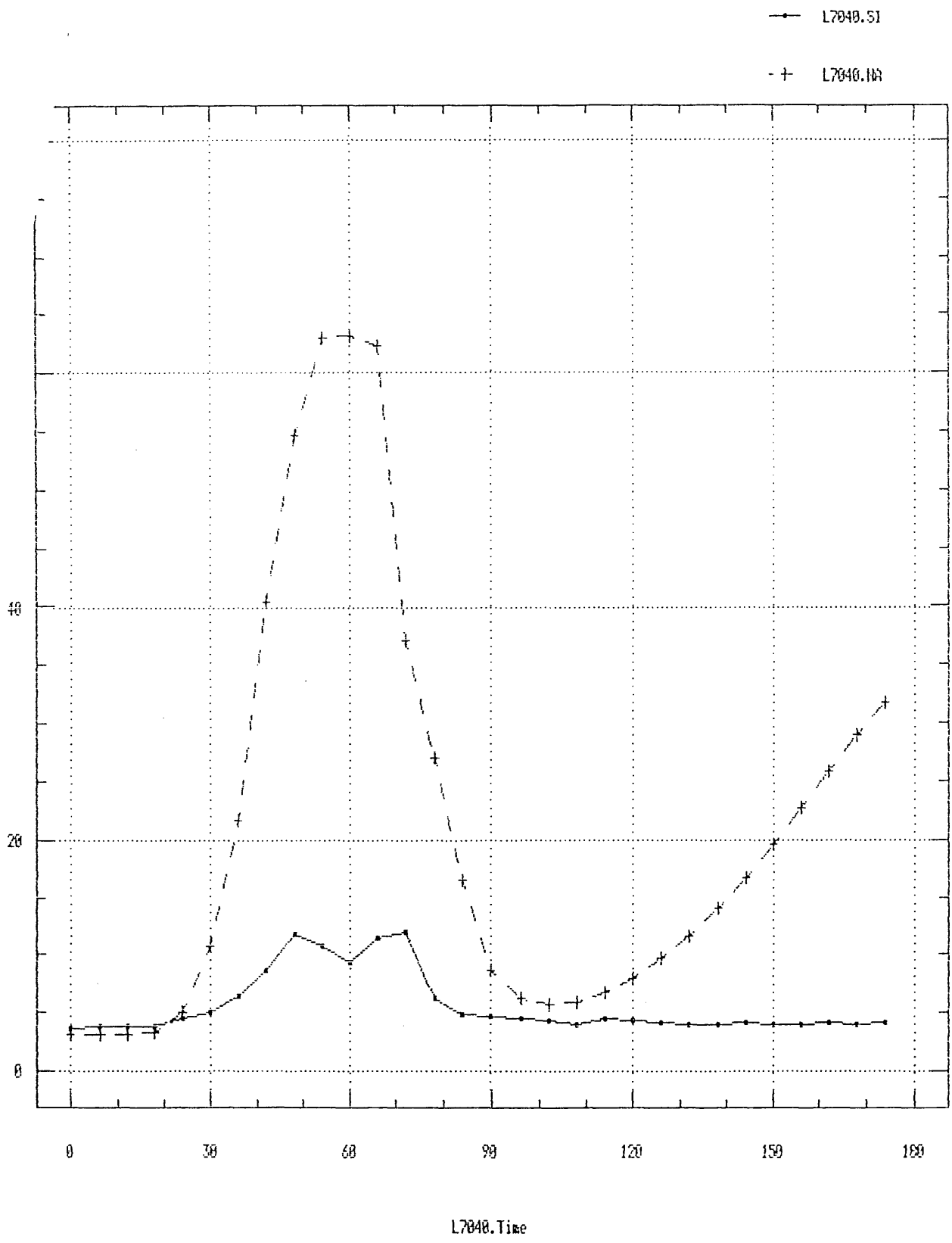
Typical profile - Type 1 quartz (sample PMQ1)



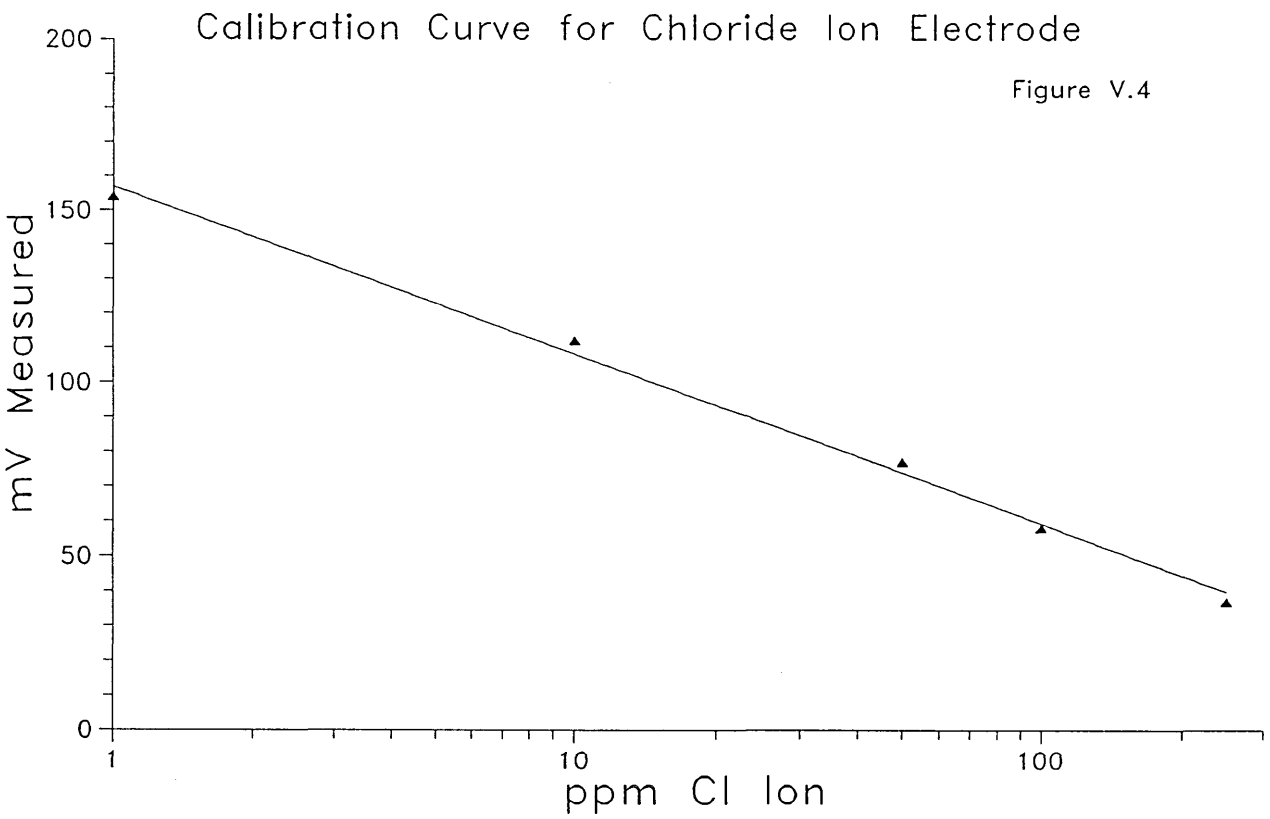
Typical profile - Type 2 quartz (sample A10-21b)



Typical profile - Type 4 quartz (sample 26-14)



Chloride ion electrode calibration curve



Detection Limits for DICP Analyses Calculated from Machine Blanks			
Element	Average	Standard Deviation	Detection Limit
Se	14.10	0.254	0.42774
Zn	9.79	0.208	0.03702
Sr	6.47	0.122	0.00390
Sb	30.95	0.408	0.28285
Pb	242.38	2.400	0.37376
Bi	59.80	0.711	0.36099
Cd	63.09	0.821	0.03220
Ba	16.46	0.301	0.00987
Ni	78.49	0.722	0.10048
B	33.61	0.489	0.04958
Mn	3.61	0.025	0.01359
Fe	4.17	0.086	0.06462
P	14.60	0.591	0.42200
S	52.17	55.362	34.69382
Mg	24.45	0.459	0.47126
Mo	336.17	7.691	0.17414
Sn	47.65	0.665	0.08486
Si	53.97	1.858	0.21881
As	32.43	0.324	0.15840
Na	39.42	1.258	0.44004
Al	31.63	0.721	0.75121
V	50.97	1.011	0.04975
Be	60.57	1.833	0.00683
Ca	4.34	0.052	0.09345
Te	95.27	0.769	0.26111
Cu	37.00	0.813	0.05167
Ag	227.88	4.729	0.05727
Li	14.98	0.228	0.02547
Ti	17.43	0.383	0.04950
Co	58.95	0.937	0.03998
Zr	181.11	3.620	0.05801
W	14.20	0.247	0.28972
K	147.27	1.813	0.15349
Rb	146.63	2.143	1.71355
La	59.62	1.217	0.10165
Cr	48.79	0.832	0.04316
Hg	43.63	0.941	0.05861
Au	58.58	1.070	0.05847
Pt	60.70	0.299	0.19726
Pd	43.80	0.897	0.45646

Highlighted elements consistently above detection limit in this study

Detection Limits for Crush-Leach ICP Analyses Calculated from Machine Blanks			
Element	Average	Standard Deviation	Detection Limit
Se	13.29	0.224	0.48834
Zn	9.29	0.248	0.05726
Sr	6.68	0.149	0.00544
Sb	30.58	0.403	0.35376
Pb	233.06	3.317	0.62837
Bi	56.65	0.850	0.52496
Cd	59.70	0.767	0.03792
Ba	17.08	0.496	0.00987
Ni	75.05	0.818	0.13492
B	34.19	0.502	0.05973
Mn	3.52	0.026	0.01745
Fe	4.13	0.074	0.06492
P	15.29	1.677	1.56072
S	33.11	8.810	6.85904
Mg	24.67	0.593	0.72607
Mo	358.06	10.326	0.27568
Sn	45.09	0.615	0.10335
Si	57.71	3.507	0.47738
As	30.62	0.919	0.59730
Na	44.66	1.952	0.79988
Al	31.50	0.854	1.05254
V	53.27	1.559	0.08900
Be	70.65	2.495	0.01139
Ca	4.36	0.088	0.18208
Te	83.11	1.243	0.54254
Cu	38.02	1.176	0.08751
Ag	238.09	7.127	0.10070
Li	15.96	0.420	0.01503
Ti	18.01	0.461	0.07086
Co	57.85	1.178	0.06261
Zr	186.30	5.305	0.09959
W	13.38	0.339	0.46388
K	155.34	3.336	1.93527
Rb	156.34	3.740	3.66639
La	61.91	1.941	0.19736
Cr	51.28	1.114	0.06622
Hg	41.36	1.762	0.14881
Au	58.67	1.488	0.09028
Pt	56.60	0.436	0.32851
Pd	45.61	1.443	0.77720

Highlighted elements consistently above detection limit in this study

Fluid Inclusions - Decrepitation ICP Analysis Results - Page 1 of 2 (Results in equivalent ppm)

Sample	Type	Li	Zn	Sr	Ba	B	Fe	Na	Ca	Cu	K
PMQ-1	1	0.041	0.018	0.120	0.020	0.190	0.010	9.310	5.262	bdl	1.490
30-3	2	0.030	0.030	0.040	0.010	0.040	0.330	7.770	2.610	0.630	0.831
26-3	2	0.398	0.236	0.866	0.383	0.387	1.377	60.290	35.743	1.581	7.965
30-3	2	bdl	bdl	bdl	bdl	0.040	0.145	bdl	bdl	0.219	bdl
26-3	2	0.502	0.183	bdl	0.113	0.588	1.088	73.704	5.640	0.972	7.598
20-12	2	bdl	bdl	0.004	bdl	bdl	0.020	bdl	bdl	bdl	bdl
26-11	2	0.097	bdl	0.656	0.088	0.134	0.071	33.484	9.364	0.079	3.434
10-32a	2	bdl	bdl	0.004	bdl	0.080	bdl	2.316	0.129	bdl	bdl
10-32a	2	0.047	bdl	0.021	bdl	0.045	bdl	10.070	bdl	bdl	0.806
A10-20b	2	0.023	bdl	0.006	bdl	0.061	bdl	2.724	0.089	bdl	0.333
A10-21b	2	0.089	bdl	0.056	0.016	0.095	bdl	13.922	0.323	bdl	4.873
600/6b	2	bdl	bdl	bdl	bdl	bdl	bdl	1.020	bdl	bdl	bdl
A10-20d	2	0.026	bdl	0.009	bdl	0.050	0.081	4.735	0.129	bdl	0.708
A10-21d	2	0.124	0.041	0.078	0.022	0.112	bdl	19.143	0.418	bdl	1.448
A10-21d	2	0.067	bdl	0.032	bdl	0.051	bdl	9.000	0.228	bdl	0.615
600/6c	2	0.048	bdl	0.009	bdl	0.220	bdl	5.061	0.091	bdl	0.341
GV1	2	0.023	bdl	0.014	0.009	0.219	bdl	7.967	0.626	bdl	0.800
A10-20d	2	0.025	bdl	0.010	bdl	0.173	bdl	3.862	0.178	bdl	0.153
600/7b	2	0.020	bdl	0.004	bdl	0.167	bdl	2.766	bdl	bdl	bdl
26-11	2	0.087	bdl	0.441	0.060	0.285	bdl	25.582	5.730	bdl	2.428
BAS1	2	0.027	bdl	0.048	0.015	0.074	bdl	12.342	0.633	bdl	1.059
600/7b	2	0.023	bdl	0.005	bdl	0.091	bdl	3.150	bdl	bdl	0.190
20-12	2	0.043	bdl	0.003	bdl	0.060	bdl	0.544	2.004	bdl	0.161
600/6e	2	bdl	bdl	0.006	bdl	bdl	bdl	1.637	0.097	bdl	bdl

Fluid Inclusions - Decrepitation ICP Analysis Results - Page 2 of 2 (Results in equivalent ppm)

Sample	Type	Li	Zn	Sr	Ba	B	Fe	Na	Ca	Cu	K
600/6f	2	bdl	bdl	bdl	bdl	bdl	bdl	4.463	0.174	bdl	0.223
600/6b	2	bdl	bdl	bdl	bdl	bdl	bdl	1.940	bdl	bdl	bdl
30-3	2	0.060	0.060	0.061	0.020	0.140	0.420	11.960	3.620	0.120	1.960
400-24	3	bdl	0.052	0.141	0.019	0.037	bdl	8.620	1.431	bdl	0.325
400-24	3	0.022	0.061	0.177	0.025	0.033	bdl	14.208	1.803	bdl	0.576
26-14	4	2.060	0.970	4.440	1.050	0.640	3.350	345.790	65.130	0.810	38.033
26-14	4	1.920	1.020	4.160	0.970	0.590	3.630	318.400	63.870	0.330	34.872
30-7	4	0.767	bdl	1.107	0.364	0.471	0.716	114.176	14.835	1.068	13.005
26-2	4	0.393	bdl	0.309	0.069	0.265	0.395	51.950	3.951	0.302	6.329
20-13b	4	1.042	0.498	2.521	0.593	0.400	1.148	190.608	34.184	0.994	21.336
26-14	4	0.517	0.160	1.170	0.289	0.171	0.358	88.464	13.898	bdl	10.067
26-14	4	0.522	0.168	1.173	0.291	0.195	0.374	86.690	14.249	0.063	10.170
30-7	4	0.490	bdl	0.572	0.183	0.220	0.041	74.010	6.174	bdl	7.504
26-2	4	1.196	bdl	0.840	0.186	0.233	0.305	171.954	10.491	bdl	19.241
26-2	4	1.043	bdl	0.763	0.168	0.227	0.114	153.090	9.488	bdl	16.749
TQ-3	5	1.098	1.295	0.117	0.049	0.840	0.227	34.988	1.156	3.147	4.644
TQ-2	5	0.162	0.301	0.010	bdl	0.157	0.285	4.916	0.180	0.890	1.287
TQ-2	5	0.215	0.354	0.013	bdl	0.172	0.262	6.801	0.223	0.986	1.549
TQ-3	5	0.783	0.750	0.086	0.032	0.266	0.178	25.686	0.890	2.064	2.825
TQ-3	5	1.207	bdl	0.134	0.044	0.196	bdl	37.35	1.171	bdl	3.920
TQ-3	5	0.418	bdl	0.022	0.010	0.359	bdl	12.90	0.242	bdl	1.441
LH7	6	bdl	bdl	0.070	0.019	0.134	bdl	2.570	4.593	bdl	0.050
LH7	6	bdl	bdl	0.034	0.011	0.066	bdl	1.206	2.236	bdl	0.147

Fluid Inclusions - De-ionised Water Crush-Leach ICP Analysis Results - Page 1 of 1 (Results in equiv. ppm)

Sample	Type	Li	Zn	Sr	Ba	B	Fe	Na	Ca	Cu	K
PMQ-1	1	0.056	0.025	0.224	0.040	0.295	0.120	12.690	10.530	bdl	1.900
20-4	2	0.010	0.035	0.088	0.046	0.018	0.340	4.830	10.080	bdl	1.900
26-3	2	0.158	0.170	0.634	0.245	0.278	0.060	30.140	25.540	bdl	3.350
26-5	2	bdl	bdl	0.039	0.006	0.018	0.160	1.180	17.190	bdl	2.350
30-6	2	bdl	bdl	0.028	0.009	0.056	bdl	1.230	2.370	bdl	0.500
20-13	2	0.124	0.140	0.360	0.745	0.160	bdl	18.780	12.150	bdl	2.000
26-13	2	bdl	bdl	0.052	0.007	0.048	0.140	1.520	6.270	bdl	0.550
A10-21b	2	0.027	bdl	0.013	0.002	0.129	0.085	3.423	0.131	bdl	0.940
26-2	4	0.082	0.010	0.110	0.220	0.153	bdl	10.500	4.410	bdl	1.250
26-2	4	0.094	bdl	0.142	0.275	0.188	bdl	12.310	5.520	bdl	1.600
30-7	4	0.112	0.020	0.250	0.865	0.330	bdl	18.130	7.530	bdl	1.700
30-7	4	0.112	0.050	0.250	0.665	0.305	bdl	16.250	7.860	0.023	1.850
26-14	4	0.056	0.040	0.229	0.046	0.285	bdl	12.460	12.780	0.015	1.800
26-2	4	0.088	0.010	0.118	0.230	0.175	bdl	11.430	5.130	bdl	1.450
26-14	4	0.042	0.045	0.203	0.040	0.265	0.140	11.070	9.390	bdl	1.500
26-14	4	0.040	0.015	0.191	0.375	0.238	bdl	10.060	9.450	bdl	1.300
30-7	4	0.030	bdl	0.062	0.017	0.088	0.103	4.328	1.506	0.005	0.719
26-2	4	0.074	bdl	0.077	0.007	0.140	0.050	10.158	2.845	0.011	3.236
26-14	4	0.099	bdl	0.304	0.060	0.154	bdl	16.459	6.710	0.010	2.330
26-2	4	0.070	bdl	0.109	0.019	0.130	0.104	9.307	5.452	0.020	2.963

Fluid Inclusions - Lanthanum Solution Crush-Leach ICP Analysis Results - Page 1 of 1 (Results in equiv. ppm)

Sample	Type	Li	Zn	Sr	Ba	B	Fe	Na	Ca	Cu	K
A10-21b	2	0.016	bdl	0.038	0.014	0.145	0.662	3.627	2.975	bdl	1.797
A10-21b	2	0.012	bdl	0.055	0.016	0.157	0.630	3.771	3.353	bdl	1.775
26-14	4	0.072	bdl	0.298	0.061	0.134	0.252	14.028	12.817	bdl	2.002
26-14	4	0.068	bdl	0.301	0.054	0.171	0.201	12.017	11.257	bdl	1.951
26-2	4	0.066	bdl	0.154	0.048	0.167	0.507	11.237	12.415	bdl	3.816
30-7	4	0.061	bdl	0.148	0.061	0.224	0.113	9.564	6.854	bdl	1.210
30-7	4	0.057	bdl	0.169	0.043	0.236	bdl	10.085	7.245	bdl	1.169
26-2	4	0.084	bdl	0.196	0.061	0.256	0.485	14.427	15.624	bdl	4.753

APPENDIX VI

OXYGEN ISOTOPE DETERMINATIONS FROM QUARTZ

Samples of quartz were separated to levels of purity in excess of 95% under a binocular microscope by hand-picking. Quartz was chosen for analysis from samples where fluid inclusion wafers were available and dominantly primary fluid inclusions were present. All samples were then subjected to washing in Analar grade, concentrated HCl to remove any carbonate present as included grains in the quartz. This procedure is identical to that performed on the samples for bulk volatile analysis.

Extraction of lattice oxygen from the silicates was undertaken on the fluorination line at the NERC Isotope Geology Centre using a method based on that described by Clayton & Mayeda (1963). Accurately weighed samples between 6 and 12 mg (+/- 0.001 mg) were placed in aluminium foil containers and loaded into pressure vessels on the fluorination line under a stream of nitrogen (Figure VI.1). Analyses were performed in duplicate or triplicate, amount of sample permitting. Samples were reacted with BrF_5 for around 16 hours (i.e. overnight) at between 250 and 450 °C, and the oxygen released was cleaned using a series of liquid N_2 traps. Conversion to CO_2 was accomplished by passing the oxygen over a carbon rod exposed to an intense heat source. The CO_2 was then collected in a series of vessels after the volume had been measured using a calibrated manometer. Volume data was then converted to the reaction yield which is an estimate of the completeness of reaction, assuming a pure sample and complete reaction had occurred with no loss of products.

All determinations of $^{18}O/^{16}O$ ratios were performed on a VG MicroMass 903 mass spectrometer except for small samples which were analysed using a VG SIRA 10. Calibration was performed using a laboratory carbonate standard. Reproducability of determined $\delta^{18}O$ is excellent, the two standard reference quartz (LAGS) run in the early and late runs showed a difference of only 0.03 ‰. Throughout the programme reference gases were run twice daily on the mass-spectrometer to correct any potential beam drift. The overall analytical reproducability for $\delta^{18}O$ was better than ± 0.1 ‰. All sample results have error bars for replicate analyses plotted.

NOTES ON SULPHUR AND CARBON ANALYSES:

SULPHUR ISOTOPIC DETERMINATION FROM PYRITE

For the $\delta^{34}S$ determinations, analytical reproducibility is ± 0.1 ‰, replicate analyses are shown as error bars in the text figures.

CARBON ISOTOPIC DETERMINATION FROM CALCITE

For the carbonate analyses, $\delta^{13}C$ reproducability is better than ± 0.05 ‰, the two duplicate analyses showing differences of 0.003 and 0.017 ‰ only.

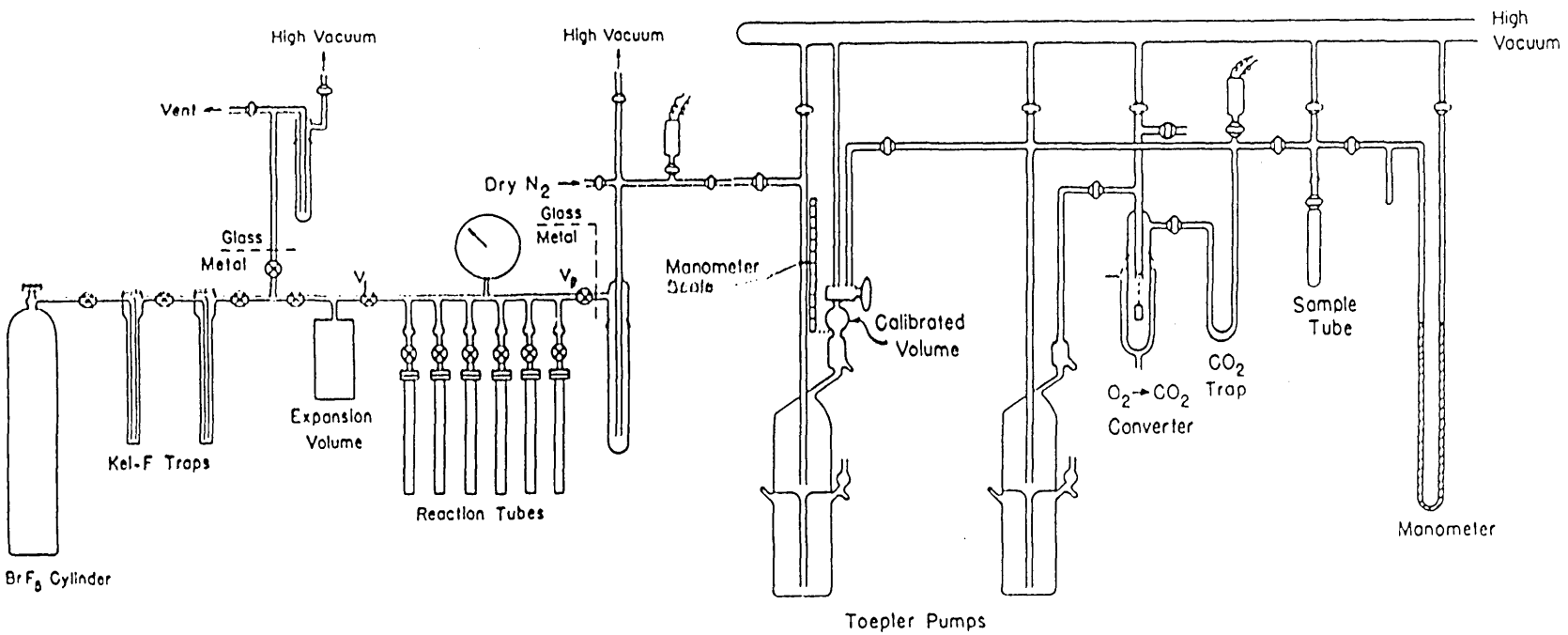
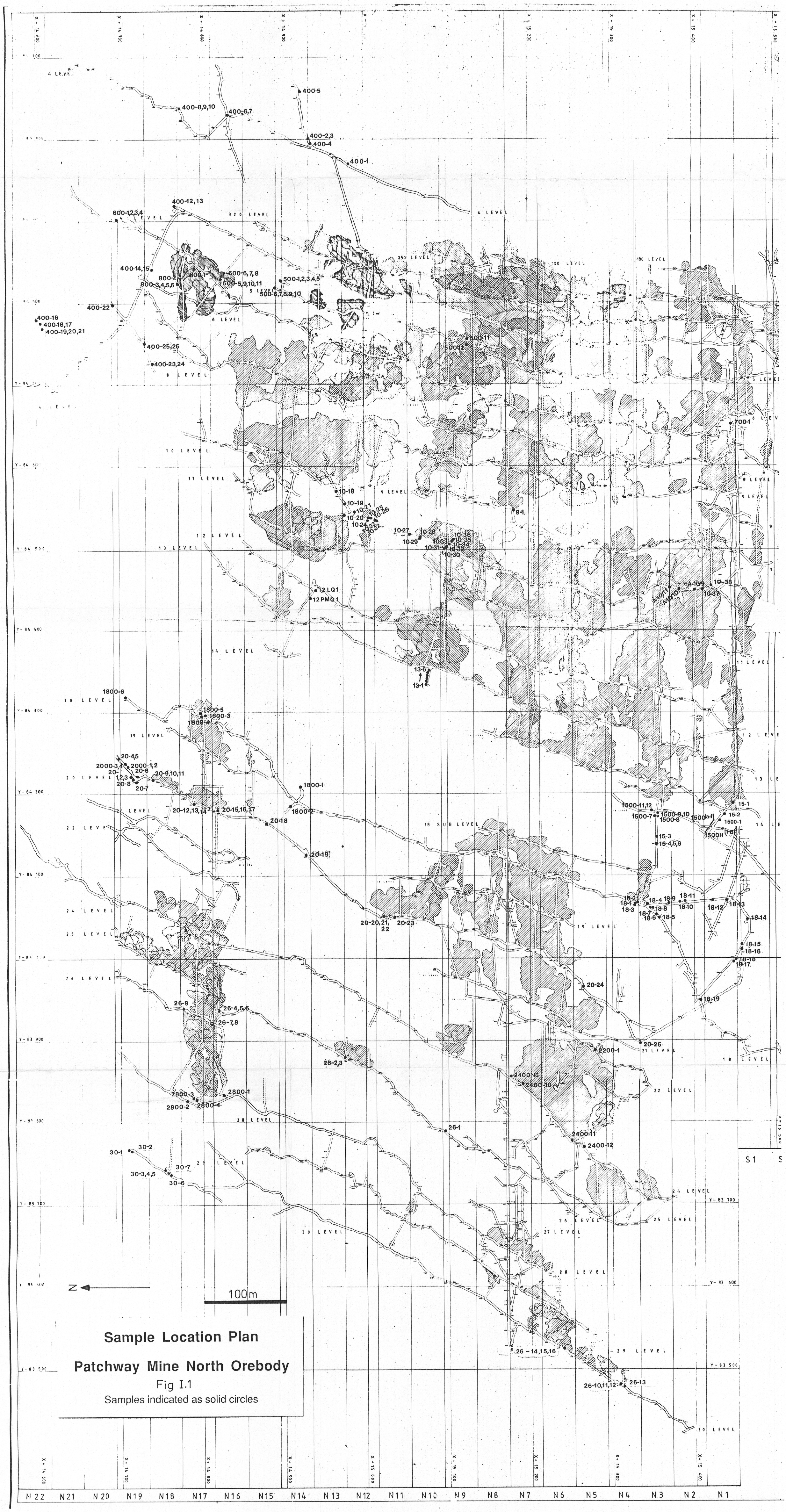
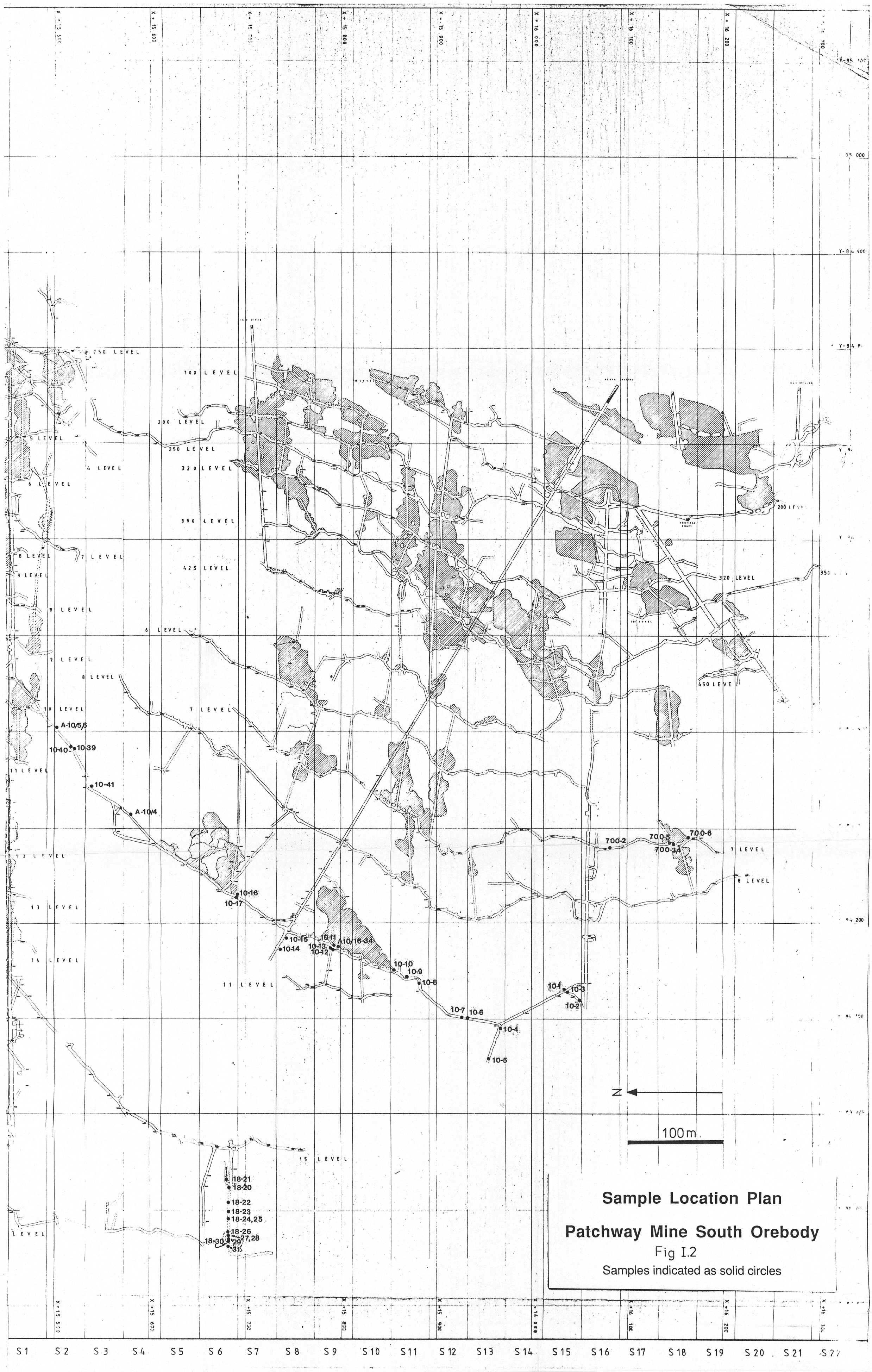

High Vacuum
High Vacuum
High Vacuum
Vent
Dry N_2
Glass
Metal
Glass
Metal
V_1
V_2
Manometer
Scale
Calibrated
Volume
Sample
Tube
CO_2
Trap
$O_2 \rightarrow CO_2$
Converter
Expansion
Volume
Kel-F Traps
Reaction Tubes
Manometer
BrF_5 Cylinder
Toepler Pumps

Fig VI.1


400-5
400-8,9,10
400-6,7
400-2,3
400-4
400-1
400-12,13
600-1,2,3,4
400-14,15
800-2
800-3,4,5,6
800-1
600-6,7,8
600-5,9,10,11
500-1,2,3,4,5
500-6,7,8,9,10
400-22
400-16
400-18,17
400-19,20,21
400-25,26
400-23,24
500-11
500-12
700-1
10-18
10-19
10-20
10-24
10-27
10-28
10-29
10-36
10-35
10-34
10-33
10-32
10-30
9-1
12 LQ1
12PMQ1
A-10W
10-38
10-37
13-6
13-1
1800-6
1800-5
1800-3
1800
20-4,5
2000-3,4
2000-1,2
20-6
20-
1,2,3
20-8
20-7
20-9,10,11
1800-1
1800-2
20-12,13,14
20-15,16,17
20-18
20-19
1500-11,12
1500-7
1500-9,10
1500-8
1500H-I
1500H-II
15-1
15-2
1500-1
15-3
15-4,5,6
18-1
18-2
18-3
18-4
18-9
18-11
18-10
18-12
18-13
18-7
18-8
18-6
18-5
18-14
18-15
18-16
18-17
18-18
20-20,21,22
20-23
20-24
18-19
20-25
2200-1
26-9
26-4,5,6
26-7,8
26-2,3
2400-13
2400-10
2800-3
2800-1
2800-2
2800-4
26-1
2400-11
2400-12
30-1
30-2
30-3,4,5
30-7
30-6
26-14,15,16
26-10,11,12
26-13
S1
N
100m
Sample Location Plan
Patchway Mine North Orebody
Fig I.1
Samples indicated as solid circles
N 22
N21
N 20
N19
N18
N17
N16
N15
N14
N13
N12
N11
N10
N9
N8
N7
N6
N5
N4
N3
N2
N1



Sample Location Plan

Patchway Mine South Orebody

Fig I.2

Samples indicated as solid circles